

FINAL SUMMARY REPORT

STUDY OF A SOFT LANDER/SUPPORT MODULE FOR MARS MISSIONS

VOLUME III - APPENDIXES

By Michael K. Mann, Billie W. Preston, and Parker S. Stafford

Distribution of this report is provided in the interest of information exchange. Responsibility for the contents resides in the author or organization that prepared it.

Prepared under Contract No. NAS1-7976 by
MARTIN MARIETTA CORPORATION
Denver, Colorado

for

NATIONAL AERONAUTICS AND SPACE ADMINISTRATION

APPENDIX A

FOREWORD

This Final Summary Report for the Soft Lander/Support Module study, a supplement to the "Study of Direct Versus Orbital Entry for Mars Missions" (NASA Contract NAS1-7976), is provided in accordance with Part III A.6 of the contract schedule as amended. This Final Summary Report is in three volumes as follows:

NASA CR-66728-1 Volume I, Summary;

NASA CR-66728-2 Volume II, Subsystem Studies;

NASA CR-66728-3 Volume III, Appendixes.

CONTENTS

	<u>Page</u>
FOREWORD	ii
CONTENTS	iii
	thru
	vii
APPENDIX A -- LM RADAR EVALUATION AND VERNIER	
PHASE SIMULATION	1
1. Definition and Scope	1
2. Summary of Results and Conclusions	4
3. Vernier Phase Control	13
4. Radar Description and Mathematical Models	32
5. Analytical Study Results	53
6. Six Degree of Freedom Simulation Results	91
7. References	102
APPENDIX B -- SIMULATION RUN SUMMARY	
TABLES AND PLOTS	105
	thru
	284
<u>Figure</u>	
A1 Radar Range Error vs Velocity for	
Velocity Beam Dropouts	10
A2 Gravity-Turn Thrust Orientation	13
A3 Typical Terminal Descent Profile and	
Propellant Utilization	17
A4 Vernier Engine Arrangement	19
A5 Guidance and Control System Block	
Diagram	21
A6 Engine-Valve Dynamics	23
A7 Attitude Control Inner Loop Root Locus	26
A8 Attitude Control Outer Loop Root Locus	27
A9 Axial Channel Root Locus, Nominal Case	28
A10 LM Radar Simulation Block Diagram	33
A11 Definition of Beam Pointing Angles with	
Respect to Vehicle Body Coordinates	35
A12 Reflectivity Models	39
A13 Spectrum Overlap due to Tracking	
High Rates	40
A14 Idealized Spectrums	41
A15 Velocity Receiver Sensitivity,	
Wideband Mode	43
A16 Velocity Receiver Sensitivity,	
Narrowband Mode	44
A17 Range Channel Acquisition Sensitivity	45

A18	Velocity Receiver Sensitivity, Wideband Mode (Modified SLPF Bandwidth of 600 Hz) . . .	46
A19	Velocity Beam Zero Doppler Dropout Velocity vs Altitude for Fixed Incidence Angle	54
A20	Critical Incidence Angle for Velocity Channel, LM Radar	55
A21	Critical Incidence Angle for the LM Radar Range Channel	56
A22	Critical Incidence Angle for Velocity Channel, Modified LM Radar	57
A23	Pitchup Model	58
A24	Tracking Rate Analysis Block Diagram	60
A25	Vehicle Attitude as a Function of Wind Gust and the Resulting Lag in the Velocity Tracker	61
A26	Range Tracker Lag during Tipup	62
A27	Parachute Phase Beam Incidence Angle Geometry	69
A28	Wind Gust Attitude Response, Maximum Continuous Headwind plus Gust, Mars Minimum Atmosphere	70
A29	Wind Gust Attitude Response, Maximum Continuous Headwind plus Gust, Mars Maximum Atmosphere	71
A30	Parachute Phase, LM Radar, H = 6000 ft, $V_{WIND} = \pm 242$ fps (3σ)	74
A31	Parachute Phase, LM Radar, H = 6000 ft, $V_{WIND} = \pm 165$ fps (3σ)	75
A32	Parachute Phase, LM Radar, H = 6000 ft, $V_{WIND} = \pm 242$ fps (3σ)	76
A33	Parachute Phase, LM Radar, H = 6000 ft, $V_{WIND} = \pm 165$ fps (3σ)	77
A34	Parachute Phase, Modified LM, H = 6000 ft, $V_{WIND} = \pm 242$ fps (3σ)	79
A35	Parachute Phase, Modified LM, H = 6000 ft, $V_{WIND} = \pm 242$ fps (3σ)	80
A36	Parachute Phase Mean and Standard Deviations of Radar Range and Velocity Beam Incidence Angles	82
A37	Tipup Phase Beam Incidence Angle Geometry	83

A38	Tipup Phase, LM Radar, H = 4000 ft, V _{WIND} = ± 242 fps (3 σ)	84
A39	Tipup Phase, LM Radar, H = 4000 ft, V _{WIND} = ± 165 fps (3 σ)	85
A40	Tipup Phase, LM Radar, H = 4000 ft, V _{WIND} = ± 242 fps (3 σ)	86
A41	Tipup Phase, LM Radar, H = 4000 ft, V _{WIND} = ± 165 fps (3 σ)	87
A42	Range Equation Incidence Angle Dependent Coefficient	90
A43	Terminal Descent Phase Simulation	93
A44	Simulation Processing Order for a Single Iteration	94
A45	Range Errors with Velocity Beams Out	97
A46	Range Errors with Velocity Beams Out	98
B1	} Soft Lander, Runs 1-1 thru 1-14	106
thru		{ thru
B14	} Soft Lander, Runs 2-1 thru 2-14	120
B15		{ thru
thru	} Soft Lander, Runs 3-1 thru 3-14	121
B28		{ thru
B29	} Soft Lander, Runs 4-1 thru 4-14	134
thru		{ thru
B42	} Soft Lander, Runs 5-1 thru 5-14	136
B43		{ thru
thru	} Soft Lander, Runs 6-1 thru 6-14	149
B56		{ thru
B57	} Soft Lander, Runs 7-1 thru 7-14	151
thru		{ thru
B70	} Soft Lander, Runs 8-1 thru 8-14	164
B71		{ thru
thru	} Soft Lander, Runs 9-1 thru 9-14	166
B84		{ thru
B85	} Soft Lander, Runs 10-1 thru 10-14	179
thru		{ thru
B98	} Soft Lander, Runs 11-1 thru 11-14	181
B99		{ thru
thru	} Soft Lander, Runs 12-1 thru 12-14	194
B112		{ thru
B113	} Soft Lander, Runs 13-1 thru 13-14	196
thru		{ thru
B126	} Soft Lander, Runs 14-1 thru 14-14	209
B127		{ thru
thru	} Soft Lander, Runs 15-1 thru 15-14	211
B140		{ thru

B141 } thru } B154 } B155 } thru } B160 } B161 } thru } B166 }	Soft Lander, Runs 11-1 thru 11-14	{ 256 thru { 269 { 272 thru { 277 { 279 thru { 284
	Soft Lander, Runs 13-1 thru 13-6	
	Soft Lander, Runs 14-1 thru 14-6	

Table

A1	Compatibility of LM Radar Materials to Planetary Mission	7
A2	Parts Sterilization Impact, Ryan LM Radar Package	7
A3	Parameters Used in Simulation Representing the LM Radar	40
A4	Mode Switching Criteria	47
A5	Functions Triggered as a Result of Threshold Criteria	49
A6	LM Radar Existing Search Rates and Limits	50
A7	Search Limits and Rates Proposed for the Modified LM Radar	50
A8	Noise Effect on System Variables	64
A9	Constants Used for Noise Analysis	64
A10	3 σ Velocity and Range Channel Error as Determined by Ryan during Various Phases of the Mission	65
A11	Radar Noise Comparison (1 σ) after 200-msec Smoothing Time (Velocity in fps)	66
A12	Impact Conditions	67
A13	Cross Coupling Isolation, Unit P42	88
A14	Simulation Run Summary	96
B1	Run 1, Autonomous Capsule/LM Radar/ Range Velocity/0 Slope	105
B2	Run 2, Autonomous/LM Radar/ Range Velocity/-19° Slope	120
B3	Run 3, Autonomous/LM Radar/ Range Velocity/-27° Slope	135
B4	Run 4, Autonomous/LM Radar/ Range Velocity/-33° Downslope	150
B5	Run 5, Autonomous/LM Radar/ Range Velocity/0 Slope/0 Doppler	165
B6	Run 6, Autonomous/Modified LM/ Range Velocity/-27° Slope	180

B7	Run 7, Autonomous/Modified LM/ Range Velocity Contour/27° Upslope	195
B8	Run 8, Autonomous/Modified LM/ Range Velocity/0 Slope/0 Doppler	210
B9	Run 9, Autonomous/Modified LM/ Altitude Velocity/0	225
B10	Run 10, Autonomous/Modified LM/ Altitude Velocity/27° Upslope	240
B11	Run 11, Autonomous/Modified LM/ Altitude Velocity/0 Slope	255
B12	Run 12, Configuration 1B/LM Radar/ Range Velocity/26.7° Downslope	270
B13	Run 13, Configuration 1B/LM Radar/ Range Velocity/26.7° Downslope	271
B14	Run 14, Configuration 1B/Modified LM/ Range Velocity/26.7° Downslope	278

APPENDIX A

LM RADAR EVALUATION AND VERNIER PHASE SIMULATION

APPENDIX A

1. DEFINITION AND SCOPE

This appendix documents the results of a detailed study of the applicability of the LM radar to the Mars soft lander mission. It was conducted through the use of small digital programs in conjunction with an extensive six degree of freedom simulation of the vernier descent and landing phase. The appendix contains a summary of the results with recommended radar changes and guidance and control system changes. Next, a discussion of the vernier descent guidance laws and control system stability is given. Following that, a description of the radar mathematical models used in this study is presented. Two detailed sections are then presented documenting the various analytical results and most of the six degree of freedom simulation runs. The authors are deeply indebted to personnel of Ryan Aeronautical Co., builders of the LM radar, for their help and criticism of the results, particularly to R. Harrington.

Mission Description

The portions of the Mars soft lander mission where the LM radar would be used are the parachute phase and the vernier descent phase. The parachute phase is preceeded by an entry through the Martian atmosphere where the lander is enclosed in a blunt cone aeroshell. At parachute deployment, this aeroshell falls away and the radar is turned on. During the parachute descent, in the absence of wind gusts, the parachute vehicle follows a gravity-turn trajectory, approaching vertical as the altitude decreases. The presence of wind gusts cause attitude excursions from the gravity-turn trajectory, which can cause the radar to break lock on one or more beams because of poor incidence angles, tracking rate, or very low doppler frequency received by the beams.

At a predefined altitude, typically 4000 ft above the terrain, the vernier engines of the lander are ignited and the parachute is released. The lander then orients the thrust vector along the velocity vector and follows a gravity-turn descent, modulating the total thrust to follow a preplanned contour of range (or altitude) vs velocity. Sensing the ignition altitude accurately is quite important to a safe landing, because if the altitude measurement is too low, the lander will not have enough altitude (or time) to remove the velocity remaining at the end of the parachute phase. If the measurement is high, the lander may run out of propellant before reaching the surface.

APPENDIX A

During the attitude maneuver to align the thrust to the velocity vector (hereafter called the tipup maneuver) the radar beams may lose lock due to tracking rate or incidence angle.

Problems Studied

An attempt was made to study the most serious problems in the application of the LM radar to the mission described above and devise radar changes or backup modes using other equipment that would allow adequate performance.

The first area concentrated on was the various situations that could cause beam unlocks, as discussed above. On the parachute, use was made of previous parachute dynamics studies (ref. A1) plus more recent work (ref. A2) to define the effects of wind gusts. The ability of the radar to track the changing signal caused by worst-case gusts was studied. Also, a Monte Carlo probability program was constructed to define the probabilities associated with single and double beam unlocks in the radar velocity beams, as well as the range beam. Similar studies were conducted for the tipup maneuver phase. These results are presented in section 5 of this appendix.

Secondly, a careful assessment of the random fluctuation noise from the radar was made. The effect of this noise on control **variables** was calculated analytically. Furthermore, the noise was modeled and injected into most of the six degree simulation runs. In addition, expected bias and random errors were calculated by Ryan (ref. A3) using trajectory data from a typical six degree of freedom run. These data are summarized in section 5.

Finally, the six degree of freedom simulation program was augmented by a detailed functional mathematical model of the LM radar as defined in sections 4 and 6. This program was used to evaluate the radar and control system performance. Two capsule configurations were used:

- 1) Configuration 1B from the Mars Mission Mode Study, three engines, out of orbit mode;
- 2) Autonomous capsule, from the recent follow-on study, four Kidde engines, direct mode.

APPENDIX A

The six degree of freedom runs verified the beam dropout logic, noise analysis, and control system studies. Various control modes for radar backup were analyzed and simulated. Recommended radar changes were also validated by these runs.

APPENDIX A

2. SUMMARY OF RESULTS AND CONCLUSIONS

The guidance and control system recommended for the autonomous capsule (excluding stellar sensors) and for any other soft lander configuration using the LM radar is as follows:

- 1) Inertial measurement unit (IMU) - 3 gyros, 3 accelerometers;
- 2) Guidance and control computer (GCC) - General-purpose digital computer, 4000 to 8000 words memory;
- 3) High-altitude altimeter - Aeroshell phase operation;
- 4) Low-altitude altimeter - Parachute and vernier phase operation;
- 5) Modified LM radar - 3 velocity beams, 1 range beam in center of pattern along thrust axis.

The recommended guidance modes, trajectory constraints, and radar changes are discussed below.

LM Radar Changes

The present LM radar configuration is described in considerable detail later in this appendix and in other available literature (ref. A3). Simply, it is a cw velocity, linear FM ranging radar with three offset velocity beams and one offset range beam. It was designed for the manned lunar landing mission for use with a full-scale filtered inertial navigation system on a well-controlled descent onto a zero atmosphere planet. As a result of the studies documented herein, necessary changes have been defined to allow its use on the Mars mission with satisfactory success probability.

Center range beam.- The use of an offset range beam as on the present LM radar requires a preferred roll orientation of the lander. If not, the range becomes a wildly varying function of vehicle attitude and surface slope. This makes a design of a range vs velocity descent contour for the vernier phase very difficult, with associated undesirable effects on thrust and propellant requirements of the propulsion system. Secondly, the range error in sensing the vernier ignition altitude is very large (about ± 1800 ft) even over flat terrain. If a preferred

APPENDIX A

roll orientation were used, a roll maneuver would be required to place the random wind velocity vector in the pitch plane. To perform a roll attitude change in a reasonably short time, a very high torque roll attitude control system is required.

Because an early design version of the LM radar had an antenna with a center range beam, the choice was made to go back to that design for the Mars lander. This removes all the problems discussed above, because radar range is then insensitive to roll.

Acquisition time.- The time required in the present LM design to complete one cycle of searching the total frequency range while trying to acquire the signal is about 6 sec. For the Mars mission, because the radar operating time is much shorter than the lunar mission, it would be desirable to reduce the search time as much as possible. With fairly simple changes to the radar search limits and search rates, the acquisition time can be reduced to 3 sec. This will improve the radar beam lock probability on the parachute phase and require shorter operating time without complete radar data during the vernier descent phase.

Mode switch altitude.- The present LM radar changes modes from a wide bandwidth (high mode) to a smaller bandwidth (low mode) at a range of 2500 ft. A simple change that will allow more freedom in descent trajectory design is to change this mode switch point to 1250 ft. The reason for this, as discussed in sections 5 and 6, is that the radar tracking rate capability is better in the high mode. Performing a tipup maneuver in the low mode can cause unlock of the range beam. However, in all capsule designs considered to date, the tipup maneuver will never occur as low as 1250 ft. By that altitude, the lander is flying the controlled descent contour and approaching a vertical attitude.

Bandwidth change.- To improve the receiver sensitivity of the LM radar, the velocity channel step low pass filter (SLPF) bandwidth in the high mode can be reduced from 2800 to 600 Hz. This significantly reduces the probability of beam unlocks during the parachute phase as shown in section 5. This change does not affect the beam tracking rate capability for the region of interest on the Mars lander.

APPENDIX A

Output format.- The present LM output interfaces with a filtered inertial navigator used on a relatively long-time descent trajectory. The four outputs (three velocity components and range) are essentially sampled at an interval of 0.4 sec. Although this effect has not been thoroughly studied to date using digital control analysis techniques for the Mars mission, preliminary results indicate that a much faster sample rate is necessary. The sequential sampling technique suffers from increased fluctuation and quantization noise when the sample time of 0.4 sec is significantly reduced. Two alternatives have been considered. The first is to add three more digital registers so that a fast sampled parallel output is available to the GCC. A second approach is to convert the four signals to analog format, which can be sampled as necessary by the GCC. This approach appears much simpler for the LM electronics package, but required addition of four A/D converters in the GCC input circuitry. It does have the advantage of allowing analog filtering of the radar data. This is the recommended approach at present.

In addition, it appears that more useful information to the GCC would be the actual radar beam velocity data and range data rather than the axial plus two lateral velocity components currently provided by the LM. Implementing this change results in a simplification to the LM circuitry and allows the GCC to make better use of partial radar data in conjunction with its internally generated inertial velocity data. Four discretes indicating the lock status of each beam must be provided to the GCC. These discretes currently exist in the LM radar but are not provided externally.

Antenna tilt mechanism.- The present LM antenna has a gimbal that can be locked in two different positions in the pitch plane. This capability cannot be used on the Mars mission, so it is recommended that the tilt mechanism be removed.

Sterilizability.- A detailed review of LM radar materials and electronic parts was made to define the changes needed for sterilization compatibility. The results are summarized in tables A1 and A2. In the materials area, 11 types must be qualified exclusively for LM radar use. Forty types requiring qualification are common to other electronic equipment in the soft lander. One material that is used for rf shielding is known to require development for the program. In the parts area, 24 parts requiring qualification are common to other electronic equipment.

TABLE A1.- COMPATIBILITY OF LM RADAR MATERIALS TO PLANETARY MISSION

Material category	Compatible	Not compatible	Number of substitutes to be qualified by Martin Marietta program
Metals	16	3	3
Adhesives	10	9	9
Coatings	4	9	0
Elastomers	1	4	4
Encapsulants	3	13	13
Films	4	0	----
Lubricants	1	0	----
Reinforced plastics	5	0	----
Tapes and cloth	13	4	4
Electrical	11	6	6
Ink	0	2	0
Molded plastics	<u>5</u>	<u>1</u>	<u>1</u>
Total	73	51	40

TABLE A2.- PARTS STERILIZATION IMPACT, RYAN LM RADAR PACKAGE

Class	Quantity per Package	Types	Number of types not sterilizable	Number of substitutes to be qualified by Martin Marietta program
1. Capacitor	859	12	2	2
2. Diode	602	19	1	1
3. Inductor	86	27	20	20
4. Integrated circuit	407	9	0	0
5. Resistor	2277	14	1	1
6. Transistor	539	19	0	0
7. Crystals, others	12	4	0	0
8. RCA transmitter	<u>188</u>	<u>Study in progress</u>		----
Total	4970	104	24	24

APPENDIX A

For the limitations imposed by the assumptions used in this study and the available test data, with the defined changes in conjunction with the guidance and control system changes discussed below, the LM radar performance is adequate for the mission. The error analysis results indicate that suitably accu-cutoff conditions can be achieved. The sensitivity of the control system to velocity fluctuation noise requires use of an inertial navigation mode for the final 100 ft of the descent. Range and velocity beam tracking rates are adequate for all expected worst-case conditions.

The probability of beam unlocks during the parachute phase is very sensitive to the assumption of the surface reflectivity model. Because of the conservative nature of the analyses described herein, it is felt that an acceptably high probability exists that the radar beam lock time during the parachute phase will be adequate.

The study of the radar beam cross-coupling problem has, to date, been very limited. Potential problems in this area and other problems that may be uncovered during the Apollo program testing should be carefully studied in the future.

Guidance and Control System Changes

The guidance and control (G&C) system for use with the modified LM radar described above is more complex than that that would be required to operate with a more complex landing radar design such as a Bessel sideband radar with five beams providing range and velocity on each beam. This is due to the fact that loss of one or two beams on the five-beam radar can be accepted with no loss of the necessary data. For the LM, unlock of one velocity beam can cause loss of (or serious errors in) two velocity components and range. The probability of one or even two beam unlocks as shown in section 5 is high enough to require backup modes of operation until the radar relocks. The G&C system changes described below are recommended to minimize the effects of beam dropouts, and radar noise.

APPENDIX A

Low-altitude altimeter.- Because the LM range beam frequency (centered in pattern or not) is a function of both range and velocity due to the modulation technique, the two coplanar velocity beams must provide valid data to produce an accurate computation of range. Figure A1 shows the range error as a function of velocity for velocity beam unlock conditions. Note that at high velocity and high angles between the velocity direction and the range beam axis, the range error is quite large. This is the situation that can occur when the vernier ignition altitude must be sensed. Because an error this large is intolerable, a low-altitude altimeter was added to the G&C system. The prime function of this altimeter is to sense the altitude mark for vernier ignition. The center range beam would be used for backup of this function. A secondary function of the altimeter data will be to update the inertial navigator estimate of altitude during both the parachute and vernier phases. In fact, simulations reported in section 6 show that the range vs velocity contour can be followed adequately using inertial estimates of range aided by the altimeter data, in spite of the existence of a surface slope.

Additional Accelerometers.- Normally only the thrust axis accelerometer is necessary for thrust control system damping if the radar data are used as the prime guidance data for the entire vernier phase. However, to implement a complete inertial navigator for radar backup, the two lateral accelerometers should be added, primarily for sensing wind accelerations.

Inertial navigation.- Except for the addition of the two accelerometers, this change represents only a software complication if a digital guidance and control computer is used. As indicated above, it is recommended that a radar and altimeter-aided inertial navigator be implemented for backup operation during radar beam unlocks. It is not required on the parachute phase of the mission, but, during that phase, the altimeter and the radar data (as available) should be used to update the inertial navigation equations. Whenever all radar velocity beams are locked, plus the altimeter, the inertial navigator can be completely initialized. Navigator initialization can occur also through use of only two velocity beams with the altimeter and range beam in a Kalman filtered inertial navigator update (or possibly a simpler filter mechanization). Although the filter approach was not investigated in this study, its feasibility was established on the Voyager Phase B study (refs. A4 and A5).

APPENDIX A

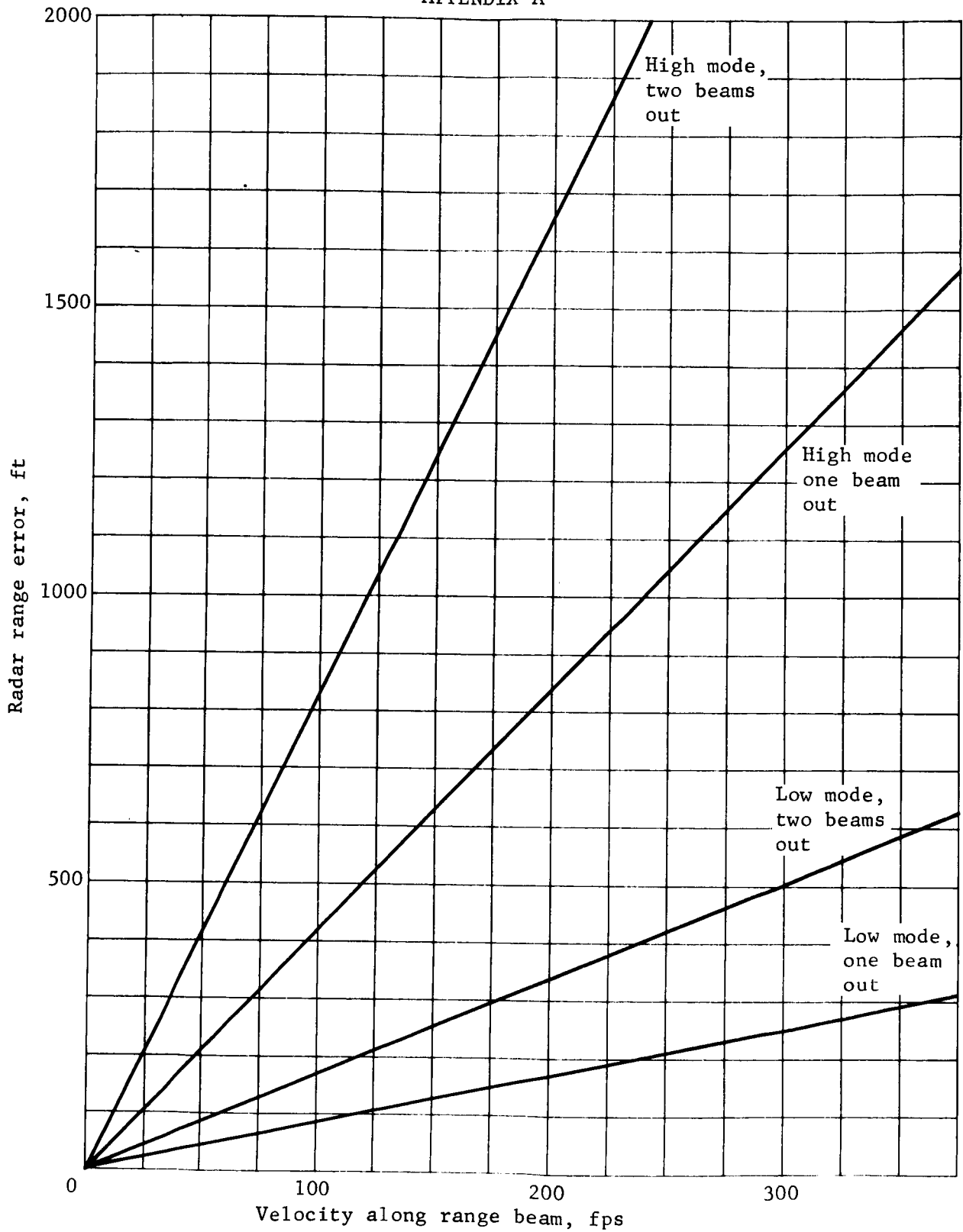


Figure A1.- Radar Range Error vs Velocity for Velocity Beam Dropouts

APPENDIX A

During the vernier phase, including the tipup, a simple conventional radar-aided inertial navigator was successfully flown in the six degree of freedom simulations described in section 6. The conclusions reached there regarding the navigator modes are:

- 1) Use of altimeter data to aid the inertial calculation of range results in soft landings for various 3σ combinations of surface slopes and wind velocities, even if the radar range beam is unlocked for the entire descent;
- 2) Use of the range data during velocity beam unlocks, even though the range data are in error, produces a soft landing because the range error goes to zero as the vehicle nears the cutoff conditions as shown in figure A1;
- 3) A simple navigator, using body velocity equations slaved to the radar data when available and a range calculation slaved to the average of the radar range data and the altimeter data, produces good results. More sophisticated filtering schemes such as a Kalman filter not necessary during the vernier phase. Either radar data or inertial data can be used as the prime control signals;
- 4) Use of the inertial navigator data for the last 100 ft of the descent eliminates the vehicle transients due to radar noise, resulting in more accurate landings with smoother thrust history near the surface.

Capsule System Changes

At the start of this study, an attempt was made to define constraints on the entry vehicle and parachute configuration to allow the LM radar to operate in the prime mode. As the study proceeded, using more inclusive effects in the radar modeling, it became evident that no practical parachute design could accomplish this goal in conjunction with landings on high-altitude terrain and worst-case entry angle. In general, design of the entry and parachute trajectory to provide near vertical approaches at high velocity (two incompatible goals) improves the radar beam lock probability as shown in section 5. **Although picking a desirable** probability for beam unlocks is an argumentative problem, it is obvious from the curves of section 5 that zero-wind parachute velocities less than 150 fps and zero-wind parachute angles

APPENDIX A

from vertical greater than 20° are very poor. The capsule design should attempt to provide at least 10 sec of trajectory time where the velocity and angle conditions are better than these with as high probability as possible.

Possible Alternatives

This study resulted in various types of vernier phase simulation runs from which conclusions about other mechanizations could be drawn. One is that either a range vs velocity or an altitude vs velocity contour can be successfully implemented in spite of wind and surface slope combinations.

This means that a system alternative that could be considered is a three-beam doppler radar with a low-altitude altimeter and an inertial navigator backup. This is probably a less costly system than either the modified LM or the five-beam Bessel side-band system. A second alternative is to change the range channel in the LM radar to a fourth velocity beam, resulting in a rectangular velocity beam pattern. This pattern would be less susceptible to loss of velocity data due to incidence angle and zero doppler **dropouts**. Both of these alternatives have the disadvantages of removing the range/altitude redundancy available in the modified LM/altimeter system or the five-beam Bessel side-band system.

A capsule system sequence change that would greatly improve the probability of achieving a total LM radar lock condition can be made with little cost (i.e., ignite the vernier engines on the parachute and close the attitude control loops to drive the lander to a vertical attitude and zero rate). This can be done in 3 sec or less, so an additional 3 sec would ensure the radar could lock all beams with the shorter acquisition time recommended. Implementing this mode would require 5 to 10 lb more vernier propellant and a throttle ratio large enough to keep from collapsing the parachute. A study of this dynamic condition should be undertaken.

APPENDIX A

3. VERNIER PHASE CONTROL

Control Law Selection

The control system for the vernier phase of the mission is required to perform two functions:

- 1) Control the total thrust of all four engines so the vehicle acceleration and, therefore, velocity follow a predetermined contour as a function of range to the ground;
- 2) Control the differential thrust of the four engines so that the vehicle's attitude is constrained to a control law.

The attitude control law selected will affect the descent contour. This can be seen by considering the problem of the terminal descent phase in detail. The vehicle will have a vertical velocity associated with the terminal velocity of the parachute phase. It can also have a horizontal velocity dependent on the atmospheric winds encountered by the parachute phase. These velocities must be reduced to a sufficiently low level so that the vehicle will impact on the planet surface with a small velocity, and its attitude will remain erect after landing. An efficient method of reducing both horizontal and vertical velocities with practical-sized thrusters is to maintain the vehicle attitude to thrust directly opposite to the total velocity vector. This produces a so-called gravity-turn descent where the vehicle attitude asymptotically approaches the local vertical as the vehicle velocity is reduced. A vector diagram of the thrust direction is shown in figure A2.

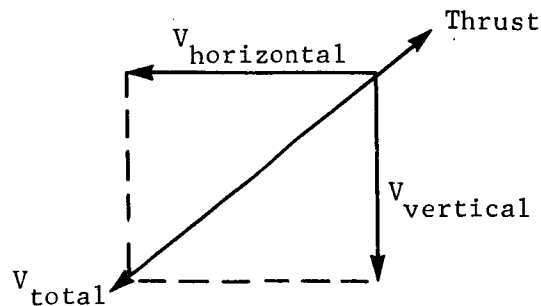


Figure A2.- Gravity-Turn Thrust Orientation

APPENDIX A

It is seen that the larger the horizontal velocity, the more thrust is imparted to the vehicle in the horizontal direction.

An example of another control law mechanization would be to initially thrust opposite to the horizontal velocity until it has been reduced to zero, then realign the vehicle to vertical to reduce the vertical velocity. This scheme allows a rather high vertical velocity to build up, however, and makes no provision for removing horizontal velocities that may build up due to winds after the vehicle has aligned itself to the vertical.

The steering law selected, then, was to thrust directly opposite to the total velocity vector. This type of steering law entails nulling the body transverse velocities. In mechanizing such a control law it is desirable to make the gain in the steering channel inversely proportional to velocity. At high body velocities, any slight angular deviation of the body about the velocity vector produces sizable body side velocities. If the steering channel were trying to null the body side velocities to some fixed gain, this would produce a very tight tolerance on angular deviation when the vehicle velocity was high and a loose one when low. The steering laws selected than are:

$$q_c = G_\alpha \frac{w}{u}$$

$$r_c = G_\beta \frac{v}{u}$$

$$q_c = \text{pitch rate command}$$

$$r_c = \text{yaw rate command}$$

u, v, w = vehicle body referenced velocities along roll,
pitch, and yaw

$$G_\alpha, G_\beta = \text{control gains} \tag{A1}$$

Many types of descent contours have been considered in the literature (ref. A6 thru A9). **The contour used herein is a modification of the approach used on the Surveyor moon lander.** The approach used is to define the worst set of parachute final conditions and simulate the trajectory via a three degree of freedom

APPENDIX A

open-loop computer simulation. The simulation includes an accurate simulation of the propulsion system. In general, the propulsion system may use a nonregulated (blowdown) propellant feed system so that the thrust decreases from its initial maximum value as a function of propellant used.

This three degree of freedom simulation assumes the body is always aligned to the velocity vector and thrusting opposite to it at a constant percentage of available thrust; hence, the axial channel is considered open loop and the attitude channel is considered closed and nulling the body side velocities to zero. A thrust level of 85% was selected to allow a 10% margin in thrust for attitude control purposes plus a 5% margin for increases in thrust due to surface slopes and craters.

The descent contour thus derived results in a velocity vs range contour that, when followed, gives the desired final conditions. The contour is used in the control system to generate a velocity error signal that controls the vehicle acceleration so that the descent contour is followed. The axial control laws are:

$$\begin{aligned} a_c &= k_v V_e \\ V_e &= V - V_d \\ &= V - k (R - R_b)^m \end{aligned} \tag{A2}$$

where

a_c = acceleration command;

V = vehicle total velocity;

V_e = velocity error;

V_d = velocity desired;

R = range;

R_b = range bias;

k, m = constants.

APPENDIX A

In eq. (A2), if a purely vertical descent were obtained with a constant acceleration, a , the coefficients would have the values $k = (2a)^{\frac{1}{2}}$, $m = \frac{1}{2}$. However, studies have shown that using a contour with these values produces increasing values of acceleration if the vehicle develops a nonvertical flightpath angle. Furthermore, it does not compensate for the decrease in thrust produced by a blowdown propulsion system.

Thus, for the vehicle class described herein, the simulation approach described above is preferred because the contour can be shaped to allow for the worst-case propellant consumption (worst-case blowdown effect) and worst-case initial conditions. The simulation is generated using constant throttle position commands so that if less severe cases are encountered, less throttle is commanded, resulting in a distribution of the control margin throughout the trajectory. If altitude is to be used as the controlling variable rather than range, an H-V contour can be generated in the same manner.

Before reaching the descent contour, the vehicle must be allowed to achieve the correct attitude for the gravity turn. To accomplish this, a 3-sec fall at minimum thrust is allowed between parachute release and reaching the contour in the highest velocity case. During this period, the attitude loops are operative and command the vehicle to point its thrust vector opposite to the total velocity vector. The vehicle then flies the programmed descent contour to a preset range and/or velocity at which the descent contour is changed to a constant velocity phase. This phase allows for adjustments in thrust to remove final velocity errors. At a preset range, thrust is terminated and the vehicle falls to impact. Figure A3 shows a typical descent contour.

Control System Mechanization

Because the terrain may be irregular and winds unpredictable, the velocity and range data used during the soft landing terminal phase must be measured from the vehicle to the surface. In view of these requirements, the basic guidance sensor is a radar backed up by an inertial navigator that is mechanized in the guidance and control computer with inputs from the IMU.

APPENDIX A

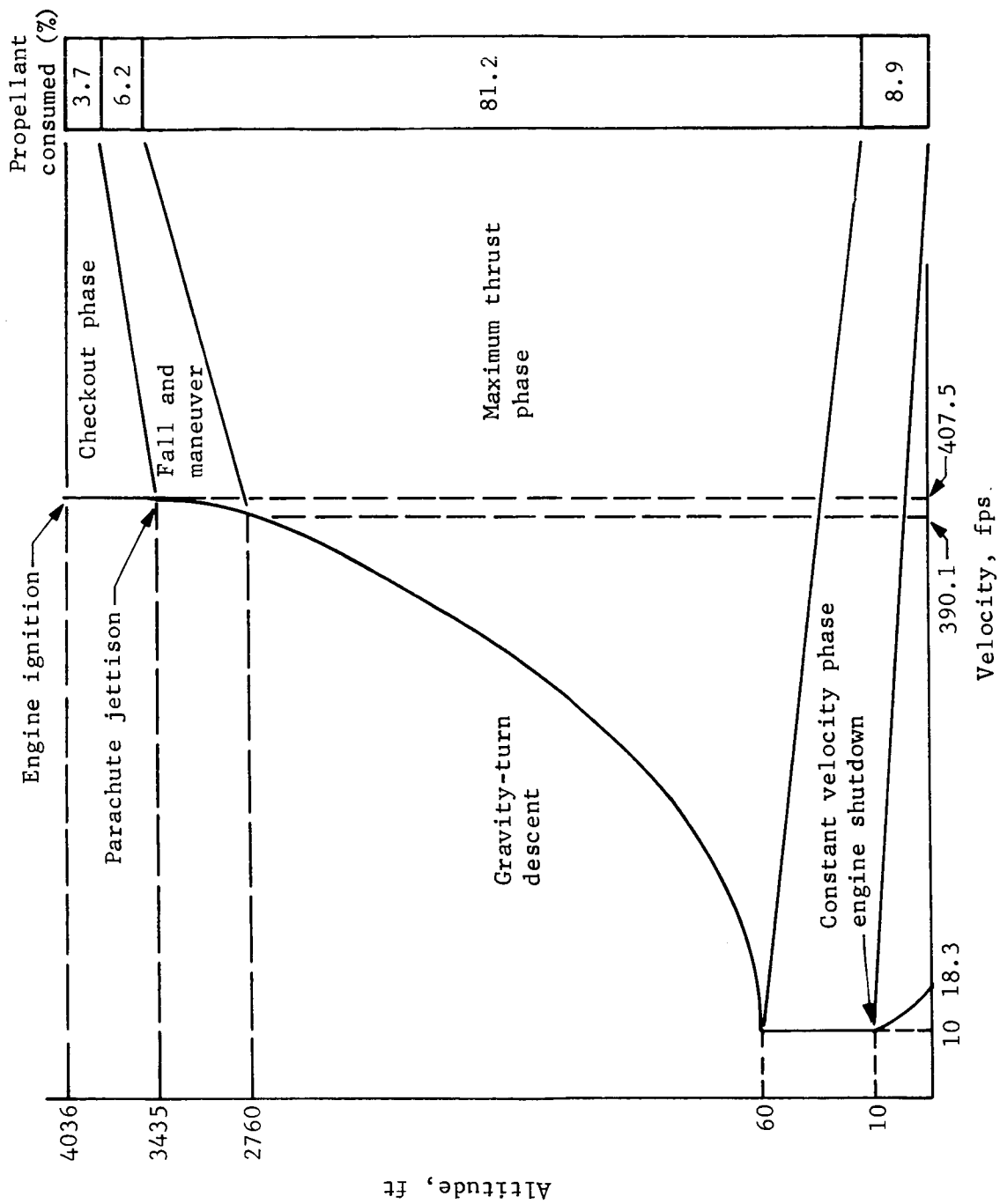


Figure A3.- Typical Terminal Descent Profile and Propellant Utilization

APPENDIX A

As discussed elsewhere in this appendix the radar beams may become unlocked under certain operating conditions thereby causing loss of input signals from the radar. An inertial navigator is provided as a backup to the radar under beam unlock conditions. The navigator outputs of range and velocity are used by the control system in the same manner as the radar outputs are used so the control system performance of either will be the same.

In addition, three gyros provide body attitude rate and incremental attitude data in roll, pitch and yaw; and three accelerometers are aligned along the three vehicle axes. Control torquers must also be provided for roll, pitch, and yaw.

Because a soft lander must have a low center of gravity and a large diameter (essentially a saucer shape) to provide good landing stability, gimbaled engines are poor candidates to provide attitude control. Because of the short moment arm, the gimbal torquers must be large and high power devices to provide the response required in pitch and yaw. Studies have shown that the best choice for pitch and yaw control is to differentially throttle the engines used for velocity control. This means that at least three engines are required. If four engines are provided, roll control can be achieved by canting the engines. However, the roll control requirements are simply to maintain a fixed roll attitude against small disturbing torques. This can be accomplished by auxiliary control jets that are required anyway during earlier mission phases.

Four throtttable engines are used for pitch, yaw, and velocity control. The four engines are throttled in unison to provide the desired total thrust, and differentially to control moments. Using figure A4 as reference, the following signal mixing matrix will accomplish the desired three axis control.

$$\begin{bmatrix} F_{c1} \\ F_{c2} \\ F_{c3} \\ F_{c4} \end{bmatrix} = \begin{bmatrix} 1 & +k_p & 0 \\ 1 & 0 & +k_y \\ 1 & -k_p & 0 \\ 1 & 0 & -k_y \end{bmatrix} \begin{bmatrix} F_c \\ \epsilon_\theta \\ \epsilon_\psi \end{bmatrix} \quad (A3)$$

APPENDIX A

where

$F_{c1} \rightarrow F_{c4}$ are engine thrust commands;

F_c is the axial channel command;

ϵ_θ is the pitch channel command;

ϵ_ψ is the yaw channel command;

k_p, k_y are pitch and yaw gains.

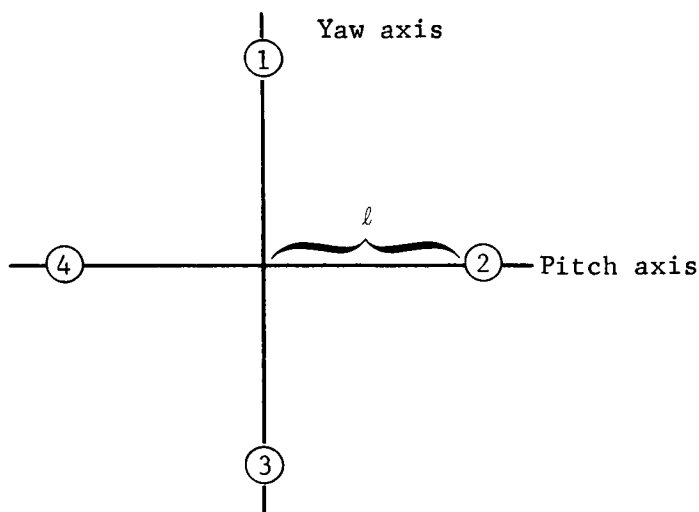


Figure A4.- Vernier Engine Arrangement

The individual engine thrusts, F_i , are related to the commanded thrust, F_{c_i} , by the propulsion system dynamics, which include the throttle valve, propellant feed system and thrust chamber effects.

$$F_i = G_p(s) F_{c_i} \quad (A4)$$

where $G_p(s)$ is the propulsion system dynamics, to be described later.

Combining eqs. (A3) and (A4) with the force and moment equations shows the three control channels to be decoupled.

$$\begin{bmatrix} F \\ M_{\theta} \\ M_{\psi} \end{bmatrix} = G_p(s) \begin{bmatrix} 4 & 0 & 0 \\ 0 & k_p(2\ell) & 0 \\ 0 & 0 & k_y(2\ell) \end{bmatrix} \begin{bmatrix} F_c \\ \epsilon_{\theta} \\ \epsilon_{\psi} \end{bmatrix} \quad (A5)$$

Figure A5 shows a block diagram of the guidance and control system using the control laws described above. The engine command mixing block is a mechanization of eq. (A3). The valve and engine dynamics produce the thrust for each engine, F_i , based on the commands, F_{c_i} . From the vehicle dynamics, the body attitude rates p , q , and r , are sensed by the strapdown gyros (not shown). The thrust acceleration a is sensed by the axial accelerometer (not shown). These signals are fed back in the inner loops shown to damp the pitch, yaw, and axial control channels.

Figure A5 shows the system with the radar in the prime control mode. Other alternative modes using inertial navigation will be described later. From the physical velocities of the vehicle resolved on to body coordinates, u_{BA} , v_{BA} , w_{BA} , the radar measures doppler frequencies, converts these to beam velocities, and generates the measured body velocities, u , v , and w . In addition, range along the vehicle thrust axis is measured. Note as described by eq. (A1) that the pitch and yaw loops null the v and w radar velocity components. The division by the axial velocity, u , is essentially an automatic gain changer that makes the gain of the attitude loops independent of velocity. The filters shown with time constants τ_v , τ_w , τ_r , and τ_d are for the purpose of smoothing the noisy radar data. To compensate the loop stability for the addition of these filters in the attitude loops, the inputs q/s and r/s are used as shown in the figure. These inputs are discussed in the next section. The proportional plus integral feed-forward blocks are used to reduce the effects of torque unbalances due to engine misalignments or aerodynamics on the steering accuracy. The limiters on the pitch and yaw rate commands are used to keep from driving the vehicle at rates that would exceed the gyro torquer capability.

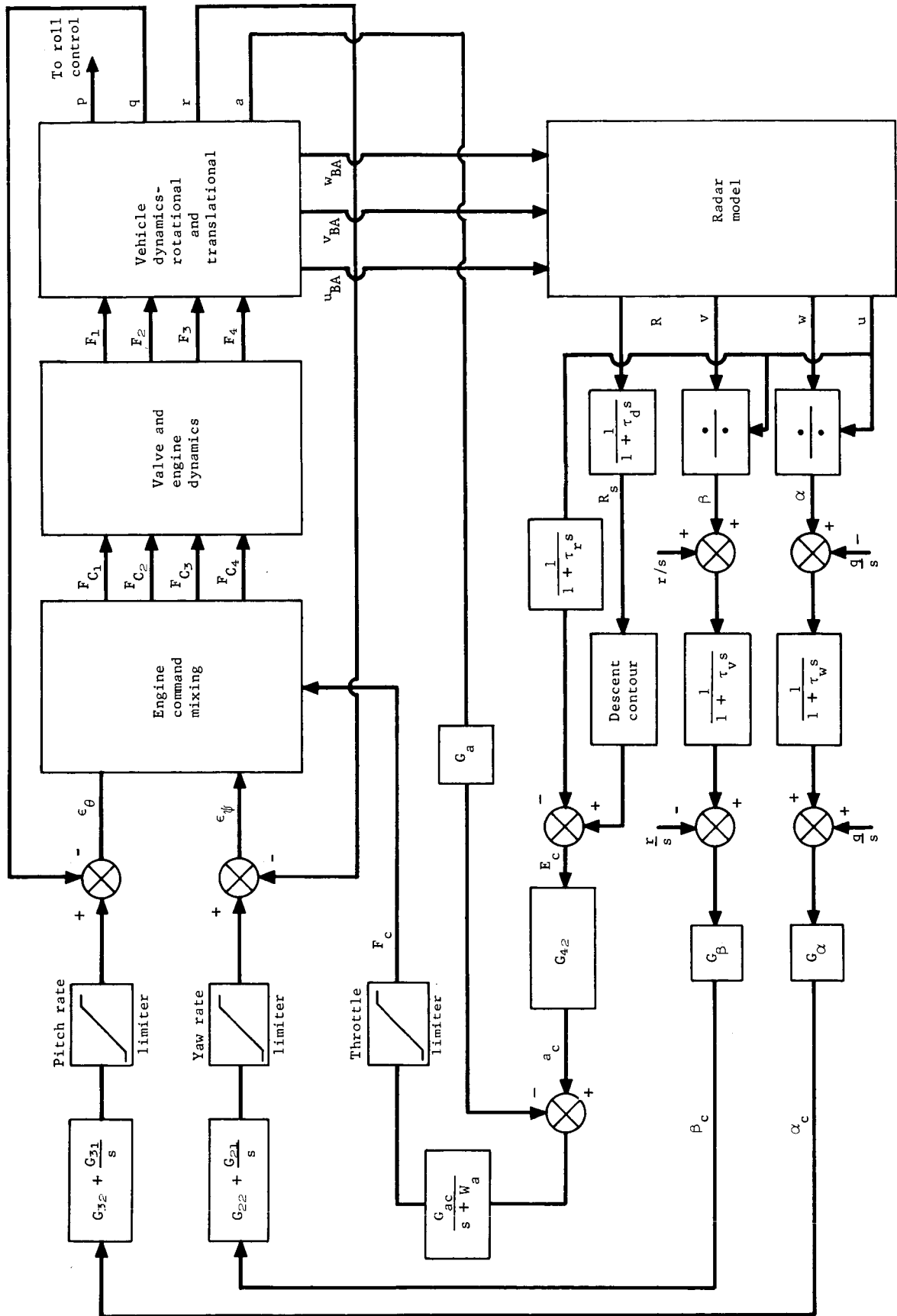


Figure A5.- Guidance and Control System Block Diagram

APPENDIX A

In the axial control channel, the radar range is used to generate the desired velocity from the descent contour as discussed earlier. The error velocity is used as the command to the inner acceleration control loop. The filter with frequency, W_a , is used to reduce accelerometer noise. The throttle limiter is used to keep the thrust command from driving to large maximum or minimum values that would hold all the engines at either maximum or minimum thrust, thus causing loss of attitude control by differential throttling. Normally the maximum and minimum on the throttle limiter is set to leave 10% of the engine thrust available for control at any thrust setting.

Control System Performance

There were basically two analysis techniques that were used to examine the performance of the control system. The first was to determine the stability and response of the system by linear analysis root locus techniques. The second technique used a six degree of freedom digital computer simulation that incorporated the full rotational and translational dynamics and also included system nonlinearities, as described in section 6. The basic block diagram shown in figure A5 applies to both analyses; however, with the linear analysis, each control channel was examined separately, and all nonlinearities were, of course, ignored. This meant that the dynamics had to be linearized.

The engine and valve dynamics were of some concern because of the differentially throttleable control method used. The transfer function for an electromagnetic type of valve is second order. Reference A10 defined the requirements for the valve response as being that the valve shall have dynamic dominant poles greater than 30 rad/sec with a damping ratio greater than 0.70 ($\zeta \geq 0.70$). This specification will be used for the valve dynamics herein.

The engine transfer function is not well known for this type of throttling operation. After considerable analysis and discussions with various engine manufacturers, it was concluded that the engine dynamics could be adequately represented by a single first-order lag of 8 msec (ref. A10). Feed system dynamics were considered to be negligible as the feedlines were purposely designed to be very short. The resulting F/F_C transfer function is shown in figure A6. The digital simulation accounted for changes in propellant tank pressure as propellant was used and the subsequent effect on flow rate while the linear analysis assumed operation about a nominal operating point.

APPENDIX A

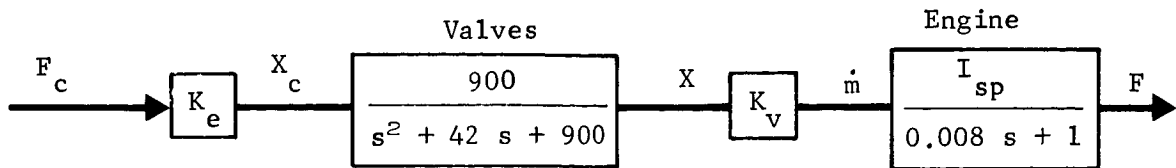


Figure A6.- Engine-Valve Dynamics

Referring to figure A5, the main control signals u , v , w , and R are derived directly from the output of the radar. The radar outputs are corrupted by noise so the signals are filtered through a first-order lag. It has been previously shown by analog simulation (ref. A10) and verified by more recent digital simulations, that the magnitude of the noise requires a filter with a break at 2 rad/sec for the attitude channel to adequately filter the noise. The axial channel filter can be as high as 10 rad/sec.

The stability of the three control channels, the axial thrust channel, and the two attitude channels, came under considerable concern because of the low frequency of the radar filters used. These radar filters have a severe deterioration on system stability and response and auxiliary loop compensation is required to stabilize the attitude channel. The axial channel does not require any auxiliary compensation techniques other than usual compensation in the inner loop because the radar is less noisy in the outputs used for this channel and the radar filters are not of such low frequency. The compensation for the attitude channels takes the form of feeding back the integral of the body rates in conjunction with the radar outputs. To show the effect that this feedback has it is necessary to look at the equations of motion for each attitude channel.

The control sensors are referenced to the moving body axis coordinate system (X_b, Y_b, Z_b) . The equation of motion in this system is:

$$\frac{d\vec{V}}{dt} = \frac{\partial \vec{V}}{\partial t} + \vec{\Omega} \times \vec{V} = \frac{\sum \vec{F}}{m} \quad (A6)$$

where

$\frac{\delta}{\delta t}$ denotes differentiation in the body axis system;

$\vec{\Omega}$ is the vehicle angular rate with components p , q , r ;

\vec{V} is the vehicle velocity with components u , v , w .

The scalar form of eq. (A6) is:

$$\begin{aligned}\dot{u} &= \frac{F_x}{m} - qw + rv + g \cos \theta \cos \psi \\ \dot{v} &= \frac{F_y}{m} + pw - ru - g \cos \theta \sin \psi \\ \dot{w} &= \frac{F_z}{m} - pv + qu + g \sin \theta\end{aligned}\tag{A7}$$

where θ and ψ are Euler angles with respect to local vertical in pitch and yaw, respectively.

In these equations, F_y and F_z are small because they are due to thrust misalignments and aerodynamics. The roll rate is held to negligible values by a reaction jet control system. Except for an initial transient, q , r , v , and w are small due to the action of the control system. Linearizing eq. (A7) by the method of small perturbations, and deleting second-order terms and zero terms yields

$$\begin{aligned}\dot{u} &= \frac{F_x}{m} + g (\cos \theta_o \cos \psi_o - \Delta\theta \cos \psi_o \sin \theta_o - \Delta\psi \cos \theta_o \sin \psi_o) \\ \dot{v} &= -ru_o - g (\cos \theta_o \sin \psi_o + \Delta\psi \cos \theta_o \cos \psi_o - \Delta\theta \sin \theta_o \sin \psi_o) \\ \dot{w} &= qu_o + g (\sin \theta_o + \cos \theta_o \Delta\theta)\end{aligned}\tag{A8}$$

APPENDIX A

For small angles about vertical the coupling terms in the gravity expressions are negligible. Because $\dot{\Delta\theta} \simeq q$ and $\Delta\psi \simeq r$, the second two equations yield by Laplace transform,

$$\frac{w}{q} = \frac{u_o \left(s + \frac{g \cos \theta_o}{u_o} \right)}{s^2} \quad (A9)$$

$$\frac{v}{r} = \frac{-u_o \left(s + \frac{g \cos \theta_o}{u_o} \right)}{s^2} \quad (A10)$$

The magnitude of the term $(g \cos \theta_o)/u_o$ is small.

Looking at the equation, we see that the fastest varying part of w is $u_o \frac{q}{s}$. Recalling that the control law is $\alpha = \frac{w}{u}$ then a rough approximation to α is to simply feedback q/s . It turns out that this does improve loop stability when the radar output is heavily filtered; however, there are certain vehicle maneuvers that could cause a significant bias signal to be integrated and fed back in error. To counter this large error the q integral was fed back negative to the original q/s feedback ahead of the radar filter. This essentially wipes out the long term effects of q/s feedback but the stabilizing effects on the loop are retained. These are the q/s and r/s inputs shown in figure A5 near the radar filters.

In figure A7 a root-locus plot of the pitch or yaw attitude control inner loop is shown. This locus assumes an engine time constant of 25 msec rather than 8 msec as shown in figure A6. A lead lag compensation network of transfer function $(s+15)/(s+100)$ is used. Figure A8 shows the root locus of the outer attitude control loop using the radar in the primary control mode. The radar tracker time constant is assumed to be 50 msec with the smoothing filter $\tau_w = 0.5$ sec. The system defined by these root loci was used in the six degree of freedom simulation runs described in section 6 of this appendix. The transient response of the system during pitchup maneuvers and noise transients can be seen on the plots presented there.

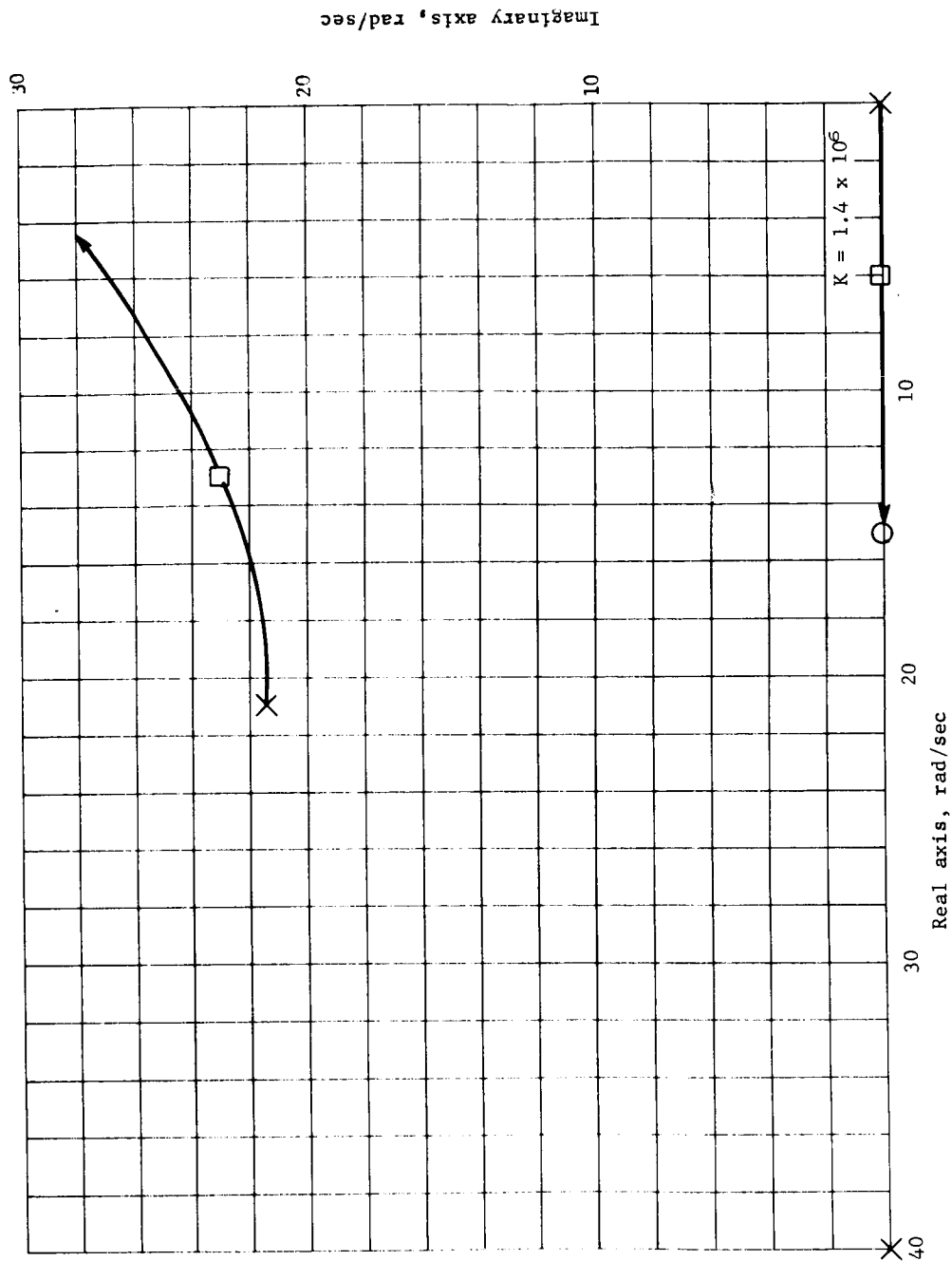


Figure A7. - Attitude Control Inner Loop Root Locus

APPENDIX A

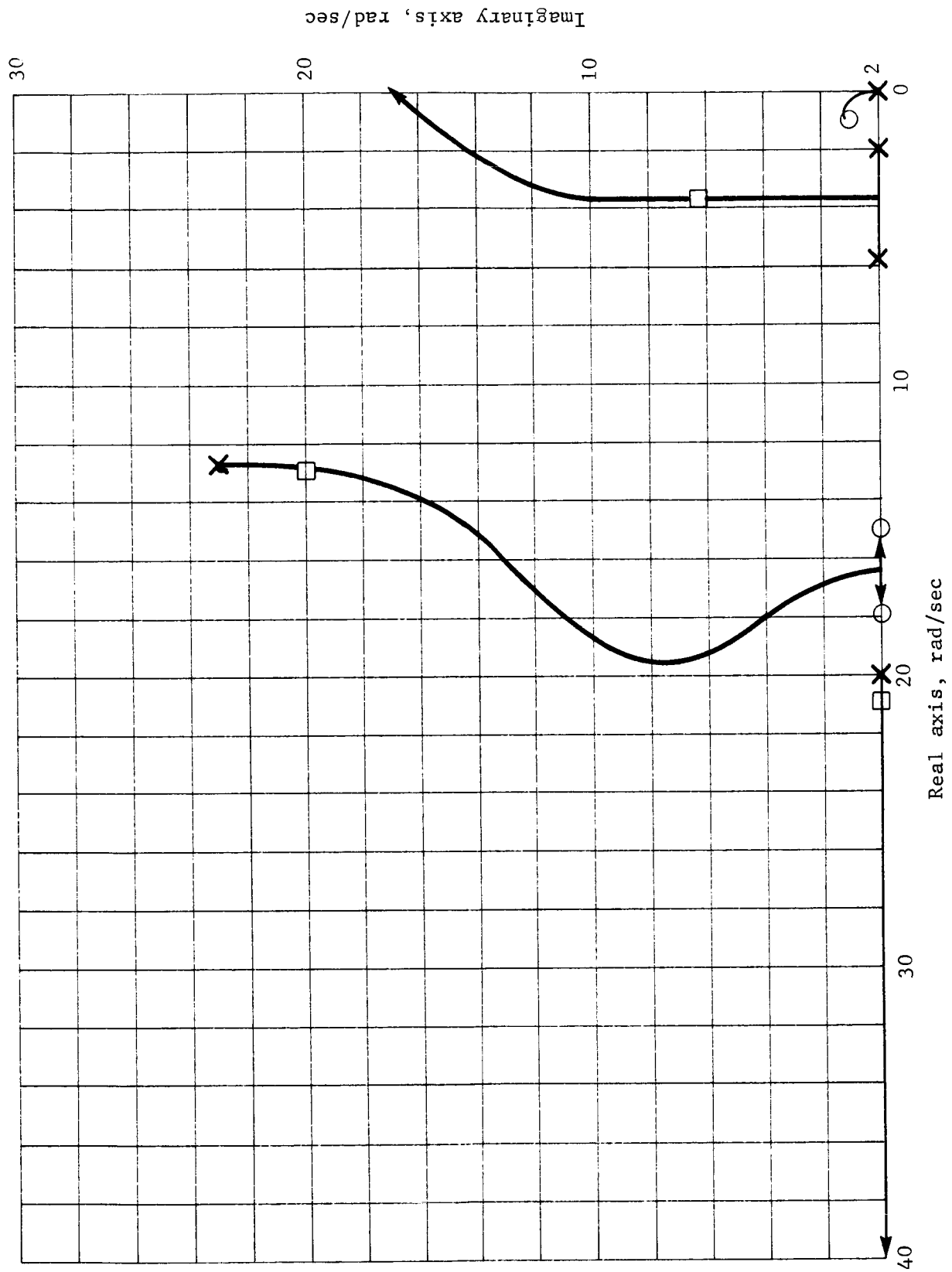


Figure A8.- Attitude Control Outer Loop Root Locus

APPENDIX A

The axial channel stability is not as sensitive as the attitude channel to the radar smoothing or the propulsion system dynamics. A root locus for it is shown in figure A9.

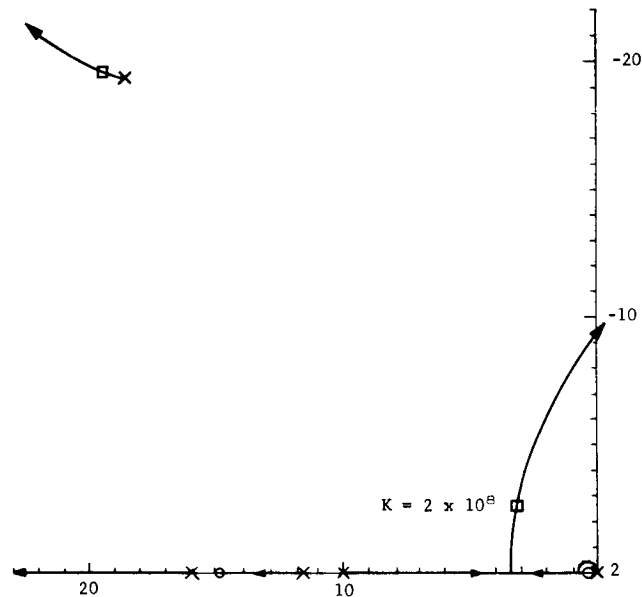


Figure A9.- Axial Channel Root Locus,
Nominal Case

Inertial Navigator Equations

Simple radar-aided inertial navigation equations were devised for use in the six degree of freedom vernier phase simulation program. Other backup algorithms for use during radar dropouts were considered but discarded when it became apparent that many different algorithms were required for the various possible conditions that could occur during the descent. A simpler approach was to use an inertial navigator, slaved to the radar data when valid, and going open loop during unlock periods. During the simulation runs, the radar data were used as the prime control system input whenever possible to assess the effect of radar noise on the system. During velocity beam dropouts, inertial velocity was switched in to the control system, but radar range was used if the range beam was locked. If the range beam was unlocked, inertial range was then used.

APPENDIX A

To slave the inertially computed velocities, the difference between the radar data and the inertial data was used as a forcing term as shown below.

$$\begin{aligned}
 \dot{u} &= \frac{F_x}{m} - qw + rv + g A_{13} + K_u(u_R - u) \\
 \dot{v} &= \frac{F_y}{m} + pw - ru - g A_{23} + K_v(v_R - v) \\
 \dot{w} &= \frac{F_z}{m} - pv + qu + g A_{33} + K_w(w_R - w)
 \end{aligned} \tag{A11}$$

where

$$A_{13} = \cos \theta \cos \psi$$

$$A_{23} = \cos \theta \sin \psi$$

$$A_{33} = \sin \theta$$

The body attitude rates, p , q , r , and the accelerations F_x/m , F_y/m , F_z/m are sensed by the strapdown gyros and accelerometers, respectively. θ and ψ are angles from local vertical.* u_R , v_R , w_R are the radar body axis velocity components. Whenever a radar velocity beam unlock was obtained, K_u , K_v , and K_w were switched to zero. Otherwise their value was one.

For the inertially computed range, a similar approach was used. First the estimated altitude was computed using the equations:

$$\begin{aligned}
 \ddot{Z} &= g + \frac{F_x}{m} A_{13} + \frac{F_y}{m} A_{23} + \frac{F_z}{m} A_{33} \\
 \dot{Z}_A &= \dot{Z} + G_R (H - R_R A_{13}) + G_H (H - H_A) \\
 H &= H_O - Z_A \\
 R &= H/A_{13}
 \end{aligned} \tag{A12}$$

*The direction cosines A_{13} , A_{23} , A_{33} would normally be available in a strapdown navigator referenced to the local vertical without computing θ and ψ .

In eqs. (A12), R_R is the radar measured range. The R_R A13 term would be the altitude represented by that range if the terrain were assumed flat. If the radar range beam unlocks, G_R is set to zero. The H_A term denotes altitude as measured by a low-altitude widebeam altimeter. In the simulation runs, initially the altimeter was not used. In the event of a range beam unlock over a sloping surface, the inertially computed range assuming a flat terrain becomes a very poor estimate. Use of the altimeter data as shown produces very good results because the surface slope error eventually becomes negligible as the altitude decreases to zero. The navigation eqs. (A11) and (A12) produced very good results in the simulation runs shown in section 6; however, a comprehensive analysis of inertial sensor error effects was not done. The assumption was made that IMU updating on the parachute phase prior to the vernier phase had occurred.

Referring again to figure A5, the simulation used the radar data as the controlling signals whenever those data were valid. During that operating mode, the inertial navigator eqs. (A11) and (A12) were slaved to the radar and altimeter data through use of the gains K_u , K_v , K_w , G_R , and G_H . If radar velocity was lost, the inertial navigator with K_u , K_v , K_w set to zero provided the velocity data in place of the radar data. The stability of the control system was the same with either mode. Similarly, the radar range data was replaced by inertial range whenever a range beam unlock was obtained. The range beam unlocks were not normally obtainable without intentionally creating an abnormal case.

Although this mode of operation produced good simulation results, it is not necessarily the best mode of operation for flight operations. In the study, the intent was to assess the radar capability to operate in the prime mode and the navigator used only as a backup to prevent vehicle crashes when radar beam unlocks occurred. The recommended use of the radar and inertial navigator is as follows. The radar will provide beam velocity data to the guidance computer rather than body velocity data. Range data will also be provided. Discretes indicating the status of the beam trackers (locked or unlocked) will be provided for each velocity beam and the range beam.

APPENDIX A

The computer will use gyro and accelerometer measurements to estimate the velocities along the body axes in a manner such as eqs. (A11) indicate. However, the inertial data and the radar data will then be combined to produce a composite estimate of the required velocity and range signals. This can be done by a Kalman filter or a simplified version of one. The result will be a smoother operation of the control loops due to the increased smoothing of the radar noise. The filters and special q/s and r/s feedback loops shown in figure A5 would not be required in the form shown. Further studies in this area will be undertaken.

4. RADAR DESCRIPTION AND MATHEMATICAL MODELS

LM Radar Description

The radar selected as the primary sensor for this study is a modified version of the landing radar for the Apollo Lunar Module. The LM radar is, in turn, a development based on the Surveyor RADVS. Both radars are products of the Ryan Aeronautical Company.

The radar measures the velocity and range of the lander with respect to the planet surface by a three-beam doppler velocity sensor and a single beam altimeter (slant range).

The velocity sensor is a direct to audio cw doppler system with coordinate conversion from beam velocity to body axis components. One component of velocity is used to correct the range measurement of the altimeter beam for the velocity error inherent in the linear FM/cw modulation used in this radar.

Modifications to the basic LM radar include relocating the range beam to the antenna pattern centerline, deleting the antenna tilt mechanism, changing the velocity compensation logic for the altimeter beam, and tailoring the acquisition and mode change circuits to match the requirements for the Mars lander mission.

The interface between the radar data converter and the guidance computer is changed from the low rate sequential sampling used by the LM to a parallel analog that offers a data rate compatible with the Mars lander.

The radar is composed of two assemblies -- the antenna assembly and the electronic assembly. The antenna assembly consists of the two transmitters, four receivers, and the cluster of phased array antennas needed to generate the four active beams of the system. The electronics assembly contains the frequency trackers, data converter, and power supplies for the radar.

Radar Mathematical Models

The approach used in simulating the LM radar was that of a black box or functional simulation as opposed to a one-to-one type of modeling. The following will describe the math models used in the simulation; as a guide to this discussion, a block diagram of the simulation is shown in figure A10 (the following text will refer to block A or B etc. from this figure).

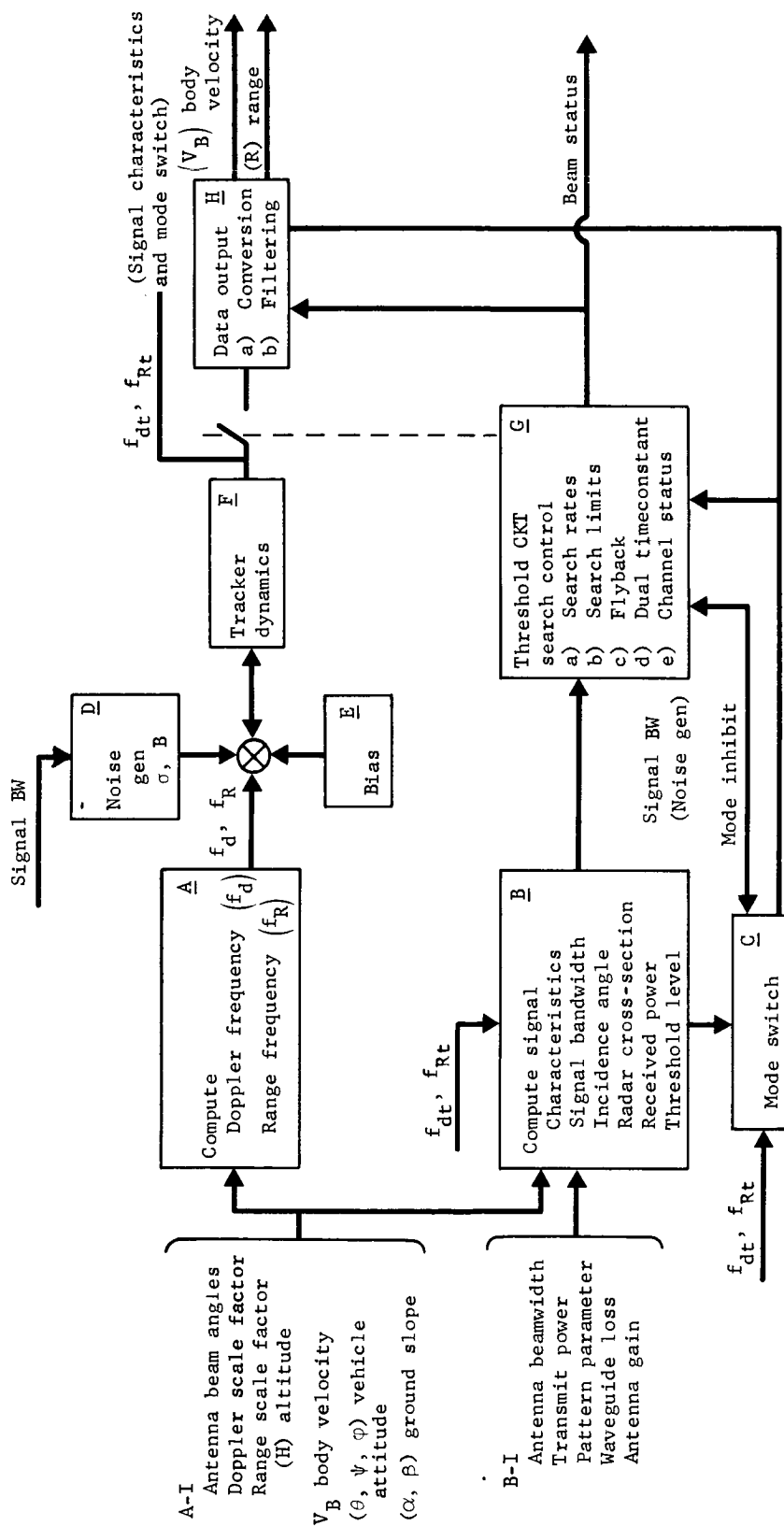


Figure A10.- LM Radar Simulation Block Diagram

APPENDIX A

Figure A10 is representative of the flow of calculations carried out on a per beam basis within the six degree of freedom simulation program. Figure A11 indicates the relative beam geometry, note that the range beam appears in the center of the beam pattern, this is a recommended change to the system and the LM radar has been evaluated with the range beam as shown.

Doppler and range frequency calculation (block A). - The in-beam doppler frequency and range frequency is calculated in the following manner (1) transforming vehicle inertial velocity into body axis velocities, (2) transforming body axis velocity components into antenna beam velocity components, (3) converting velocity components along the beam into doppler frequency, (4) converting vehicle inertial position into position in the vehicle coordinate system, and (5) transforming position in the body coordinate system into a component along the range beam 4.

The in-beam velocities are obtained by the following equations.

$$\vec{V}_B = \underline{A} \vec{V}_I \quad (A13)$$

$$V_{B1} = \vec{\mu}_{B1} \cdot \vec{V}_B$$

$$V_{B2} = \vec{\mu}_{B2} \cdot \vec{V}_B$$

$$V_{B3} = \vec{\mu}_{B3} \cdot \vec{V}_B \quad (A14)$$

where

\underline{A} = inertial to body transformation matrix;

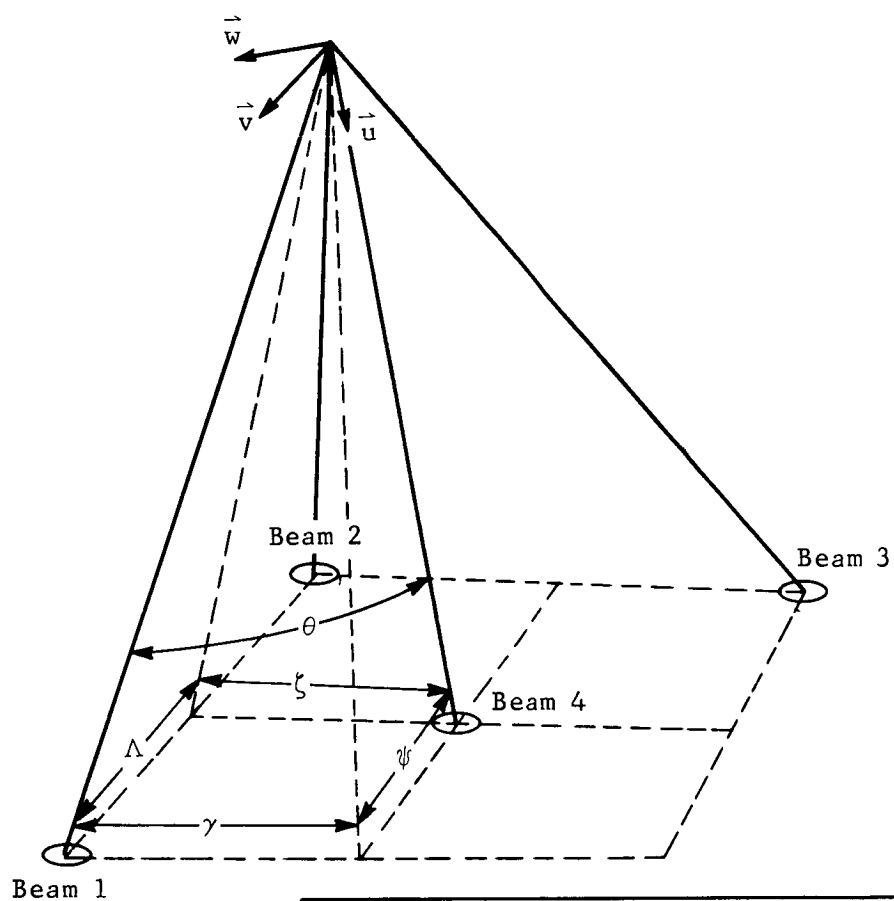
\vec{V}_I = vehicle inertial velocity vector;

\vec{V}_B = vehicle velocity in body coordinates;

$\vec{\mu}_{B1}, \vec{\mu}_{B2}, \vec{\mu}_{B3}$ = unit vectors in body coordinates in the beams 1, 2, and 3 direction, respectively;

V_{B1}, V_{B2}, V_{B3} = vehicle velocity components in the beams 1, 2, and 3 direction.

APPENDIX A



Note: 1. Beam 4 is the range beam. Configuration angles of beams 2 and 3 are nominally identical to beam 1.

2. $\zeta = 20^\circ 22' 48''$, $\Delta = 13^\circ 59' 22''$, $\theta = 24^\circ 33'$, $\psi = 14^\circ 53'$, and $\gamma = 19^\circ 45'$.

Figure All.- Definition of Beam Pointing Angles with Respect to Vehicle Body Coordinates

For range,

$$\begin{aligned}\bar{\mu}_{I4} &= \underline{A}^T \underline{B}_4 \bar{\mu}_{B4} \\ \cos \theta_4 &= \bar{\mu}_{I4} \cdot \bar{\mu}_N \\ D &= \bar{X} \cdot \bar{\mu}_N \\ R &= D / \cos \theta_4\end{aligned}\tag{A15}$$

where

- \underline{A}^T = body to inertial transformation matrix;
- \underline{B}_4 = beam 4 to body transformation matrix;
- $\bar{\mu}_{B4}$ = unit vector in body coordinates, the beam 4 pointing direction;
- $\bar{\mu}_N$ = unit vector normal to the terrain;
- $\bar{\mu}_{I4}$ = beam 4 pointing direction in inertial coordinates;
- θ_4 = incidence angle for beam 4;
- \bar{X} = position vector of the vehicle;
- D = perpendicular distance from the vehicle to the ground;
- R = slant range of beam 4 - the range beam.

The simulation assumes an infinite ground plane, which can slope in a defined direction. To obtain the doppler frequencies for the velocity beams, the following is used:

$$f_d = \frac{2 V_{B4}}{\lambda}\tag{A16}$$

APPENDIX A

where

V_{B1} = beam velocity;

λ = wavelength.

To obtain the range beam frequency,

$$f_R = K \times R + \frac{2 V_{B4}}{\lambda} \quad (A17)$$

where K = scale factor corresponding to the range transmitter frequency modulation.

Signal characteristics (block B)..- This description pertains to block B of figure A10; the calculations are in regard to the signal spectrum characteristics, bandwidth and power level, the proportion of received power in the tracker step low pass filter (SLPF), and the power level required by the threshold circuitry (as determined by the tracker output).

Incidence angle: The incidence angle of each beam is calculated in the following manner:

$$\bar{\mu}_{Ij} = \underline{A}^T \underline{B}_j \bar{\mu}_{Bj} \quad j = 1, 2, 3, 4 \quad (A18)$$

$$\cos \theta_j = \bar{\mu}_{Ij} \cdot \bar{\mu}_N \quad (A19)$$

where \underline{A}^T , \underline{B}_j , μ_{Bj} , and θ_j , μ_{Ij} , μ_N are as previously defined for eq. (A15); the subscript here refers to the calculation being made for each of the radar antenna beams.

Radar cross section: The radar cross section as seen by each beam in illuminating the terrain is calculated for use in the radar range equation. The reflectivity model used is based on the Muhleman equation (ref. A11) given below:

$$\sigma_o(\theta) = \frac{\eta \kappa \cos \theta}{(\sin \theta + \alpha \cos \theta)^3} \quad (A20)$$

where

α, κ = wavelength dependent;

η = reflectivity compared with a perfect reflecting sphere;

θ = incidence angle;

$\sigma_o(\theta)$ = cross section per unit surface area.

An example of three reflectivity models (ref. A12) is given in figure A12. Curve 2 was used for all analyses and the simulation described in this report, i.e., $\alpha = 0.035$, $\kappa = 0.037$, and $\eta = 0.063$. Radar evaluation is extremely dependent on the reflectivity model that is used, this is brought out in the Monte Carlo results (section 5) and the simulation results (section 6). It is very desirable to further investigate this area.

Radar range equation: The radar range equation that is used in this simulation to calculate power received at the antenna is given by the following:

$$P_R = \frac{\sigma_o K P_t G_o \lambda^2}{(4\pi)^2 R^2 \cos \theta} \quad (A21)$$

where

σ_o = cross section per unit surface area;

K = antenna pattern parameter;

P_t = transmitter power;

G_o = two-way antenna gain;

λ = wavelength;

R = slant range;

θ = incidence angle;

P_R = received power.

APPENDIX A

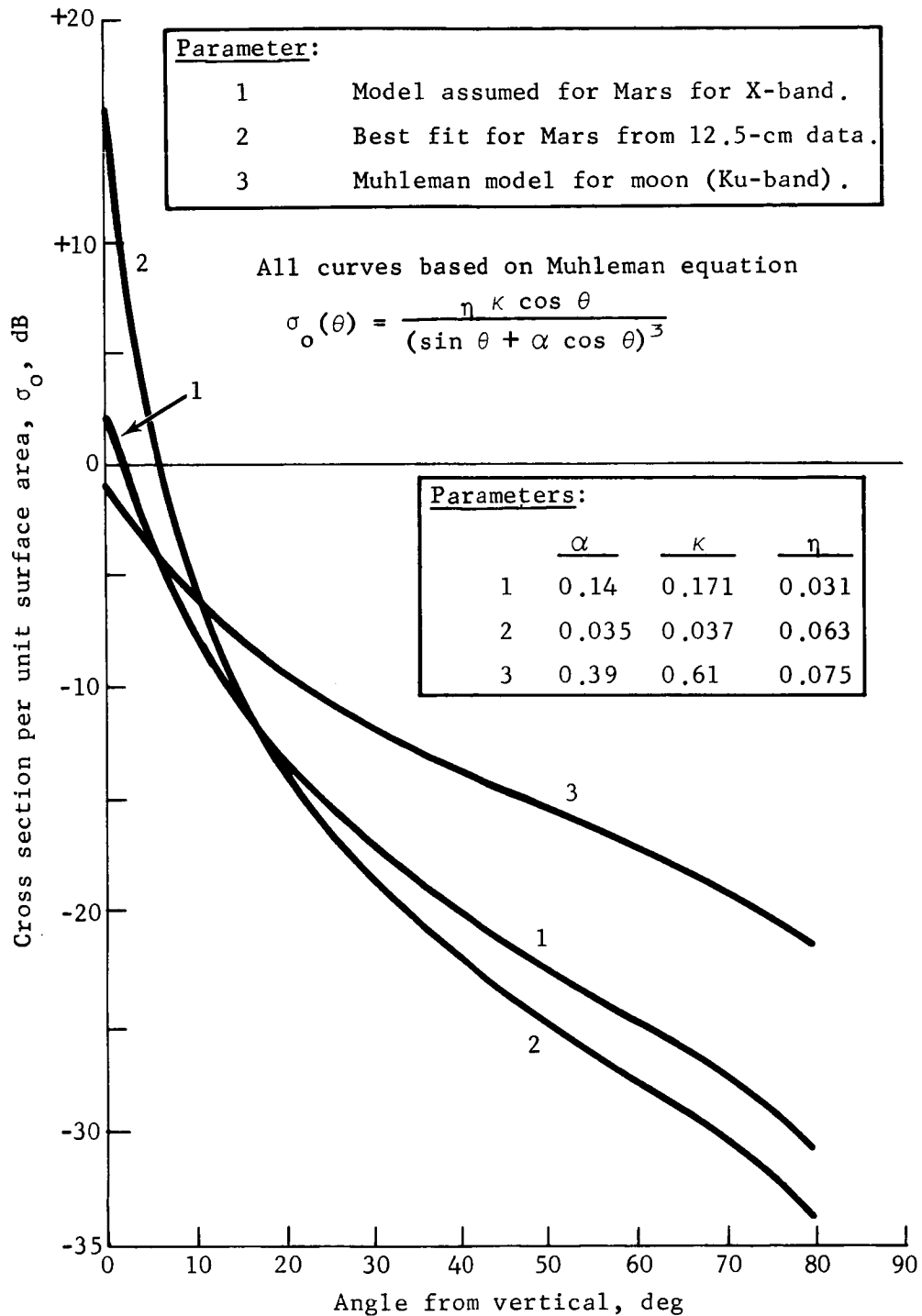


Figure A12.- Reflectivity Models

APPENDIX A

The parameters used in the simulation representing the LM radar (ref. A13) are given in table A3.

TABLE A3.- PARAMETERS USED IN SIMULATION REPRESENTING
THE LM RADAR

Parameters	Range	Velocity
Transmitter power	-14.1 dBw	-13. dBw
Waveguide loss	-1.8	-1.8
Pattern parameter	-6.0	-6.0
Antenna gain	27.2	28.2
Wavelength	-19.8	-20.6

It becomes necessary to determine the signal power that is seen by the tracker for the sake of comparing it to the tracker threshold. The spectrum seen by the tracker may be modified somewhat due to lag of the tracker output. That is, the tracker step low pass filters (SLPF) may, in effect, due to high tracking rates, straddle the incoming doppler spectrum as shown in figure A13.

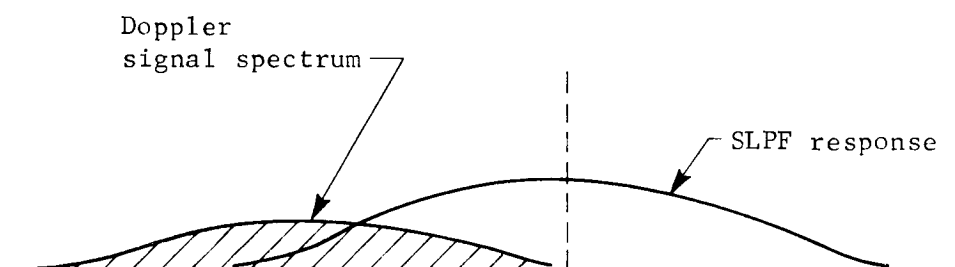


Figure A13.- Spectrum Overlap Due to Tracking High Rates

When this situation is detected in the simulation the power received as calculated by the range equation is modified by the following:

$$P_{RT} = P_R + 10 \log \frac{\Delta BW}{BW_S} \quad (A22)$$

APPENDIX A

where

P_R = power received, dBw;

ΔBW = that portion of the signal spectrum appearing in the tracker SLPF bandwidth when both bandwidths are idealized as shown in figure A14;

BW_S = doppler signal spectrum 3-dB bandwidth.

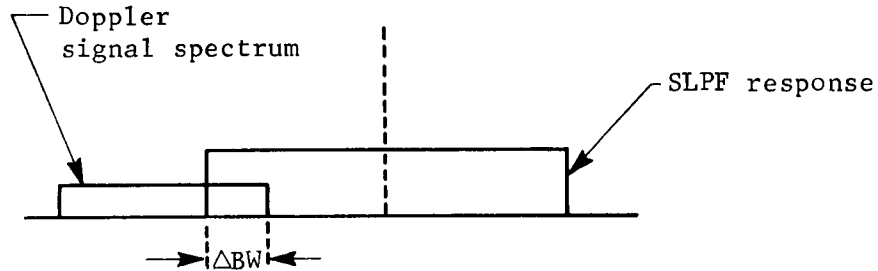


Figure A14.- Idealized Spectrums

Signal bandwidth: The doppler signal spectrum bandwidth (ref. A14) is calculated as follows:

$$\Delta f_d = \frac{2\Delta\gamma}{\lambda} |\bar{V}_B| \sin \gamma \quad (A23)$$

where

$\Delta\gamma$ = the average antenna 3-dB beamwidth;

$|\bar{V}_B|$ = vehicle total velocity;

γ = the angle between the beam centerline and the velocity vector.

The spectrum bandwidth is taken to be proportional to the component of velocity perpendicular to the beam pointing direction as modified by the 3-dB beamwidth of the antenna. The spectrum shape is taken to be Gaussian.

APPENDIX A

Tracker threshold level: The simulation made use of the receiver sensitivity curves (ref. 13) shown in figures A15 thru A18 to determine the adequacy of signal to noise ratio required for tracking (referred to the antenna). Figure A15 is the velocity receiver sensitivity for the wideband mode of operation. This curve can be used as described -- a doppler spectrum centered at 5000 Hz with a bandwidth of 390 Hz and power level (as calculated by the radar range equation and modified by the amount of spectrum overlap in the SLPF) exceeding -139 dBw -- satisfies the track criteria. Figure A16 shows the velocity receiver sensitivities applicable for low mode operation of the radar. Figure A17 presents the range receiver sensitivities. The curves shown in figures A15 thru A17 were originally derived for LM radar test requirement. Figure A18 is the velocity receiver sensitivity for wideband operation given the suggested change in bandwidth of SLPF response during this mode, i.e., from current 2800 to 600 Hz. The curves shown in figures A15 thru A18 were curve fit with straight line segments for use in the digital simulation. Each of the curves is then represented by equations of the form:

$$P_{TH} = g(f_{dt}, f_{Rt}) \quad (A24)$$

where

P_{TH} = threshold tracking criteria referenced to the antenna, dBw;

f_{dt}, f_{Rt} = tracker output frequency, doppler and range channel, respectively.

Mode switch (block C)..- The mode switching is based on range and velocity tracker outputs, and affects the SLPF bandwidths, tracker search limits, search rates, range scale factor, and receiver sensitivity. Table A4 describes the mode switching criteria. The criteria numbered 1, 2, 3, and 4 in table A4 apply for the LM radar mode switching criteria as it presently exists (ref. A13), and the criteria numbered 1-a, 2-a, 3-a, and 4-a apply for the suggested mode criteria change, i.e., from 2500 to 1250 ft. Both criteria were evaluated via analysis and in the simulation.

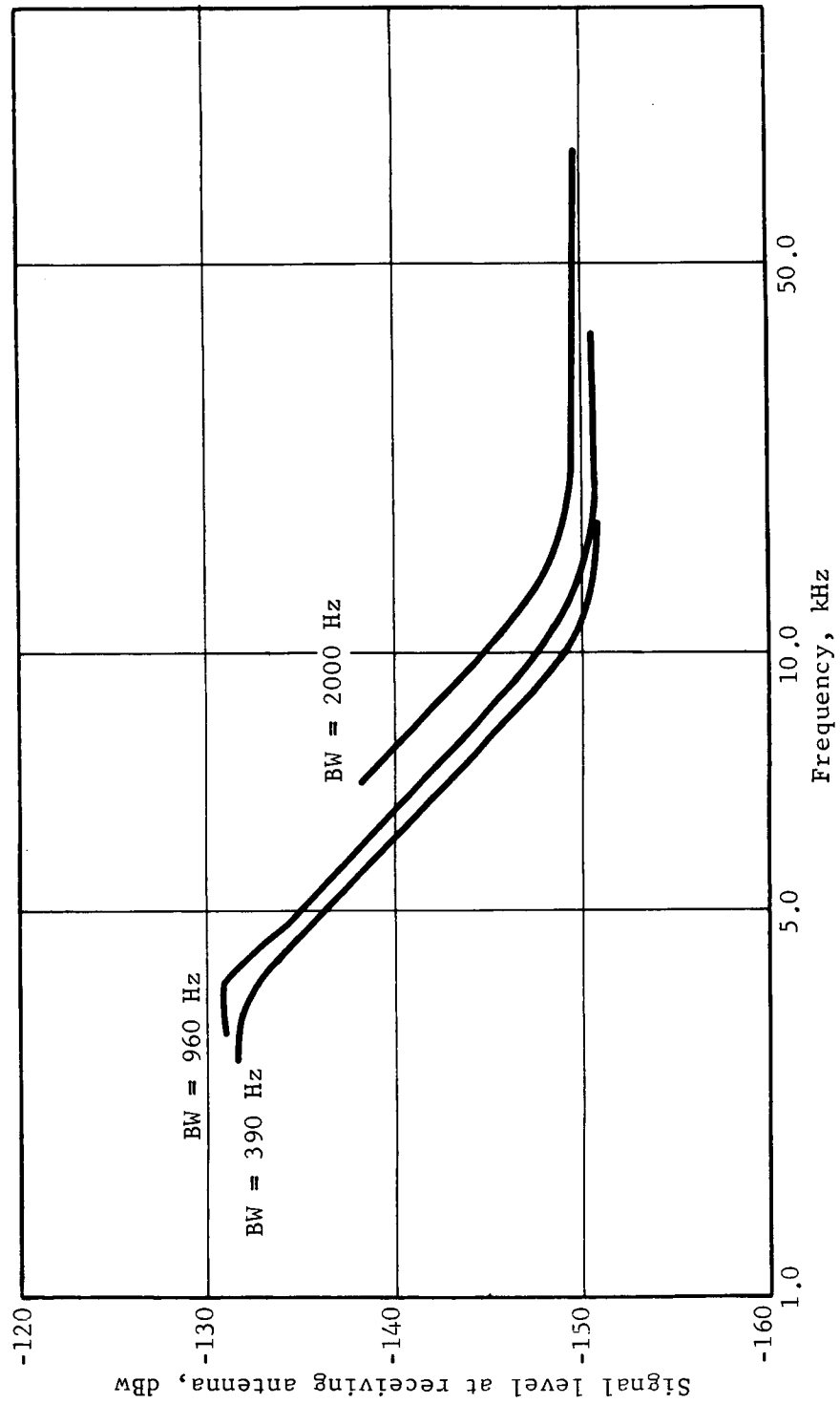


Figure A15.- Velocity Receiver Sensitivity, Wideband Mode

APPENDIX A

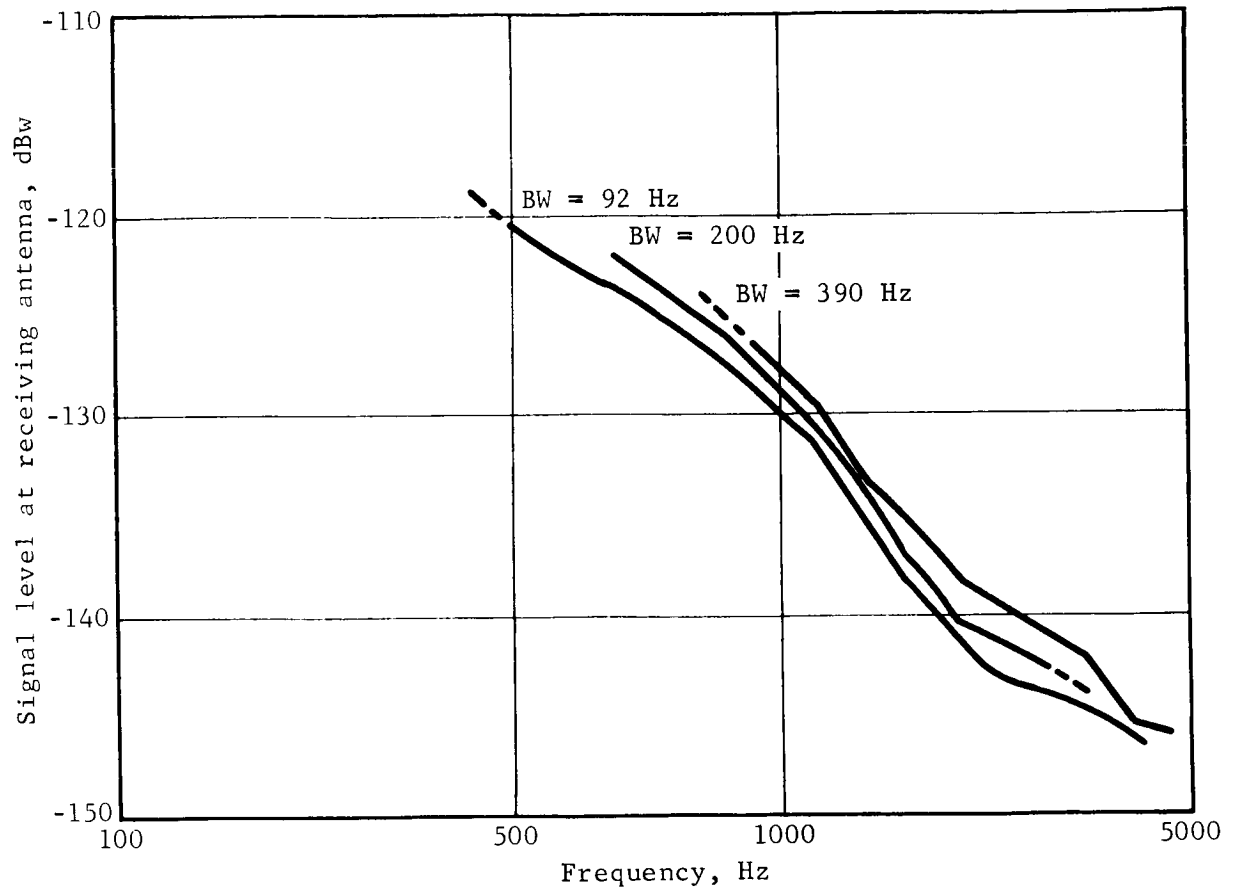


Figure A16.- Velocity Receiver Sensitivity, Narrowband Mode

APPENDIX A

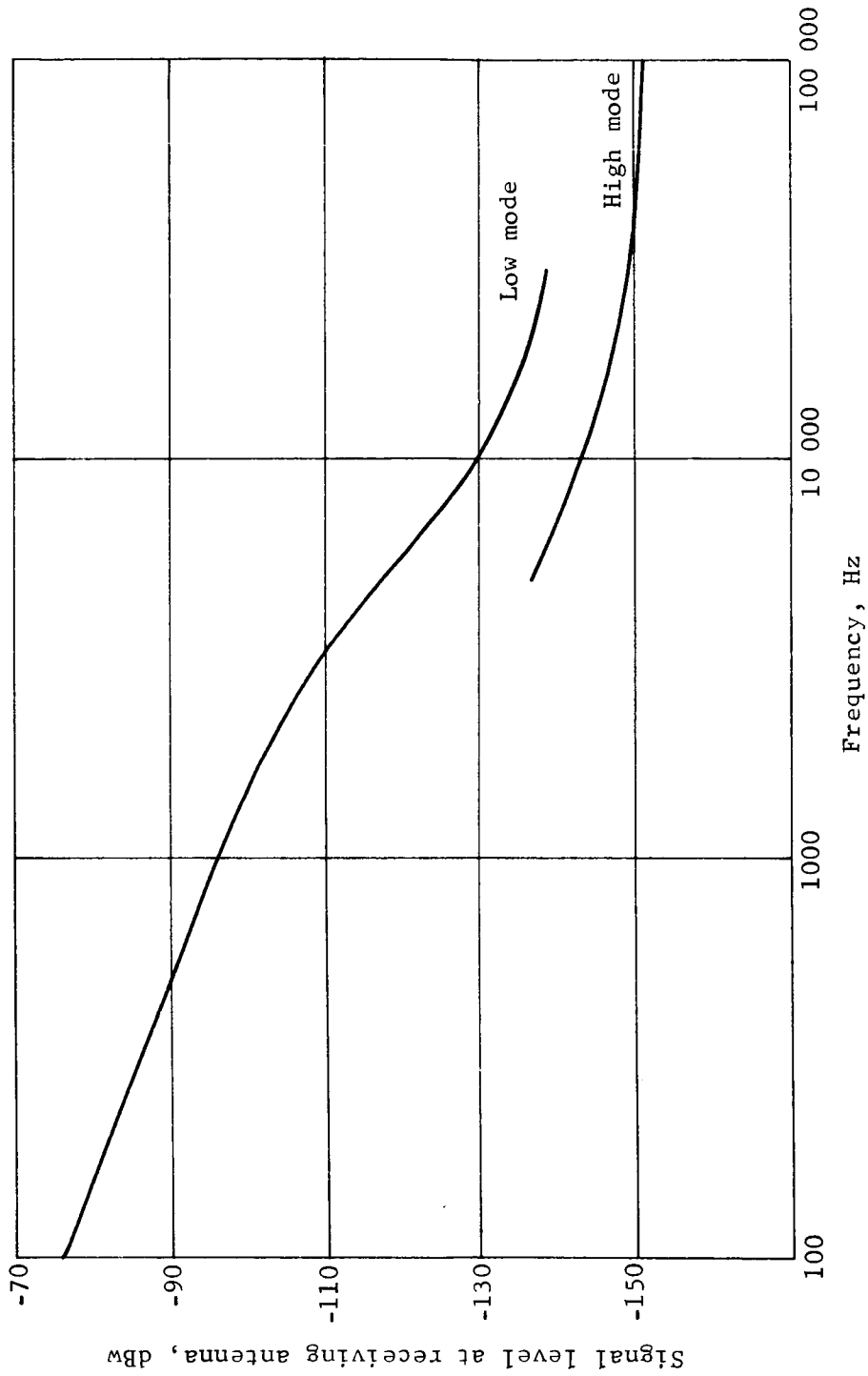


Figure A17.- Range Channel Acquisition Sensitivity

APPENDIX A

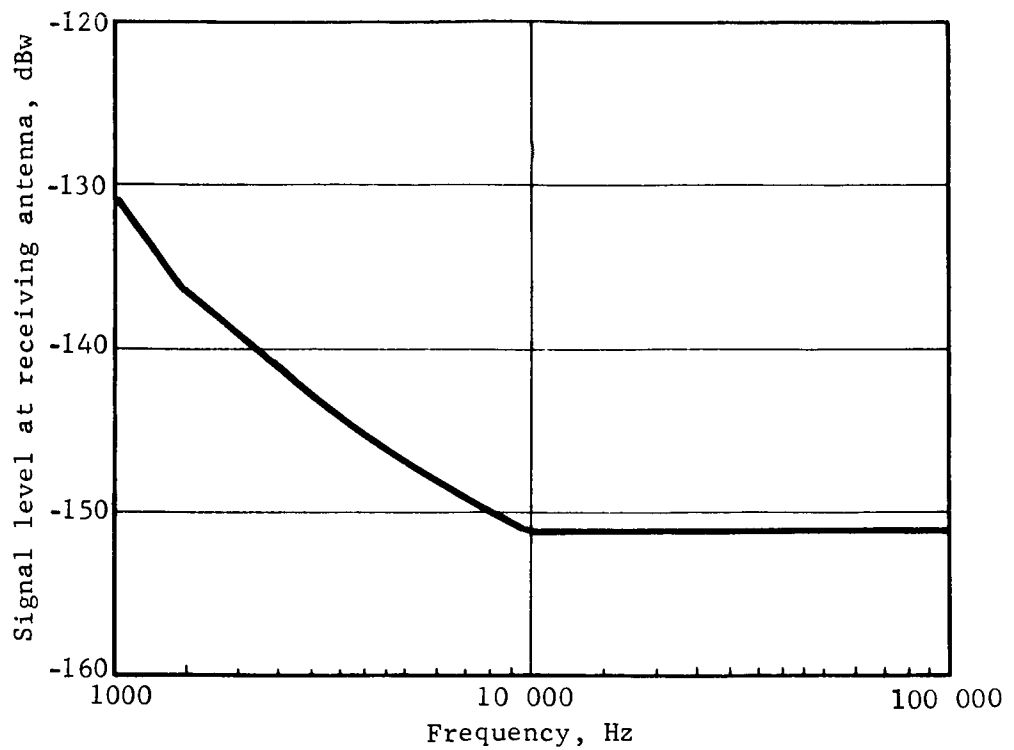


Figure A18.- Velocity Receiver Sensitivity, Wideband Mode
(Modified SLPF Bandwidth of 600 Hz)

TABLE A4.- MODE SWITCHING CRITERIA

Criteria	Mode
1. Range < the frequency equivalent of 2500 ft 1-a. Range < the frequency equivalent of 1250 ft	Low mode throughout the system
2. Range > the frequency equivalent of 2500 ft 2-a. Range > the frequency equivalent of 1250 ft	High mode except the velocity in any individual velocity tracker between the equivalent frequency limits of ± 65.5 fps will switch the SLPF bandwidths to the low mode equivalent in that channel
3. If low mode has been achieved, then: Range > the frequency equivalent of 3100 ft 3-a. If low mode has been achieved, then: Range > the frequency equivalent of 1850 ft	High mode applies as described above.
4. Mode inhibit if the range beam or either of its compensating beams are in search mode 4-a. Same as 4.	Status quo

Noise generator (block D).- The statistical characteristics of the tracker output are obtained by adding the appropriate jitter or noise to the doppler and range frequencies f_d and f_R .

The standard deviation and time constant of the noise are a function of the doppler spectrum bandwidth (ref. A14), and, therefore, a function of velocity as described by the following:

$$\sigma = \frac{BW_S}{2} \quad (A25)$$

APPENDIX A

$$\tau = \frac{1}{\pi BW_S} \quad (A26)$$

where

σ = rms level of the frequency jitter;

τ = the time constant of the noise.

It was assumed that the noise is Gaussian. Another assumption was that the range signal spectrum took on the characteristics of the doppler spectrum seen by the range beam. The accuracy of this assumption requires further investigation; however, it is felt to be a reasonable assumption. Each of the velocity channels and the range channel has its own noise generator producing the variations on respective signals according to the parameters defined by eqs. (A25) and (A26).

Bias (block E)..- Although the simulation has the capability to add biases to the signals, as is indicated in figure A10, no runs were made with biases because the outcome is predictable and is not a problem in any sense.

Tracker (block F)..- The closed loop transfer function of the tracker is represented by a first-order lag, i.e.,

$$1/(1 + \tau S) \quad (A27)$$

where $0.05 < \tau < 0.07$. The closed loop time constant τ of the tracker is specified to be within the limits shown in eq. (A27) (ref. A13). The mean of this range has been used in the simulation to date, $\tau = 0.06$.

Threshold and search control (block G)..- The threshold circuit indicated in this block merely takes the threshold power level criteria indicated from the sensitivity curves, eq. (A24) and compares it with the received power indicated in the tracker, eq. (A22). Then the functions described in table A5 are carried out depending on the results of the comparison just described and the current state of the tracker.

The 0.5-sec lockout time mentioned in tracker state 2 of table A5 refers to the time allowed the tracker to observe the signal, while it is below the threshold power level, before initiating search. The 0.1 sec mentioned in tracker state 4 of table A5 is the time that the received signal must remain above threshold (during search mode) before normal track is initiated.

TABLE A5.- FUNCTIONS TRIGGERED AS A RESULT OF THRESHOLD CRITERIA

Tracker state	Threshold criteria	Function
1. Tracking	$P_{RT} > P_{TH}^a$	Continue tracking
2. Tracking	$P_{RT} < P_{TH}$	Commence 0.5 sec lockout. If $P_{RT} > P_{TH} - 3 \text{ dBw}$, the tracker is held at the last value it had during the lockout time. If $P_{RT} < P_{TH} - 3 \text{ dBw}$, the tracker continues tracking during the lockout time.
3. Search	$P_{RT} < P_{TH}$	Continue search
4. Search	$P_{RT} > P_{TH}$	Commence 0.1 sec proof time.
^a P_{RT} = received power seen by the tracker as referred to the antenna; P_{TH} = receiver threshold sensitivity as referred to the antenna.		

Search control: The search mode of operation occurs in the simulation on an individual channel basis according to the radar mode with limits and rates described in table A6 as per existing LM radar and table A7 with the suggested changes to these parameters. Flyback requires 0.2 sec for all beams regardless of radar mode and is, therefore, not shown in the chart. Flyback refers to driving the tracker VCO from its low limit of search range to the high limit of the search range.

Channel status: The status of output data is flagged in the following manner: if all velocity channels are tracking, a discrete is initiated indicating same; if the range beam and its velocity compensating beams are tracking, a discrete is also available indicating this. These two discrettes are current LM radar data flags. A suggested change, and presently used in the simulation, is a discrete for each individual channel indicating a tracker lock or search condition.

TABLE A6.- LM RADAR EXISTING SEARCH RATES AND LIMITS

Beam	Radar mode	Search limits	Search rates
1 and 2	High	-41.5 kHz < f < 52.4 kHz	27.4 kHz/sec for 1.44 kHz < f < 52.4 kHz 2.3 kHz/sec for -1.44 kHz < f < 1.44 kHz 27.4 kHz/sec for -41.5 kHz < f < -1.44 kHz
3	High	-20.3 kHz < f < 77 kHz	26.4 kHz/sec for 1.44 kHz < f < 77 kHz 2.3 kHz/sec for -1.44 kHz < f < 1.44 kHz 26.4 kHz/sec for -20.3 kHz < f < -1.44 kHz
1, 2, and 3	Low	-5.24 kHz < f < 7.4 kHz	2.3 kHz/sec
4	High	830 Hz < f < 141.6 kHz	25.6 kHz/sec
4	Low	830 Hz < f < 38.5 kHz	6.85 kHz/sec

TABLE A7.- SEARCH LIMITS AND RATES PROPOSED FOR THE MODIFIED LM RADAR

Beam	Radar mode	Search limits	Search rates
1, 2, and 3	High	0 < f < 12. kHz	2.3 kHz/sec for f < 1.44 kHz 6.6 kHz/sec for 1.44 kHz < f < 12. kHz
1, 2, and 3	Low	0 < f < 6. kHz	2.14 kHz/sec
4	High	1 kHz < f < 66. kHz	23.2 kHz/sec
4	Low	1 kHz < f < 19. kHz	6.4 kHz/sec

Data output (block H)..- The velocity tracker outputs are converted to body axis velocities by the following relationships:

$$V_u = \frac{\lambda}{4 \cos \Lambda \cos \zeta} (D_1 + D_3) \quad (A28)$$

$$V_v = \frac{\lambda}{4 \sin \Lambda} (D_1 - D_2) \quad (A29)$$

$$V_w = \frac{\lambda}{4 \cos \Lambda \sin \zeta} (D_2 - D_3) \quad (A30)$$

where

λ = wavelength;

Λ, ζ = beam configuration angles as defined in figure A11, $13^\circ 59' 22''$ and $20^\circ 22' 48''$;

D_1, D_2, D_3 = doppler frequencies of beams 1, 2, and 3, respectively;

V_u, V_v, V_w = body axis velocities as described in figure A11.

The velocity trackers of beams 1 and 3 are used to correct the velocity component of the beam 4 range tracker output by the following relationship:

$$R = \frac{f_R - \frac{\lambda_1}{2 \lambda_2} (D_1 + D_2)}{M_K} \quad (A31)$$

where

f_R = range tracker output;

M_K = range scale factor,

2.32, high mode,

11.6, low mode;

R = range along the u axis (see fig. A11);

λ_1 = range transmitter wavelength;

λ_2 = velocity transmitter wavelength.

APPENDIX A

For the simulations of section 6 the radar outputs were filtered by analog filters with time constants of 0.5 sec. in the lateral velocity channels, 0.1 sec. in the axial velocity channel, and 0.08 sec. in the range channel. For the purpose of comparing the simulation with Ryan Aeronautical Co. error analysis data, 0.2 sec. time constants were used on all channels.

5. ANALYTICAL STUDY RESULTS

Three conditions exist that may cause velocity or range beam unlocks -- (1) incidence angle, a combination of vehicle attitude and ground slope, (2) zero doppler dropout due to receiver noise compensation by receiver preamp at low frequency, and (3) tracking rate, i.e., loss of signal due to high tracking rates. The curves shown in figures A19 thru A22 indicate some of the conditions in which dropout would occur.

Figure A19 indicates a region termed zero doppler dropout as a function of perpendicular distance to the terrain; a velocity beam incidence angle of 35° was used. Because of threshold dependence on velocity, there is some minimum velocity below which the tracker can no longer function. This curve would move to the left with higher incidence angles.

Figure A20 indicates velocity beam dropout incidence angles as a function of velocity and perpendicular distance to the terrain. These curves were generated using the wideband receiver sensitivity curves. Figure A21 presents similar curves for the range channel, and figure A22 is the same type of data using receiver sensitivity curves suggested for the wideband SLPF change.

These curves are intended to illuminate the more detailed analysis results to follow. The curves shown assume static conditions. The tracking rate analysis to follow accounts for a dynamically changing signal. The Monte Carlo results calculate beam dropout probabilities considering random number selections of the random variables of surface slope, wind, and gusts.

Tracker Rate Analysis

As the tracker lags the signal due to a large rate of change of velocity (velocity channel) or range and velocity (range channel), the signal spectrum may become straddled by the step low pass filter (SLPF) of the tracker to the extent that the signal power drop in the SLPF will be sufficient to cause breaklock. Two situations exist during descent that will cause extreme tracking rates -- (1) when the vehicle is swinging on the parachute due to wind gusts, and (2) during the vehicle pitchup maneuver (to null cross velocities).

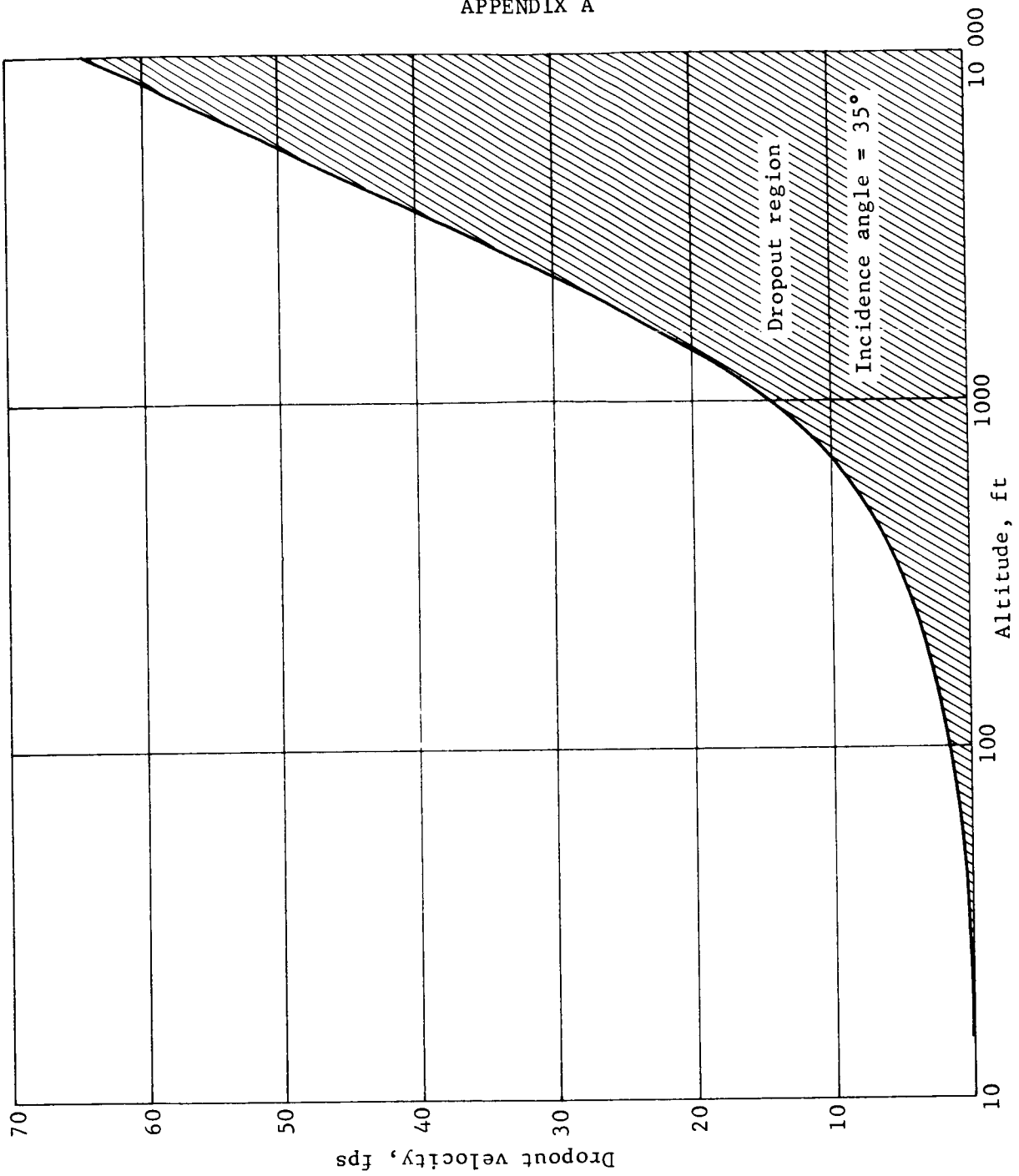


Figure A19.- Velocity Beam Zero Doppler Dropout Velocity vs Altitude for Fixed Incidence Angle

APPENDIX A

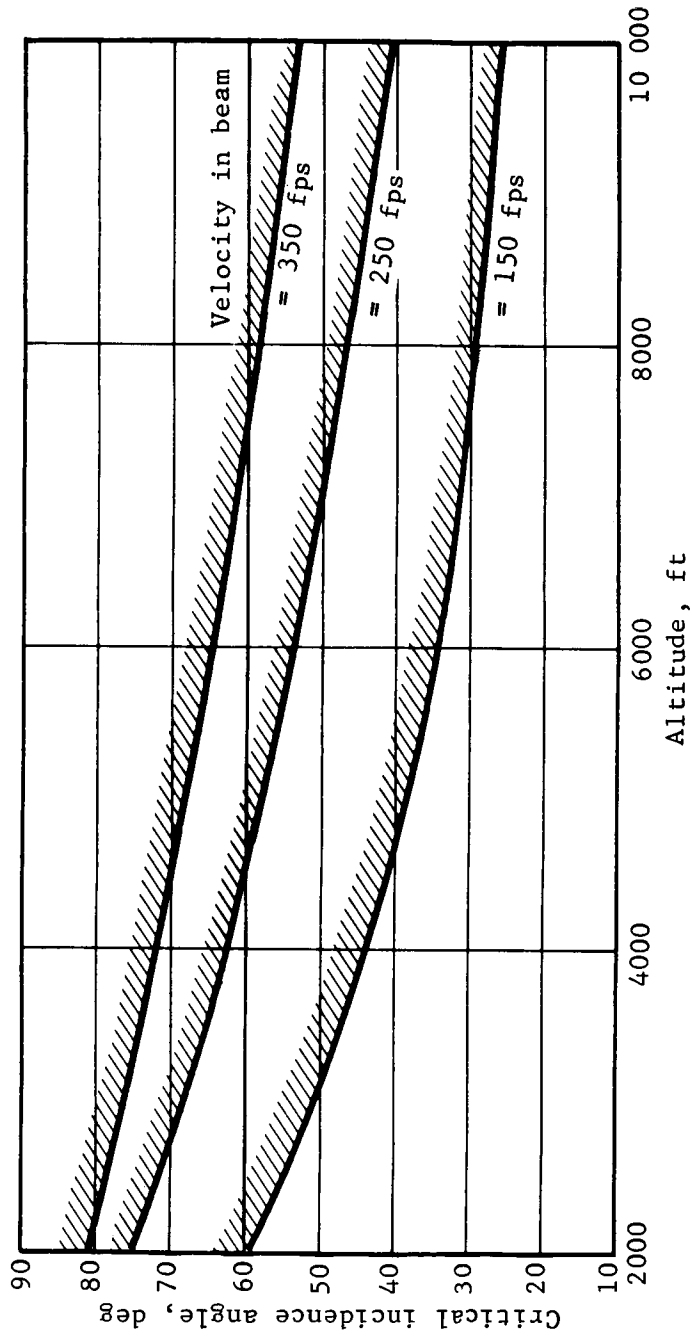


Figure A20.- Critical Incidence Angle for Velocity Channel, LM Radar

APPENDIX A

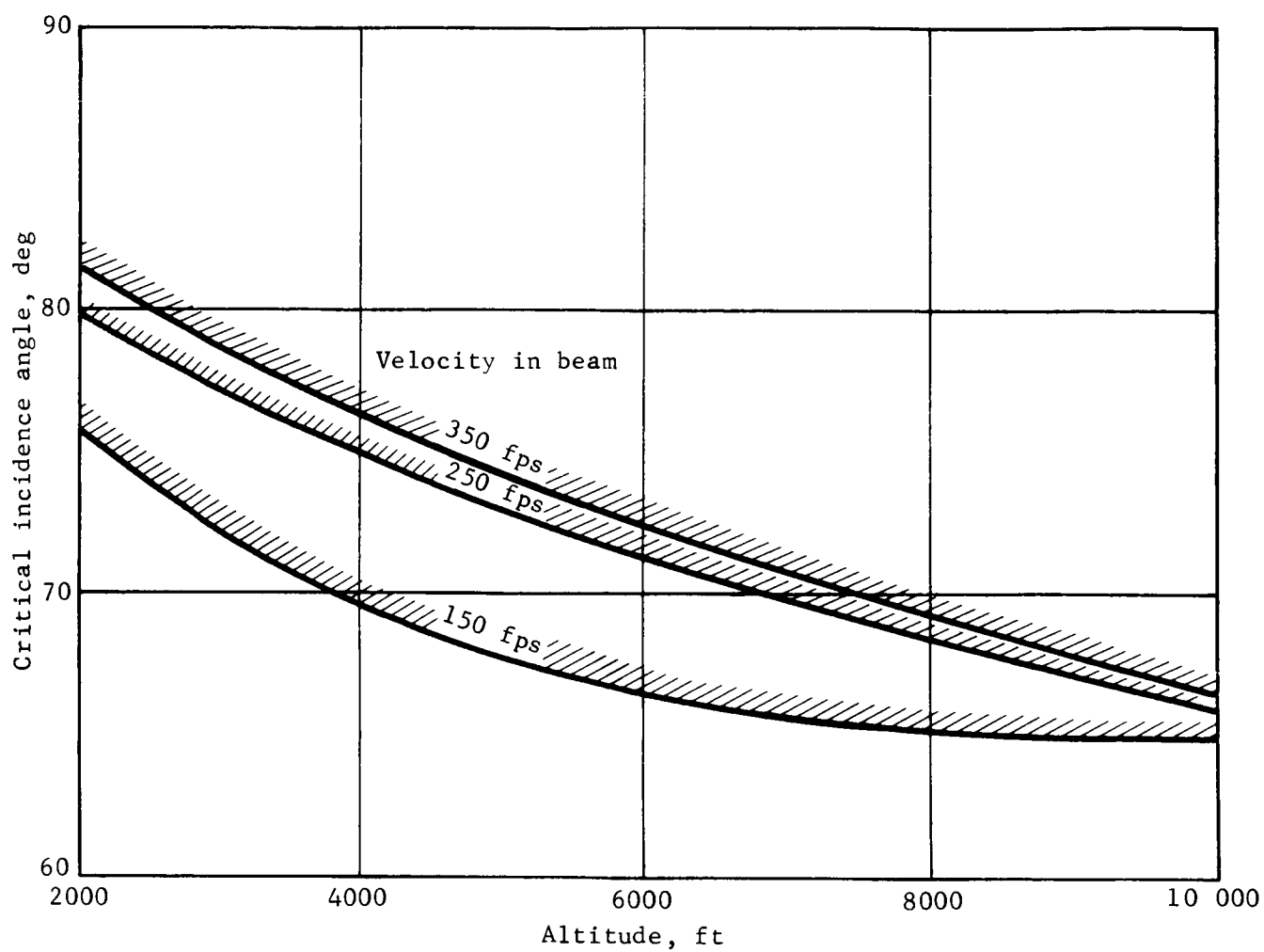


Figure A21.- Critical Incidence Angle for the LM Radar Range Channel

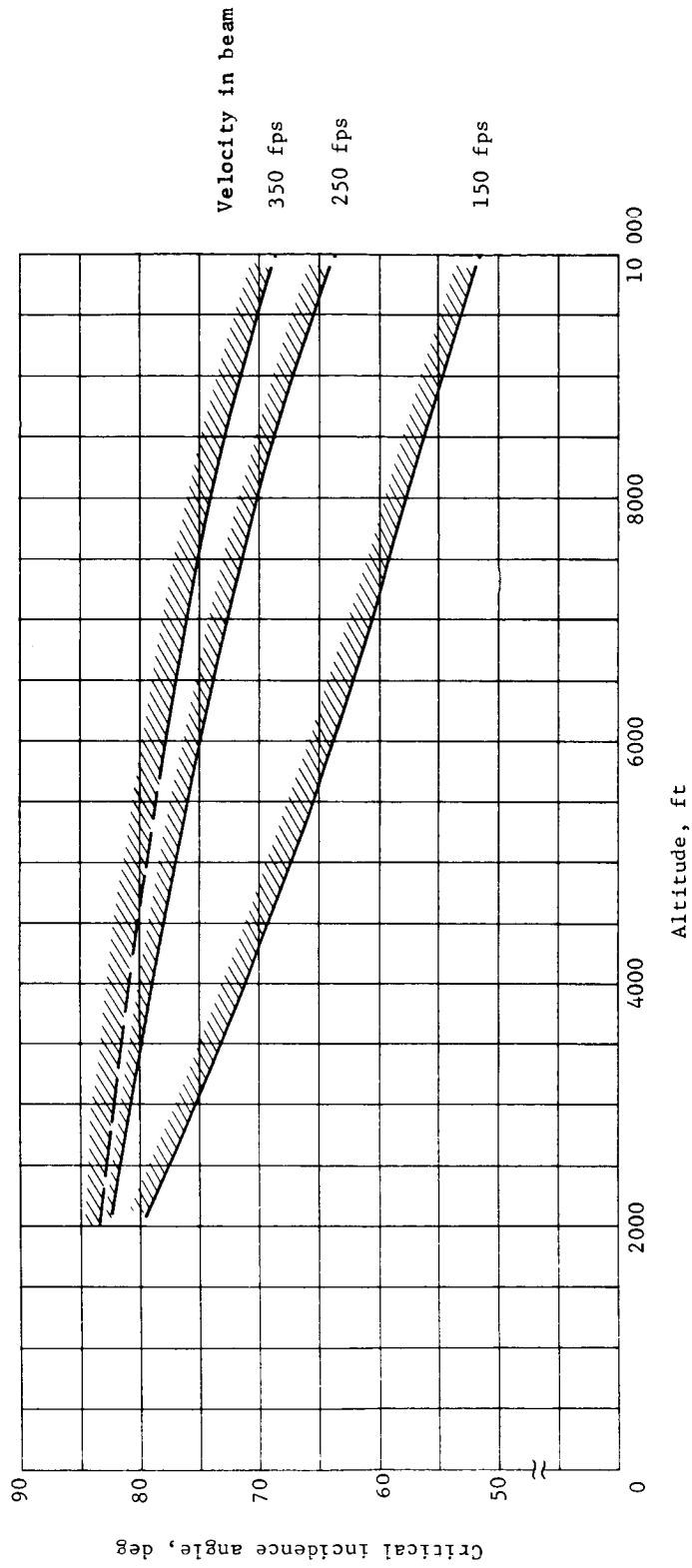


Figure A22.- Critical Incidence Angle for Velocity Channel, Modified LM Radar

APPENDIX A

The two situations just described were modeled in an uncomplicated manner for a worst-case gust condition (for the parachute condition) and worst-case pitch rate (for the pitchup maneuver) to determine whether the radar would break lock under these severe conditions. The following tabulation notes the cases examined analytically.

	Velocity channel		Range channel	
	High	Low	High	Low
Pitchup	x	x	x	x
Parachute	x	Does not exist	x	Does not exist

The analysis was first performed using original LM radar parameters, and two of the combinations listed in the tabulation indicated a break lock condition, this was in the range channel, low and high mode, during the pitchup maneuver. Latter analysis considering the mode switch to be at 1250 ft (high-to-low mode range criterion) and 1850 ft (low-to-high mode range switch criterion) indicated that the above low-mode break lock condition will not exist, i.e., pitchup will occur well above this altitude. Corresponding LM radar original switching criteria are 2500 and 3100 ft, respectively. In addition, the suggested change in high-mode velocity channel SLPF bandwidth (2800 to 600 Hz) was evaluated with regard to tracking rate and it was determined to be no problem.

The analysis was accomplished using the IBM 1130 computer, the models are described briefly as follows with some example results shown.

For the pitchup maneuver, the following geometry was used (fig. A23).

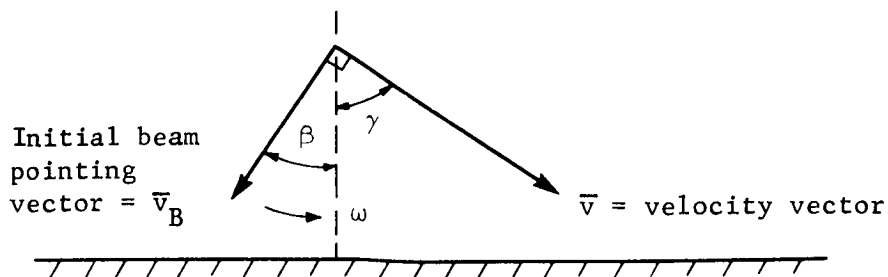


Figure A23.- Pitchup Model

APPENDIX A

The pitchup was assumed to occur over a full 90° , i.e., so that a beam is initially 90° from the velocity vector and is pitched at an angular rate (ω) toward the velocity vector. This situation produces the fastest change in doppler frequency. The change in velocity and range due to thrust and aerodynamics during the maneuver was assumed to be negligible. The tracker closed-loop time constant was taken to be 0.07 sec. As the beam is swept toward the velocity vector in the pitchup maneuver, the power received is calculated and compared with the appropriate threshold, which is frequency dependent.

Figure A24 is a block diagram of the simulation used to evaluate the tracking rate effects. The dynamics and equations are the same as those described in section 4. The output easily distinguishes a break lock due to zero doppler, incidence angle, and tracker lag.

Some example results are shown in the curves of figures A25 and A26.

Figure A25 indicates the velocity tracker lag during a typical wind gust condition causing a vehicle attitude change as shown. Figure A26 demonstrates range tracker lag during the tipup maneuver (vehicle attitude rate was $30^\circ/\text{sec}$). The tracker broke lock soon after the beam passed 61° incidence angle. It is seen (section 6) that runs 2, 3, and 6 broke lock in the range channel during pitchup with 3σ environmental conditions. Further investigation is required to determine a pitch rate that can be tolerated without a range beam unlock under 3σ conditions.

Error Analysis

The noise model (ref. A14) defining the statistical characteristics of the doppler frequency is given in eqs. A32 thru A34.

$$BW = \frac{2}{\lambda} |\bar{V}| (\Delta\gamma) \sin \gamma \text{ Hz} \quad (\text{A32})$$

$$\sigma_{fd} = \frac{BW}{2} \text{ Hz} \quad (\text{A33})$$

$$\tau = \frac{1}{\pi BW} \text{ sec} \quad (\text{A34})$$

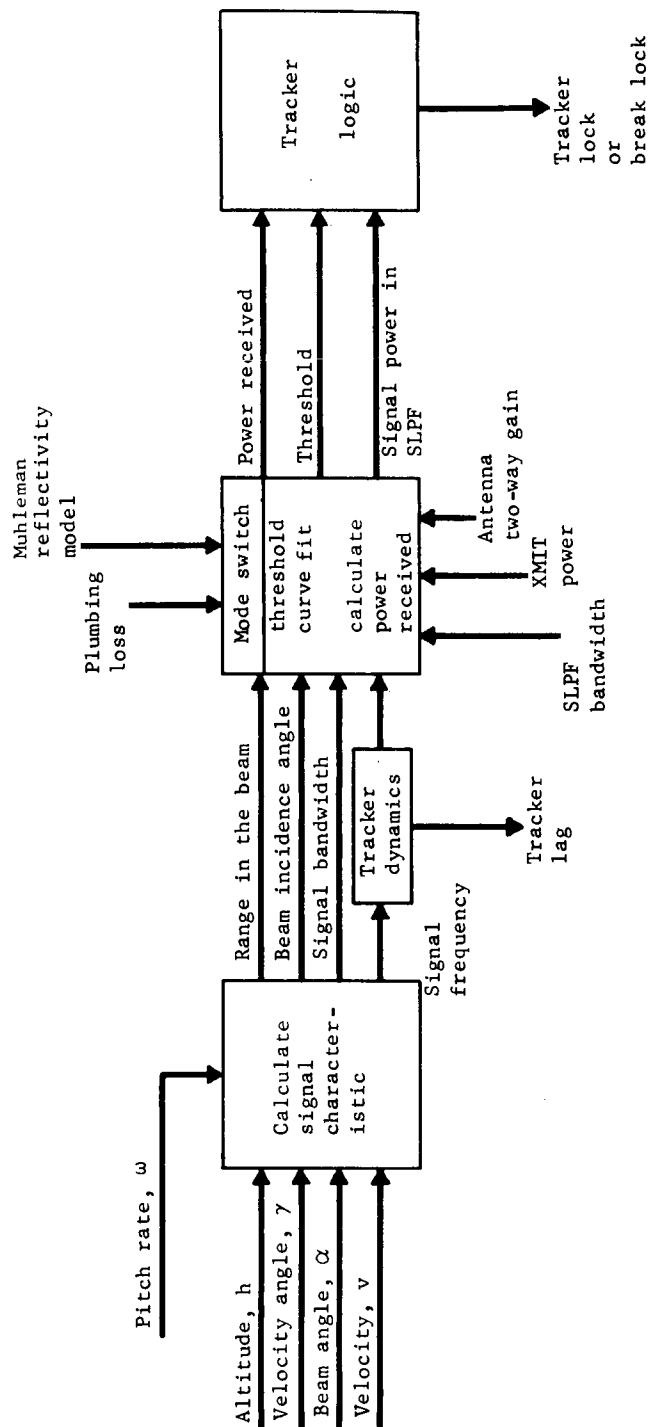


Figure A24.- Tracking Rate Analysis Block Diagram

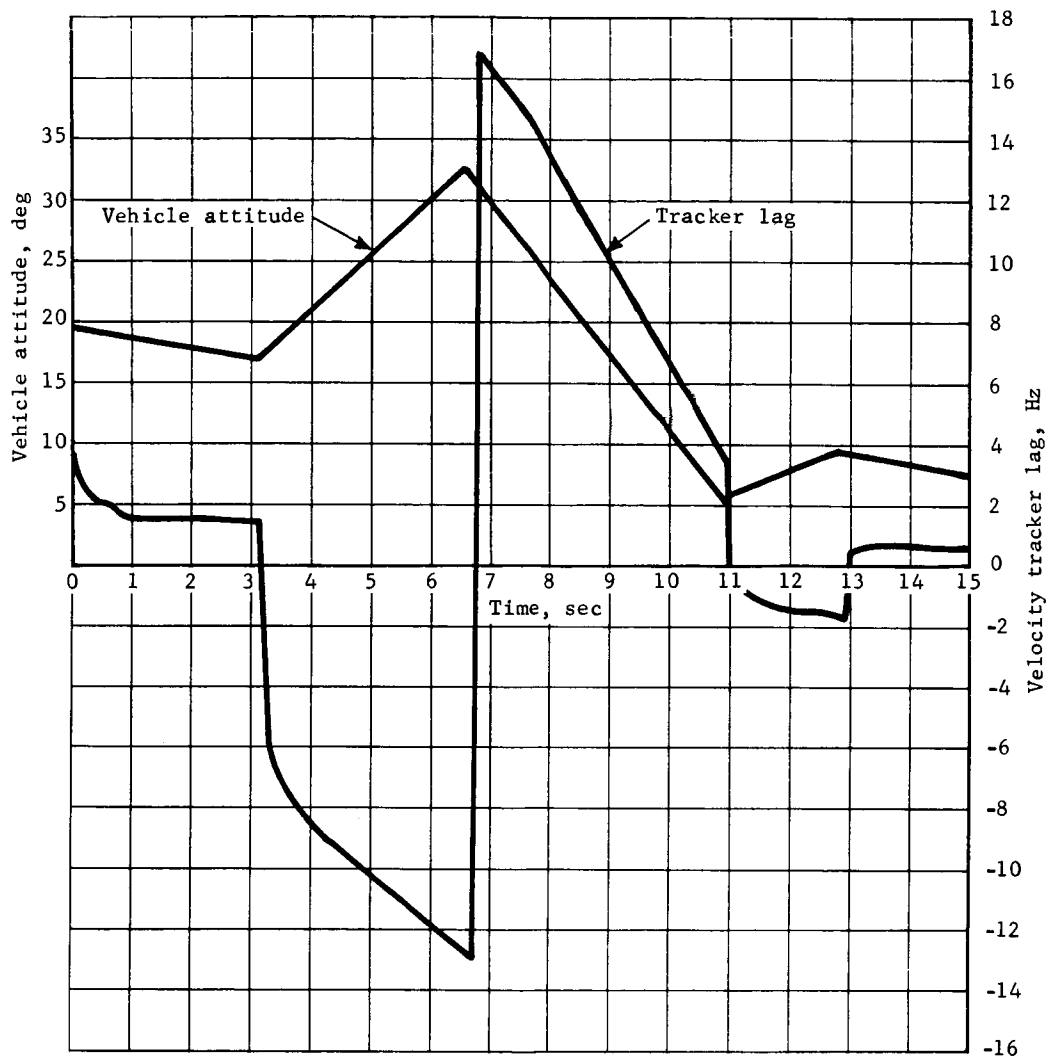


Figure A25.- Vehicle Attitude as a Function of Wind Gust
and the Resulting Lag in the Velocity Tracker

APPENDIX A

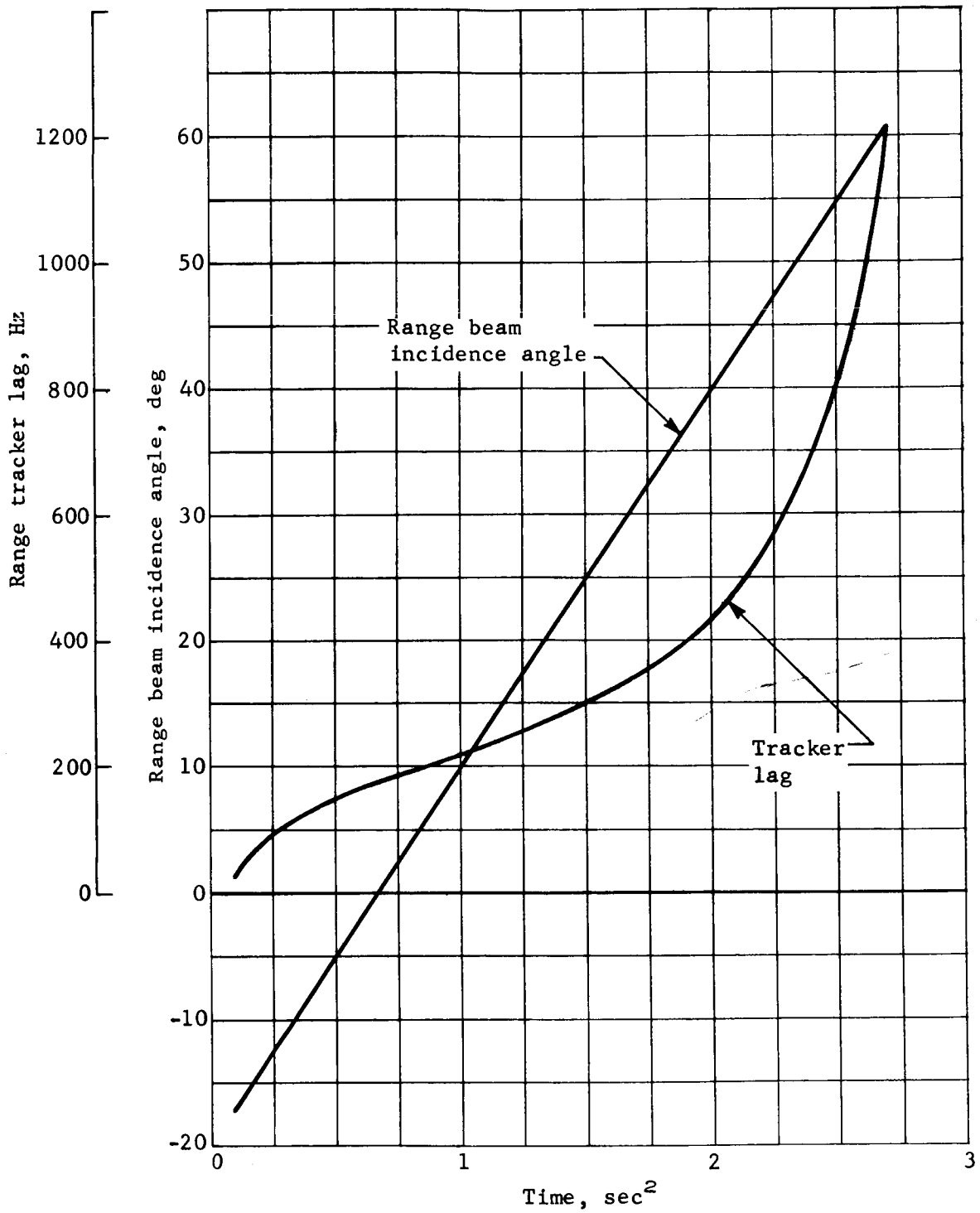


Figure A26.- Range Tracker Lag during Tipup
($\omega = 30^\circ/\text{sec}$, Altitude = 4000 ft,
Velocity = 250 fps)

APPENDIX A

where

- $|\bar{V}|$ = vehicle velocity magnitude;
- $\Delta\gamma$ = antenna beamwidth;
- γ = angle between \bar{V} and the antenna beam line of sight.

It is assumed that the probability density function of frequency about the mean doppler frequency is **Gaussian**. The effects of the doppler noise on the system has been evaluated in several ways -- (1) modeling the noise for the six degree of freedom simulation as described in section 4, (2) determining the effect on particular vehicle parameters in an rms sense, and (3) calculation of the effects on body axis velocities.

The noise as it effects system variables has been investigated using the following relationship (ref. A15):

$$\sigma_x^2 = \frac{1}{2\pi} \int_{-\infty}^{\infty} |G(j\omega) N(j\omega)|^2 d\omega \quad (A35)$$

where

- $G(j\omega)$ = control system transfer function;
- $N(j\omega)$ = power spectral density of the noise source;
- σ_x^2 = mean squared value of x .

Equation (A35) requires the closed loop transfer function between the noise as input and the location of the variable of interest as the output (e.g., see fig. A5). With the noise on (v) body axis velocity as the input, the closed loop transfer function $[G(s)]$ is obtained, say for yaw rate r , between v and r . The noise on (v) is defined by the coefficient of eq. (A29), i.e.,

$$\sigma_v = \sqrt{2} \sigma_{fd} \frac{\lambda}{4 \sin \Lambda} \quad (A36)$$

$$\sigma_v = k \sigma_{fd} \quad (A37)$$

APPENDIX A

The analysis was performed using the parameters of the Bessel Sideband Radar proposed in the Voyager Phase B Study by the Martin Marietta Corporation, and the LM radar parameters. The results of this investigation are shown in table A8, and the parameters used are shown in table A9.

TABLE A8.- NOISE EFFECT ON SYSTEM VARIABLES

Variable	LM radar (1 σ values)		Bessel sideband radar (1 σ value)	
	V = 10	V = 350	V = 10	V = 350
Attitude rate, deg/sec	4.2	0.5	2.0	0.3
Attitude, deg	1.4	0.16	.7	0.08
Lateral velocity, fps	.3	1.0	.14	0.5

TABLE A9.- CONSTANTS USED FOR NOISE ANALYSIS

Parameter	LM radar	Bessel sideband radar
Antenna beamwidth, $\Delta\gamma$, deg	5.2	3
Wavelength, λ , ft	.09358	.0734
Angle between the velocity vector and beam, γ , deg	24.6	15
Constant, k, ft/sec/Hz	.1367	.104

The peak **values** observed for velocity noise in the lateral channel of the LM radar module of the six degree of freedom simulation (this is the worst axis with regard to noise susceptibility) were tabulated. The highest value was **2.7 ft/sec.** In addition, the peak value of attitude rate due to velocity sensor noise observed is 5.7°/sec. Both of these numbers do not seem unreasonable as compared with the analytical results of table A8. However, it is felt that the attitude rate that can occur due to velocity noise at engine cutoff will not be tolerable on a 3 σ basis; this is one reason for using a full inertial system during the final 100 ft of the descent.

APPENDIX A

The noise model used in the LM radar module of the six degree of freedom simulation was cross checked with the model used by the Ryan Aeronautical Company. That is, a statistical analysis of the noise on the body axis velocities occurring in the six degree of freedom simulation was performed. This was done by freezing the simulation at various trajectory points (allowing only the noise generators, tracker, and data conversion modules to continue running, see fig. A10) and recording the output velocities along the body axis. A statistical analysis was performed on the recorded data. The trajectory points used in the above-described procedure were given to R. Harrington, Ryan Aeronautical Company. Ryan's error analysis program for the LM radar was then used to determine the body velocity errors and range errors at these trajectory points. Table A10 summarizes the Ryan error analysis results. In addition, hand calculations were made with regard to body velocity errors due to doppler fluctuation noise. A summary of the results for all three investigation sources is shown in table A11. The correlation of results in this table is felt to be reassuring.

TABLE A10.- 3σ VELOCITY AND RANGE CHANNEL ERROR AS DETERMINED BY RYAN DURING VARIOUS PHASES OF THE MISSION

Time	Range				U axis ^a		V axis				W axis			
	Digital		Analog		Digital		Analog		Digital		Analog		Digital	
	Fluctuating	Bias	Fluctuating	Bias	Fluctuating	Bias	Fluctuating	Bias	Fluctuating	Bias	Fluctuating	Bias	Fluctuating	Bias
Vernier engine	6.8	39.7	6.8	72.7	4.4	7.13	5.27	3.67	7.13	3.6	1.22	4.15	1.66	2.12
Tipup	29.9	53.3	29.9	107.6	3.01	3.08	3.06	2.16	4.24	2.04	.81	5.23	1.13	.48
Contour	8.6	57.0	8.6	95.9	2.45	1.61	2.52	1.54	3.5	1.38	.66	3.63	.92	.35
Engine cutoff	2.2	.9	2.2	3.1	.59	.33	.59	.83	.83	.46	.18	.81	.26	.20

^aThere is no analog channel for this axis in existing LM design.

APPENDIX A

TABLE A11.- RADAR NOISE COMPARISON (1σ) AFTER 200-msec SMOOTHING TIME (VELOCITY IN fps)

Time	U axis			V axis			W axis		
	Ryan	Calc	Mod6D	Ryan	Calc	Mod6D	Ryan	Calc	Mod6D
Vernier ignition	0.55	0.55	1.04	2.4	1.7	2.9	1.5	1.5	2.0
Tipup	0.37	0.38	.57	1.4	1.2	1.9	1.0	1.0	1.12
Contour	0.30	0.4	.4	1.2	1.1	1.07	.8	1.1	1.03
Engine cutoff	0.07	0.11	.36	.26	.42	.2	.16	.3	.2

The biases of the LM radar are not large enough to be of concern with regards to mission performance or success. The biases are of interest only with regards to that portion of the mission near engine cutoff. While on contour it is easily shown that the biases are insignificant, i.e., a lateral velocity bias causes the vehicle to take on an equivalent lateral velocity error (one might think an attitude error would result, this is not the case, as steady-state attitude error equals zero). For example the Y axis 3σ analog velocity bias on contour shown in table A10 is 1.54 fps, which is not significant as far as mission performance is concerned.

Using the rss of 3σ fluctuating errors and bias errors at cutoff (taken from table A10) the worst-case impact conditions were determined and are shown in table A12. Note that the worst-case vertical velocity is 20.6 fps as compared with a specified velocity of 25 fps and lateral velocity of 0.95 fps compared with a spec value of 10 fps.

Monte Carlo Beam Unlock Analysis

The probability of obtaining beam dropouts for the modified LM radar was studied by use of a Monte Carlo digital simulation program.

The radar function while on the parachute phase of the mission is to acquire the signal on each of its beams and provide the data to the guidance and computer. The velocity data are used primarily to initialize and drive the navigation equations in the computer.

APPENDIX A

TABLE A12.- IMPACT CONDITIONS

	Vertical velocity, fps	Lateral velocity, fps	Altitude, ft
Specified landing requirements	25	10	
Nominal cutoff conditions	10	0	10
Nominal impact conditions	18.5	0	0
Ryan error analysis results at engine cutoff (3 σ)	.68	.95	2.4
Impact conditions using the error analysis results as maximum condition	20.6	.95	0
Impact conditions using the error analysis results as a minimum condition	16.4	.95	0

The mode used to initialize the navigator depends on the number of beams that can be expected to achieve lock with acceptably high probability. These modes are discussed elsewhere in this report. This section describes an analysis to determine the probability of achieving one, two, or three velocity beam locks as a function of the parachute velocity and angle and other random variables.

The radar function for the vernier descent phase is to provide velocity and range data for steering the lander and controlling the thrust magnitude. Radar beam unlocks, if they occur during this phase, will occur during the attitude maneuver to align the thrust vector along the velocity vector.

Parachute phase.- Beam unlocks during the parachute phase are caused by a combination of poor beam incidence angles and the zero doppler effect. Beam incidence angles are a function of the vehicle attitude and the slope of the surface. The zero doppler effect refers to the degradation in receiver sensitivity as velocity along the beam direction is decreased (see figs. A19 thru A22).

APPENDIX A

Figure A27 is a simple diagram of this geometry in a single plane.

The parachute/vehicle descends through the atmosphere with a velocity, V_T , and angle, θ_T with respect to the atmosphere. These are parameters that depend on the parachute and aeroshell design. The atmosphere may be moving with respect to the surface at a velocity designated V_{WIND} in figure A27. Although figure A27 is a planar sketch, V_{WIND} may be in any horizontal direction. The wind may have random gusts superimposed on it that do not significantly affect the velocity of the vehicle, V , but do cause time varying changes in the vehicle attitude, designated θ_{GUST} in figure A27. θ_{GUST} is most likely to occur in the same direction as V_{WIND} . The dynamics of the parachute/lander subjected to wind gusts are described by Moog (ref. A1). The maximum excursion of the lander attitude is related directly to the onset rate of the gust. The worst gust onset rate was applied to the parachute/lander in a simulation by Moog (ref. A2) to produce the curves shown in figures A28 and A29. Note that the maximum change in attitude due to a gust is 22.5° . This was considered to be a 3σ number in the subsequent data.

The radar beam line of sight is fixed with respect to the lander geometric axes and makes an angle, A , as shown with respect to the surface slope. The surface slope is a random variable up to 34° . Also, the slope may be in any direction with respect to the wind direction, or the trajectory direction.

APPENDIX A

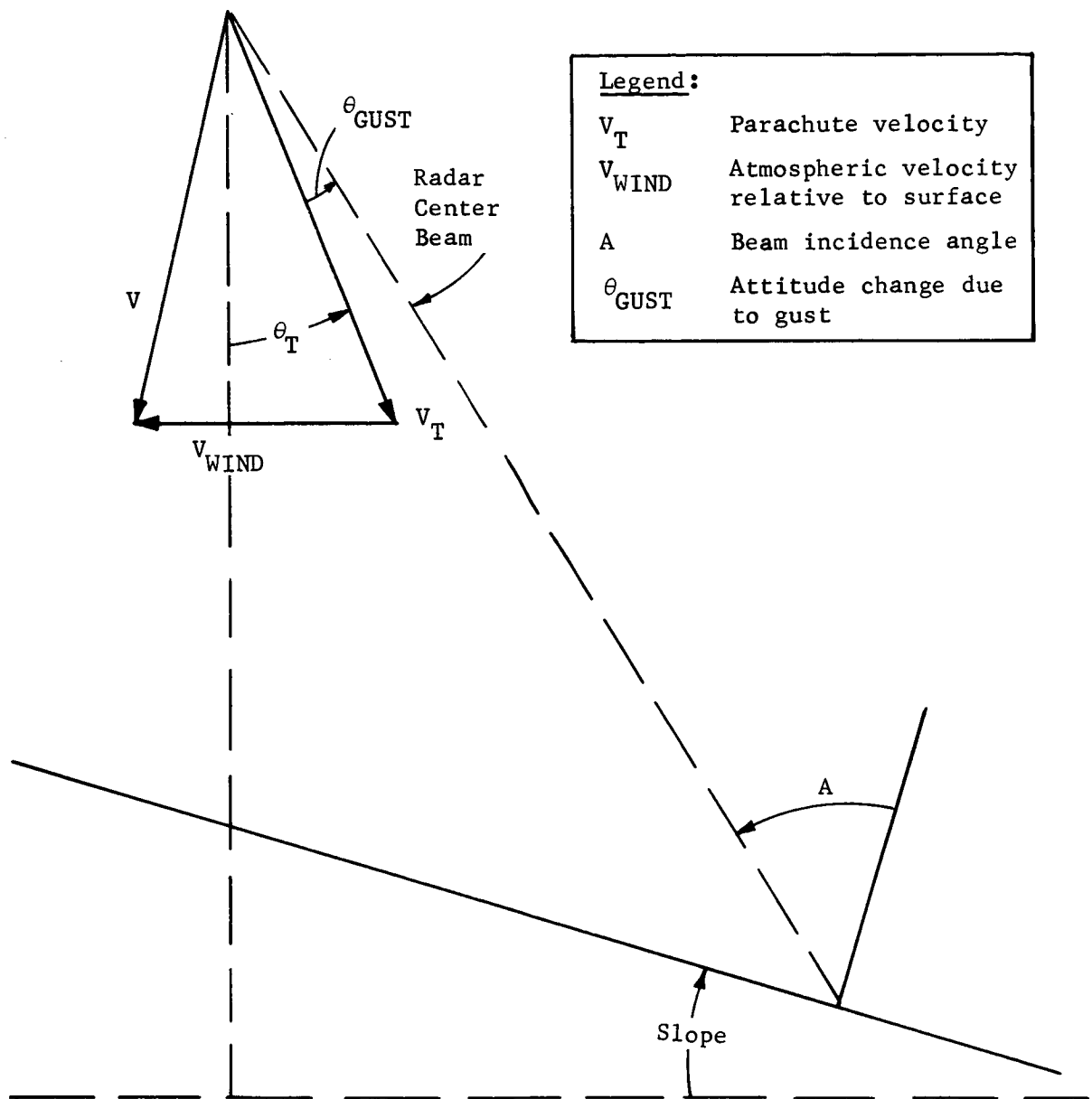


Figure A27.- Parachute Phase Beam Incidence Angle Geometry

APPENDIX A

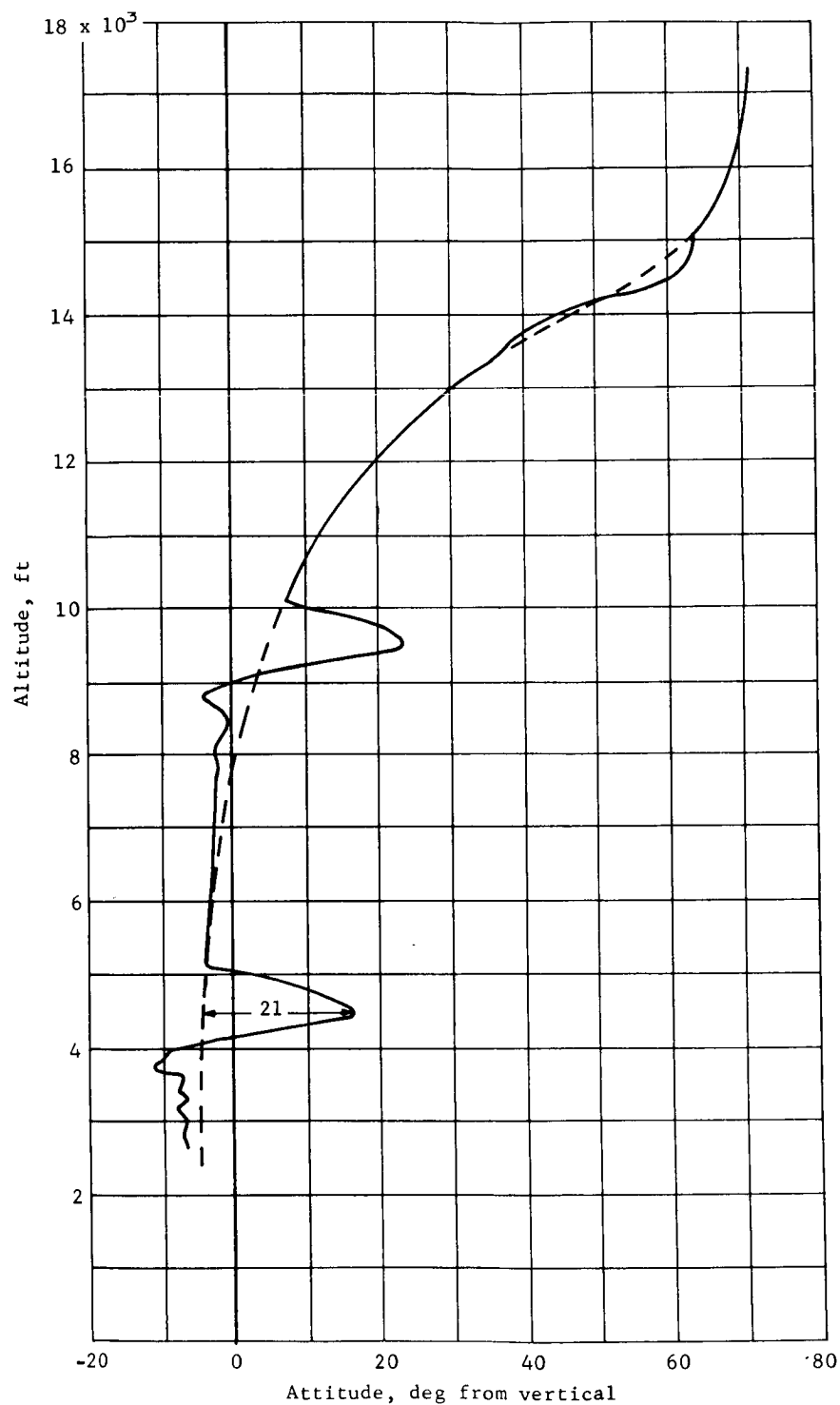


Figure A28.- Wind Gust Attitude Response, Maximum Continuous Headwind plus Gust, Mars Minimum Atmosphere (Mach 2 Deployment at 17 340 ft, Configuration 1B, 48-ft Chute)

APPENDIX A

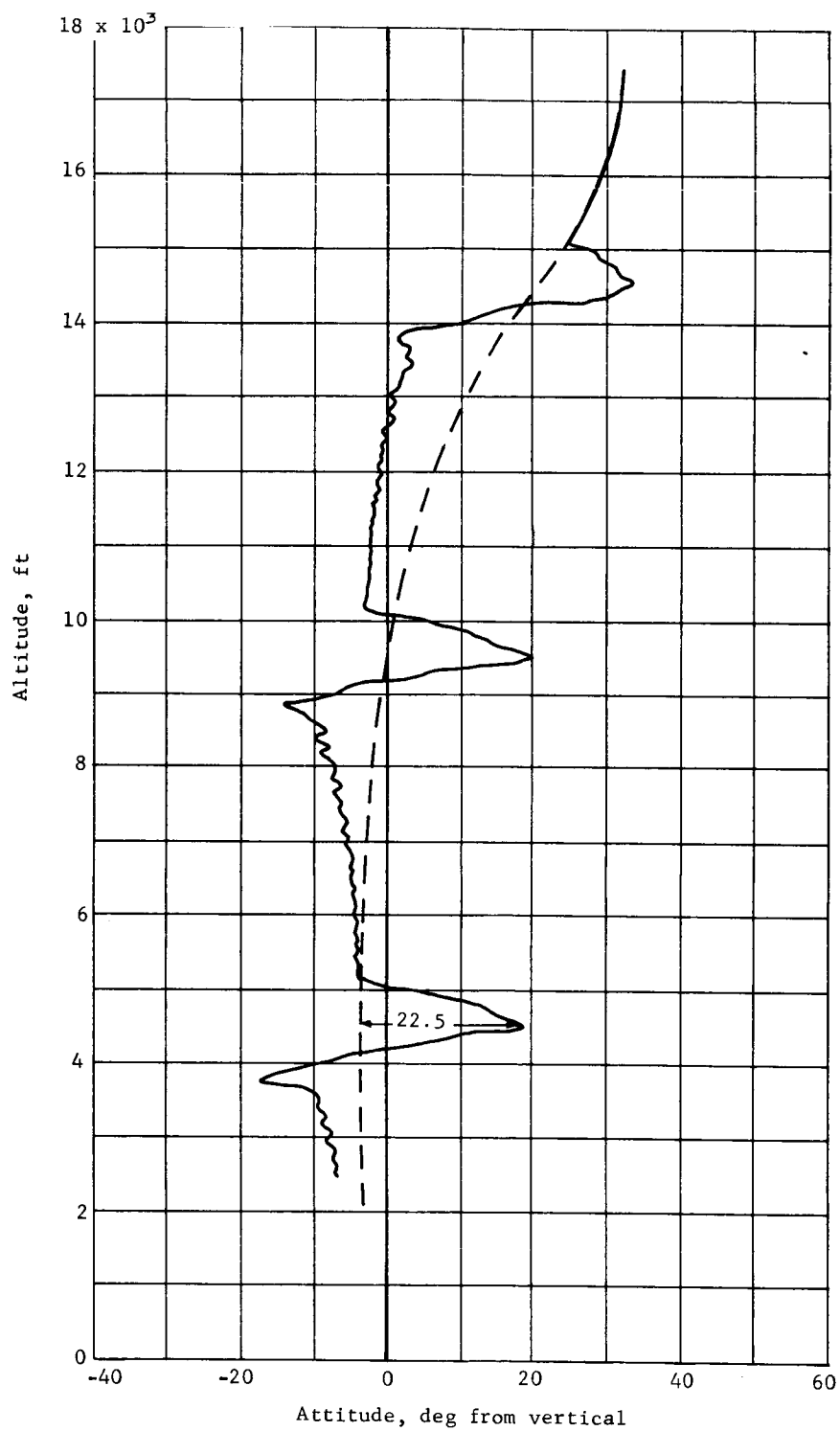


Figure A29.- Wind Gust Attitude Response, Maximum Continuous Headwind plus Gust, Mars Maximum Atmosphere (Chute Deployed at 17 340 ft, Configuration 1B, 48-ft Chute)

APPENDIX A

A digital computer program was constructed that computes the random incidence angle, A , as a function of all the variables described above. The method is summarized:

- 1) Input V_T , θ_T , and altitude, H as fixed parameters;
- 2) Compute random numbers from standard digital random number routines for the variables tabulated,

Variable	Definition	Probability distribution	Mean	Maximum
V_{WIND}^*	Wind velocity	Gaussian	0	± 242 fps (3 σ)
θ_{GUST}	Attitude change due to wind gust	Gaussian	0	$\pm 22.5^\circ$ (3 σ)
A_{WIND}	Wind azimuth	Uniform	0	$\pm 180^\circ$
Slope	Surface slope	Gaussian	0	$\pm 34^\circ$ (3 σ)
A_{SLOPE}	Direction of slope	Uniform	0	$\pm 180^\circ$
ϕ	Vehicle roll angle about centerline	Uniform	0	$\pm 180^\circ$

- 3) Compute using general geometry the incidence angles of each of the four radar beams;
- 4) Compute the velocity measured along each beam;
- 5) Compute the received power in each beam, compare to threshold curves, set lock flag to 1 if locked, to 0 if unlocked;
- 6) Repeat steps 1) thru 5) 1000 times, count number of unlocks on each beam, number of times two beams in pairs are unlocked, and average and mean square incidence angles.

* V_{WIND} is a function of altitude above the surface and the Martian season as defined in "Mars Engineering Model Parameters for Mission and Design Studies, 1968." $V_{WIND} = \pm 242$ fps is the maximum wind, worst season, at 4000 ft. The maximum wind for the worst 1973 landing date at $H = 4000$ ft is ± 165 fps, using linear interpolation between seasons.

APPENDIX A

The radar received power is calculated by the methods defined in section 4.

Results from this simulation are plotted in figures A30 thru A33. In figure A30, the probability that one of the three velocity beams is unlocked is plotted as a function of the parachute velocity with respect to the atmosphere, V_T , and the parachute angle with respect to the vertical, θ_T . Both V_T and θ_T are time-varying functions of the trajectory, decreasing as the altitude decreases as shown in figures A28 and A29. Note that the curves shown in figure A30 show quite high probabilities that one beam will be unlocked for velocities < 250 fps.

These data correspond to the original LM radar, and the worst-case seasonal maximum wind velocity of 242 fps. Reducing the wind maximum to 165 fps for the 1973 landing dates produces the curves of figure A31. Very little change is noted because the lander attitude is not affected by wind velocity.

Because the LM radar requires good velocity data to achieve an accurate range measurement, the curves of figure A30 and A31 indicate an unacceptably high probability of obtaining poor range data at the critical vernier ignition altitude. This is the main reason for adding an altimeter to the configuration to provide accurate, highly reliable altitude data on the parachute.

The velocity data for initializing the inertial navigator must be provided by the LM radar. If at any time on the parachute all three radar velocity beams are locked the inertial navigator can be initialized very quickly. If as indicated by figures A30 and A31, one beam is missing for a high percentage of time, two of the three beams can be used with the altimeter data in a filter update of the IMU as suggested by Hull (ref. A4). Therefore, the probability that two of the three beams being unlocked should be suitably low to implement this mode. Figures A32 and A33 show this probability for the same conditions as figures A30 and A31, respectively. Note that the probabilities are as high as 35% for $V_T = 150$ fps and $\theta_T = 20^\circ$. As θ_T approaches vertical the probability improves to 6.6%.

APPENDIX A

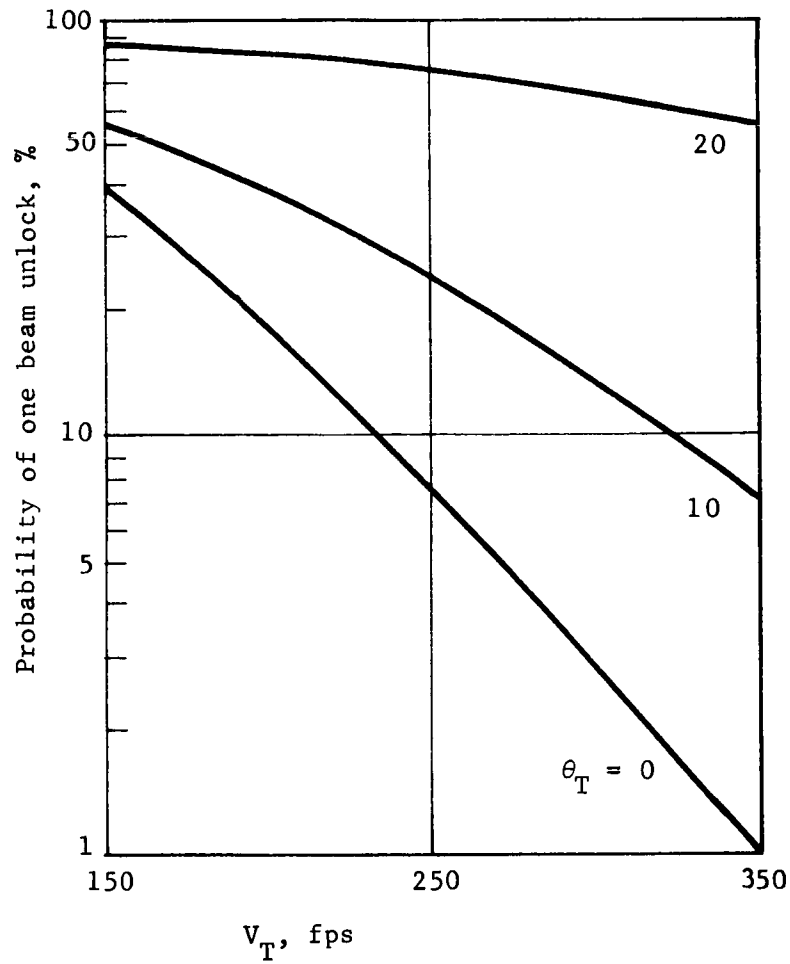


Figure A30.- Parachute Phase, LM Radar, $H = 6000$ ft,
 $V_{WIND} = \pm 242$ fps (3σ)

APPENDIX A

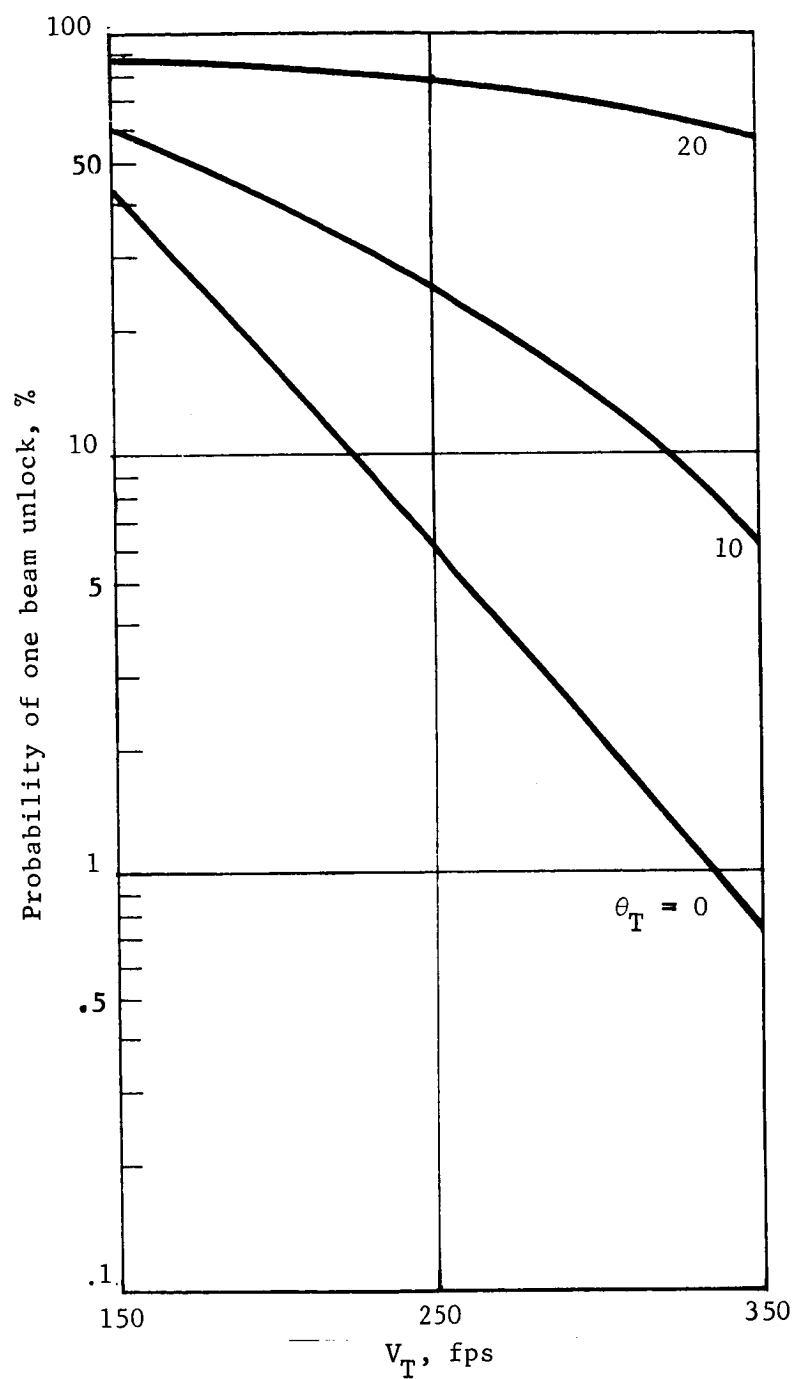


Figure A31.- Parachute Phase, LM Radar, $H = 6000$ ft, $V_{WIND} = \pm 165$ fps (3σ)

APPENDIX A

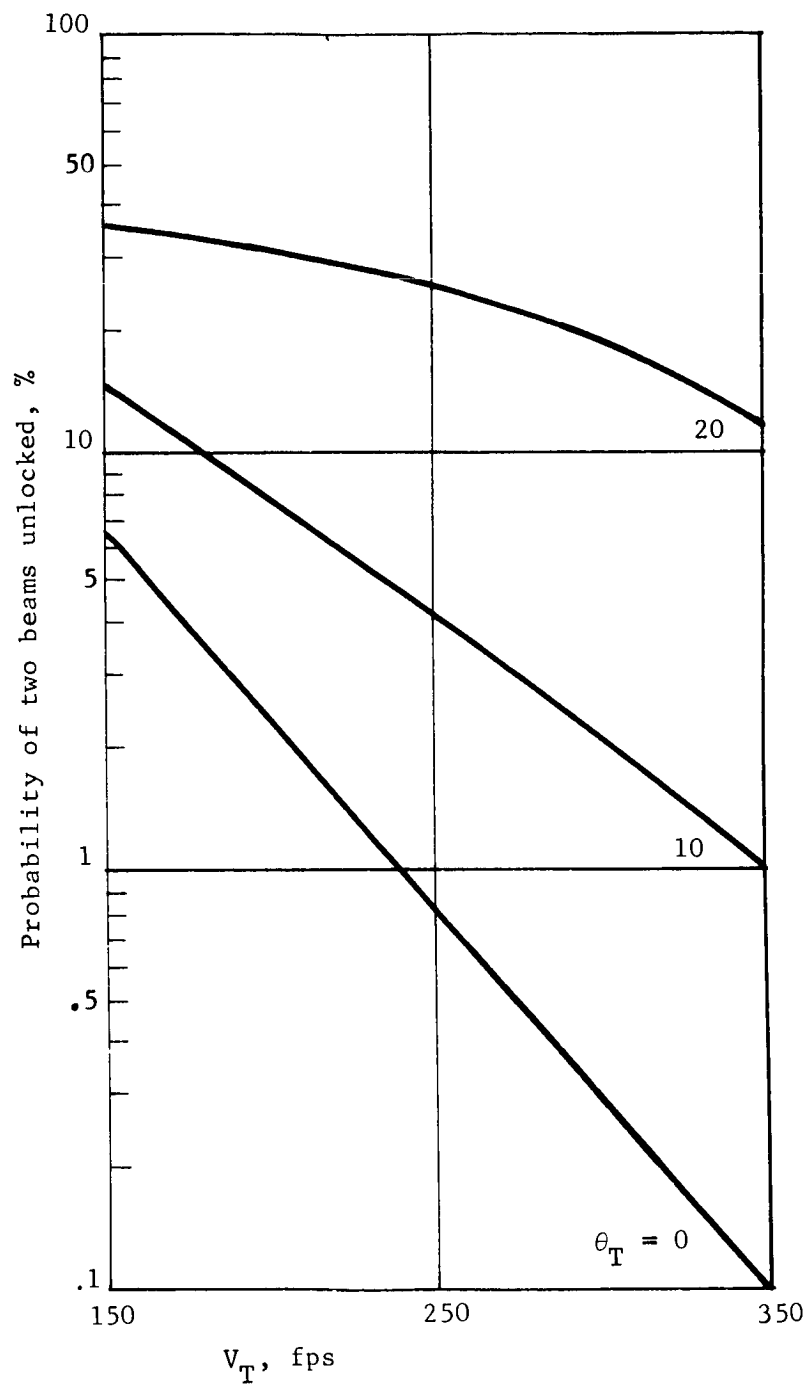


Figure A32.- Parachute Phase, LM Radar, $H = 6000$ ft, $V_{WIND} = \pm 242$ fps (3σ)

APPENDIX A

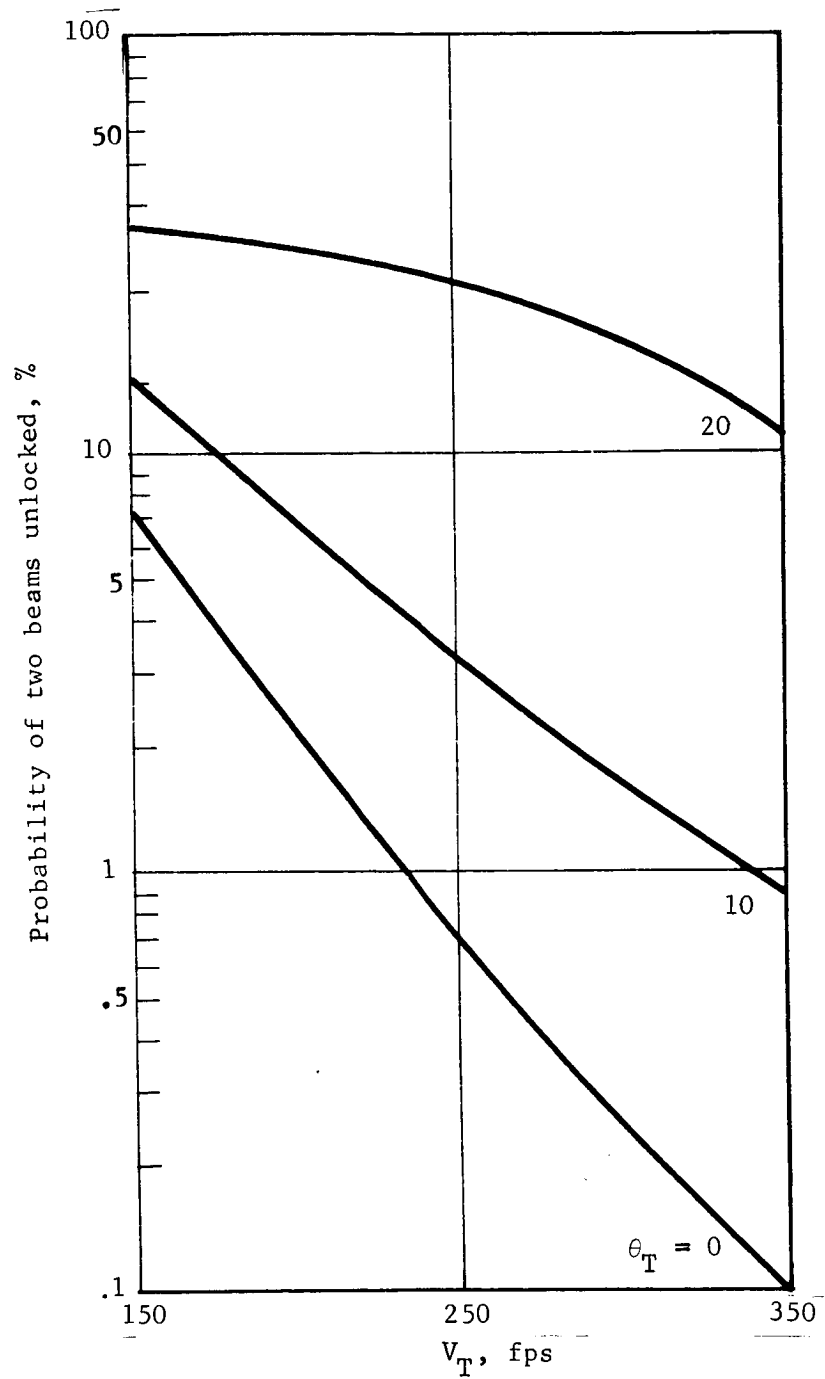


Figure A33.- Parachute Phase, LM Radar, $H = 6000$ ft, $V_{WIND} = \pm 165$ fps (3σ)

APPENDIX A

In evaluating the "goodness" of this probability, many factors must be considered. The first is that each random value computed represents one static point on a given mission. The composite 1000 cases calculated to define the number of unlocks obtained for each beam represents 1000 static points on 1000 possible missions. In actuality, as figures A28 and A29 indicate, θ_T and V_T are variables that have a continuity in time for a given trajectory. The existence of a steady wind between -242 and 242 fps (3 σ) (or -165 to 165 fps), and a random gust angle between -22.5 and 22.5° (3 σ) is assumed at every point on the trajectory. This assumption, particularly for the gusts, is probably quite conservative. In addition, the Monte Carlo results do not account for the dynamic motion vs time of the parachute/lander, which may result in fewer beam unlocks because the radar has builtin proof time delays before indicating beam dropouts. That is, if the radar beam passes through an unlock condition in less than 0.5 sec, loss of lock will not occur.

Nevertheless, to improve the probabilities shown in figures A30 thru A33, a bandwidth change is recommended for the radar velocity channels from 2800 to 600 Hz. This has the advantage of improving the radar sensitivity by about 7 dB in certain frequency regions as shown in figure A18. Reruns of the Monte Carlo simulation for the new threshold data yields the curves of figures A34 and A35. Note the marked improvement in the two beam unlock curves. It is believed that these probabilities are adequate to ensure update of the inertial navigator before vernier ignition.

The improvement shown in figures A34 and A35 due to an improvement of 7 dB in the radar sensitivity points up another very important assumption. All the data shown in this report used the Muhleman curve 2 as shown in figure A12 for the surface reflectivity model. This curve is the most conservative of all the curves shown by as much as 15 dB.

An improvement in signal strength of another 6 dB would reduce the probability of two beam unlocks to essentially zero, and greatly improve the single beam unlock data. For this reason, continued study of Mars reflectivity data is very important to final radar design as well as total guidance and control system implementation.

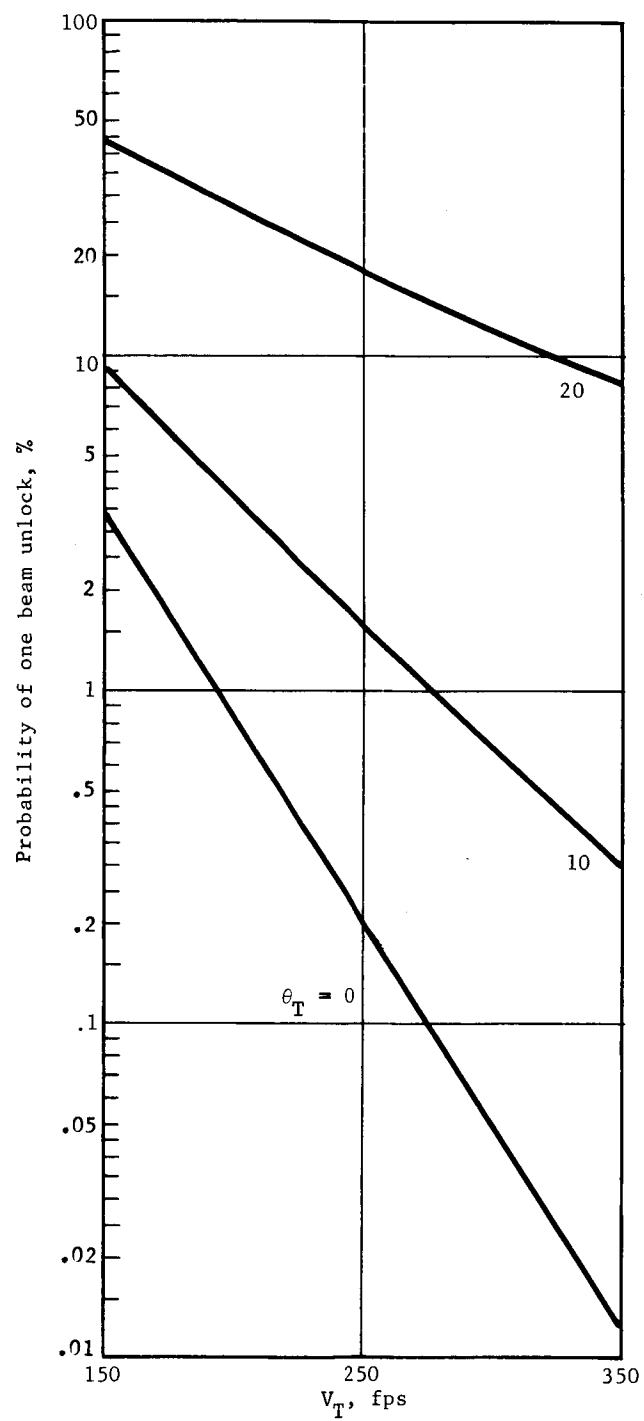


Figure A34.- Parachute Phase, Modified LM, H = 6000 ft, $V_{WIND} = \pm 242$ fps (3σ)

APPENDIX A

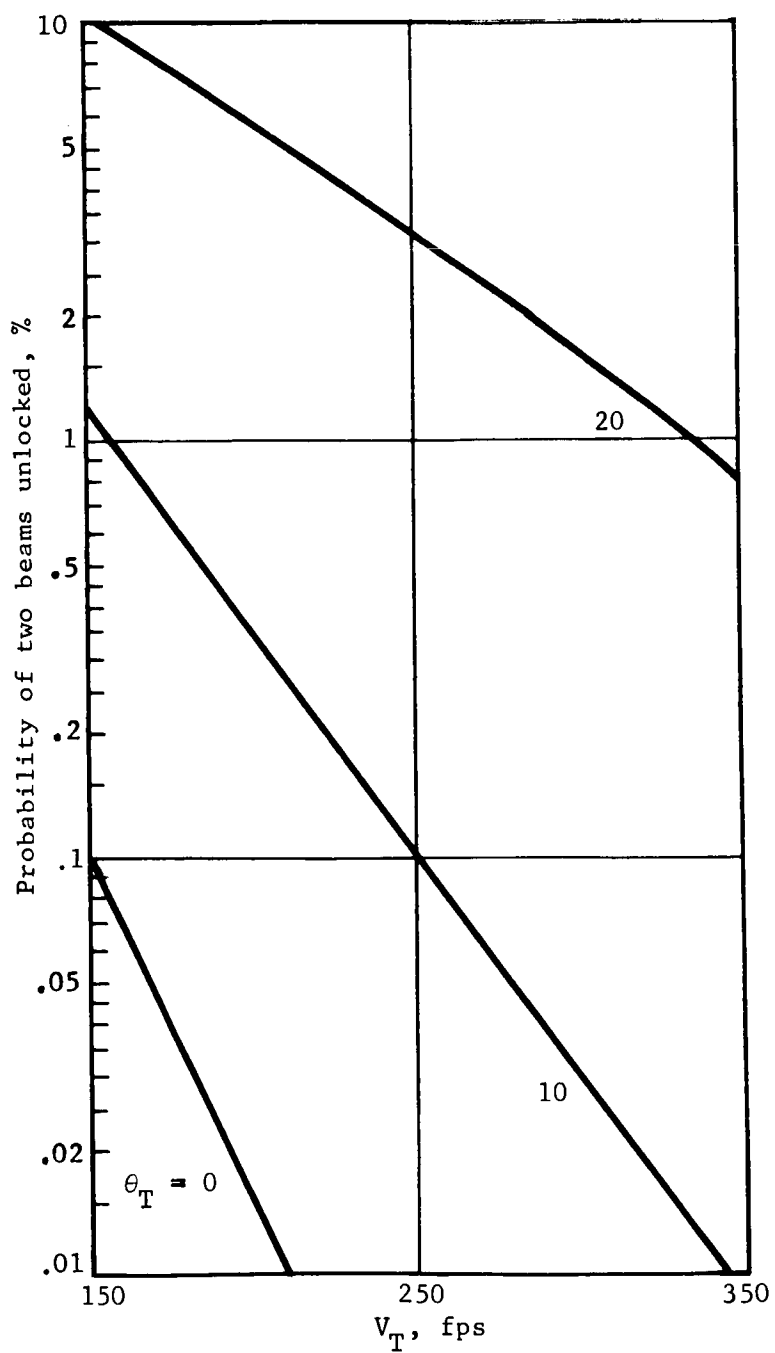


Figure A35.- Parachute Phase, Modified LM, $H = 6000$ ft, $V_{WIND} = \pm 242$ fps (3σ)

APPENDIX A

As can be seen in figures A30 thru A35, the Monte Carlo program was run only at a fixed altitude, 6000 ft above local terrain. This altitude was selected to allow about 10 sec between this altitude and the vernier ignition altitude, about 4000 ft. During this 10 sec, the probability of unlocking beams will decrease due to the increase in signal strength of the radar for lower altitude and because the parachute/lander approaches $\theta_T = 0$.

To produce the data for many altitudes would require a prohibitive amount of computer time. Thus, to get a qualitative appraisal of how the results are affected by altitude, figures A36 presents the means and standard deviations (rms) of the beam incidence angles plotted versus θ_T . These curves are unaffected by velocity or altitude. In figure A22, the critical incidence angle at which the velocity beam will unlock is plotted as a function of altitude and velocity. Similar data for the range beam are given in figure A21. Figures A21 and A22 are for the Muhleman curve 2 (see fig. A12) and for the improved radar threshold curves (bandwidth = 600 Hz). It can be seen from the curves that the range beam mean plus 3σ incidence angle is 51° for $\theta_T = 20^\circ$. From figure A21, it can be seen that essentially no range beam unlocks will occur. This was validated by the Monte Carlo simulations.

Tipup phase. - Beam unlocks during the tipup phase at the beginning of the vernier descent phase are caused primarily by loss of power due to incidence angle. The worst incidence angle condition of the entire **vernier phase will occur immediately when** the thrust vector is being aligned to the velocity vector relative to the surface.

Single plane geometry of this situation is shown in figure A37. As in the parachute phase, the incidence angle is a function of the random surface slope and azimuth and the random vehicle roll angle. The pitch angle of the vehicle is not affected strongly by gusts, so it is defined by the angle that the total velocity vector, V , makes with the local vertical. The parachute conditions θ_T and V_T are defined as before as is the wind velocity and the azimuth of the wind. The calculation of the number of beam unlocks proceeds very similarly to the parachute program.

Figures A38 thru A41 show results obtained for the tipup occurring at 4000 ft above the surface. This altitude represents a typical vernier ignition and tipup case.

APPENDIX A

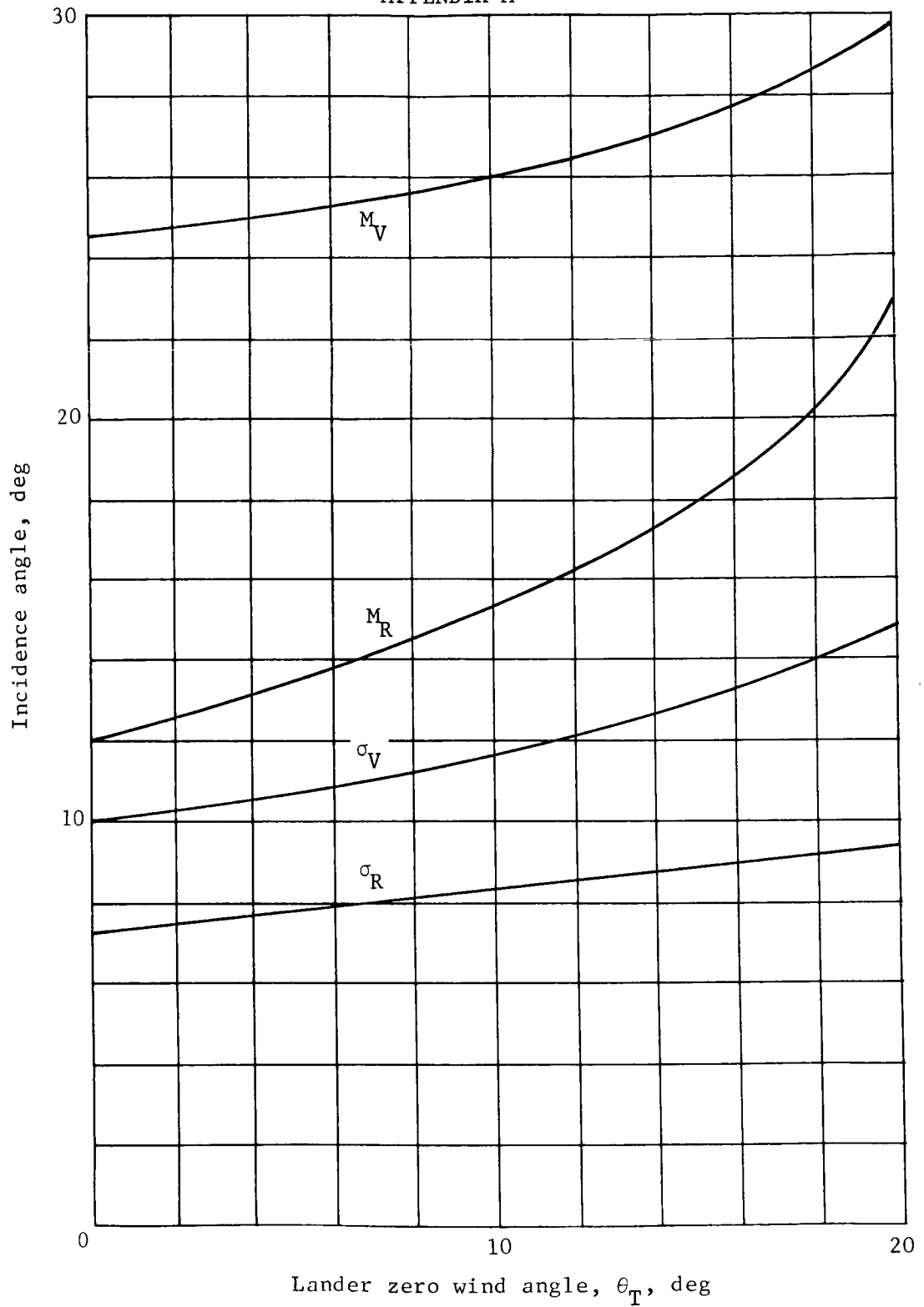


Figure A36.- Parachute Phase, Mean and Standard Deviations of Radar Range and Velocity Beam Incidence Angles

APPENDIX A

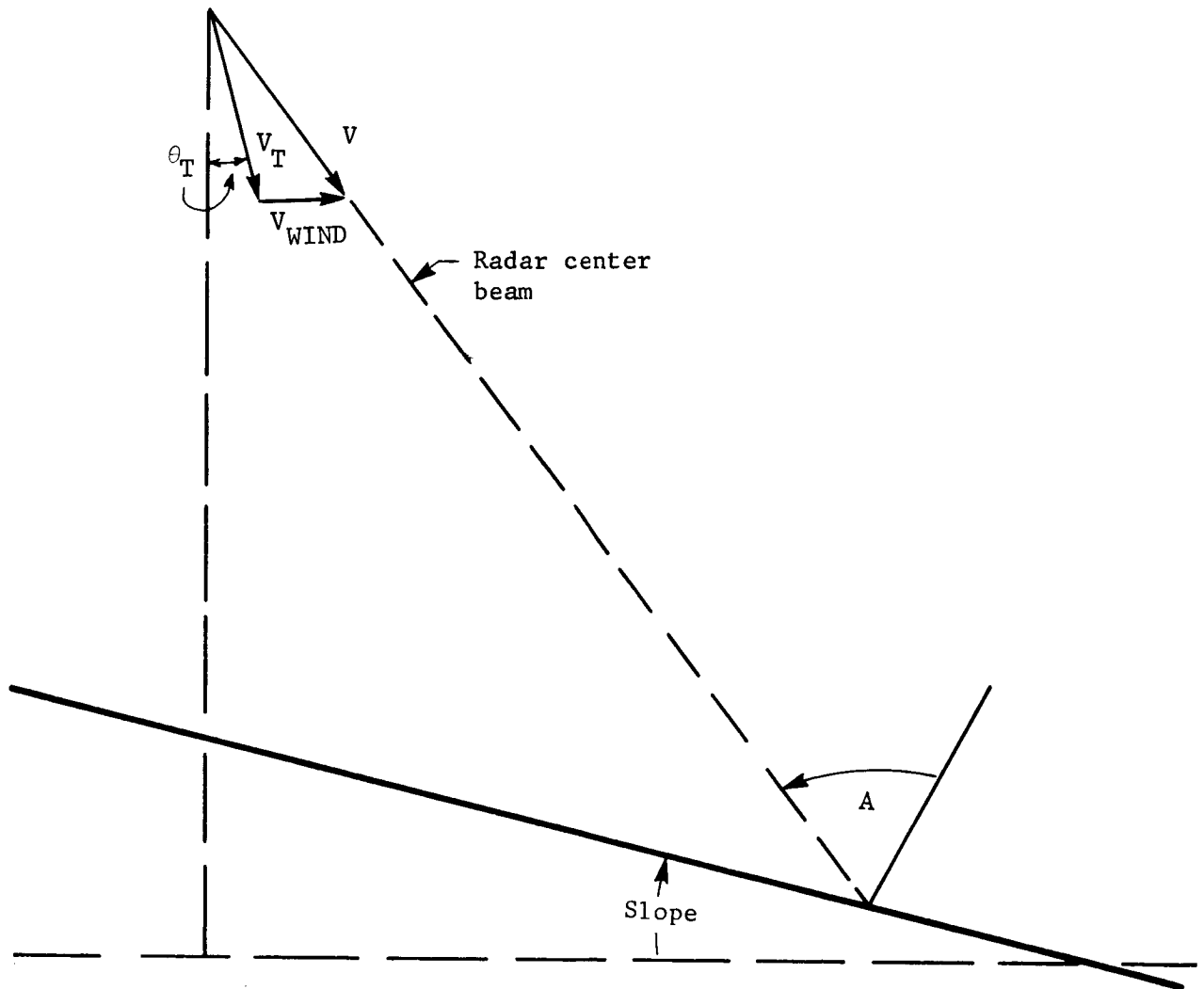


Figure A37.- Tipup Phase Beam Incidence Angle Geometry

APPENDIX A

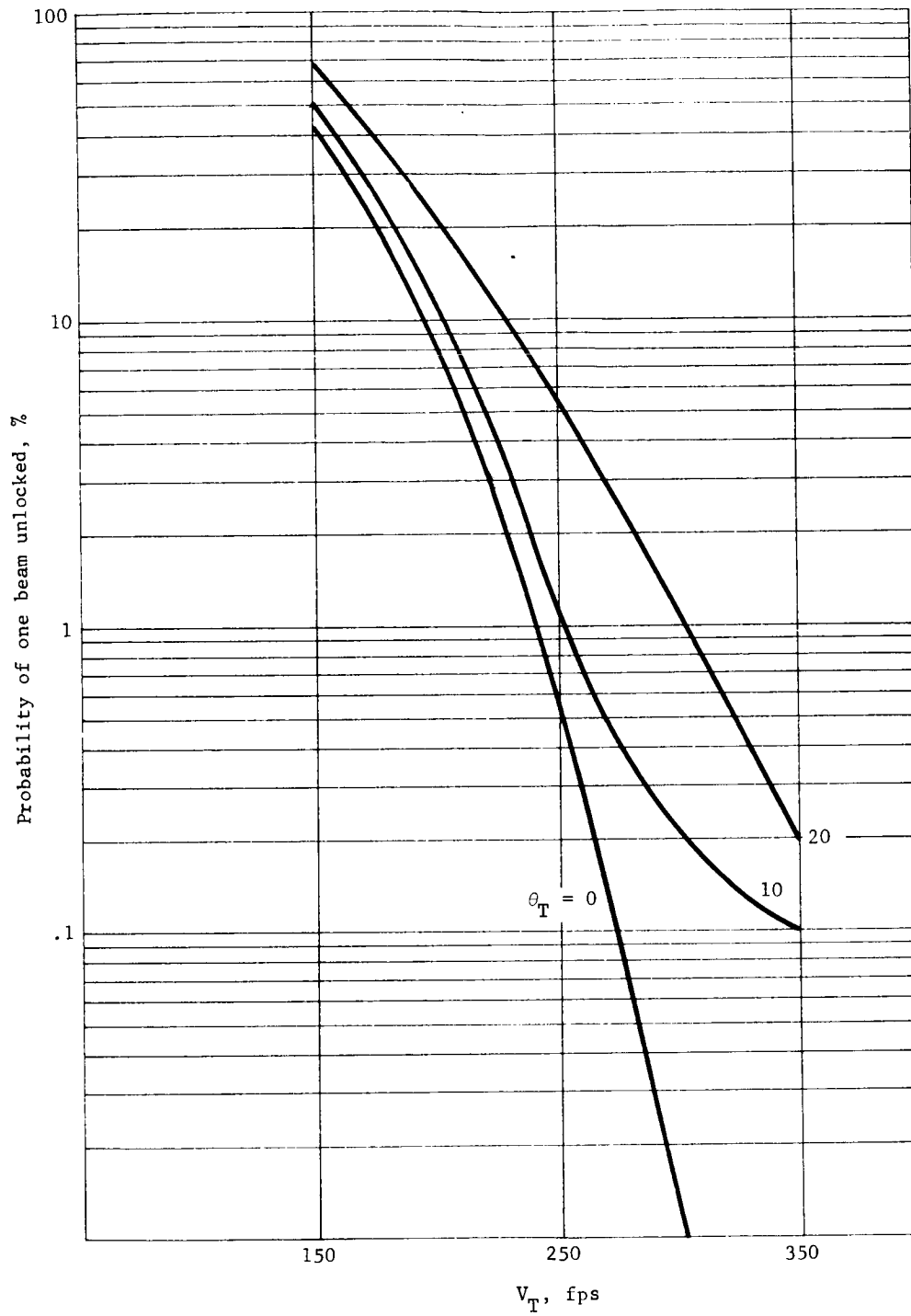


Figure A38.- Tipup Phase, LM Radar, $H = 4000$ ft, $V_{WIND} = \pm 242$ fps (3 σ)

APPENDIX A

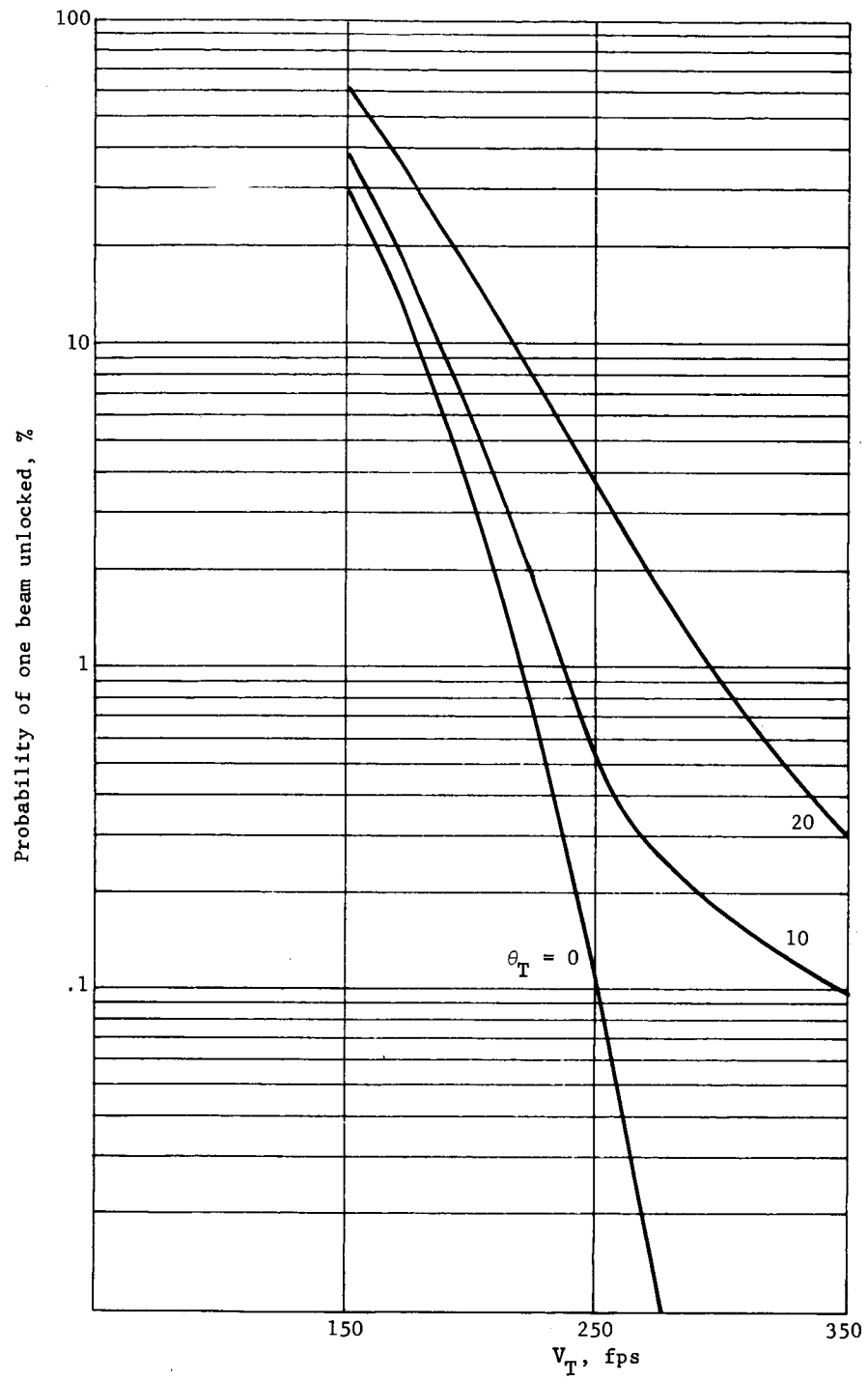


Figure A39.- Tipup Phase, LM Radar, $H = 4000$ ft, $V_{WIND} = \pm 165$ fps (3σ)

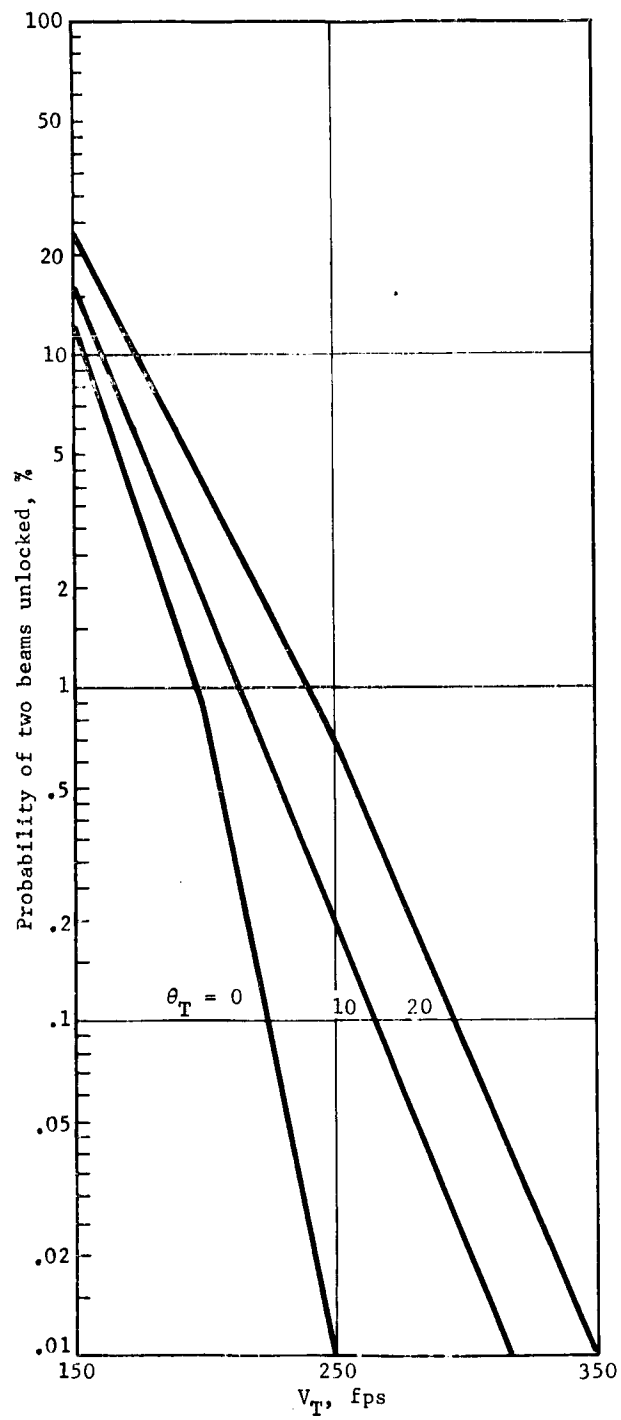


Figure A40.- Tipup Phase LM Radar, $H = 4000$ ft, $V_{WIND} = \pm 242$ fps
(3 σ)

APPENDIX A

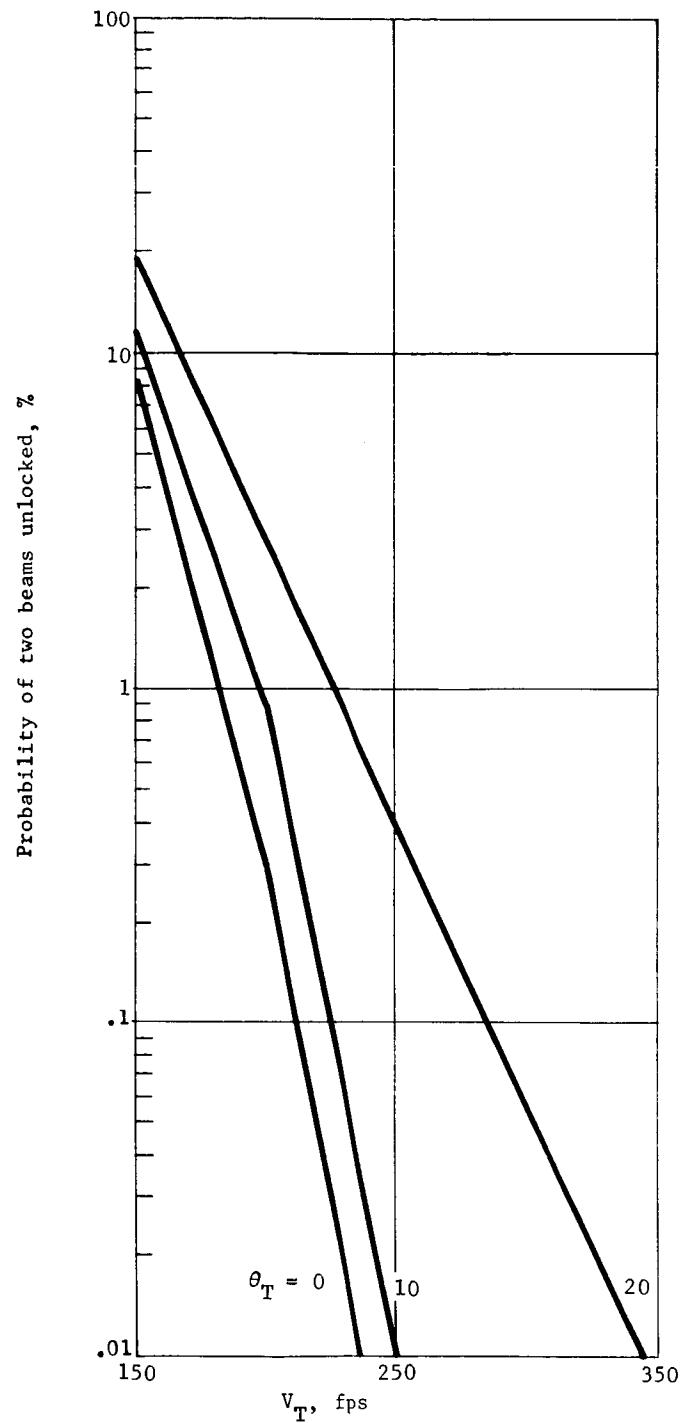


Figure A41.- Tipup Phase, LM Radar, $H = 4000$ ft, $V_{WIND} = \pm 165$ fps
(3 σ)

APPENDIX A

As in the parachute phase results, two maximum wind cases were considered. For either wind, figures A38 and A39 show that the probability of unlocking one beam is high, even for $\theta_T = 0$, for velocities (V_T) less than 200 fps. This illustrates the need for a backup inertial navigator to guide the lander during beam dropouts. The probability of two beams being unlocked as shown in figures A40 and A41 does not change this conclusion. It does point out that the probability of losing all lateral velocity data can be fairly high.

It does not appear practical to attempt to constrain the parachute design to solve all the radar unlock problems. A more reasonable approach, in terms of vehicle landed weight capability, is to provide backup modes using the existing inertial sensors, the altimeter, and the guidance and control computer. This has been studied in considerable detail using a six degree of freedom simulation of the vernier phase. The results are presented later in this report.

Cross Coupling

The cross coupling problem has not been evaluated in detail as yet. The following will attempt to indicate the source of cross coupling, possible problems due to it, and the methods that will be used to analyze the problem area.

The cross coupling occurs due to velocity receiver antenna beam side lobe aligned in the vicinity of the main lobe of another receiver beam. Some actual cross coupling data taken from LM radar unit P42 is given in table A13 (ref.A13).

TABLE A13.- CROSS COUPLING ISOLATION, UNIT P42

Beam	Port-starboard, dB	Fore-aft, dB	Diagonal, dB
1	32.5	31.0	33.5
2	30.5	34.5	42.2
3	31.0	35.3	40.3

APPENDIX A

These data refer to the relative side lobe gain with respect to the main lobe, i.e., beam 1 has a side lobe located to the port side (aligned with beam 2) that is down -32.5 dB relative to the beam 1 main lobe. Note then that the beam 1 receiver will receive a signal that will have a center frequency corresponding to the mean doppler frequency seen by the receiver of beam 2. This situation might cause a false tracker lock in either of two ways -- (1) a receiver in search mode could conceivably lock up on a cross coupled signal, and (2) during track a situation might exist where a cross coupled signal in the SLPF bandwidth might "pull" the tracker away from the correct spectrum. For the latter situation to occur, the cross coupled signal must contain more power than the true signal, all parameters being equal, (e.g., the respective transmitted power, beamwidth, and threshold), with the exception of incidence angle, i.e., the incidence angle of beam 1 main lobe and beam 1 side lobe aligned with another main beam. The incidence angle dependent term in the range equation is plotted in figure A42. Note in figure A11 that the maximum angle separating two velocity beams is about 49° . Figure A42 shows that for a 49° difference in incidence angle, the power difference is 22 dB, and, in table A13, it is seen that the worst-case cross coupling is 30.5 dB. A tentative conclusion, therefore, is that it will not be possible to "pull" a tracker off from the true signal. The problem should be examined further considering worst-case cross coupling terms, side lobe beamwidth, and a terrain model other than an infinite ground slope.

The problem of locking a receiver onto a cross coupled signal during search is felt to be more probable. A reasonable way to determine how probable will be to use the Monte Carlo program previously described; it is intended to do this in further studies.

APPENDIX A

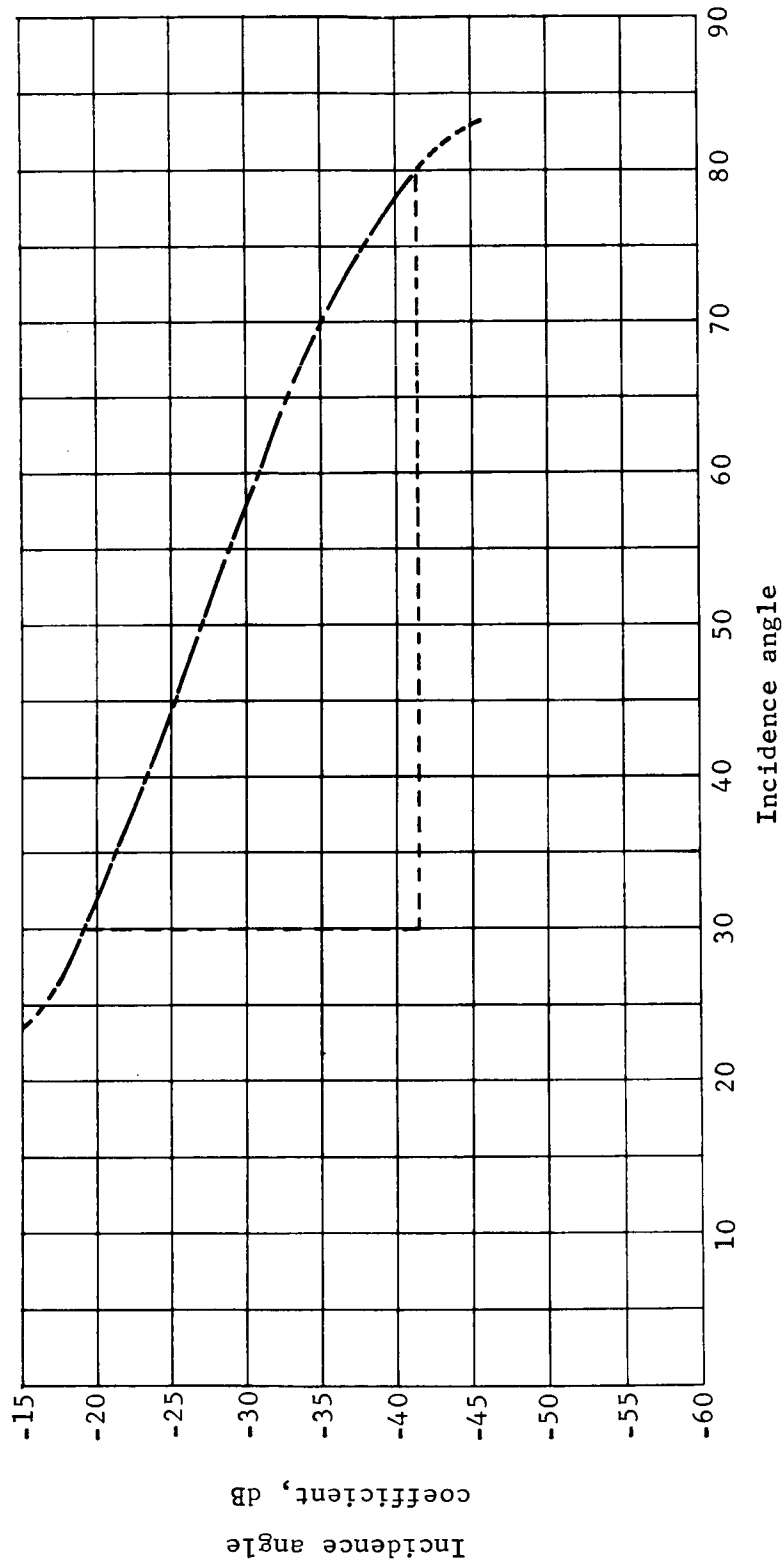


Figure A42.- Range Equation Incidence Angle Dependent Coefficient

APPENDIX A

6. SIX DEGREE OF FREEDOM SIMULATION RESULTS

Description of Simulation

The simulation of terminal descents made use of a modular, full six degree of freedom trajectory analysis program. The program consists of a set of executive subroutines to control input, output, and sequence of calling the operational subroutines that are organized on a black box basis. All data for input, output, or interface between subroutines are stored in an extensive "common" storage array. This organization of the program permits changes to any operational subroutine (i.e., radar module) without disturbing any other subroutine or requiring changes in basic executive operation.

Simulation runs may be initiated at any point in a trajectory and may be terminated for a variety of reasons. Time of flight and altitude cutoff are built-in to the program, with provision for adding any number of criteria in the operational subroutines. An example of this is the automatic run termination provided in the event of a complete loss of radar data caused by an unstable vehicle configuration. The sole purpose of this "staging" is to save computer operating time.

The executive organization is such that a series of simulations may be performed with a single input to the computer. Several options are available for selecting the amount of input to be changed at initialization for any run.

The simulations described below were performed on a CDC 6500 computer with the MACE operating system providing basic computer control and programing. Extensive use is made of library subroutines to provide various arithmetic functions and, in particular, the automatic scaling and generation of plots.

The subroutines used in this simulation are:

- 1) Executive and functional subroutines - Normal MOD6DF group for input, output, program control, and random noise generators;

APPENDIX A

- 2) Operational subroutines,
 - a) C 3 strapdown inertial navigator,
 - b) C 4 guidance computer,
 - c) C 5 engine controls,
 - d) D 1 translational dynamics,
 - e) D 2 rotational dynamics,
 - f) G 1 gravitational and coriolis acceleration,
 - g) G 5 coordinate conversion (output),
 - h) S 1 LM radar,
 - i) S 3 coordinate conversion for strapdown systems.

Note: D and G subroutines are standard program routines. C and S subroutines are specifically written for the 1 B or autonomous lander and the LM radar. The equations on which these modules are based are found in sections 3 and 4 of this appendix.

The interaction of the operational subroutines is shown in figure A43, and a listing of the order of operation for one iteration cycle is shown in figure A44.

Simulation Runs and Discussions

A series of five runs was conducted for the autonomous lander configuration using the LM radar with range beam aligned to the center of the antenna pattern and the roll axis of the vehicle. Various 3σ wind and surface slope conditions were selected to illustrate the effects on radar beam dropouts. All wind and slope conditions were restricted to the pitch plane for reference even though the program was running with the full six degree of freedom option. The effects of fluctuation noise may be seen in both pitch and yaw data. A second series of three runs was conducted with the LM radar further modified in bandwidth, acquisition search range and search rate, and in the range criterion at which the mode change occurs. These eight runs used a range/velocity descent contour.

Two more runs were conducted with the modified radar but using an altitude/velocity contour as a control law.

APPENDIX A

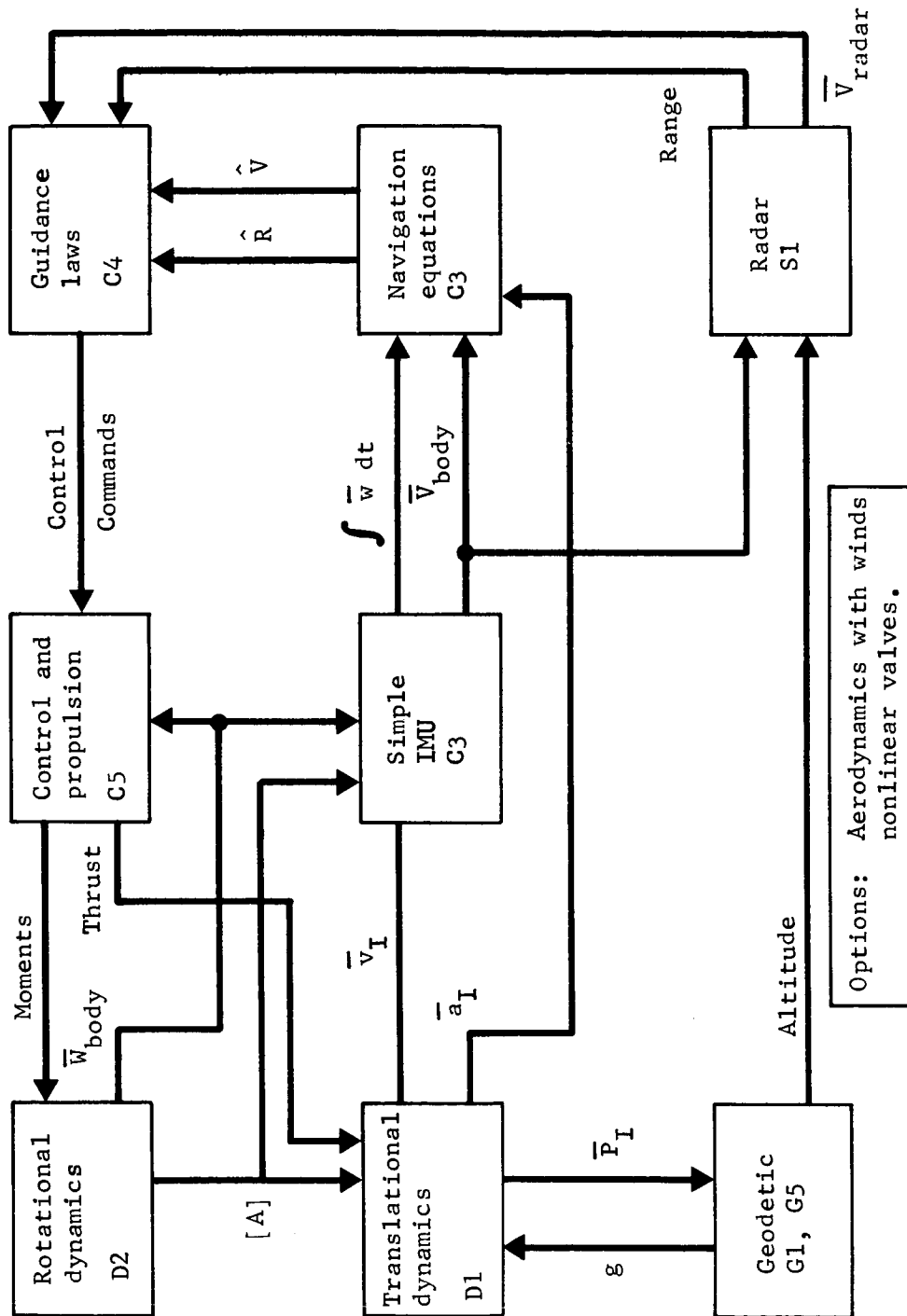


Figure A43.- Terminal Descent Phase Simulation

APPENDIX A

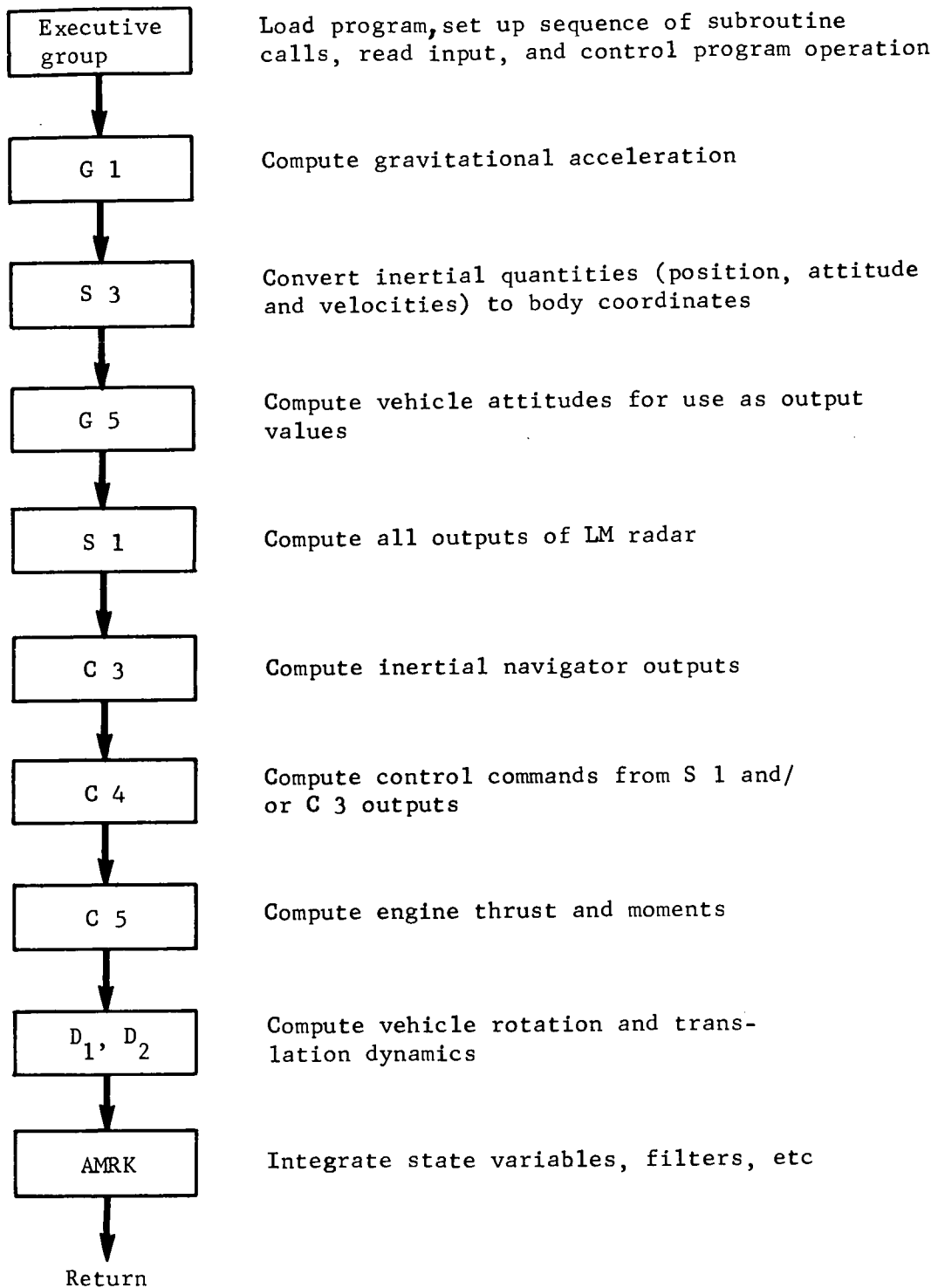


Figure A44.- Simulation Processing Order for a Single Iteration

APPENDIX A

Because the above were conducted for a minimum atmosphere to explore beam dropout due to pitchup and zero doppler effects, a run was conducted for a zero wind, zero slope condition in maximum atmosphere to compare propellant usage at extreme conditions.

Another series of runs was conducted for the three- engine 1B configuration to explore an acquisition anomaly due to interaction of flight conditions and radar mode change logic.

Table A14 presents a list and brief summary of the runs. Data from each run are summarized in tabular form in Appendix B. Appendix B also includes selected plots generated on the 280 plotter of the CDC 6500 computer.

No offsets or biases were added to compensate for system lags. This caused the fixed velocity descent to occur at about 13 fps instead of the nominal 10 fps. and the engine cutoff to occur about 8.5 ft instead of the nominal 10 ft. The control equations were left at nominal values to determine the effect of system lag on the landing parameters. A final system definition will be compensated by offsetting the appropriate limits in the computer.

A conditional reliable operator (CRO) mode is incorporated in the S1 simulation to allow use of range information from the IM radar without full velocity compensation from beams 1 and 3. Operation of this mode was demonstrated during Run 13 with beam 3 locked out.

The most likely case of dropout is shown in figures A45 and A46 by the single beam out curves.

The effect of implementing a synthetic correction factor by doubling the factor in event of beam 1 or 3 unlock is shown on the curve labeled "single beam out, double correction factor." The logic is such that no error is introduced with one beam out and vehicle aligned to velocity vector. Because the inertial system is capable of holding this alignment to within a few degrees, this implementation allows successful landings under near nominal conditions with either beam 1 or 3 out. The shaded areas of the curves show error variation introduced by misalignment of up to 10°.

TABLE A14. - SIMULATION RUN SUMMARY

Run no.	Configuration		Control	Atmos- phere	Wind, fps	Ground slope, deg	Radar beam unlock/lock, sec				Descent time, sec	Fuel used, lb	Landing conditions, fps		Atti- tude, deg	Atti- tude rate, deg/sec	Peak atti- tude rate (noise) ^d , deg/sec	Peak side velocity (noise) ^d , fps	Remarks
	Vehicle	Radar ^b					1	2	3	4			H-vel	V-vel					
1	Autonomous Lander	LM	RV	Min.	-263	0	2.6/12	2.6/12	----	----	45.2	138	0.06	18.25	1	1.4	2.1-3.2	-1.5	Range Beam (4) dropout due to tracking rate
2		LM	RV	Min.	220	-19	----	2.2/14	2.4/5.8	2.4/5.8	49.1	141.1	0.07	18.7	1.5	1.65	3.1-2.06	1.2-3.3	
3		LM	RV	Min.	170	-27	----	----	1.8/13.4	2.2/5.6	49.9	138.6	-0.06	18.4	.6	1.9	2.6-3.5	2.7-1.8	
4		LM	RV	Min.	70	-33	----	----	1.6/6.4	----	47.3	128	0.11	18.5	.3	1	3.1-3.5	2-1.1	Zero doppler run Set up with crossstalk flags
5		LM	RV	Min.	263	0	.5/4.6	.5/4.6	4.2/9	----	46.3	140.1	0.1	18.1	1	1.6	3.1-2.1	.8-2.3	
6		Mod	RV	Min.	170	-27	----	----	1.8/12.6	2.2/6.2	50	139	0.2	17.7	.1	.002	1.2-1.3	1.7-1.5	
7		Mod	RV	Min.	170	27	.6/3.4	.6/3.4	----	----	41.4	122	0.05	18.4	.2	.25	2.9-2.	1.7-2.1	Zero doppler
8		Mod	RV	Min.	263	0	.5/2.6	.5/2.6	4.2/7.6	----	45.3	138.4	0.11	18.2	.5	.11	2.1-2.6	1.4-1.3	
9		Mod	RV	Min.	263	0	----	----	2.8/6.2	----	47	141.4	0.4	18.6	2.1	2.96	5-3.3	.22-2.4	
10		Mod	RV	Min.	170	27	.6/3.4	.6/3.4	----	----	42.9	125	0.06	18.4	1.5	1.3	2.6-1.7	1.7-2.1	Landed with range beam out
11		Mod	RV	Max.	0	0	----	----	----	----	49.4	124.4	0.1	18.3	.2	.64	5.7-4.6	1.5-.9	
12		LM	RV	Min.	170	-26.7	----	2.8/8.8	1.8/11.2	1.8/11.2	31	92.6	0.5	21.4	1.7	1.6	----	----	
13	Configuration 1B	LM	RV	Min.	170	-26.7	----	----	1.8/11.2	----	27.5	85.9	0.3	18.9	.4	.45	----	1.1-2	Nominal 1B with ve- locity beam re- acquisition
14		LM	RV	Min.	170	-26.7	----	----	1.8/11.2	----	26.5	84.3	0.68	18.7	2.6	2.3	----	1.25-1.5	

^aRun numbers are arbitrarily assigned for identification only.^bLM refers to a basic LM with centered range beam and analog outputs, mod refers to radar with modified search and acquisition circuitry.^cFor wind and ground slope with same sign vehicle is traveling up slope.^dValues taken at 90° to flightpath to indicate effect of fluctuation noise on vehicle motion.

APPENDIX A

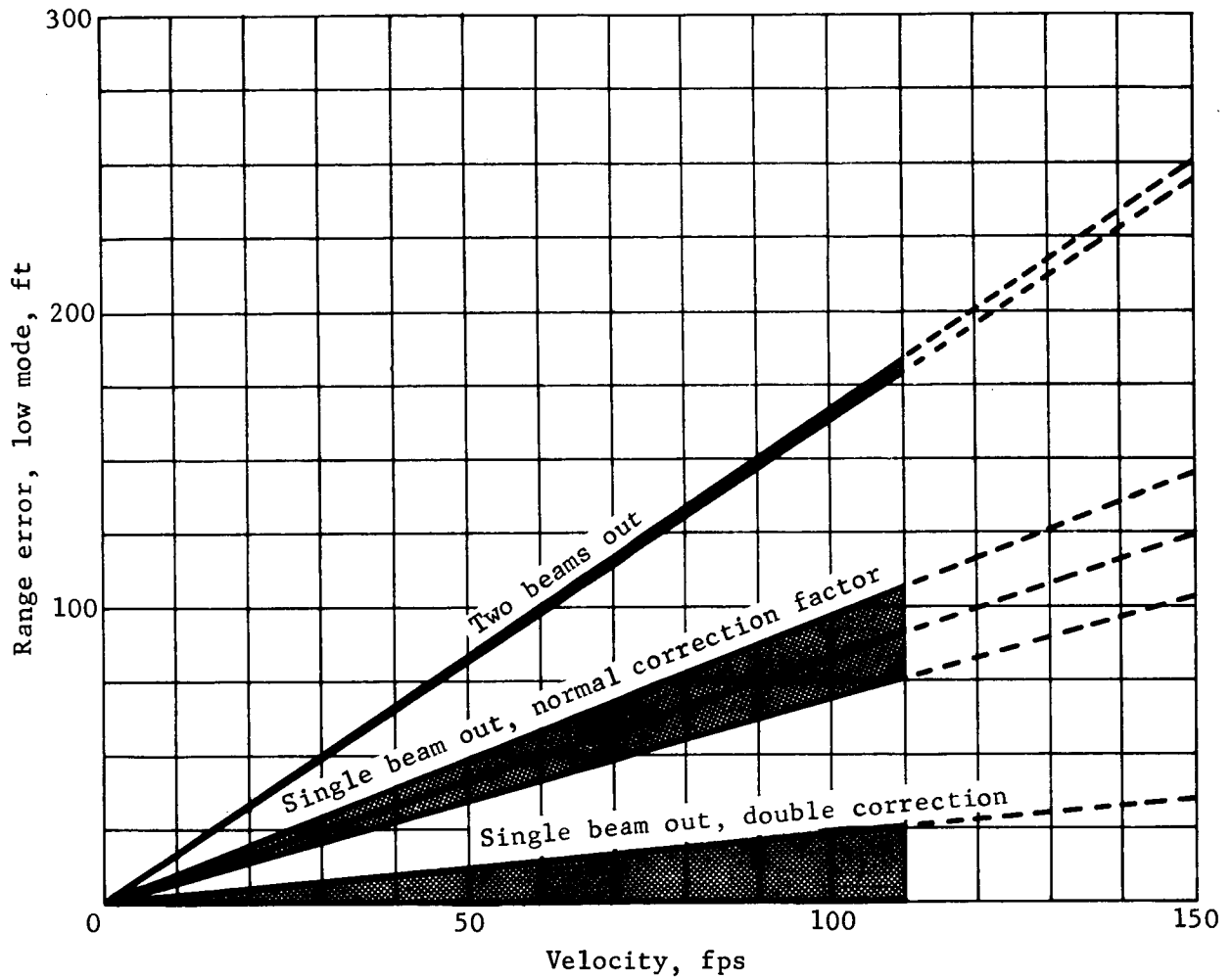


Figure A45.- Range Errors with Velocity Beams Out

APPENDIX A

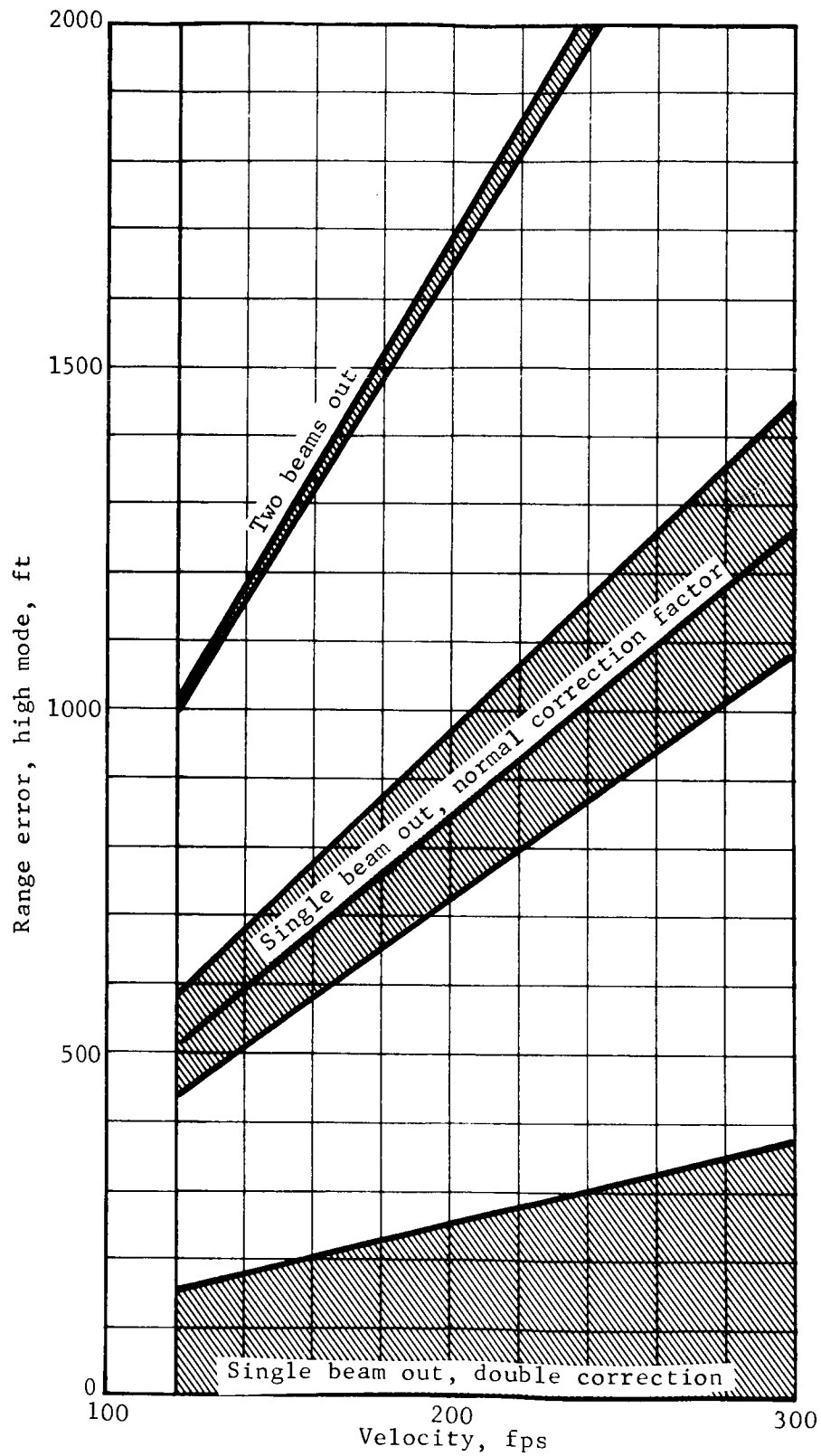


Figure A46.- Range Errors with Velocity Beams Out

APPENDIX A

Autonomous capsule runs.- A variety of wind vs slope combinations were chosen to investigate the severity of beam drop out due to the zero doppler effect and to high incidence angles encountered during the pitchup maneuver to align the vehicle thrust axis with the velocity vector at the time of parachute release. Only one case, Run 11, performed as a limit condition, does not exhibit radar drop out.

Runs 1 thru 4 were performed using the IM radar with centered range beam and analog outputs. The dropouts shown on beams 1, 2, or 3 are caused by high incidence angles due to combination of pitch angle and ground slope. The search times shown indicate that two search cycles were required in velocity channels of runs 1, 2, and 3 but that the velocity of run 4 and the range channel of runs 2 and 3 required a single cycle.

Run 5 was basically similar to run 1 except that initial conditions were chosen and timing set to force beams 1 and 2 into a zero doppler condition and thus cause the entire pitchup maneuver to be controlled from inertial data. This run was nearly terminated by the S 1 module for having all three velocity beams unlocked after 5 sec of run time (logic to save computer time in event of unstable flight). Because beams 1 and 2 relocked at 4.6 sec, the entire run was completed to a nominal landing. The difference in fuel used was due to the extra 1.1 sec of run time the increased pitch maneuver required by the off vertical initial condition.

Runs 6 and 8 are repeats of runs 3 and 5 except for the change in search range and rate to give $\frac{1}{2}$ the search cycle time. Differences in relock timing in runs 3 and 6 are due to actual values of sweep speed and range used in the S 1 module. The time involved shows that sufficient signal was not available for acquisition until $T \approx 12$ sec, so that run 3 locked on second pass and run 6 on fourth pass in velocity channels. The range beam showed a similar effect with run 3 relocking on first pass and run 6 on second pass.

Comparison of runs 5 and 8 shows that beams 1 and 2 recover from doppler dropout on first pass of search cycle and that beam 3 has sufficient signal at $T \approx 7$ sec. While there is a small difference in time of 1 sec and a 1.7 lb saving in fuel used, the primary reason for the faster search time is to assure lock-up while on the parachute so that the inertial system can be initialized with sufficient accuracy to perform the pitchup maneuver during radar drop outs.

APPENDIX A

Run 7 is a repeat of run 6 except that slope is reversed so that vehicle is flying upslope. As would be expected, the flight time decreased and so did the fuel used. This run shows that the range/velocity control law has enough margin to compensate for variations in ground slope.

Runs 9, 10, and 11 made use of an altitude/velocity control law to evaluate the capability of using altitude data in event of loss of LM radar range data or as a possible alternative implementation. Run 9 is similar to run 1, differences in flight time and fuel used are due to the chosen contour causing an early high throttle condition which lengthens the flight time. Run 10 is similar to run 7 and shows the same effect on time and fuel. Optimization of the altitude/velocity control law can be used to minimize these differences.

Run 11 shows the effect of no wind in a maximum density atmosphere. As would be expected for the slow vertical descent there were no radar drop outs and the longer flight time just about balanced out the fuel saved by a lower total velocity.

An additional operational module (S 5) was included in run 6 to investigate possible problems with cross coupling of energy between the various velocity beams. This run showed that no cross coupling could occur before 23.4 sec or above ≈ 1600 ft altitude. Below this point, various cases could occur. The effect of this would be to prevent a tracker drop out during a signal loss due to some local surface feature. Because, during the period when such cross coupling is possible, beam velocities are nominally equal, momentary dropouts are not significant. Energy in a beam must fall below threshold while cross coupled energy is above threshold for a sufficient time to affect the vehicle attitude. If proper signal balance is restored before the development of sufficient error to drive the desired signal out of the tracker bandwidth, the condition will be self-correcting. The signal levels during pitchup maneuver are such that cross coupling does not occur at this time. Further effort is needed in this area to determine the probability of unlocks from local surface features. Several techniques may be used to limit cross lock. The most practical is a reshaping of the step low pass filters to raise the thresholds at lower velocities. However, once the vehicle is aligned to the velocity vector, cross lock between beams 1 and 2 will cause a zero output in the V channel and, between 2 and 3, a zero output in the W channel. This will merely cause an attitude hold during the cross lock.

APPENDIX A

For short durations this is harmless. Cross lock between 1 and 3 can be more severe due to cross coupling between the V and W channels. This instance occurred at 1250 ft altitude in run 6. To cross lock, beam 3 signal would have to drop by ≈ 28.5 dB. In general, it may be stated that cross locks of 1 to 3, 3 to 1, 2 to 1, and 2 to 3 are cases that should be studied to a greater depth.

One method of limiting cross lock problems is to switch to inertial guidance at a preselected altitude. A criterion for selection is to compare the size of local surface features with the area illuminated by the beams. Various runs on the 1B configuration have shown that the simple strapdown navigator can control steering during the entire controlled descent.

1B configuration runs.- Runs 12, 13, and 14 were performed using the 1B configuration to evaluate a problem involving operation of the mode switch during tracker search. If the mode changes from high to low during or shortly after search flyback, search will be at low rate and acquisition time is so large that the vehicle reaches the ground before lockup can occur. Search starts at 77 kc and searches down at 26.4 kHz/sec in high mode. Low mode search starts at 7.4 kc and searches down at 2.3 kHz. If the search is near 77 kc when mode switch occurs it may require as much as 30 sec for the tracker to relock. Run 13 shows this effect for beam 3, but in actual hardware this effect applies to beam 2 only, due to logic that inhibits mode switch if beam 4 or either beam used for velocity correction is not locked. Run 14 has modified search logic, which prevents problems by sensing the trouble and reinitializing search in proper mode.

Run 13 shows the capability of the inertial system to complete a landing sequence without continuous radar velocity data after once being initialized to radar data.

Run 12 contained faulty logic in the search mode for beam 4. This logic error caused a failure to relock after a momentary drop out. Data from this run are included to show that the inertial system can recover from range drop out. Velocity at impact was marginal (about 24 fps) but just within acceptable limits.

APPENDIX A

7. REFERENCES

- A1. Moog, R. D.: Mars Lander Vehicle/Parachute Dynamics. Presented at 5th Space Congress, Cocoa Beach, Florida, Mar. 1968.
- A2. Moog, R. D.: Mars Mission Mode Configuration 1B Response to Mars Engineering Model Wind Criteria. Martin Marietta Corporation, 19 Sept. 1968.
- A3. Anon.: Description of the Landing Radar for the Apollo Lunar Module. B-162A, Ryan Aeronautical Company, 1 Apr. 1968 (53969-49).
- A4. Hull, K. H.: Terminal Descent Navigation for a Planetary Lander. Paper presented at 5th Space Congress, Cocoa Beach, Florida, Mar. 1969.
- A5. Anon.: Terminal Sensor Mechanization Trade Study. Report C7-1481-21060, Martin Marietta Corporation, June 1967 (NAA).
- A6. Meditch, J. S.: The Pontryagin Maximum Principle and Some of the Applications. Chapter 2, Advances in Control Systems, vol. 1, C. T. Leondes, ed., Academic Press, New York, 1964.
- A7. Moonan, P. J.: Dynamics of a Guided Propulsive Soft Landing Preceded by a Martian Atmospheric Deceleration. AIAA paper no. 67-170, Jan. 23, 1967.
- A8. Pfeffer, I.: Terminal Guidance for Soft Lunar Landing. Chapter 13, Guidance and Control of Aerospace Vehicles, C. T. Leondes, ed., McGraw Hill, New York, 1963.
- A9. Mankovitz, R. V.: The Analysis and Configuration of a Control System for a Mars Propulsive Lander. Report no. 32-1104, Jet Propulsion Laboratory, Mar. 1967.
- A10. Ingoldby, R. N.; and Seibel, R. P.: Terminal Descent Control System Analysis. PR-22-10-94-21, Martin Marietta Corporation, Jan. 1968.
- A11. Muhleman, D. O.: Radar Scattering from Venus and the Moon. Astron. J., vol. 69, no. 1, Feb. 1964.
- A12. Harrington, R.: Mars Radar Backscattering Coefficients. Ryan Aeronautical Co.

APPENDIX A

- A13. Harrington, R.: Ryan Aeronautical Company.
- A14. Berger, F. B.: The Nature of Doppler Velocity Measurements. IRE Trans on Aeronautical and Navigational Electronics, 1957.
- A15. Newton, Gould, and Kaiser: Analytical Design of Linear Feedback Controls. John Wiley & Sons, New York, 1957.

APPENDIX B

SIMULATION RUN SUMMARY TABLES AND PLOTS

APPENDIX B

TABLE B1.- RUN 1, SOFT LANDER/SUPPORT MODULE/RADAR/RANGE VELOCITY/O SLOPE

Flight condition	Altitude, ft	Velocity, fps		Pitch angle, deg	Pitch rate, deg/sec	Time, sec	Fuel used, lb	Beams unlocked	Time at relock
		Roll axis	Cross axis						
Initial	4600	165	263	-90	0	0	0	----	----
Mid-pitchup	4369	275.9	137.1	-121	-31.2	1.4	3.2	1, 2 at 2.6	----
Max. pitchup	4168	299.4	-38	-153	1.18	2.8	6.5	1, 2	----
Thrust aligned	3925	282.2	-22	-147	2.4	4	11.2	1, 2	12
Encounter contour	4435	240	194.6	-108.5	-29.9	1	2.5	----	----
Constant vel	49.5	12.2	.1	-90.5	.46	41.4	131.3	----	----
Cutoff eng	8.2	12.4	.12	-88.3	1.1	44.7	138	----	----
Land	.95	18.25	.06	-89	1.4	45.2	138	----	----
Remarks:									

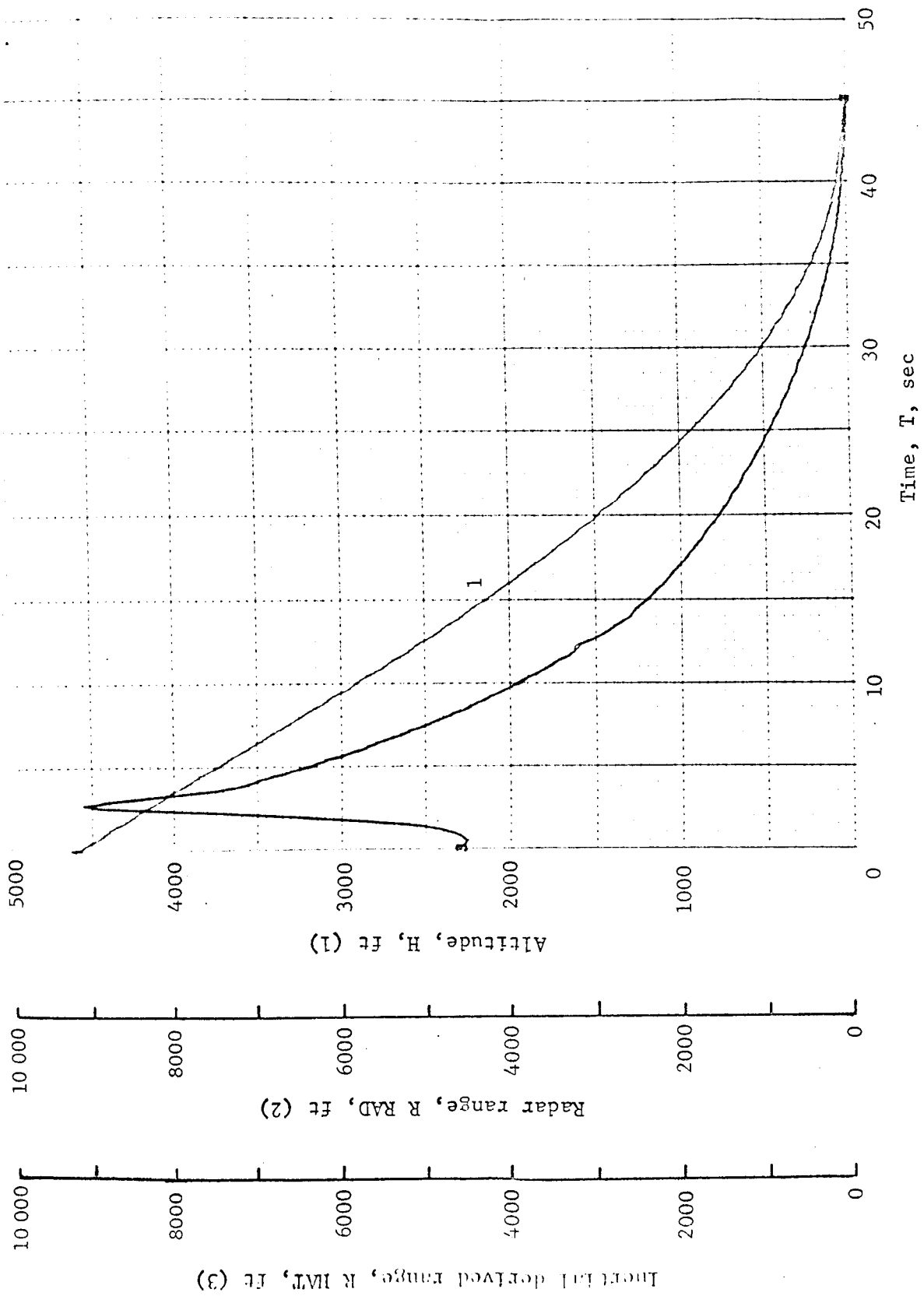


Figure B1.- Soft Lander, Run 1-1

APPENDIX B

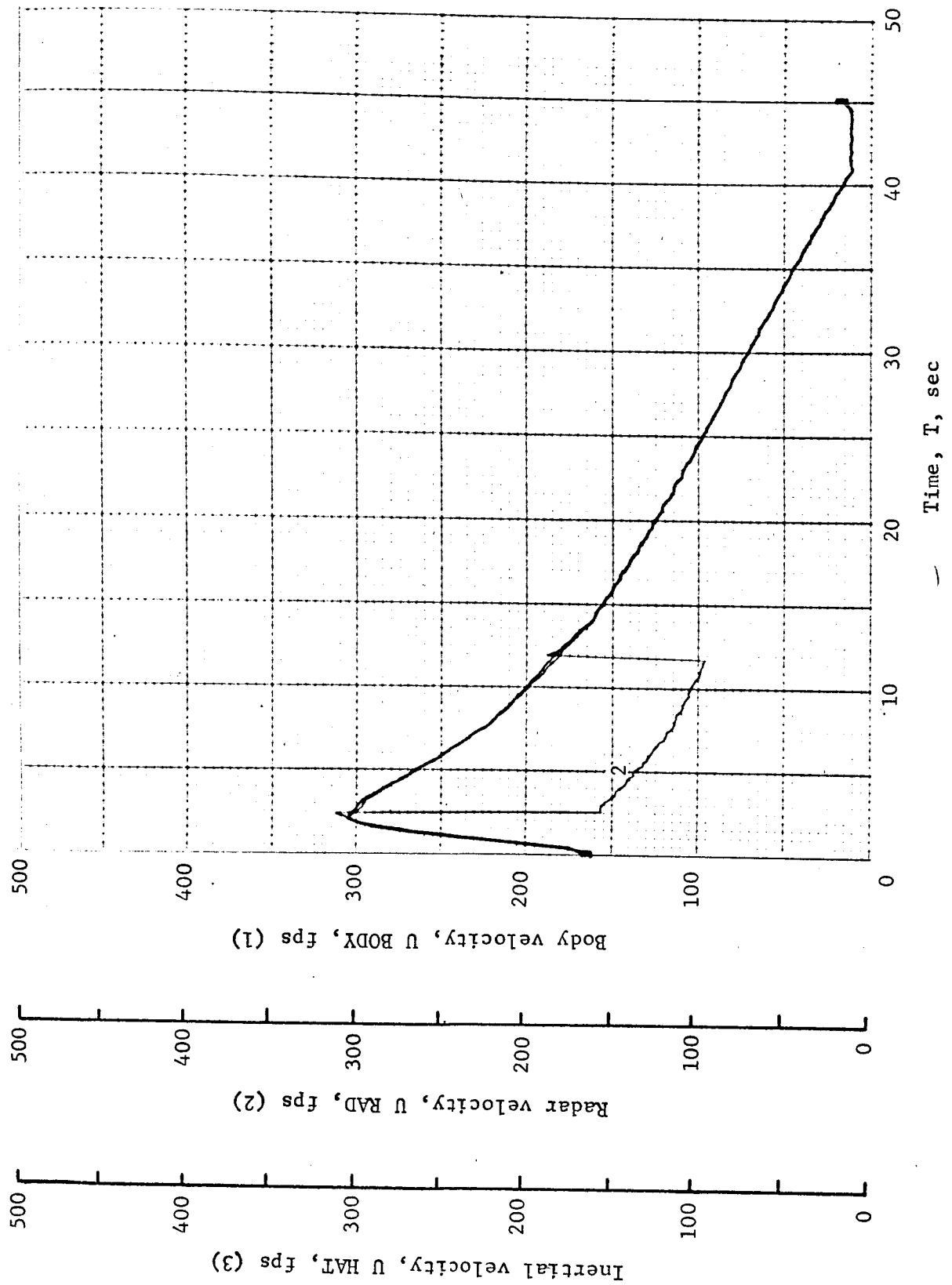


Figure B2.- Soft Lander, Run 1-2

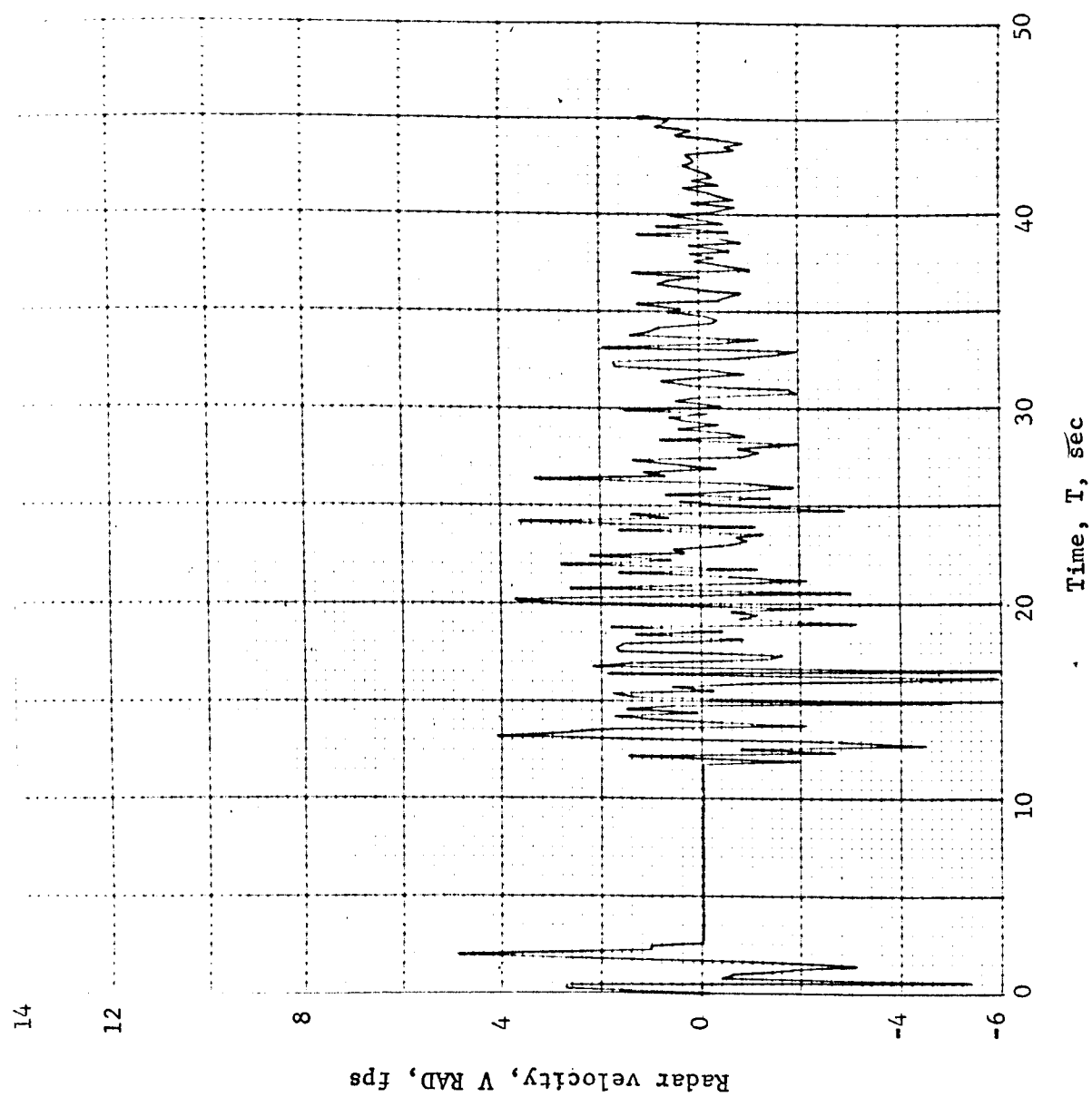


Figure B3.- Soft Lander, Run 1-3

APPENDIX B

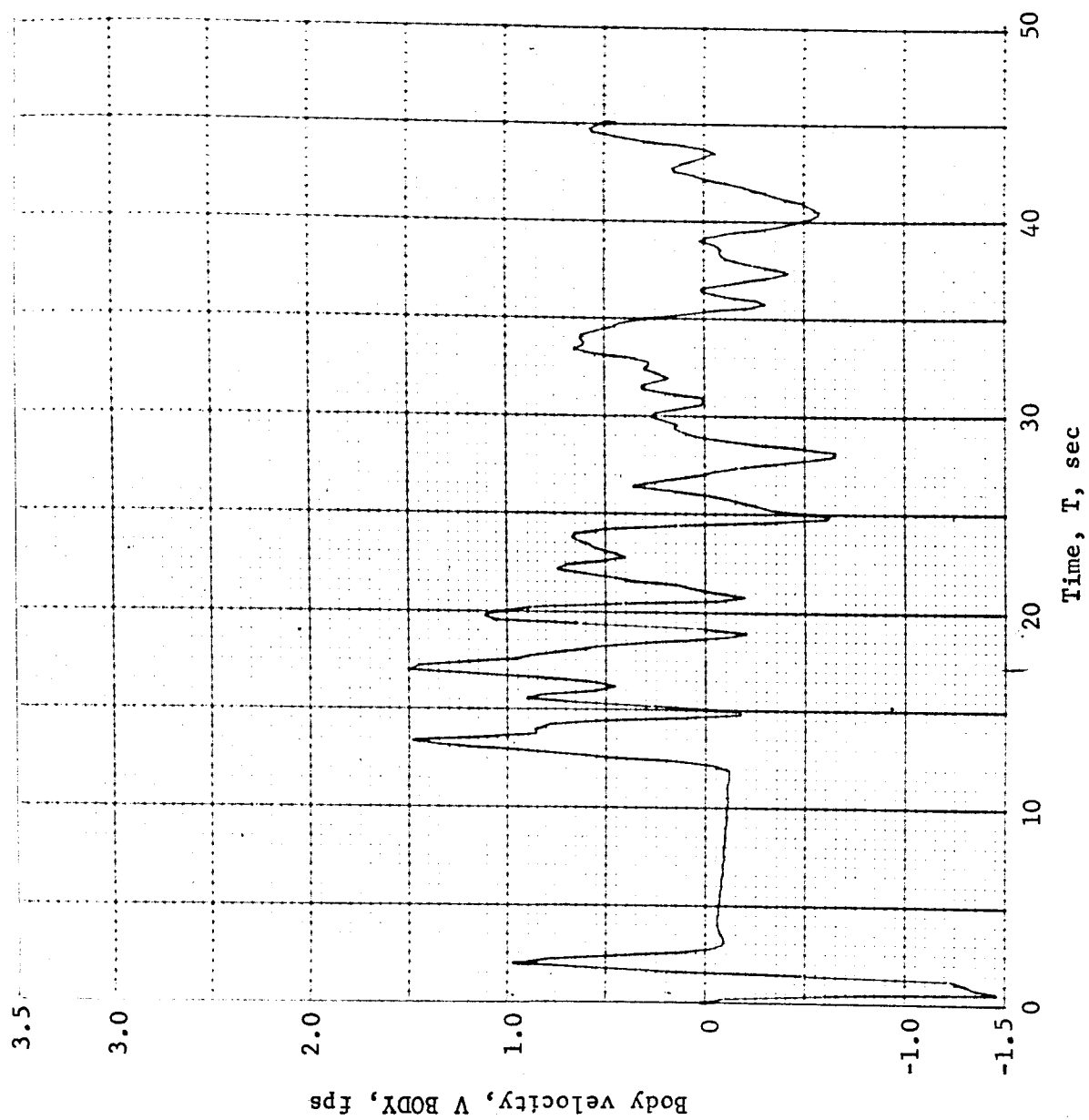


Figure B4.- Soft Lander, Run 1-4

APPENDIX B

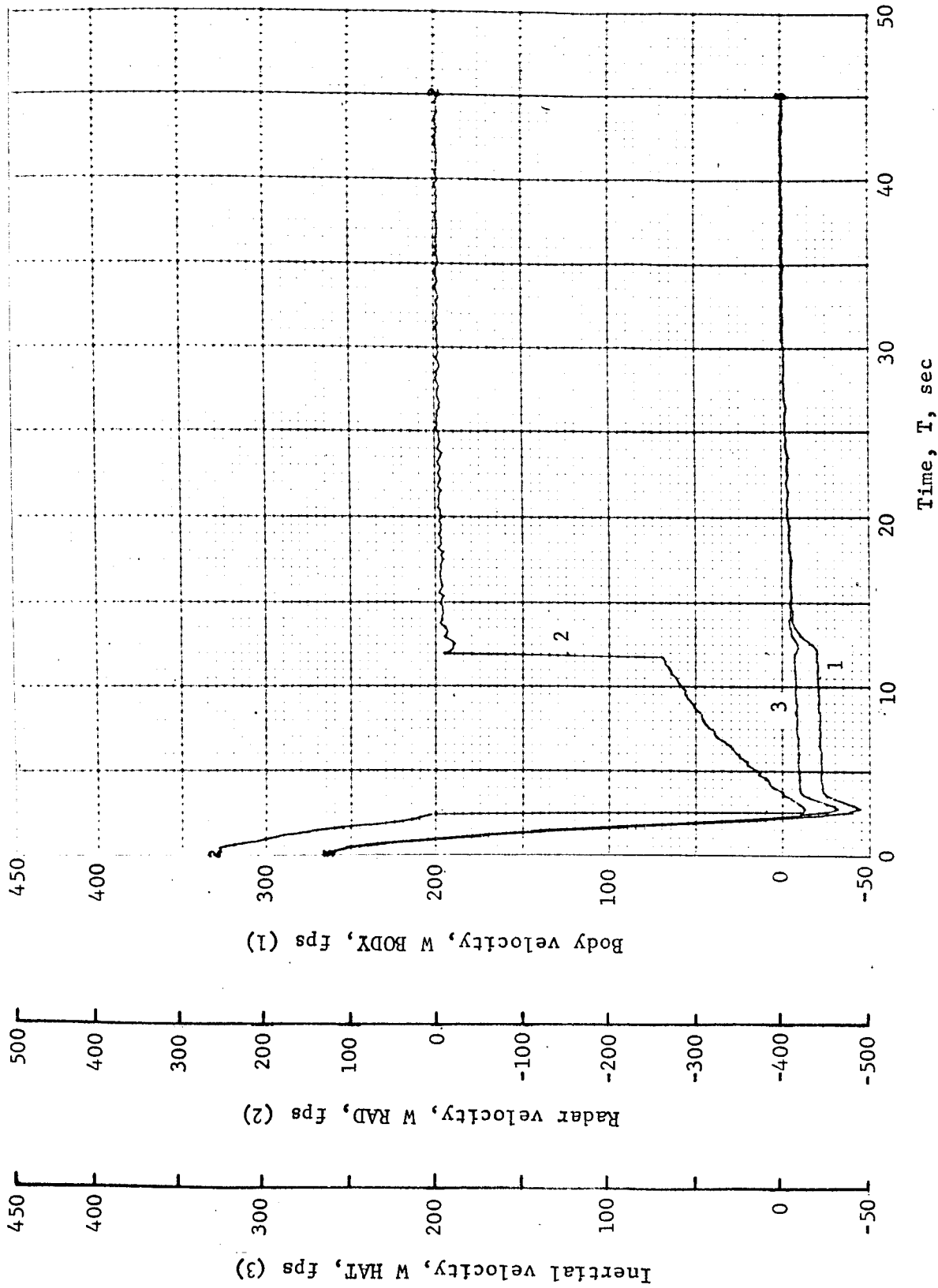


Figure B5.- Soft Lander, Run 1-5

APPENDIX B

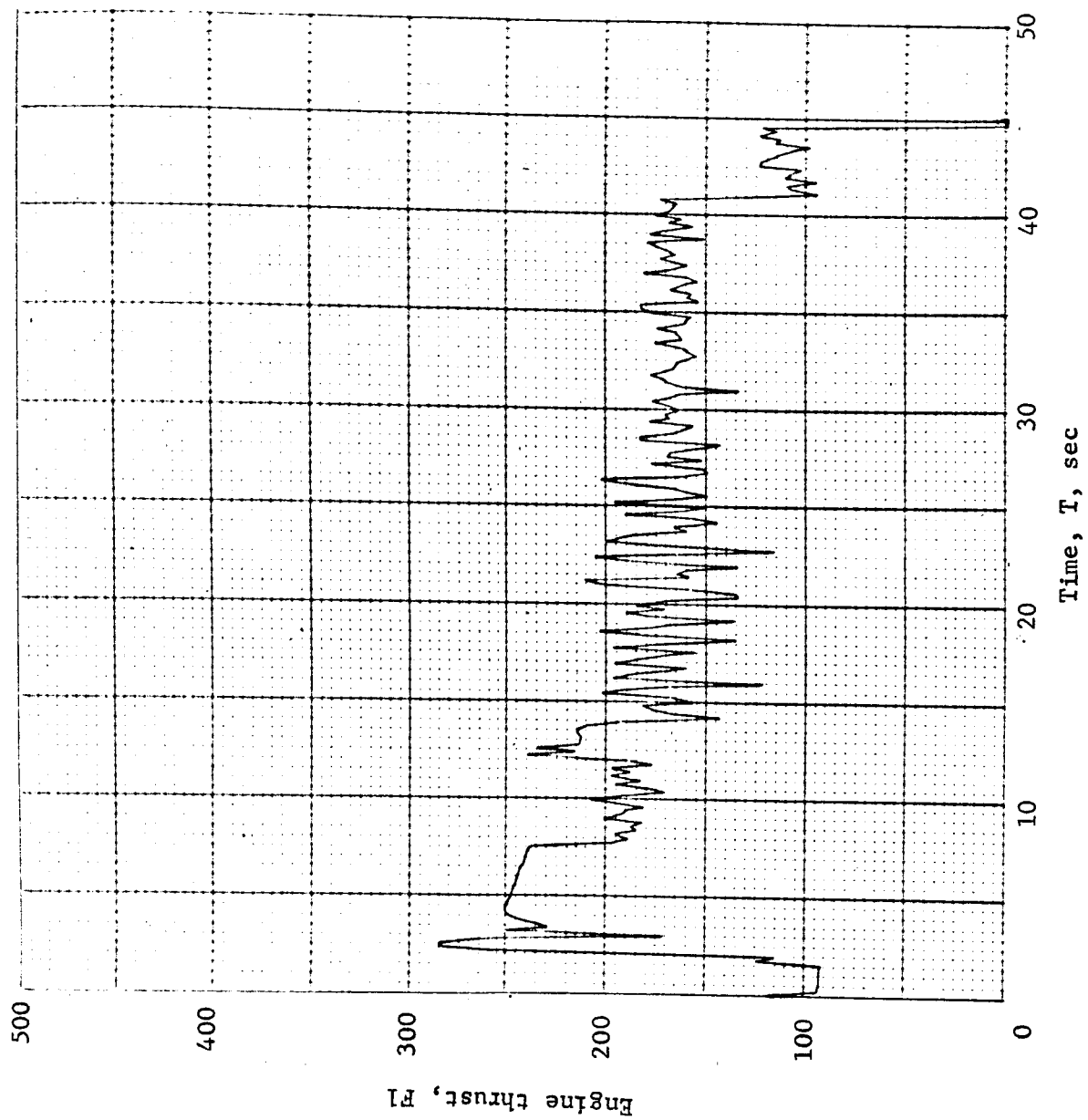


Figure B6.- Soft Lander, Run 1-6

APPENDIX B

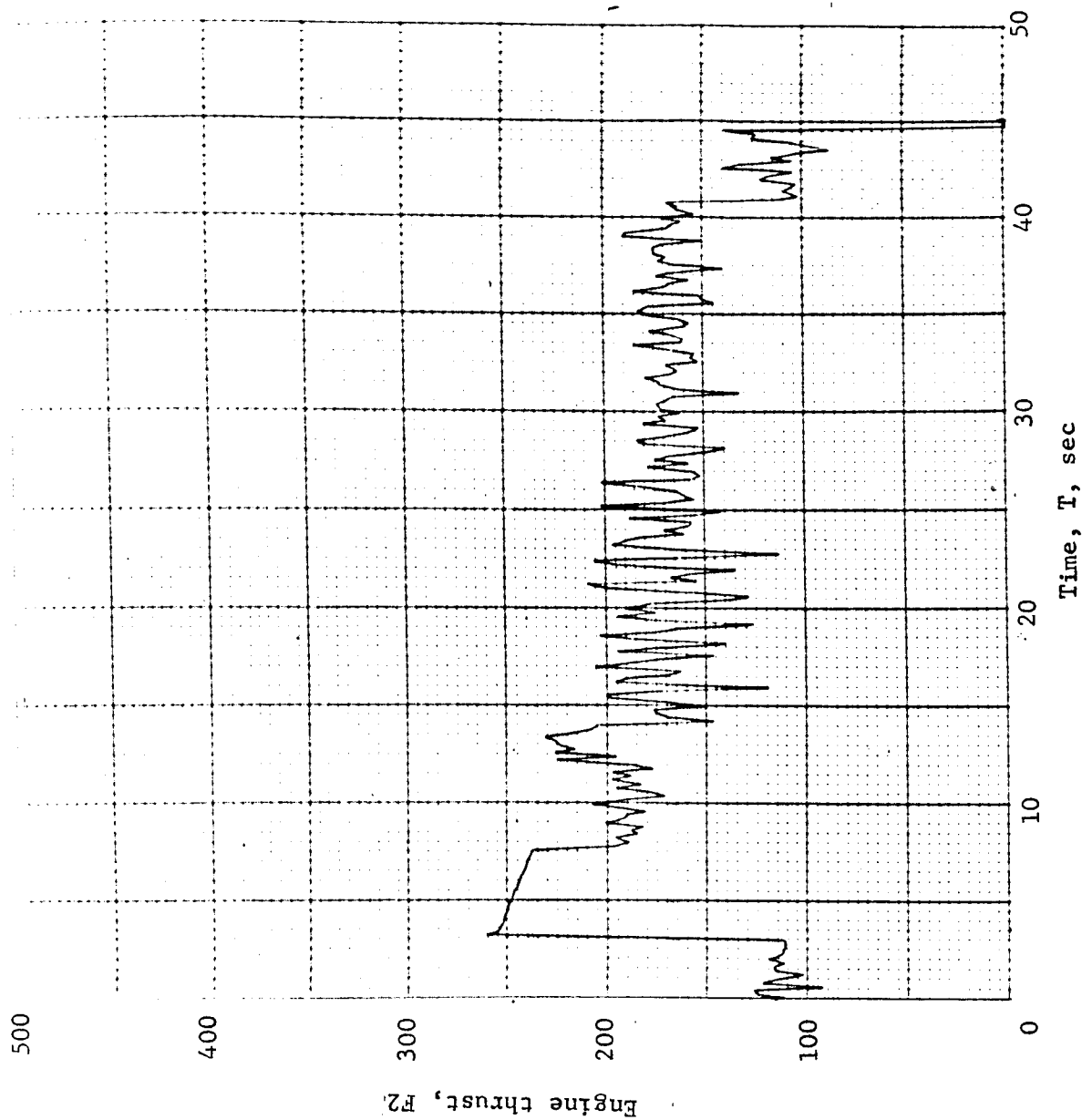


Figure B7.- Soft Lander, Run 1-7

APPENDIX B

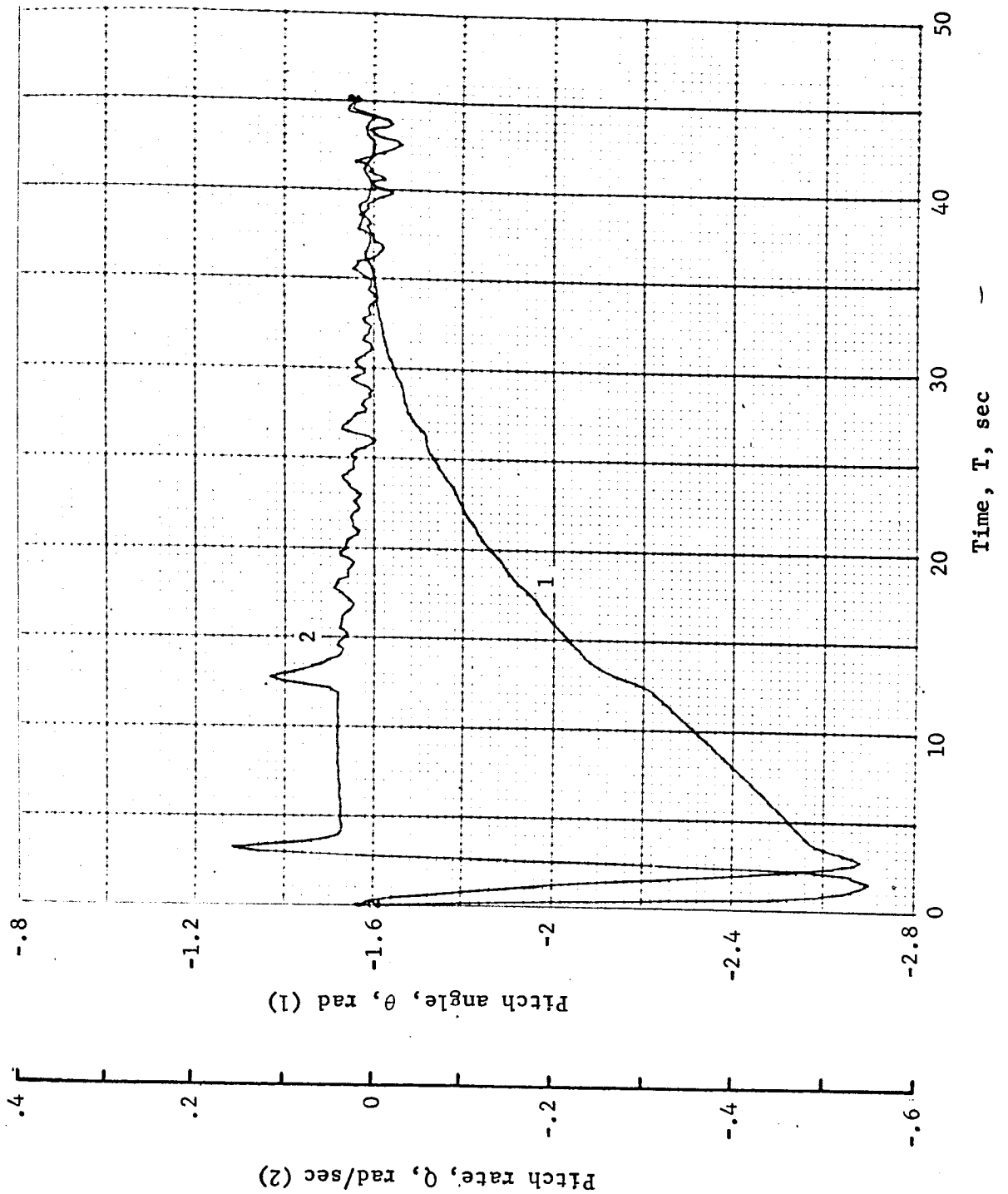


Figure B8.- Soft Lander, Run 1-8

APPENDIX B

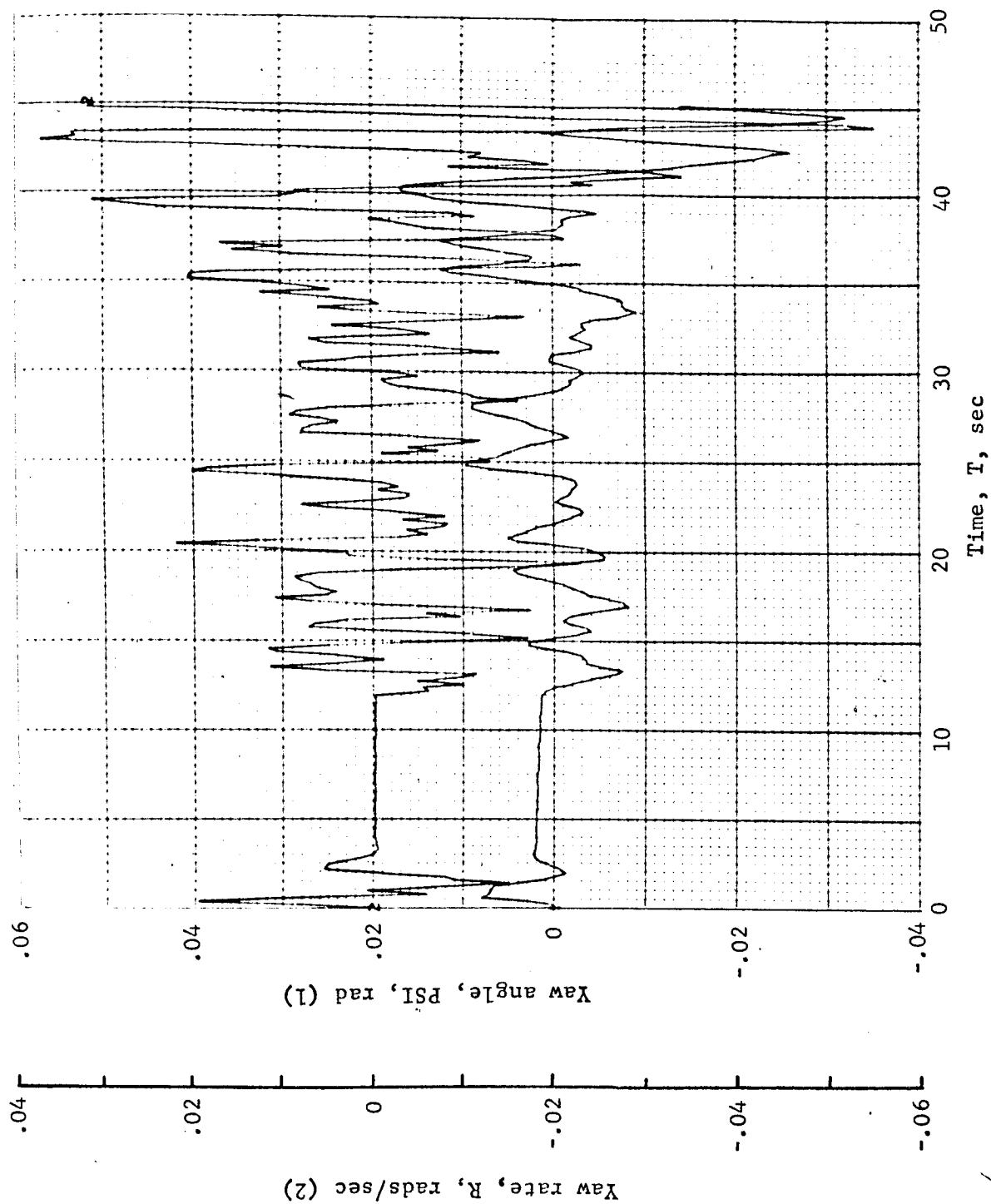


Figure B9.- Soft Lander, Run 1-9

APPENDIX B

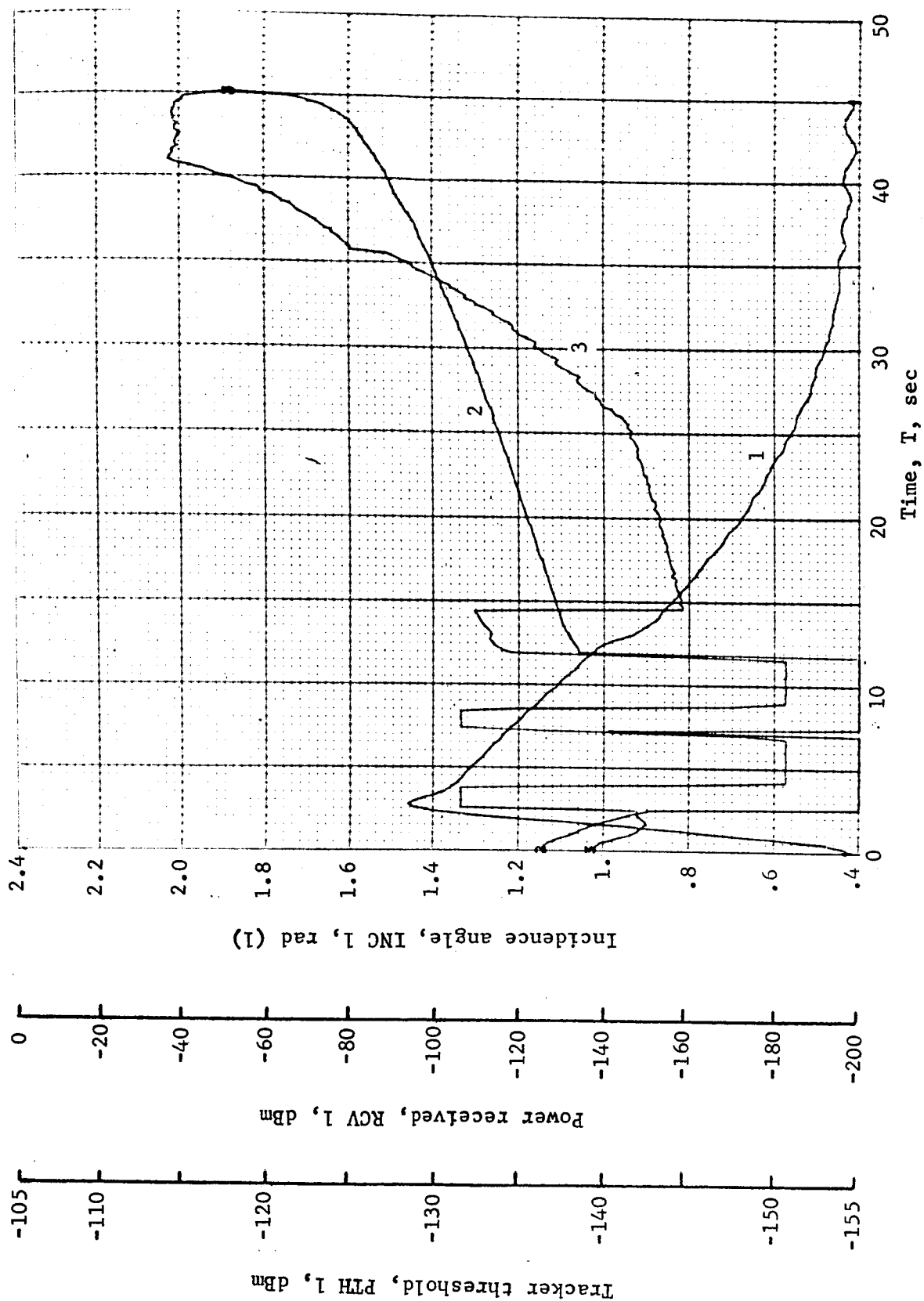


Figure B10.- Soft Lander, Run 1-10

APPENDIX B

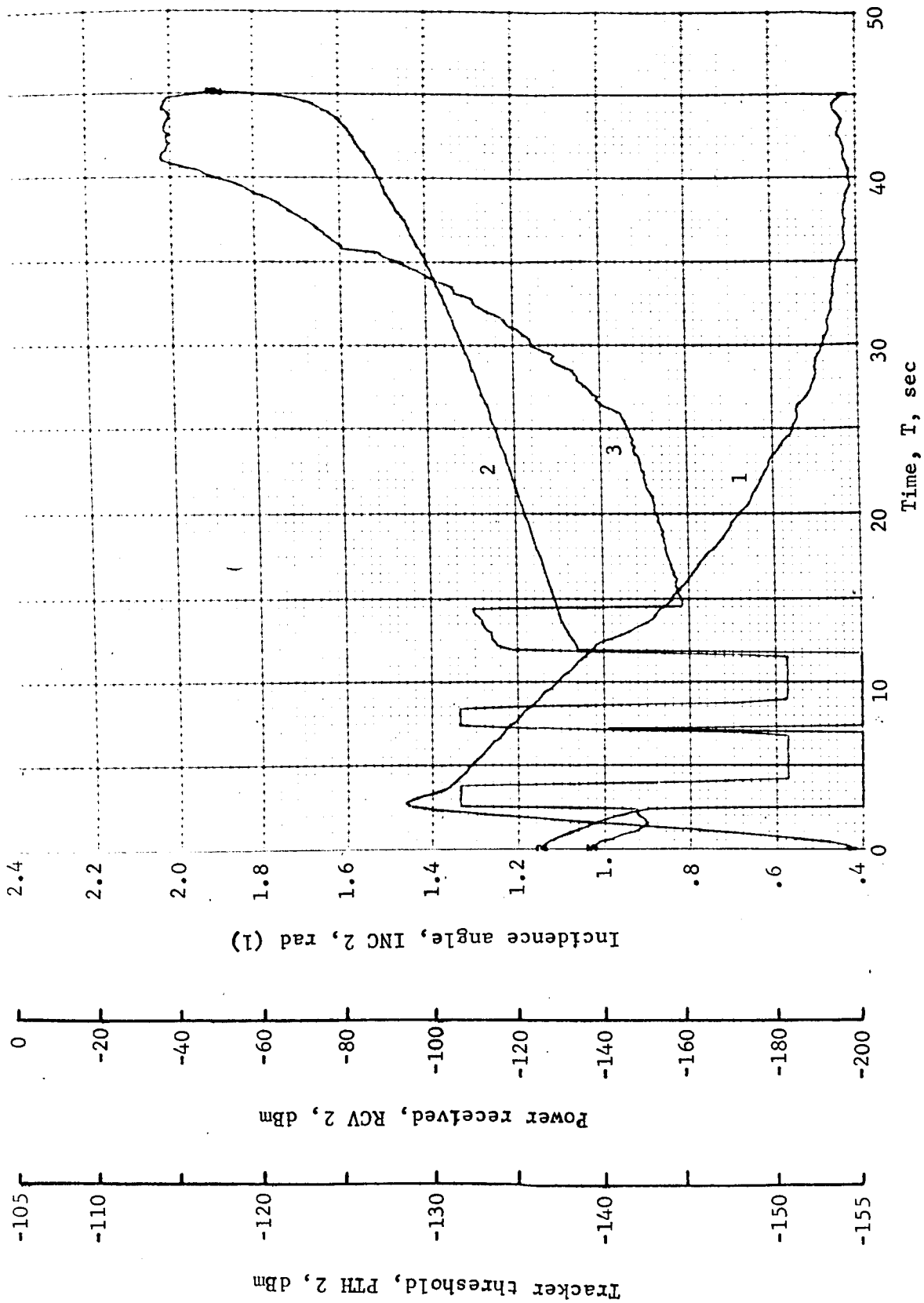


Figure B11.- Soft Lander, Run 1-11

APPENDIX B

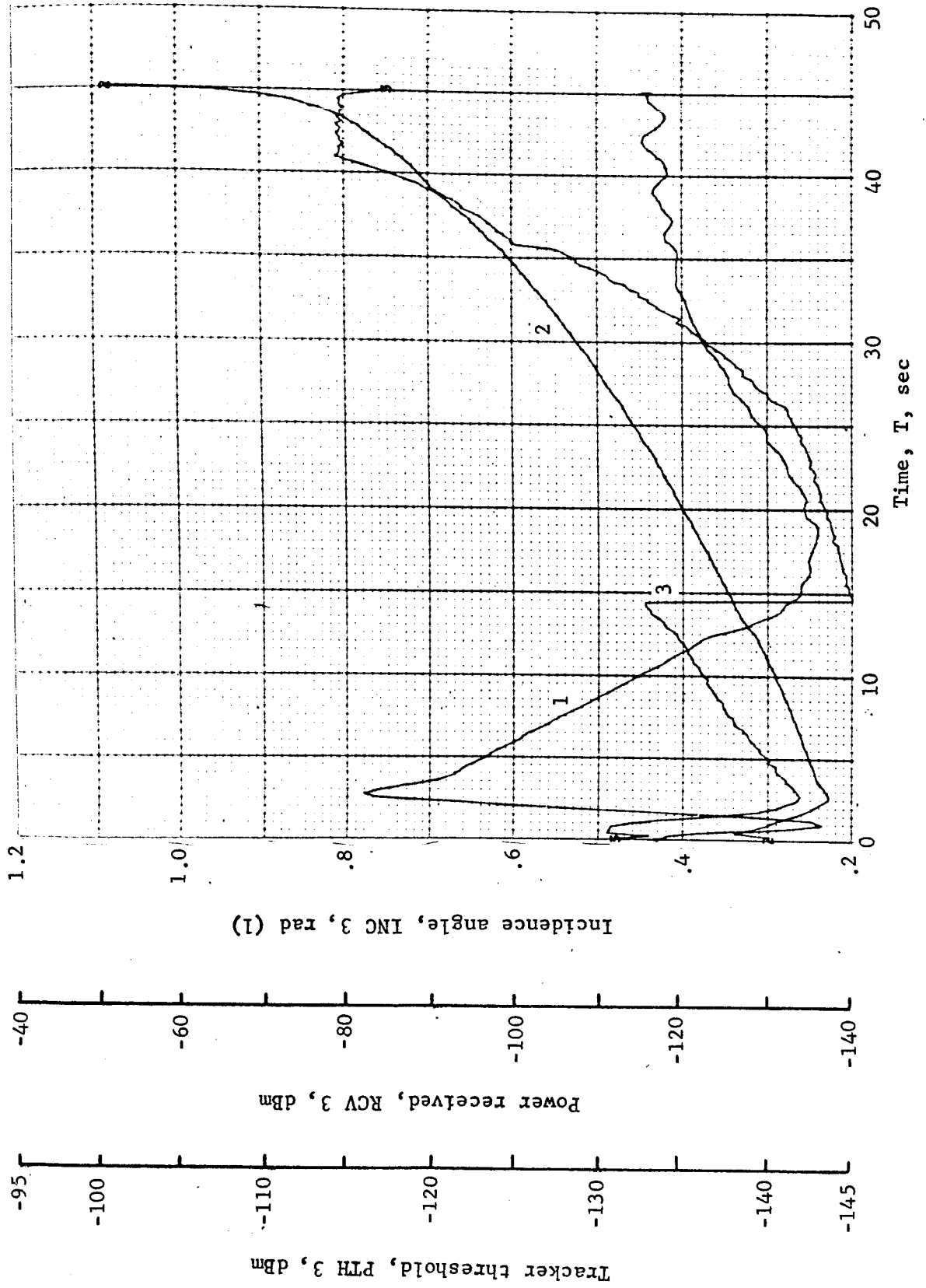


Figure B12.- Soft Lander, Run 1-12

APPENDIX B

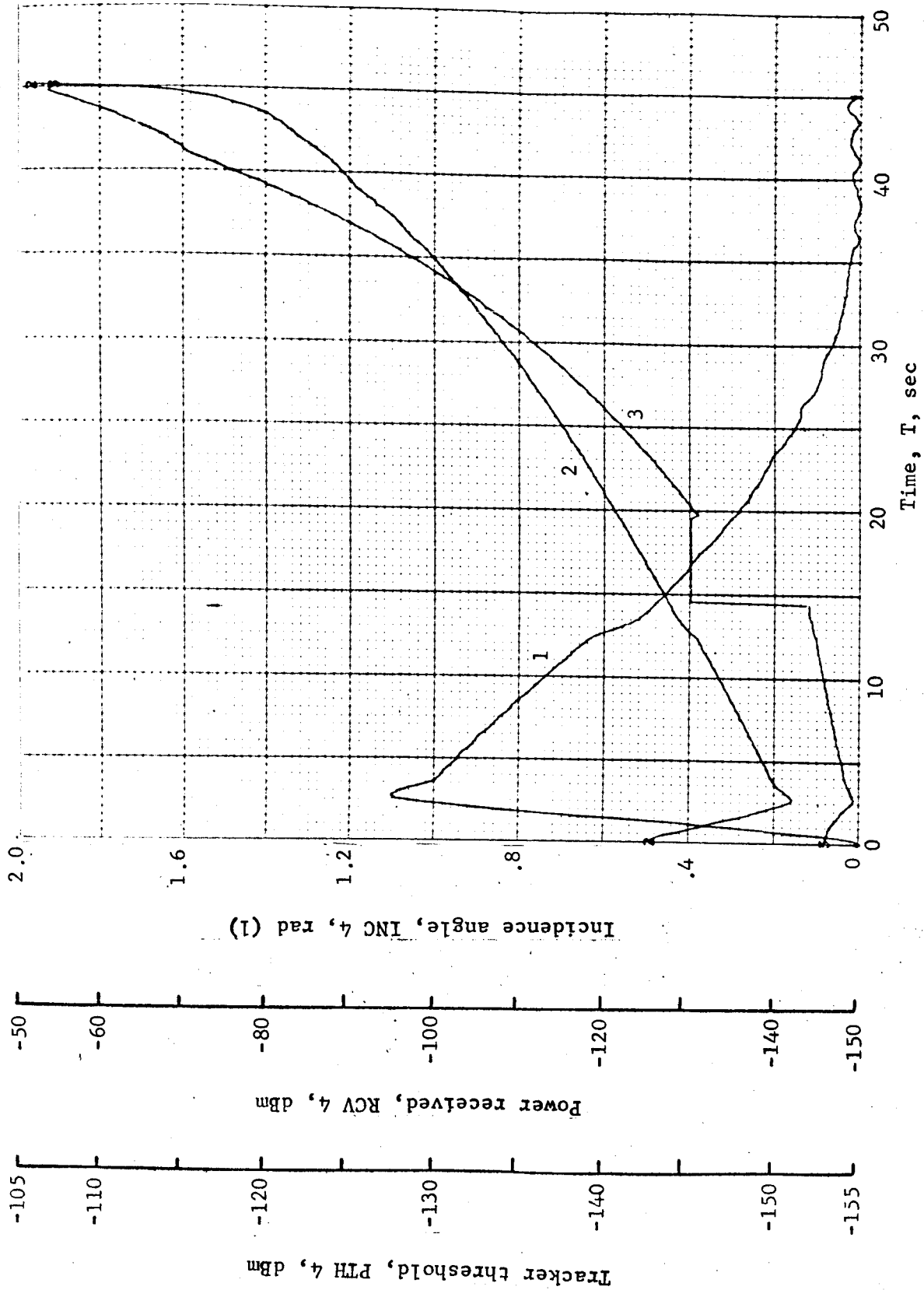


Figure B13.- Soft Lander, Run 1-13

APPENDIX B

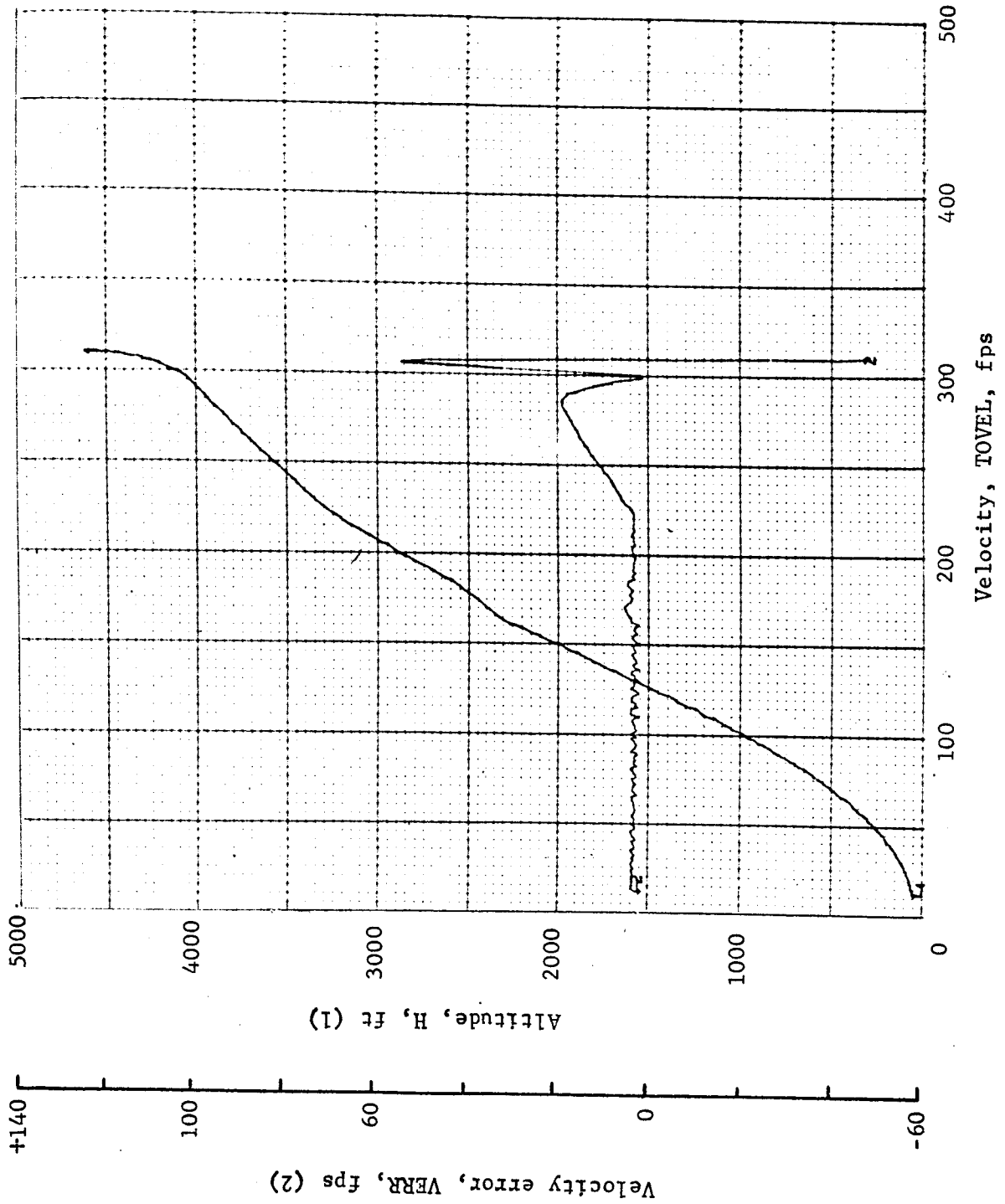


Figure B14.- Soft Lander, Run 1-14

APPENDIX B

TABLE B2.- RUN 2, AUTONOMOUS/LM RADAR/RANGE VELOCITY/-19° SLOPE

Flight condition	Altitude, ft	Velocity, fps		Pitch angle, deg	Pitch rate, deg/sec	Time, sec	Fuel used, lb	Beams unlocked	Time at reqcquire after un- lock, sec
		Roll axis	cross axis						
Initial	4600	165	-220	-90	0	0	0	----	----
Mid-pitchup	4476	253.5	-100.5	-58.5	31.2	1.4	3.2	----	----
Max. pitchup	4362.6	263.9	38.7	-31.3	1.2	2.6	6.1 4 at 2.4 3 at 2.2	----	----
Thrust aligned	4236.9	260.8	18.8	-38.3	-2.3	3.8	8.8	----	----
Encounter contour	4258.7	262.3	19.4	-37.7	-3.3	3.6	8.2	----	3 at 14.2 4 at 5.6
Constant vel	46.7	12.5	.04	-89.5	1.45	45.6	135	----	----
Cutoff eng	8.73	12.6	.3	-89.7	1.66	48.6	141.1	----	----
Land	.96	18.7	.07	-88.5	1.65	49.1	141.1	----	----
Remarks:									

APPENDIX B

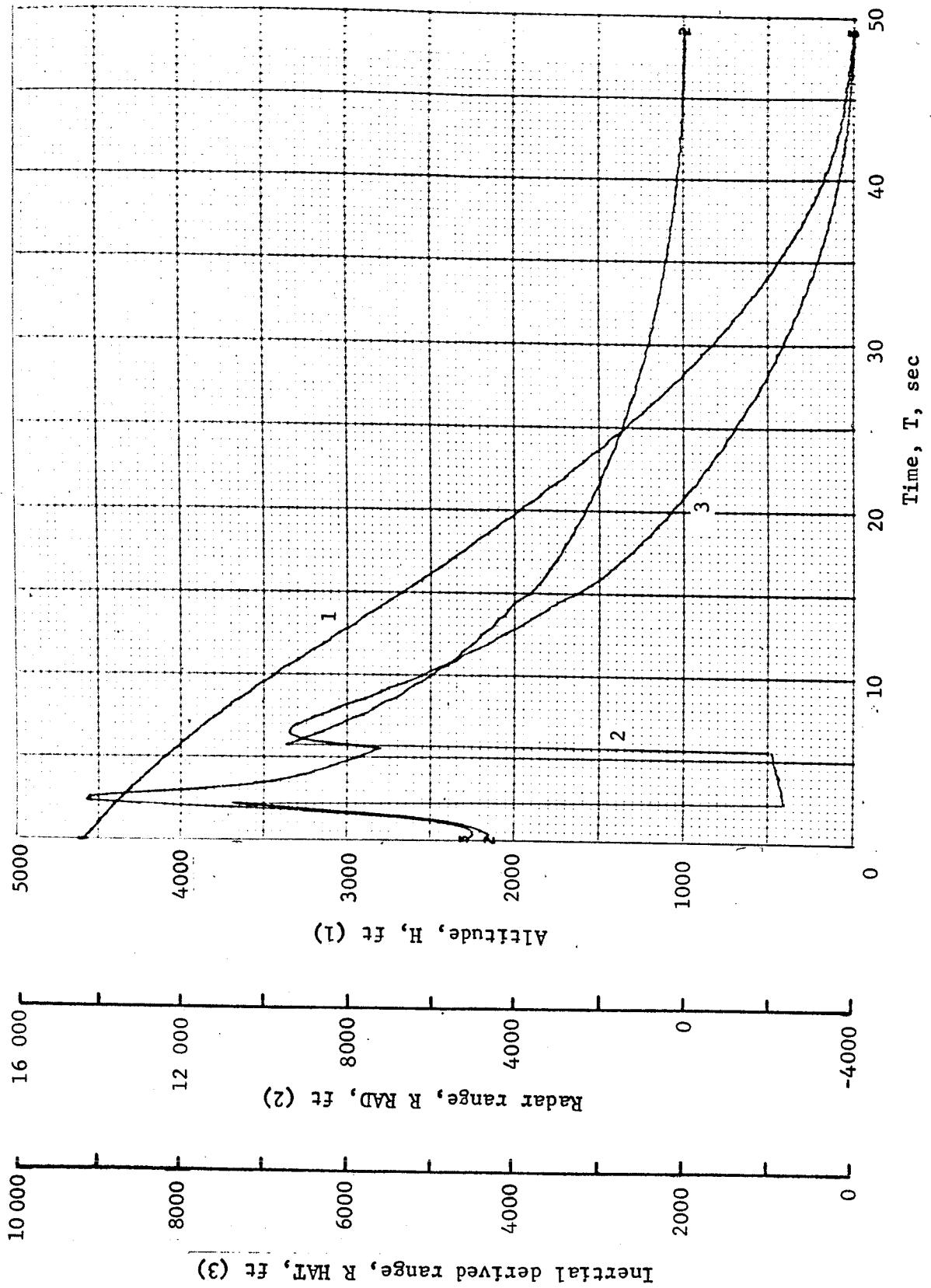


Figure B15.- Soft Lander, Run 2-1

APPENDIX B

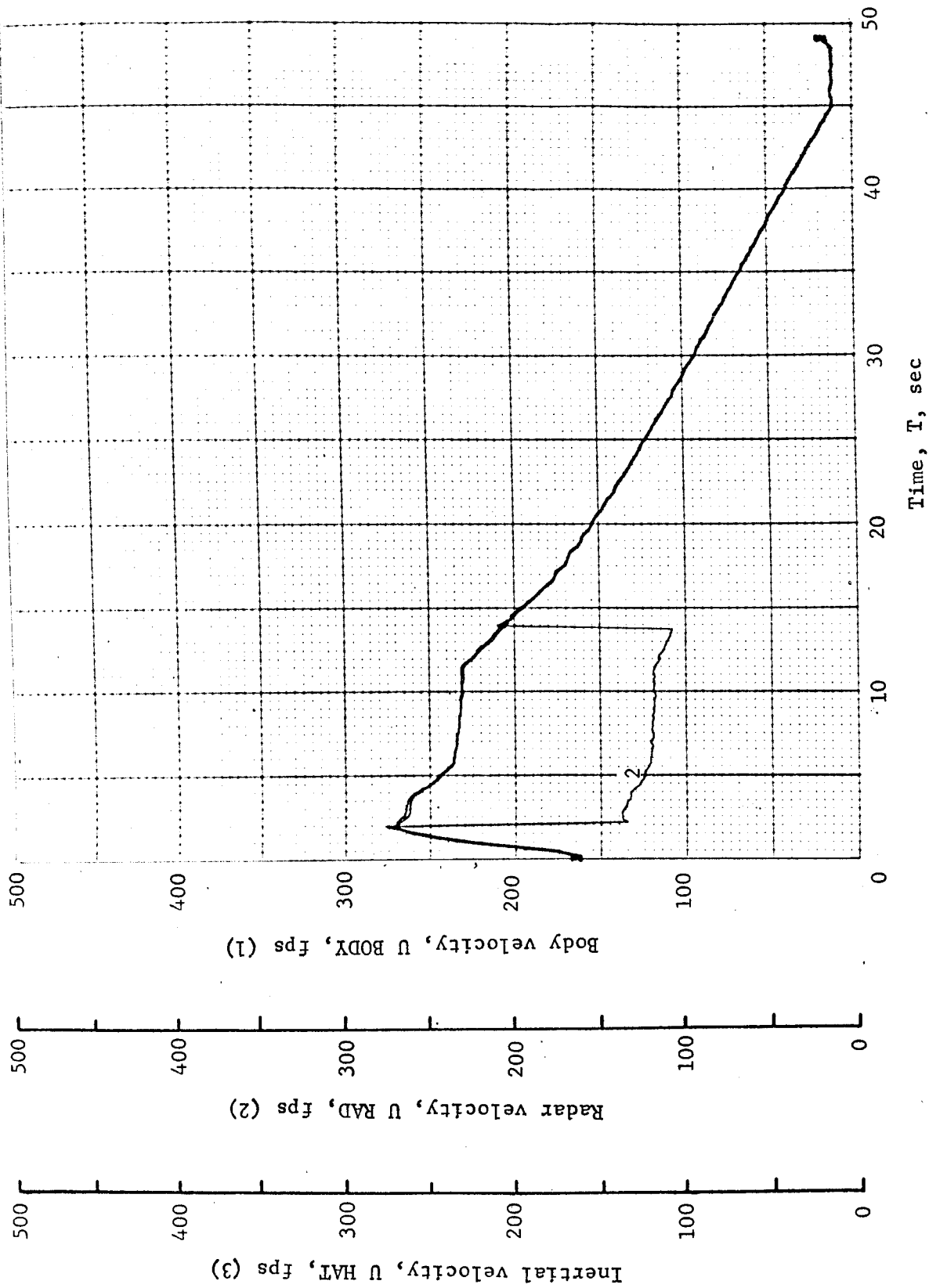


Figure B16.- Soft Lander, Run 2-2

APPENDIX B

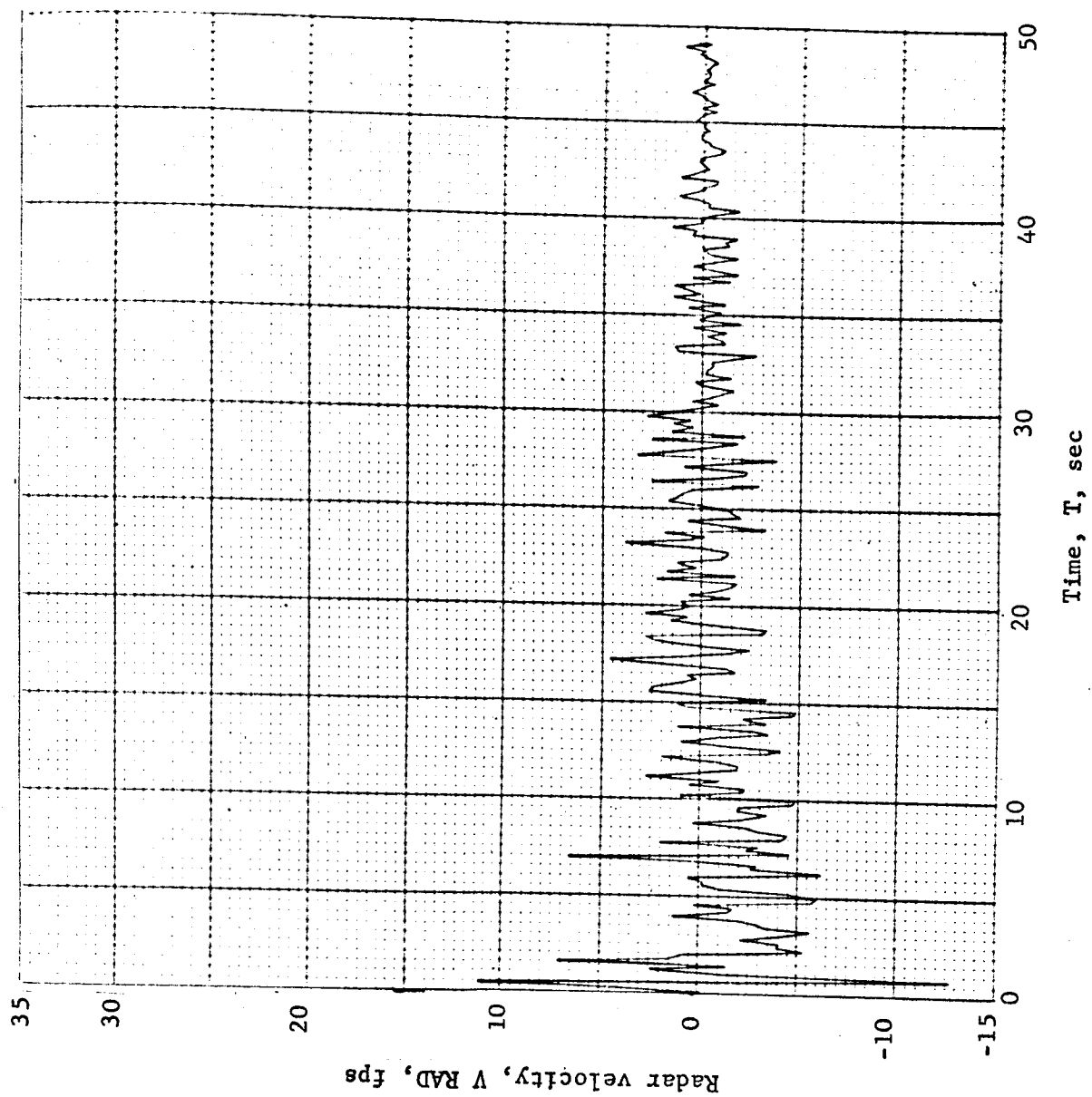


Figure B17.- Soft Lander, Run 2-3

APPENDIX B

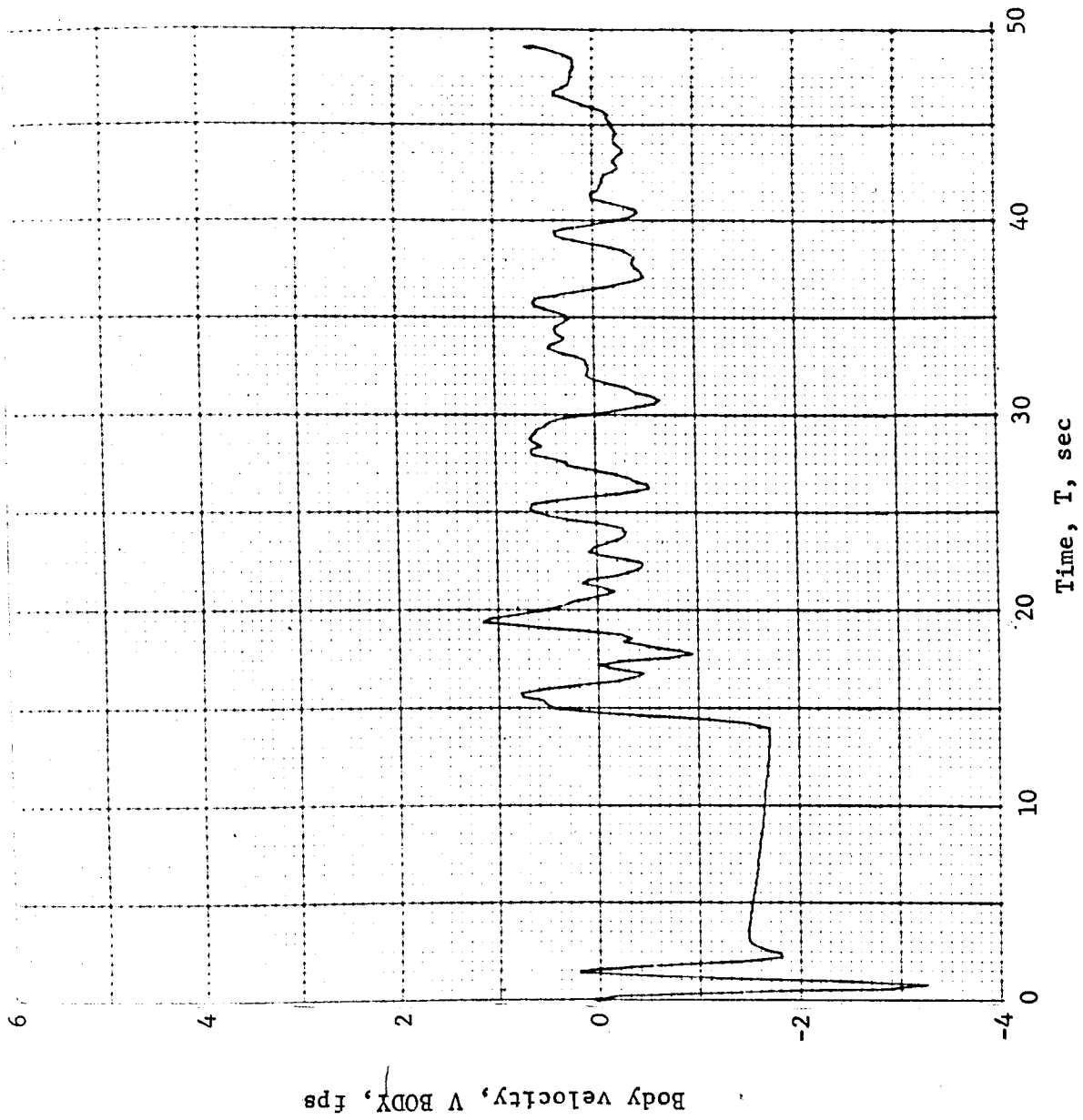


Figure B18.- Soft Lander, Run 2-4

APPENDIX B

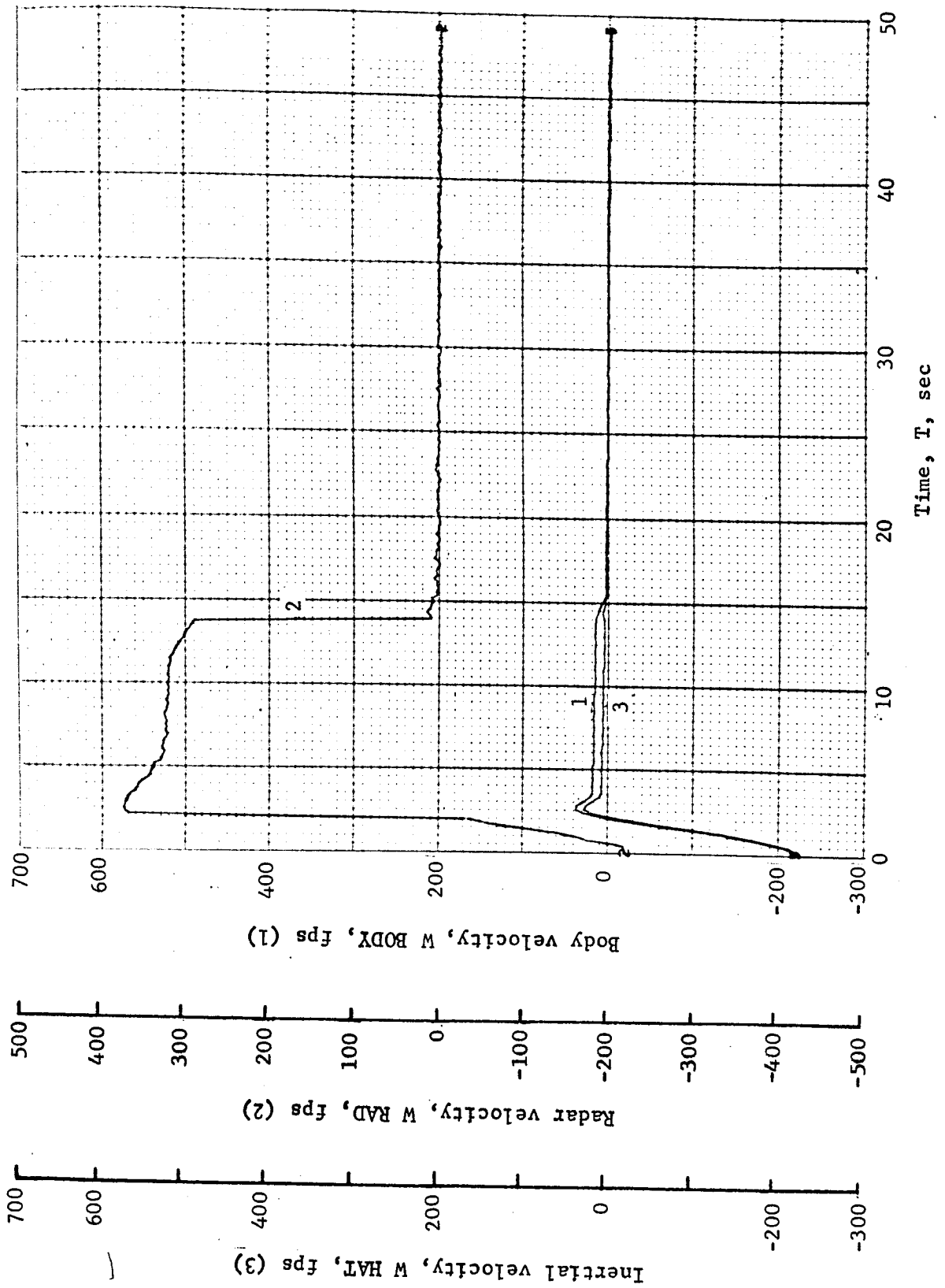


Figure B19.- Soft Lander, Run 2-5

APPENDIX B

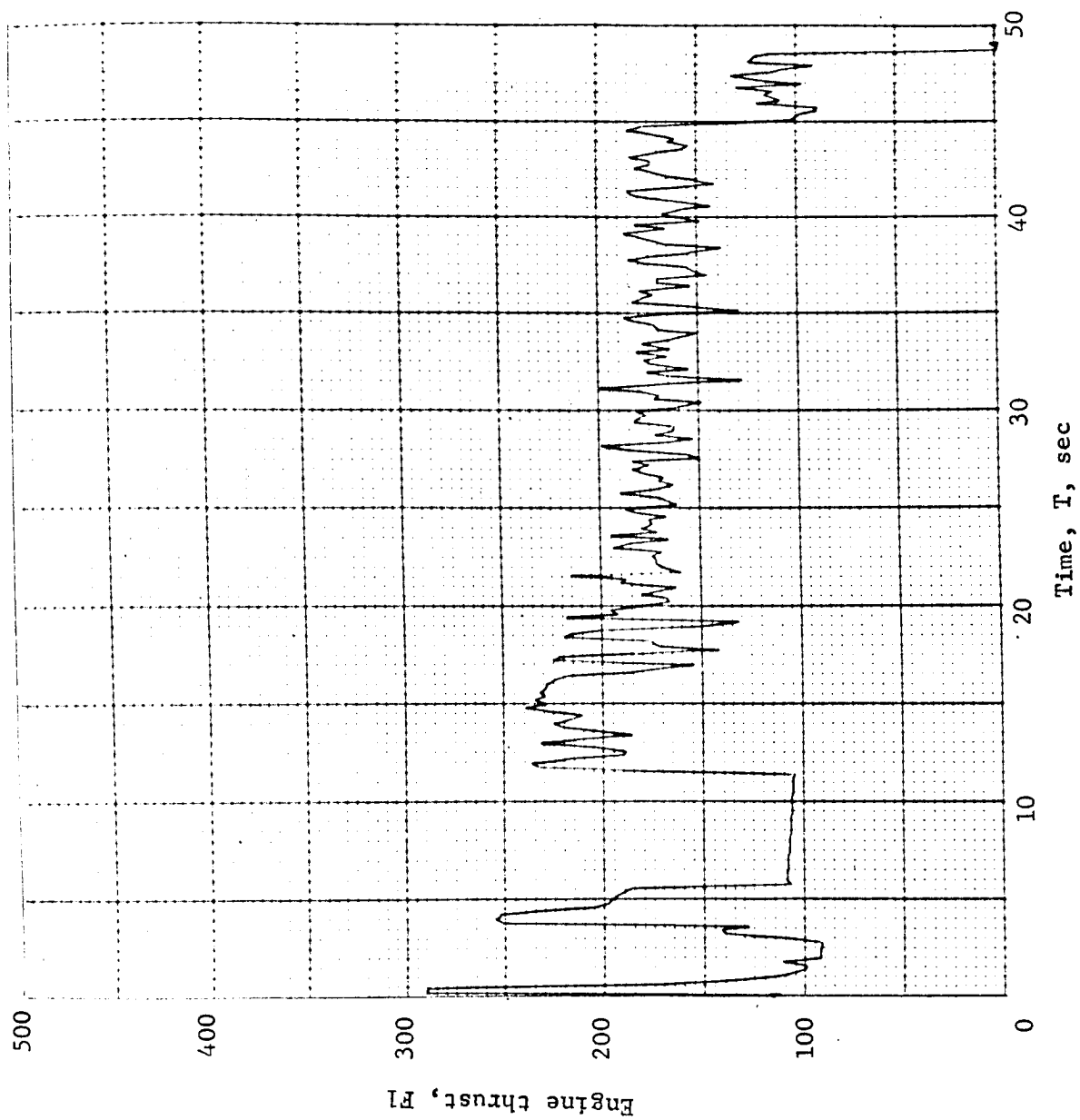


Figure B20.- Soft Lander, Run 2-6

APPENDIX B

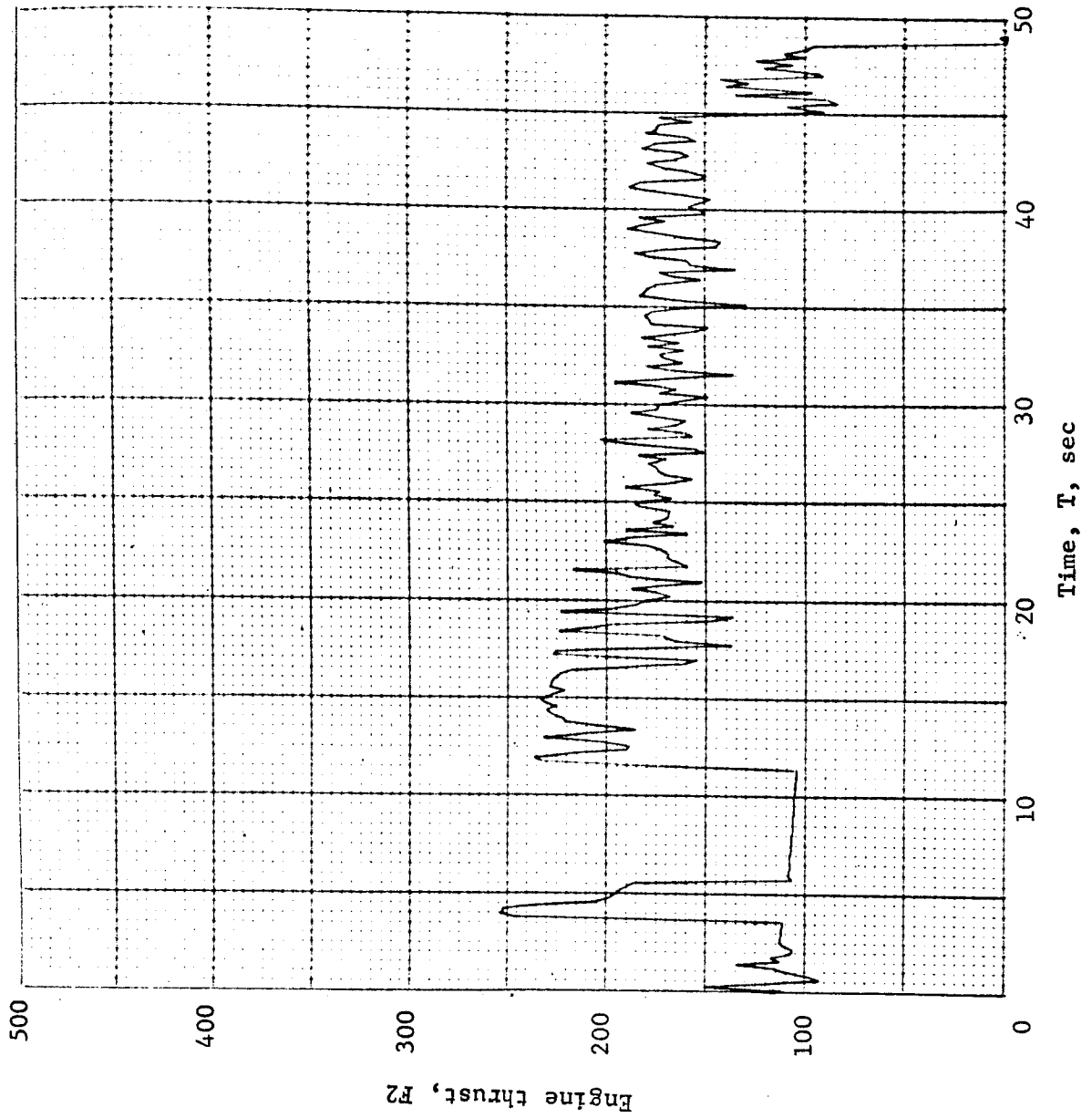


Figure B21.- Soft Lander, Run 2-7

APPENDIX B

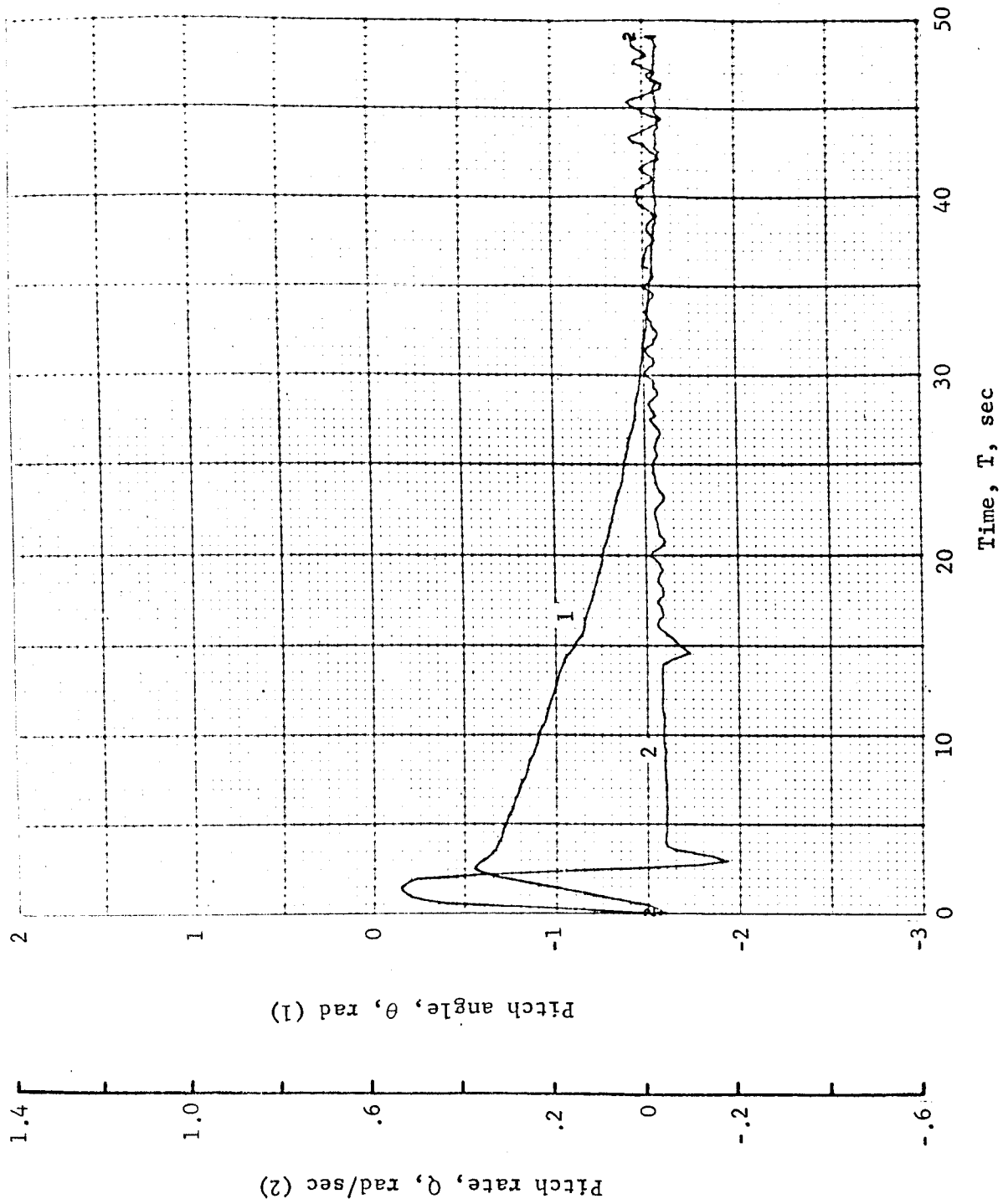


Figure B22.- Soft Lander, Run 2-8

APPENDIX B

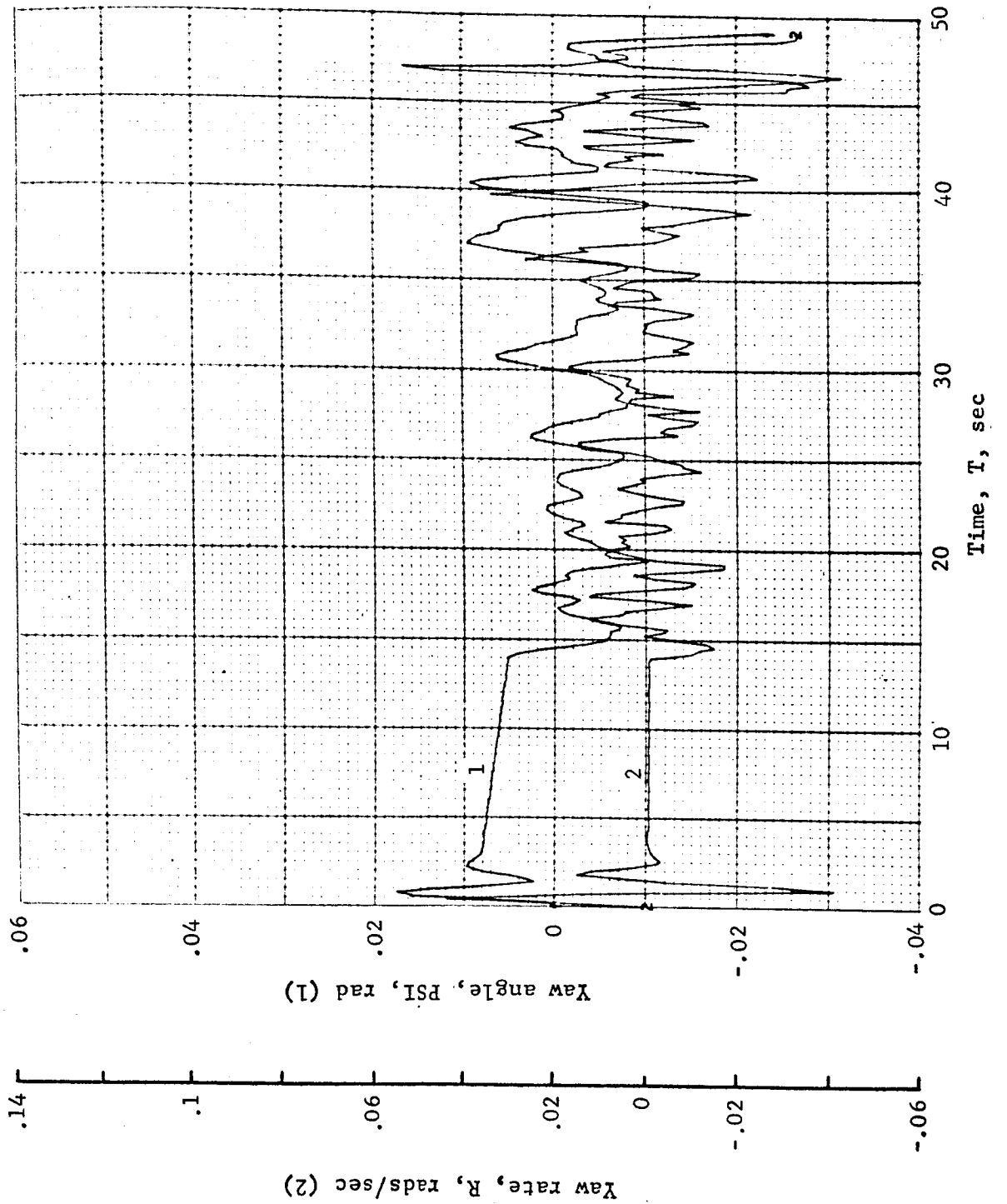


Figure B23.- Soft Lander, Run 2-9.

APPENDIX B

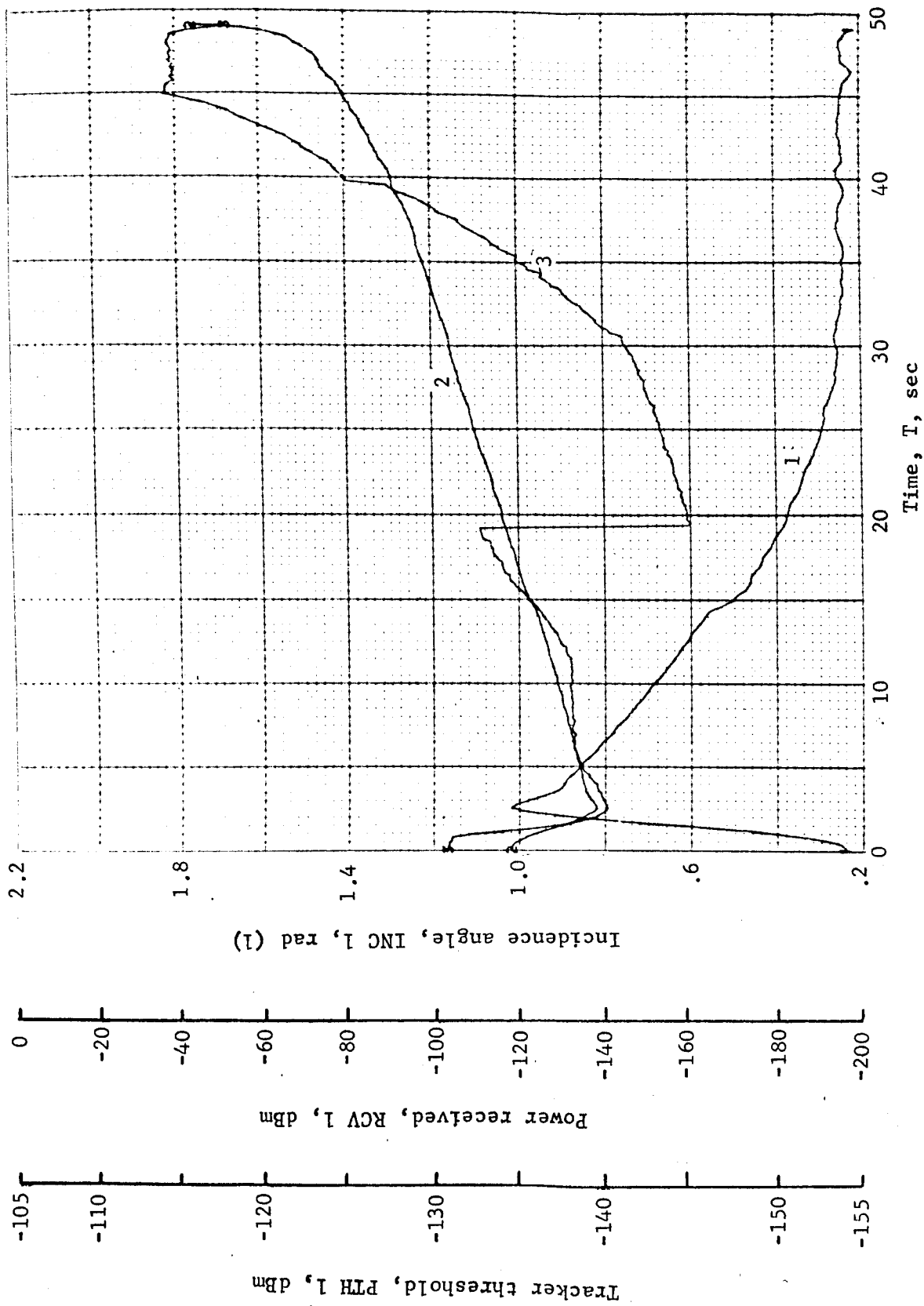


Figure B24.- Soft Lander, Run 2-10

APPENDIX B

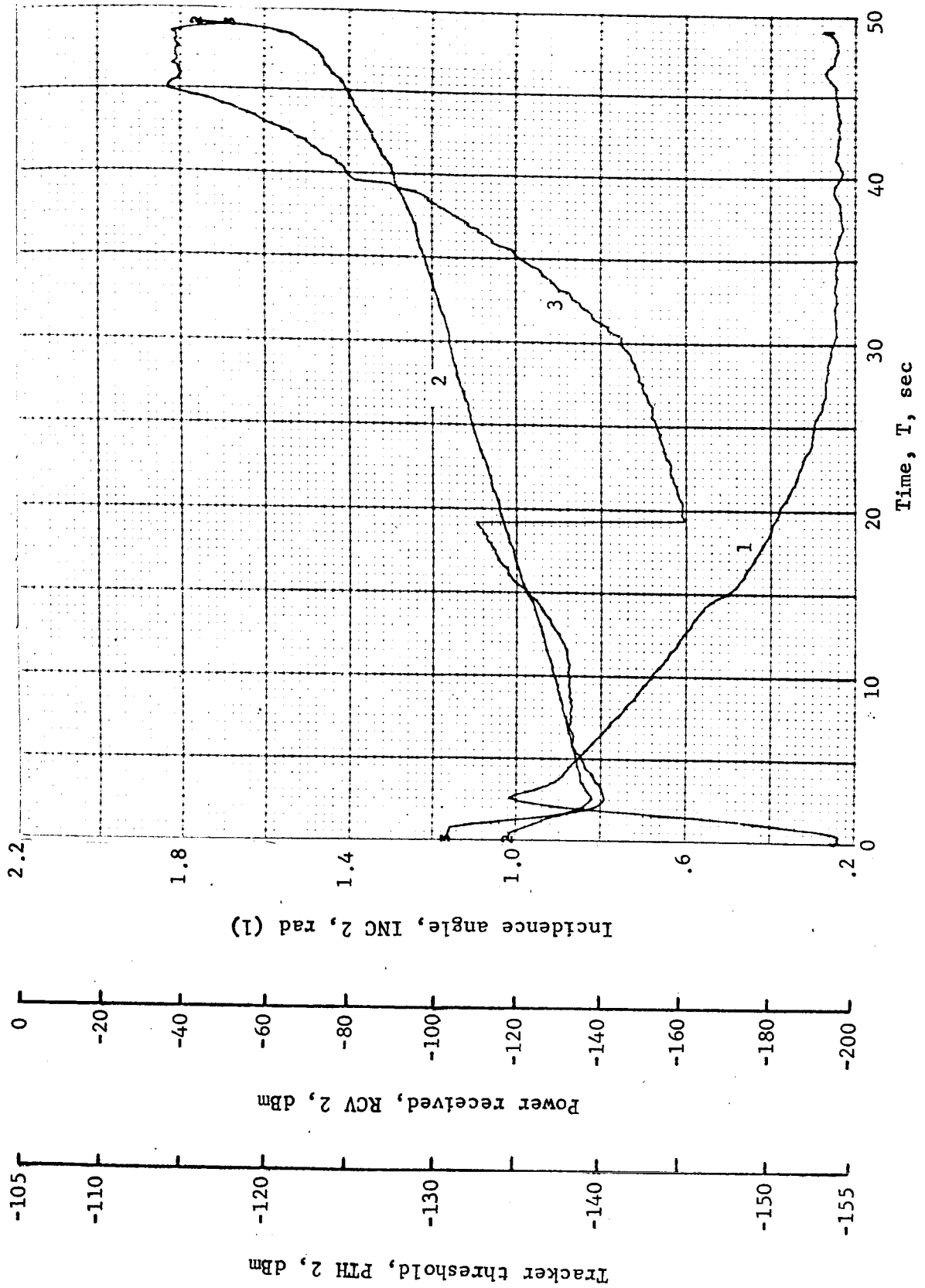


Figure B25.- Soft Lander, Run 2-11

APPENDIX B

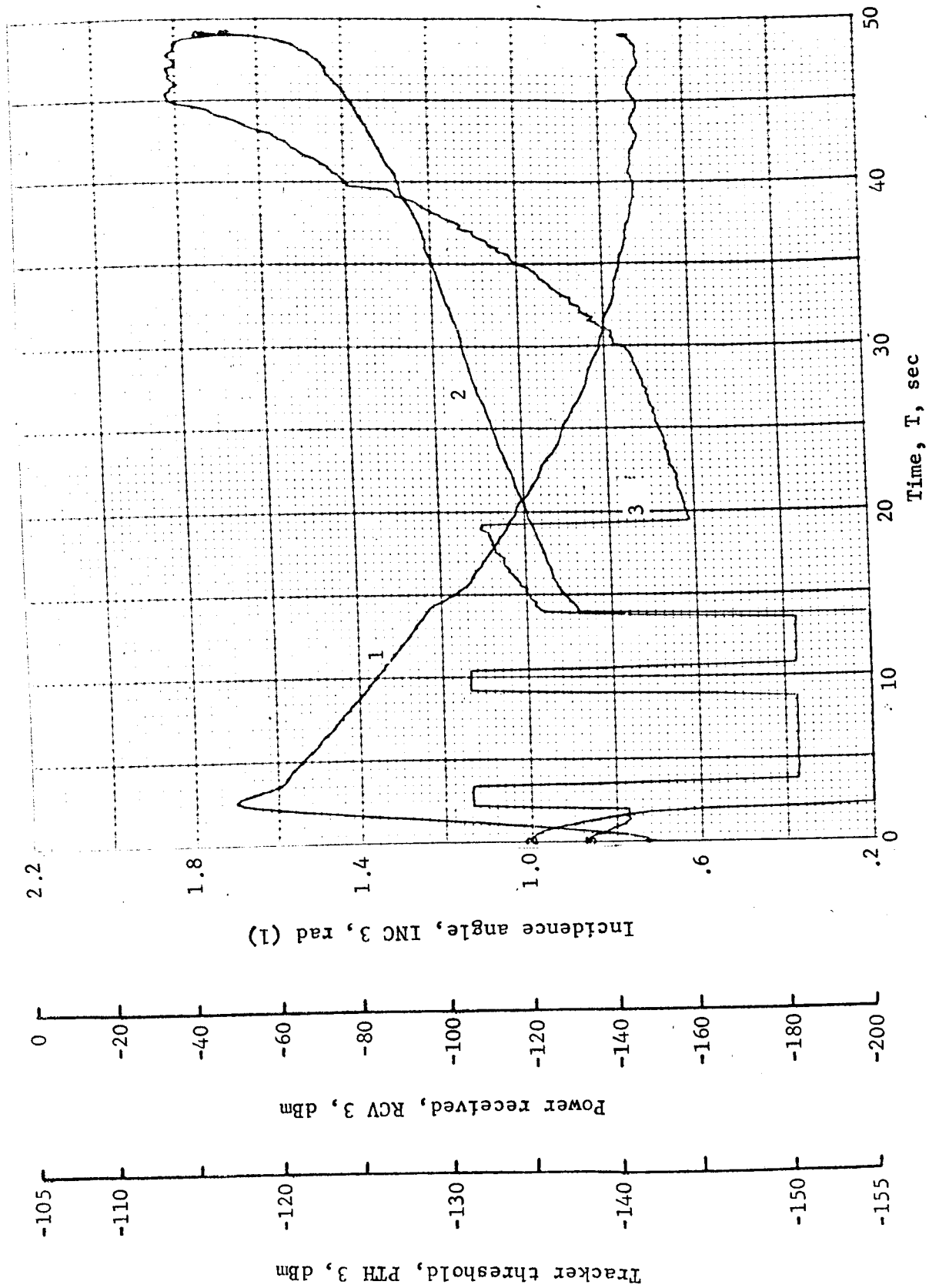


Figure B26.- Soft Lander, Run 2-12

APPENDIX B

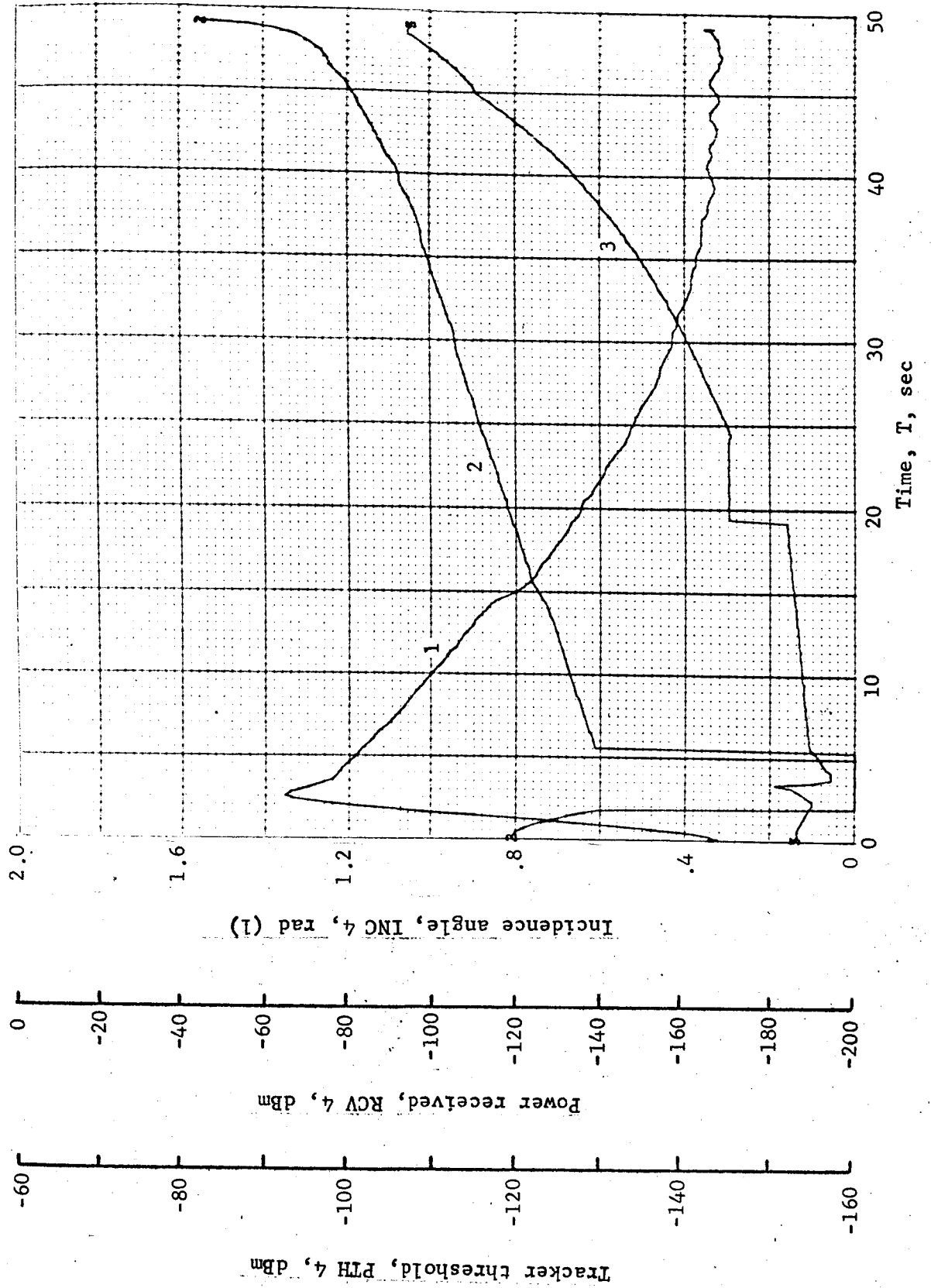


Figure B27.- Soft Lander, Run 2-13

APPENDIX B

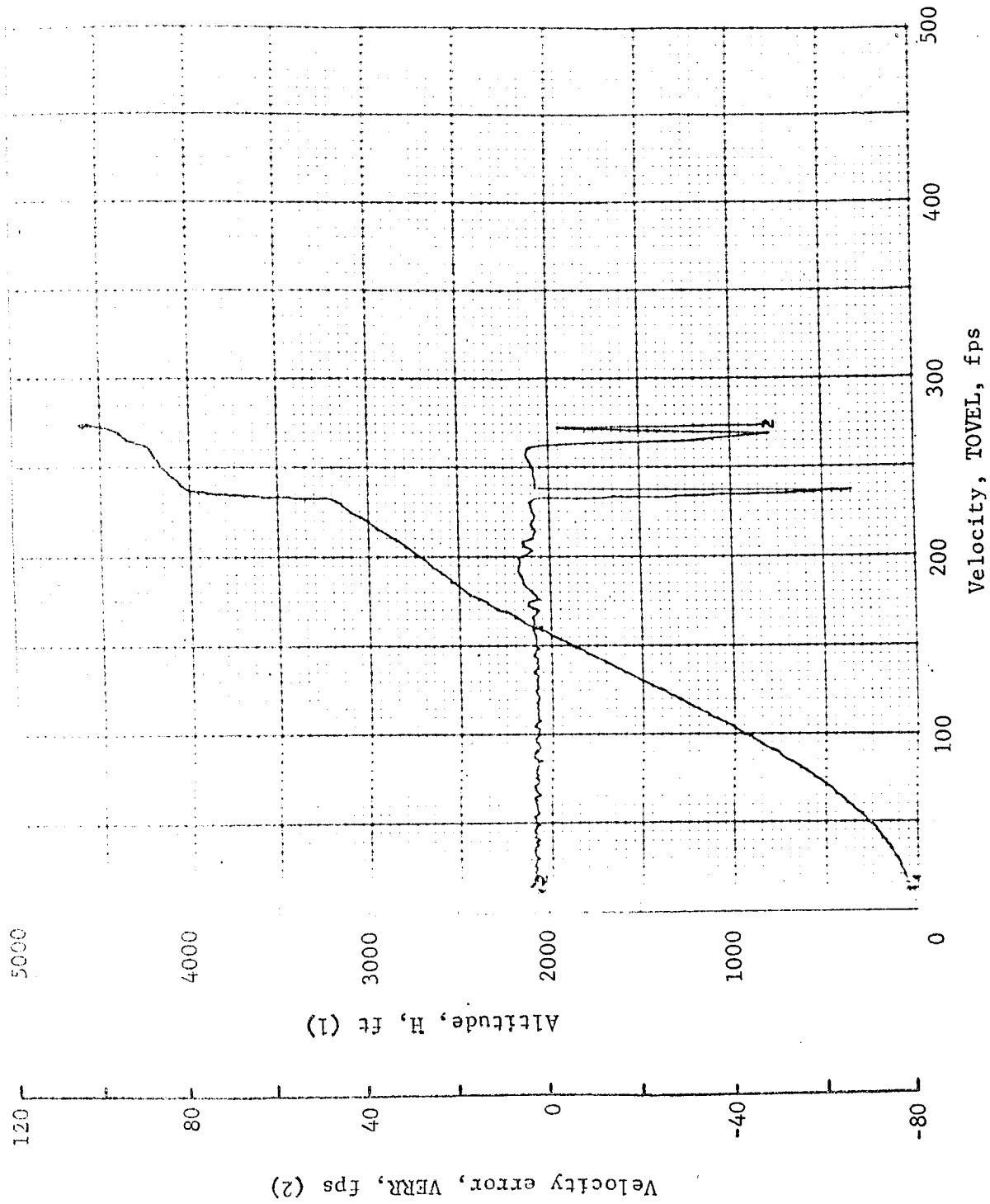


Figure B28.- Soft Lander, Run 2-14

APPENDIX B

TABLE B3.- RUN 3, AUTONOMOUS/LM RADAR/RANGE VELOCITY/-27° SLOPE

Flight condition	Altitude, ft	Velocity, fps		Pitch angle, deg	Pitch rate, deg/sec	Time, sec	Fuel used, lb	Beams unlocked	Time to reacquire after loss
		Roll axis	Cross axis						
Initial	4600	165	-170	0	0	0	0	----	----
Mid-pitchup	4507	219.8	-83.7	-65.5	30.7	1.2	2.8	----	----
Max. pitchup	4407	228.7	27.35	-40	-1.9	2.4	5.7	3 at 1.8 4 at 2.2	----
Thrust aligned	4315.3	227.7	13.7	-45.7	-2.7	3.4	7.75	3, 4	----
Encounter contour	4214.8	226.2	13.5	-47.9	-2.2	4.4	9.8	3, 4	3 at 1 13.4 4 at 5.6
Constant vel	48.2	12.3	.25	-88	-.18	46.2	132.1	----	----
Cutoff eng	8.46	12.5	.2	-90.3	-1.9	49.4	138.6	----	----
Land	.92	18.4	-.06	-90.6	-1.9	49.9	138.6	----	----
Remarks:									

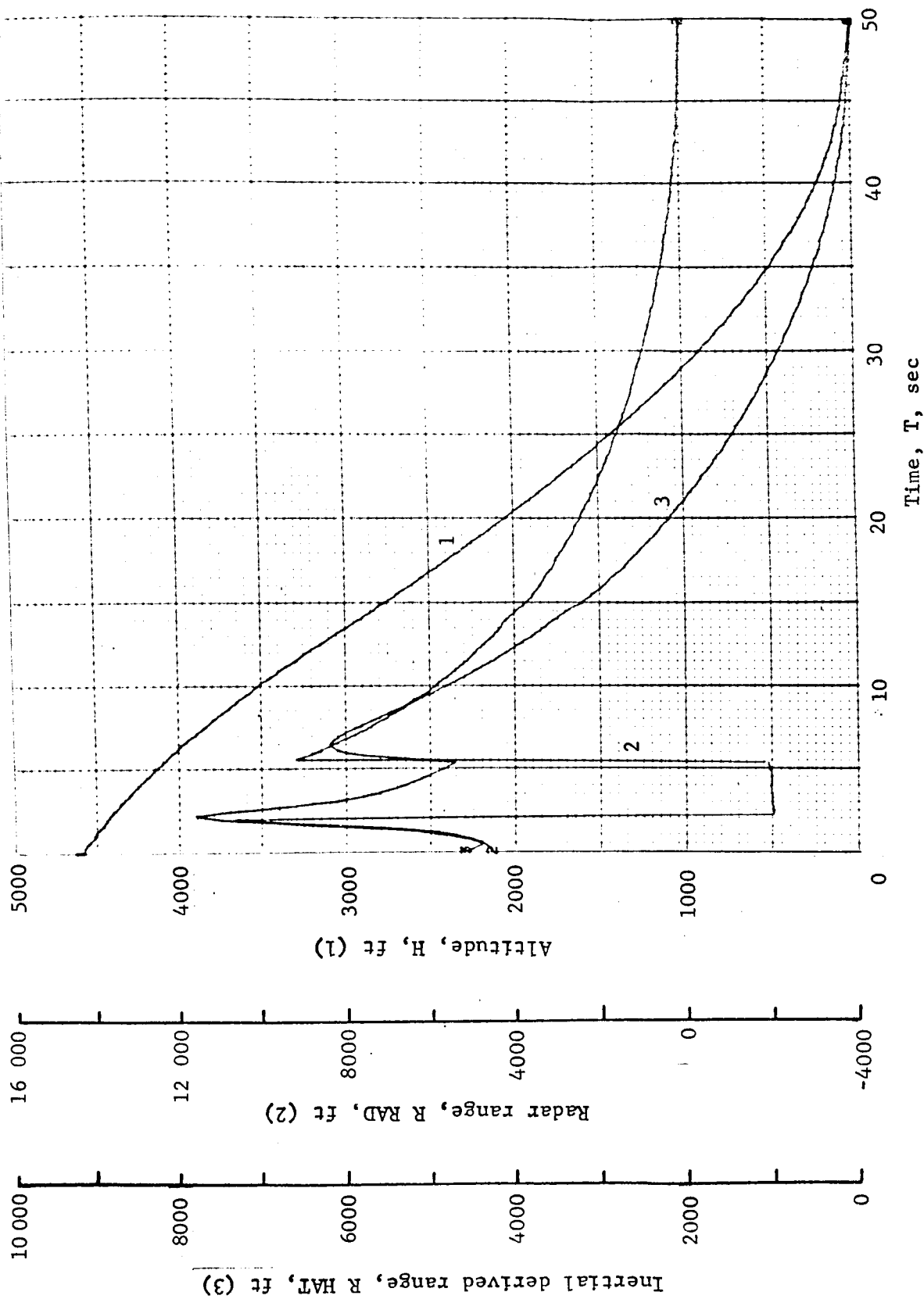


Figure B29.- Soft Lander, Run 3-1

APPENDIX B

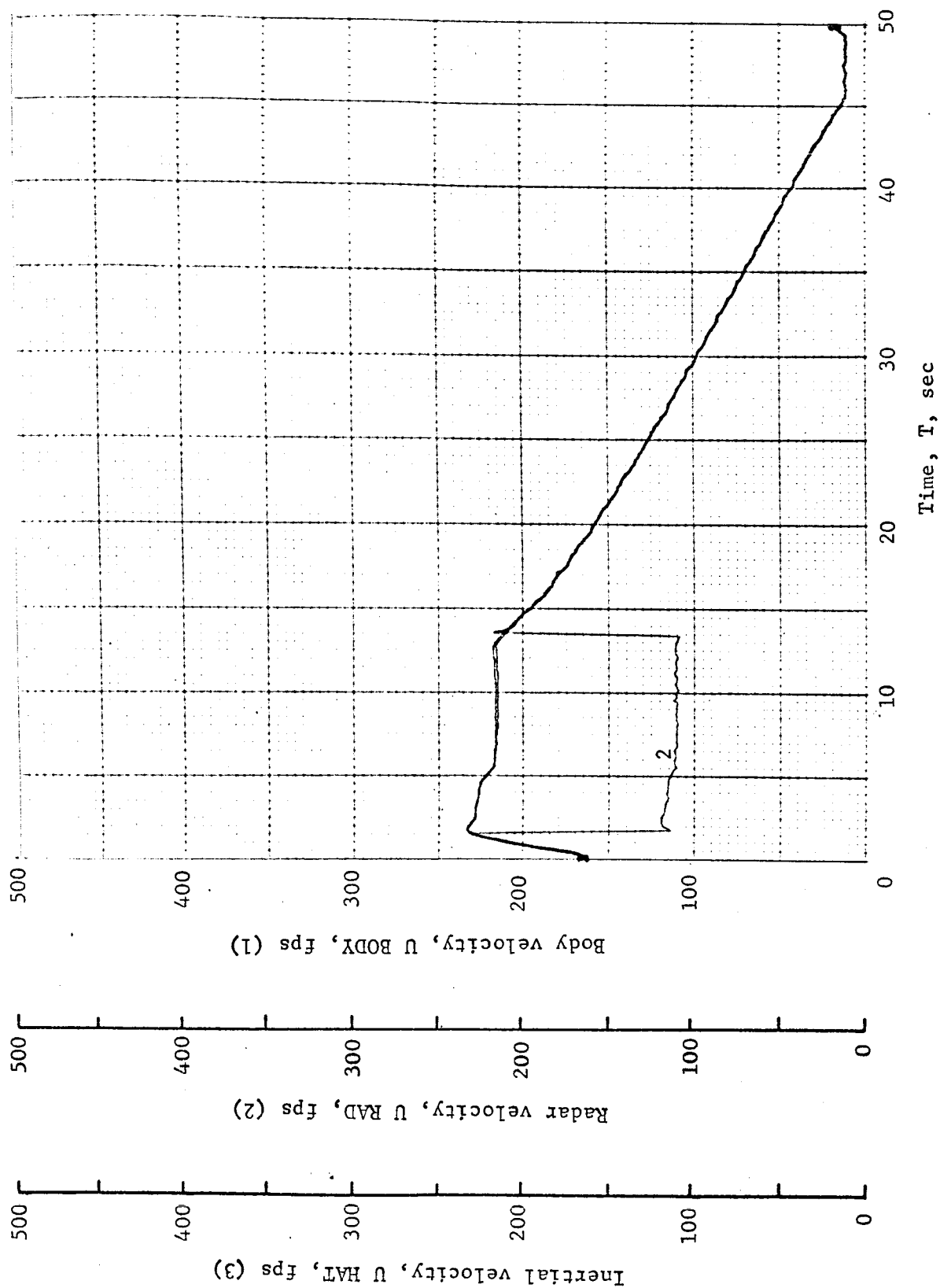


Figure B30.- Soft Lander, Run 3-2

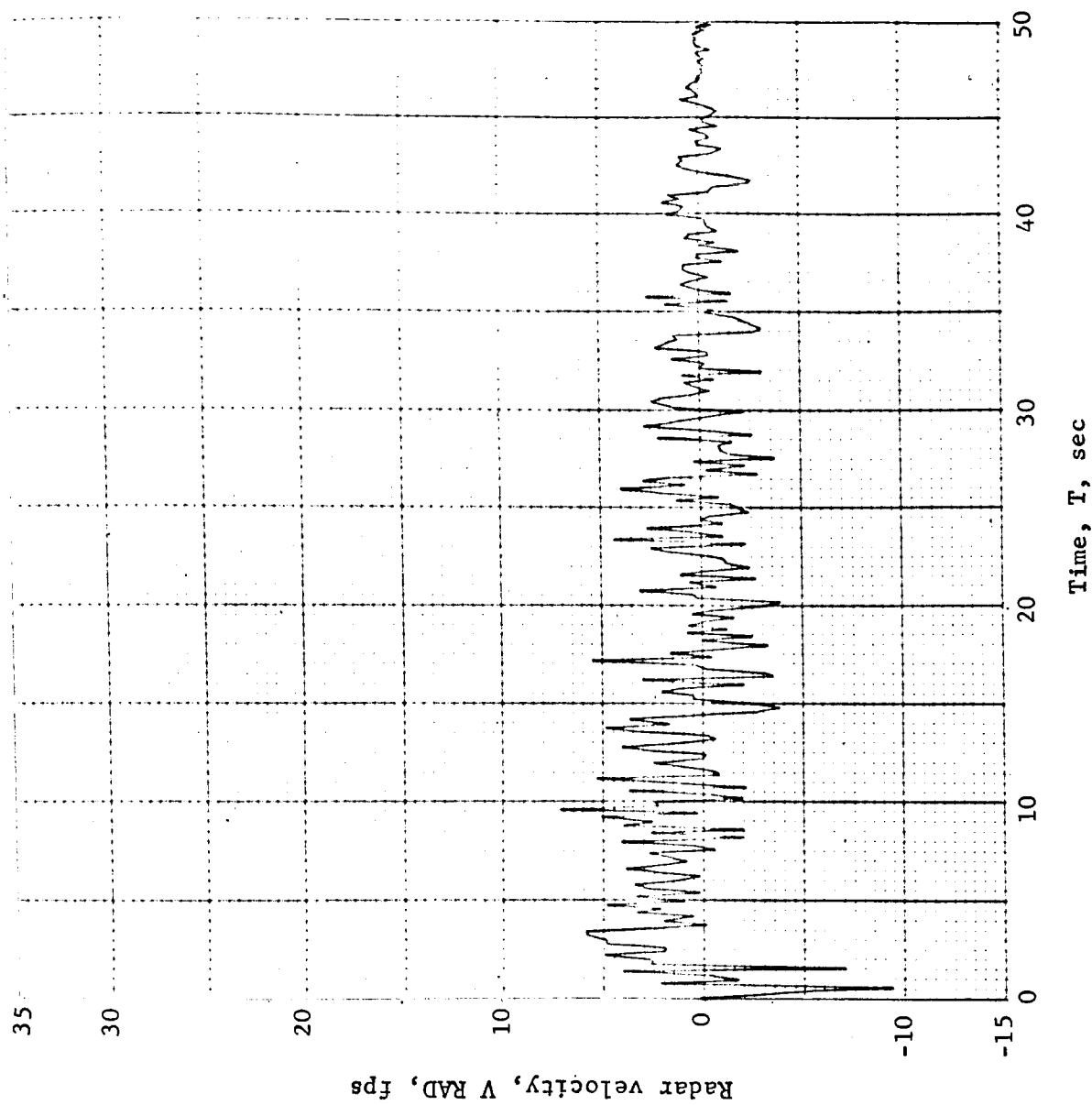


Figure B31.- Soft Lander, Run 3-3

APPENDIX B

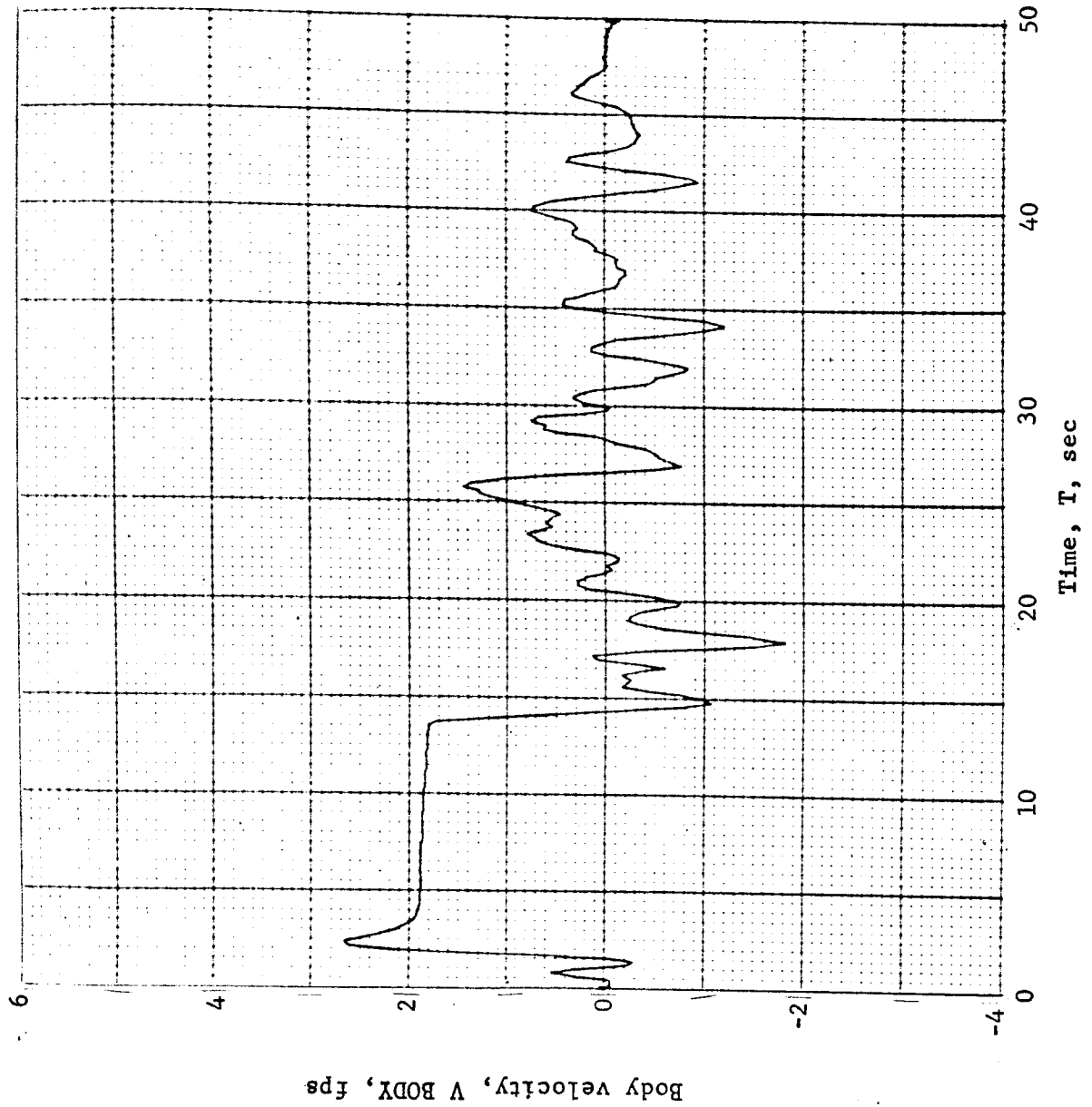


Figure B32.- Soft Lander, Run 3-4

APPENDIX B

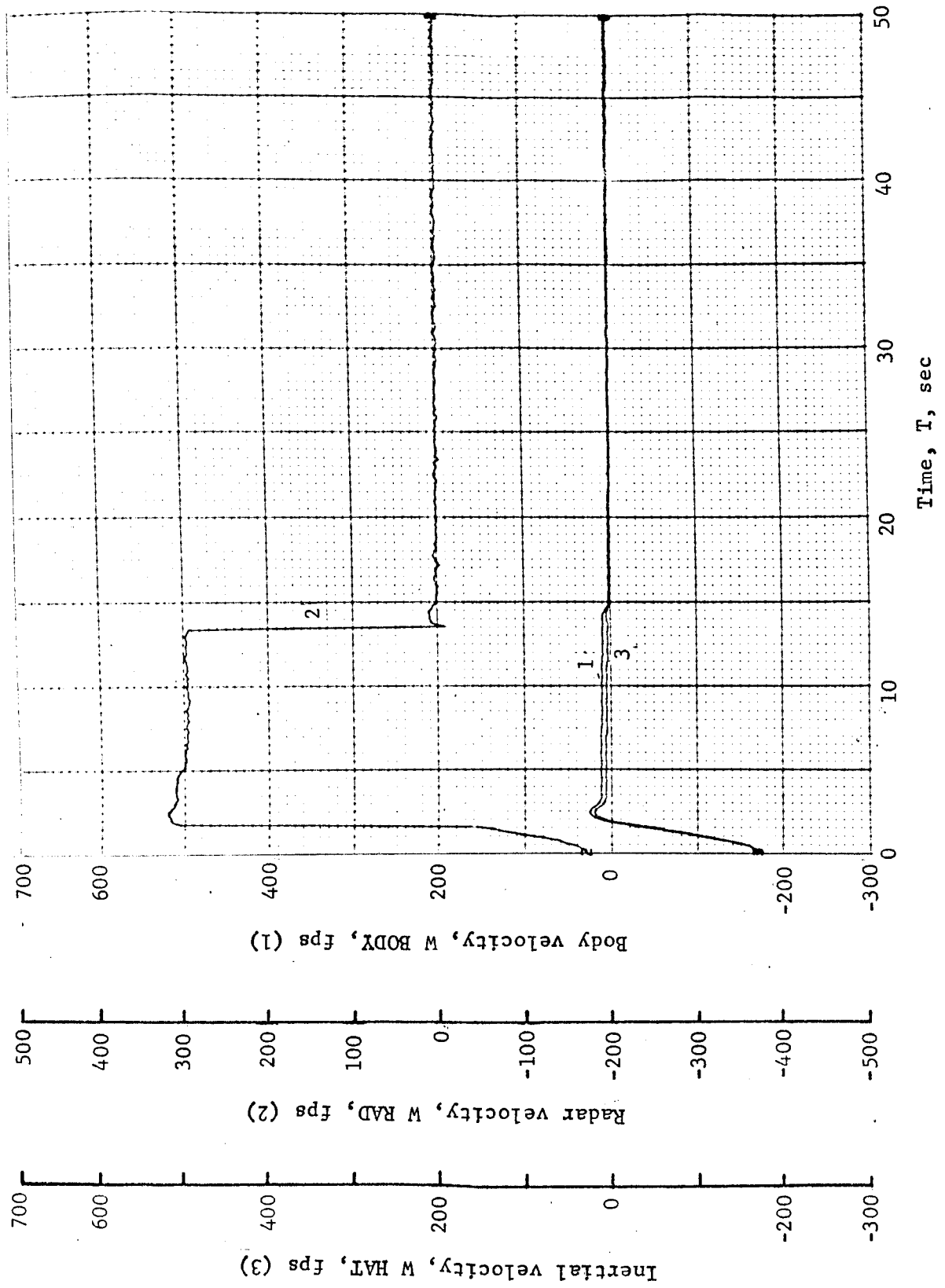


Figure B33.- Soft Lander, Run 3-5

APPENDIX B

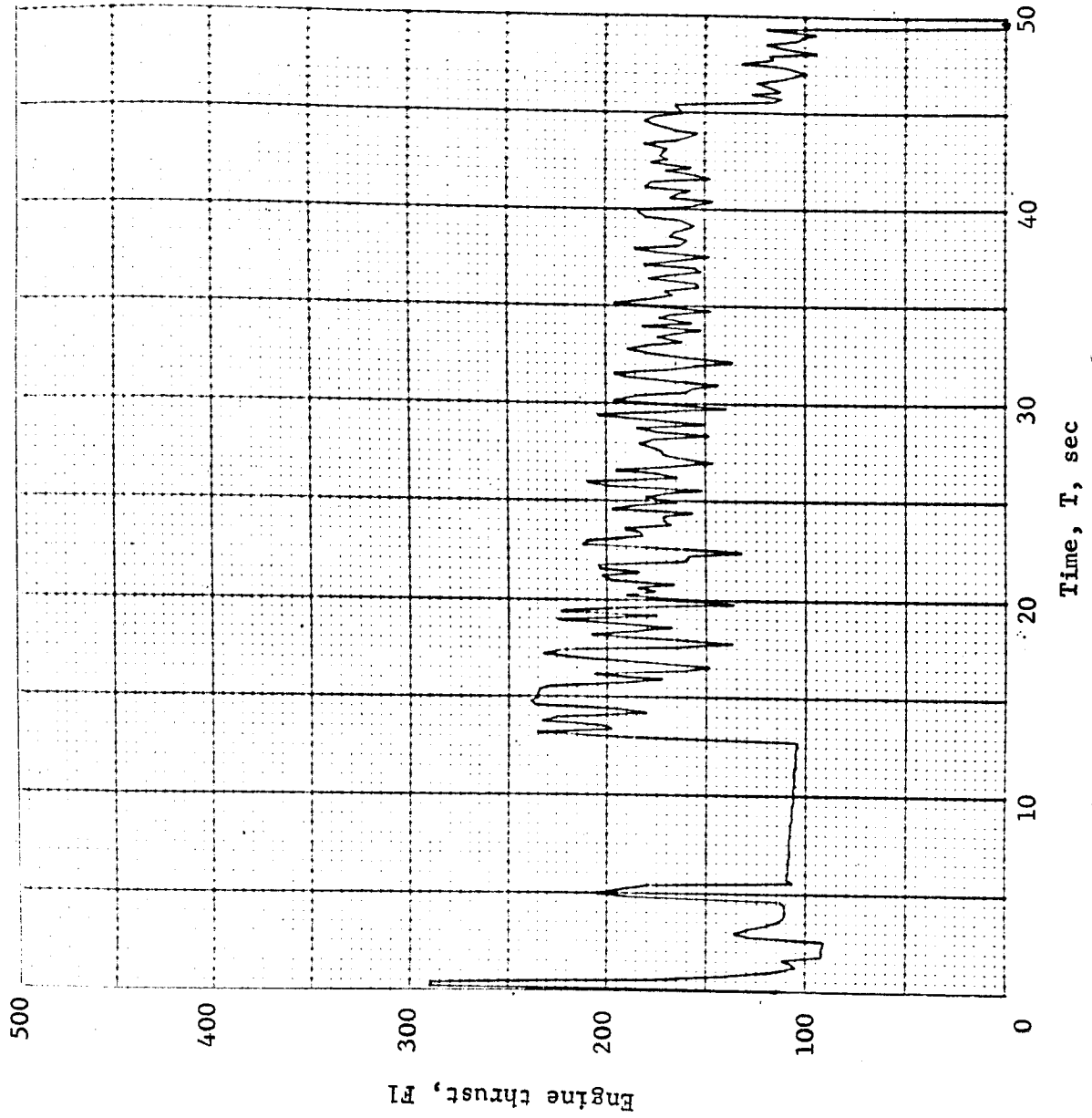


Figure B34.- Soft Lander, Run 3-6

APPENDIX B

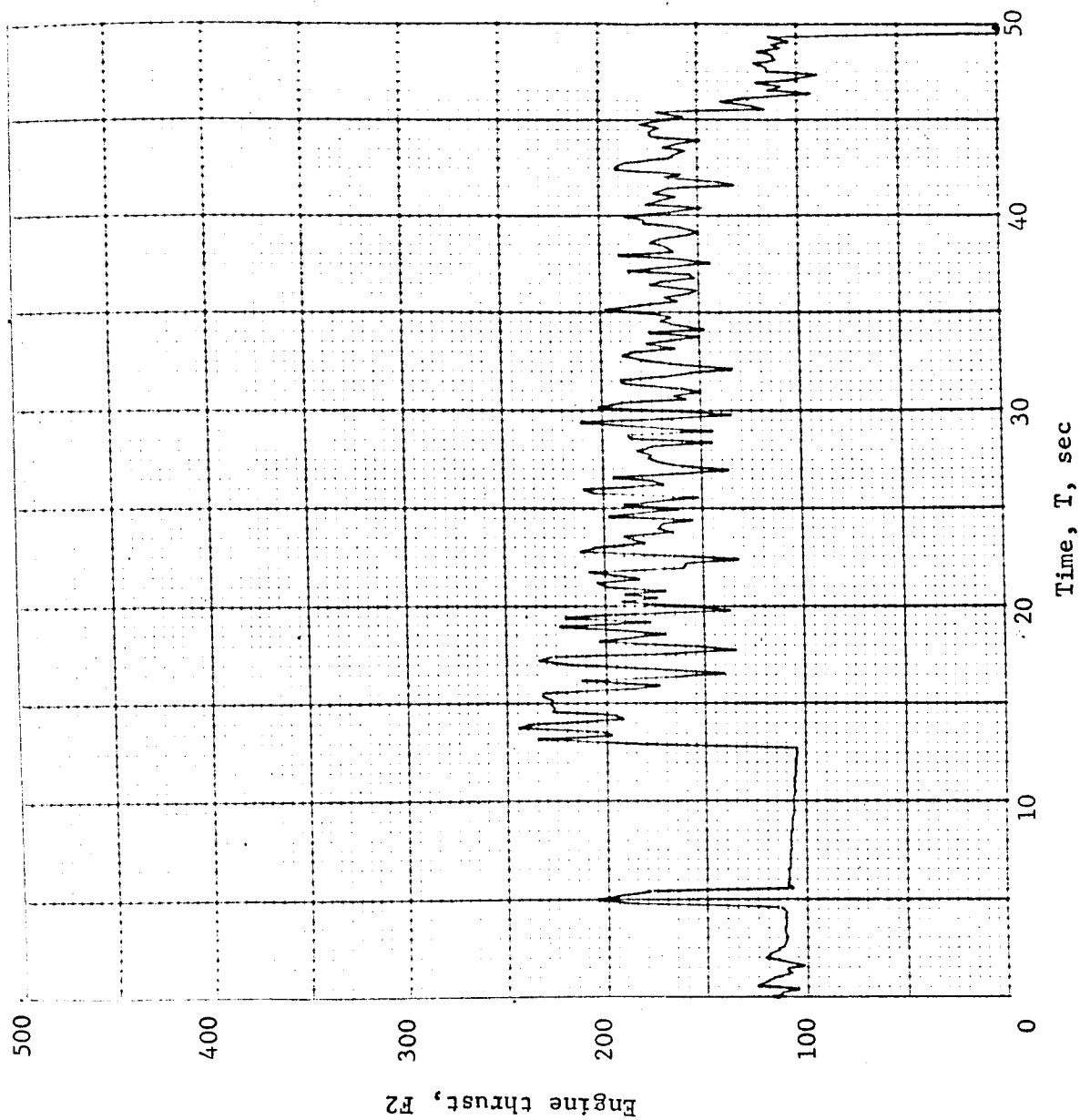


Figure B35.- Soft Lander, Run 3-7

APPENDIX B

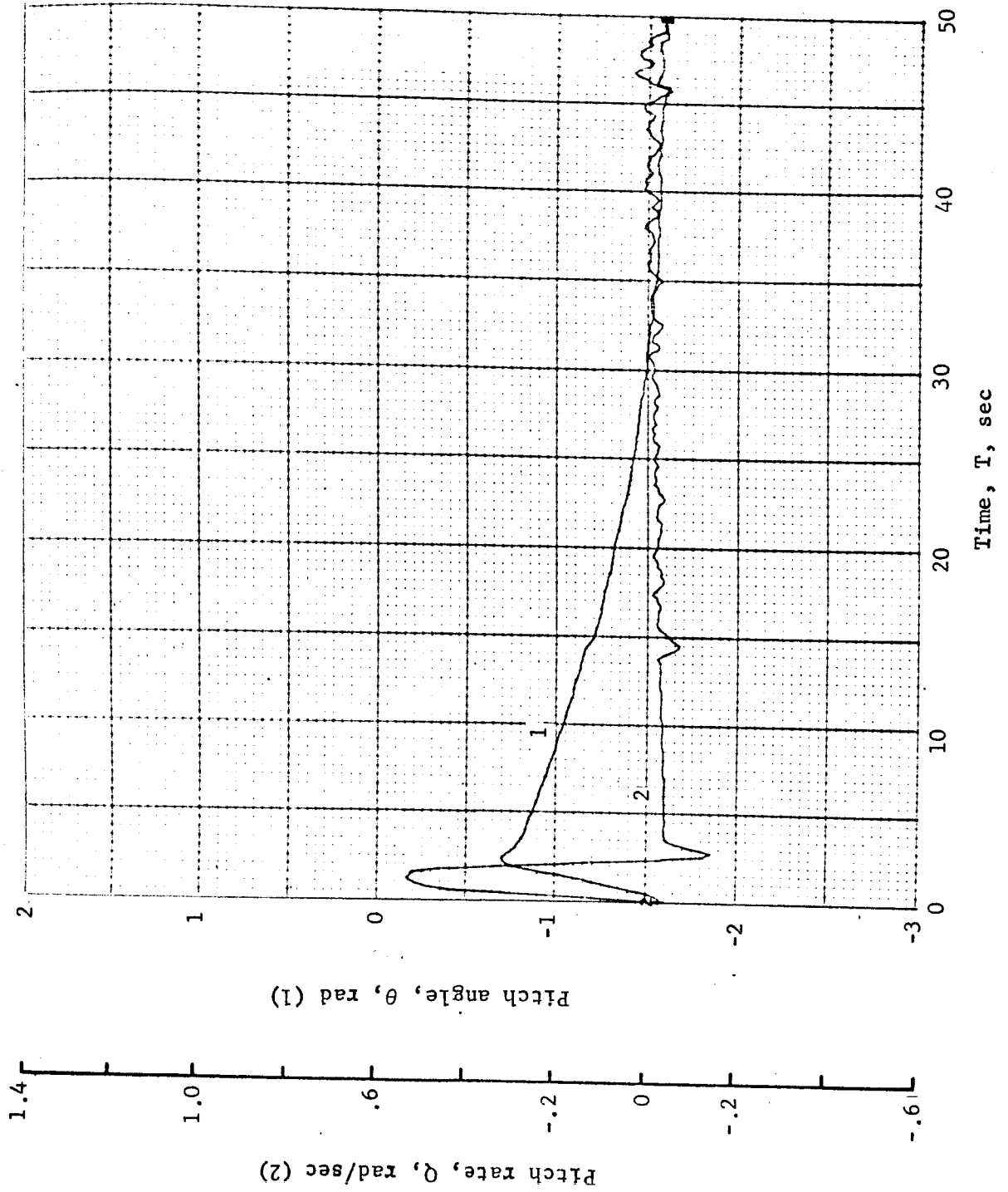


Figure B36.- Soft Lander, Run 3-8

APPENDIX B

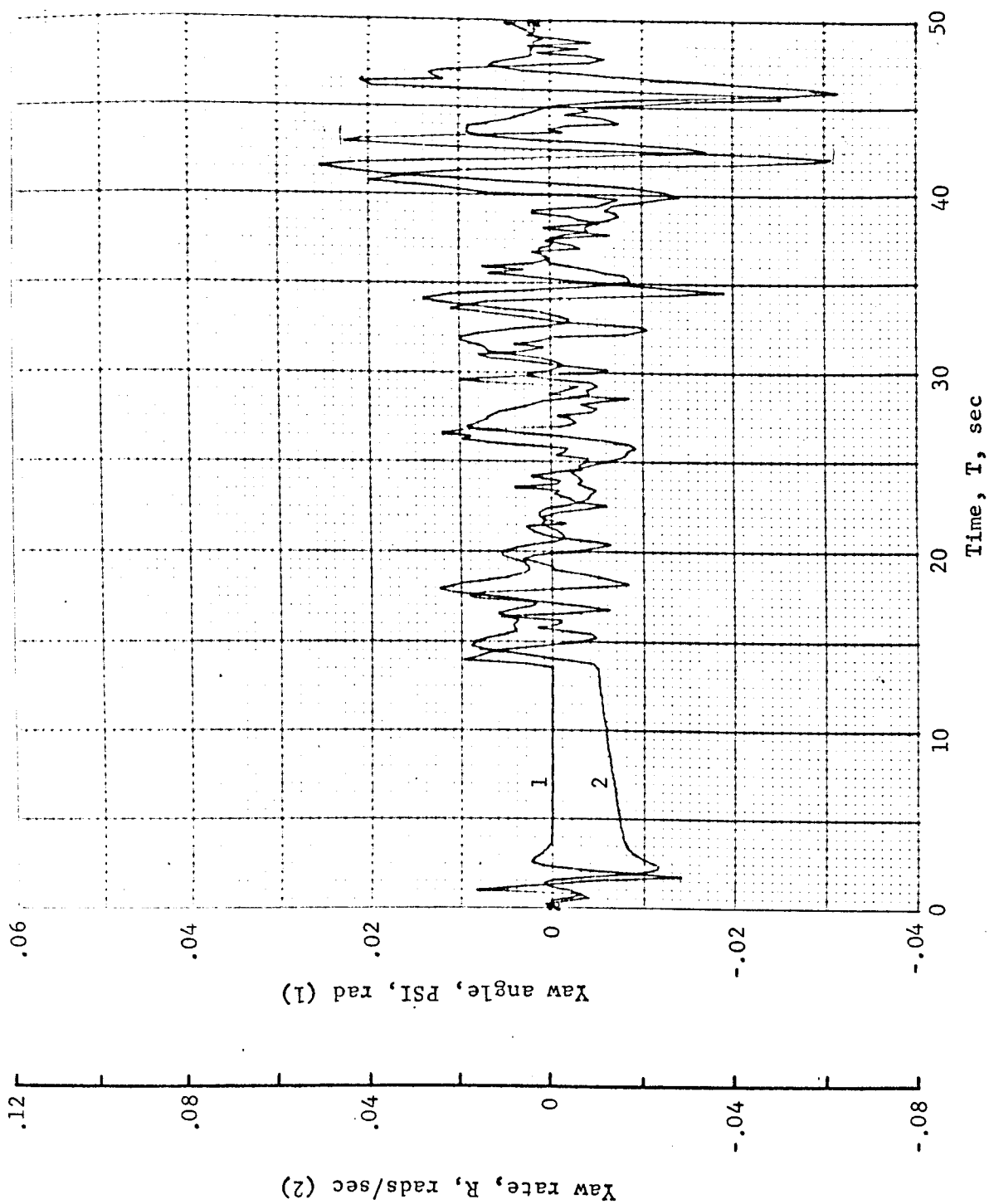


Figure B37.- Soft Lander, Run 3-9

APPENDIX B

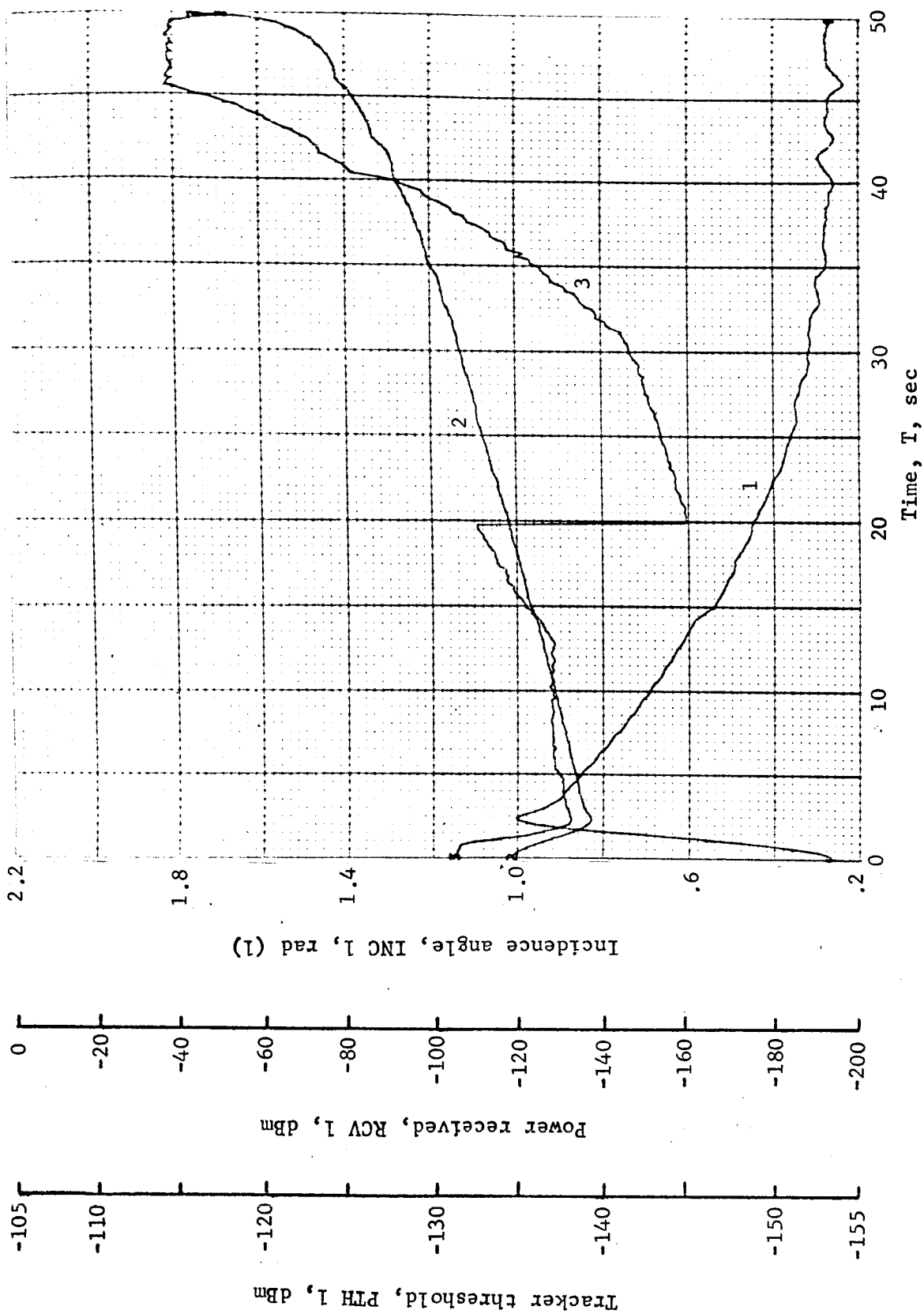


Figure B38.- Soft Lander, Run 3-10

APPENDIX B

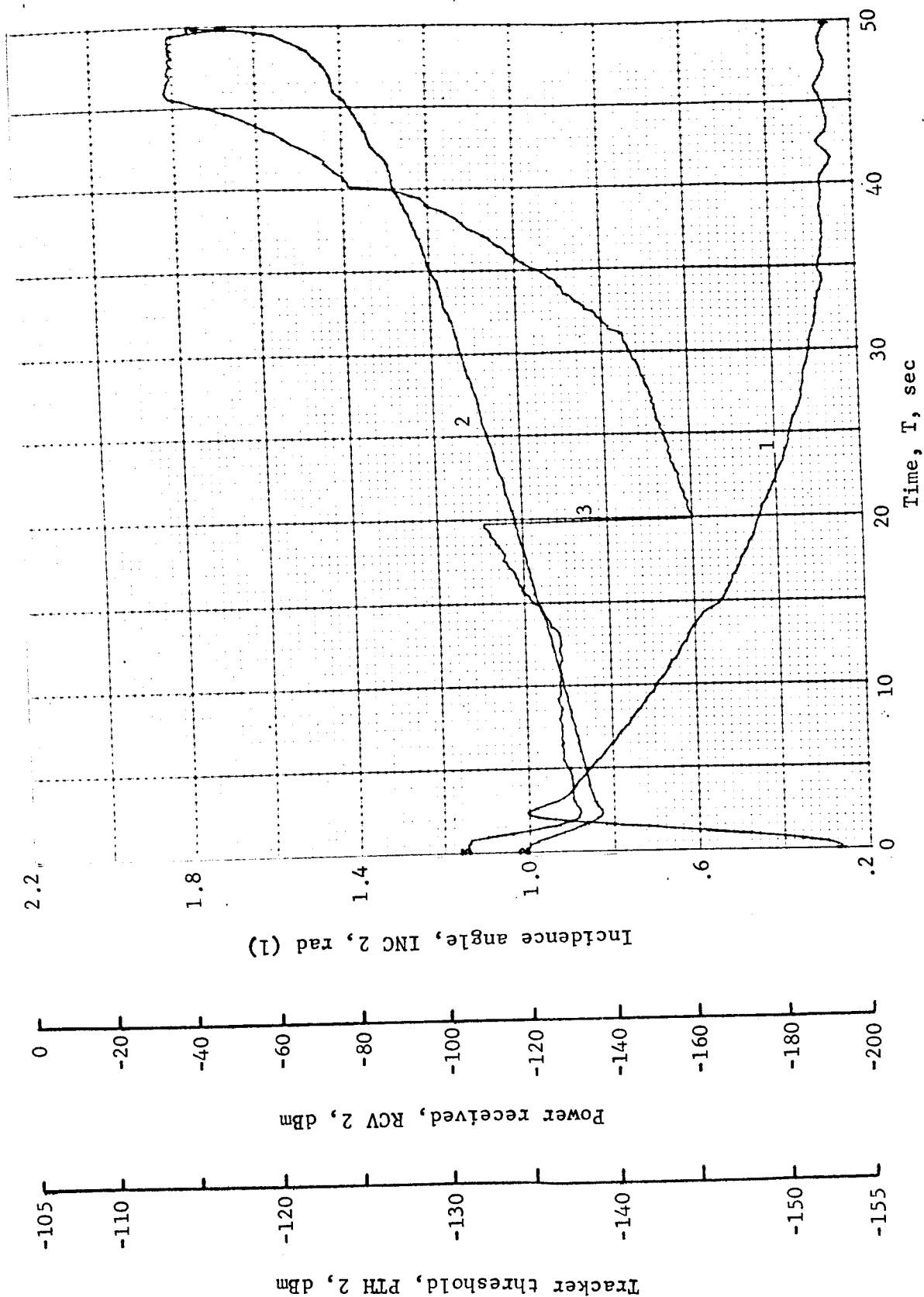


Figure B39.- Soft Lander, Run 3-11

APPENDIX B

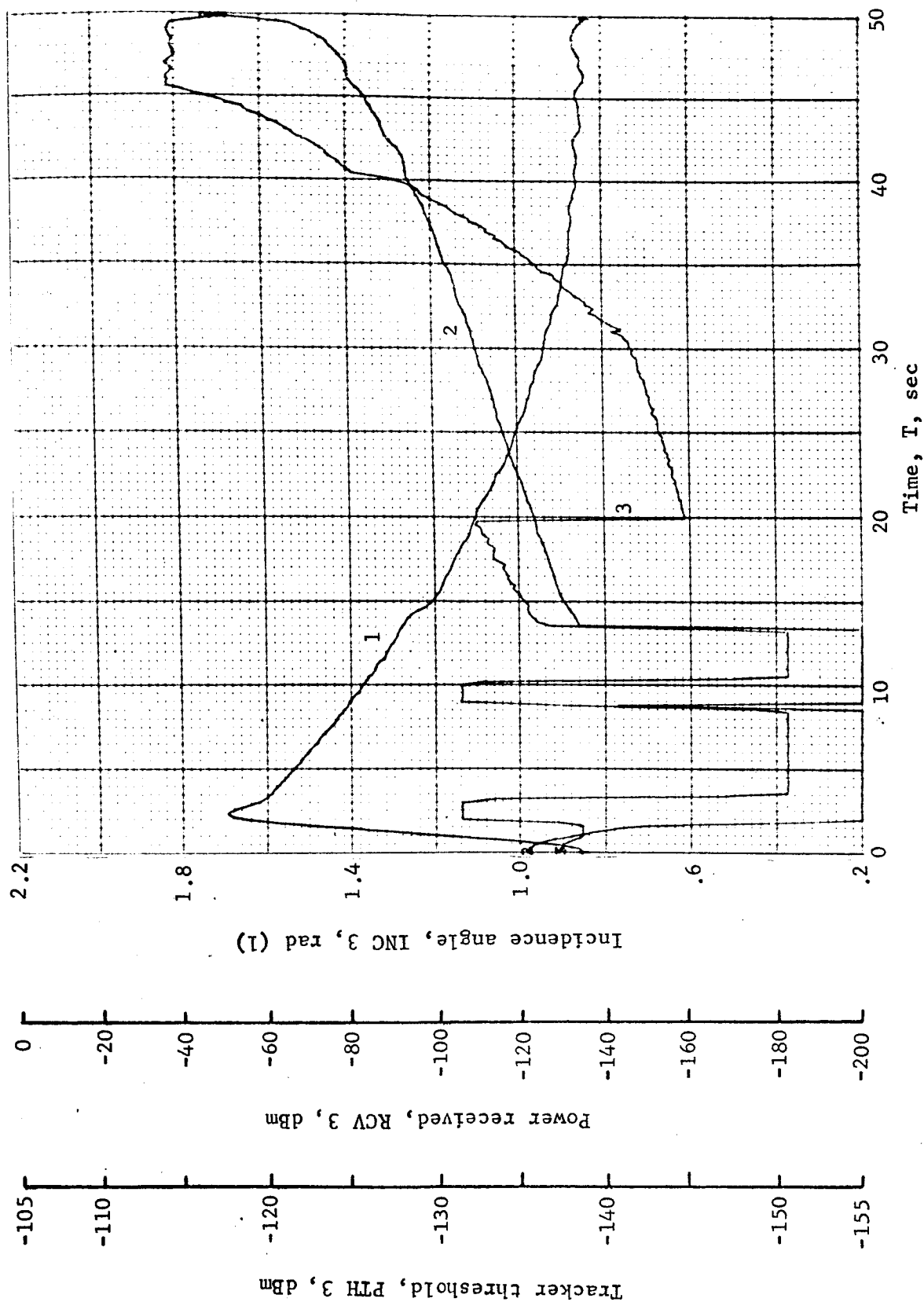


Figure B40.- Soft Lander, Run 3-12

APPENDIX B

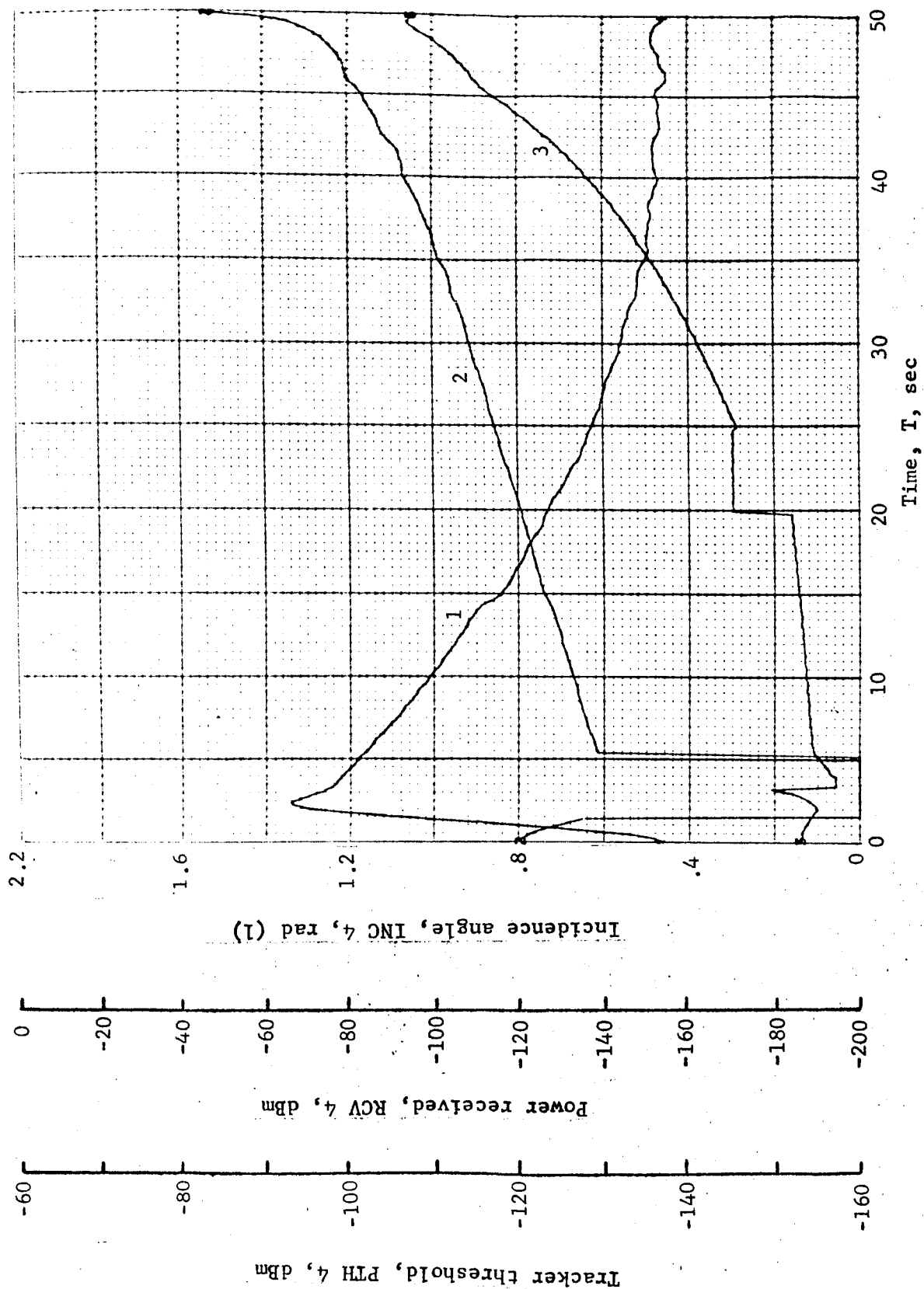


Figure B41.- Soft Lander, Run 3-13

APPENDIX B

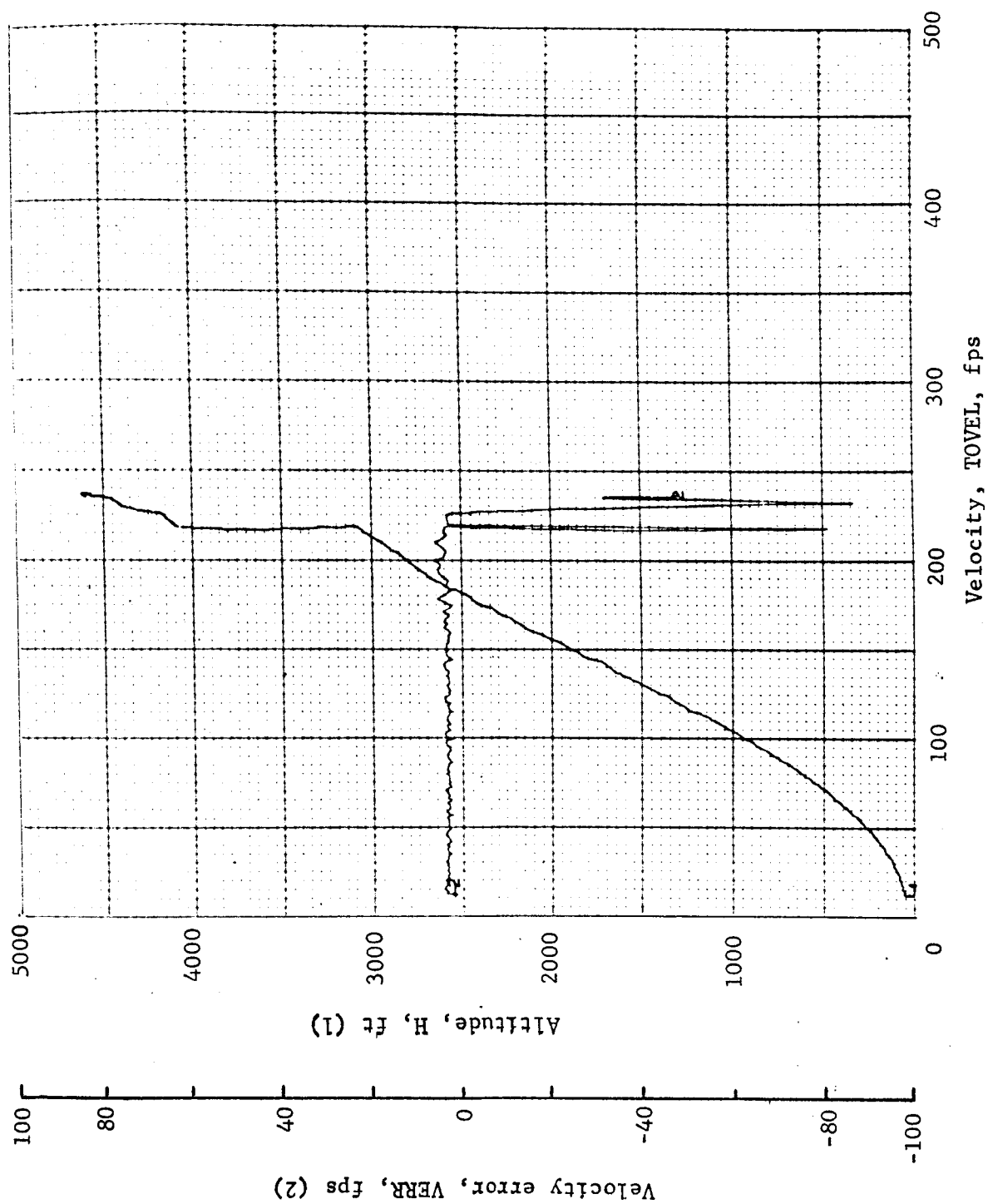


Figure B42.- Soft Lander, Run 3-14

APPENDIX B

TABLE B4.- RUN 4, AUTONOMOUS/LM RADAR/RANGE VELOCITY/-33° DOWNSLOPE

Flight condition	Altitude ft	Velocity, fps		Pitch angle, deg	Pitch rate, deg/sec	Time, sec	Fuel used, lb	Beams unlocked	Time to reacquire
		Roll axis	Cross axis						
Initial	4600	165	-70	-90	0	0	0	----	----
Mid-pitchup	4505.4	174.8	-34.1	-78.2	26.3	.8	2	----	----
Max. pitchup	4385	176.6	8.5	-65.6	.17	1.8	4.4	3 at 1.6	----
Thrust aligned	4385	176.6	8.5	-65.6	.17	1.8	4.4	3 at 1.6	----
Encounter contour	3011.1	186.5	1.7	-79	-.53	11.4	23.3	----	3 at 6.4
Constant vel	50.4	11.9	-.06	-91.5	-1.5	43.4	121.2	----	----
Cutoff eng	8.6	12.4	.26	-90.5	-1	46.8	128	----	----
Land	.96	18.5	.11	-90.3	-1	47.3	128	----	----
Remarks:									

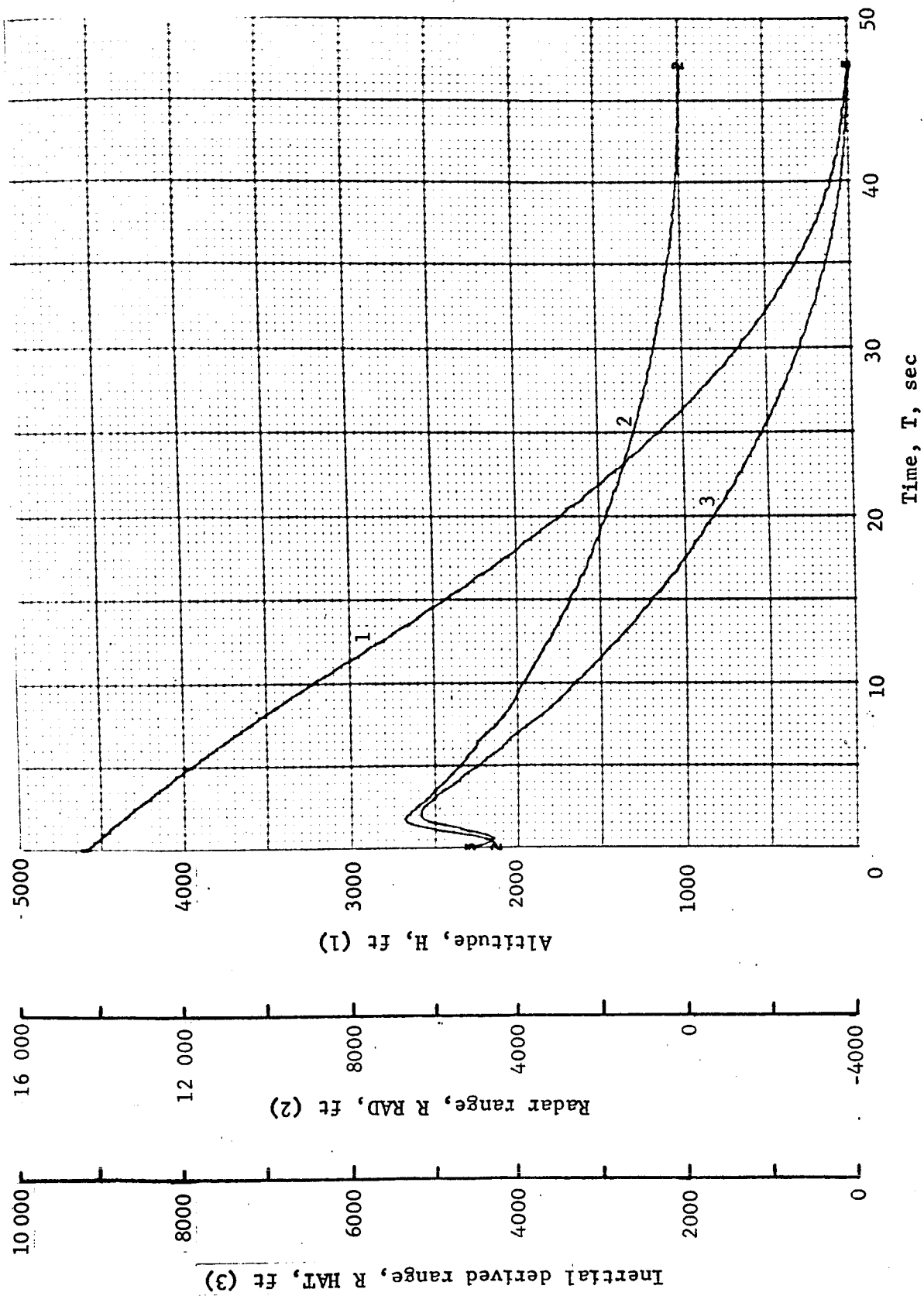


Figure B43.- Soft Lander, Run 4-1

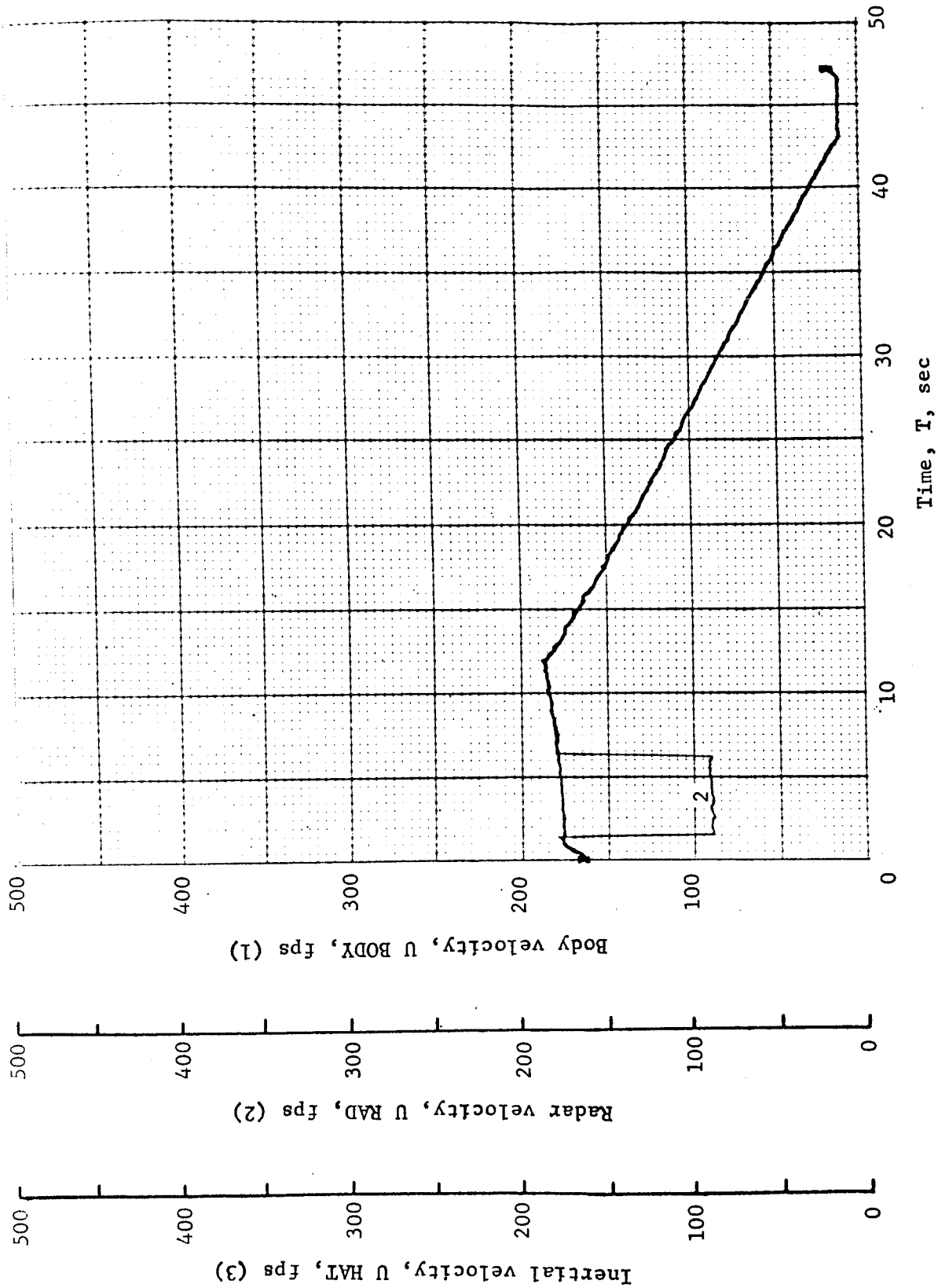


Figure B44.- Soft Lander, Run 4-2

APPENDIX B

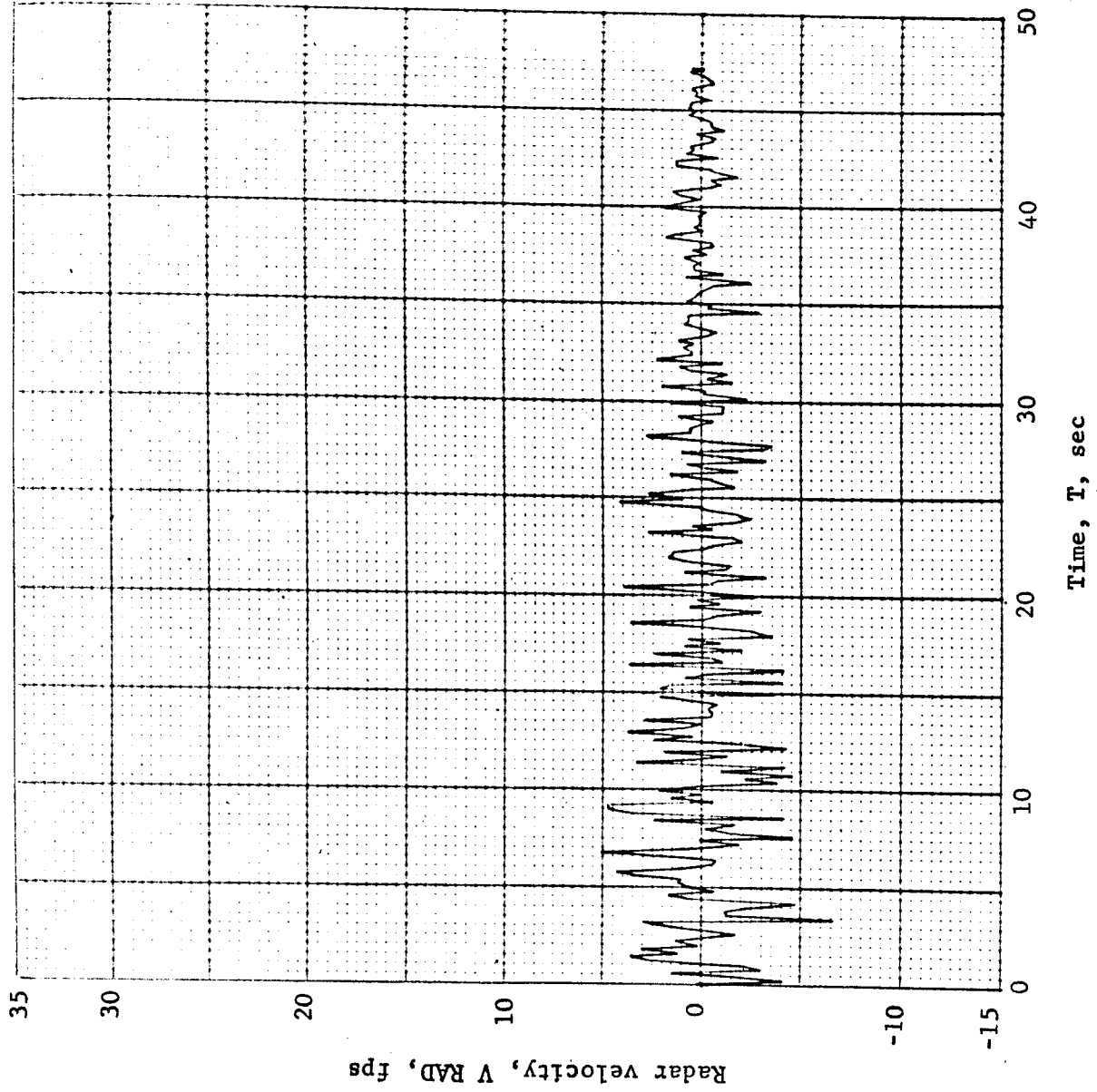


Figure B45.- Soft Lander, Run 4-3

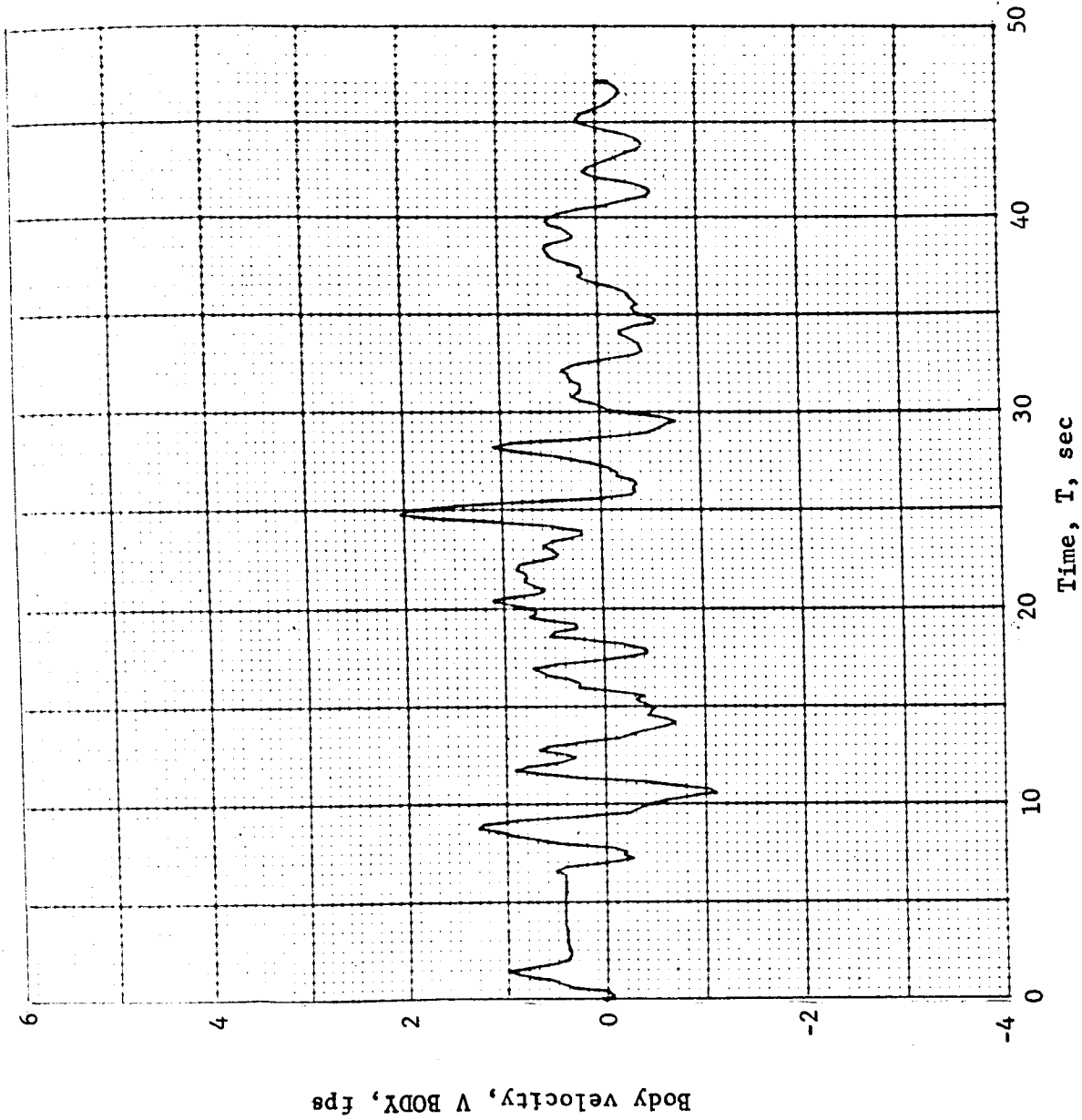


Figure B46.- Soft Lander, Run 4-4

APPENDIX B

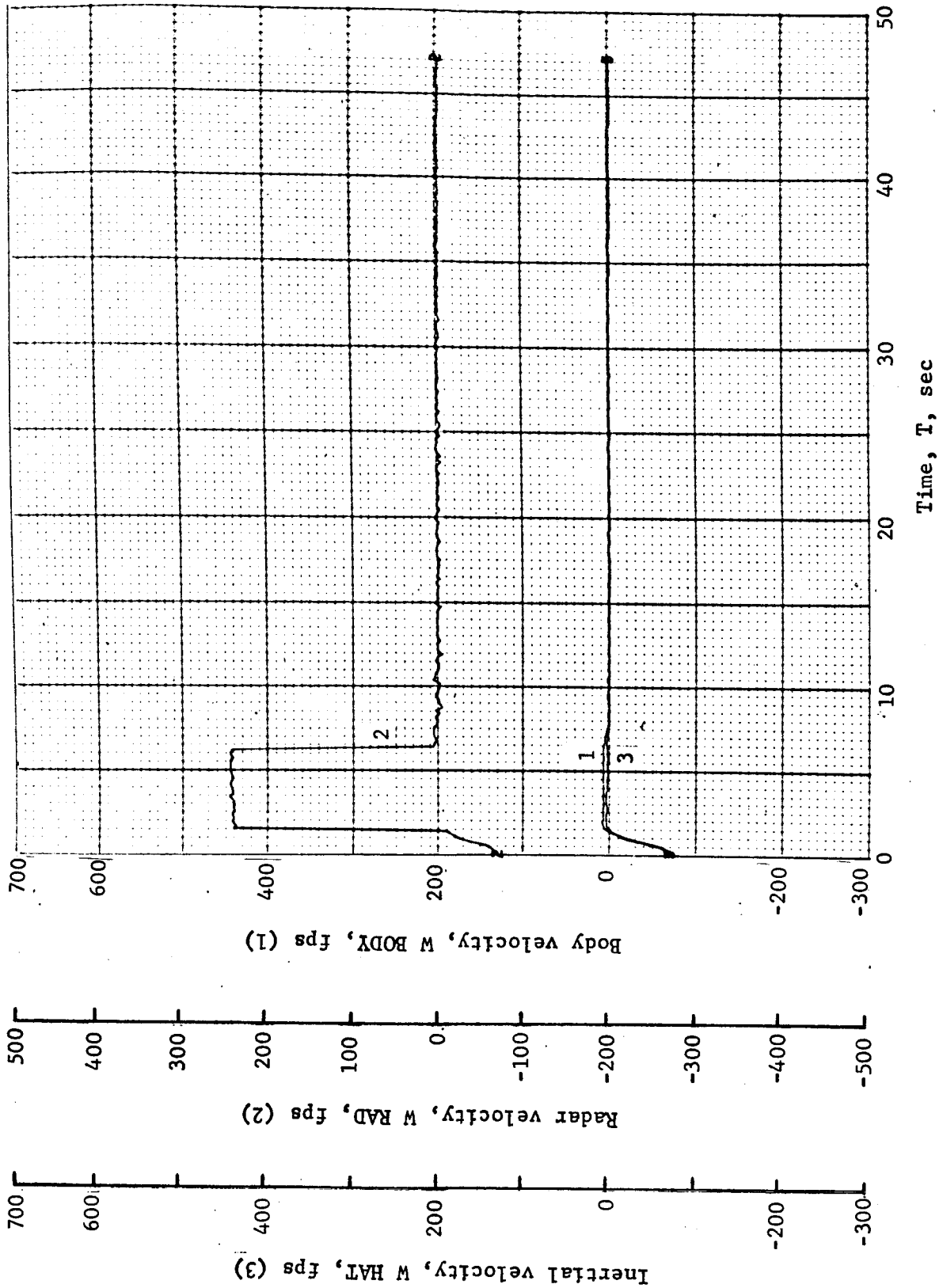


Figure B47.- Soft Lander, Run 4-5

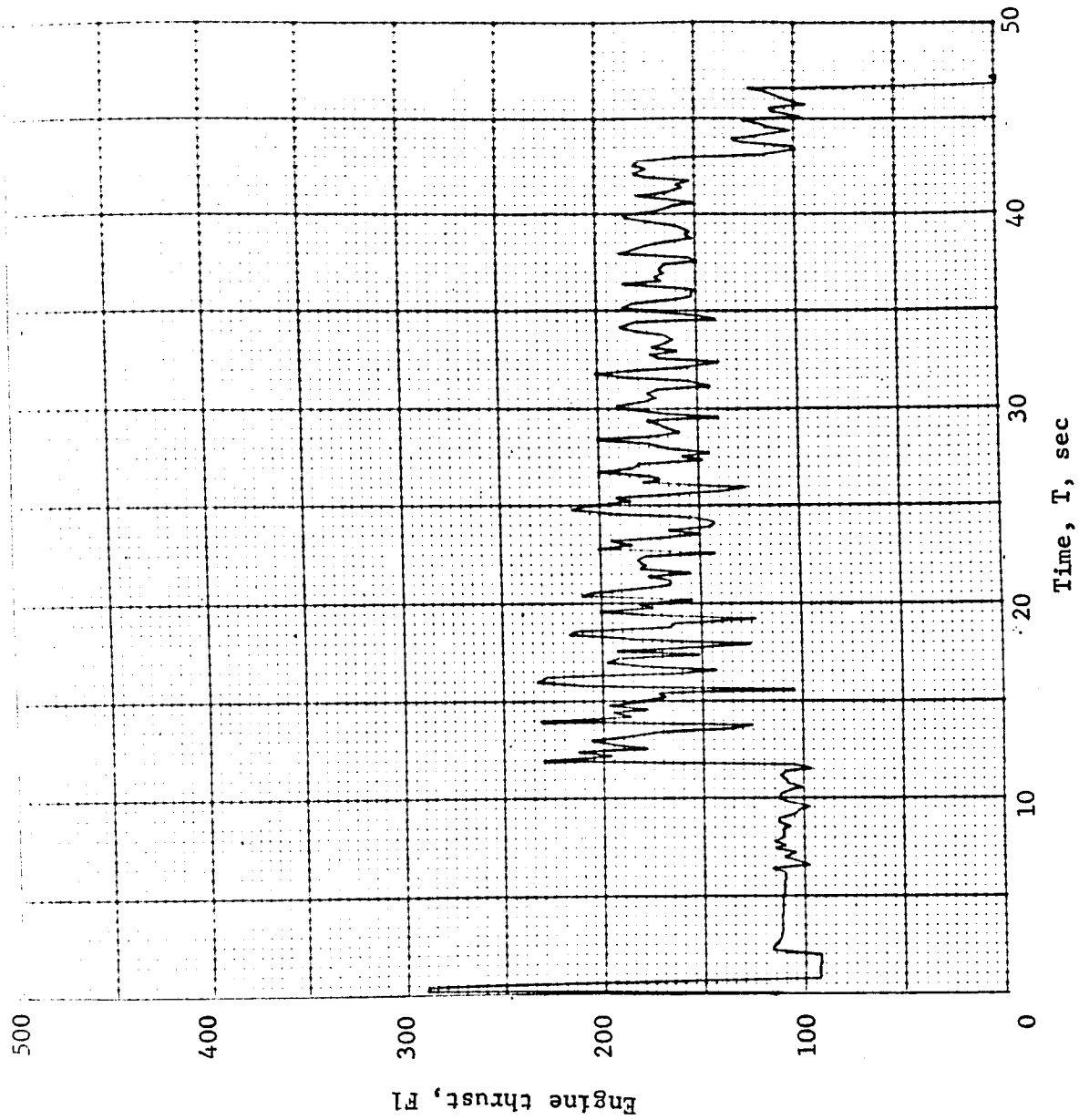


Figure B48.- Soft Lander, Run 4-6

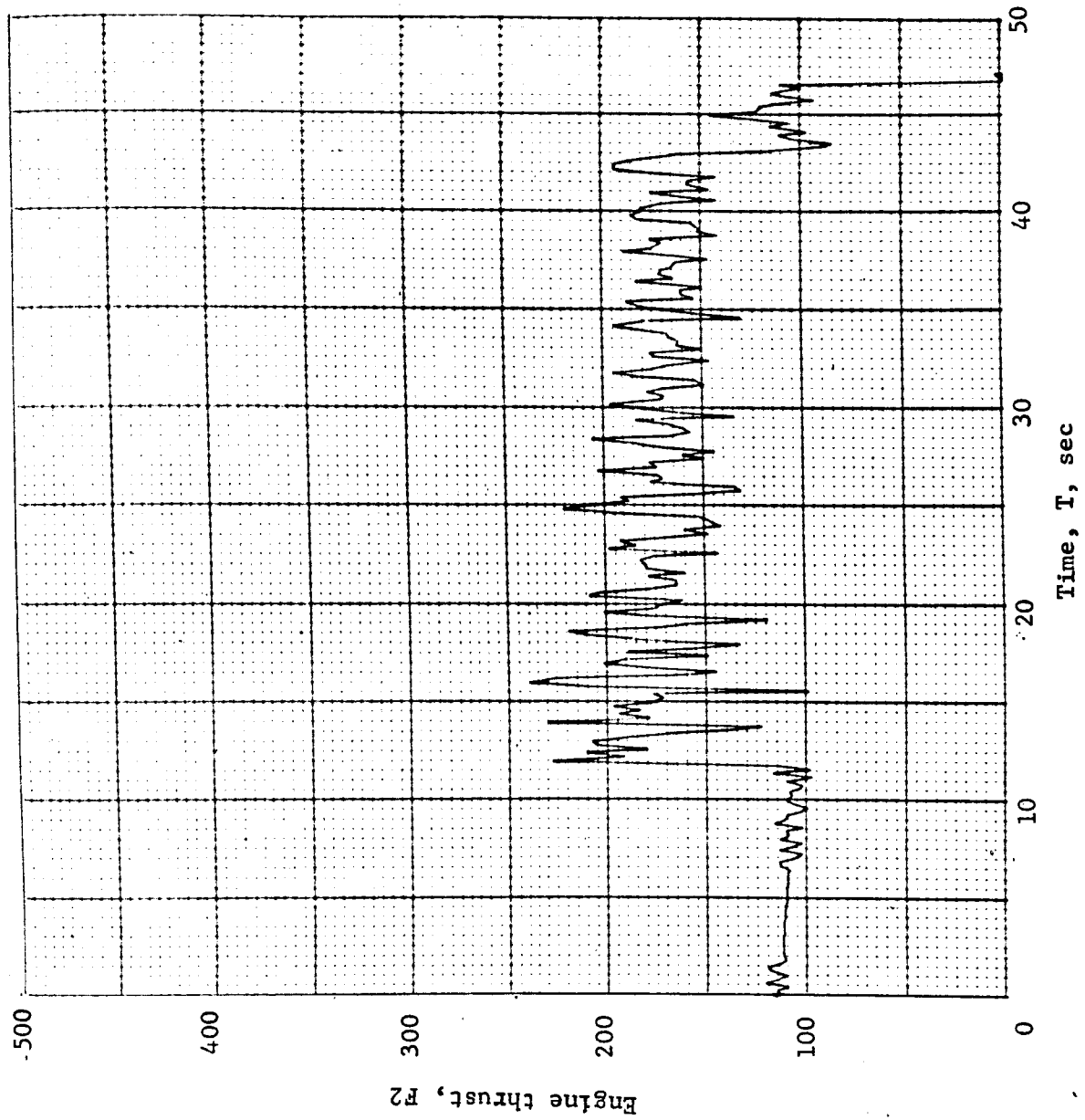


Figure B49.- Soft Lander, Run 4-7

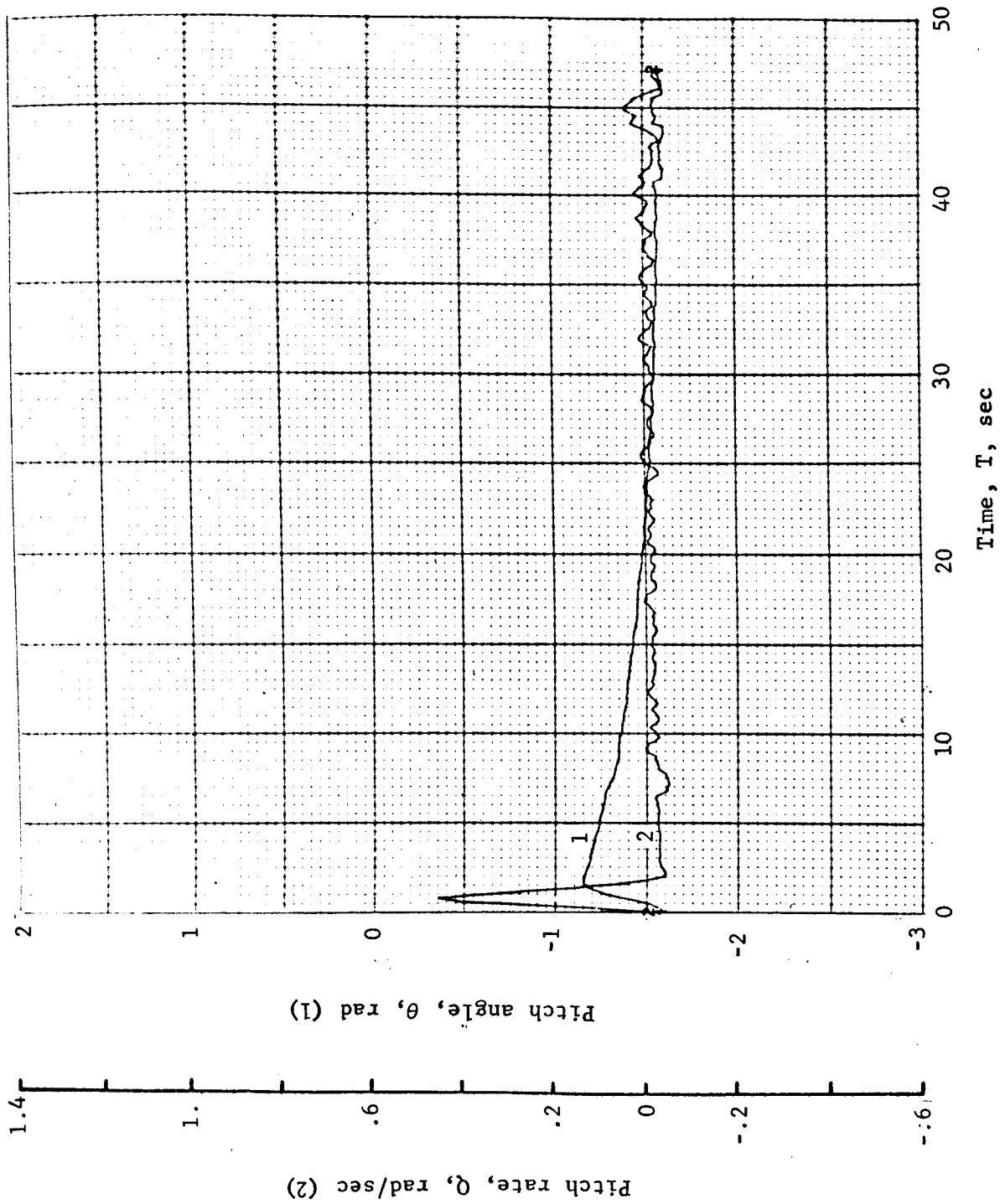


Figure B50.- Soft Lander, Run 4-8

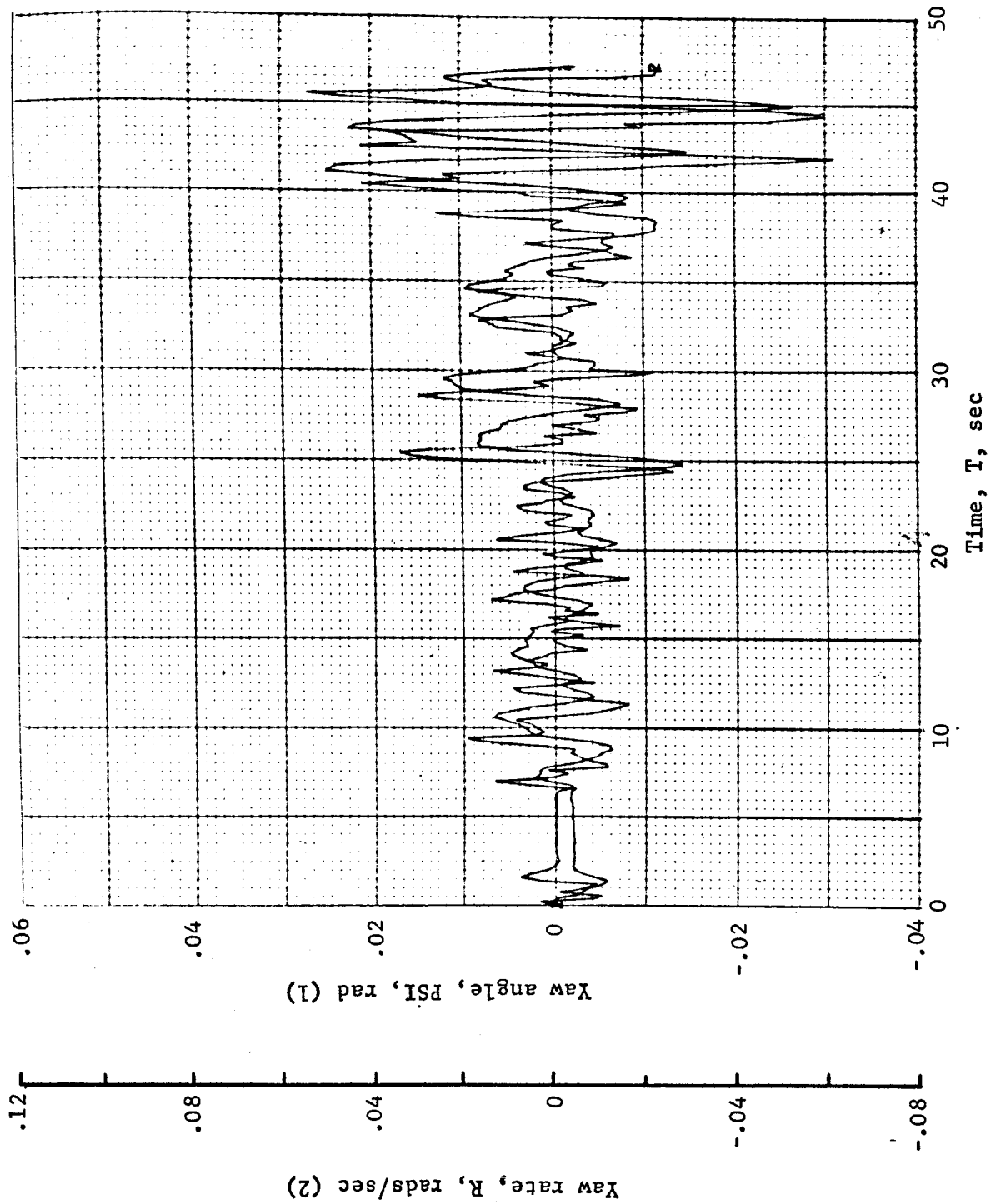


Figure B51.- Soft Lander, Run 4-9

APPENDIX B

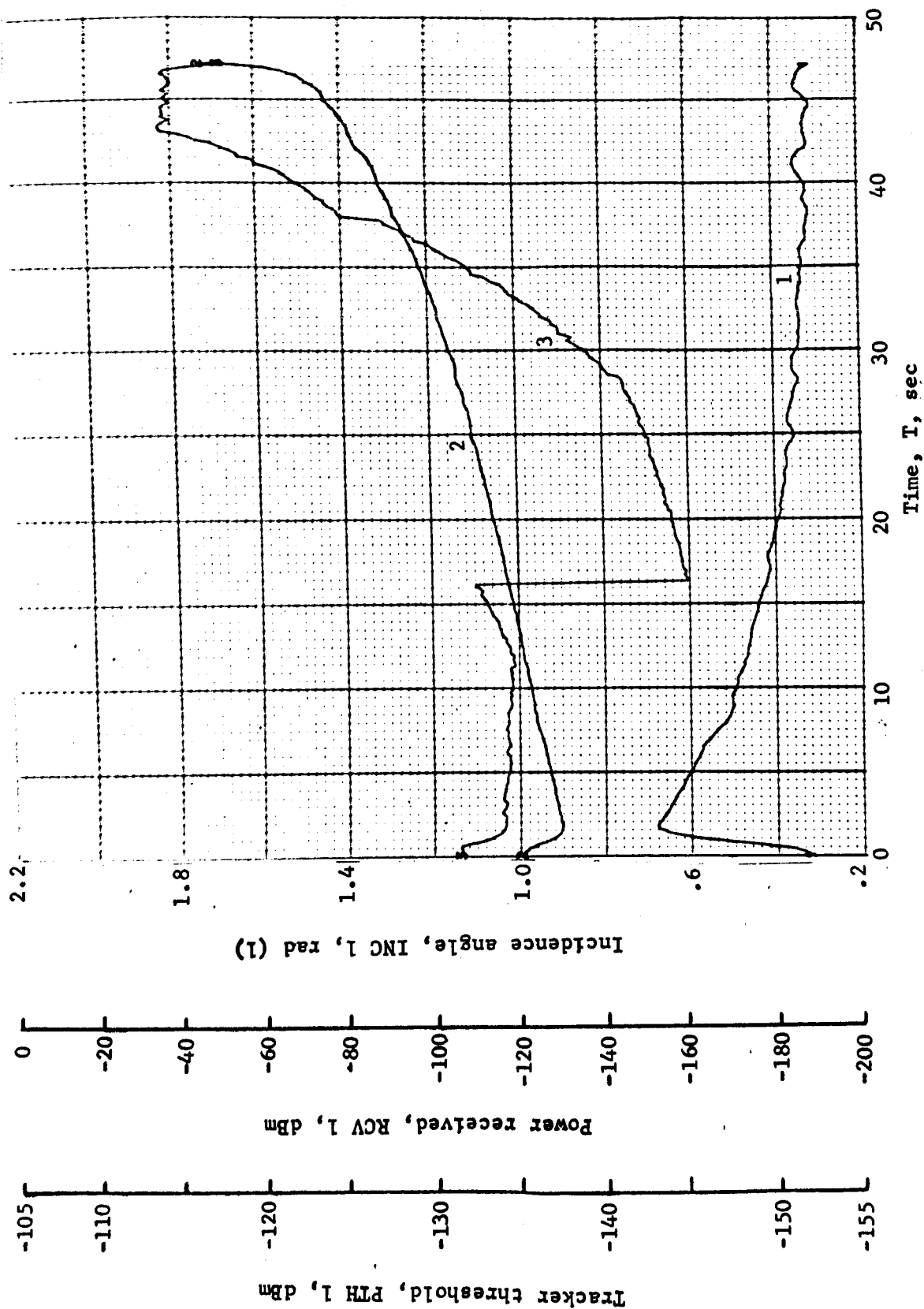


Figure B52.- Soft Lander, Run 4-10

APPENDIX B

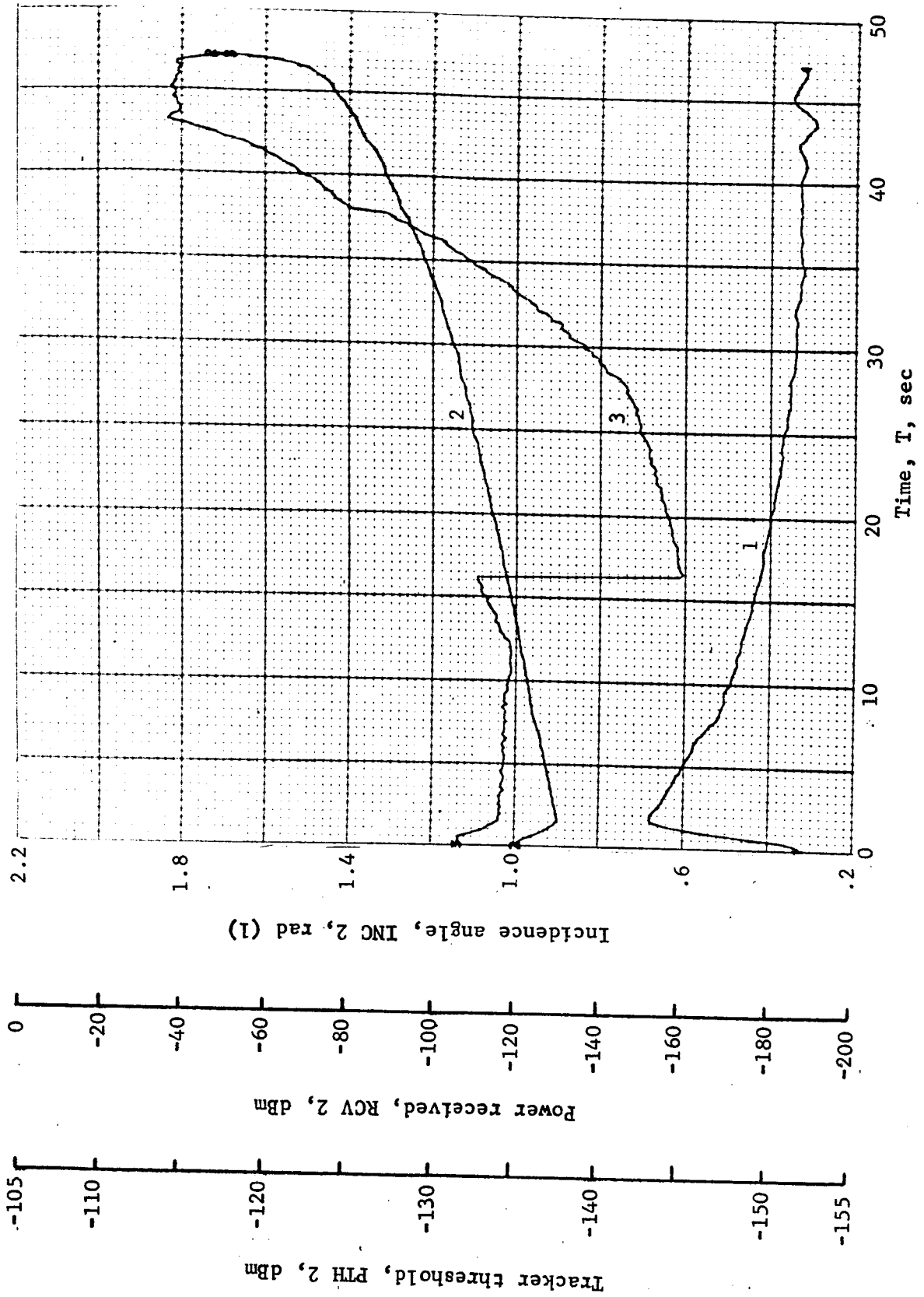


Figure B53.- Soft Lander, Run 4-11

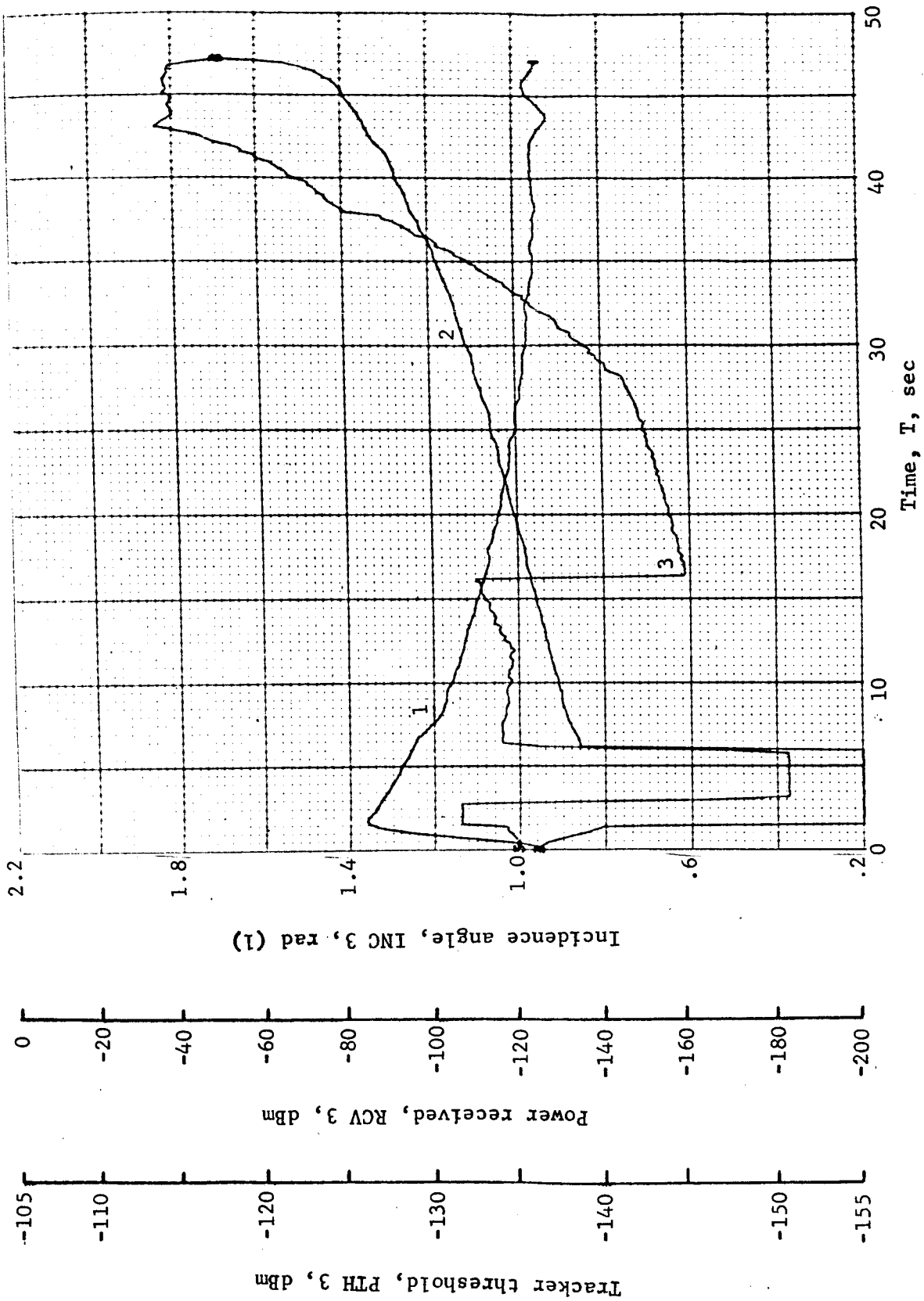


Figure B54.- Soft Lander, Run 4-12

APPENDIX B

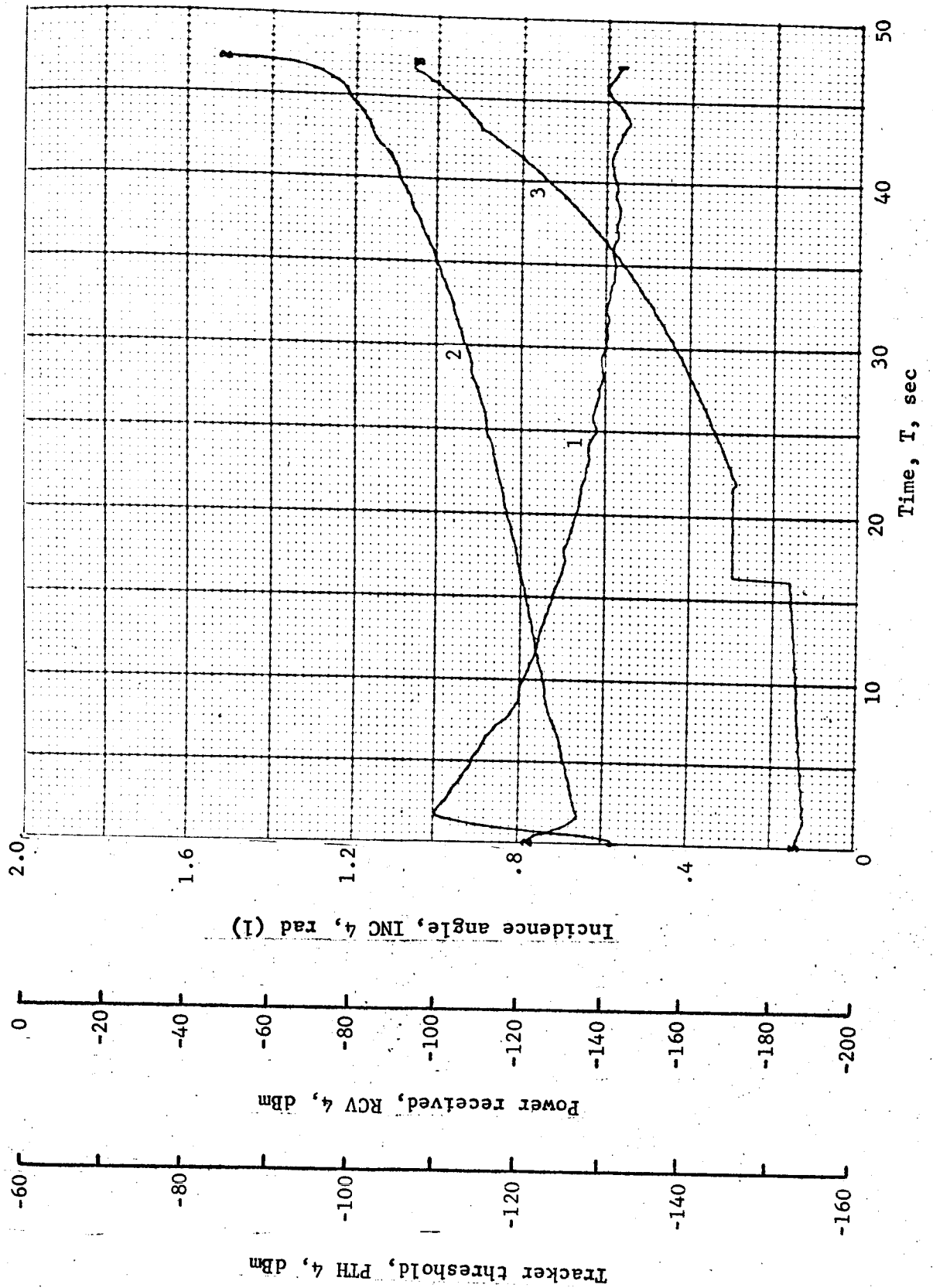


Figure B55.- Soft Lander, Run 4-13

APPENDIX B

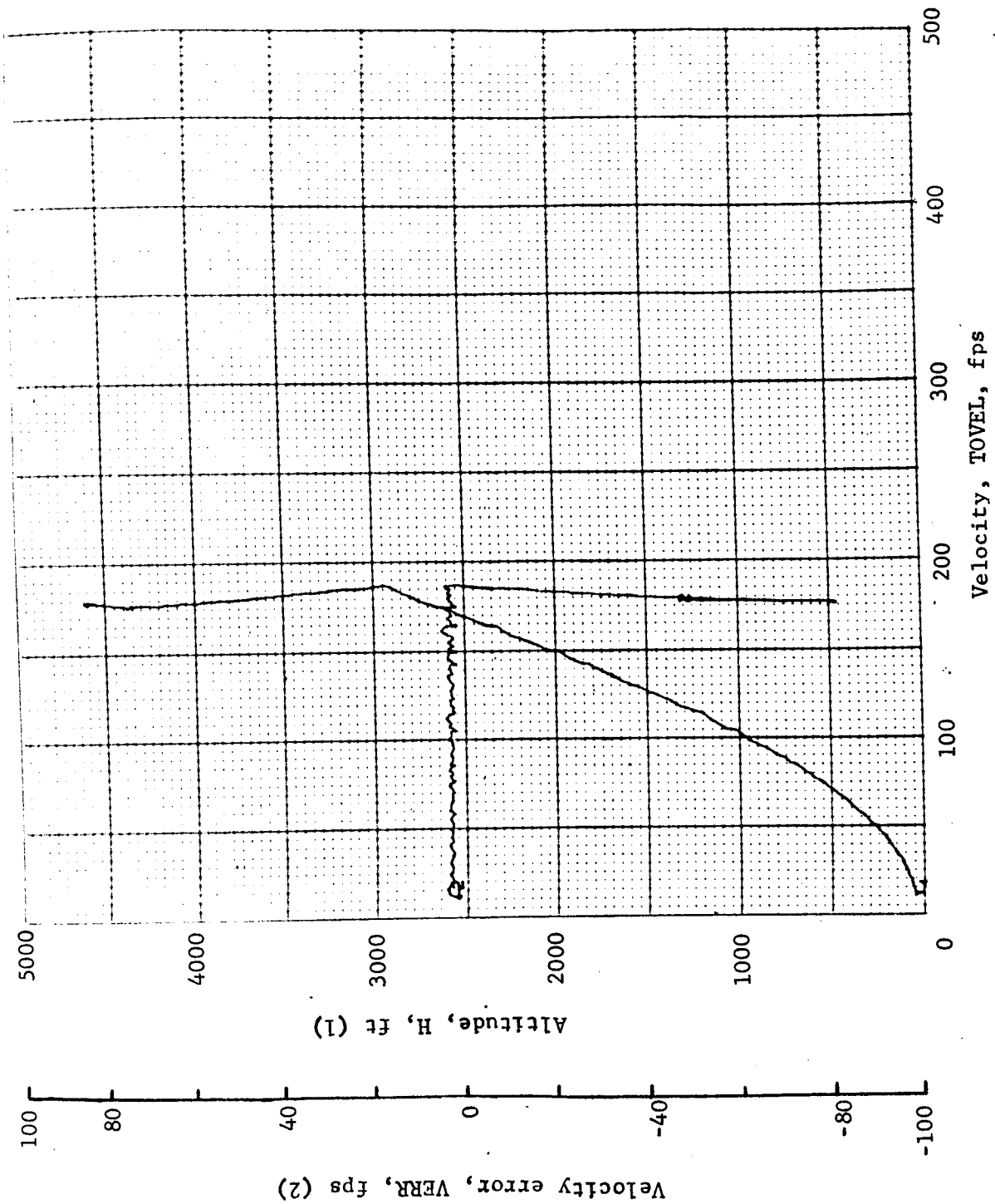


Figure B56.- Soft Lander, Run 4-14

APPENDIX B

TABLE B5.- RUN 5, AUTONOMOUS/LM RADAR/RANGE VELOCITY/O SLOPE/O DOPPLER

Flight Condition	Altitude, ft	Velocity, fps		Pitch angle, deg	Pitch rate, deg/sec	Time, sec	Fuel used, lb	Beams unlocked	Time to reacquire
		Roll axis	Cross axis						
Initial	4765	165	-263	-102	0	0	0	1, 2 at 0.5	----
Mid-pitchup	4334	267.8	-161.9	-63.4	31.4	2.6	5.6	1, 2	----
Max. pitchup	4060.9	300.7	44.6	-26.6	-.44	4.2	9.3	3 at 4.2	1, 2 at 4.6
Thrust aligned	3849	289	7.7	-36	-1.68	5.4	13.6	3	3 at 9.0
Encounter contour	4433.7	201.1	-240.7	-82	30	2	4.5	1, 2	----
Constant vel	48.7	12.4	-.05	-82.8	-1.95	42.6	133.4	----	----
Cutoff eng	7.9	12.5	.24	-91.3	-1.58	45.9	140.1	----	----
Land	.95	18.1	.1	-91	-1.58	46.3	140.1	----	----
Remarks:									

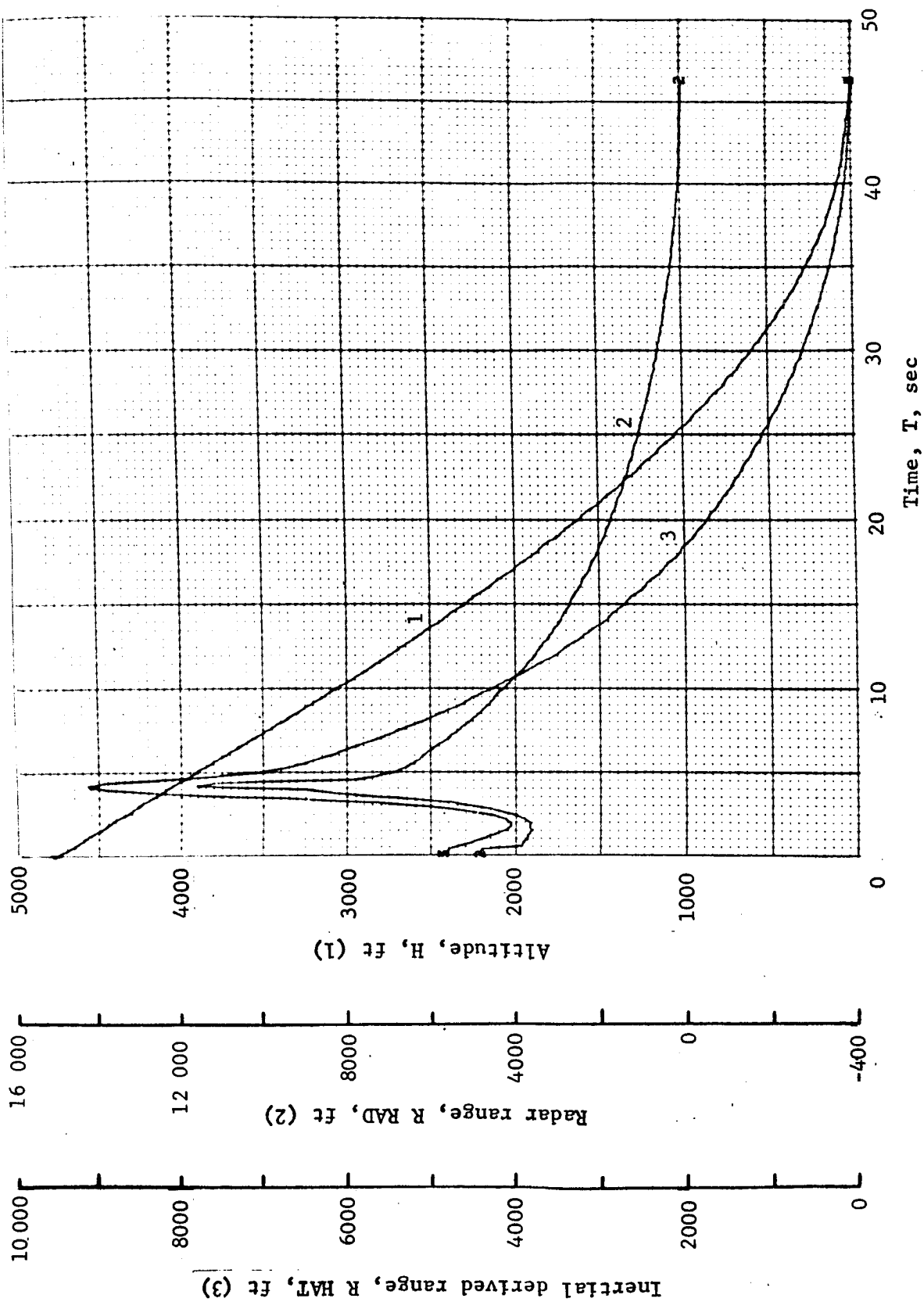


Figure B57.- Soft Lander, Run 5-1

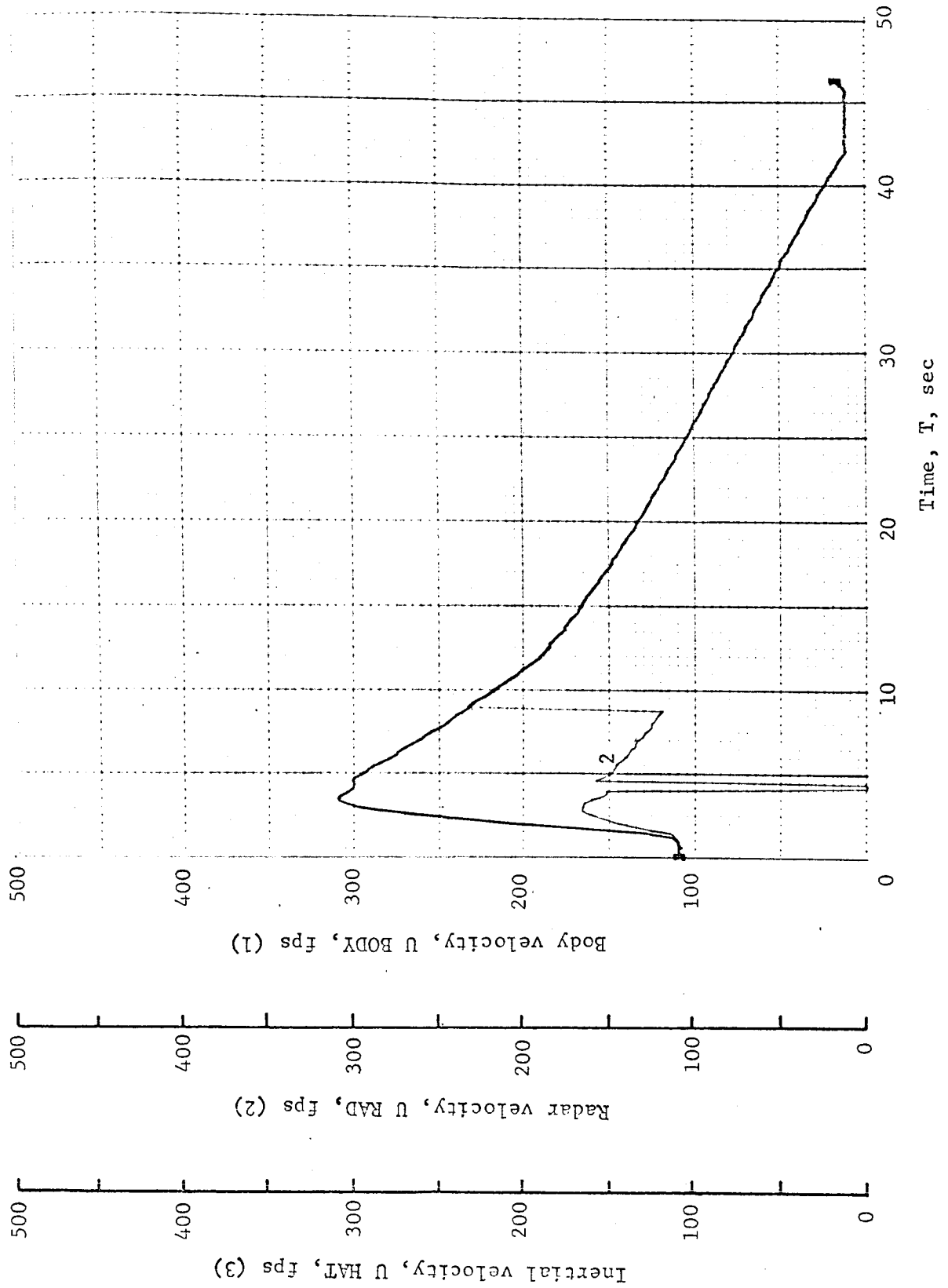


Figure B58.- Soft Lander, Run 5-2

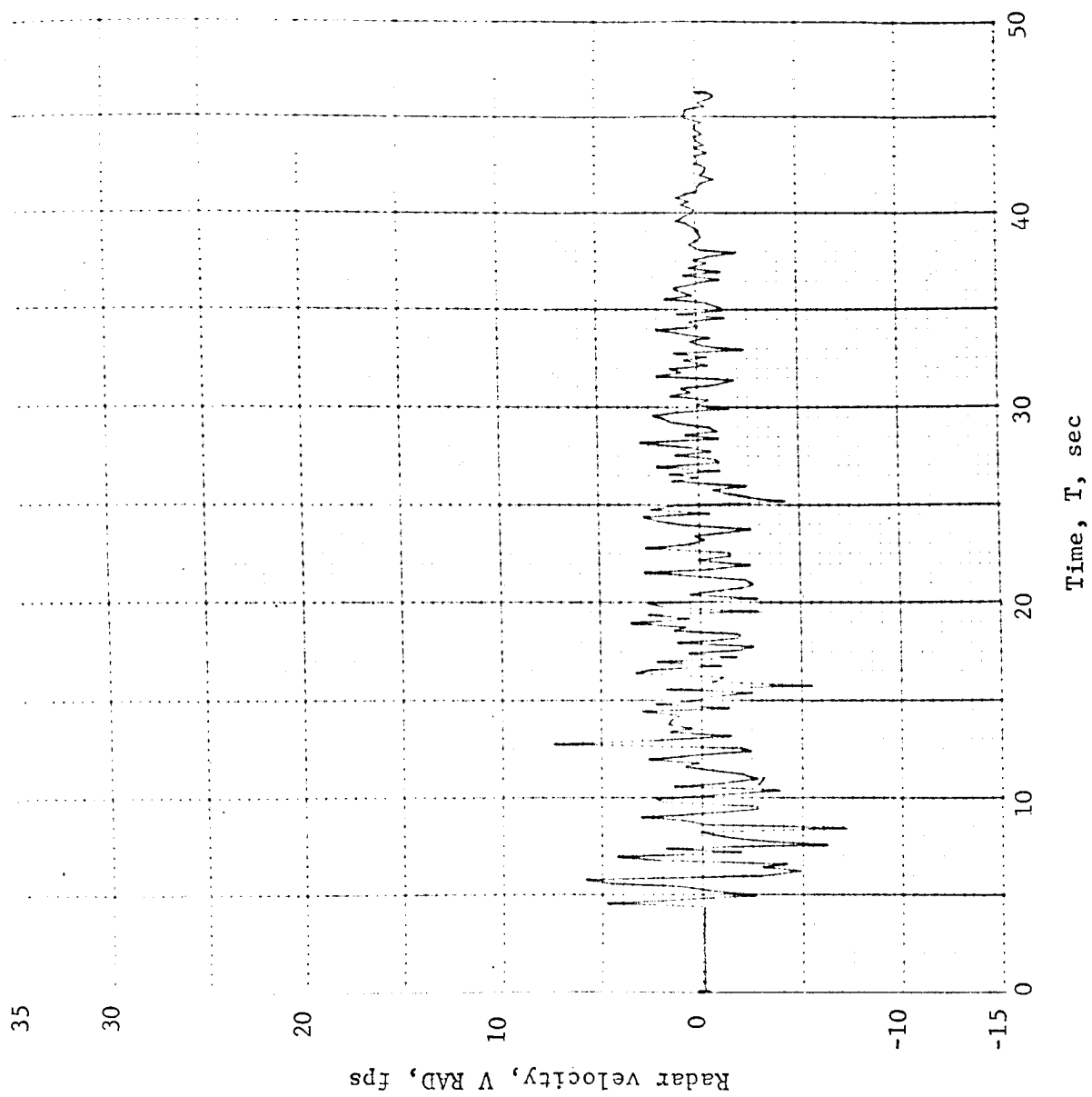


Figure B59.- Soft Lander, Run 5-3

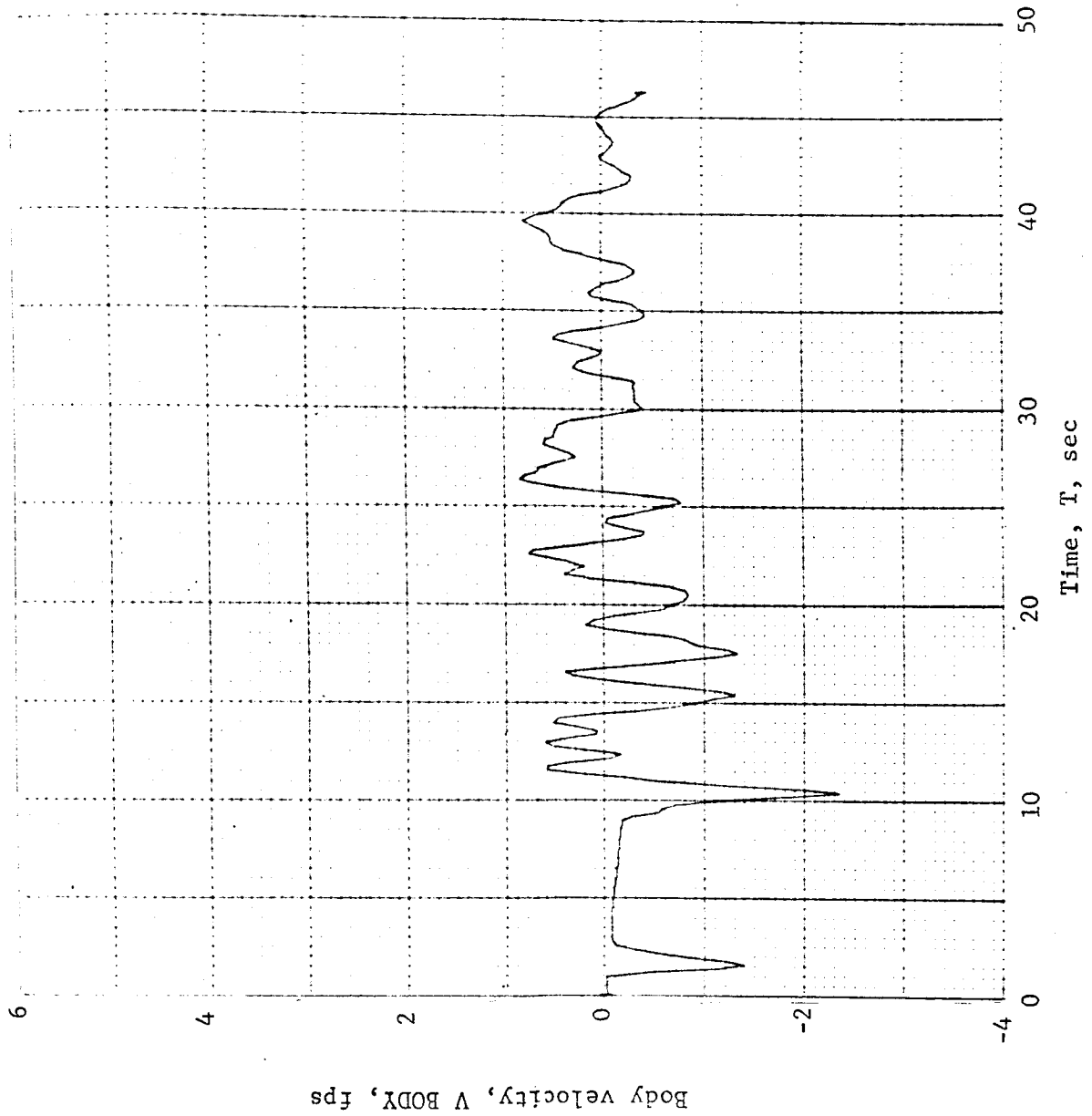


Figure B60.- Soft Lander, Run 5-4

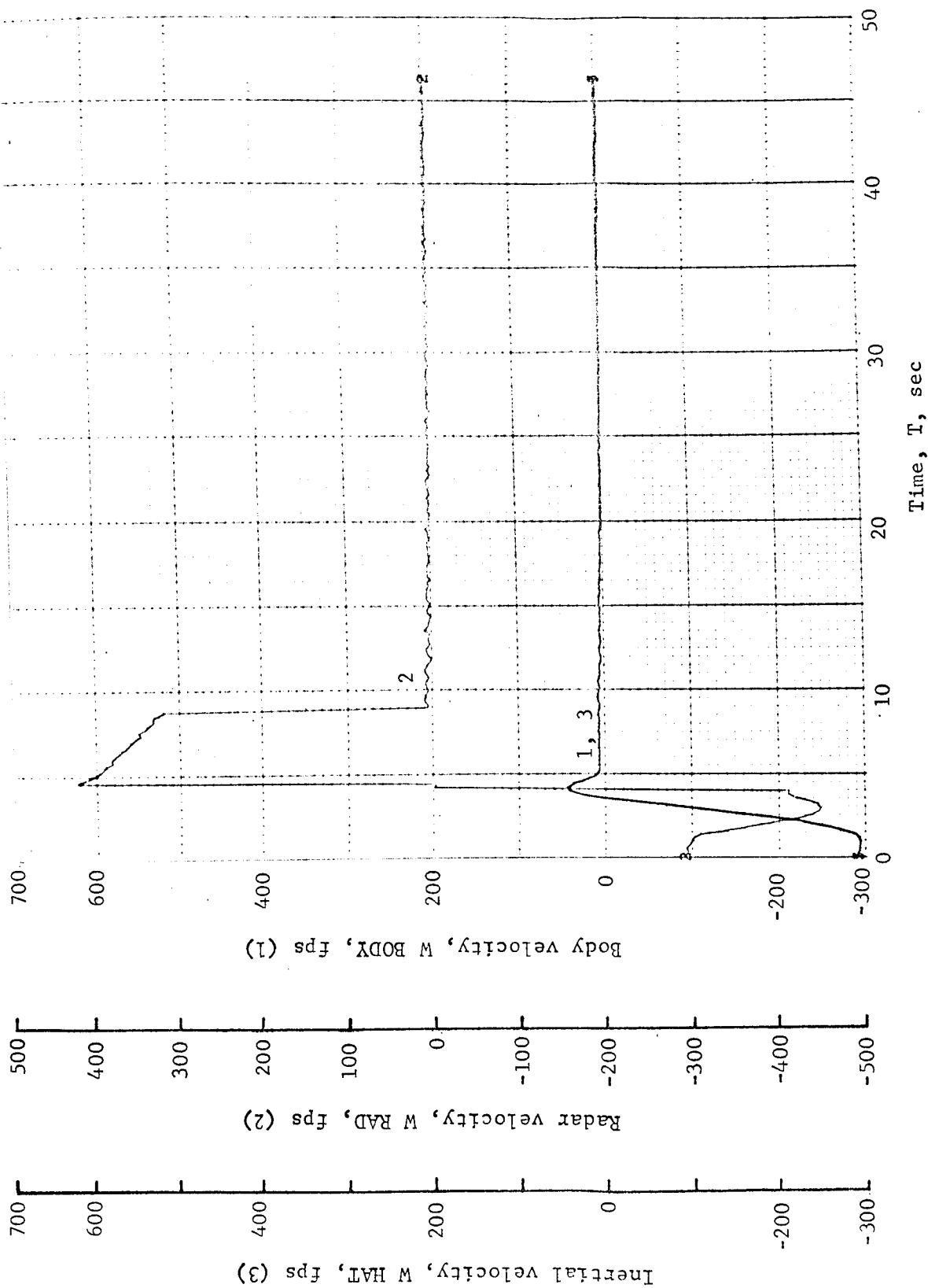


Figure B61.- Soft Lander, Run 5-5

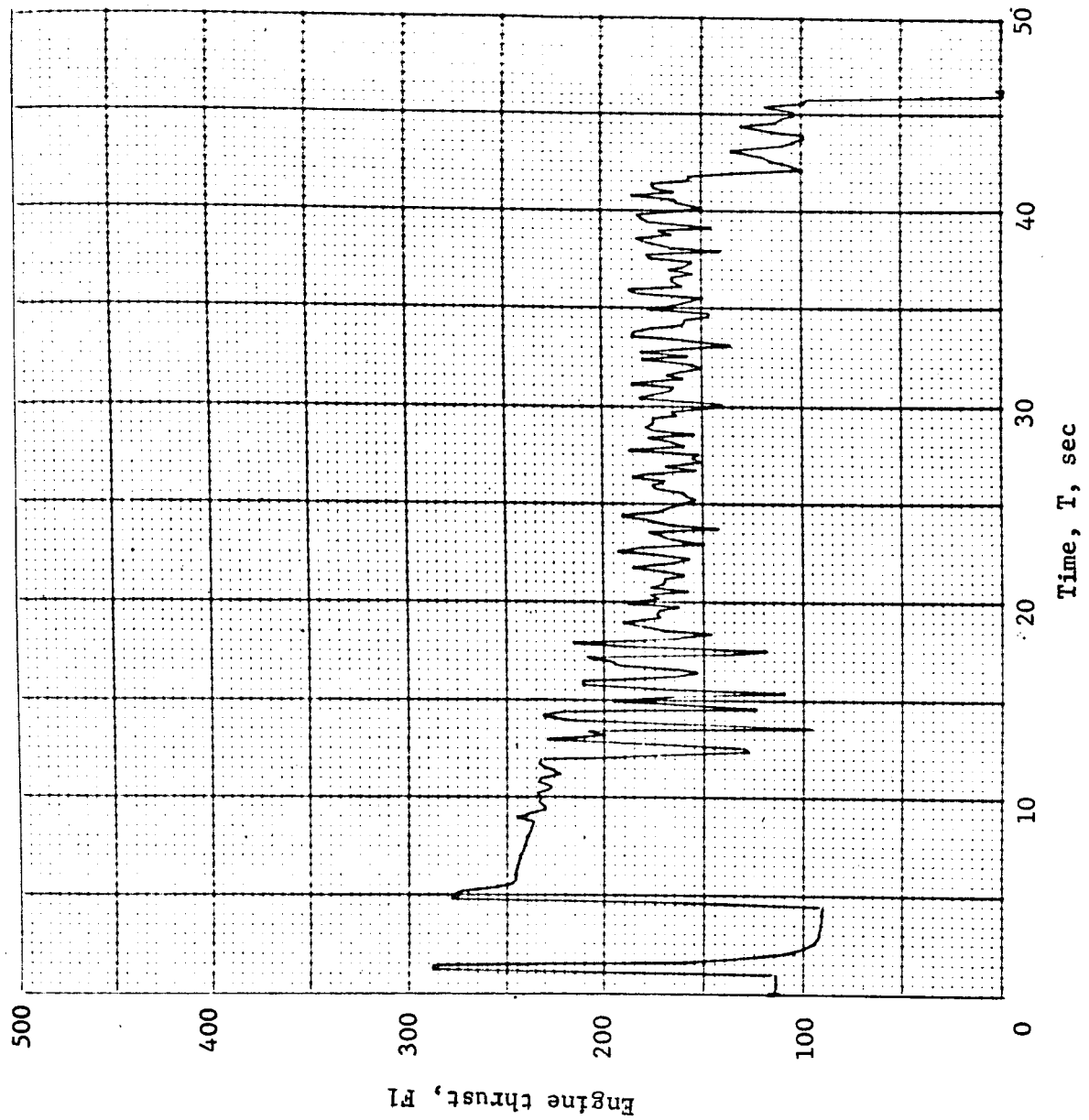


Figure B62.- Soft Lander, Run 5-6

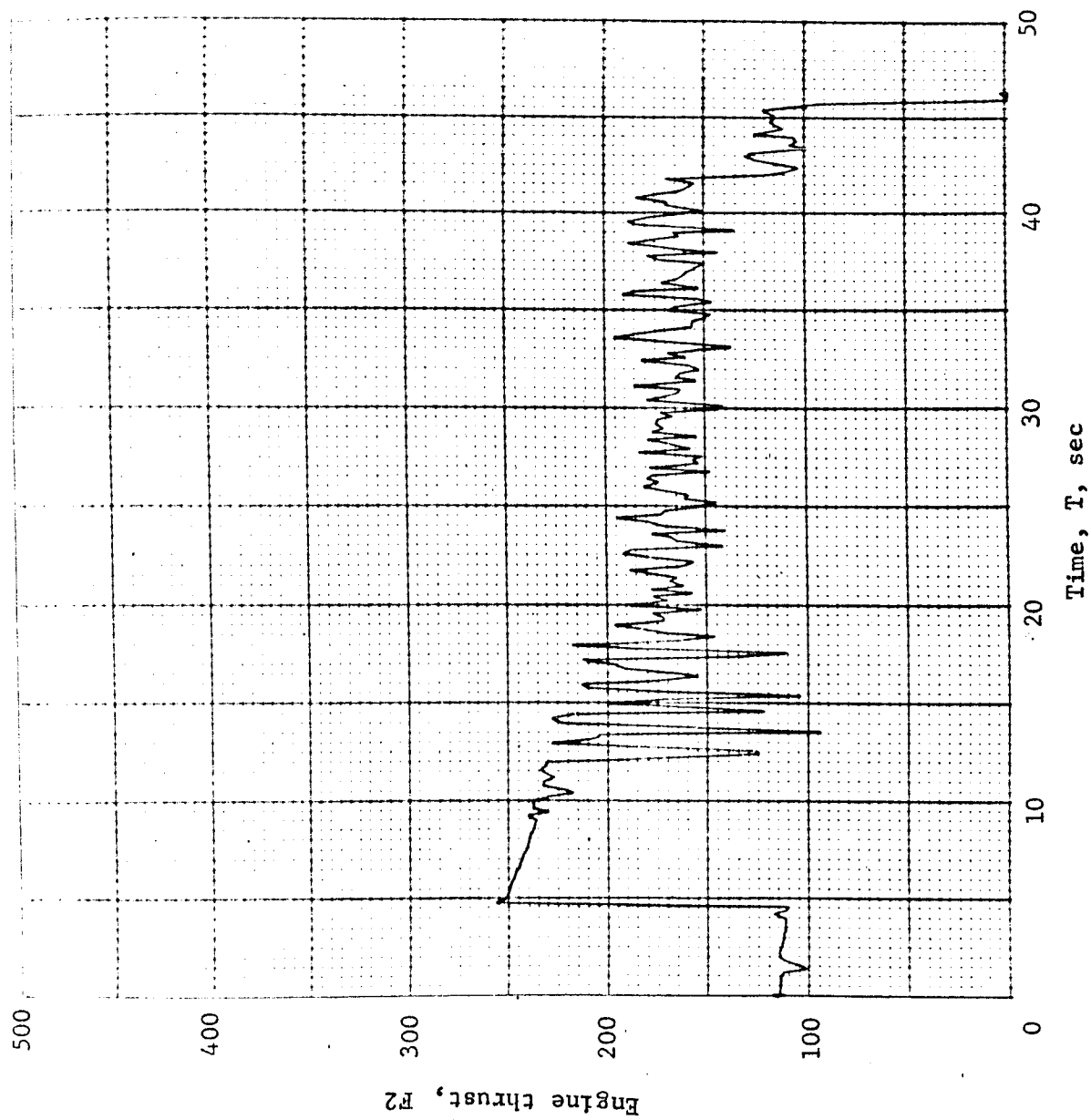


Figure B63.- Soft Lander, Run 5-7

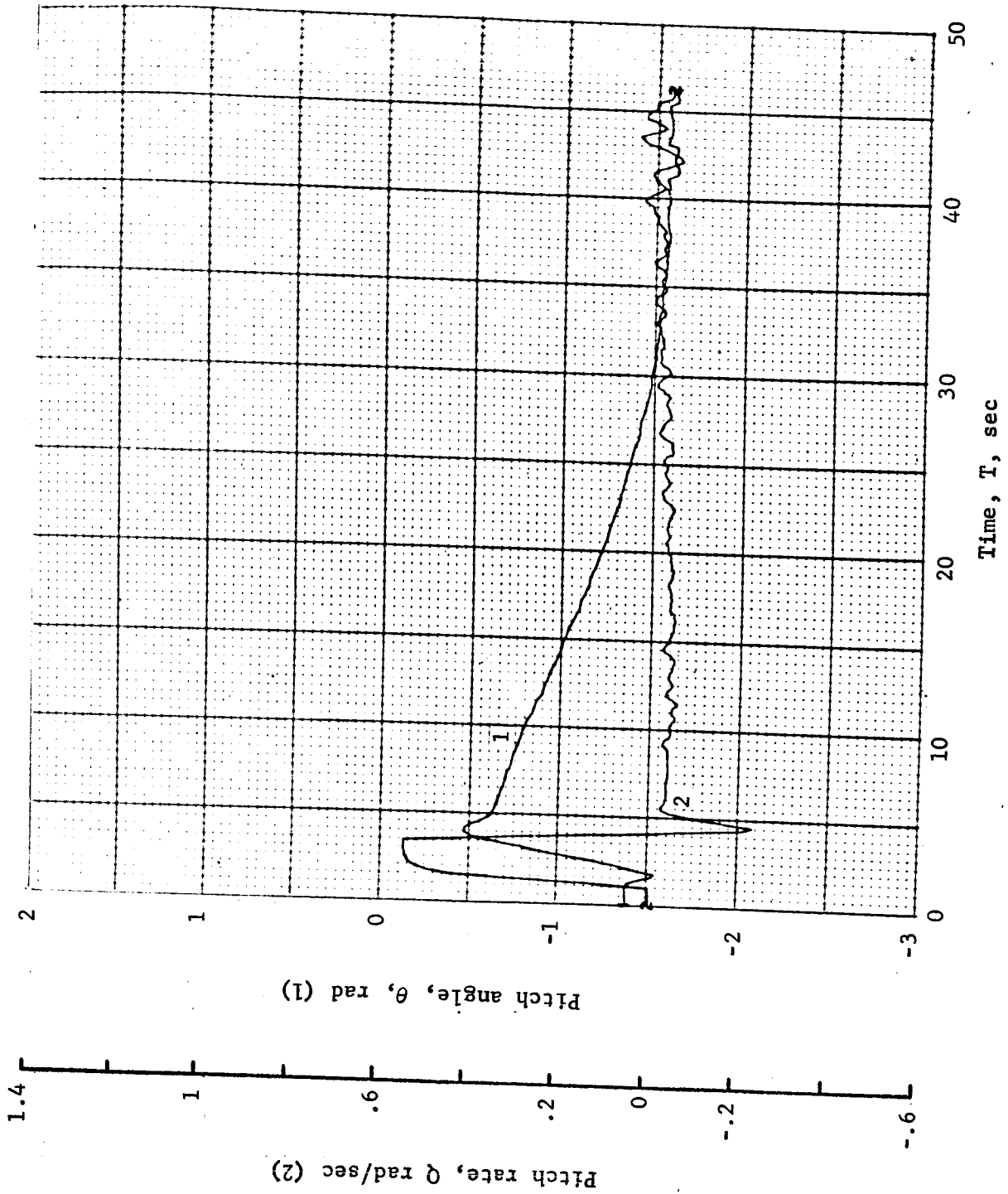


Figure B64.- Soft Lander, Run 5-8

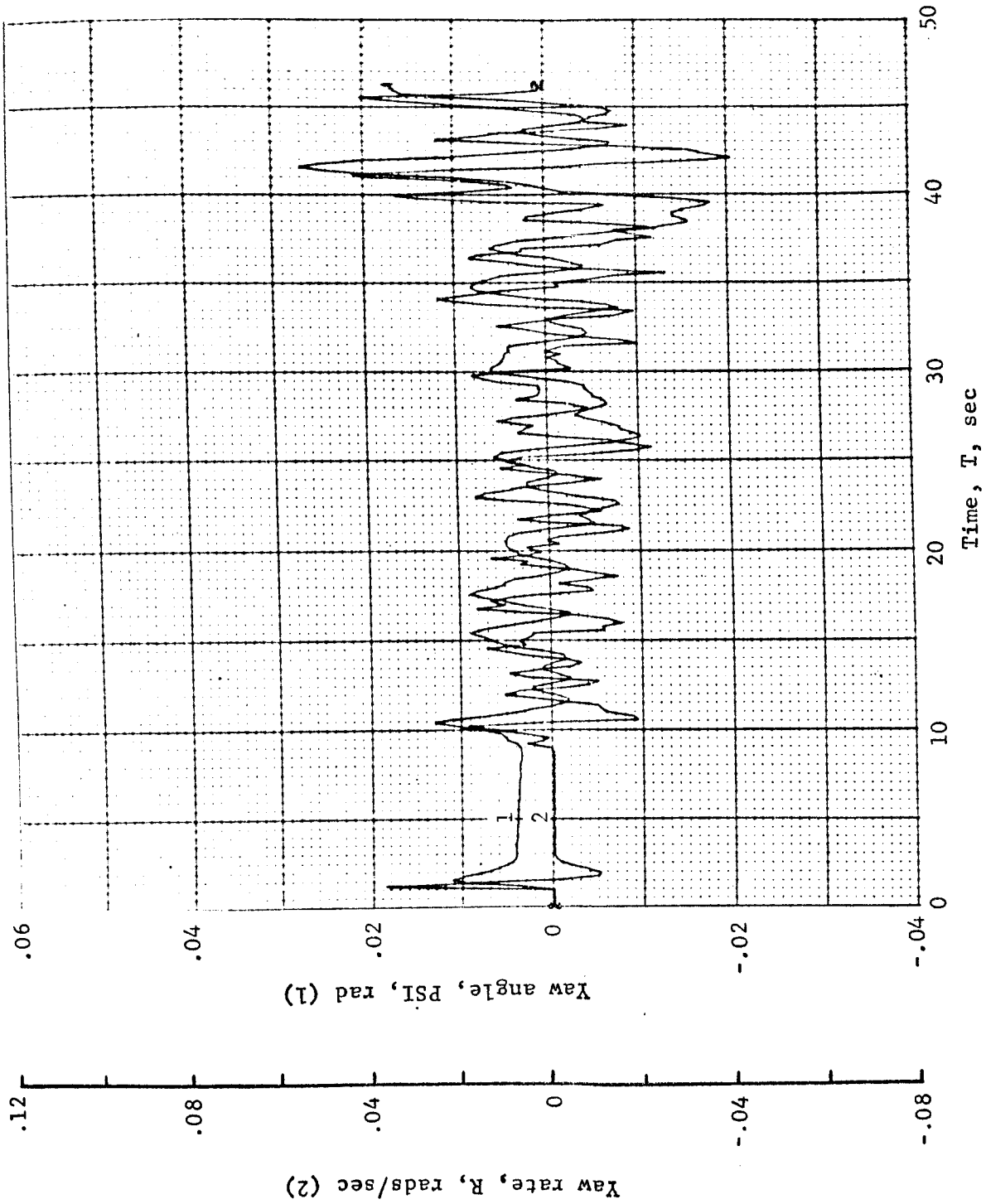


Figure B65.- Soft Lander, Run 5-9

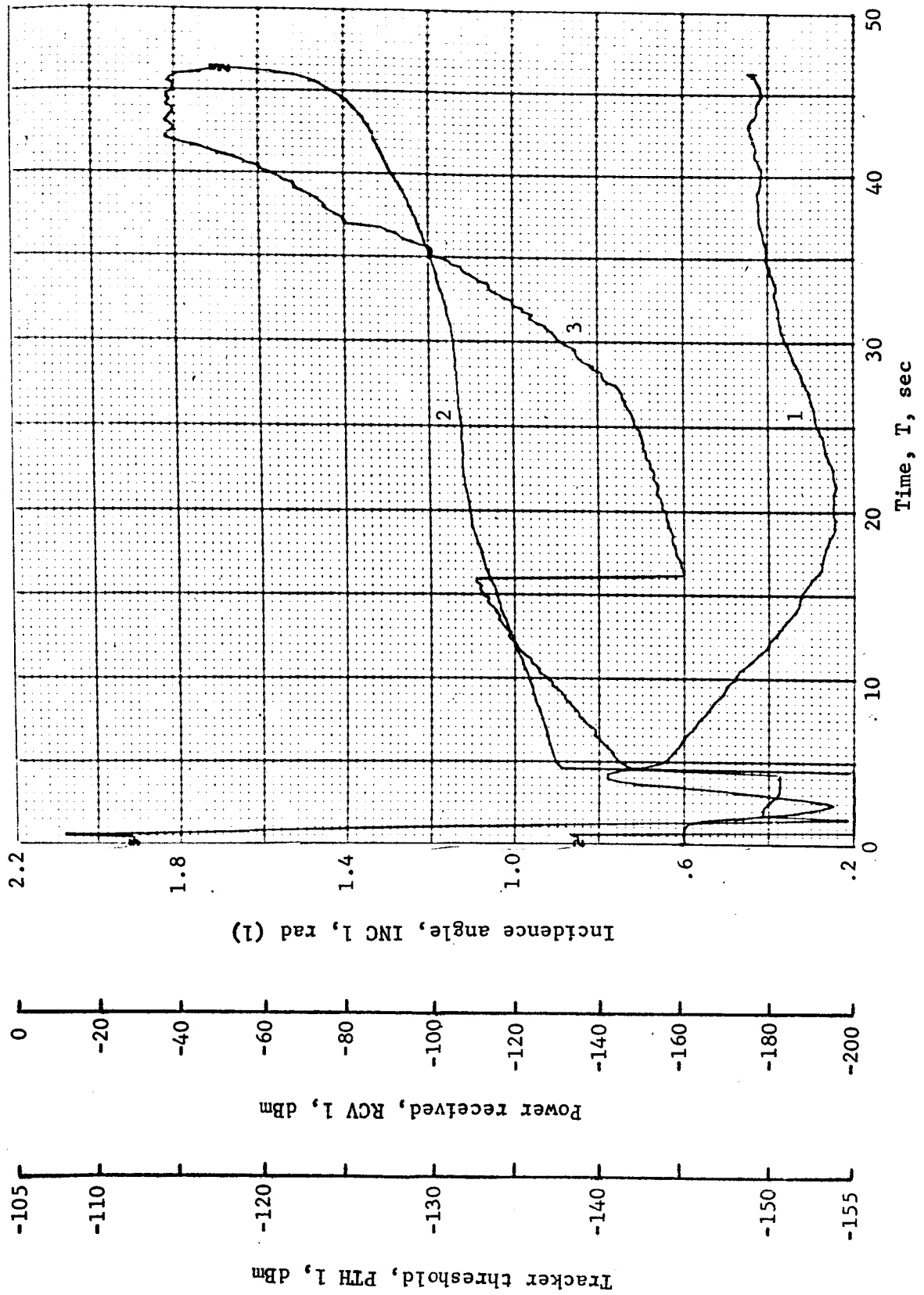


Figure B66.- Soft Lander, Run 5-10

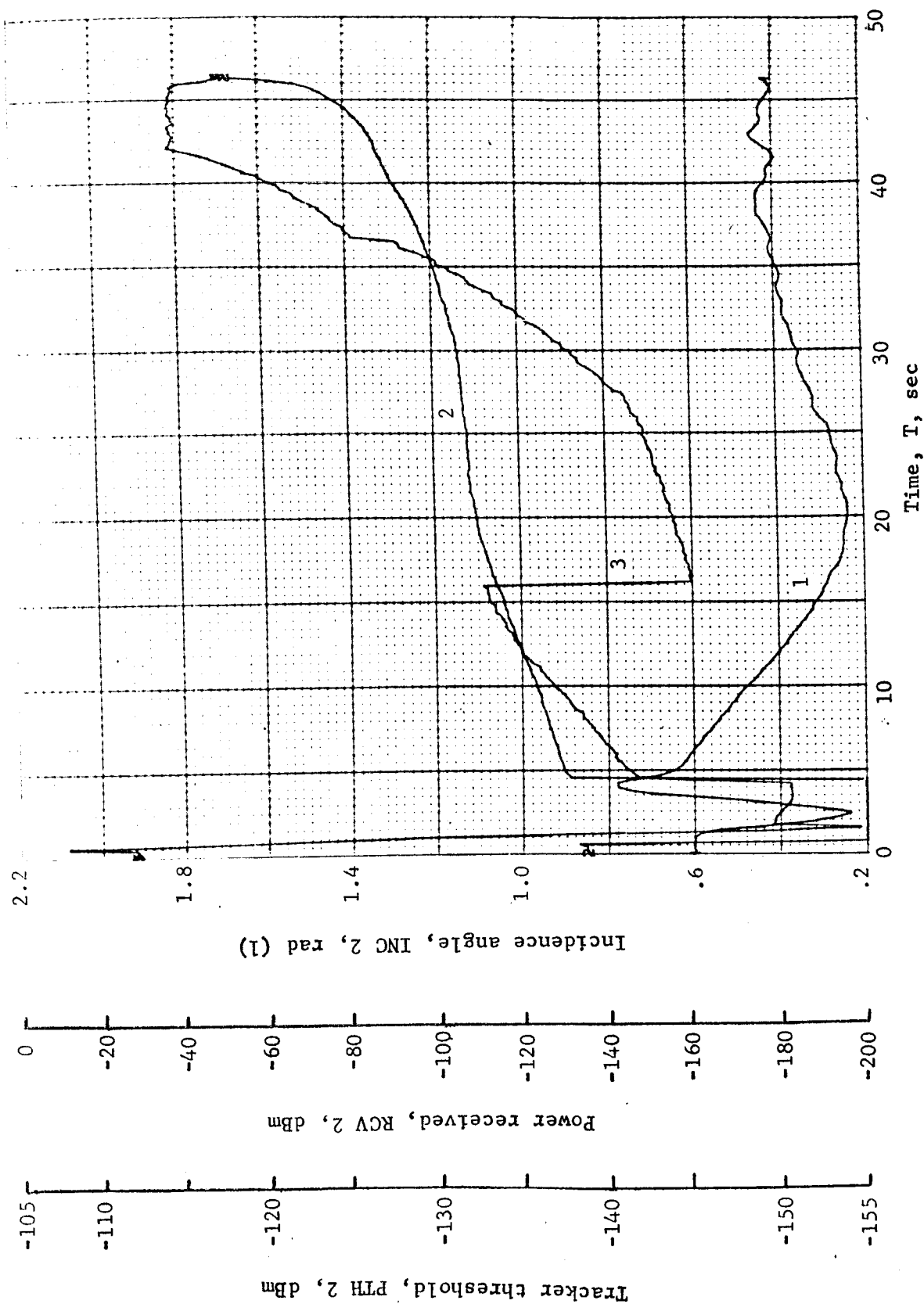


Figure B67.- Soft Lander, Run 5-11

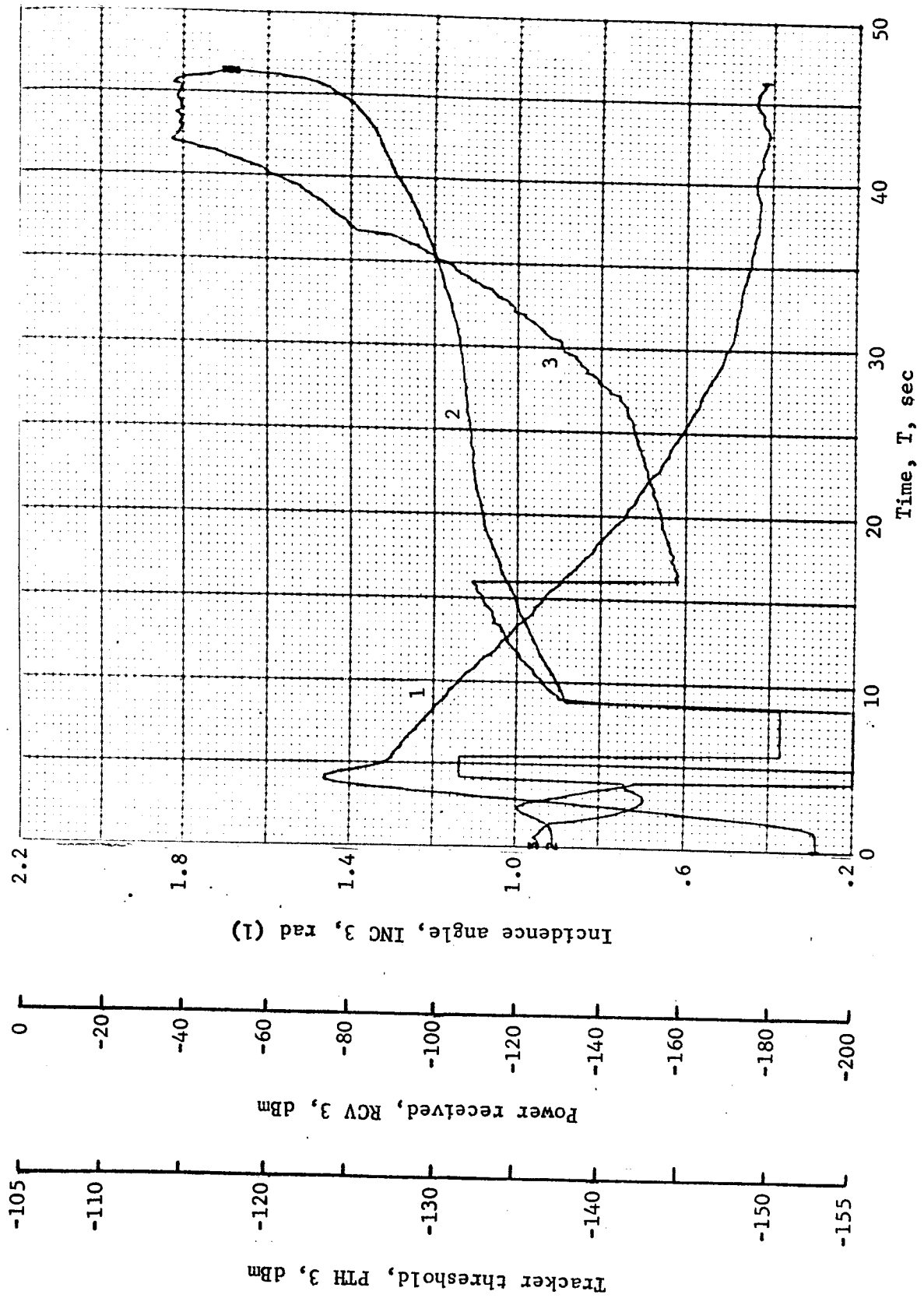


Figure B68.- Soft Lander, Run 5-12

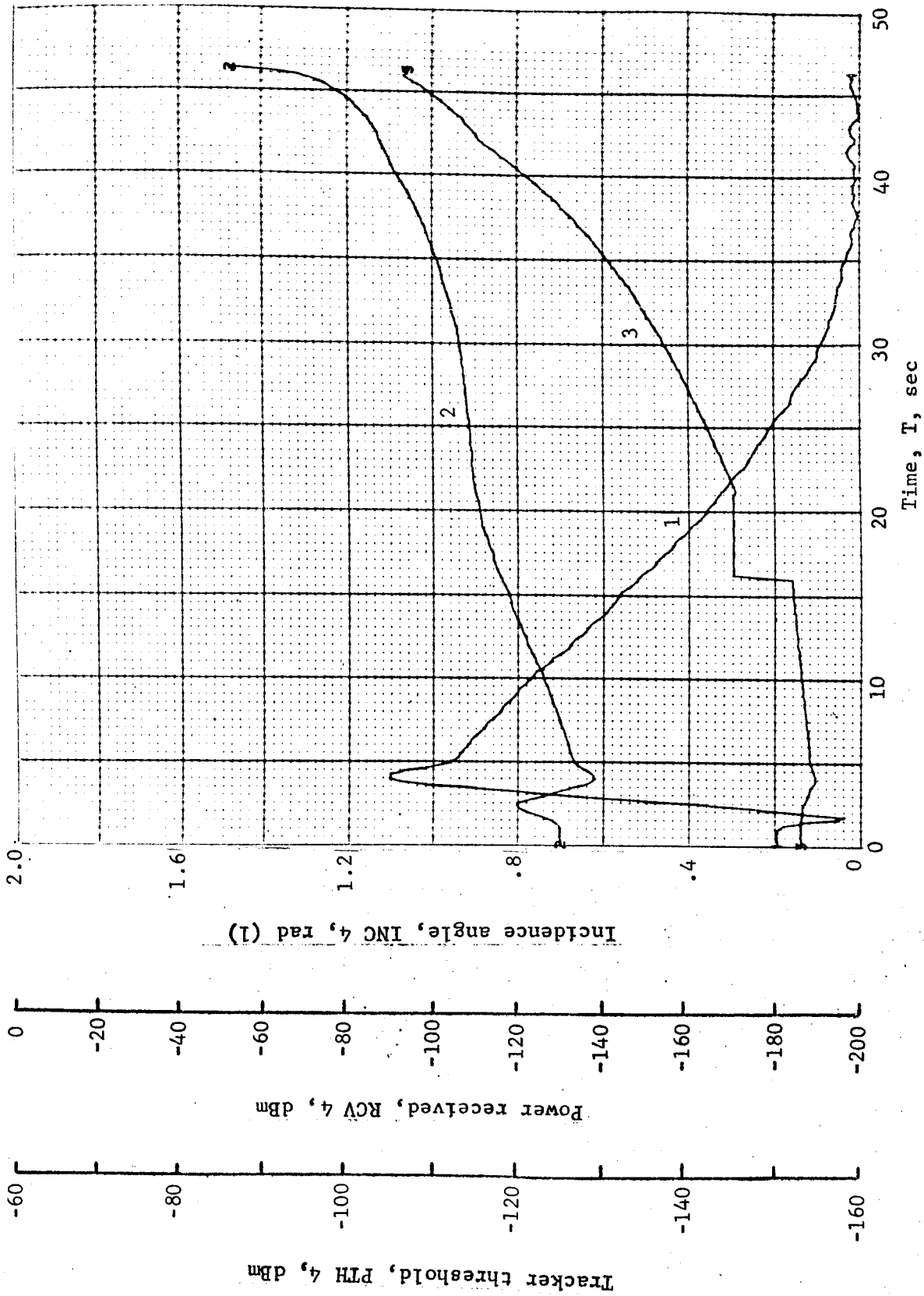


Figure B69.- Soft Lander, Run 5-13

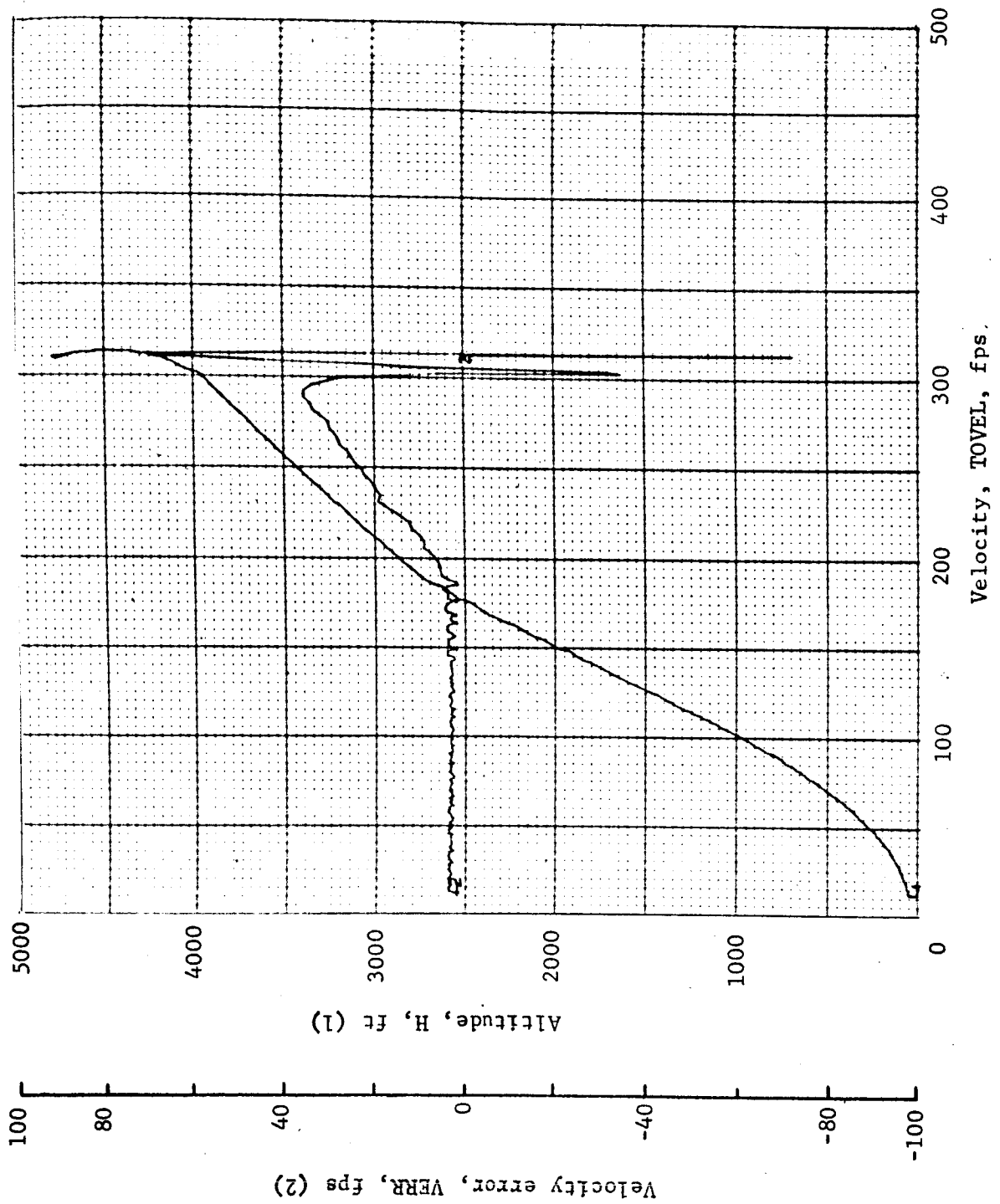


Figure B70.- Soft Lander, Run 5-14

APPENDIX B

TABLE B6.- RUN 6, AUTONOMOUS/MODIFIED LM/RANGE VELOCITY/-27° SLOPE

Flight condition	Altitude, ft	Velocity, fps		Pitch angle, deg	Pitch rate, deg/sec	Time, sec	Fuel used, lb	Beams unlocked	Time to reacquire after loss, sec
		Roll axis	Cross axis						
Initial	4600	165	-170	-90	0	0	0	----	----
Mid-pitchup	4538	197.3	-128.8	-77	28.	.8	2.1	----	----
Max. pitchup	4407	228.7	27.4	-40	-1.8	2.4	5.7	3 at 1.8 4 at 2.2	----
Thrust aligned	4295	227.3	13.4	-46.2	-2.2	3.6	8.2	3, 4	----
Encounter contour	4215	226.2	13.4	-47.9	-2.15	4.4	9.8	3, 4	3 at 12.6 4 at 6.2
Constant vel	51.57	11.8	.18	-90.1	.035	46	131.7	----	----
Cutoff eng	8.63	12	.2	-90.1	.002	49.5	139	----	----
Land	1.7	17.7	.2	-90.1	.002	50.	139	----	----
Remarks: System was forced to transfer to inertial velocity data at 100 ft altitude. This gave a smoother terminal (50 ft at 10 fps) descent and near nominal angle and rate.									

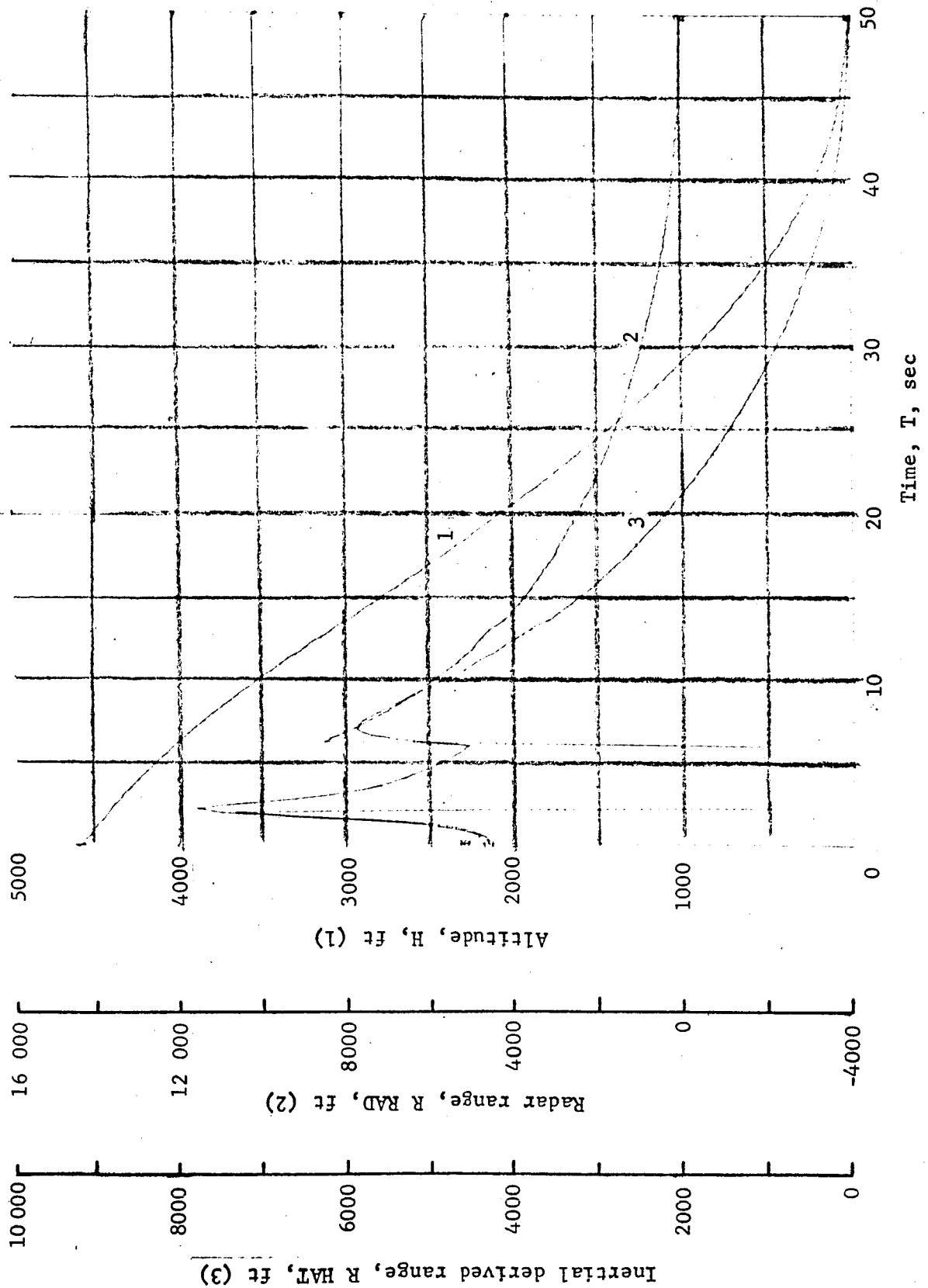


Figure B71.- Soft Lander, Run 6-1

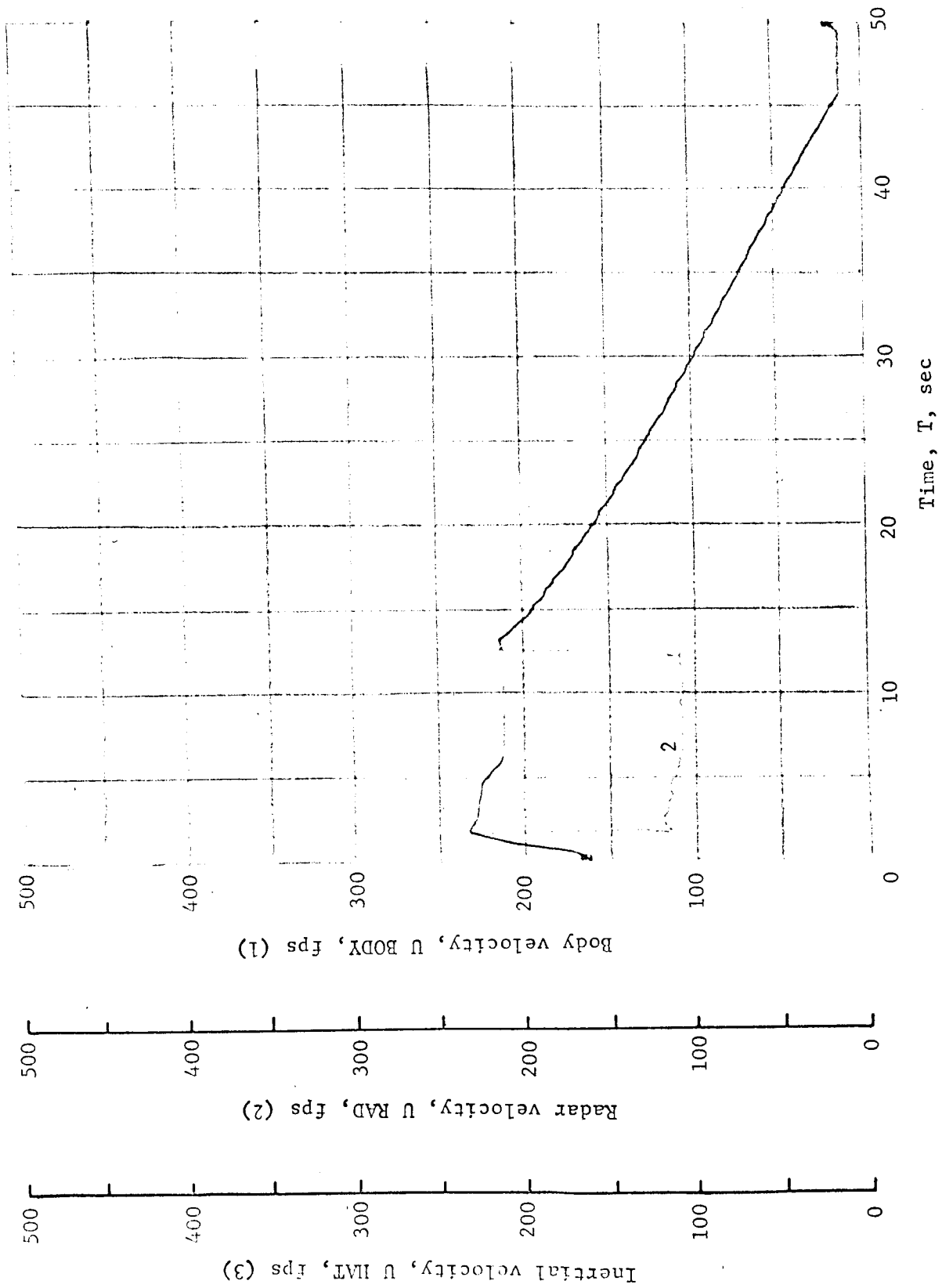


Figure B72.- Soft Lander, Run 6-2

APPENDIX B

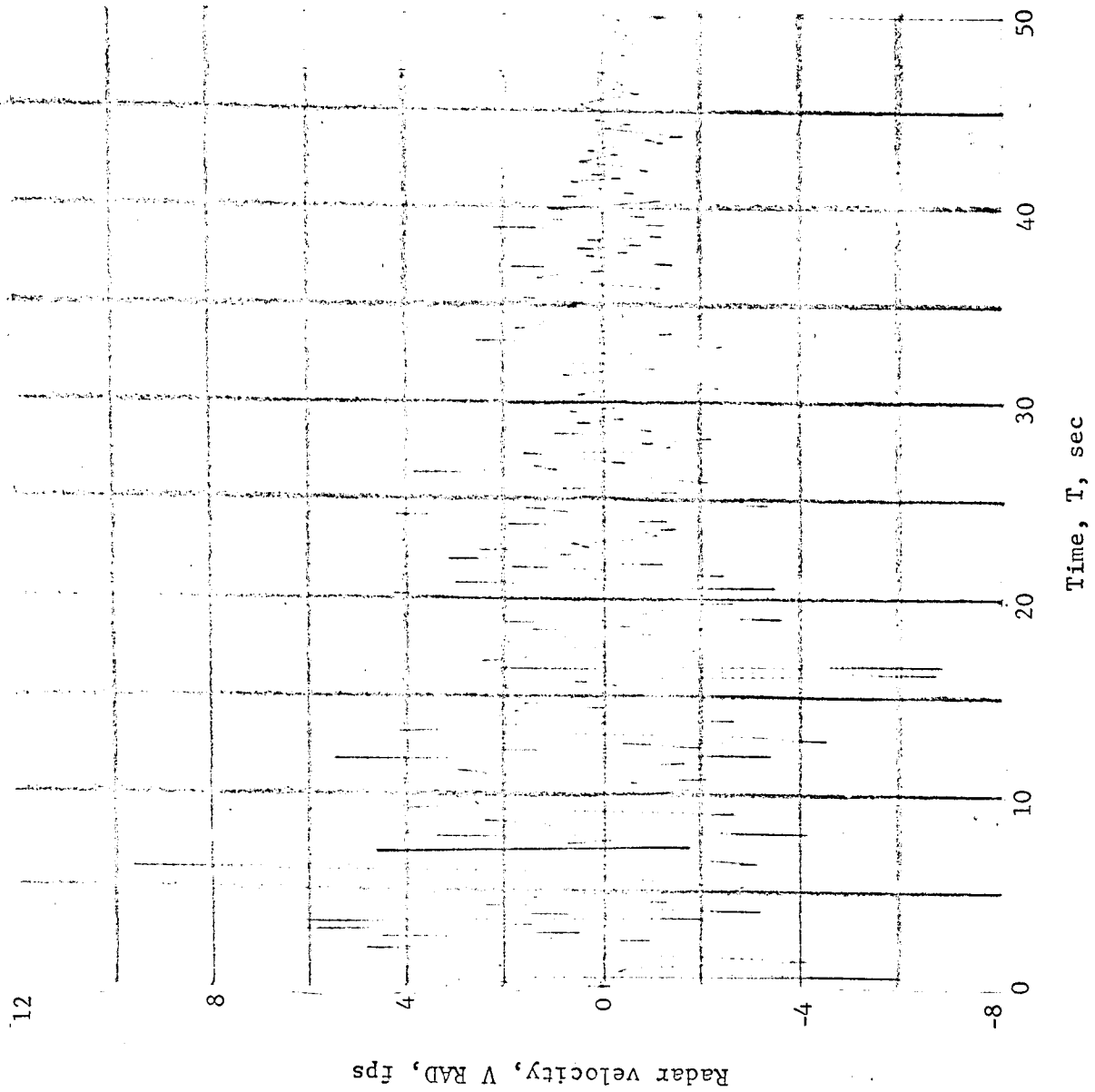


Figure B73.- Soft Lander, Run 6-3

APPENDIX B

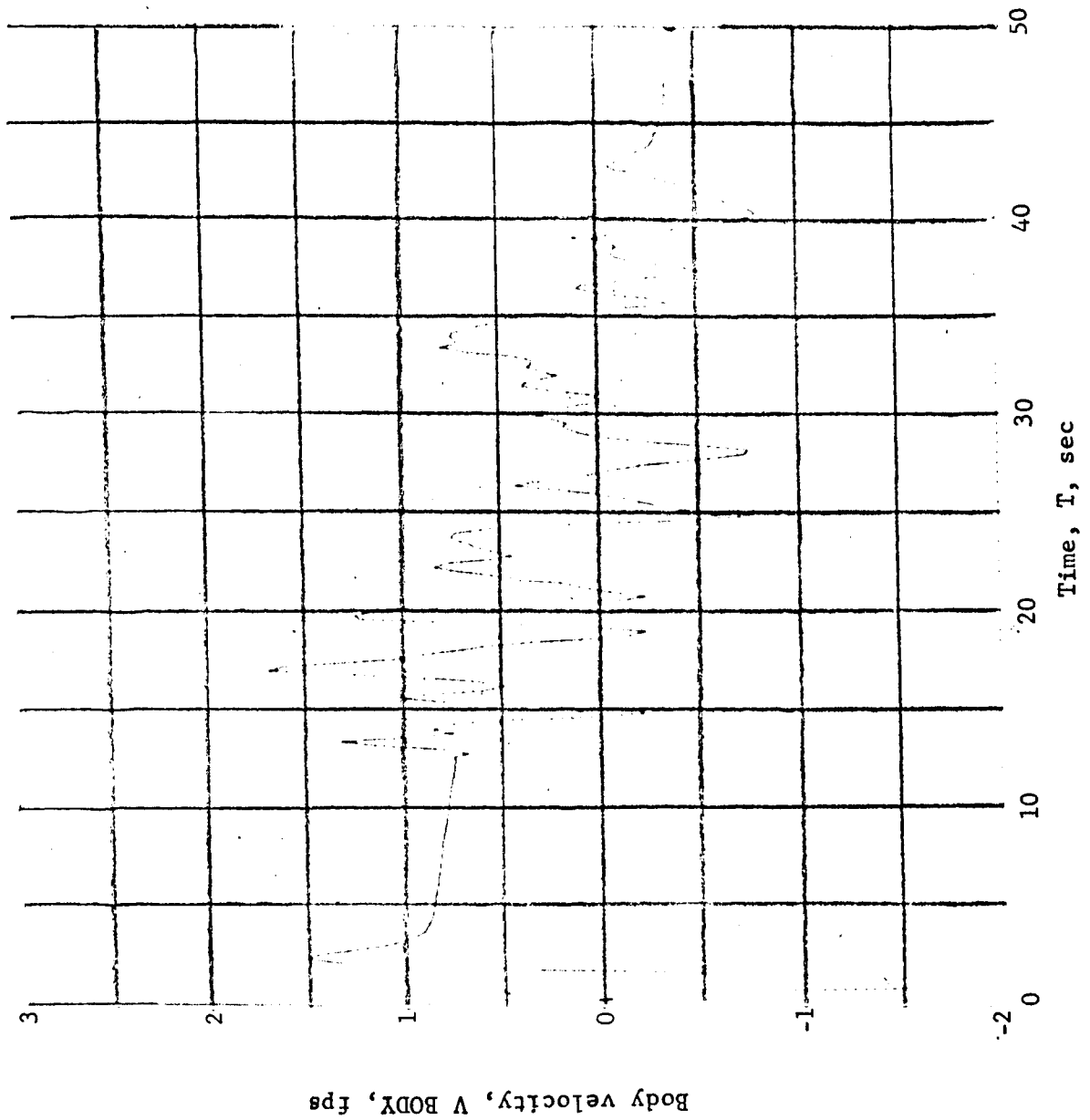


Figure B74.- Soft Lander, Run 6-4

APPENDIX B

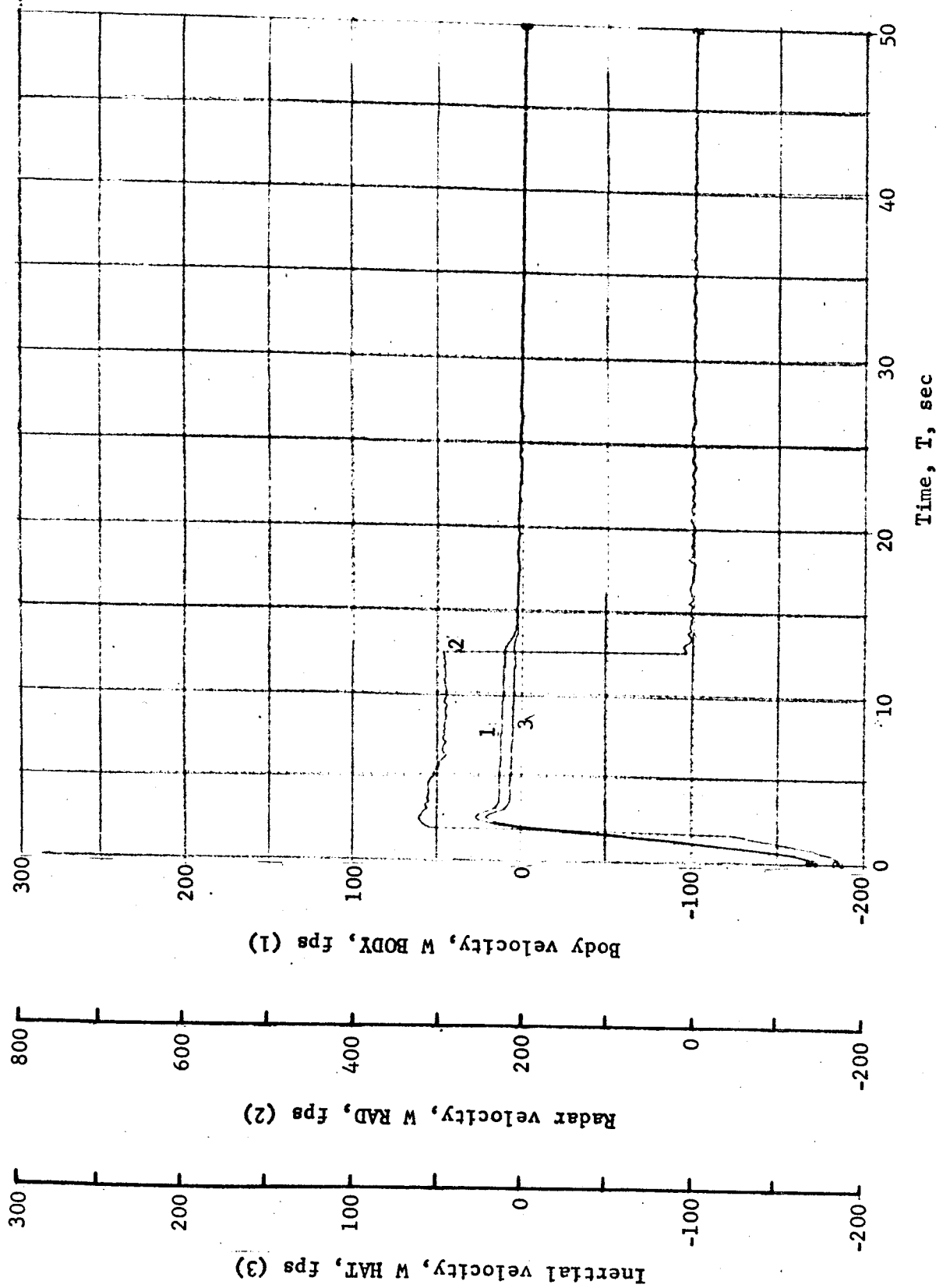


Figure B75.- Soft Lander, Run 6-5

APPENDIX B

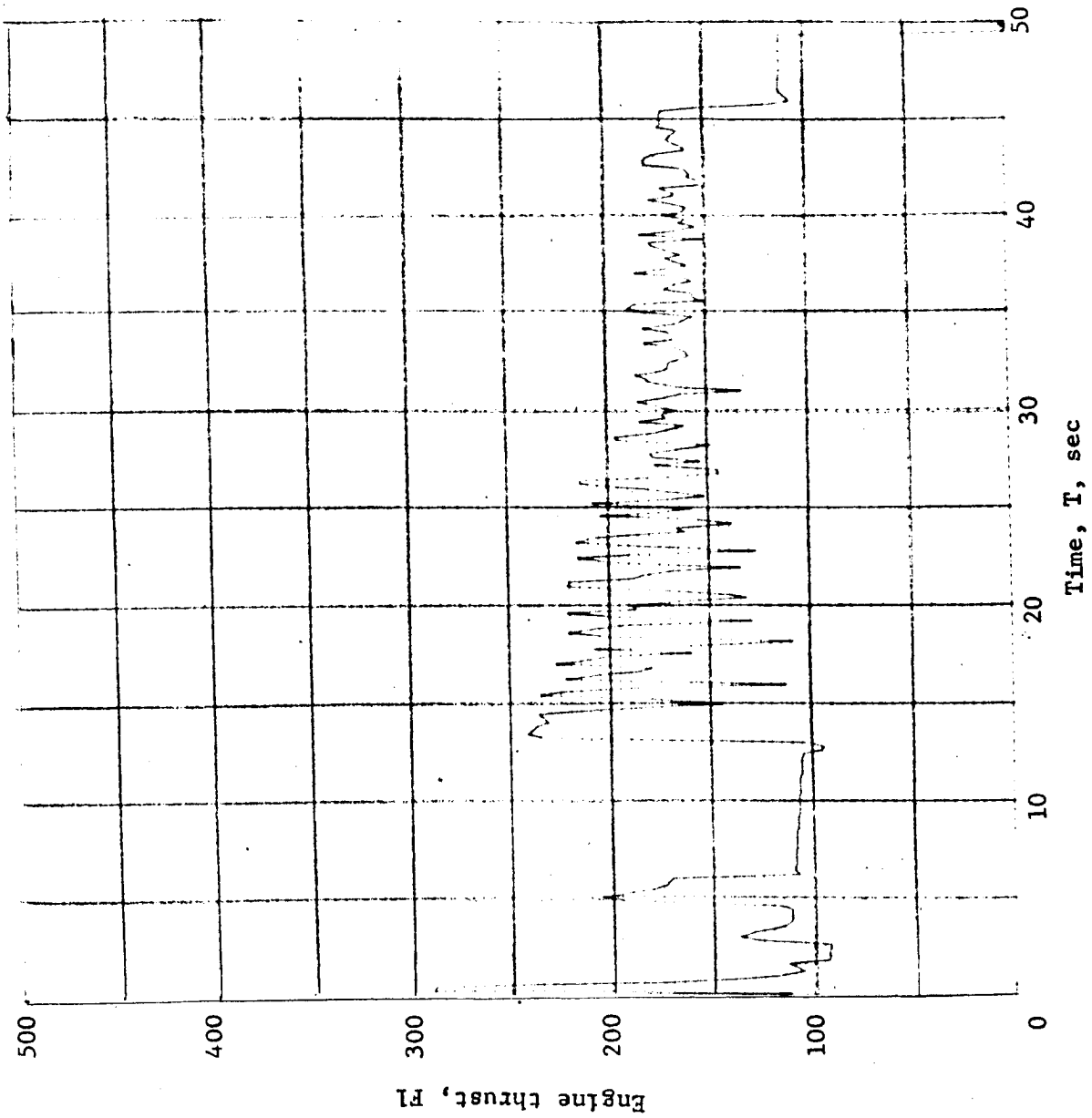


Figure B76.- Soft Lander, Run 6-6

APPENDIX B

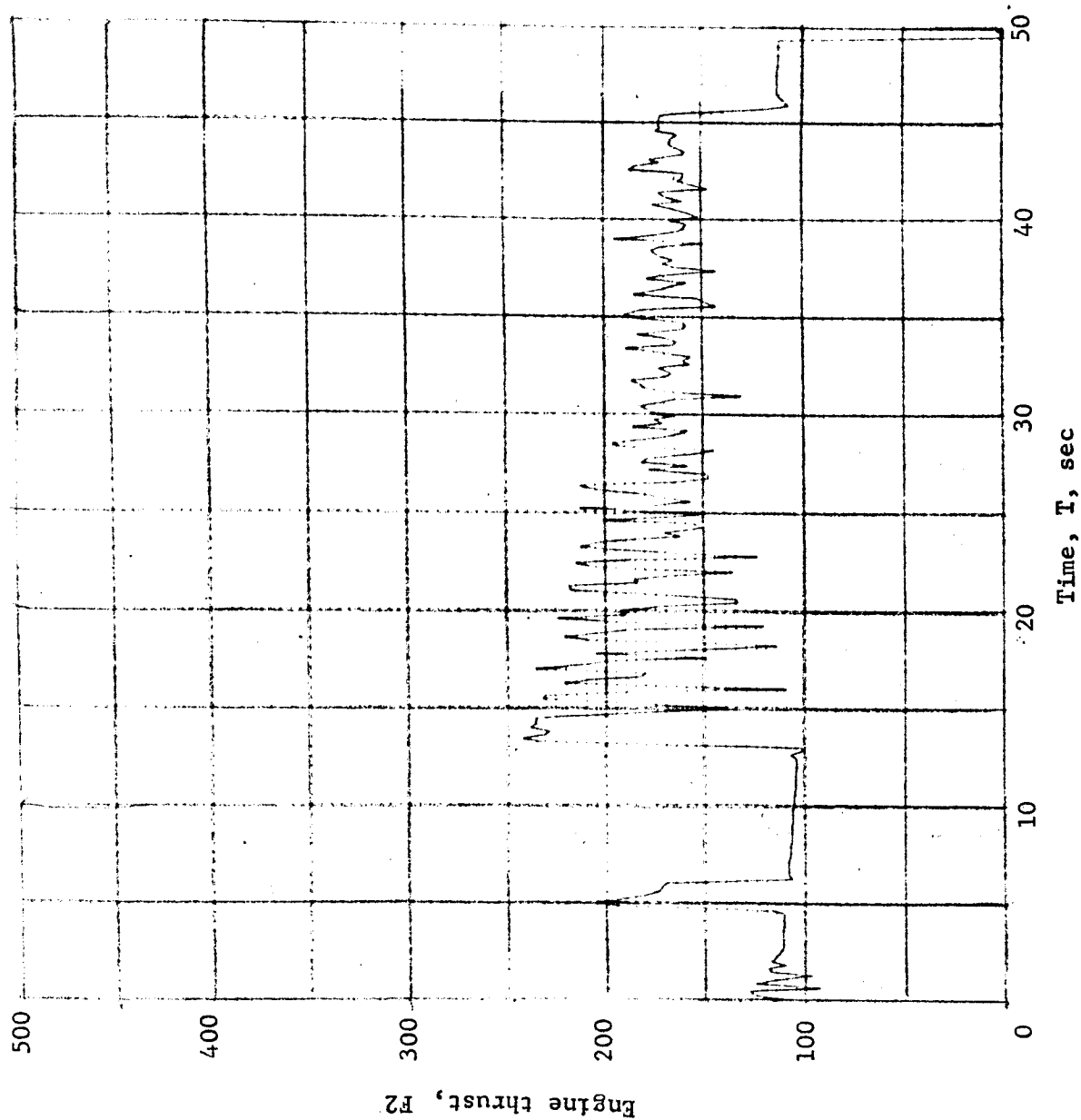


Figure B77.- Soft Lander, Run 6-7

APPENDIX B

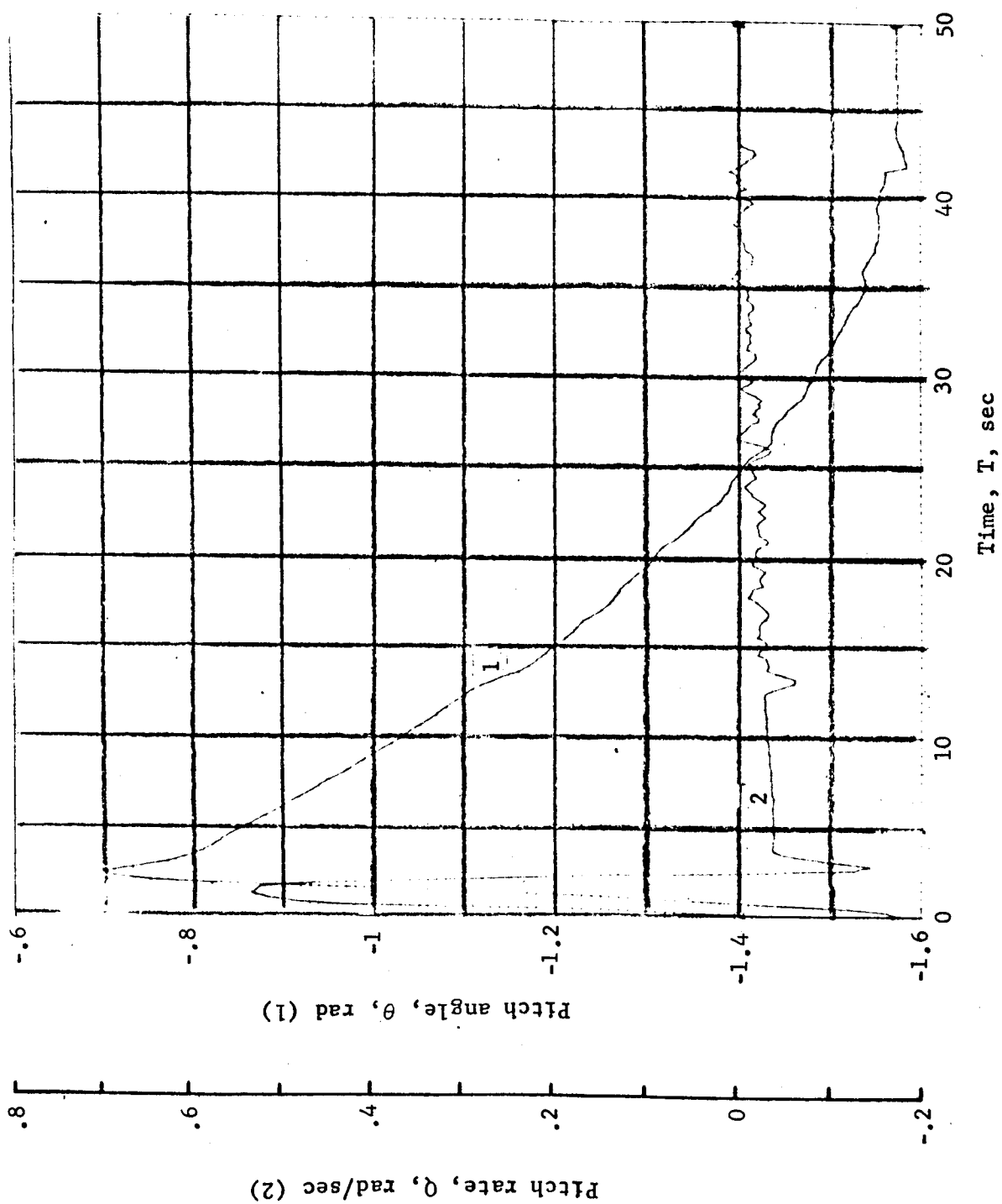
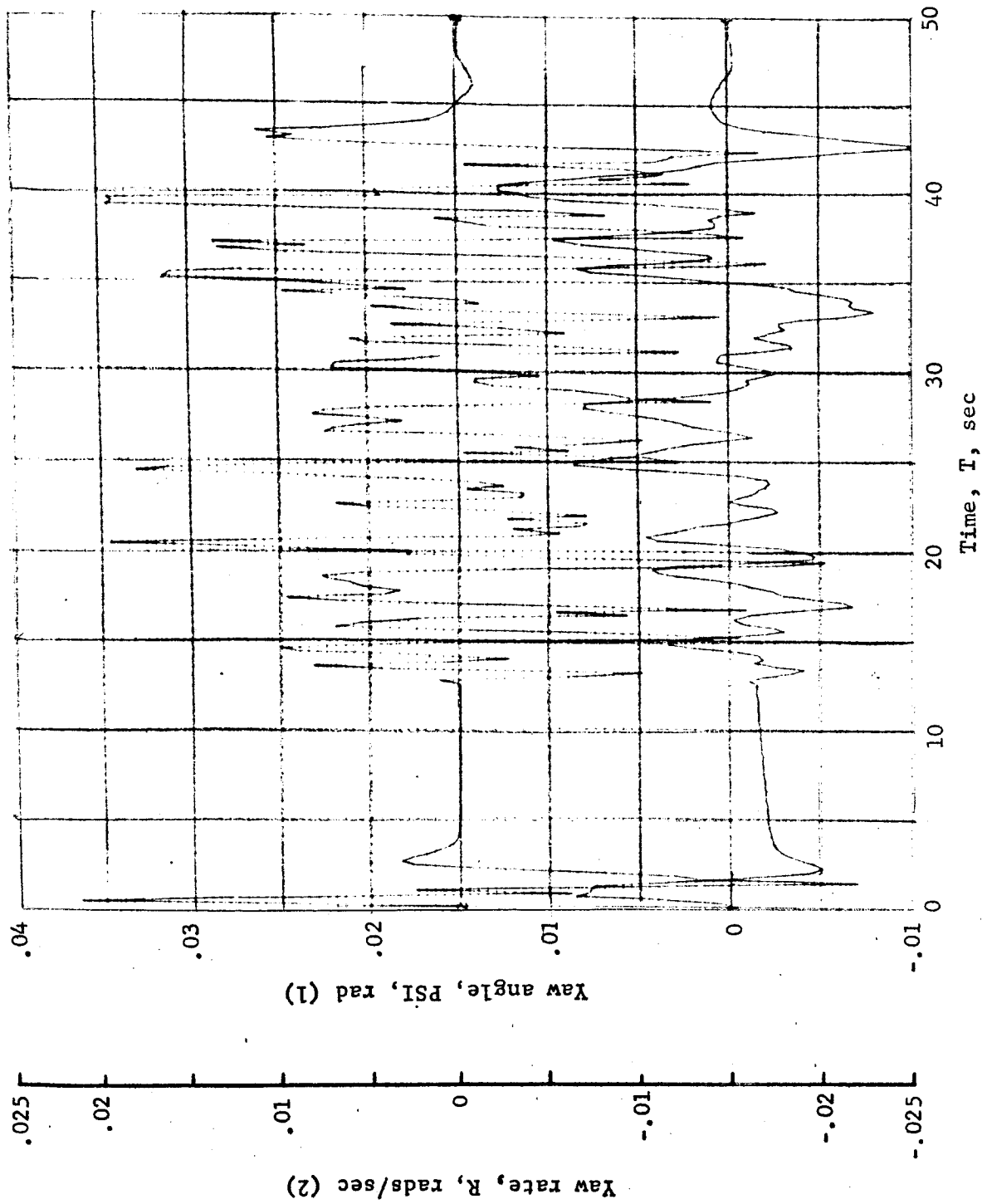


Figure B78.- Soft Lander, Run 6-8

APPENDIX B



APPENDIX B

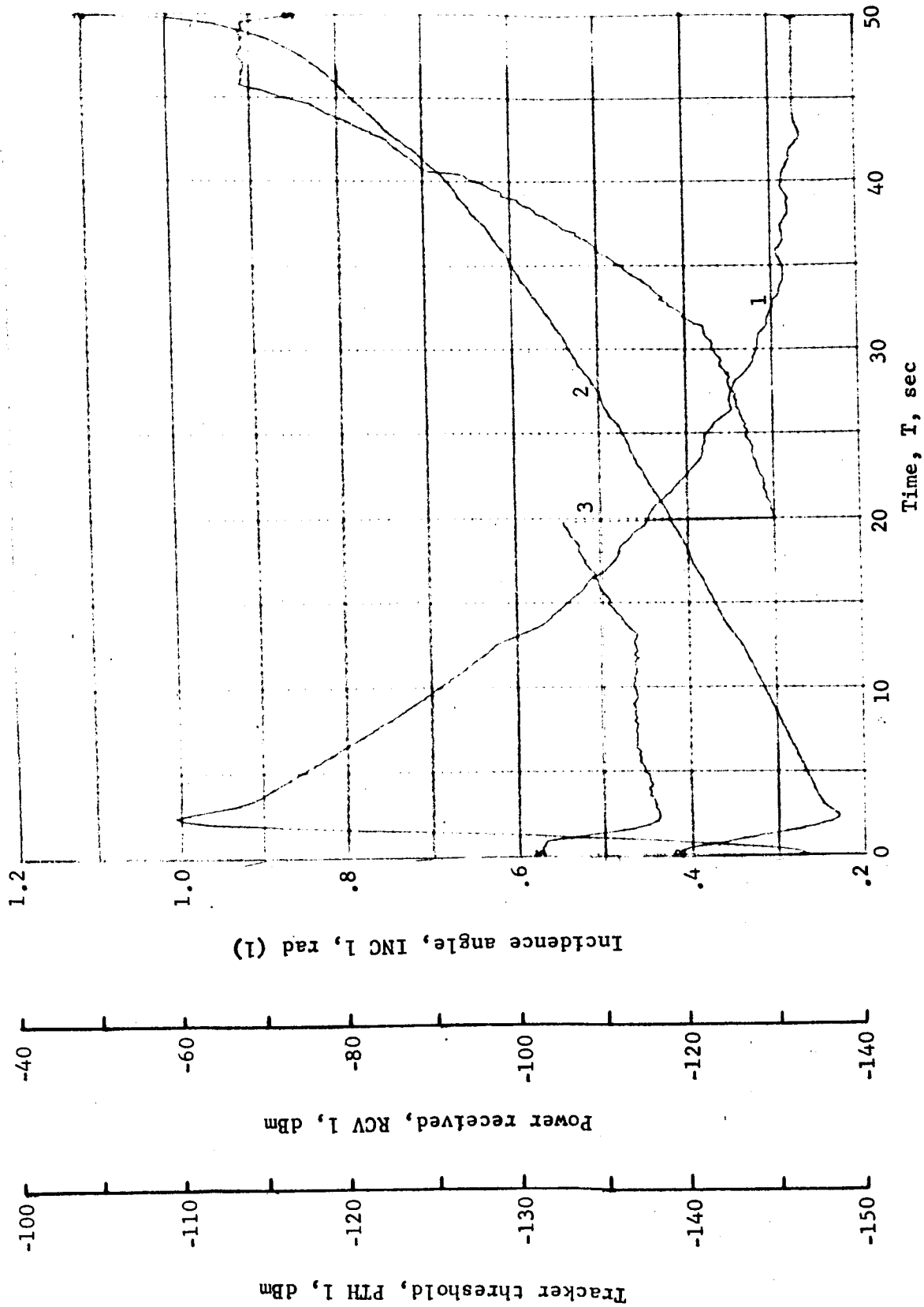


Figure B80.- Soft Lander, Run 6-10

APPENDIX B

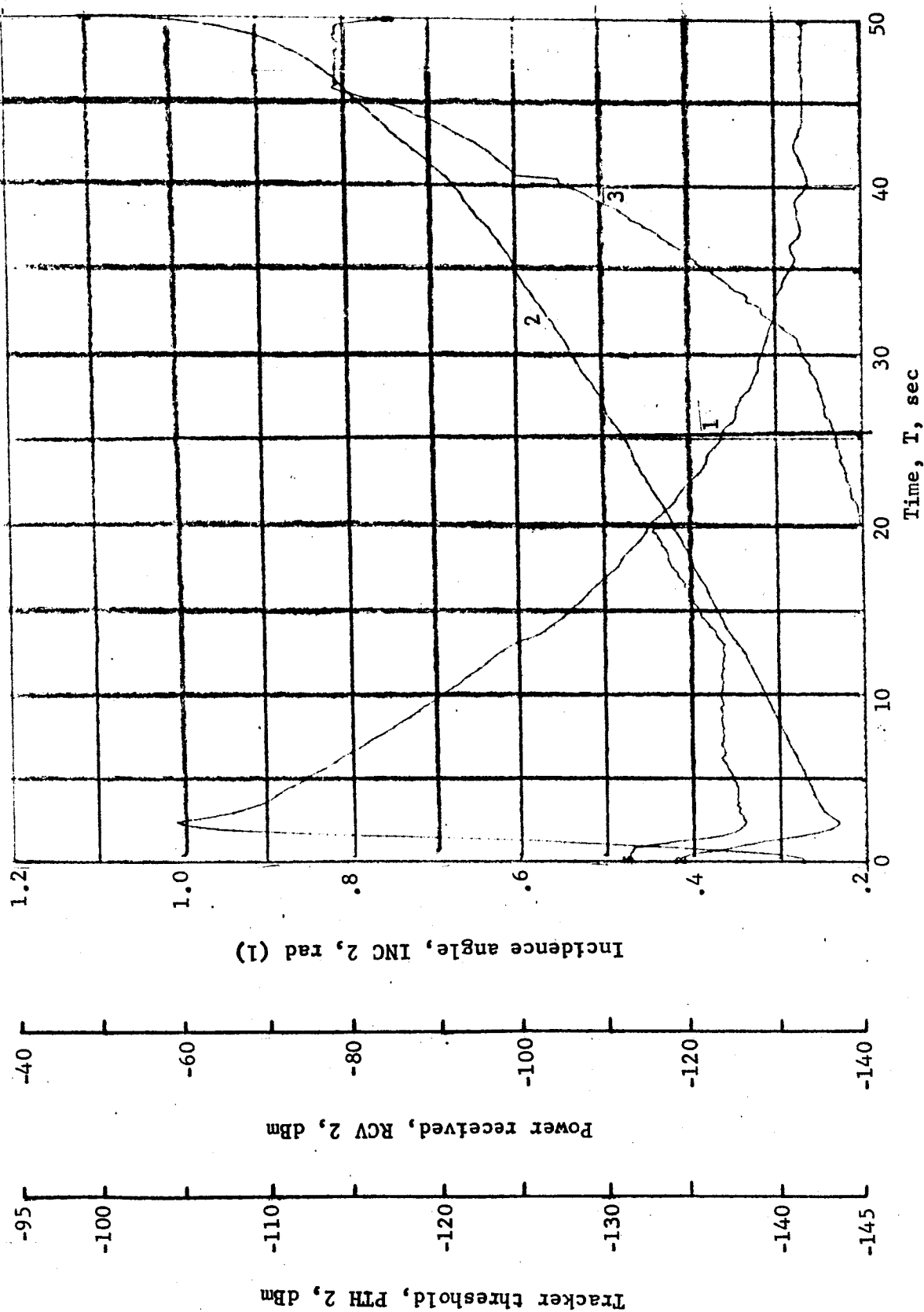


Figure B81.- Soft Lander, Run 6-11

APPENDIX B

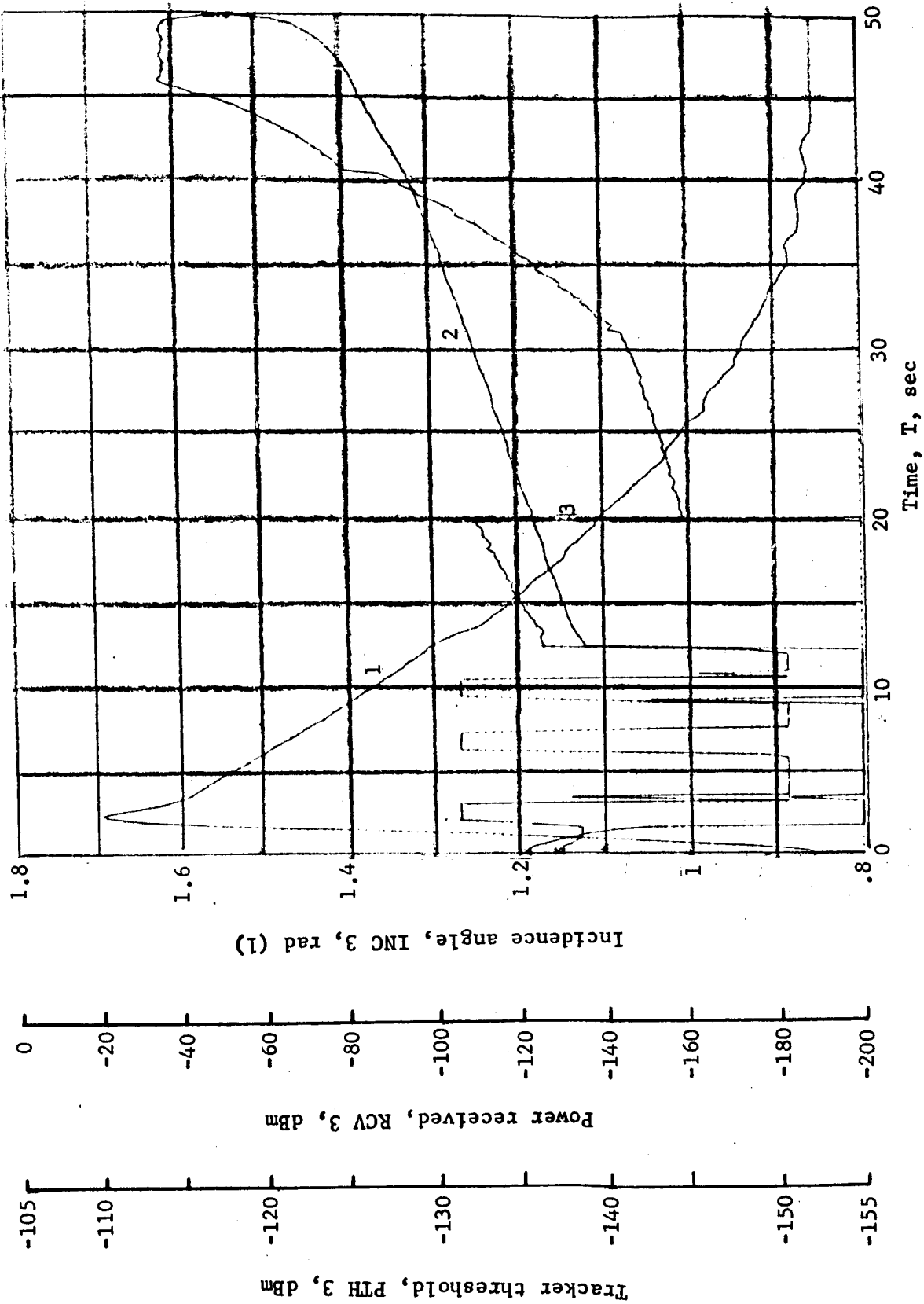


Figure B82.- Soft Lander, Run 6-12

APPENDIX B

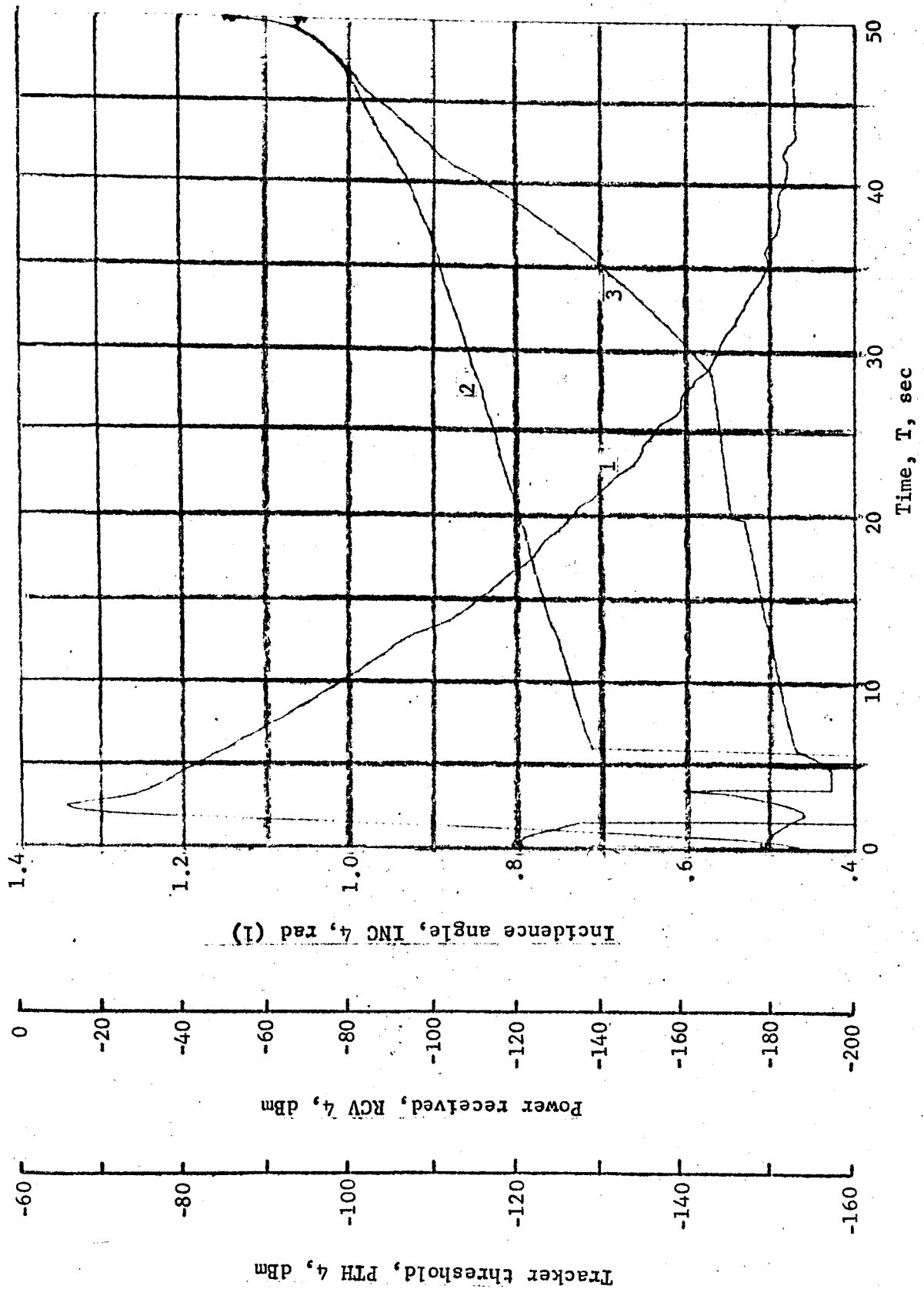


Figure B83.- Soft Lander, Run 6-13

APPENDIX B

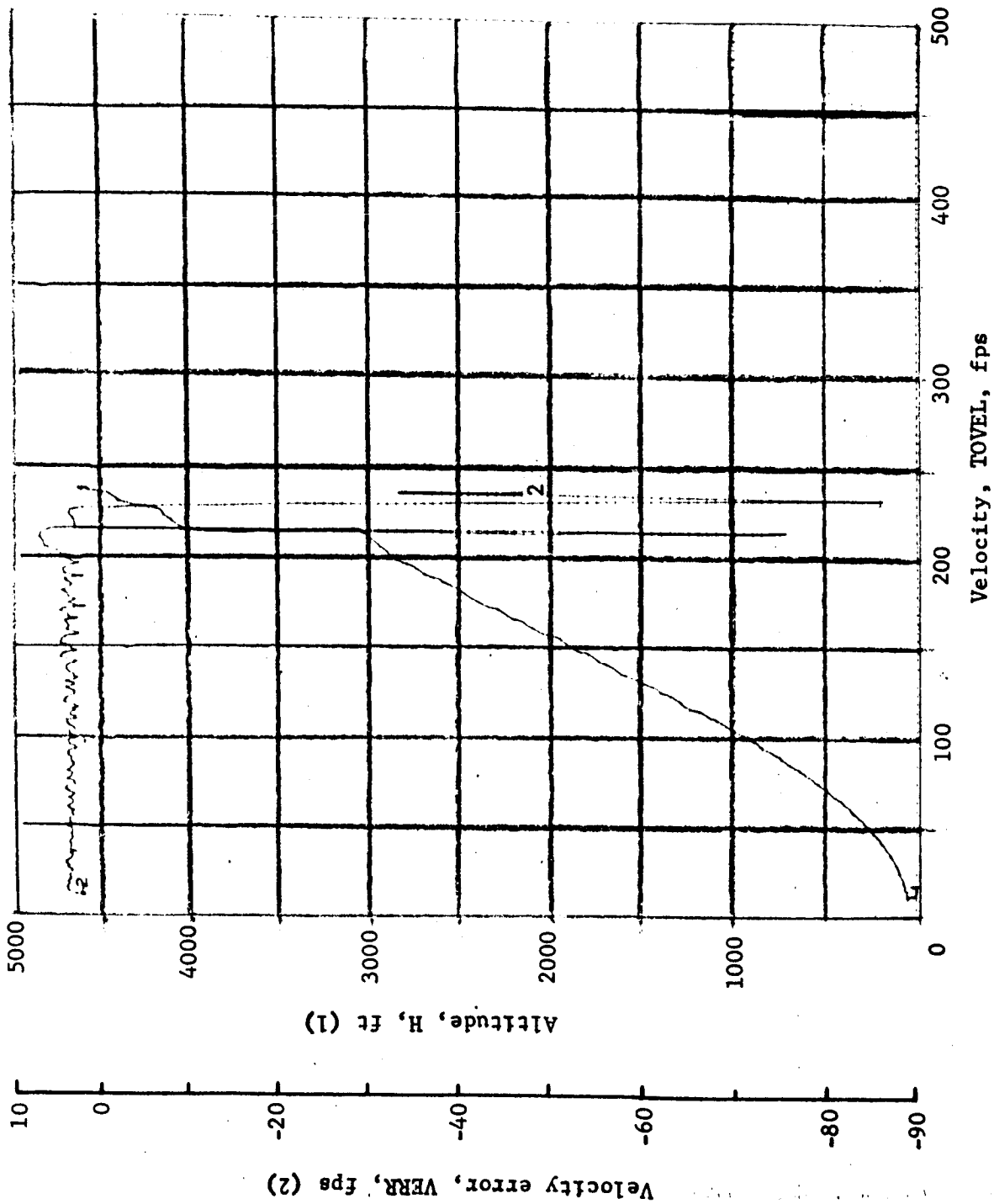


Figure 2. - Soft Lander, Run 6-14

APPENDIX B

TABLE B7.- RUN 7, AUTONOMOUS/MODIFIED LM/RANGE VELOCITY CONTOUR/27° UPSLOPE

Flight condition	Altitude ft	Velocity, fps		Pitch angle, deg	Pitch rate, deg/sec	Time, sec	Fuel used, lb	Beams unlocked	Time to reacquire, sec
		Roll axis	Cross axis						
Initial	4600	165	170	-90	0	0	0	----	----
Mid-pitchup	4296	219.8	-83.9	-65.3	30.7	1.2	2.8	1, 2	----
Max. pitchup	3999	229.4	19.2	-42	-3.6	2.4	5.7	1, 2	2.9
Thrust aligned	3703	219.9	7.1	-47.6	-2.6	3.6	9.5	----	----
Encounter contour	3850.1	228.6	9.4	-45.8	-4.7	3	6.9	1, 2	----
Constant vel	49.35	12.4	-.1	-89.5	-.1	37.6	115.1	----	----
Cutoff eng	8.5	12.3	.03	-90.7	.25	40.9	122	----	----
Land	.94	18.4	.05	-90.2	.25	41.4	122	----	----
Remarks:									

APPENDIX B

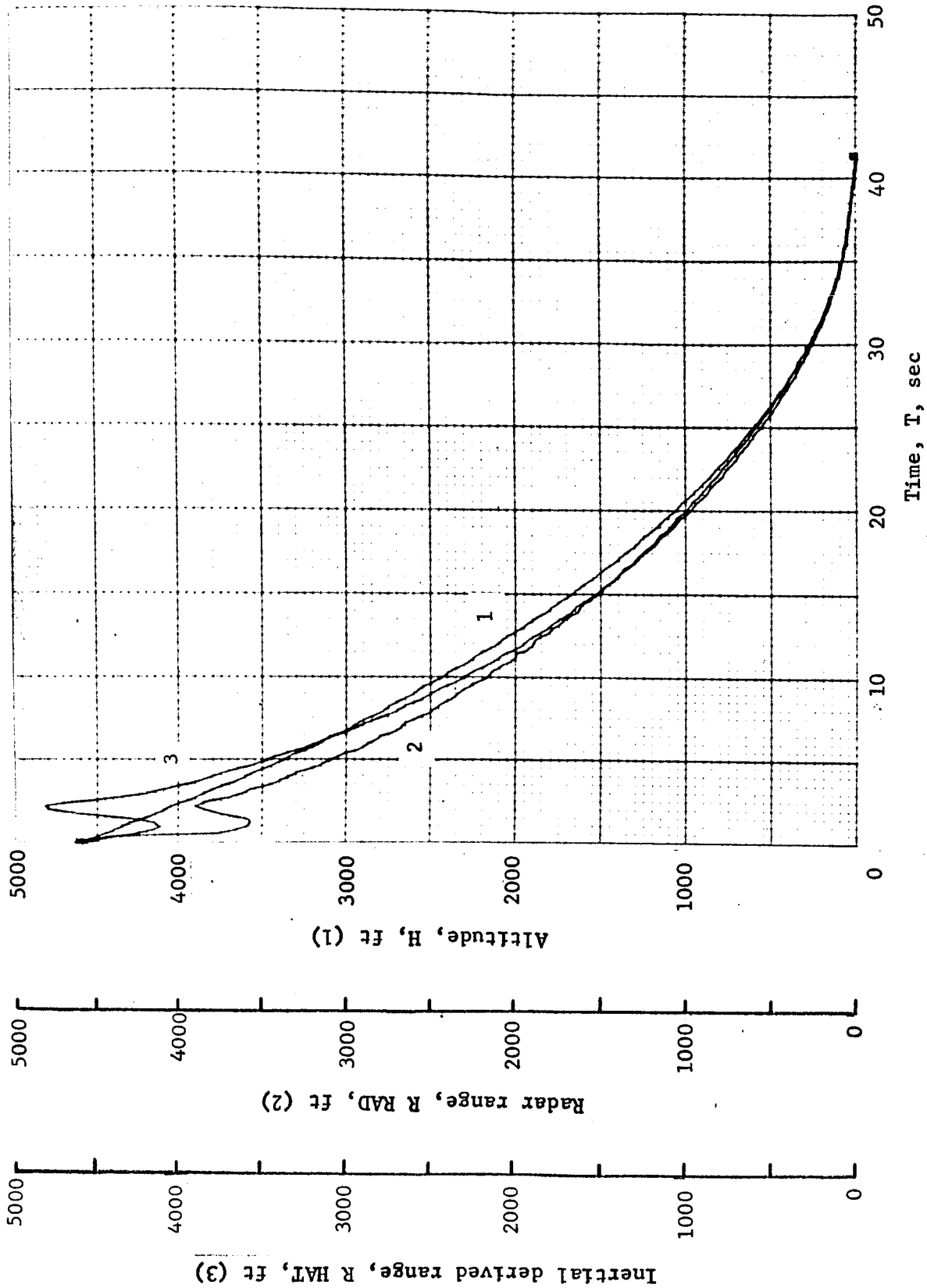


Figure B85.- Soft Lander, Run 7-1

APPENDIX B

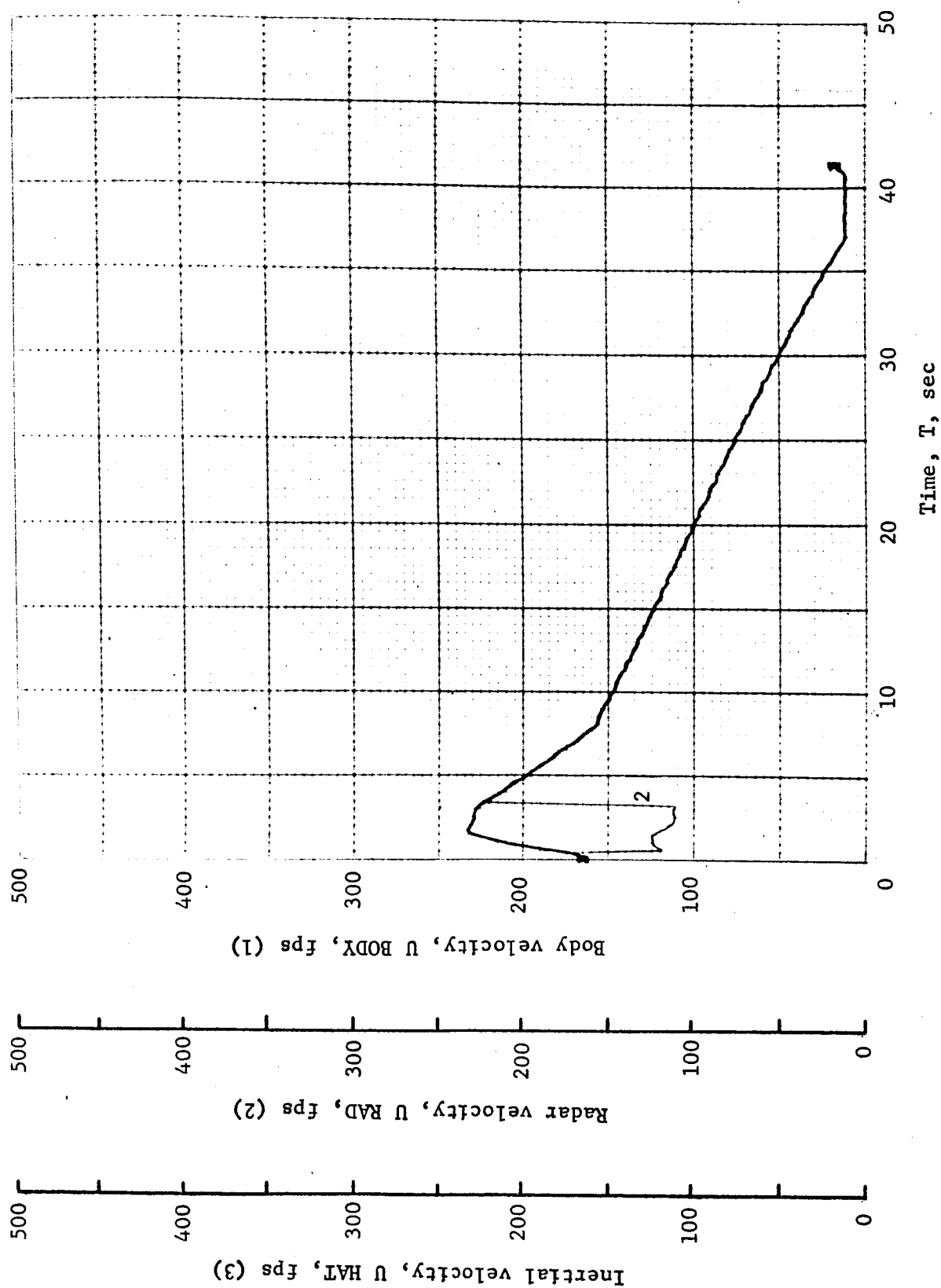


Figure B86.- Soft Lander, Run 7-2

APPENDIX B

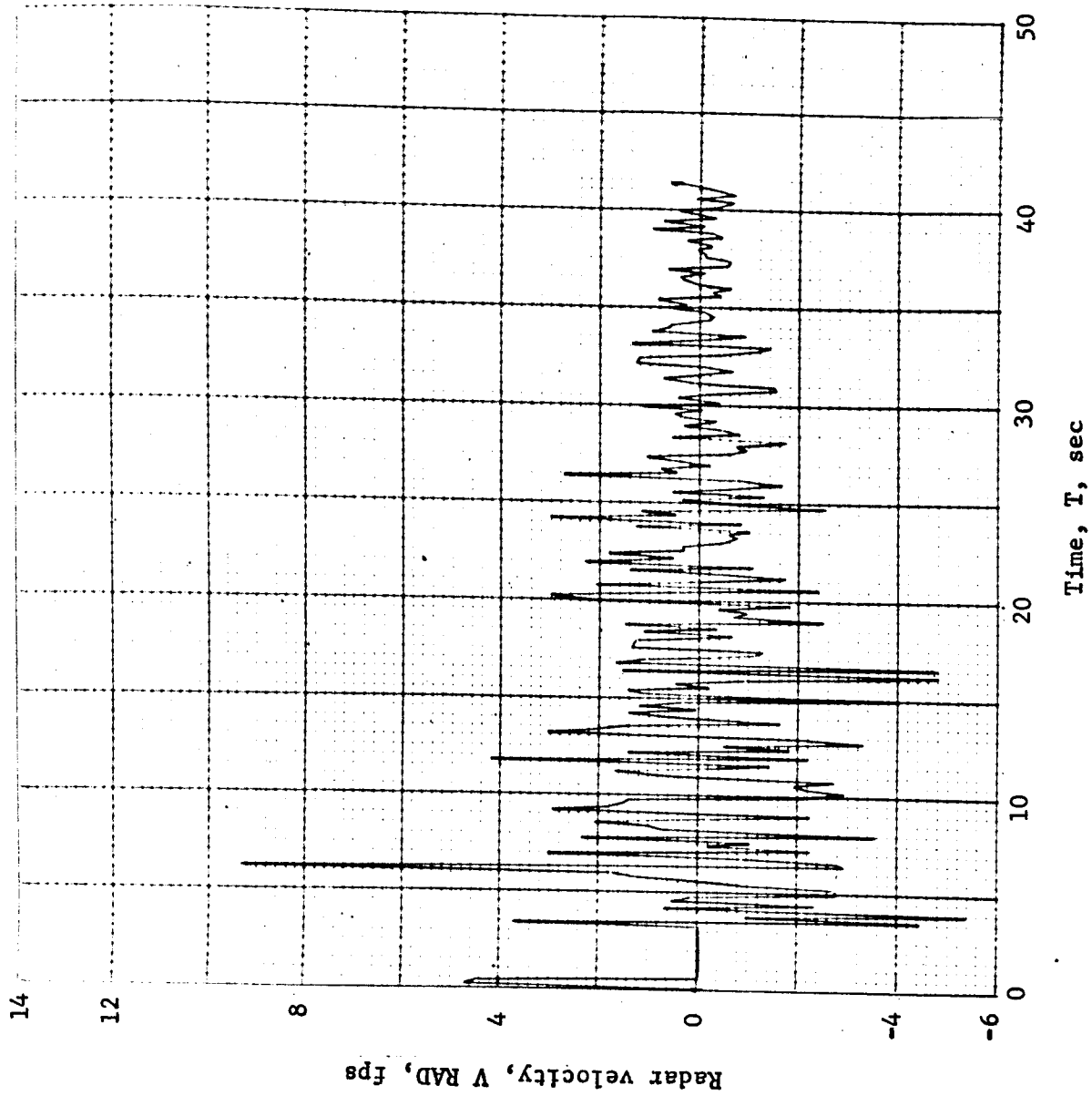


Figure B87.- Soft Lander, Run 7-3

APPENDIX B

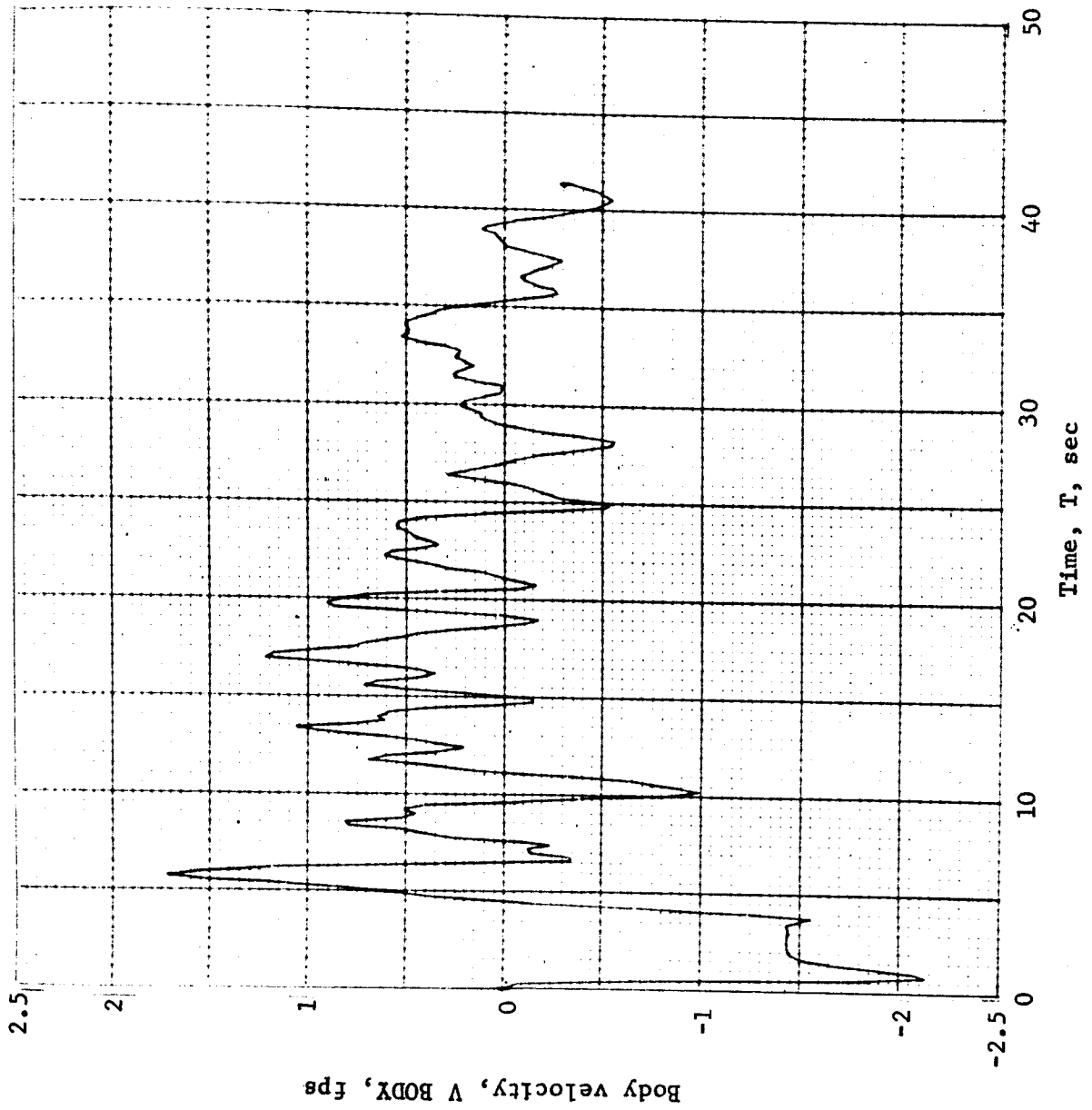


Figure B88.- Soft Lander, Run 7-4

APPENDIX B

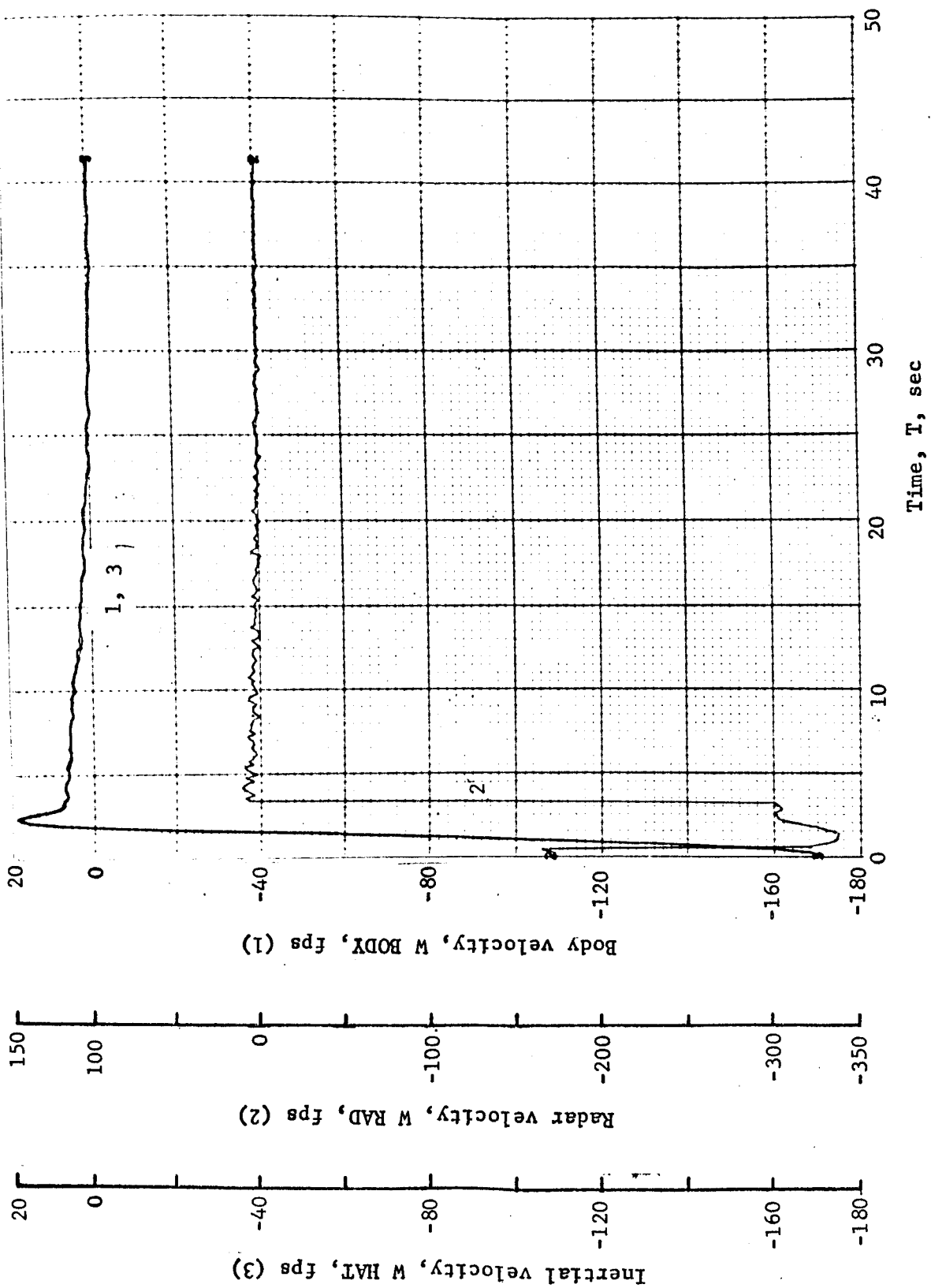


Figure B89.- Soft Lander, Run 7-5

APPENDIX B

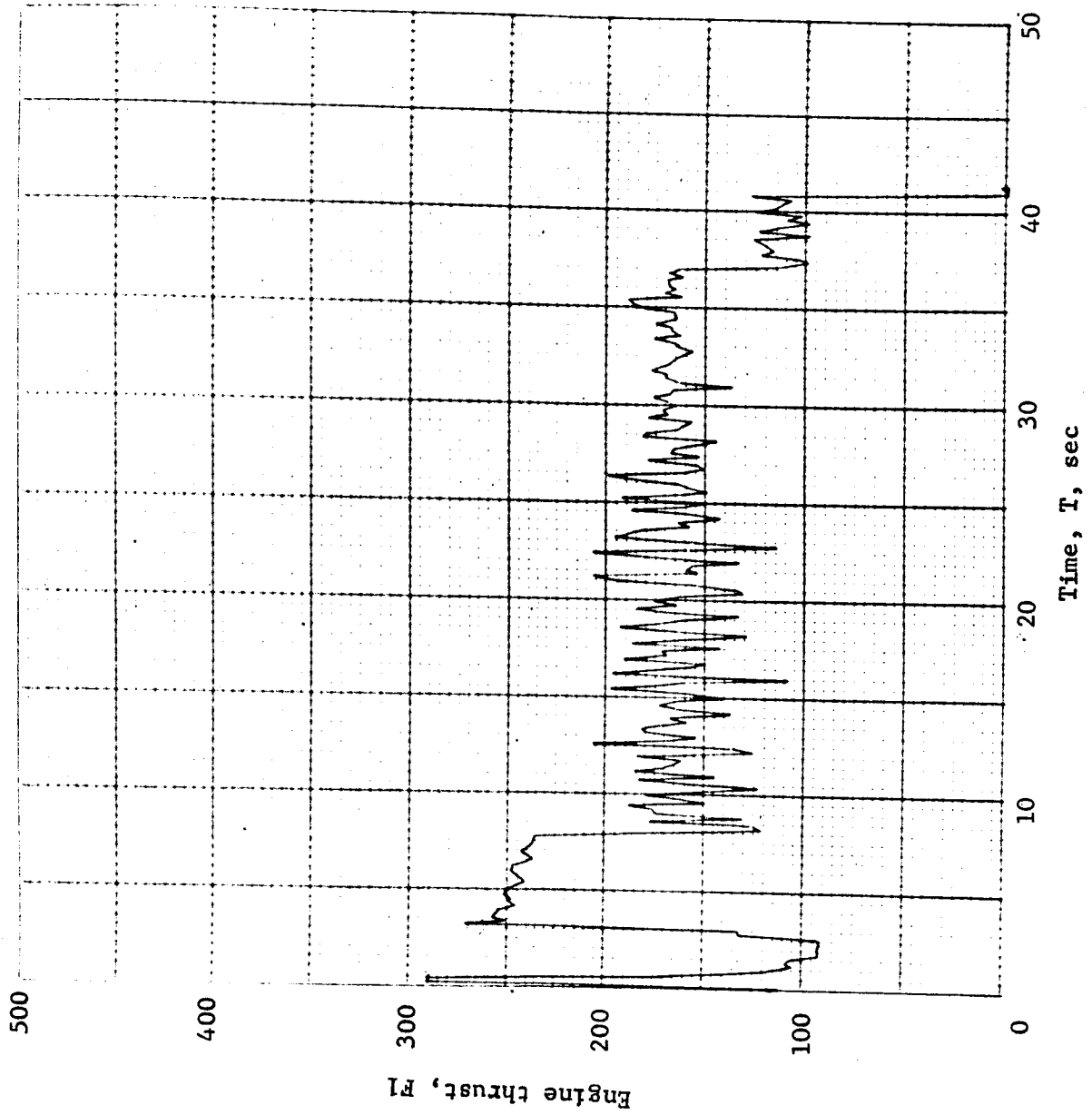


Figure B90.- Soft Lander, Run 7-6

APPENDIX B

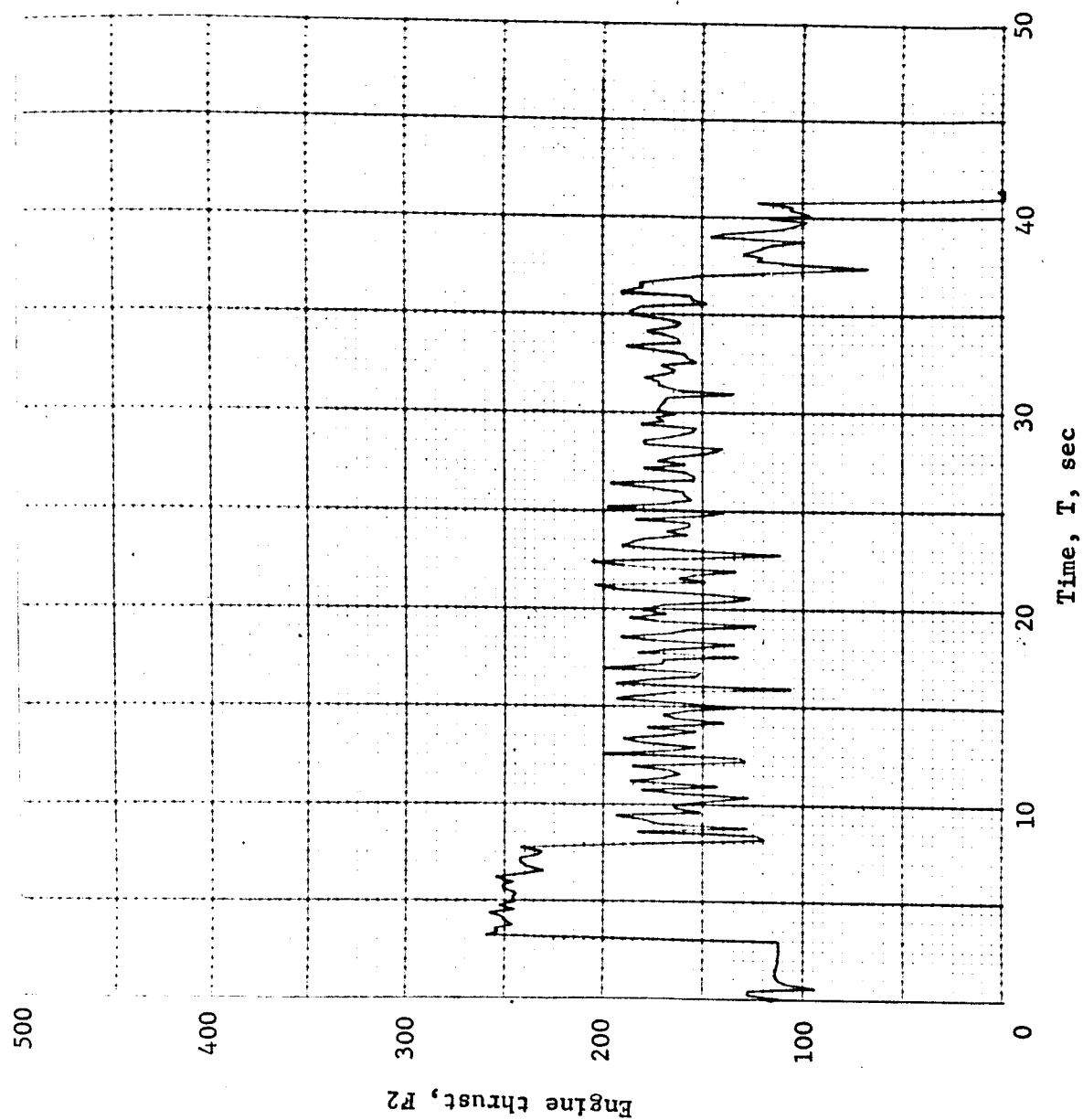


Figure B91.- Soft Lander, Run 7-7

APPENDIX B

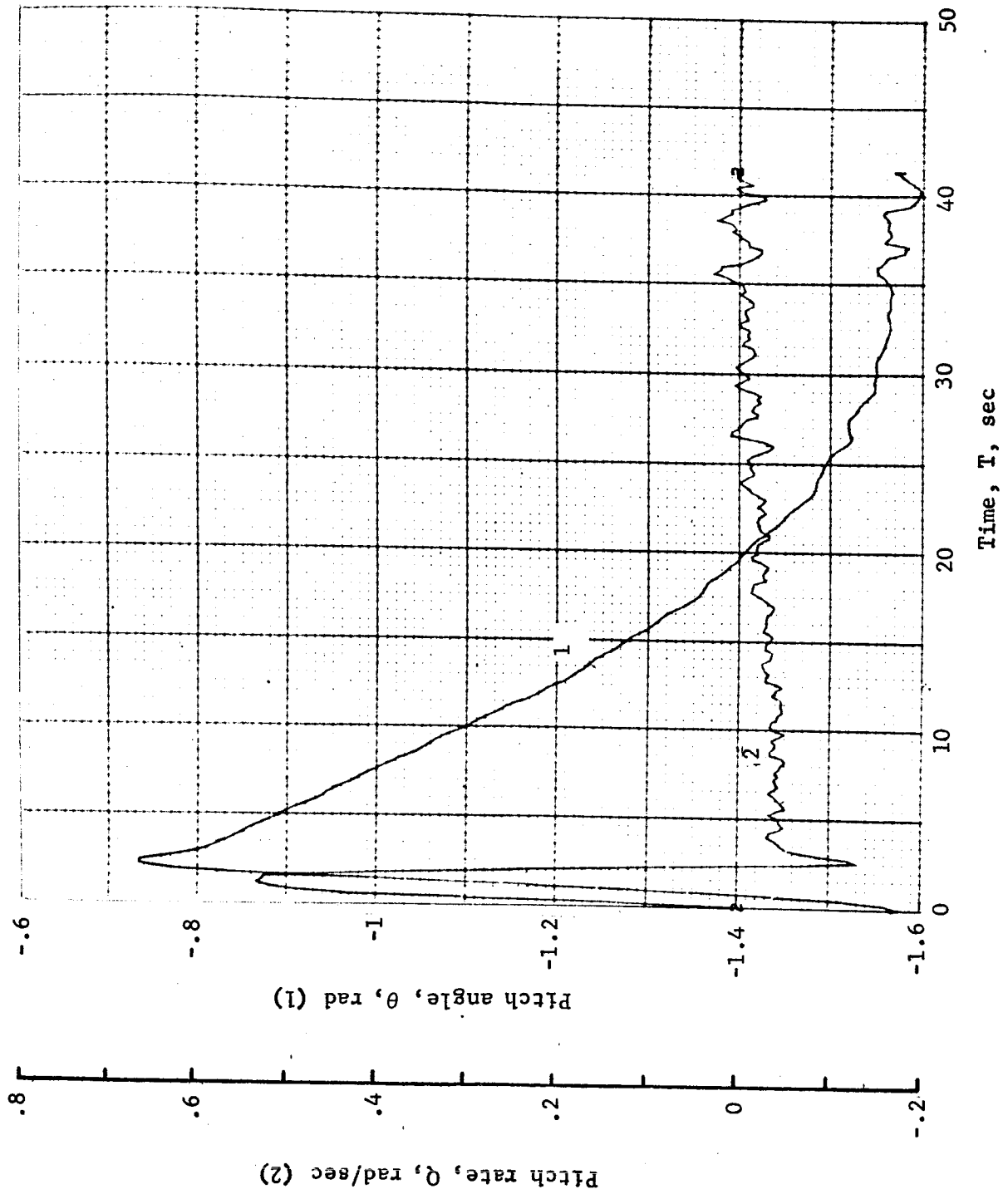


Figure B92.- Soft Lander, Run 7-8

APPENDIX B

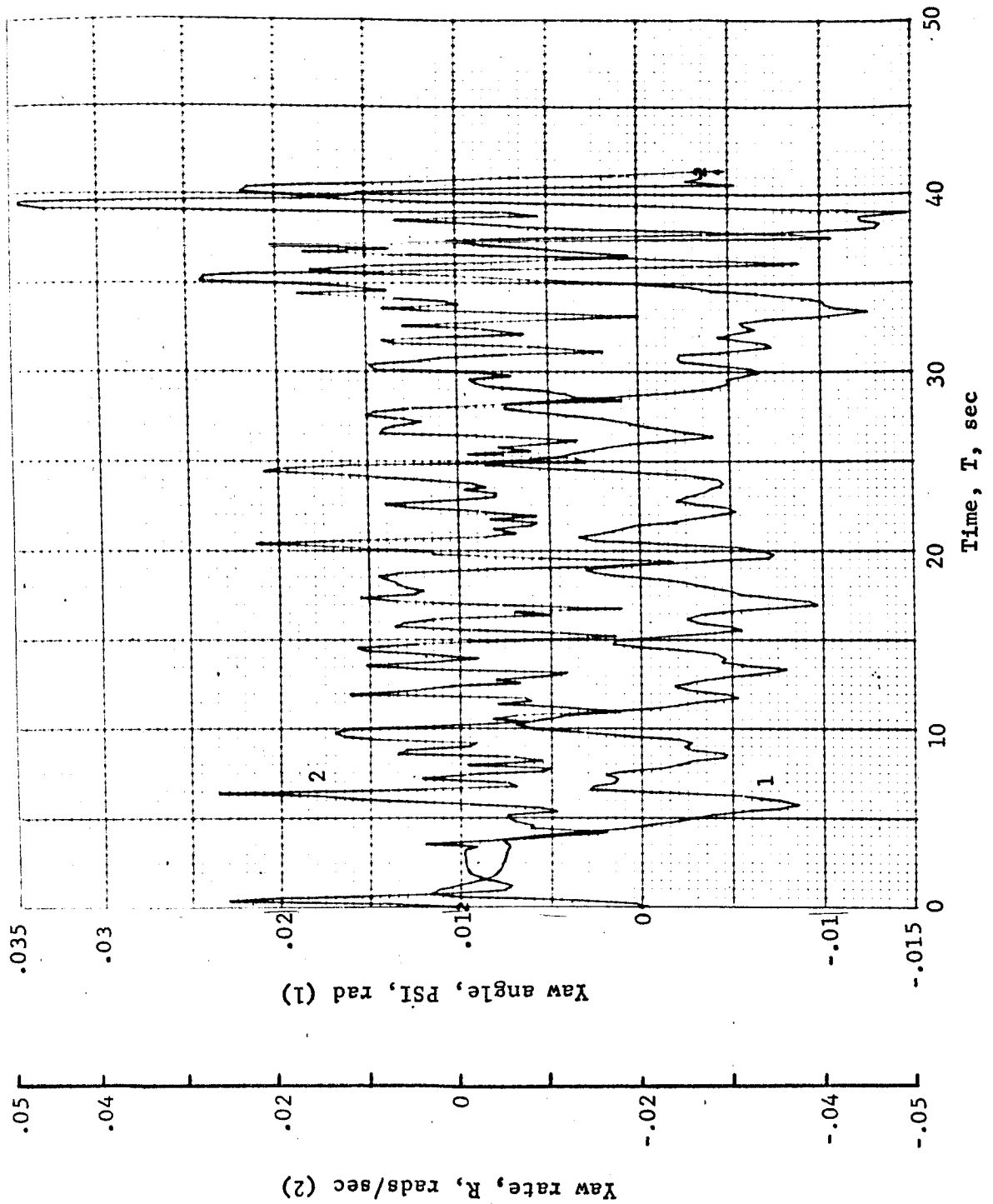


Figure B93.- Soft Lander, Run 7-9

APPENDIX B

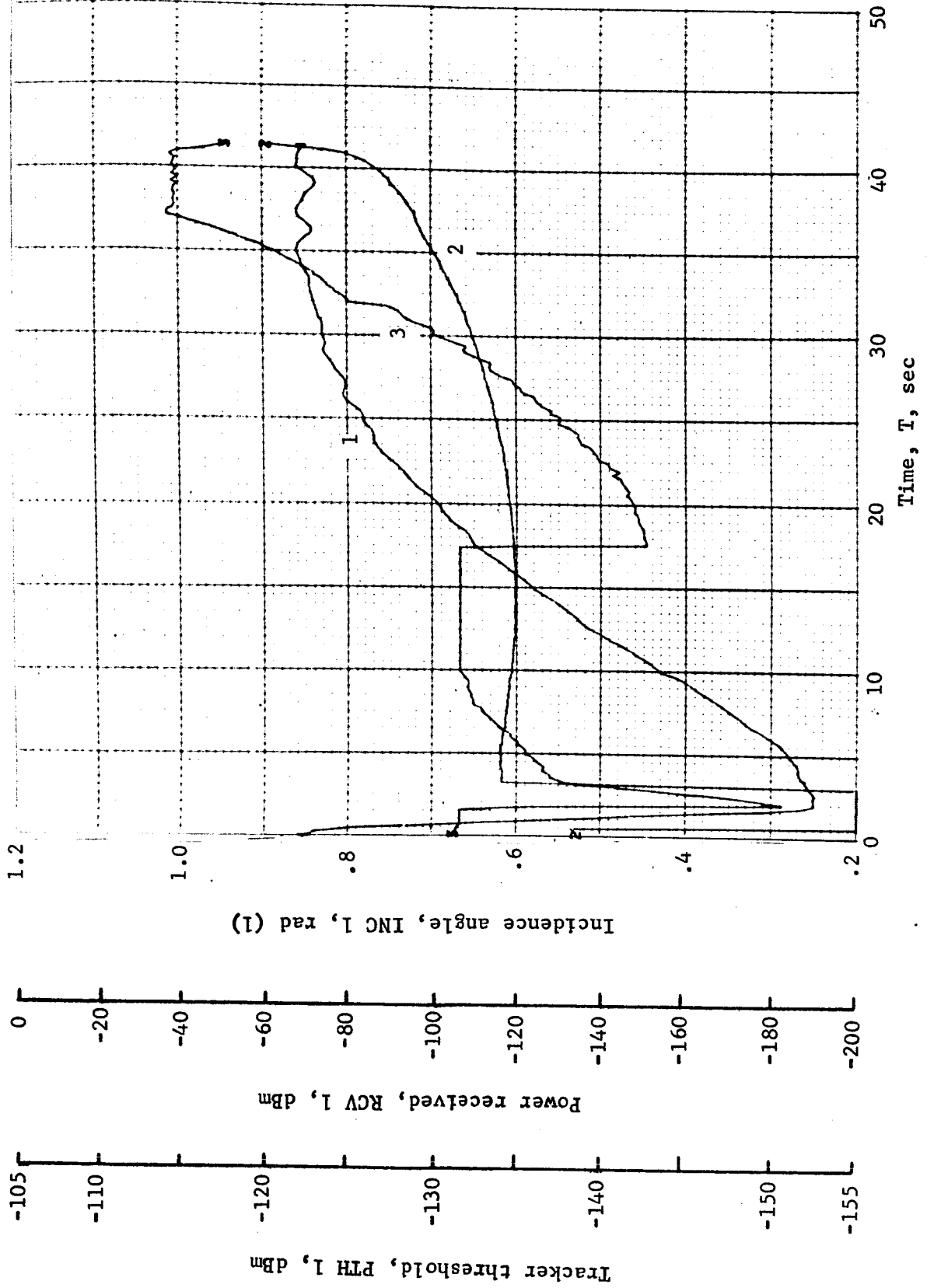


Figure B94.- Soft Lander, Run 7-10

APPENDIX B

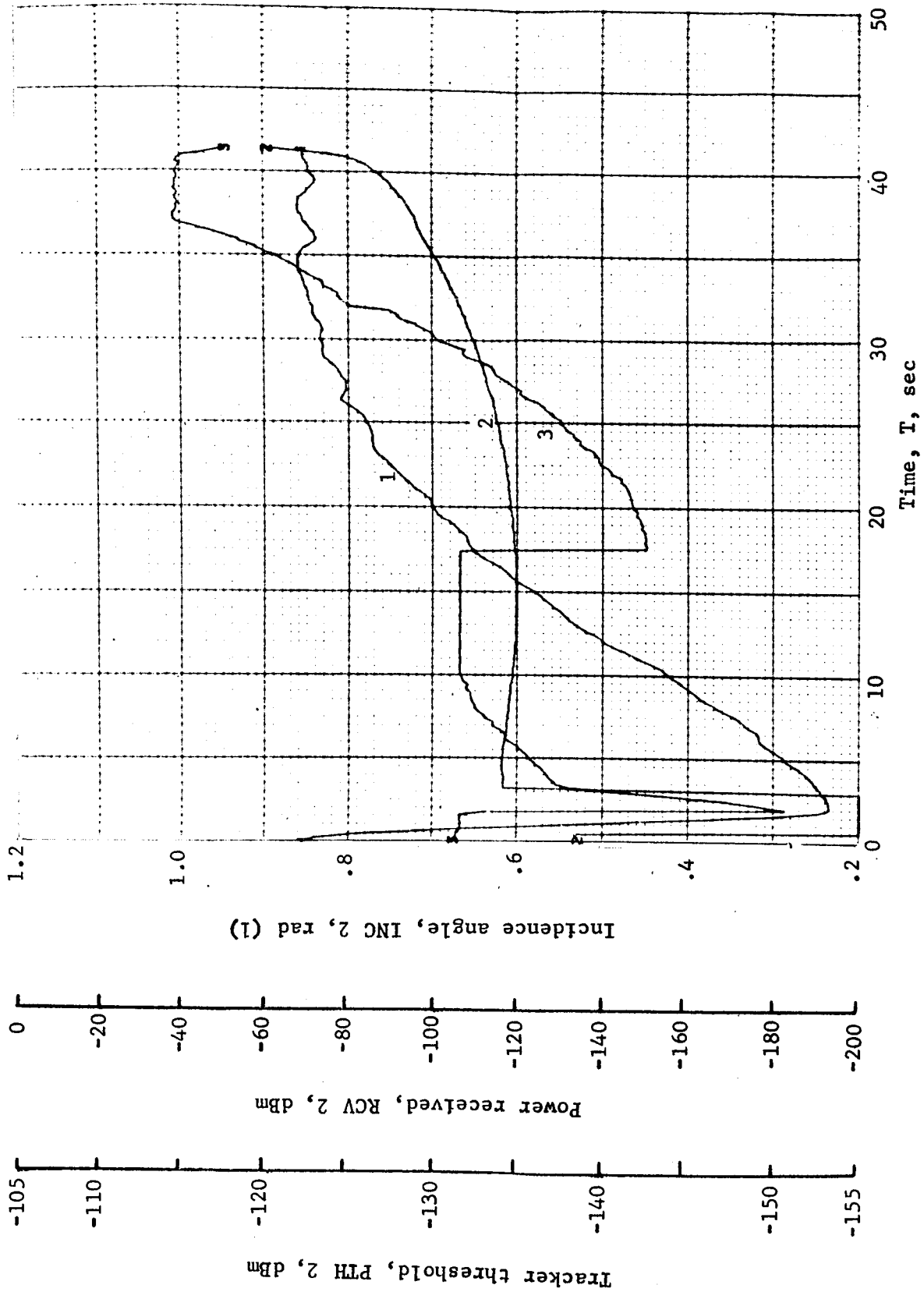


Figure B95.- Soft Lander, Run 7-11

APPENDIX B

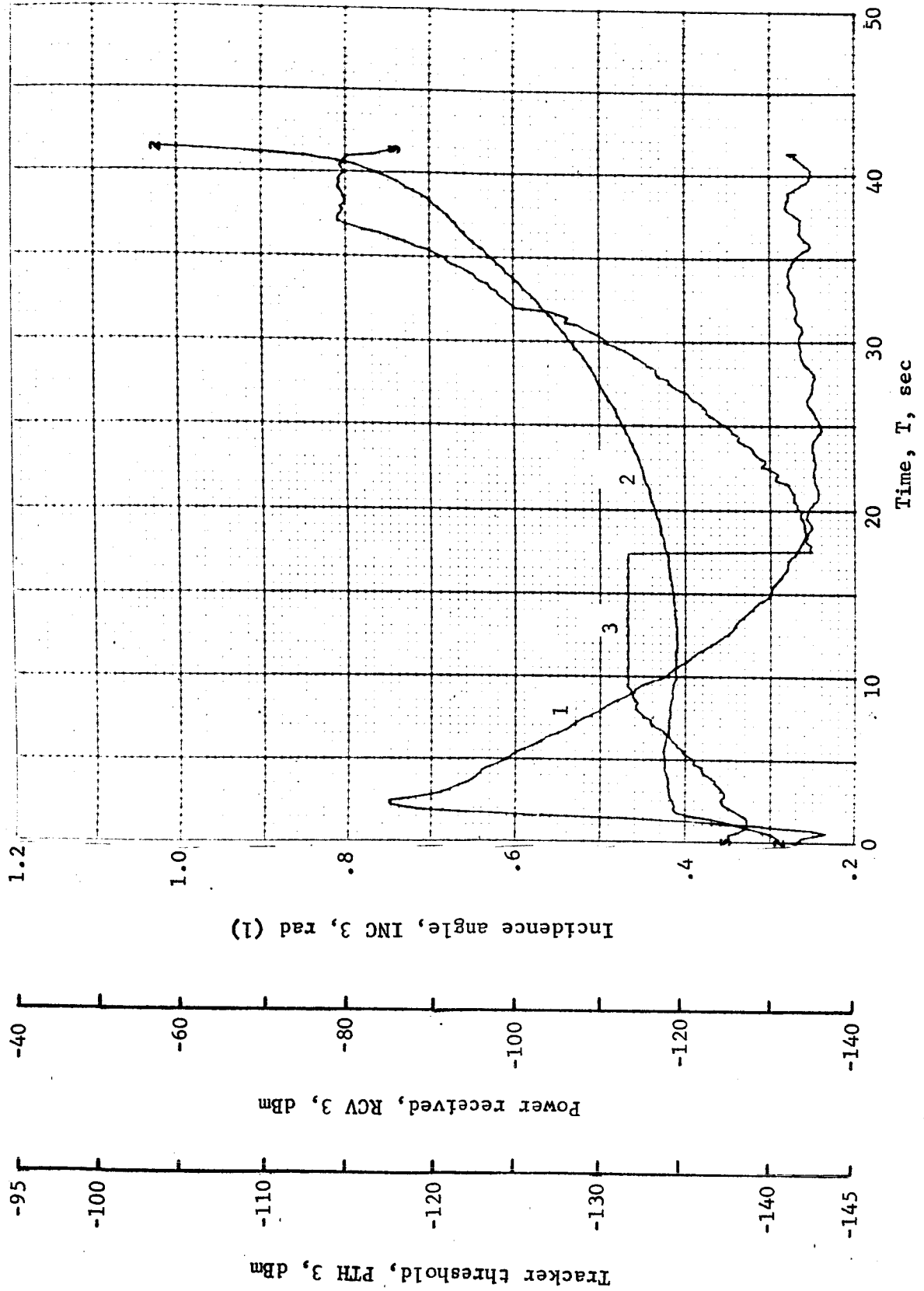


Figure B96.- Soft Lander, Run 7-12

APPENDIX B

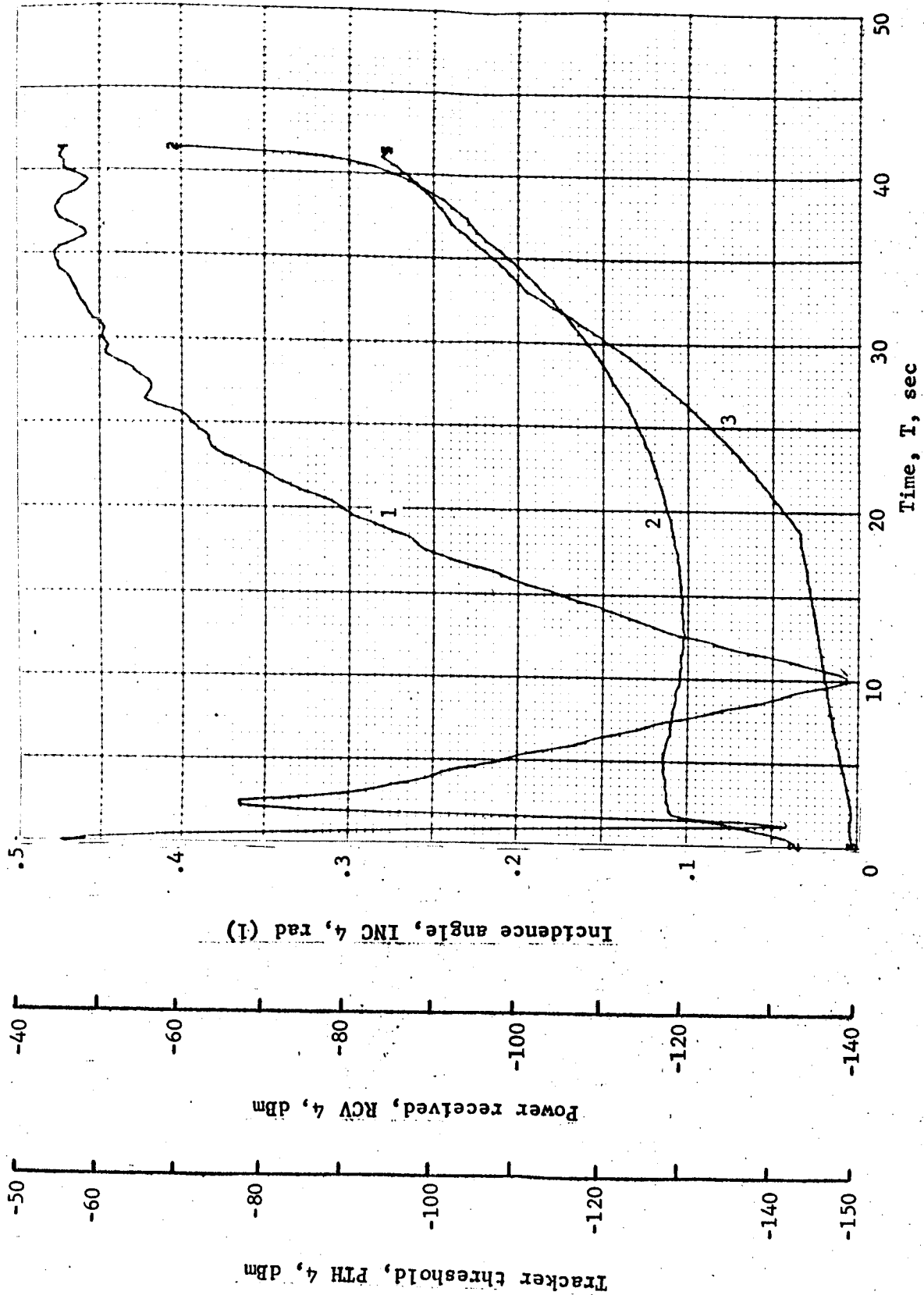


Figure B97.- Soft Lander, Run 7-13

APPENDIX B

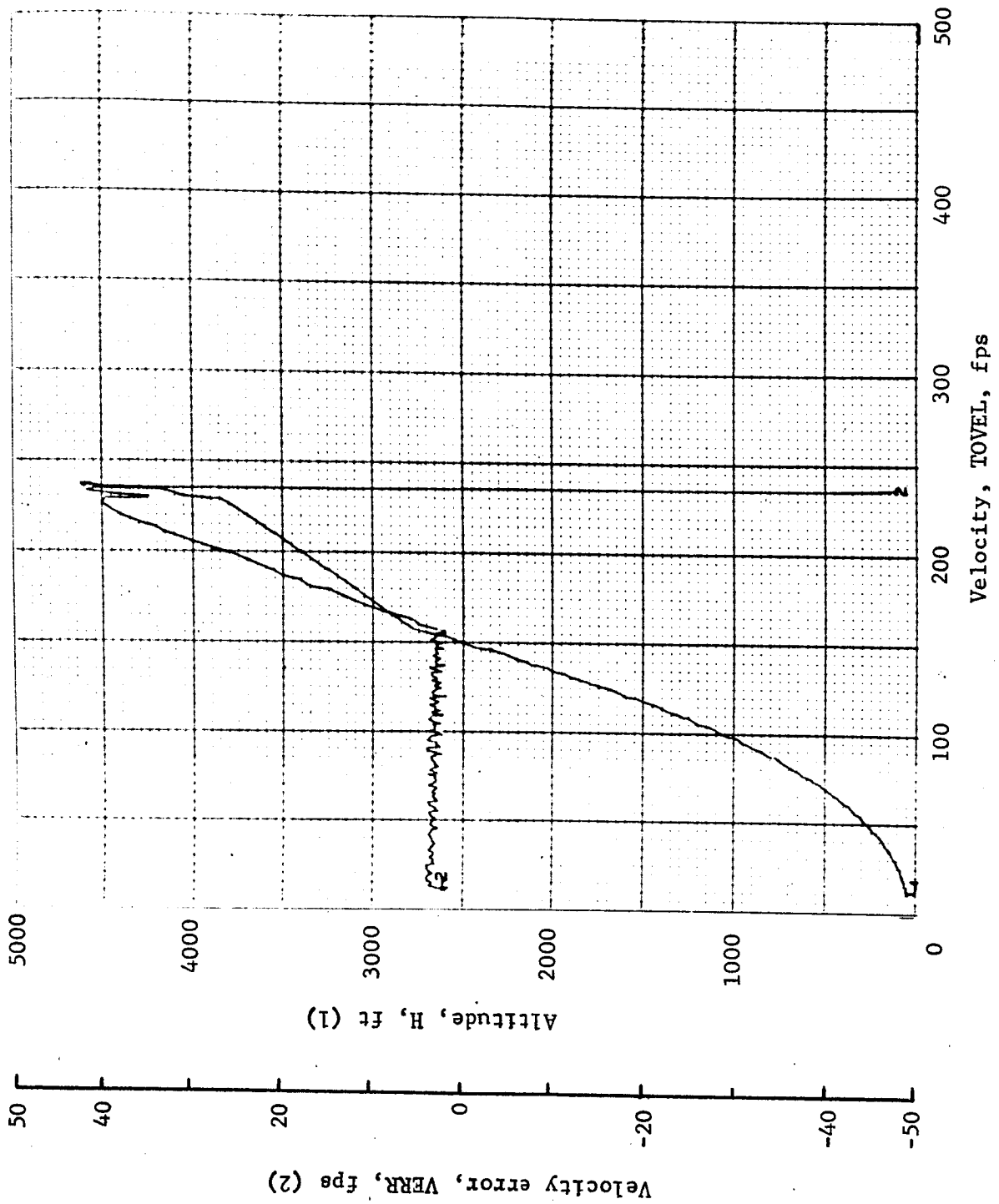


Figure B98.- Soft Lander, Run 7-14

APPENDIX B

TABLE B8.- RUN 8, AUTONOMOUS/MODIFIED LM/RANGE VELOCITY/O SLOPE/O DOPPLER

Flight condition	Altitude, ft	Velocity, fps		Pitch angle, deg	Pitch rate, deg/sec	Time, sec	Fuel used, lb	Beams unlocked	Time to reacquire, sec
		Roll axis	Cross axis						
Initial	4765	165	263	-102	0	0	0	1, 2 at 0.5	----
Mid-pitchup	4169	267.8	-161.9	-63.5	31.4	2.6	5.6	----	1, 2 at 2.6
Max. pitchup	3895	299.2	53.3	-25	-2.2	4.2	9.4	3 at 4.2	----
Thrust aligned	3135.8	233.0	9.69	-43.5	-3.4	8.6	28.4	----	3 at 1.6
Encounter contour	4269	201	241	-80	30	2	4.9	----	----
Constant vel	48.3	12.3	.14	-90.6	1.4	41.6	132	----	----
Cutoff eng	8.25	12.4	-.1	-88.5	1.5	44.8	138.4	----	----
Land	.98	18.2	.11	-89.5	.11	45.3	138.4	----	----
Remarks: 0 doppler cases initiate 165-ft higher and delay pitchup for 1 sec.									

APPENDIX B

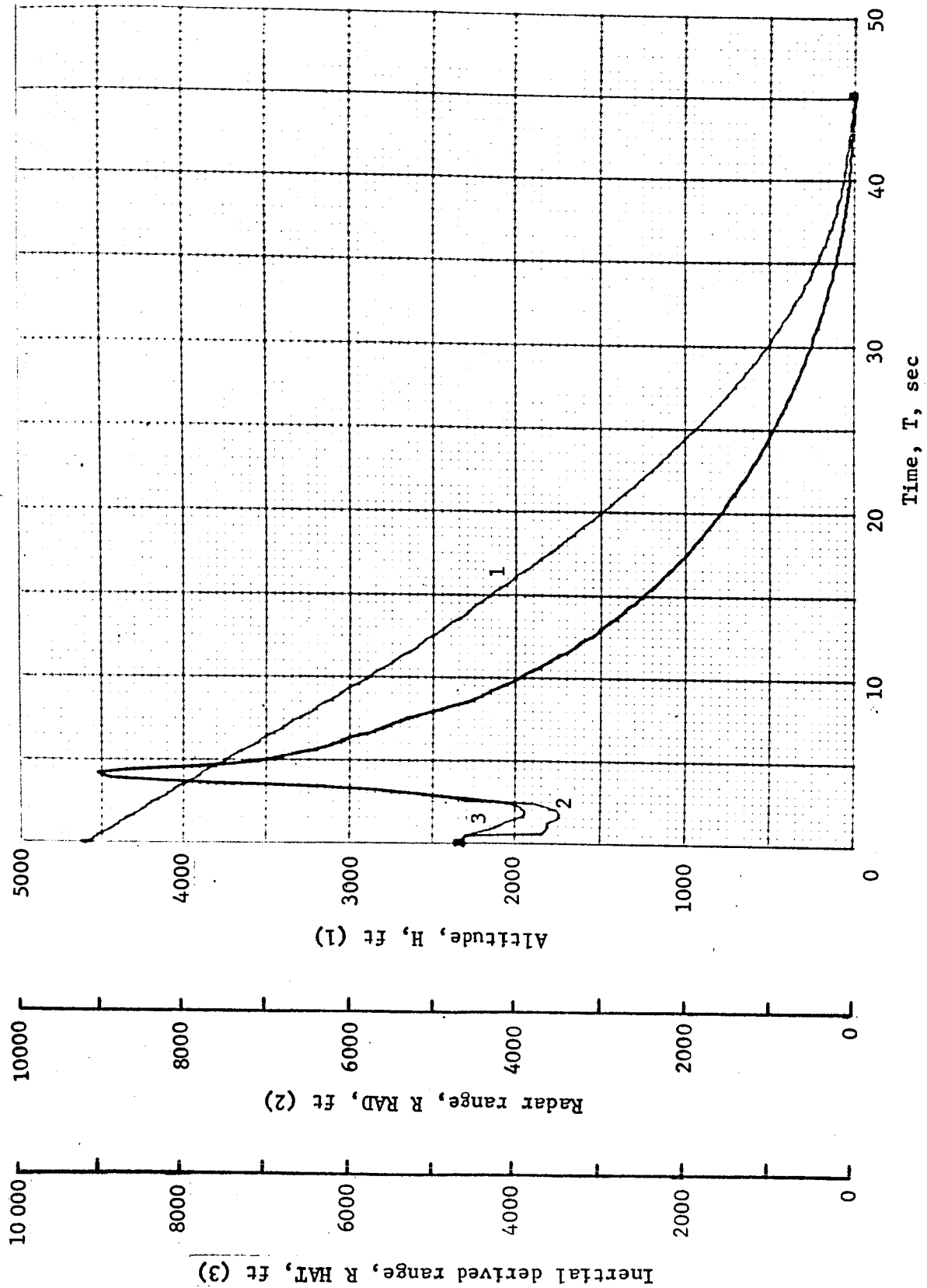


Figure B99.- Soft Lander, Run 8-1

APPENDIX B

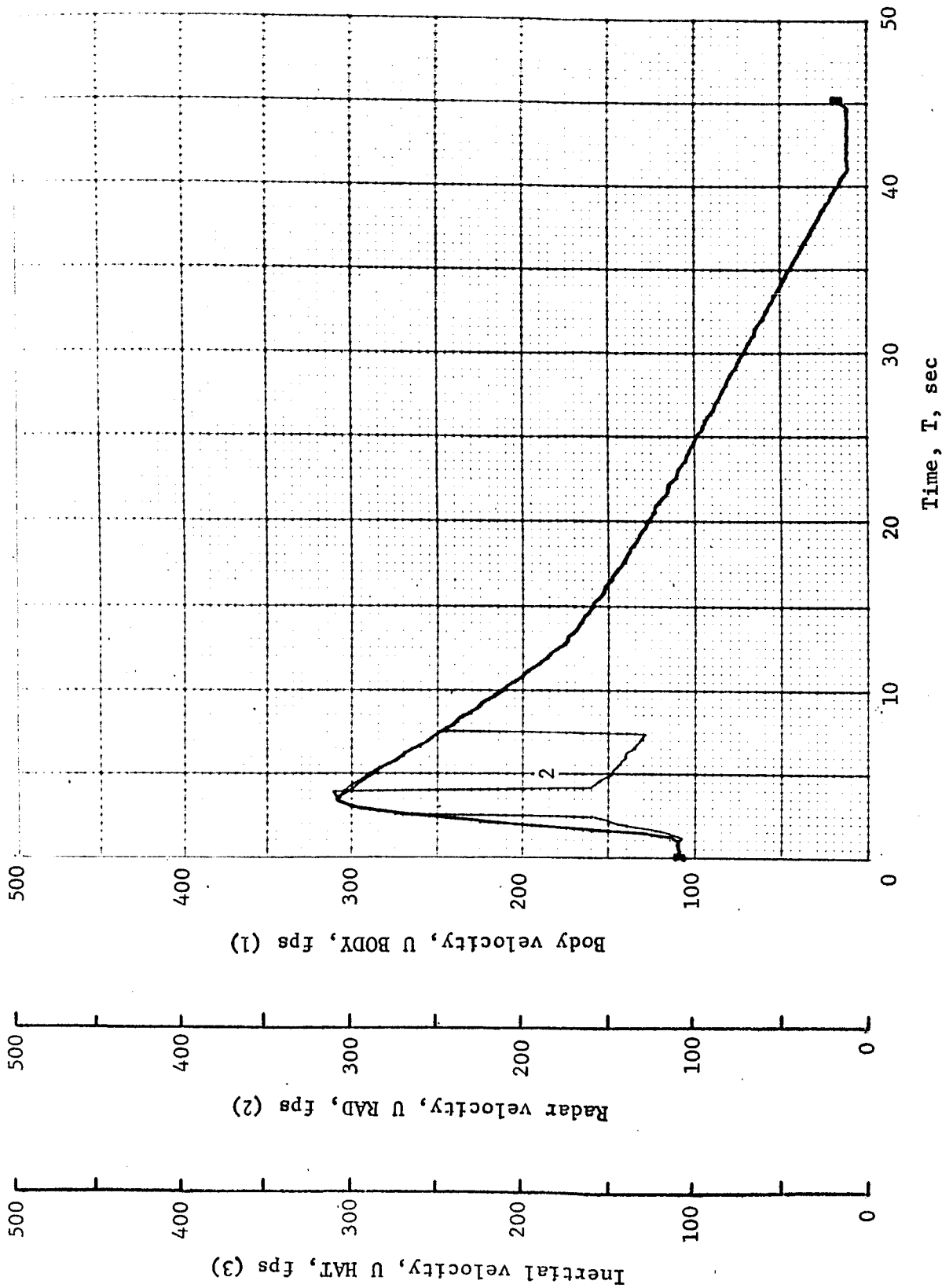


Figure B100.- Soft Lander, Run 8-2

APPENDIX B

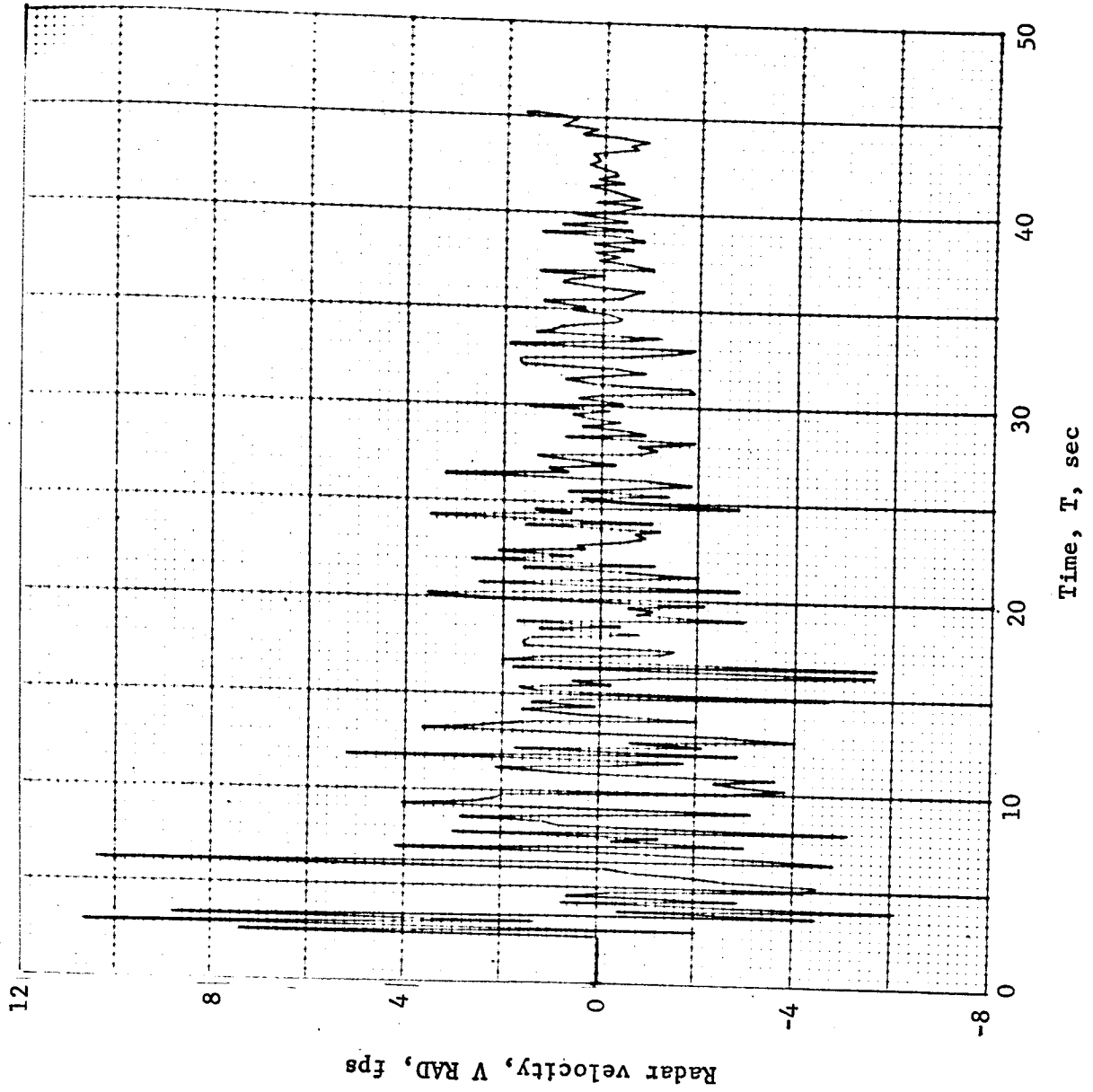


Figure B101.- Soft Lander, Run 8-2

APPENDIX B

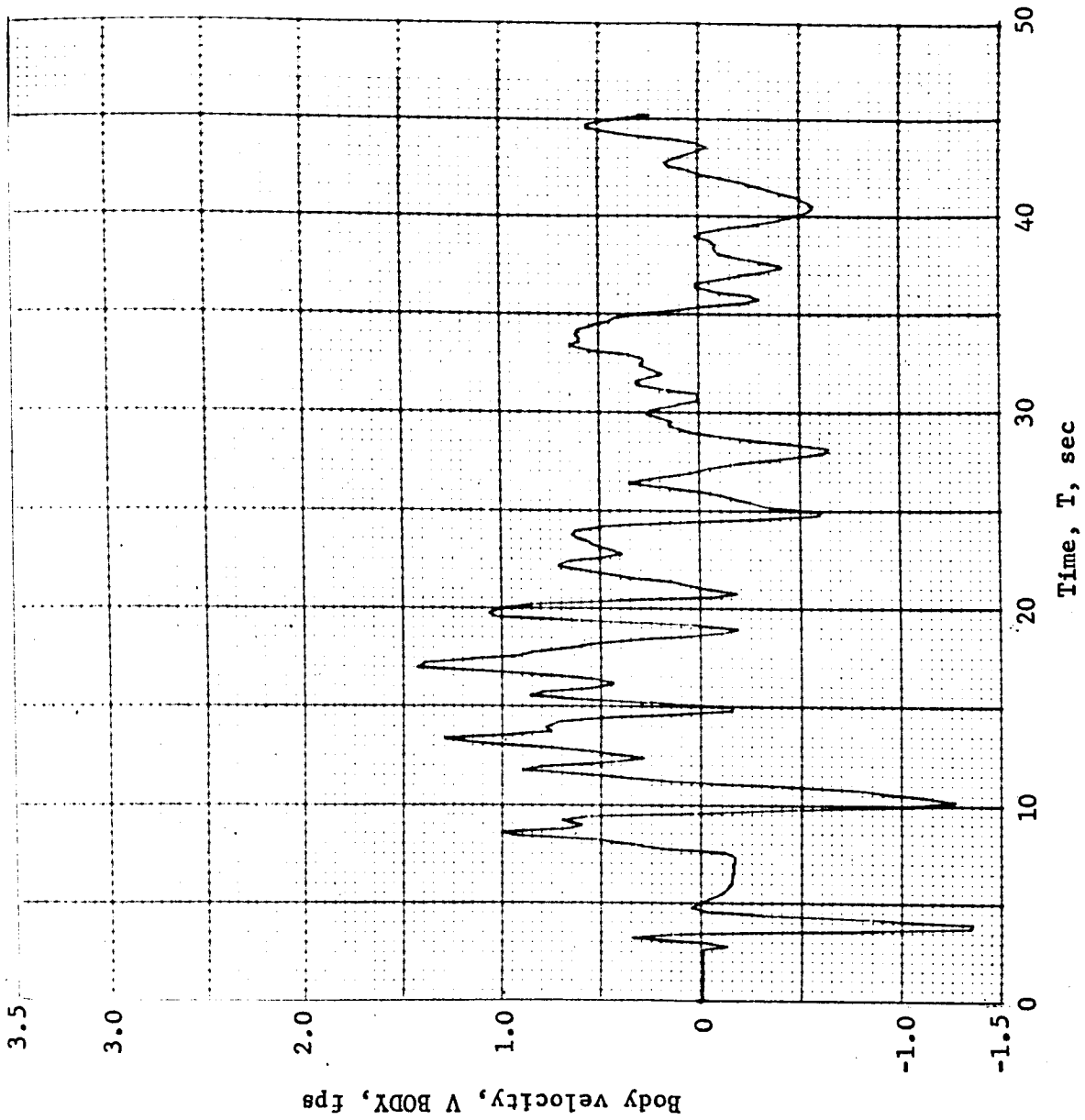


Figure B102.- Soft Lander, Run 8-4

APPENDIX B

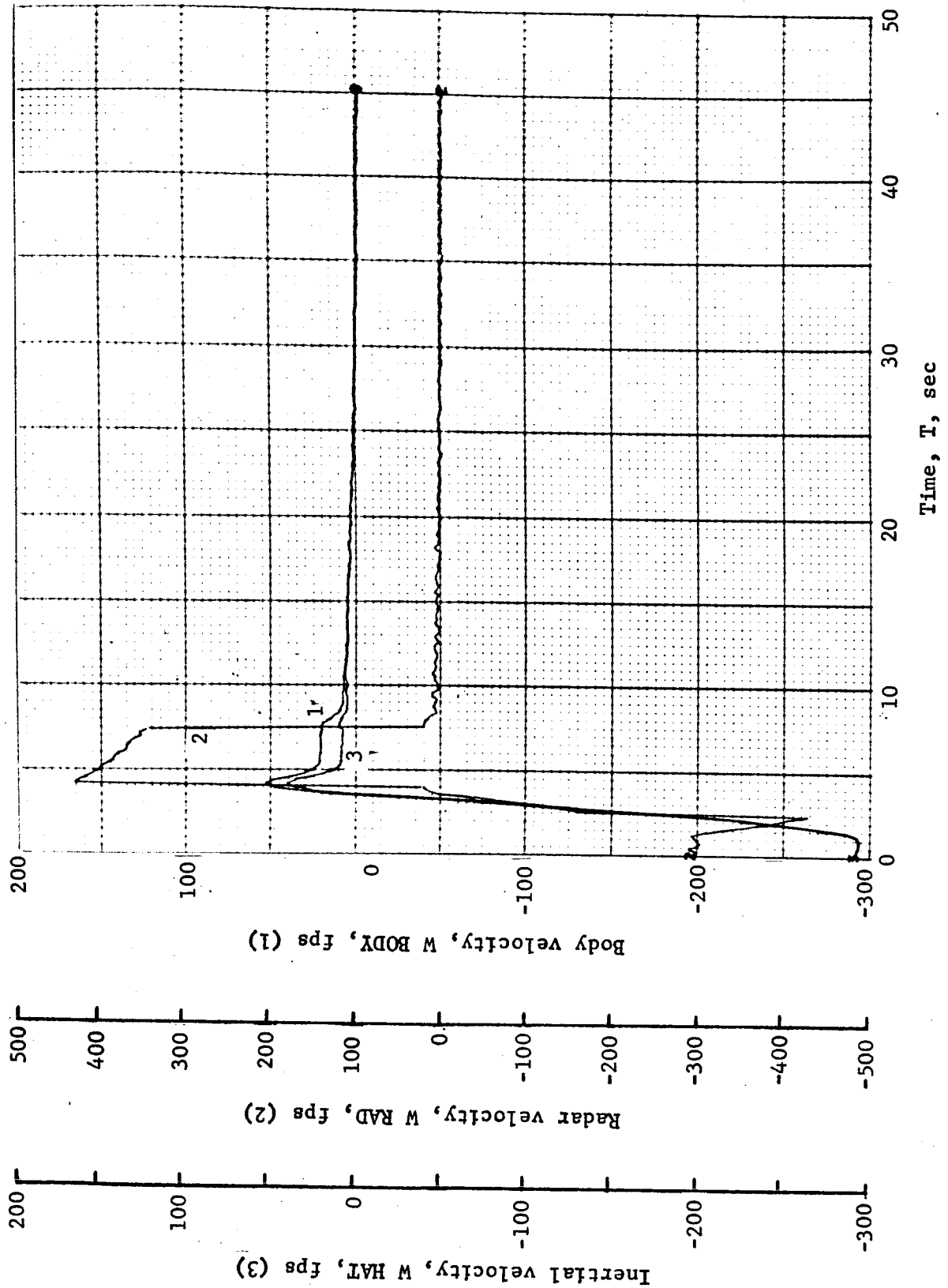


Figure B-103.- Soft Lander, Run 8-5

APPENDIX B

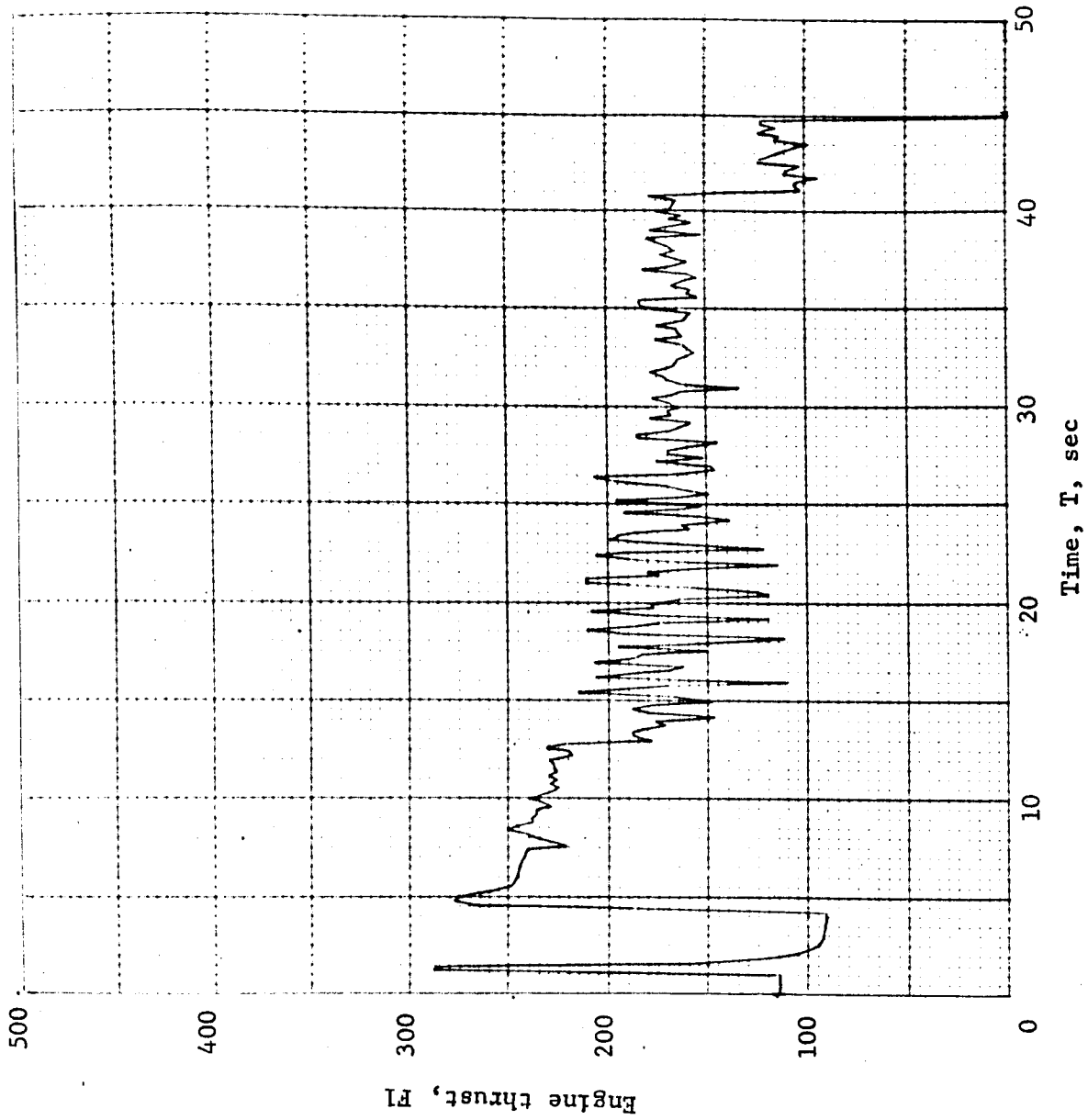


Figure B104.- Soft Lander, Run 8-6

APPENDIX B

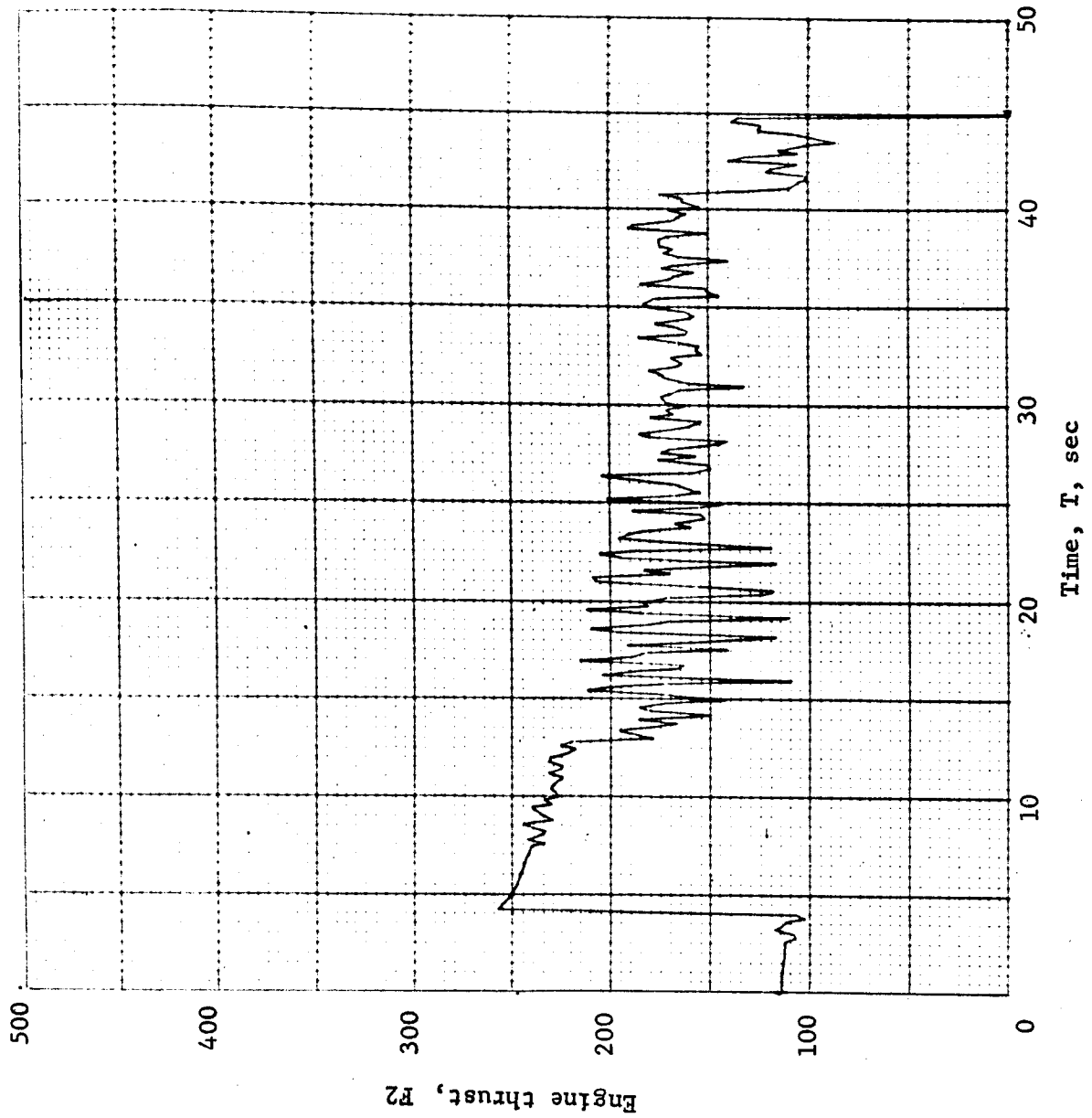


Figure B105.- Soft Lander, Run 8-7

APPENDIX B

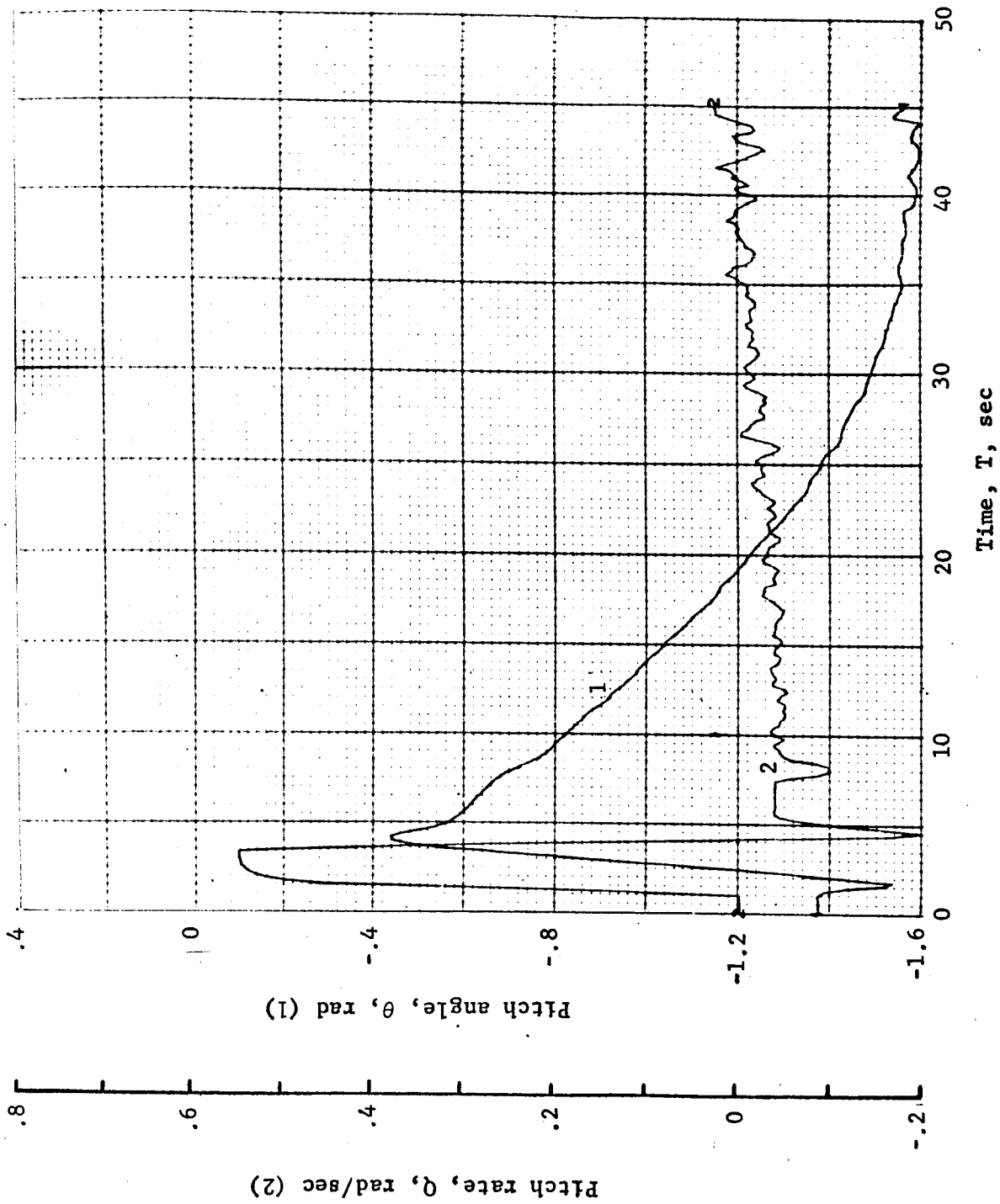


Figure B106.- Soft Lander, Run 8-8

APPENDIX B

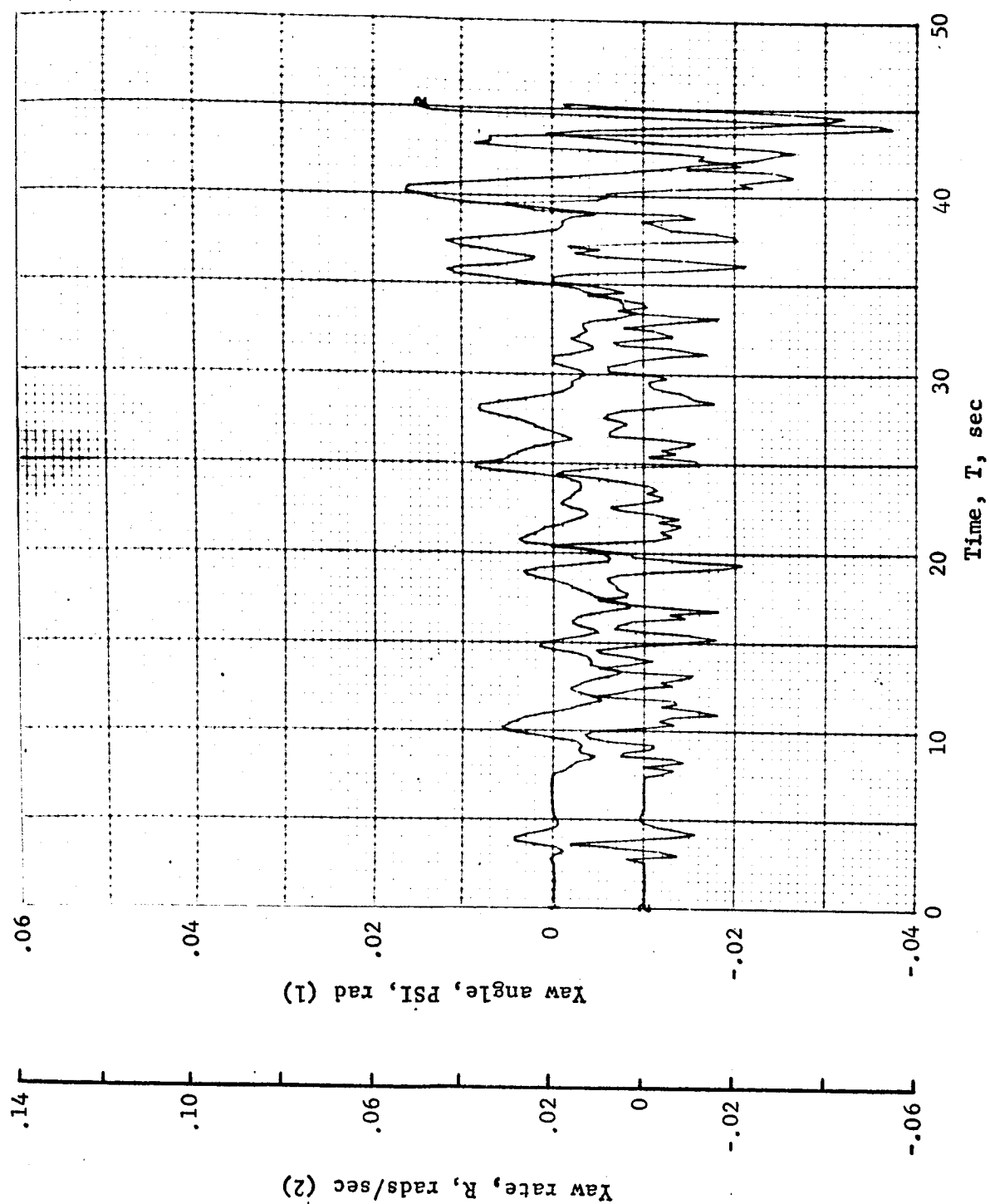


Figure B107.- Soft Lander, Run 8-9

APPENDIX B

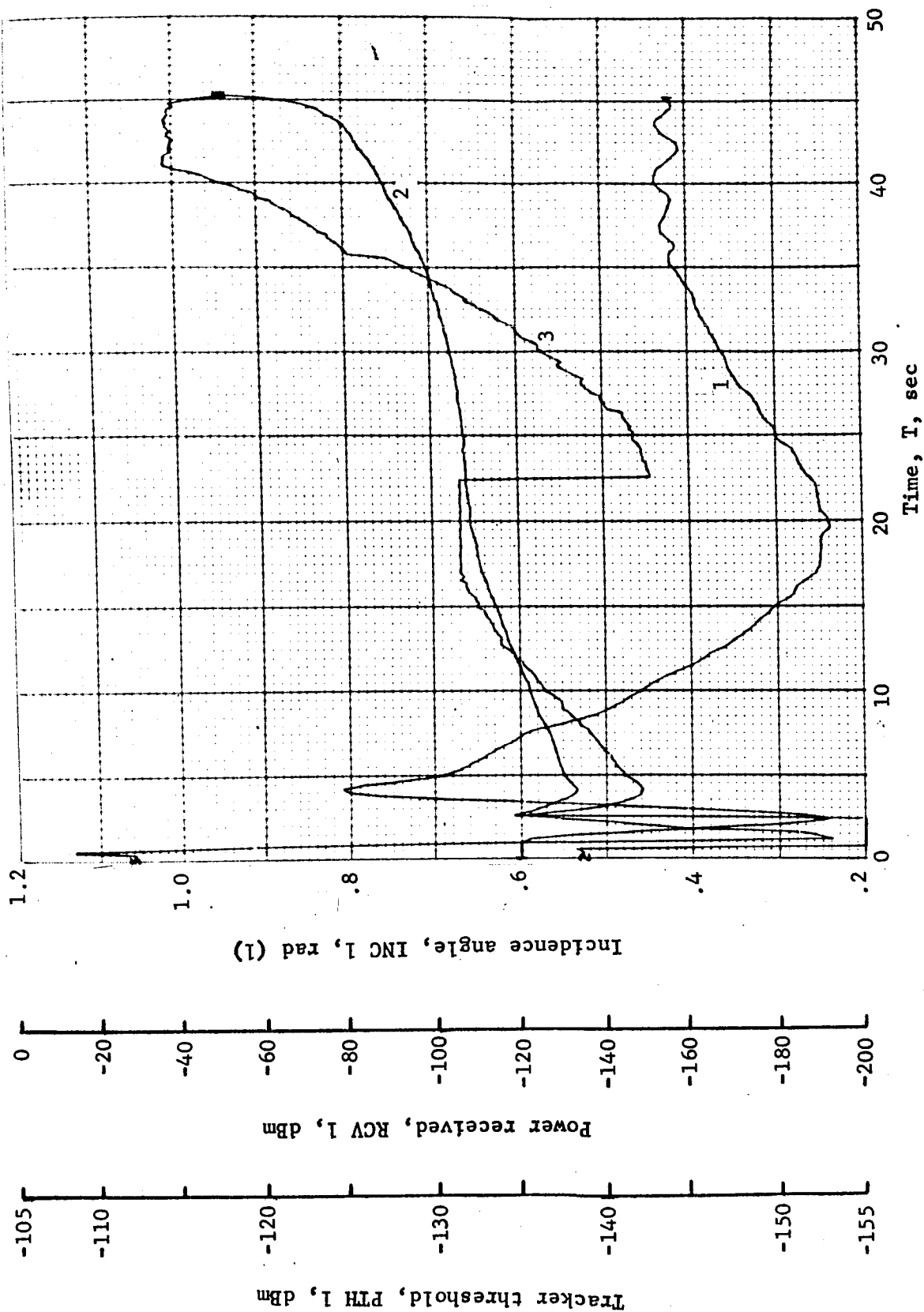


Figure B108.- Soft Lander, Run 8-10

APPENDIX B

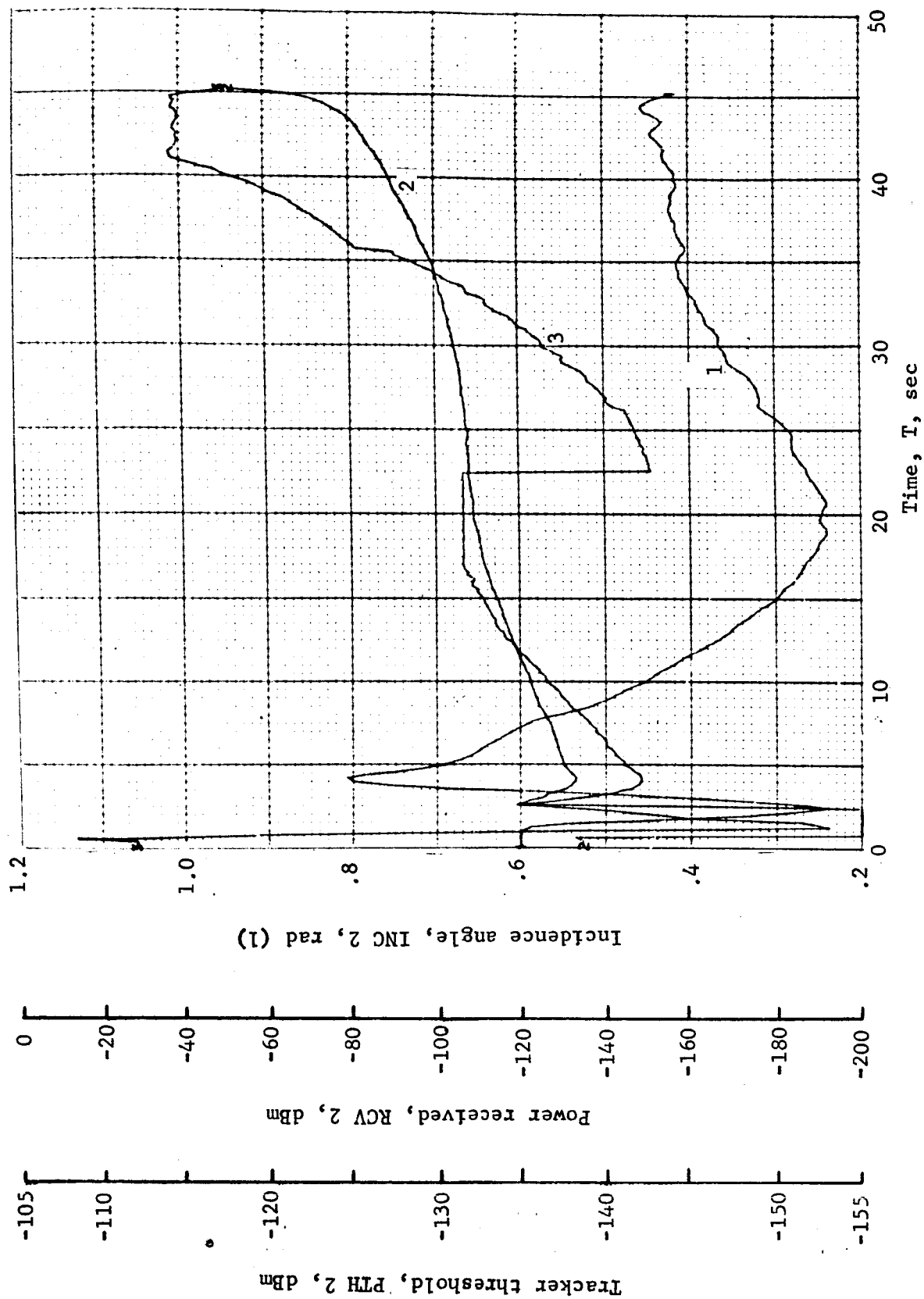


Figure B109.- Soft Lander, Run 8-11

APPENDIX B

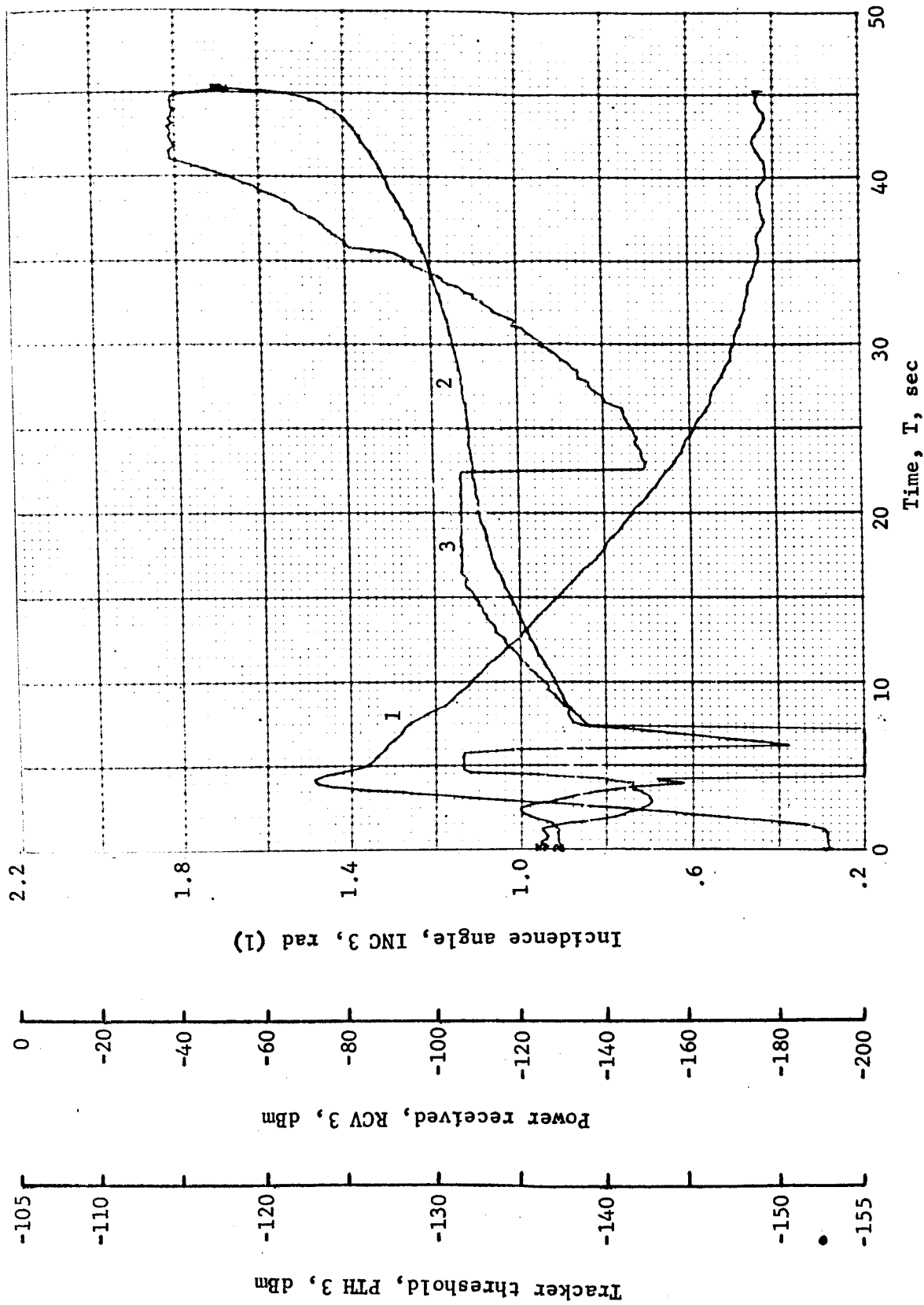


Figure B110.- Soft Lander, Run 8-12

APPENDIX B

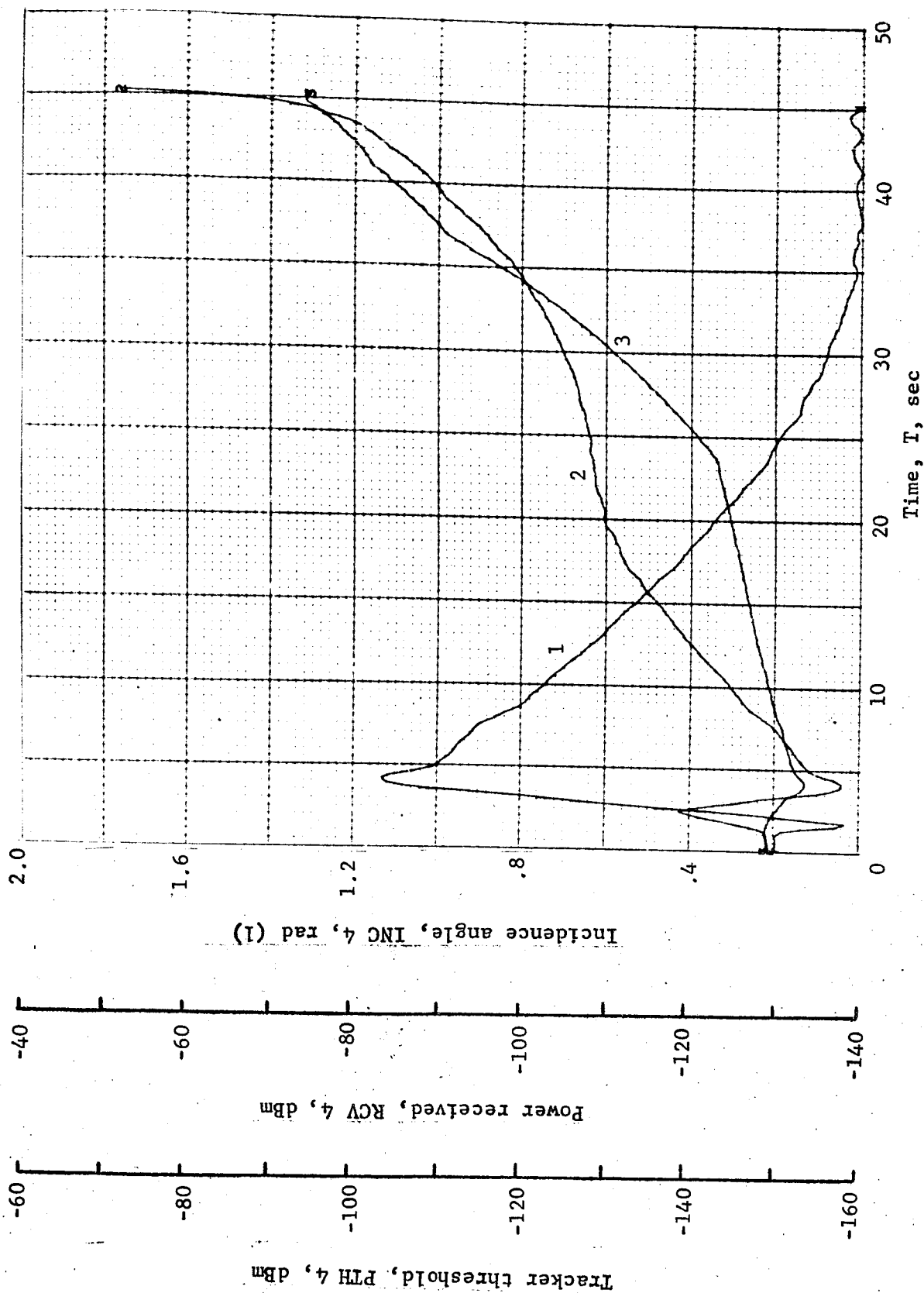


Figure B11.- Soft Lander, Run 8-13

APPENDIX B

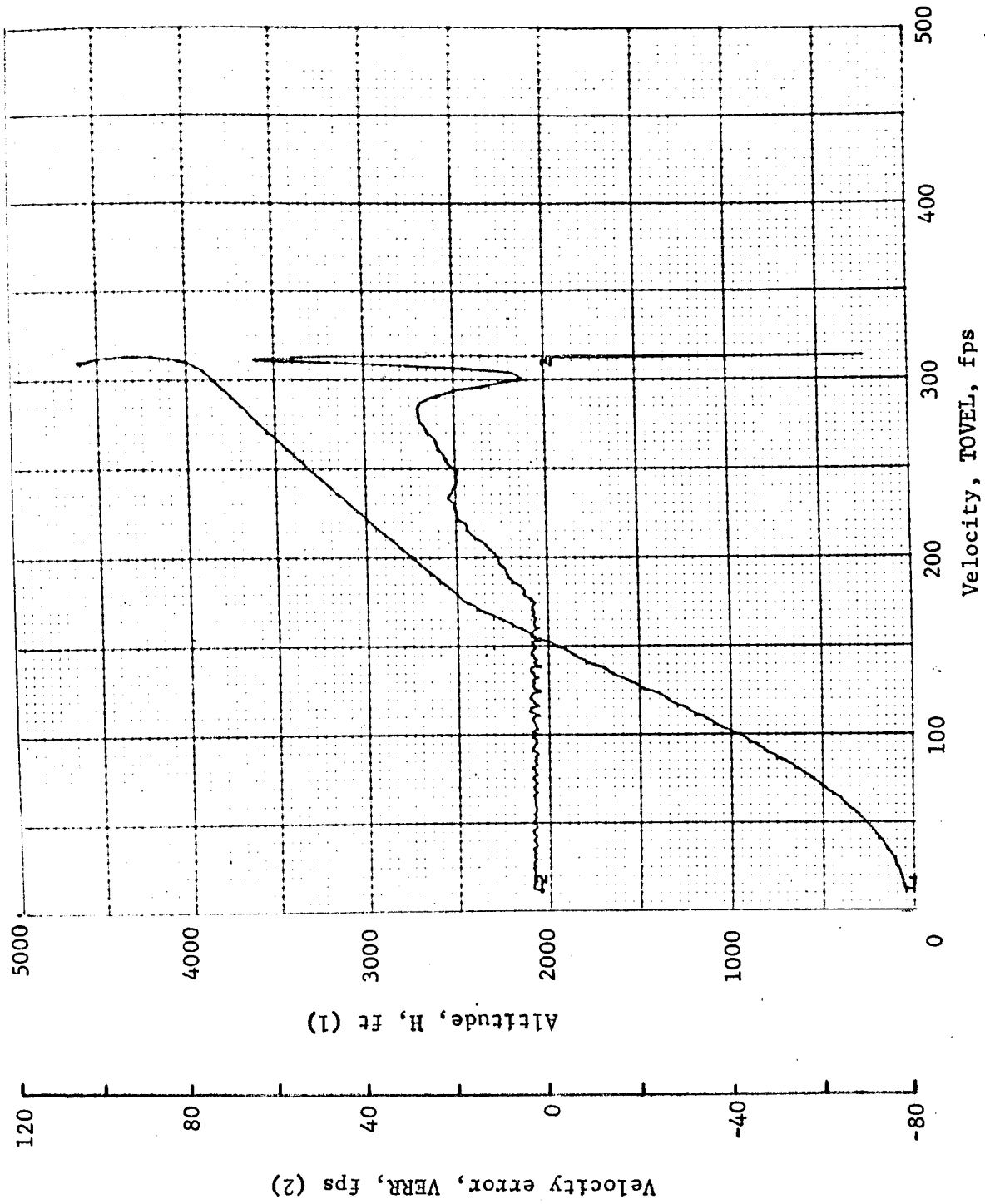


Figure B112.- Soft Lander, Run 8-14

APPENDIX B

TABLE B9.- RUN 9, AUTONOMOUS/MODIFIED LM/ALTITUDE VELOCITY/O

Flight condition	Altitude, ft	Velocity, fps		Pitch angle, deg	Pitch rate, deg/sec	Time, sec	Fuel used, lb	Beams unlocked	Time to reacquire, sec
		Roll axis	Cross axis						
Initial	4600	165	-263	-90	0	0	0	----	----
Mid-pitchup	4336.7	289.2	-104	-52.5	31.4	1.6	3.6	----	----
Max. pitchup	4134	297.3	41.7	-27	-1.6	2.8	6.5	3	----
Thrust aligned	3822.7	271.3	20.1	-35	-1.65	4.6	14	3	----
Encounter contour	4099.5	296.6	39	-28	-7.1	3.0	6.9	3	----
Constant vel	49.8	12.2	.06	-90.8	-.15	43.2	135	----	----
Cutoff eng	8.7	12.4	.12	-91.5	-2.86	46.5	141.4	----	----
Land	.94	18.6	-.4	-92.1	-2.96	47	141.4	----	----
Remarks:									

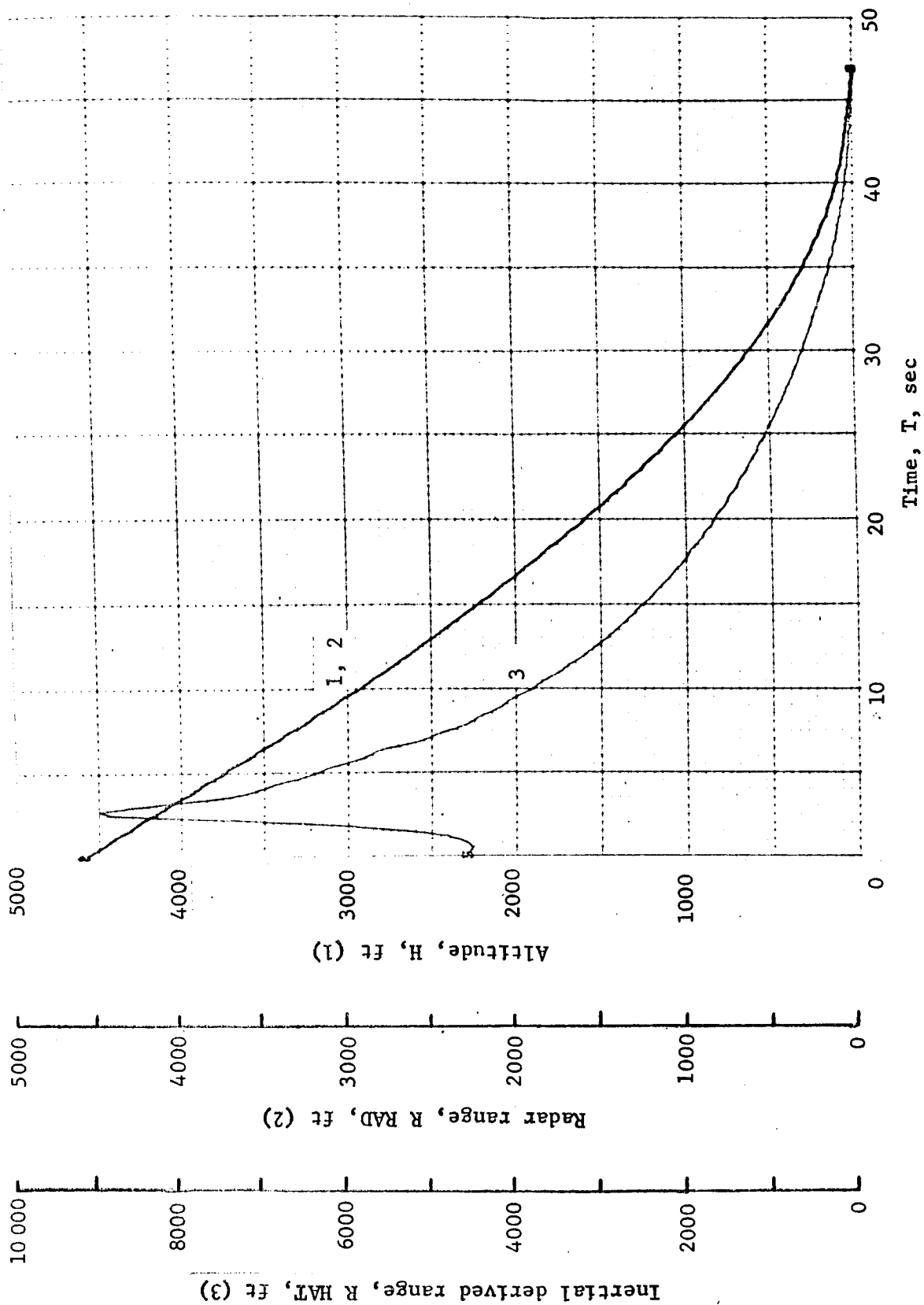


Figure B113.- Soft Lander, Run 9-1

APPENDIX B

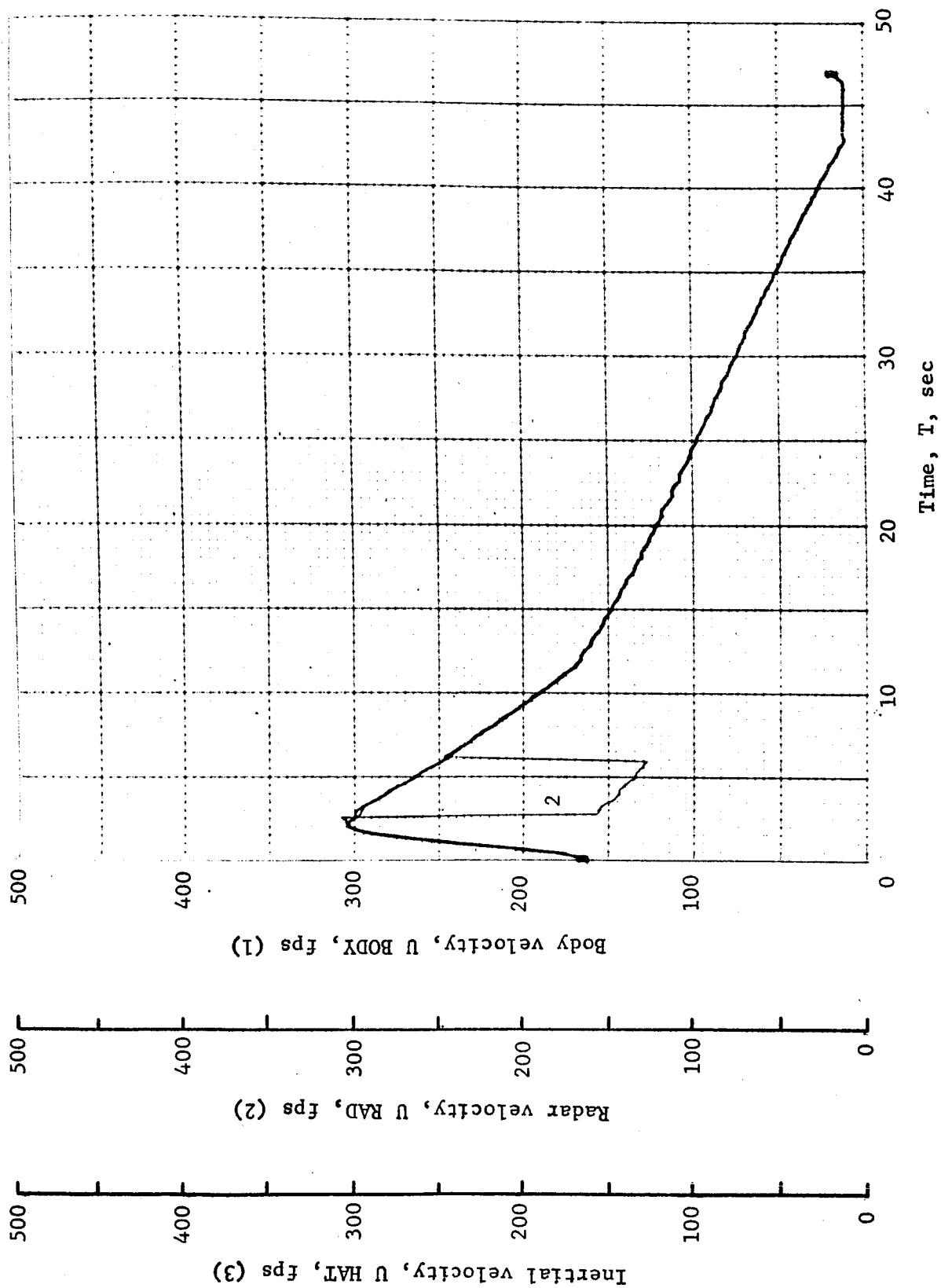


Figure B114.- Soft Lander, Run 9-2

APPENDIX B

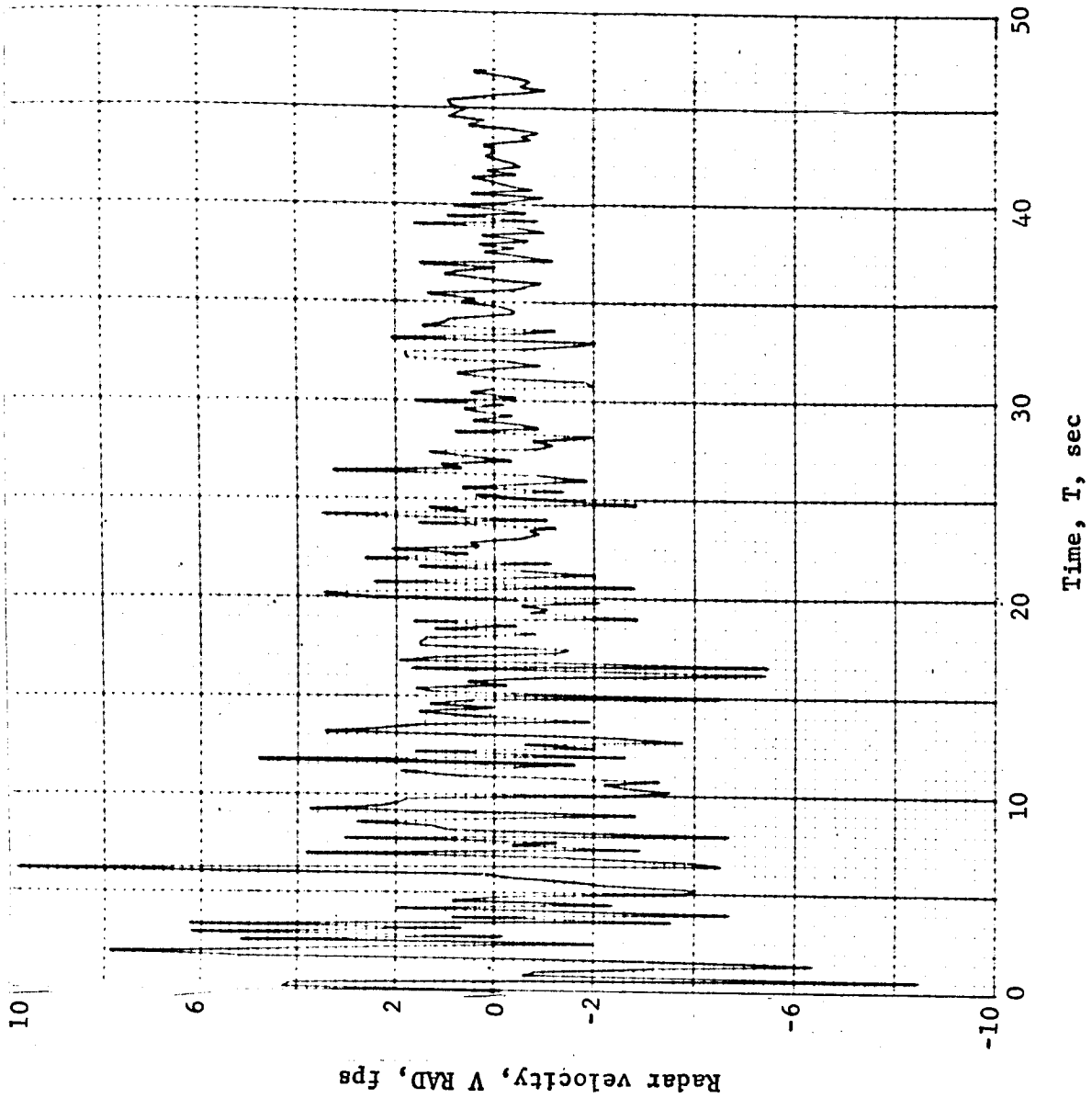


Figure B115.- Soft Lander, Run 9-3

APPENDIX B

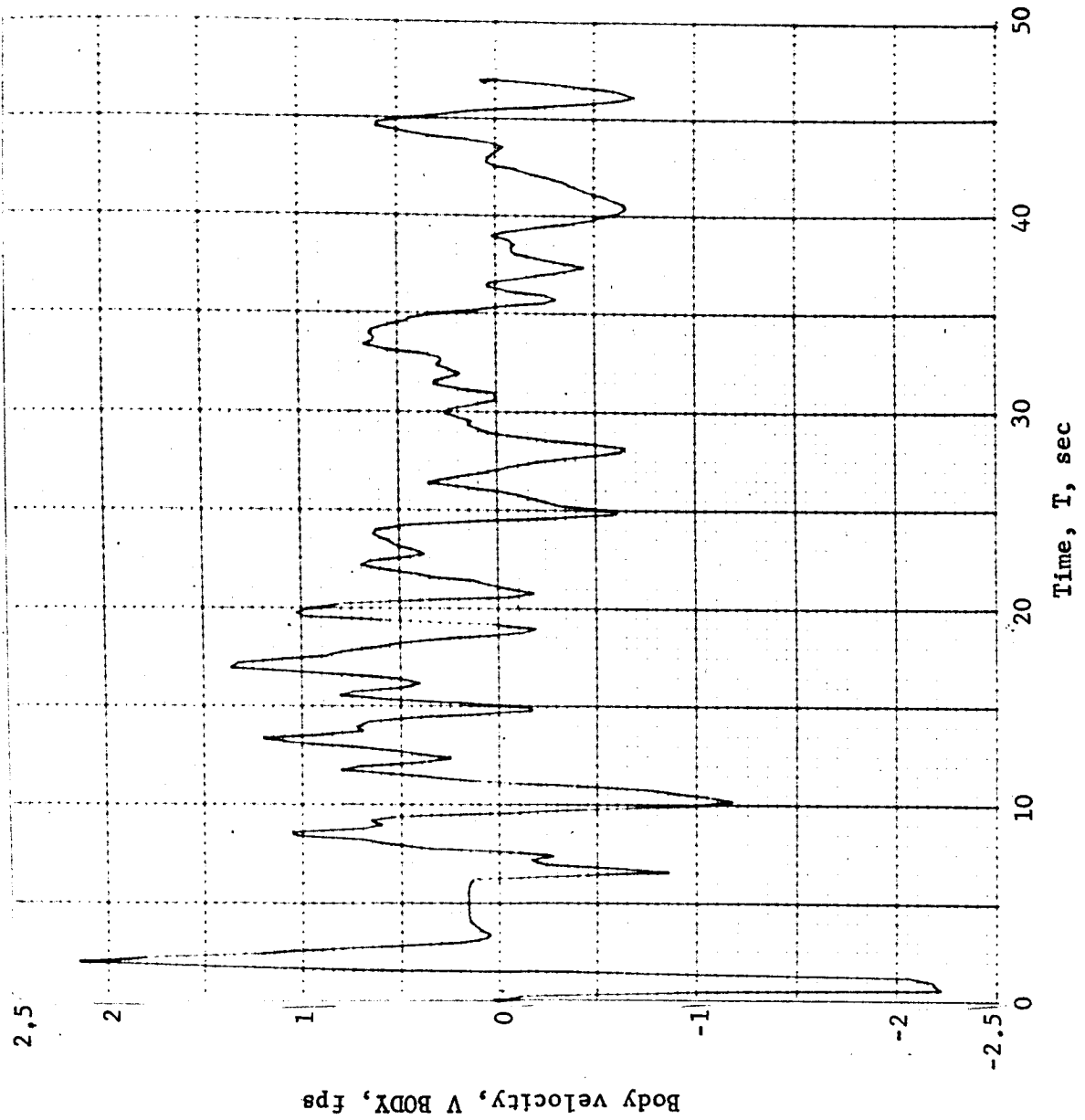


Figure B116.- Soft Lander, Run 9-4

APPENDIX B

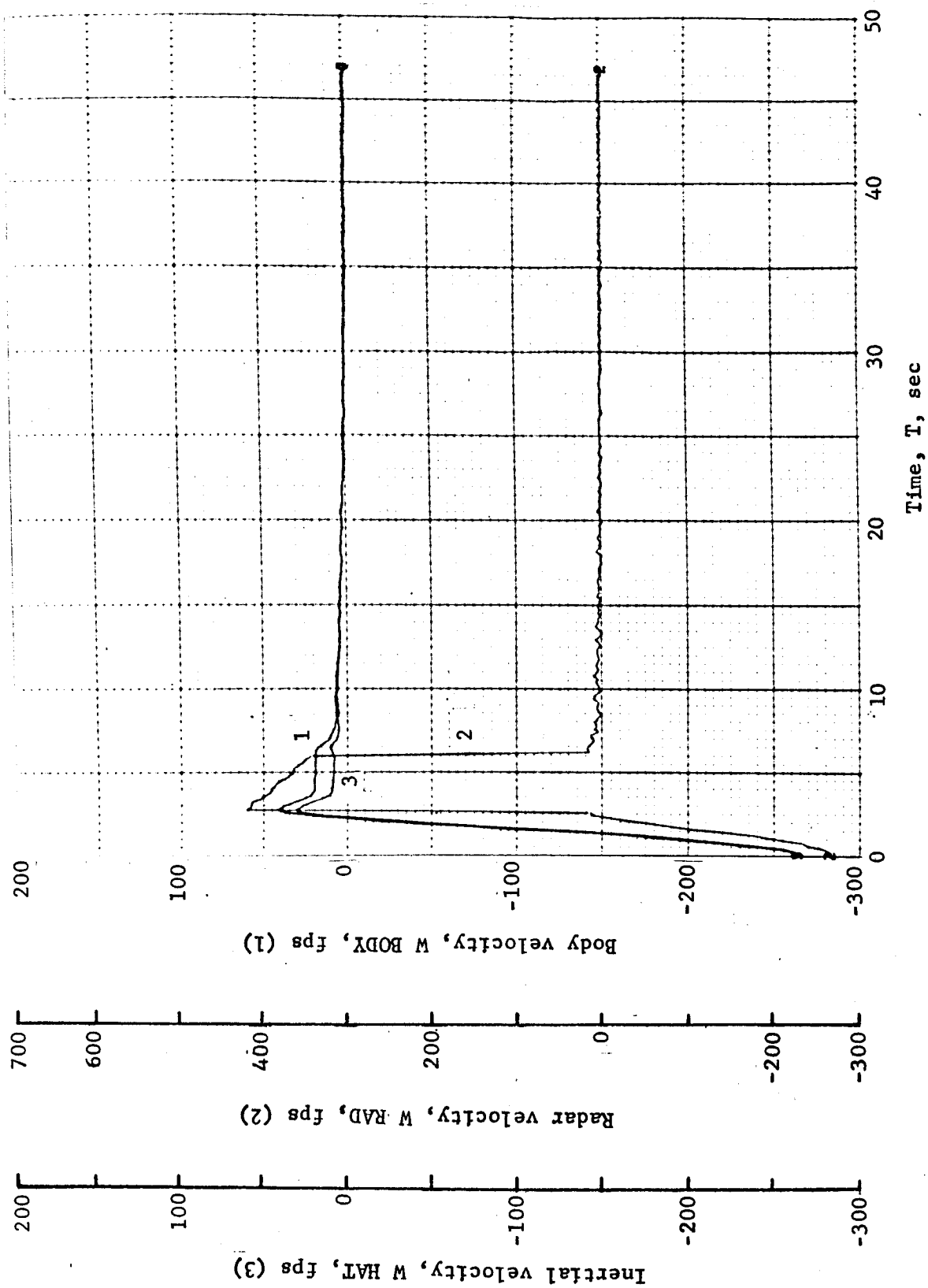


Figure B117.- Soft Lander, Run 9-5

APPENDIX B

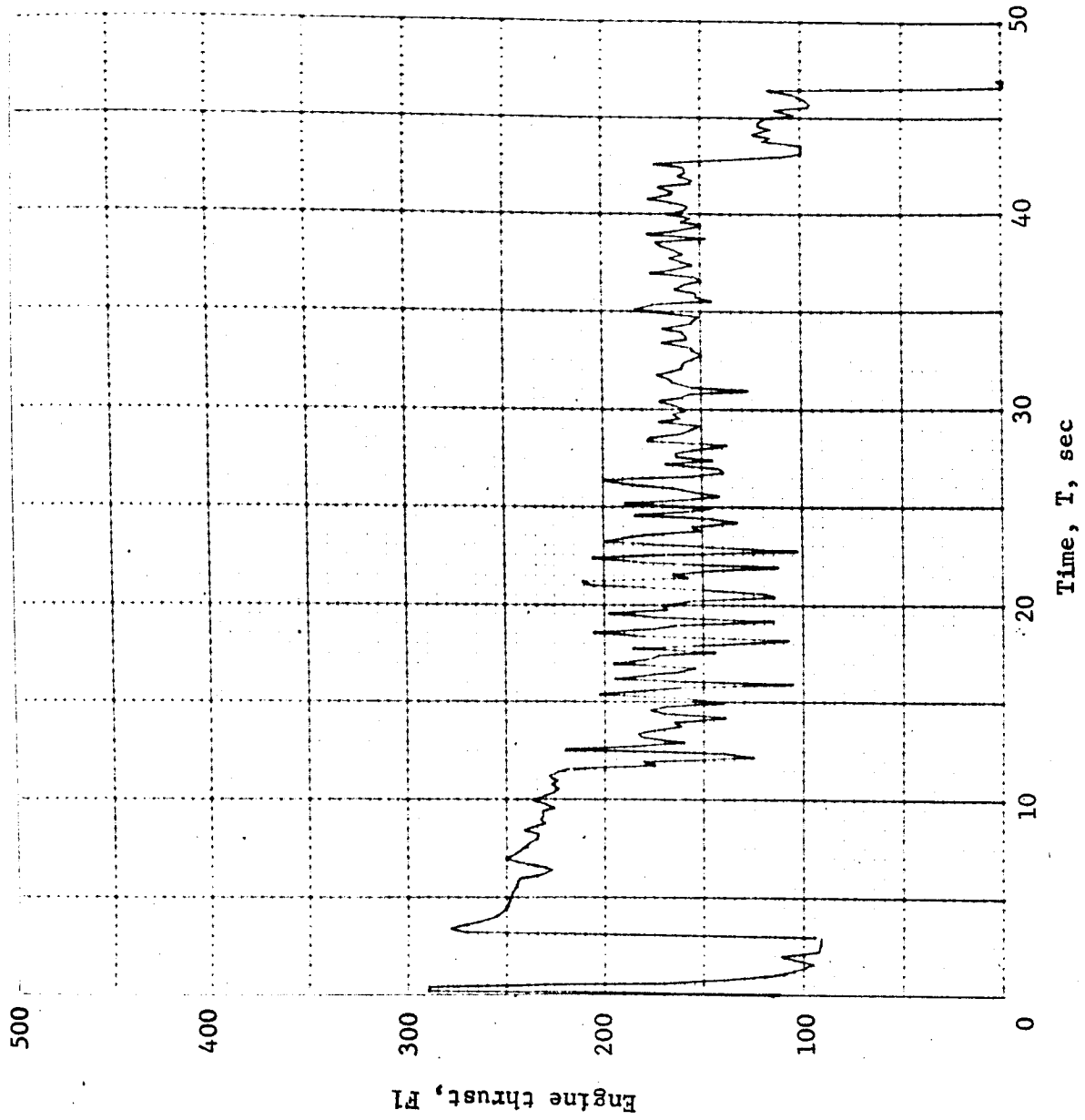


Figure B118.- Soft Lander, Run 9-6

APPENDIX B

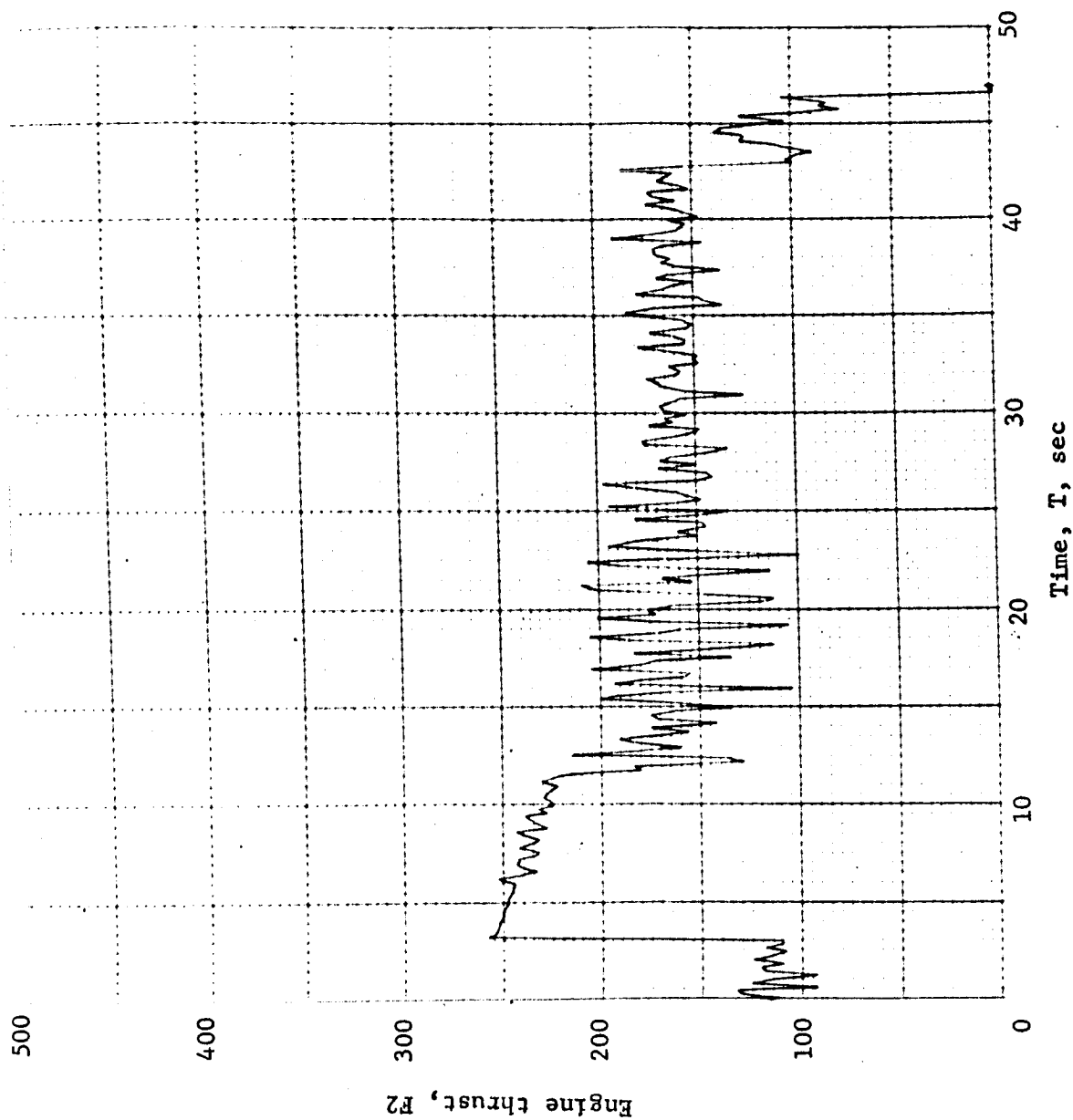


Figure B119.- Soft Lander, Run 9-7

APPENDIX B

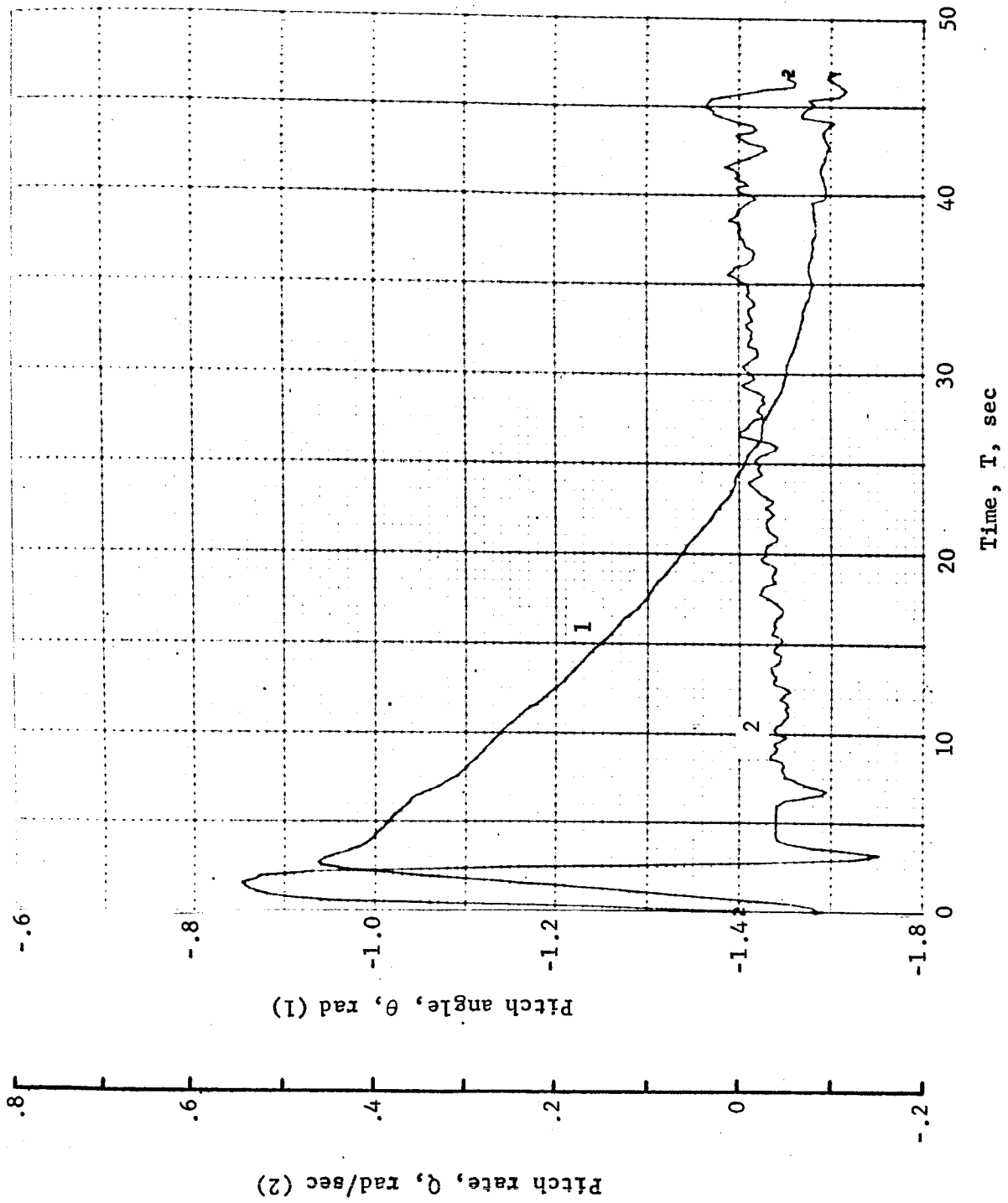


Figure B120.- Soft Lander, Run 9-8

APPENDIX B

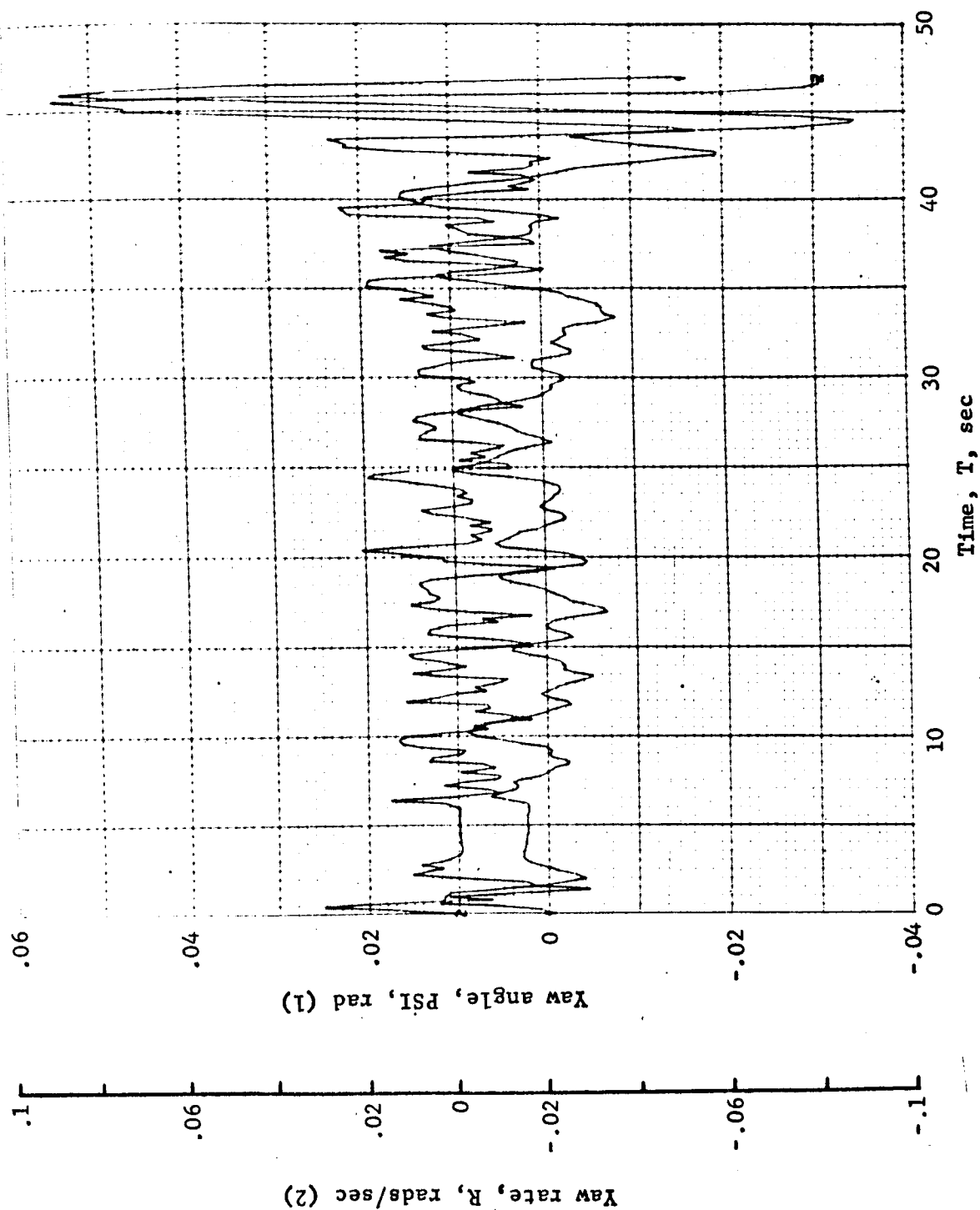


Figure B121.- Soft Lander, Run 9-9

APPENDIX B

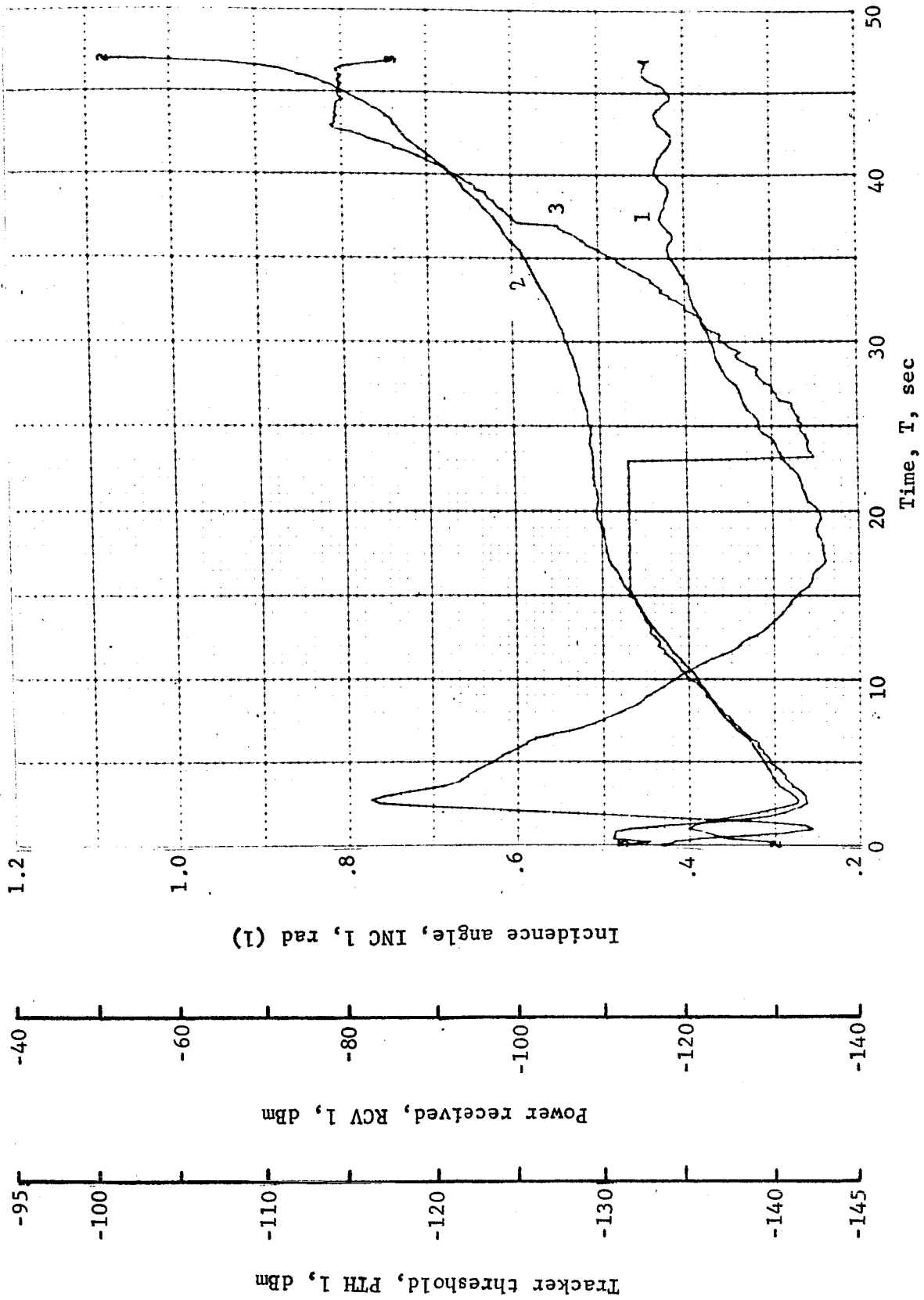


Figure B122.- Soft Lander, Run 9-10

APPENDIX B

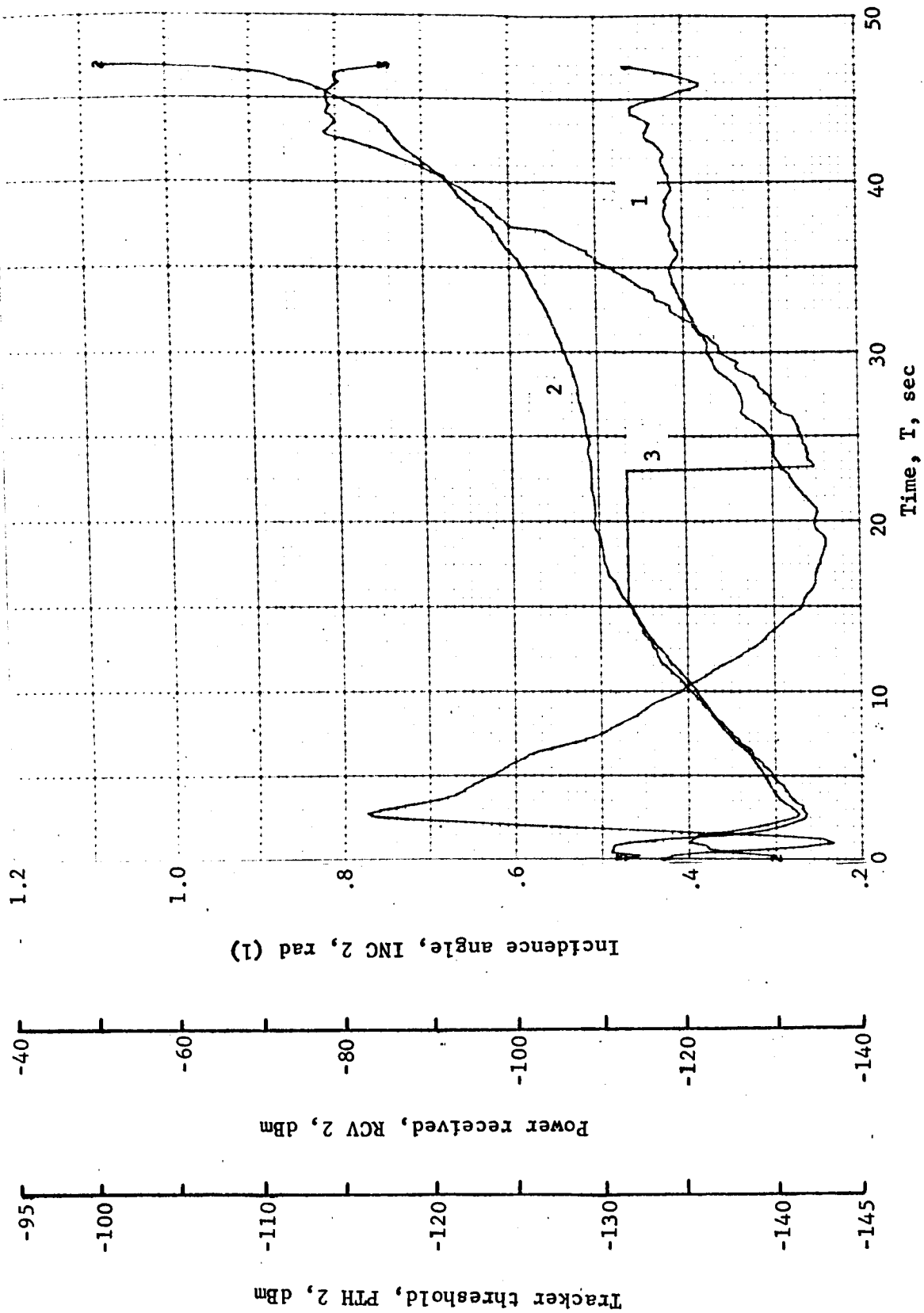


Figure B123.- Soft Lander, Run 9-11

APPENDIX B

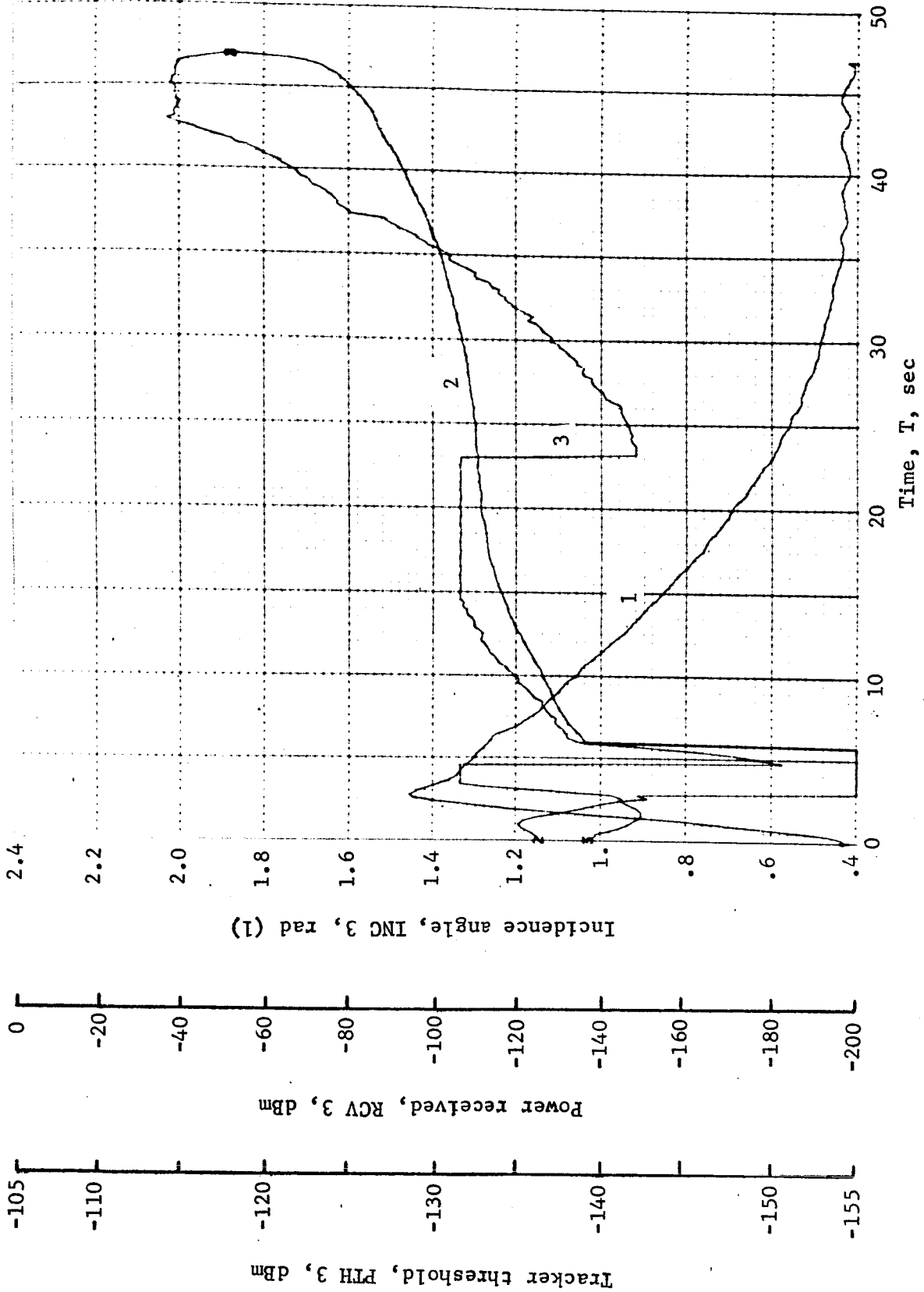


Figure B124.- Soft Lander, Run 9-12

APPENDIX B

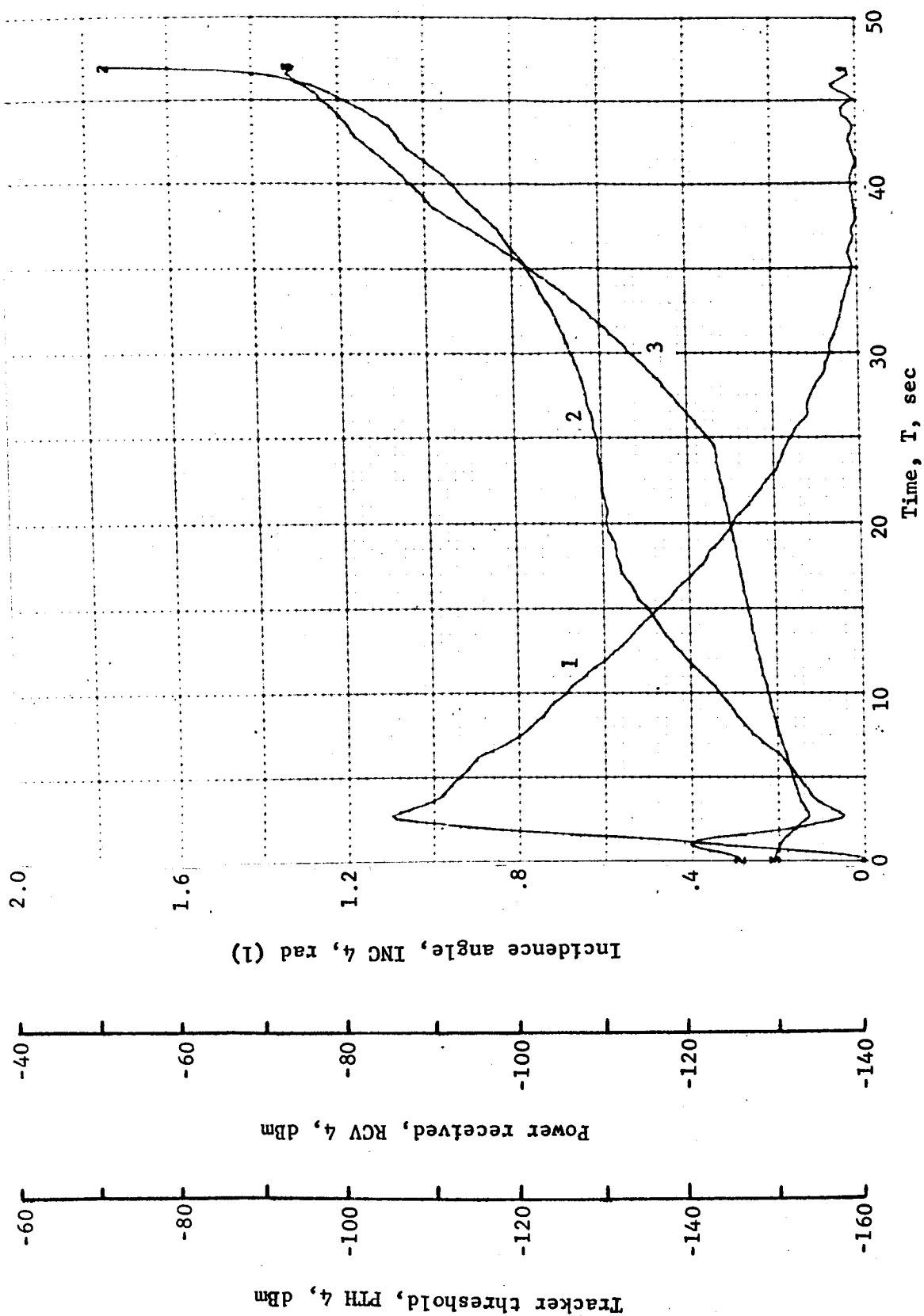


Figure B125.- Soft Lander, Run 9-13

APPENDIX B

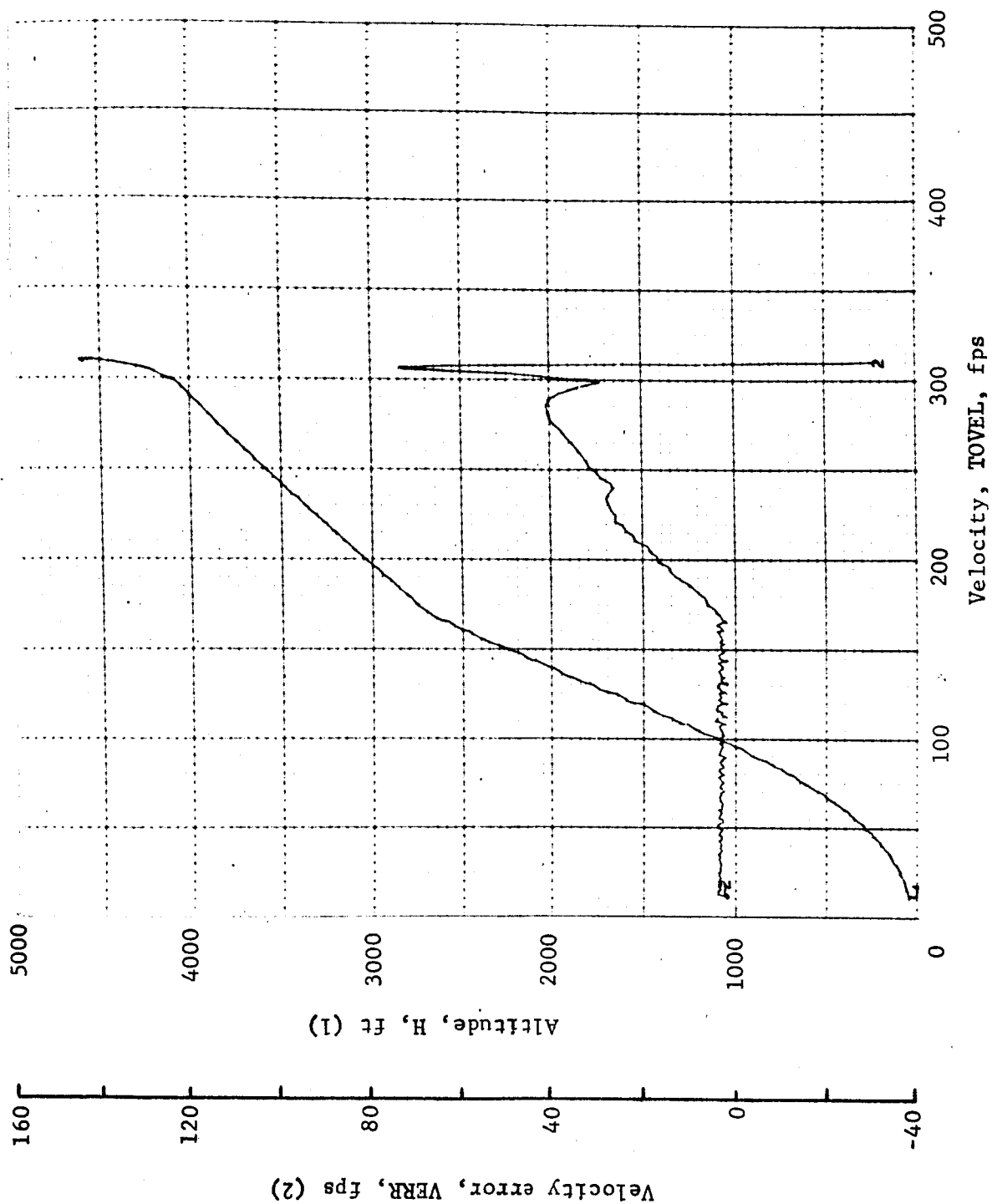


Figure B126.- Soft Lander, Run 9-14

APPENDIX B

TABLE B10.- RUN 10, AUTONOMOUS/MODIFIED LM/ALTITUDE VELOCITY/27° UPSLOPE

Flight condition	Altitude ft	Velocity, fps		Pitch angle, deg	Pitch rate, deg/sec	Time, sec	Fuel used, lb	Beams unlocked	Time to reacquire, sec
		Roll axis	Cross axis						
Initial	4600	165	-170	-90	0	0	0	----	----
Mid-pitchup	4298.6	219.8	-83.9	-65.4	30.7	1.2	2.8	1, 2	----
Max. pitchup	3999	229.4	19.2	-42	0	2.4	5.7	1, 2	----
Thrust aligned	3655.6	217.0	6.9	-48.1	1.43	3.8	10.4	----	2.8
Encounter contour	3850	228.6	9.4	-45.8	-4.58	3.0	7	1, 2	----
Constant vel	55.11	11.8	0	-89.4	1.4	38.58	118	----	----
Cutoff eng	8.3	12.45	.24	-91.2	-1.2	42.4	125	----	----
Land	.9	18.4	.06	-91.5	-1.3	42.9	125	----	----
Remarks									

APPENDIX B

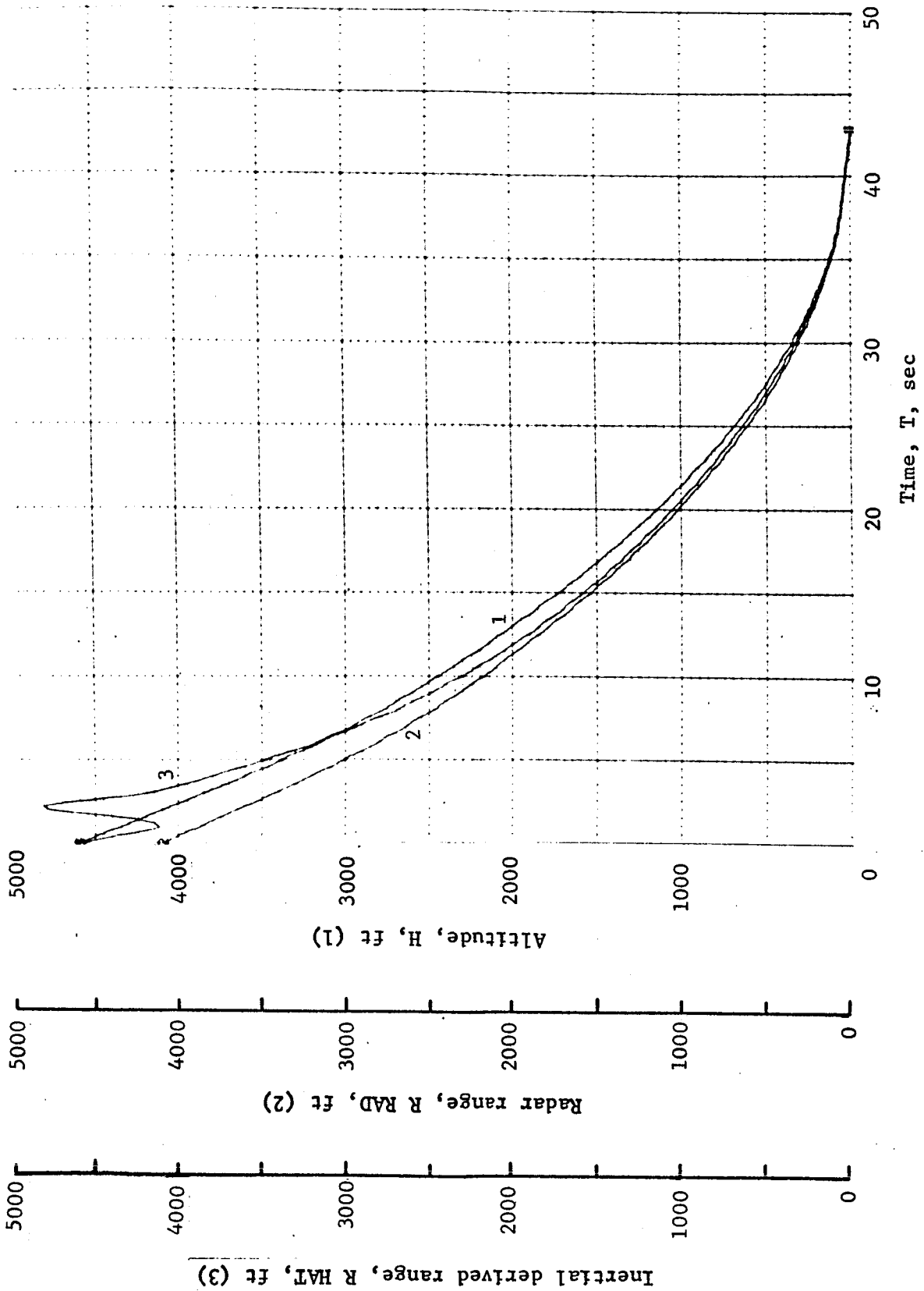


Figure B127.- Soft Lander, Run 10-1

APPENDIX B

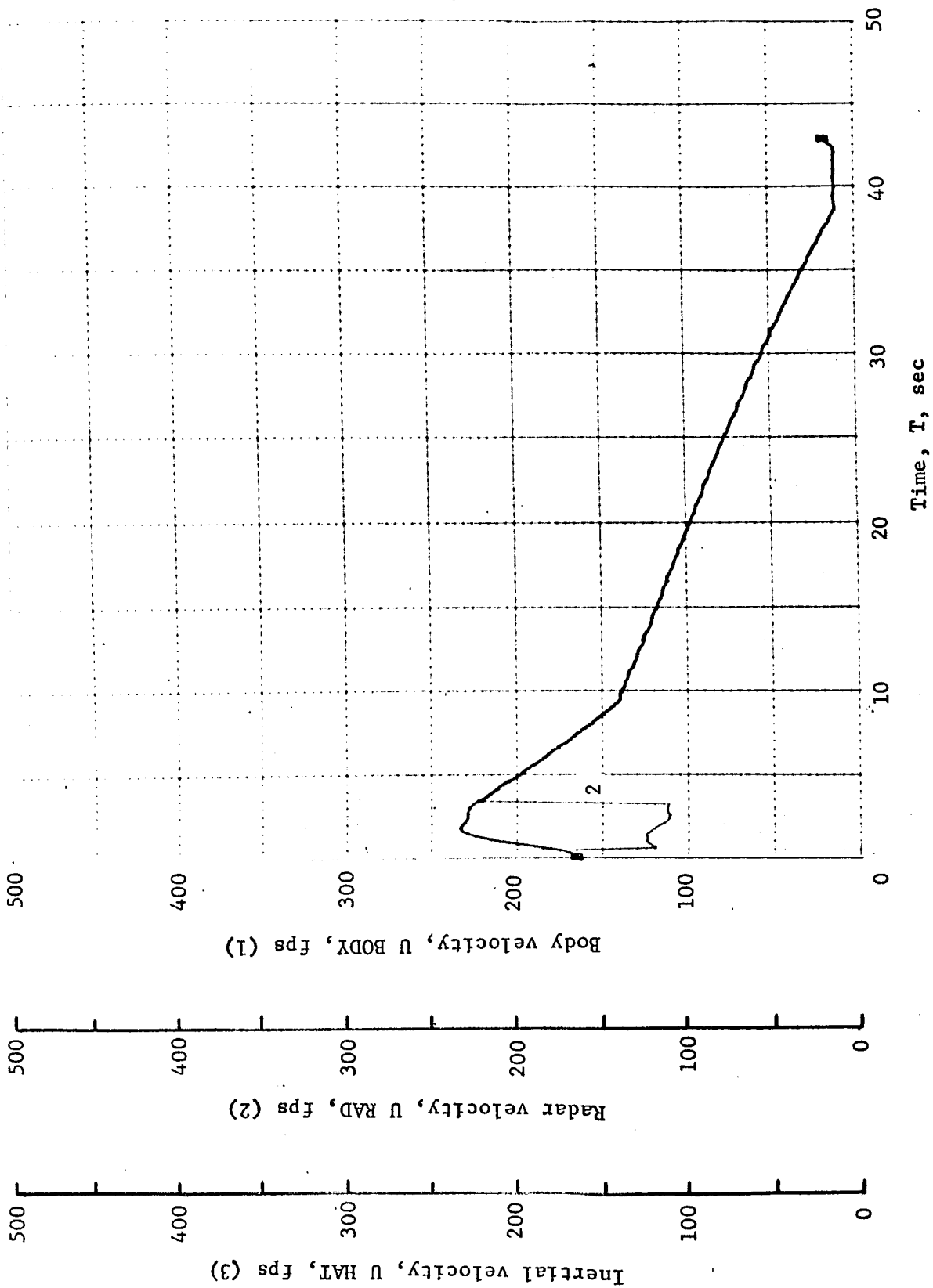


Figure B128.- Soft Lander, Run 10-2

APPENDIX B

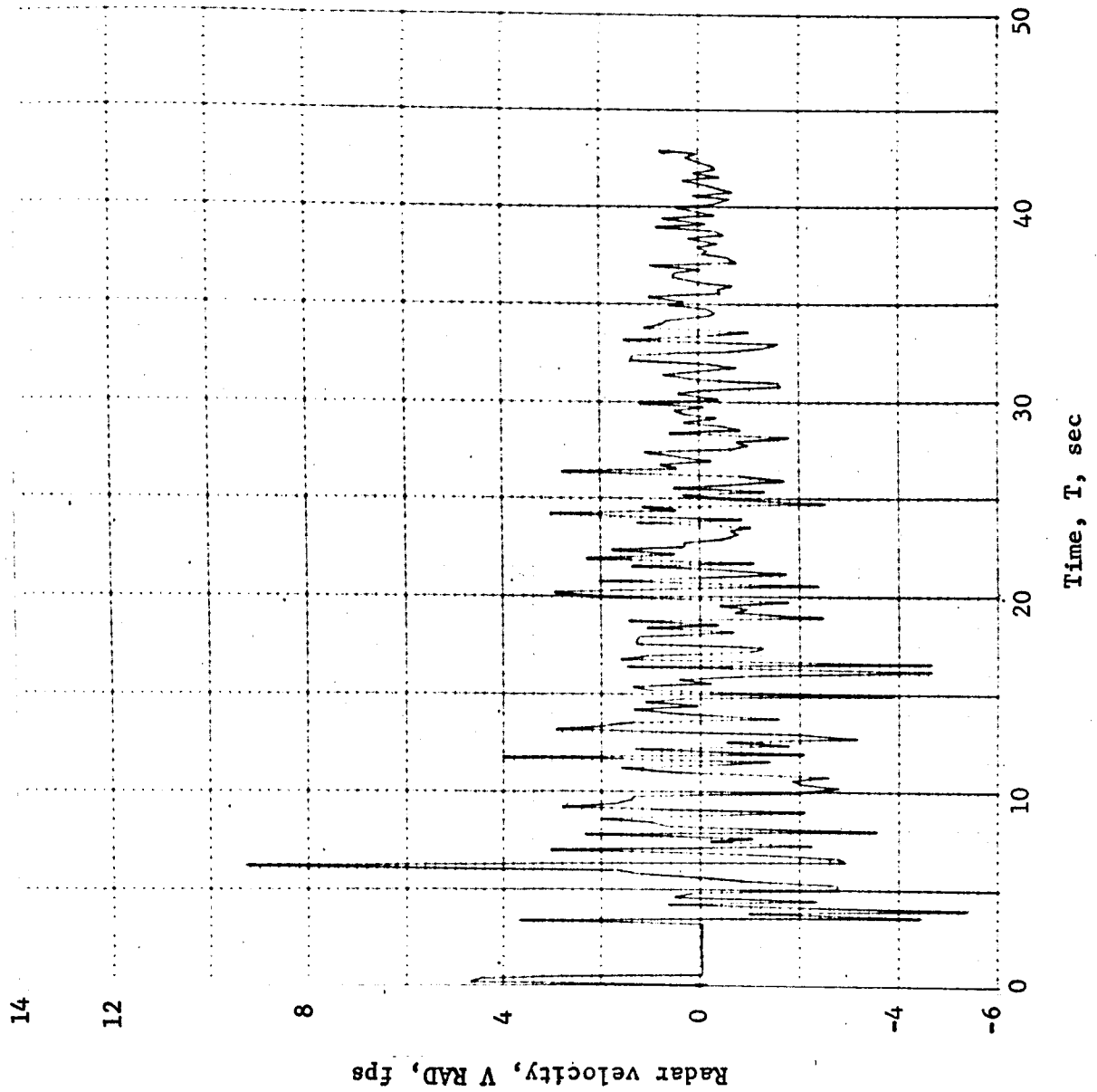


Figure B129.- Soft Lander, Run 10-3

APPENDIX B

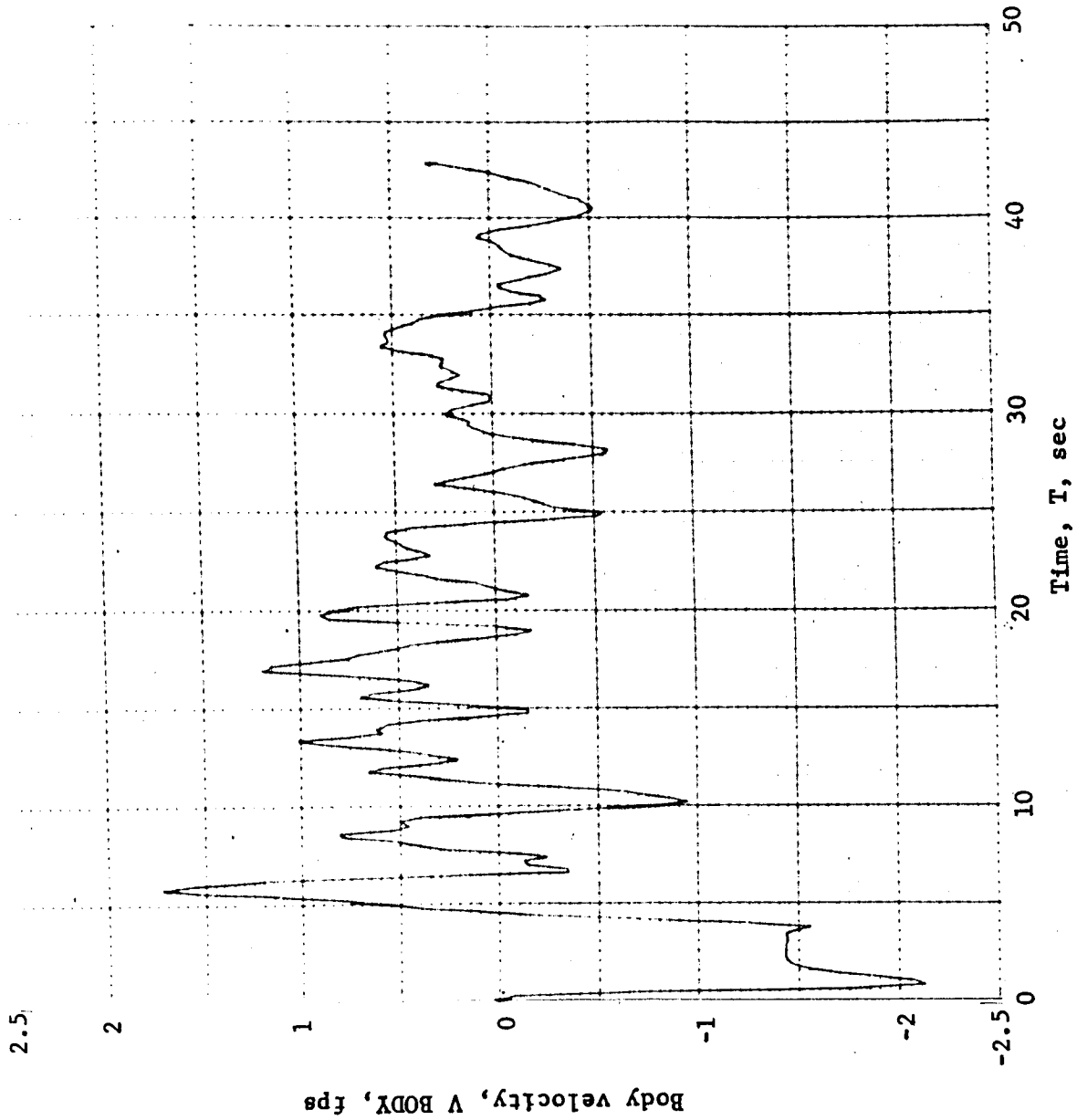


Figure B130.- Soft Lander, Run 10-4

APPENDIX B

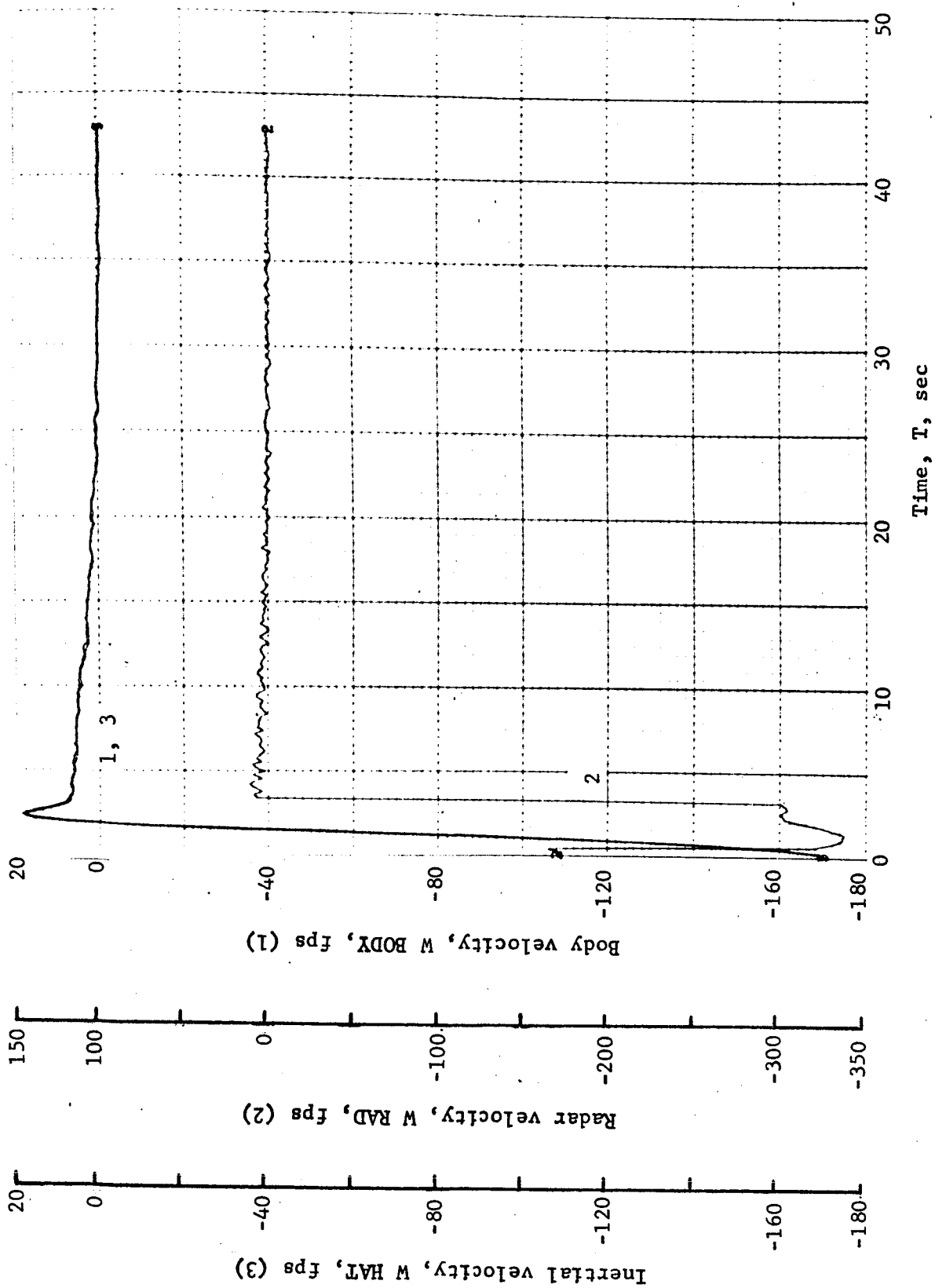


Figure B131.- Soft Lander, Run 10-5

APPENDIX B

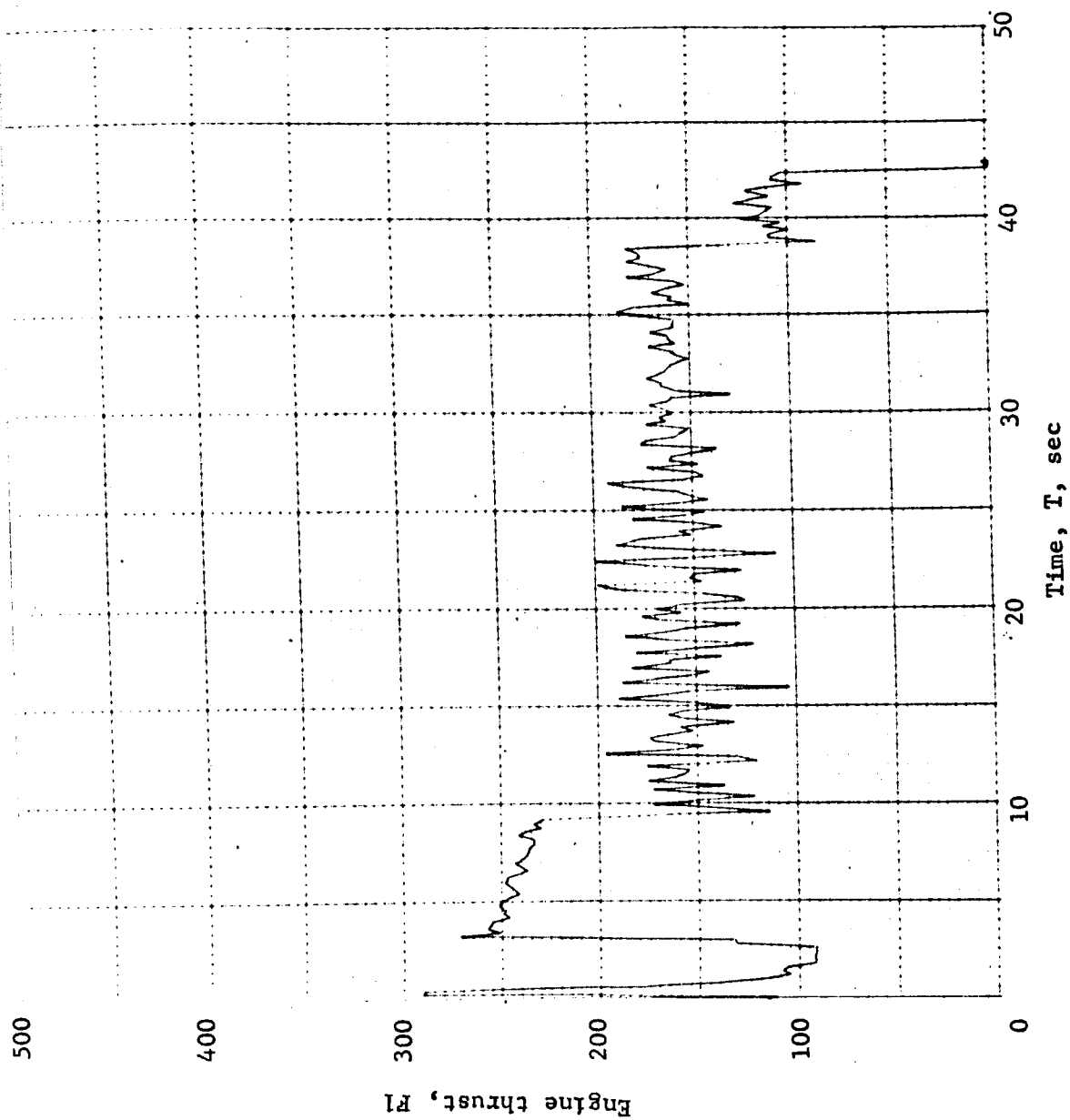


Figure B132.- Soft Lander, Run 10-6

APPENDIX B

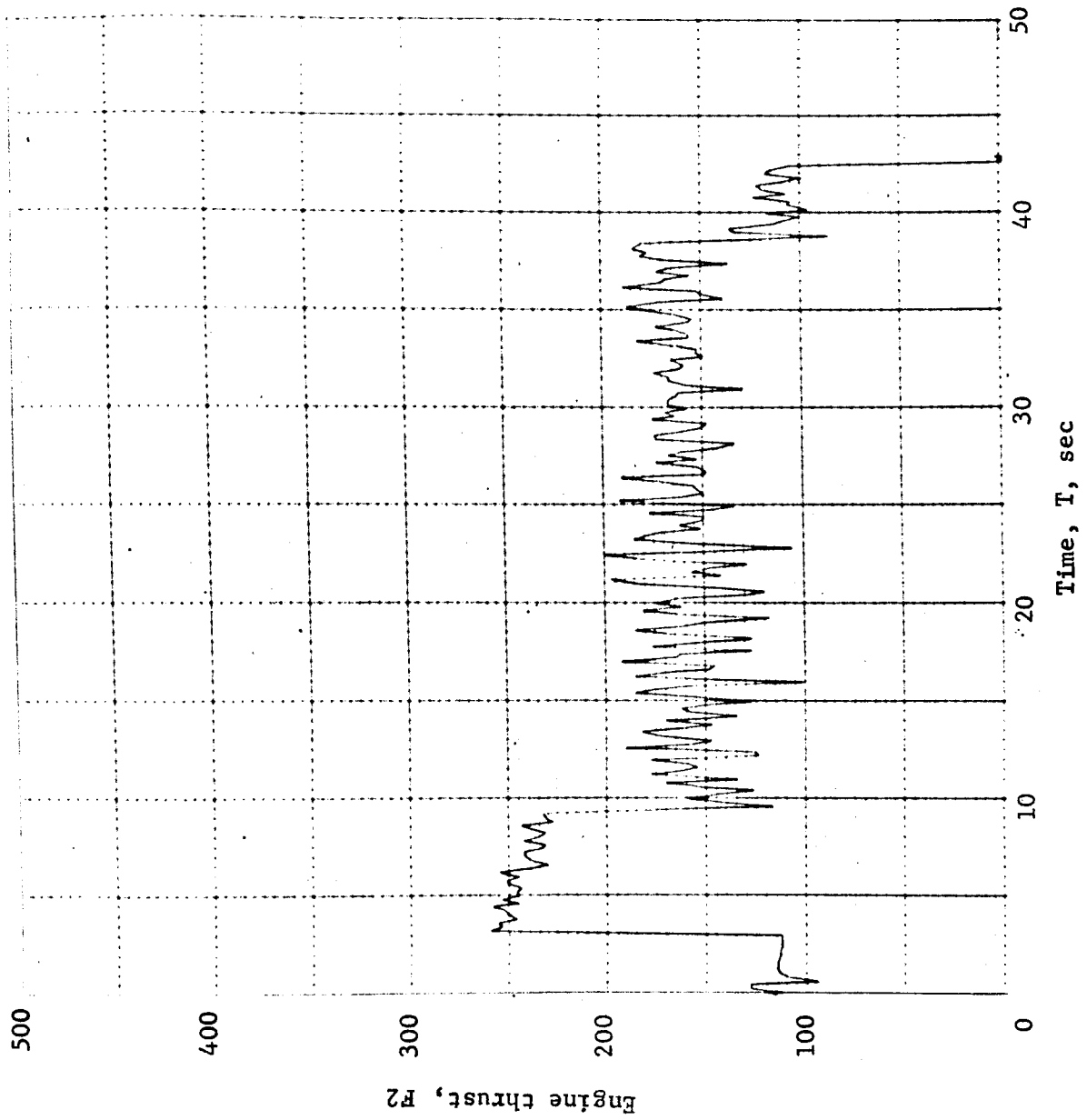


Figure B133.- Soft Lander, Run 10-7

APPENDIX B

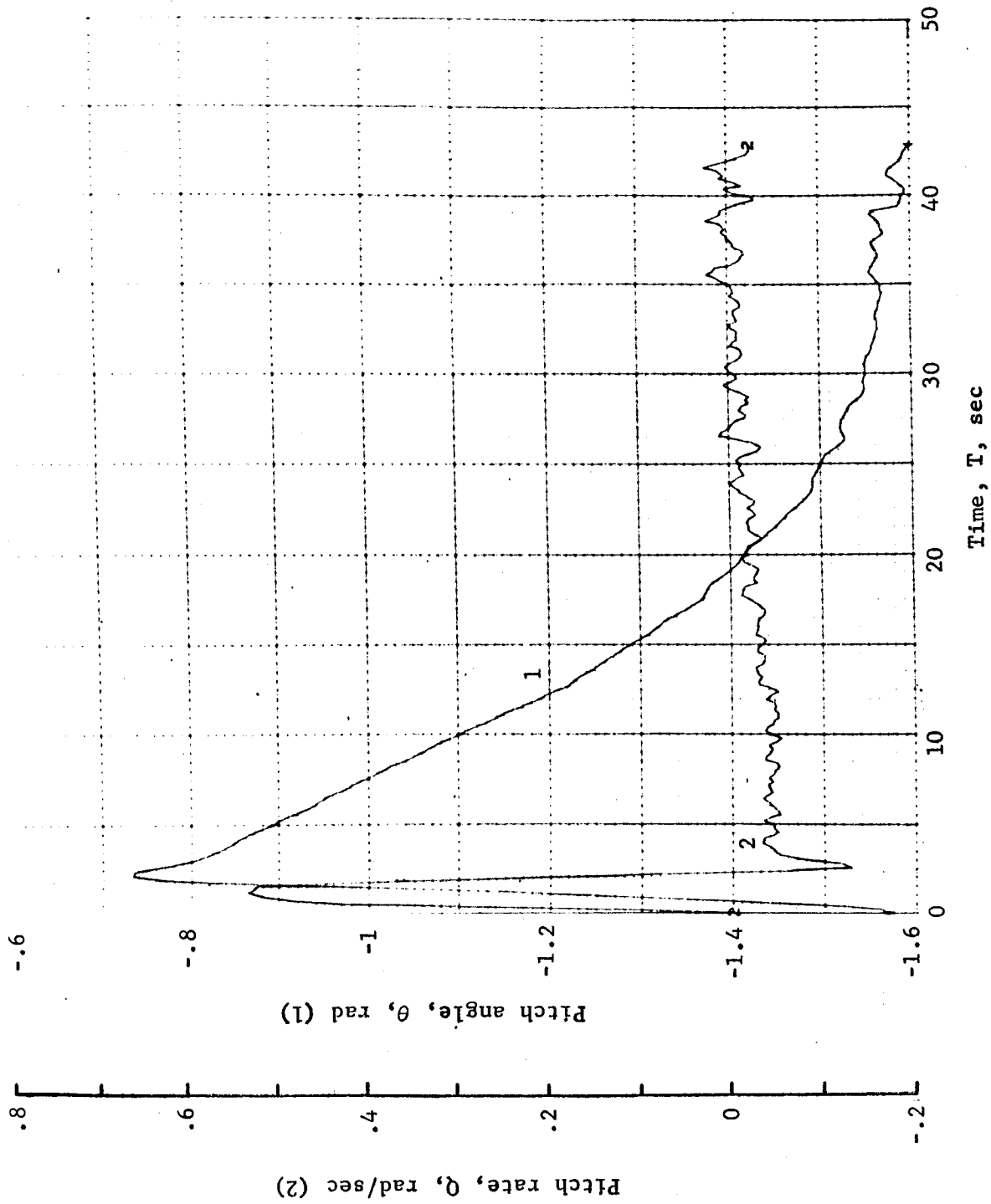


Figure B134.- Soft Lander, Run 10-8

APPENDIX B

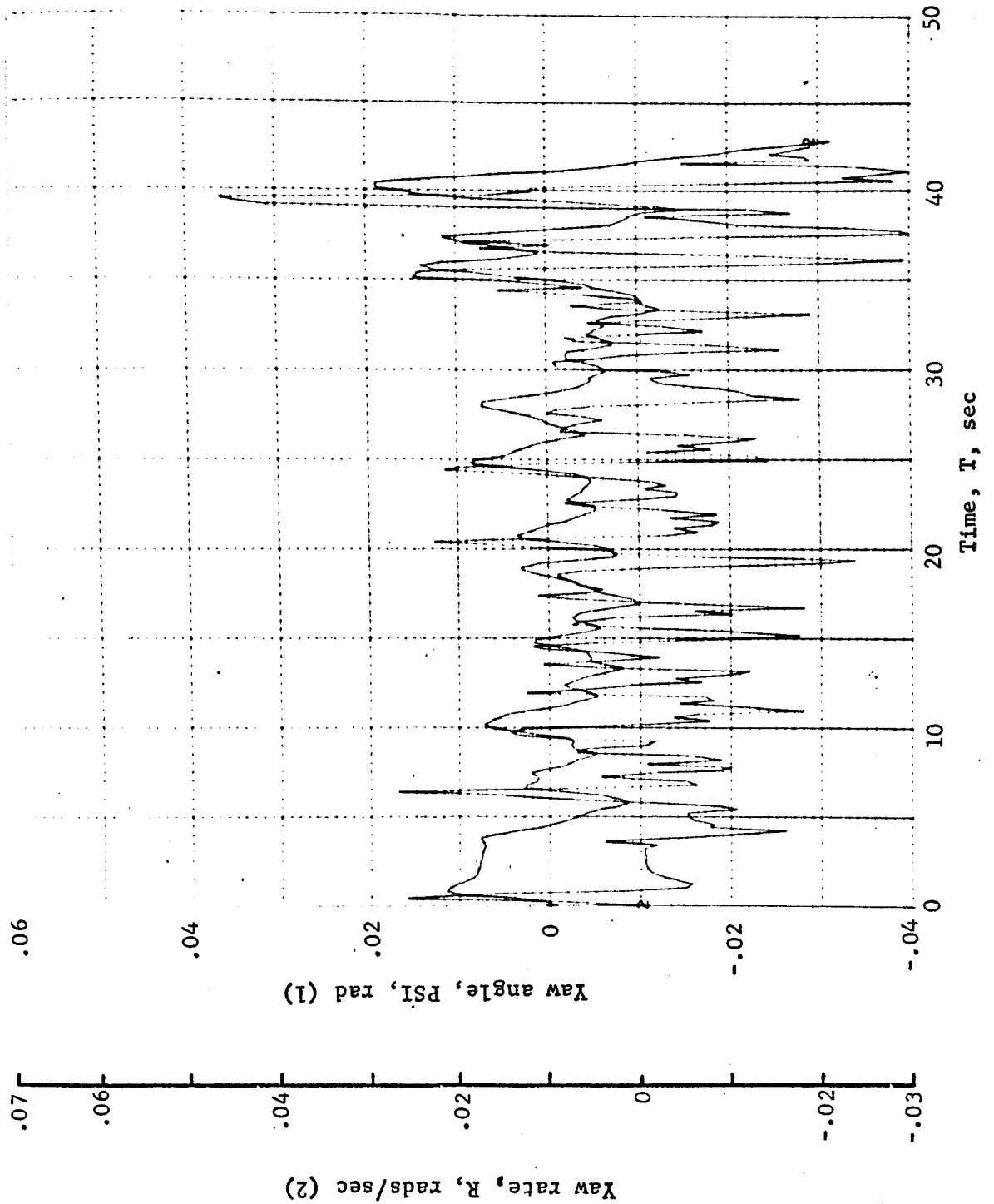


Figure B135.- Soft Lander, Run 10-9

APPENDIX B

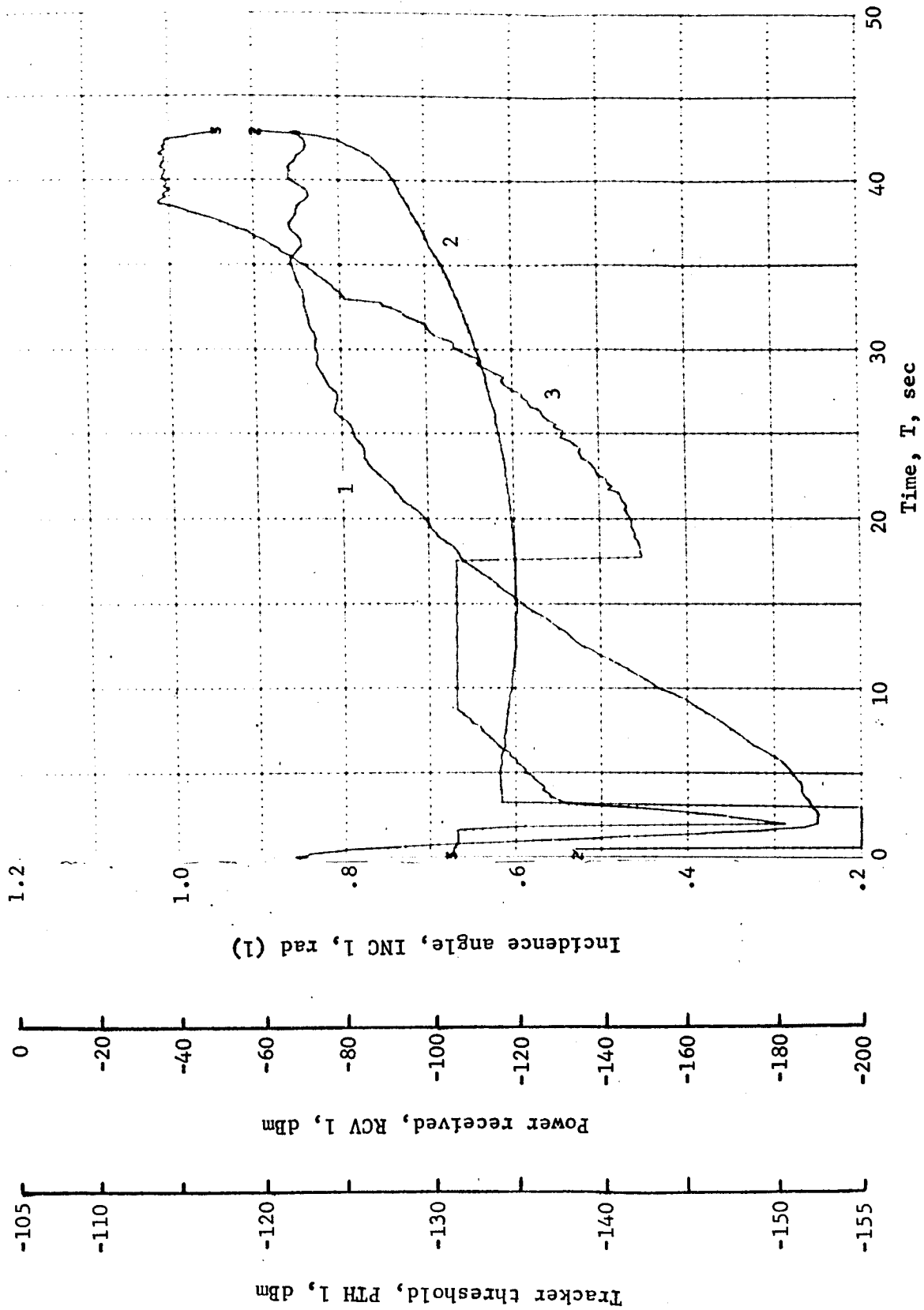


Figure B136.- Soft Lander, Run 10-10

APPENDIX B

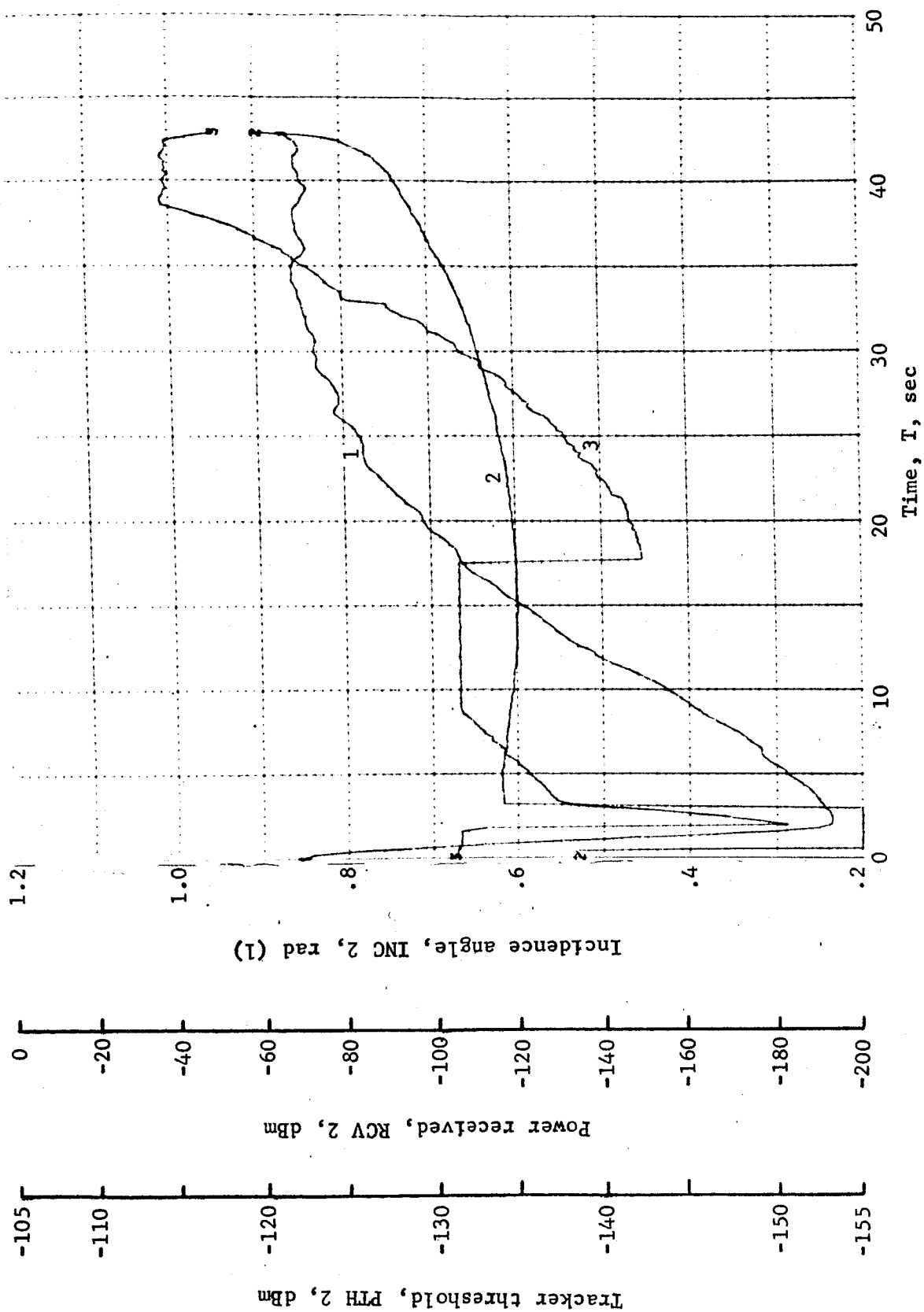


Figure B137.- Soft Lander, Run 10-11

APPENDIX B

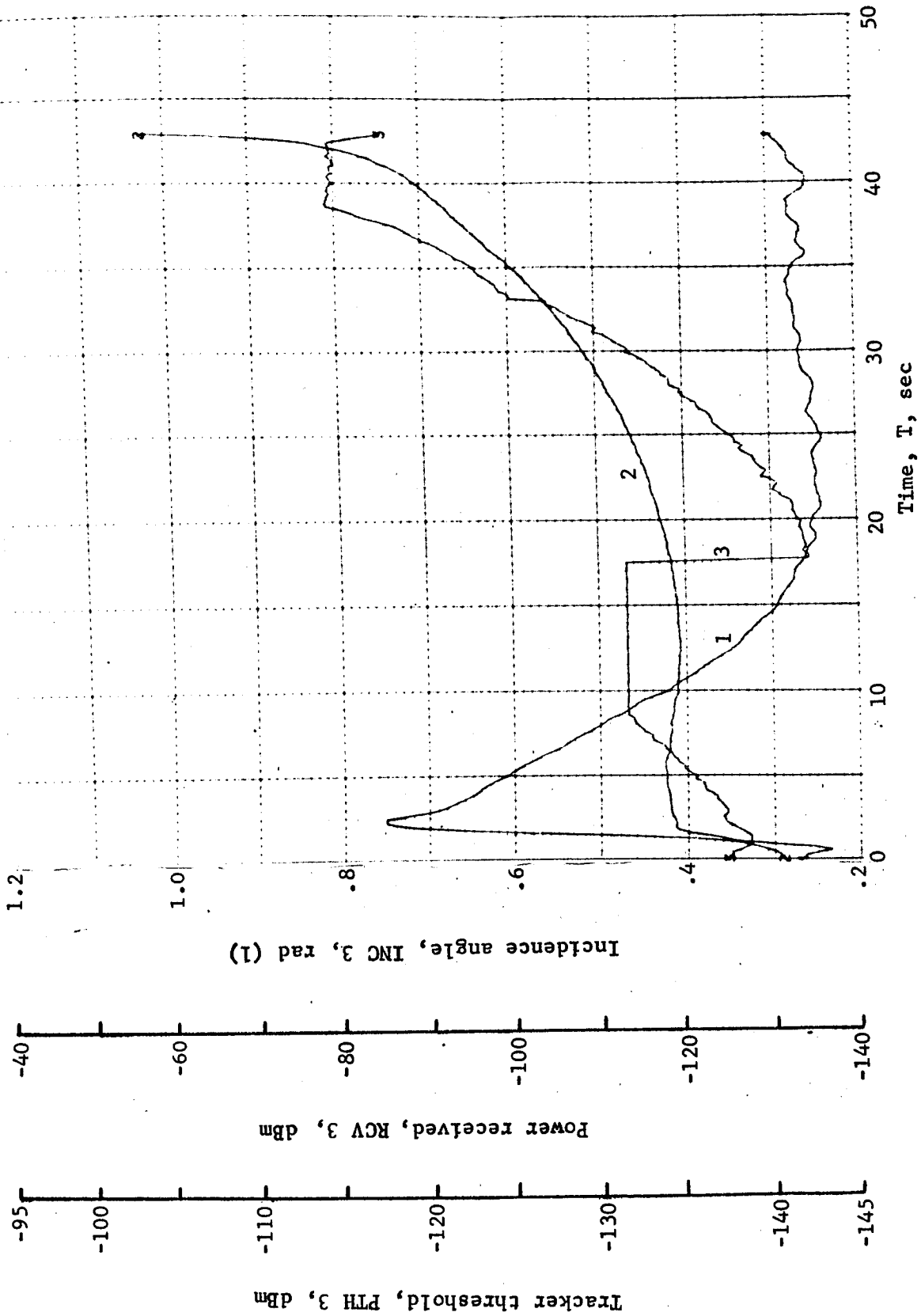


Figure B138.- Soft Lander, Run 10-12

APPENDIX B

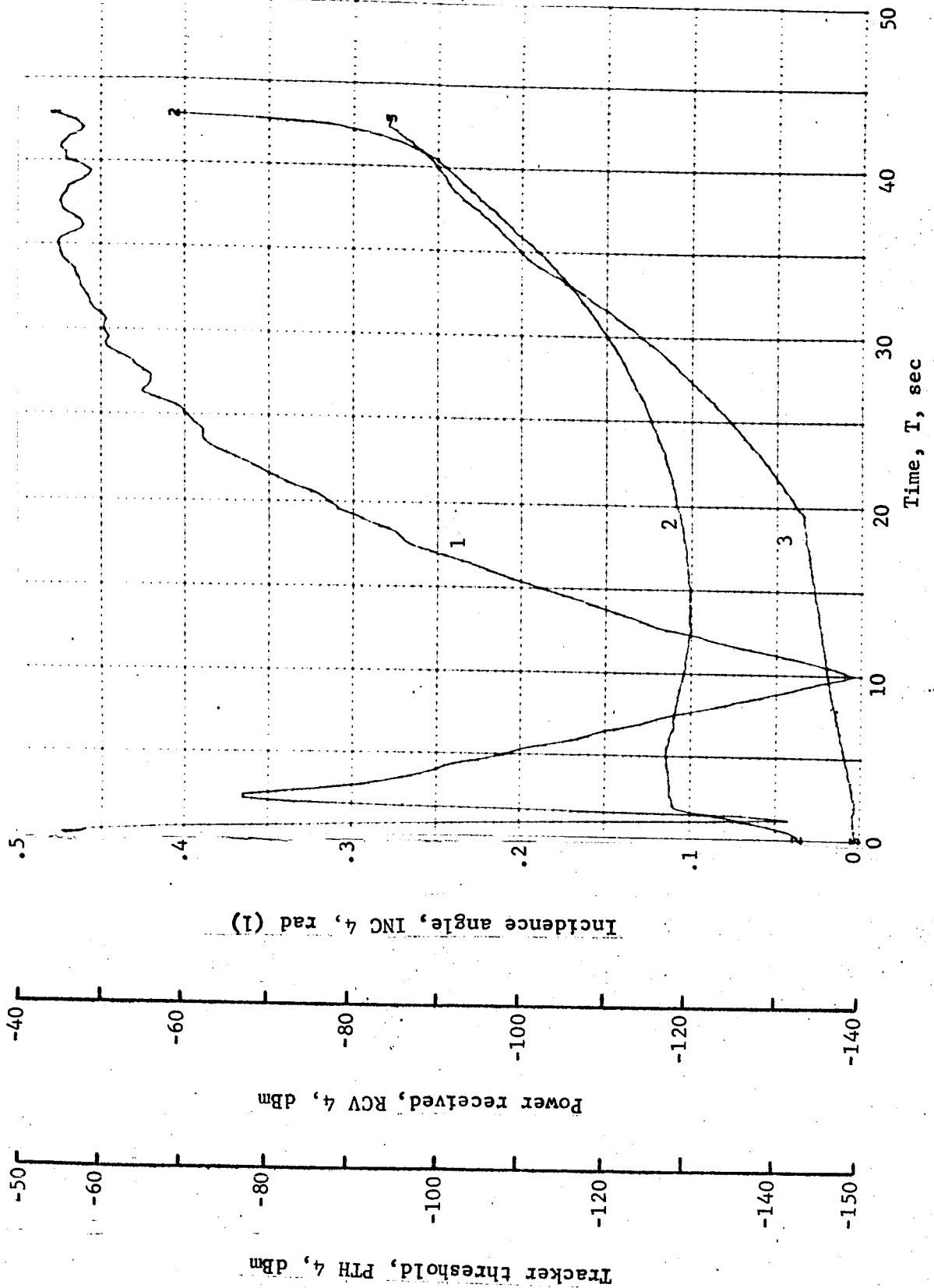


Figure B139.- Soft Lander, Run 10-13

APPENDIX B

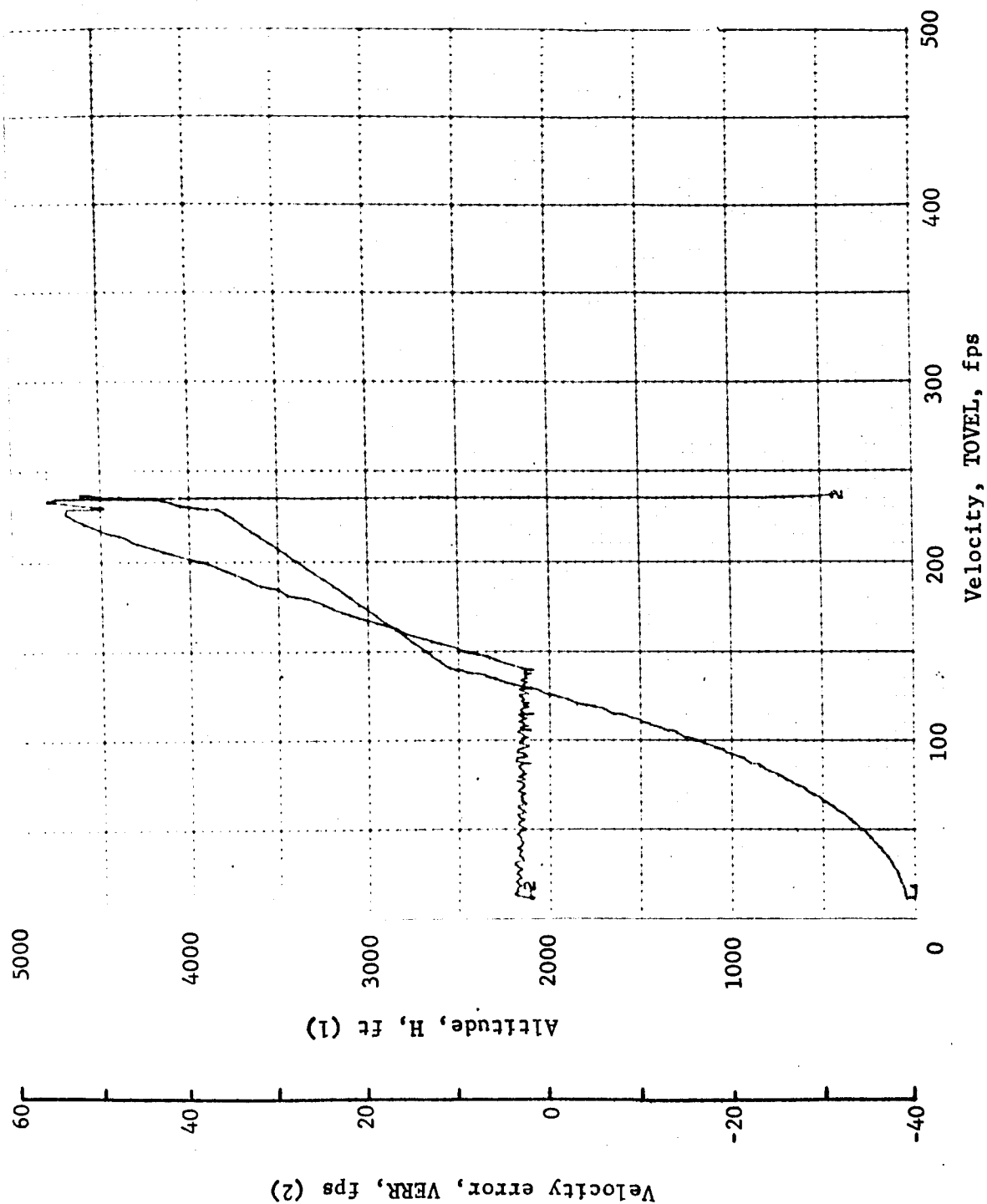


Figure B140.- Soft Lander, Run 10-14

APPENDIX B

TABLE B11.- RUN 11, AUTONOMOUS/MODIFIED LM/ALTITUDE VELOCITY/O SLOPE

Flight condition	Altitude, ft	Velocity, fps		Pitch angle, deg	Pitch rate, deg/sec	Time, sec	Fuel used, lb	Beams unlocked	Time to reacquire, sec
		Roll axis	Cross axis						
Initial	4600	123	0	-90	0	0	0	----	----
Mid-pitchup	----	----	----	----	----	----	----	----	----
Max. pitchup	----	----	----	----	----	----	----	----	----
Thrust aligned	----	----	----	----	----	----	----	----	----
Encounter contour	2516.8	146.3	-.2	-89.6	.3	15.6	30.7	----	----
Constant vel	50	12.3	.25	-92.2	1.24	45.6	117.5	----	----
Cutoff eng	8.1	12.5	-.17	-88.9	.64	49	124.4	----	----
Land	.92	18.3	-.1	-89.8	.64	49.4	124.4	----	----
Remarks:									

APPENDIX B

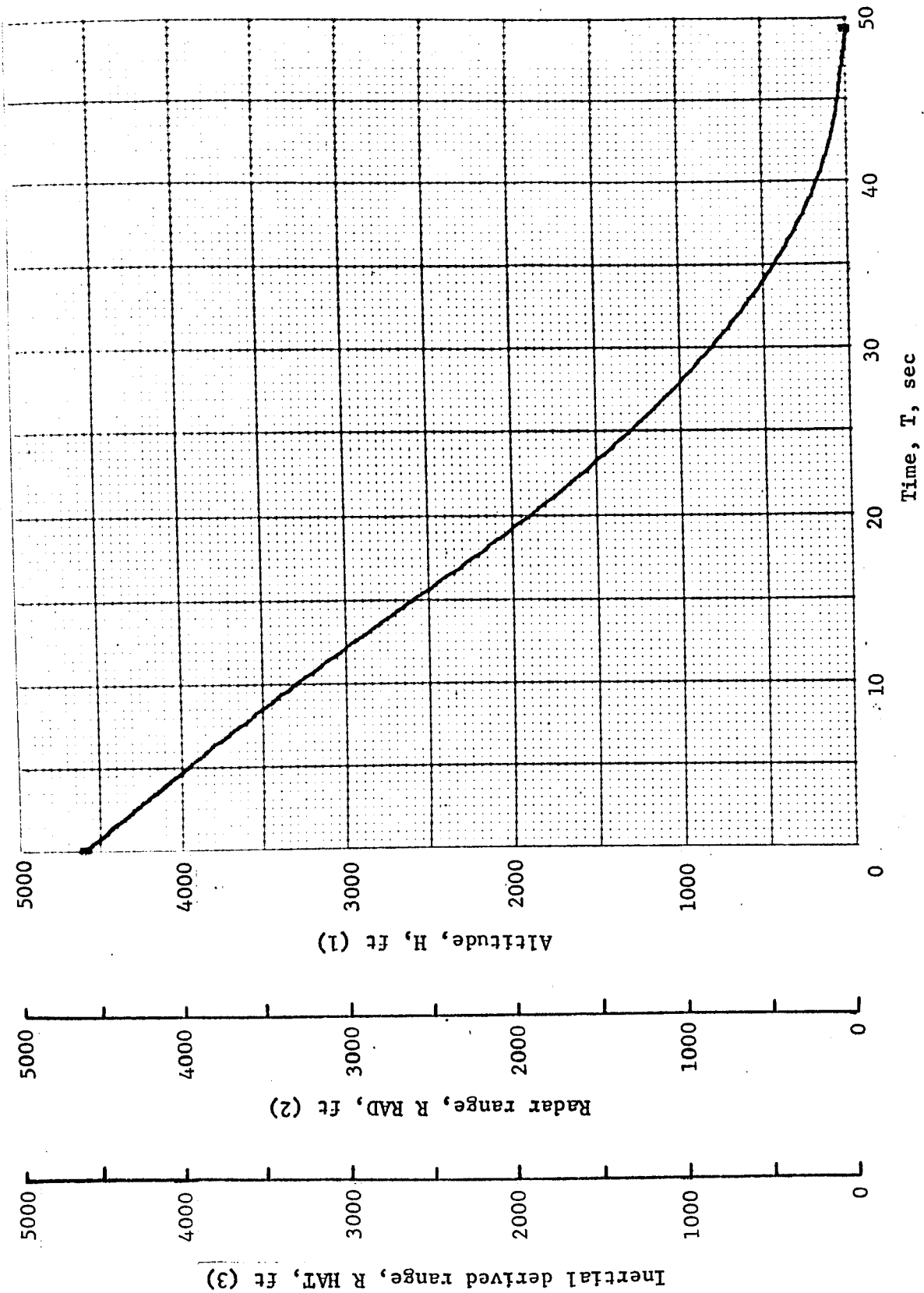


Figure B141.- Soft Lander, Run 11-1

APPENDIX B

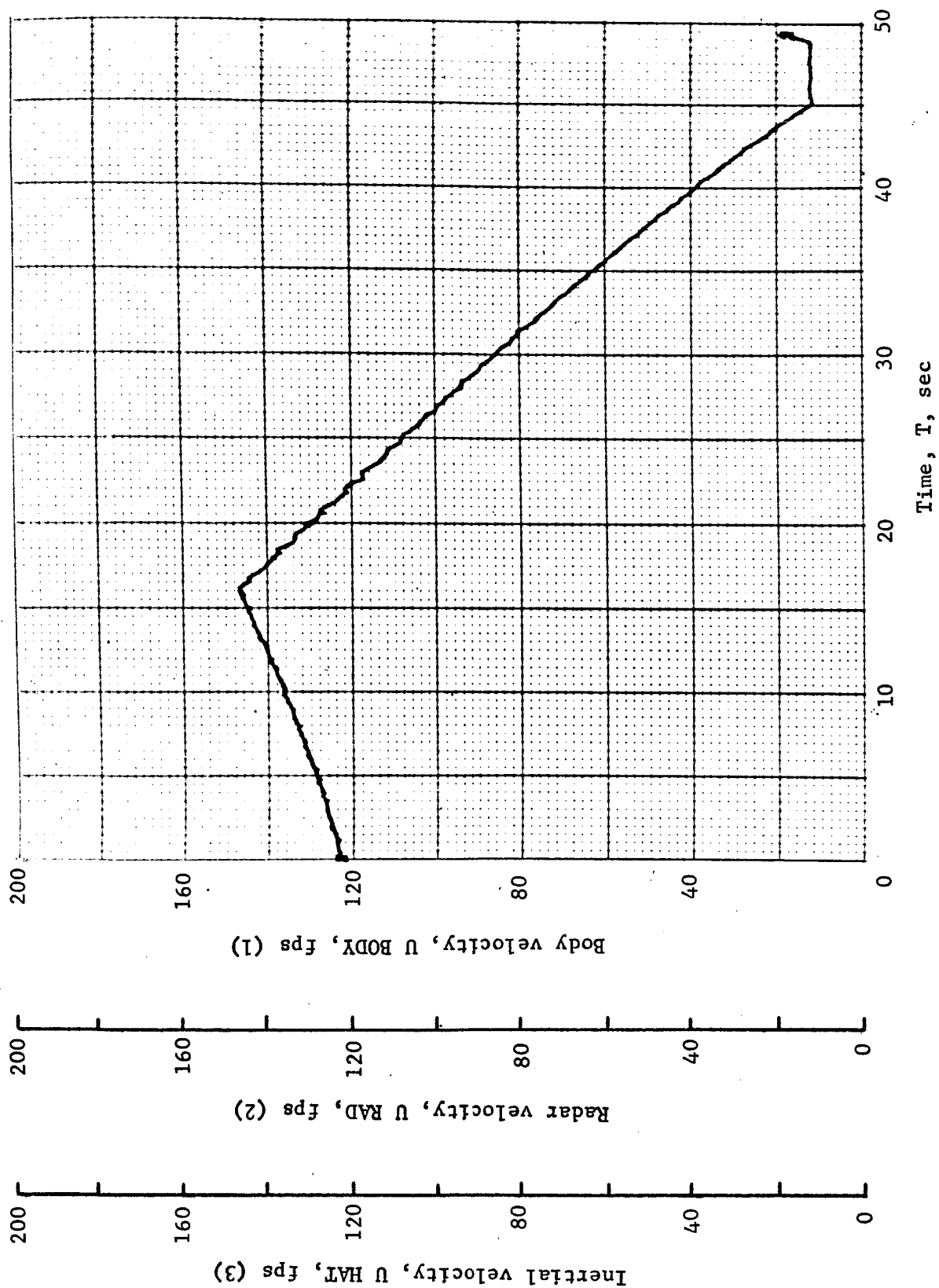


Figure B142.- Soft Lander, Run 11-2

APPENDIX B

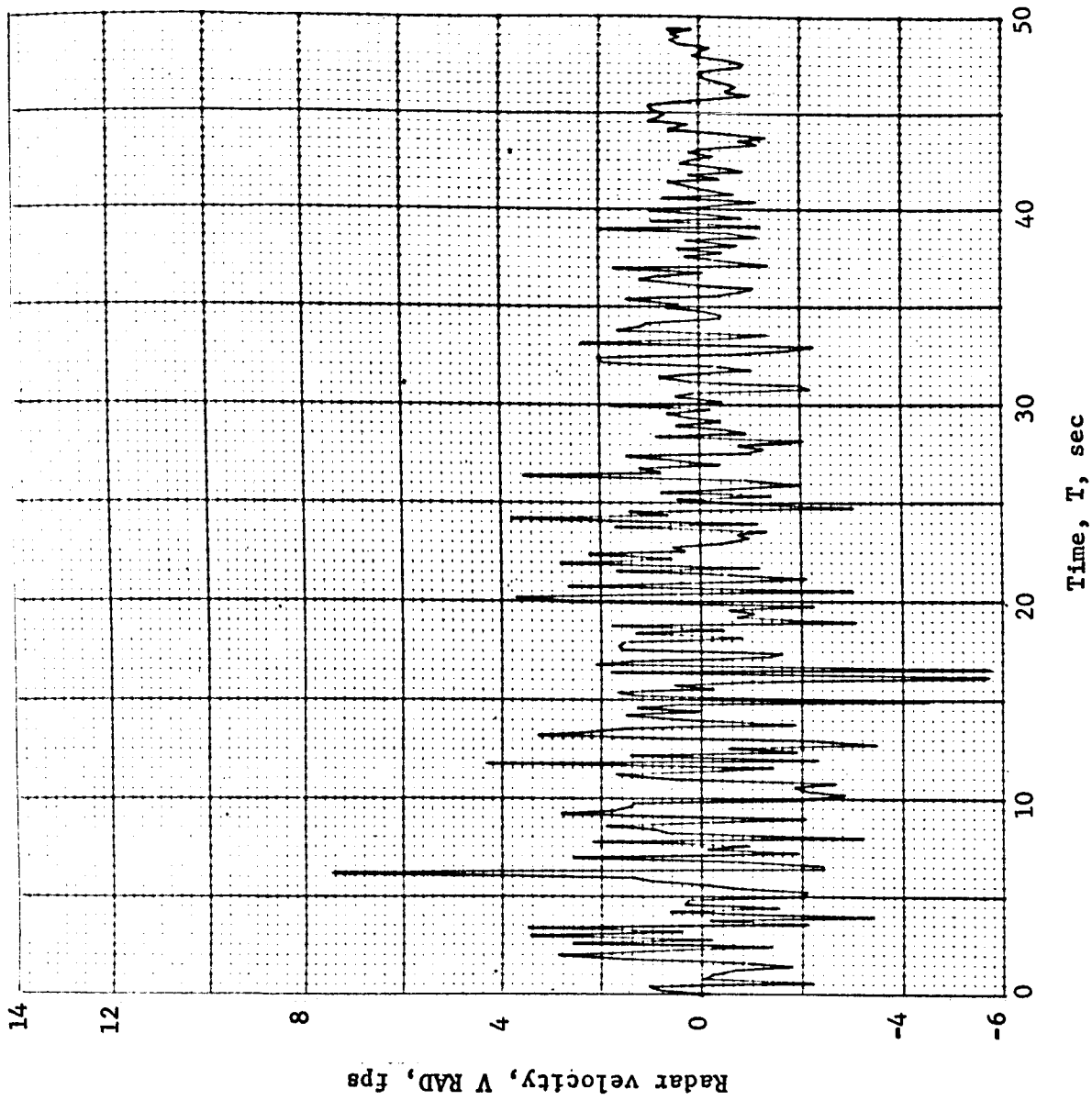


Figure B143.- Soft Lander, Run 11-3

APPENDIX B

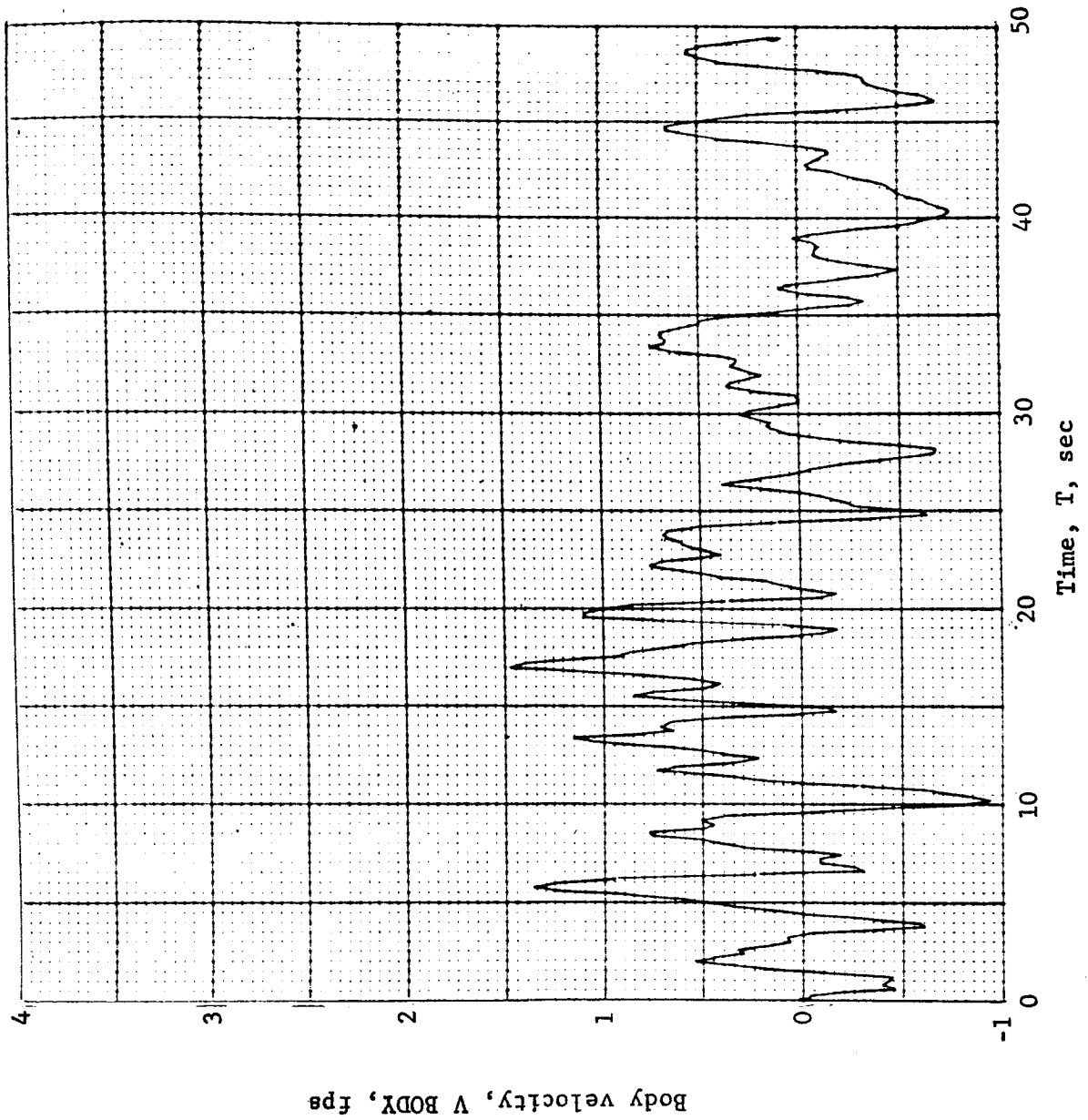


Figure B144.- Soft Lander, Run 11-4

APPENDIX B

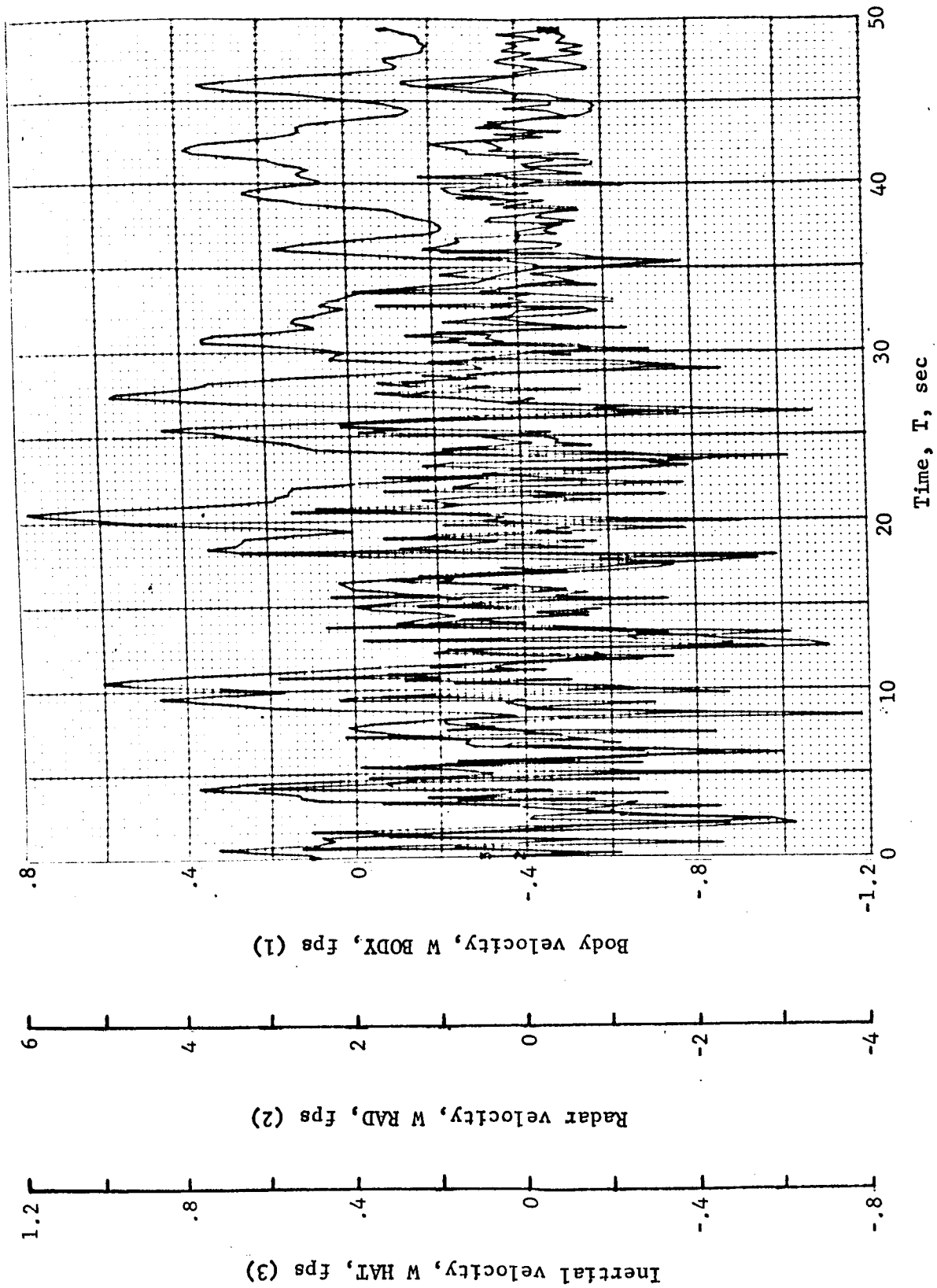


Figure B145.- Soft Lander, Run 11-5

APPENDIX B

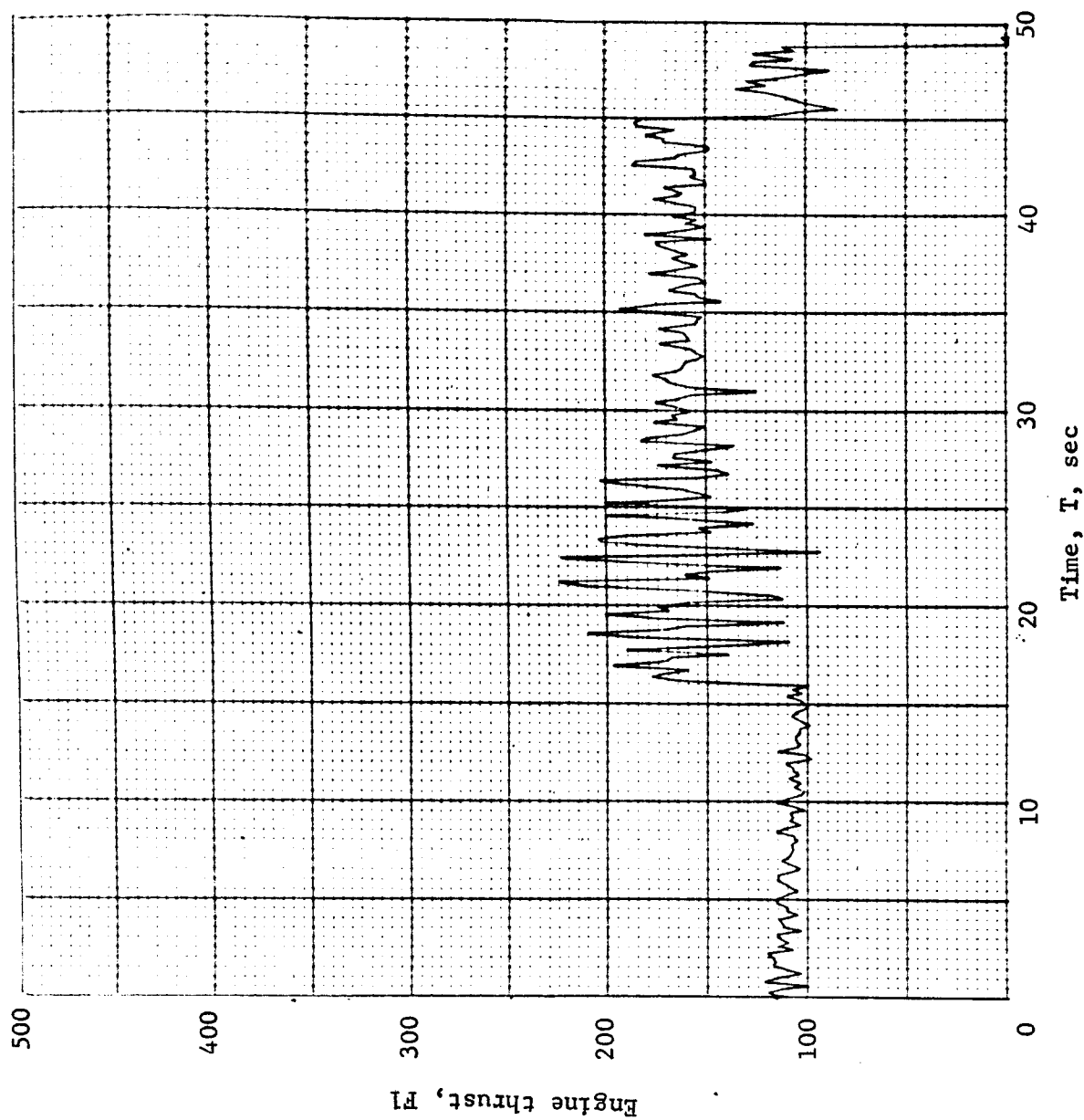


Figure B146.- Soft Lander, Run 11-6

APPENDIX B

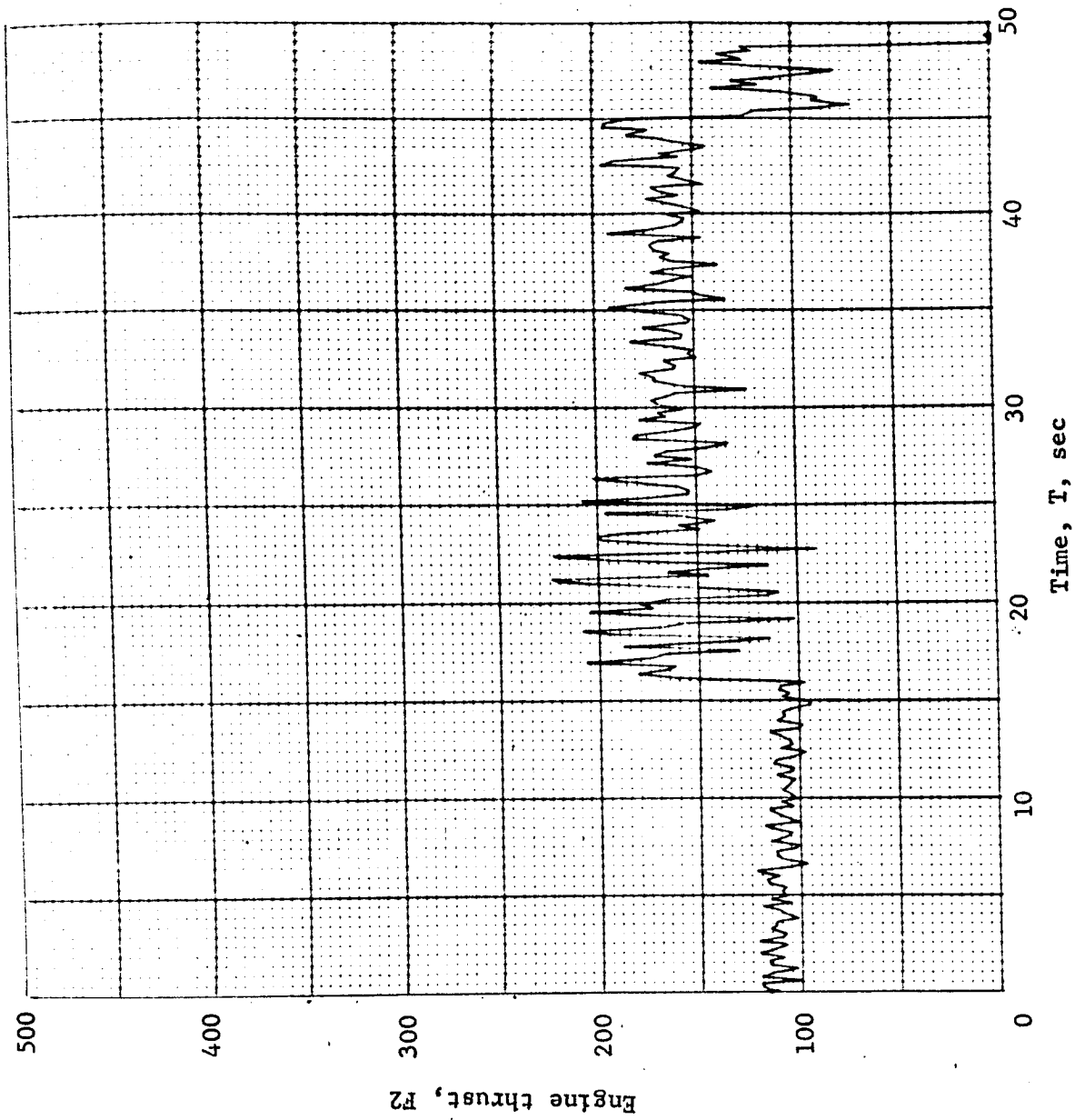


Figure B147.- Soft Lander, Run 11-7

APPENDIX B

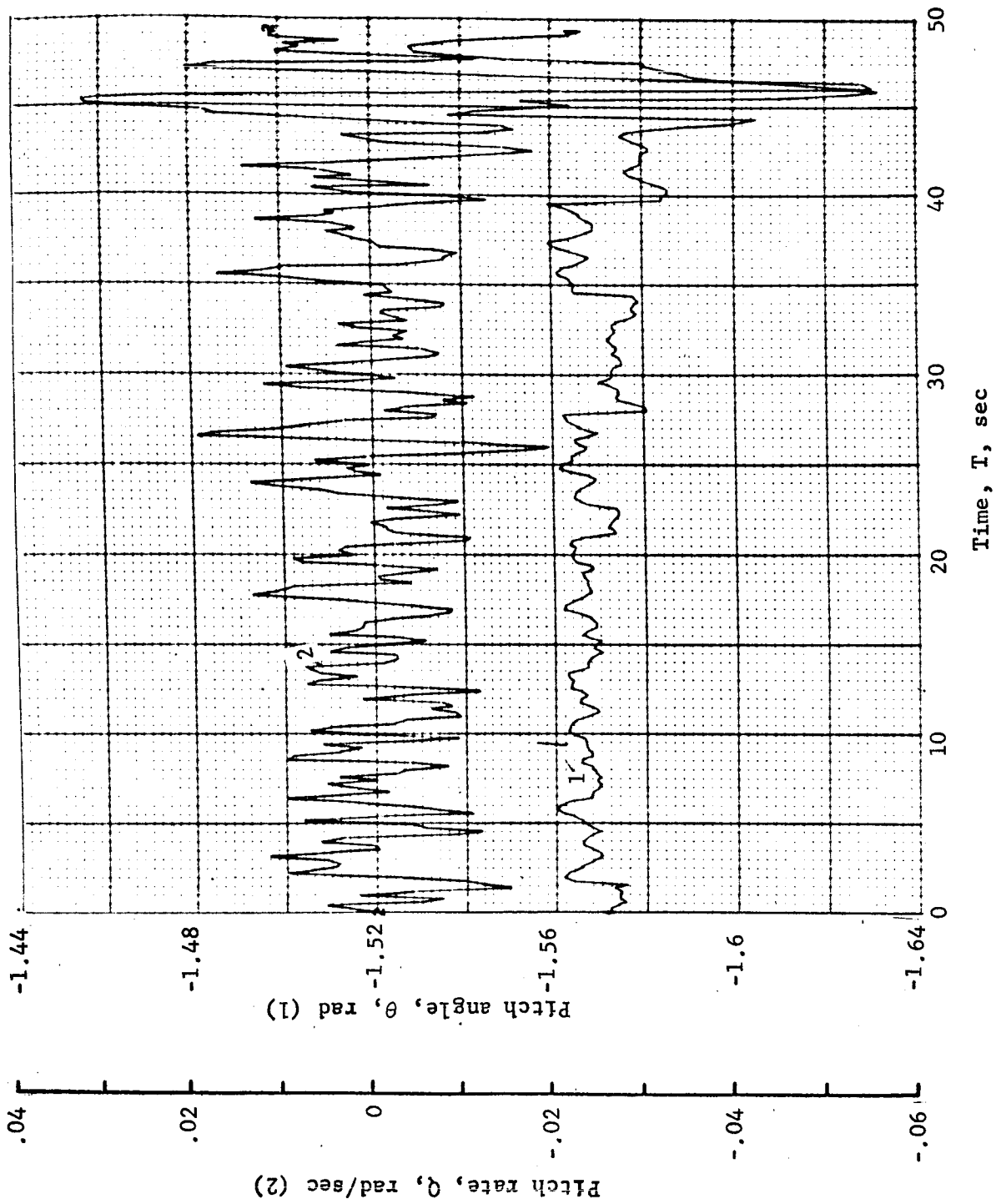


Figure B148.- Soft Lander, Run 11-8

APPENDIX B

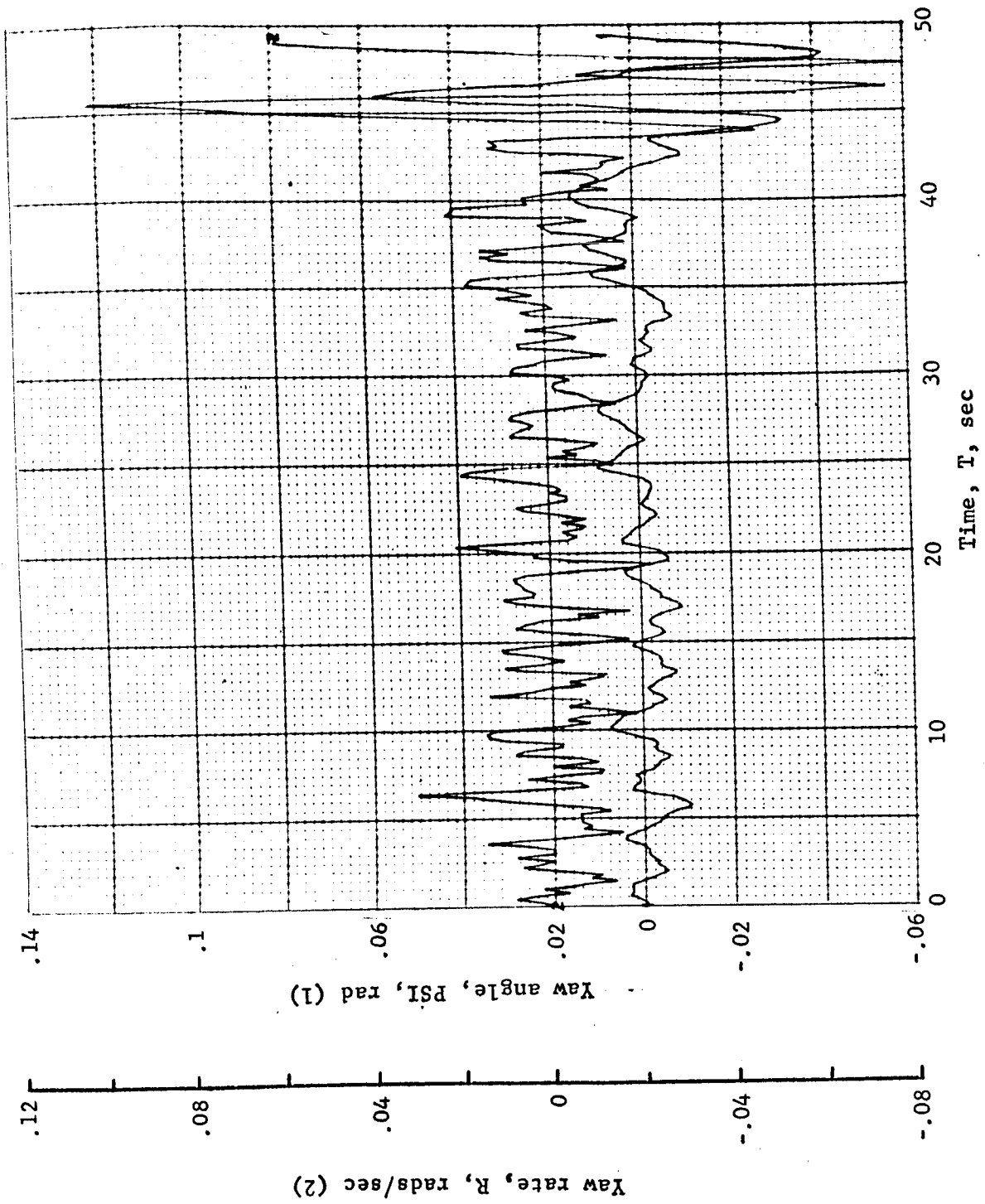


Figure B149.- Soft Lander, Run 11-9

APPENDIX B

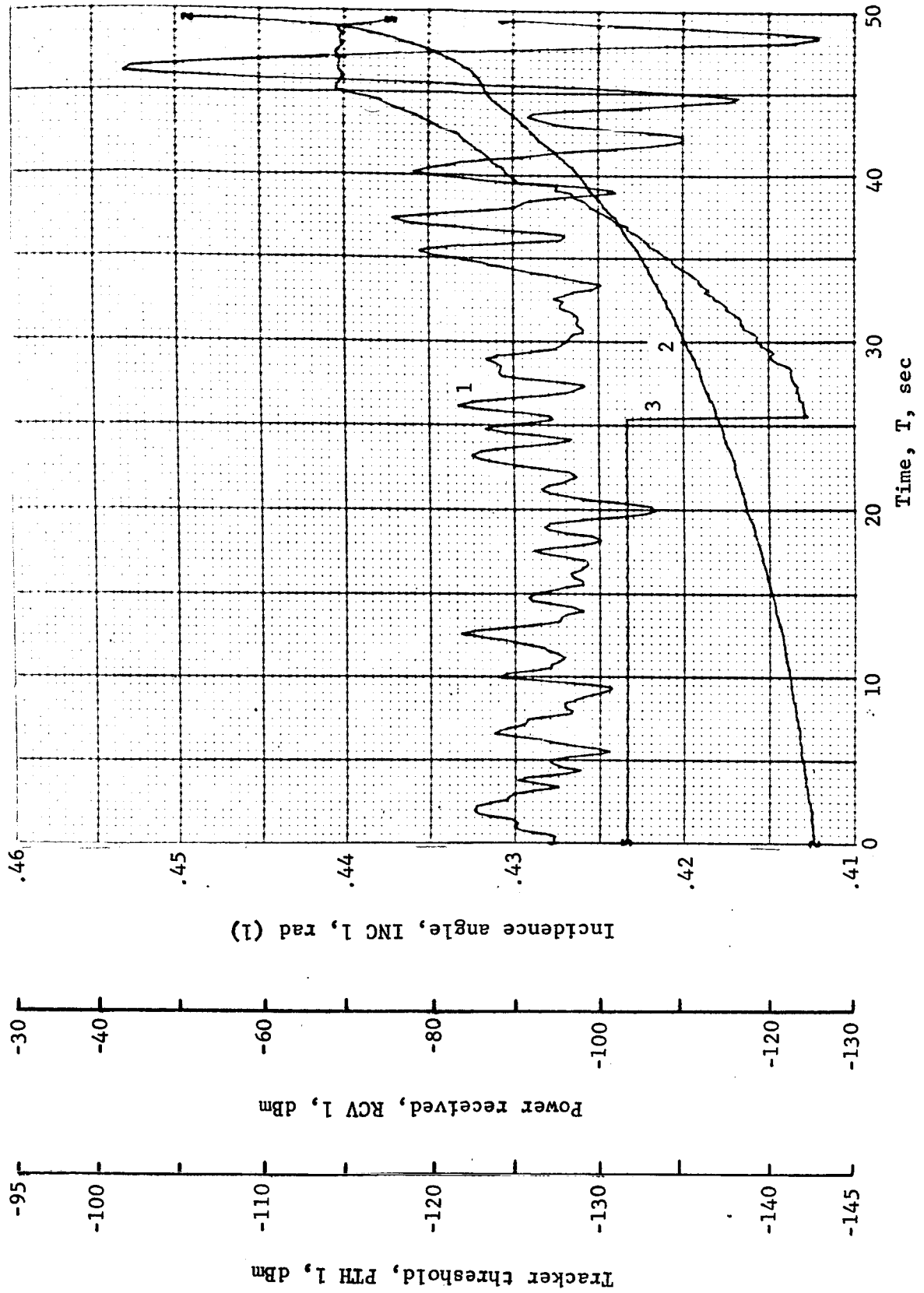


Figure B150.- Soft Lander, Run 11-10

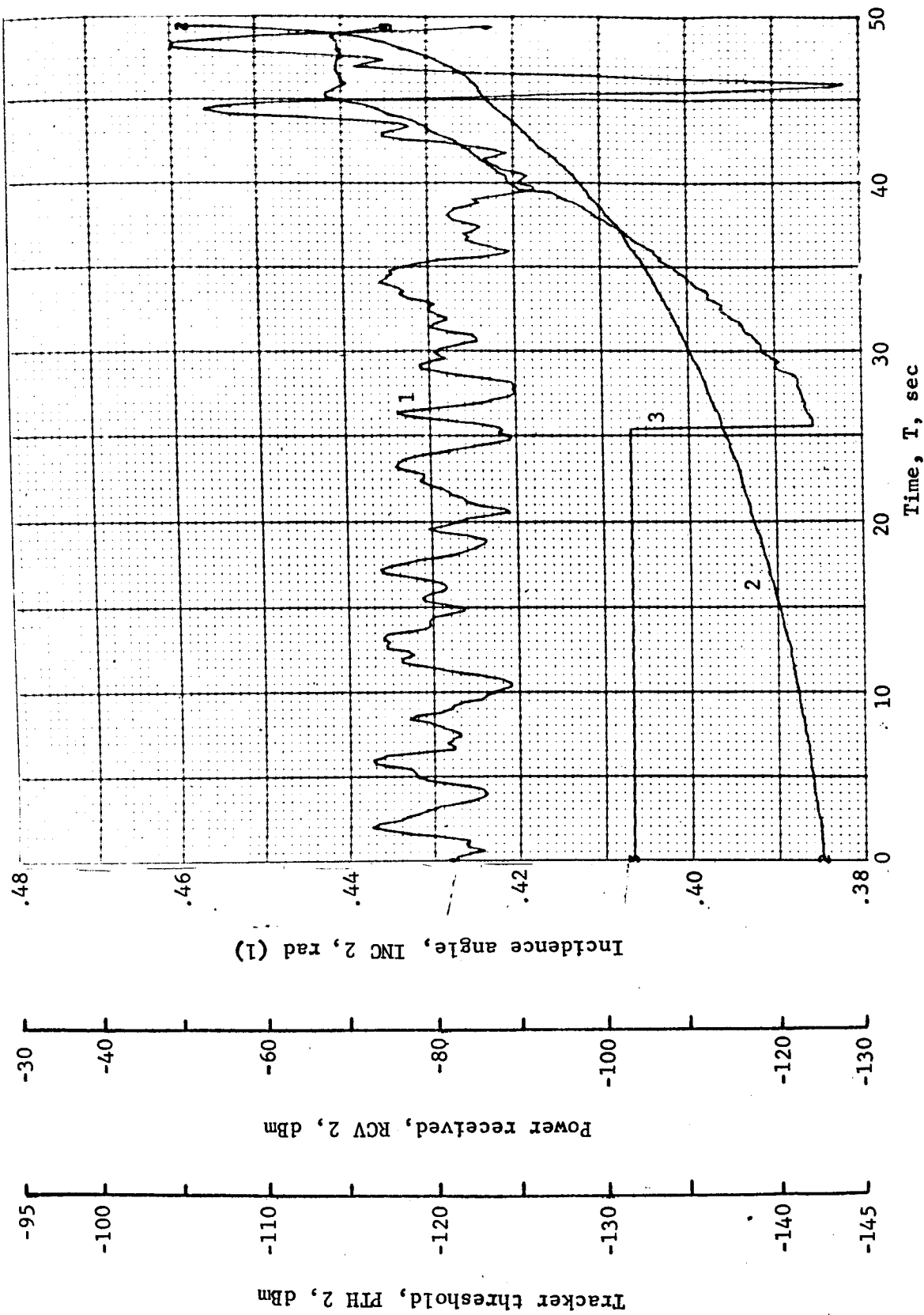


Figure B151.- Soft Lander, Run 11-11

APPENDIX B

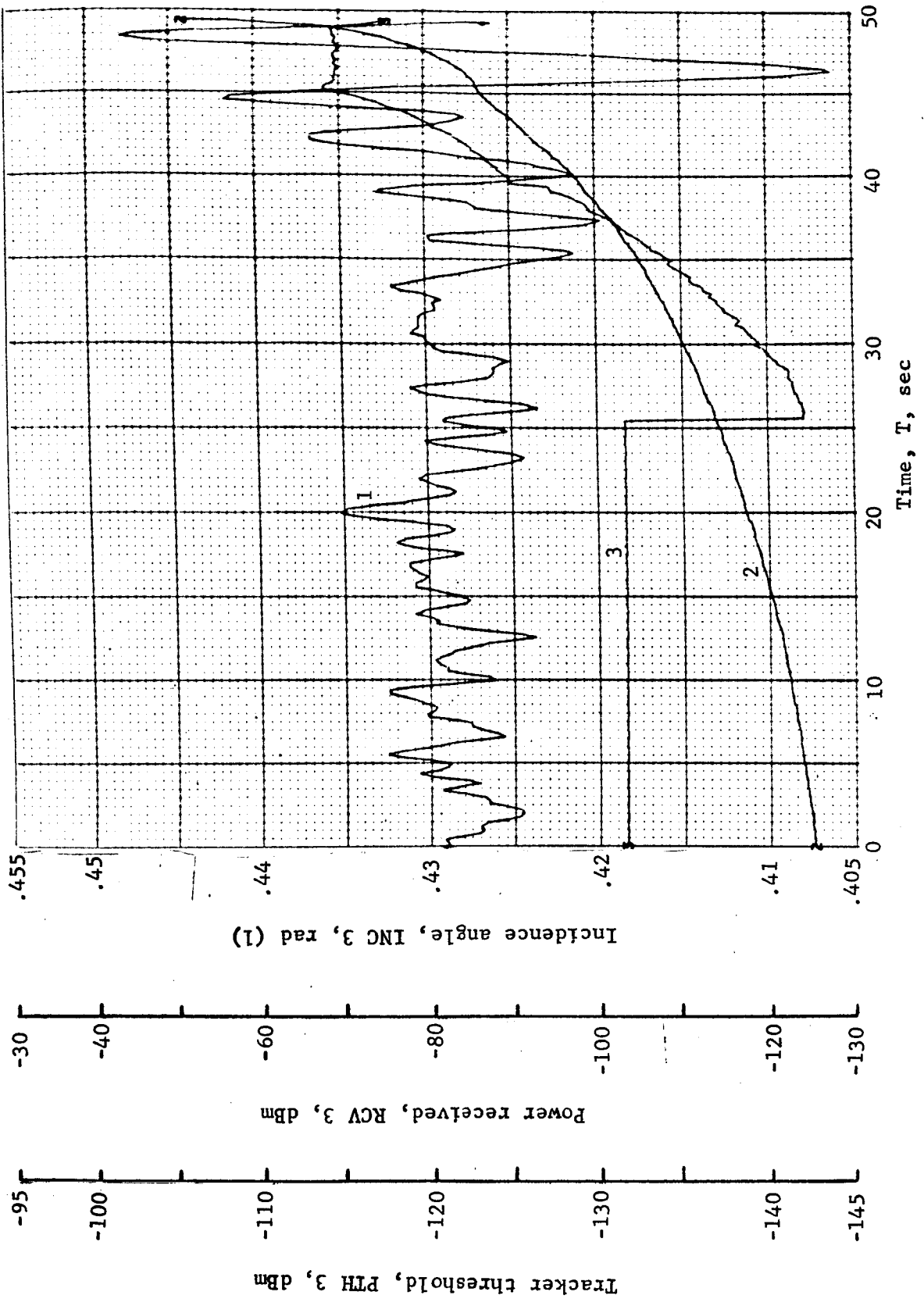


Figure B152.- Soft Lander, Run 11-12

APPENDIX B

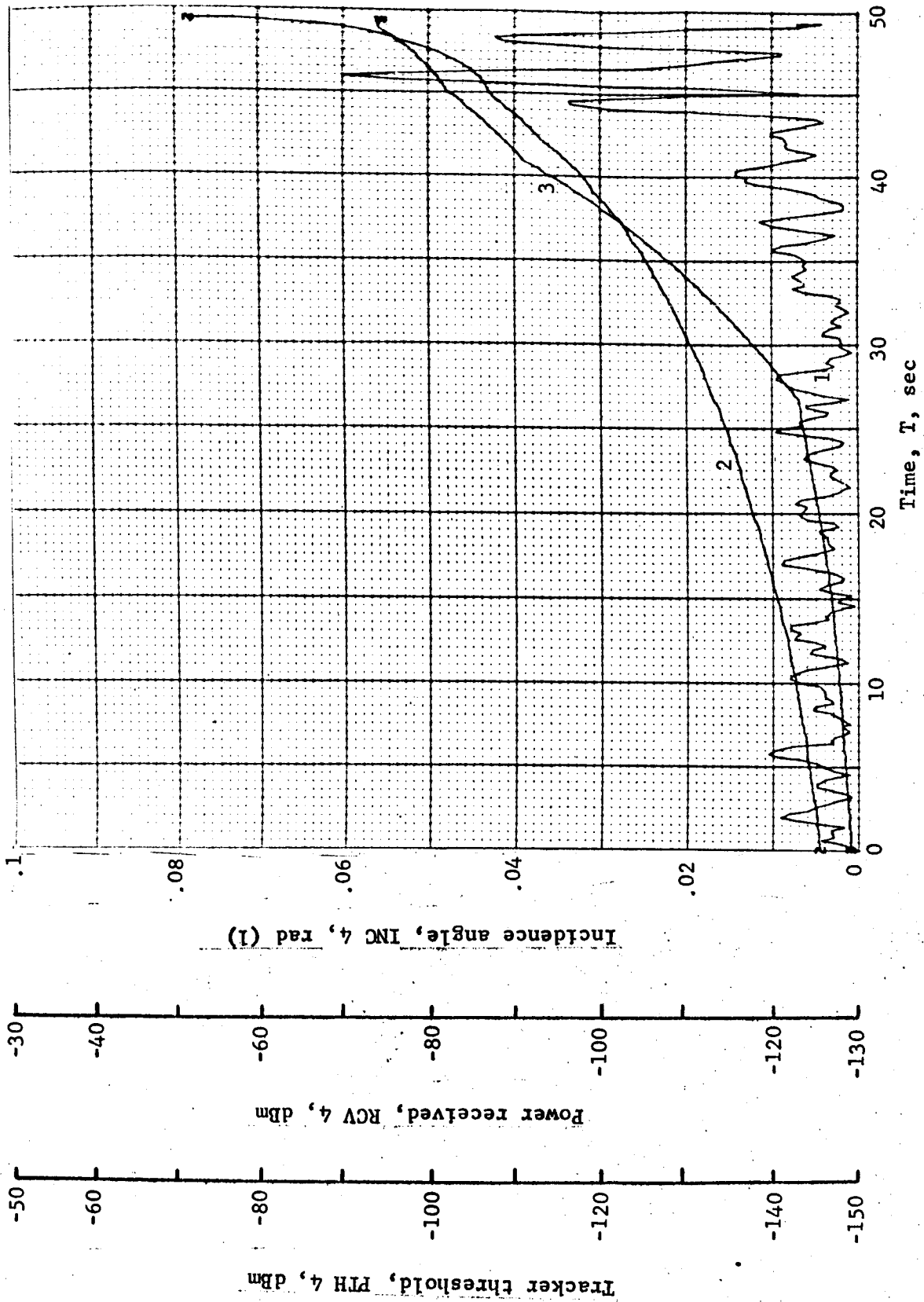


Figure B153.- Soft Lander, Run 11-13

APPENDIX B

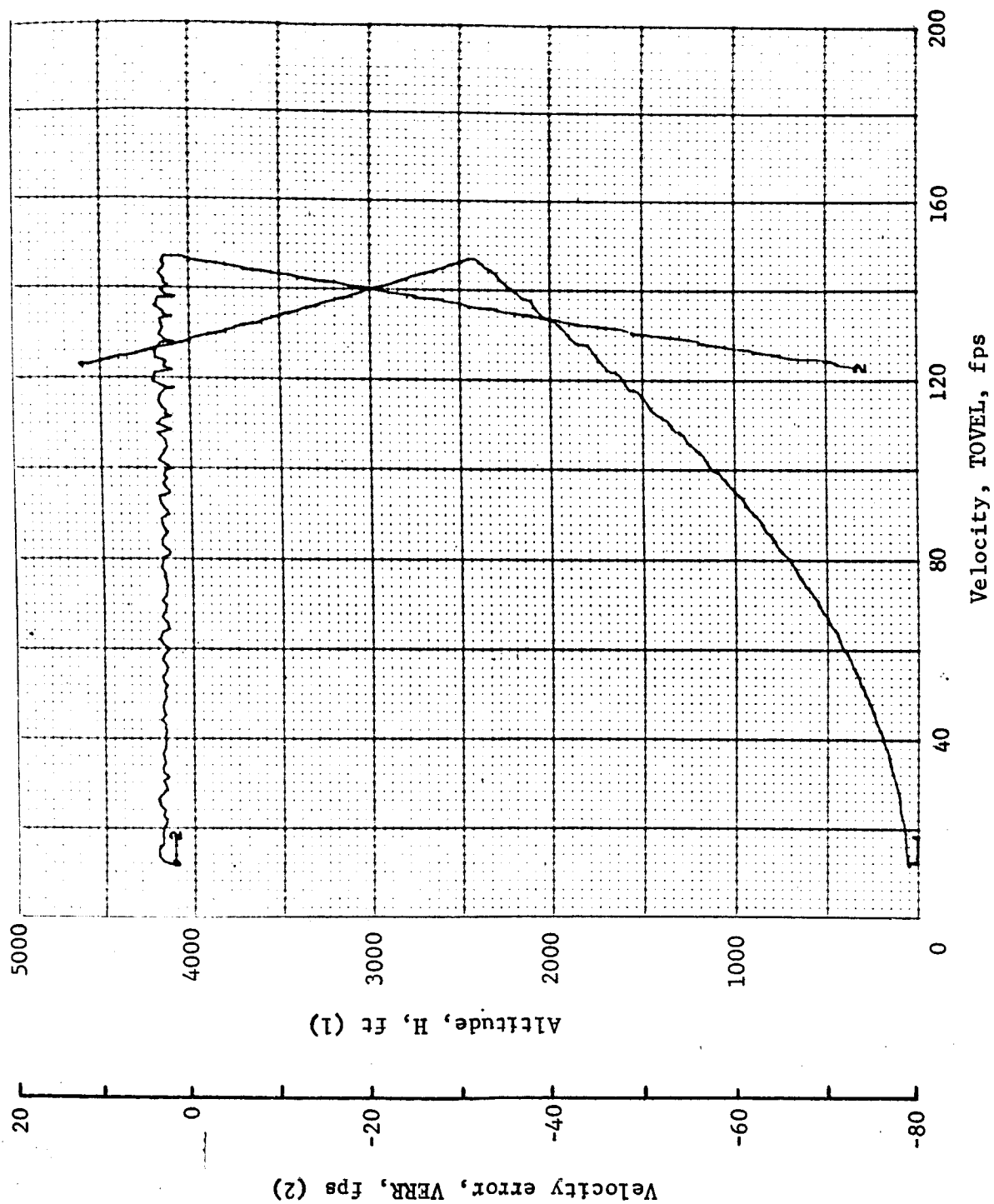


Figure B154.- Soft Lander, Run 11-14

APPENDIX B

TABLE B12.- RUN 12, CONFIGURATION 1B/LM RADAR/RANGE VELOCITY/26.7° DOWNSLOPE

Flight condition	Altitude, ft	Velocity, fps		Pitch angle, deg	Pitch rate, deg/sec	Time, sec	Fuel used, lb	Beams unlocked	Time to reacquire, sec
		Roll axis	Cross axis						
Initial	2300	165	-170	-90	0	0	0	-----	----
Mid-pitchup	2224	218.5	-81	-64	30.6	1	2.7	4	----
Max. pitchup	2111	225.3	13.7	-43	-.8	2.4	6.1	3, 4	----
Thrust aligned	2111	225.3	13.7	-43	-.8	2.4	6.1	3, 4	----
Encounter contour	1493	205.9	13.4	-55	-2.	8.2	19.1	-----	----
Constant vel	56.5	12.9	.07	-89.6	1.5	27.2	85.5	4	----
Cutoff eng	14.9	14	.06	-89.5	1.5	30.4	92.6	4	----
Land	4.26	21.4	.5	-88.2	1.5	31	92.6	4	----
Remarks: Program logic caused lockout of range beam at 1 sec. Run continued under inertial control to landing.									

APPENDIX B

TABLE B13.- RUN 13, CONFIGURATION 1B/LM RADAR/RANGE VELOCITY/26.7° DOWNSLOPE

Flight condition	Altitude, ft	Velocity, fps		Pitch angle, deg	Pitch rate, deg/sec	Time, sec	Fuel used, lb	Beams unlocked	Time to reacquire, sec
		Roll axis	Cross axis						
Initial	2300	165	170	-90	0	0	0	----	----
Mid-pitchup	2224.3	218.5	-81.1	-64.2	30.6	1	2.7	----	----
Max. pitchup	2127.9	226.5	10.8	-43.4	-1.44	2.2	5.6	3	----
Thrust aligned	2161.1	228.8	2.4	-44.6	.99	1.8	4.6	3	----
Encounter contour	972.7	200.8	4.7	-64.2	-1.6	12.2	27.4	3	----
Constant vel	48.5	12.85	.67	-90.5	-2.5	24	80	3	----
Cutoff eng	9.5	12.89	.21	-90.1	.48	27	85.9	3	----
Land	.91	18.9	.3	-90.4	.45	27.5	85.9	3	----
Remarks: Program logic caused lockout of beam 3 at 1.8 sec. Run continued to landing using inertial velocity data.									

APPENDIX B

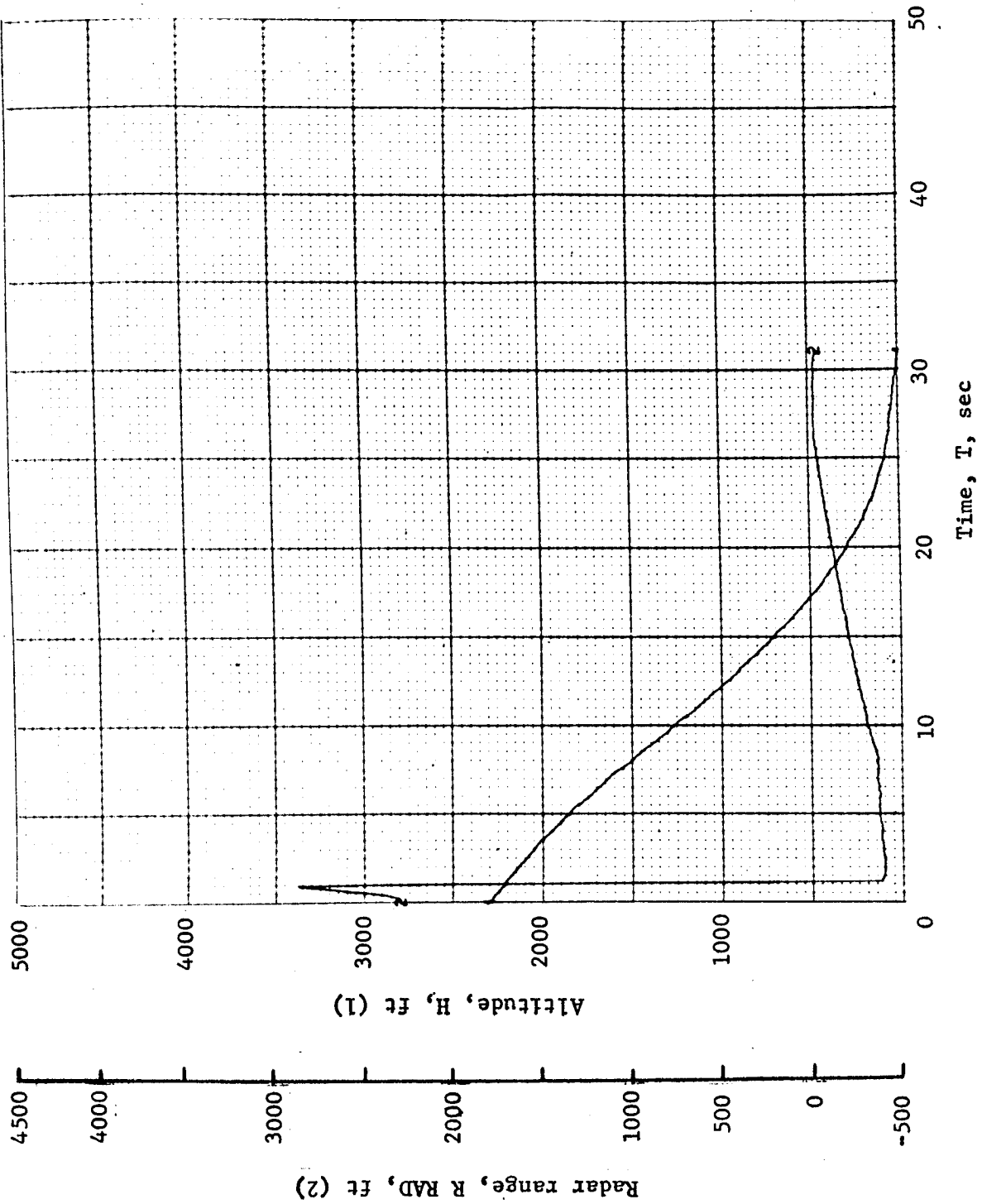


Figure B155.- Configuration 1B, Run 13-1

APPENDIX B

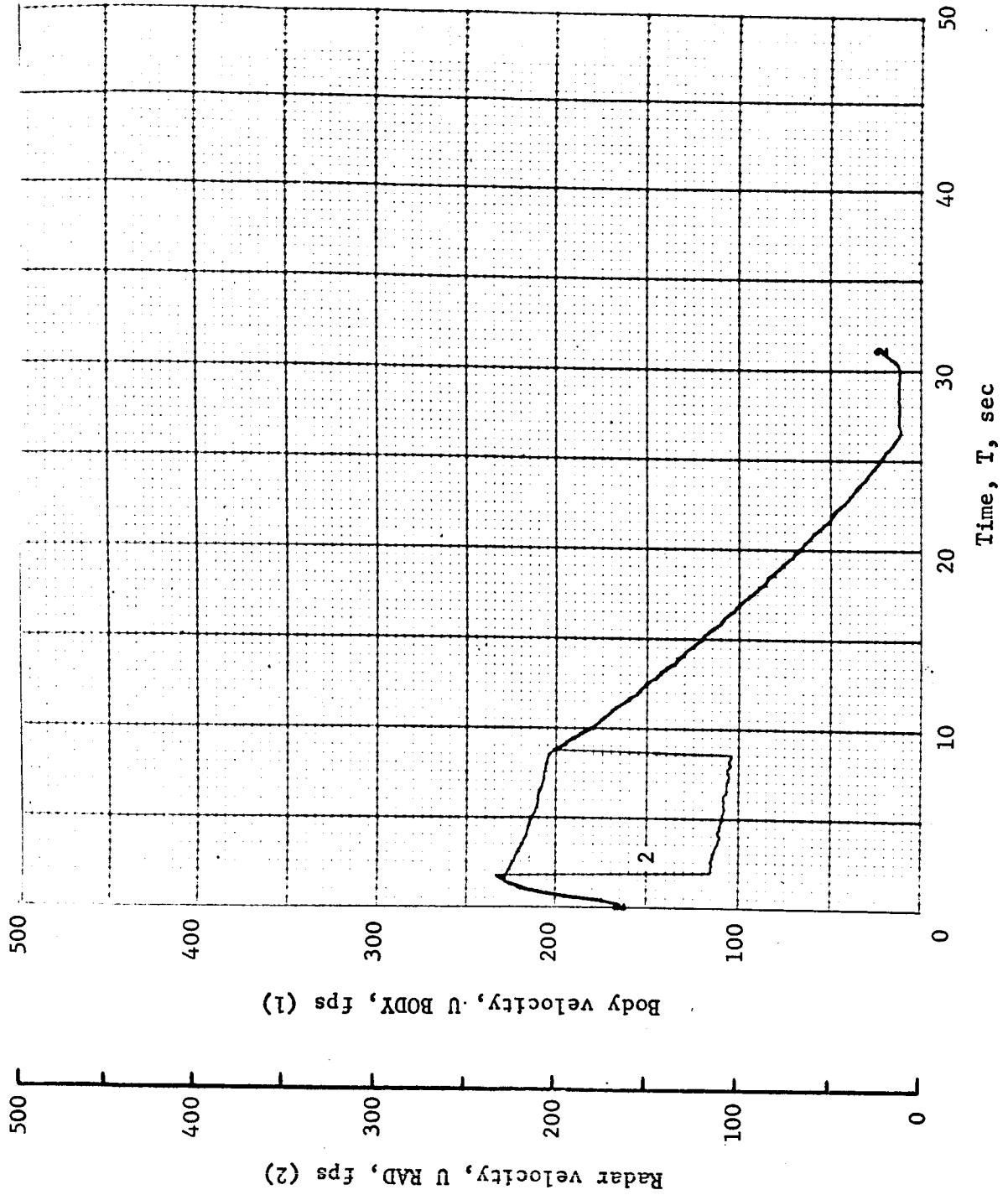


Figure B156.- Configuration 1B, Run 13-2

APPENDIX B

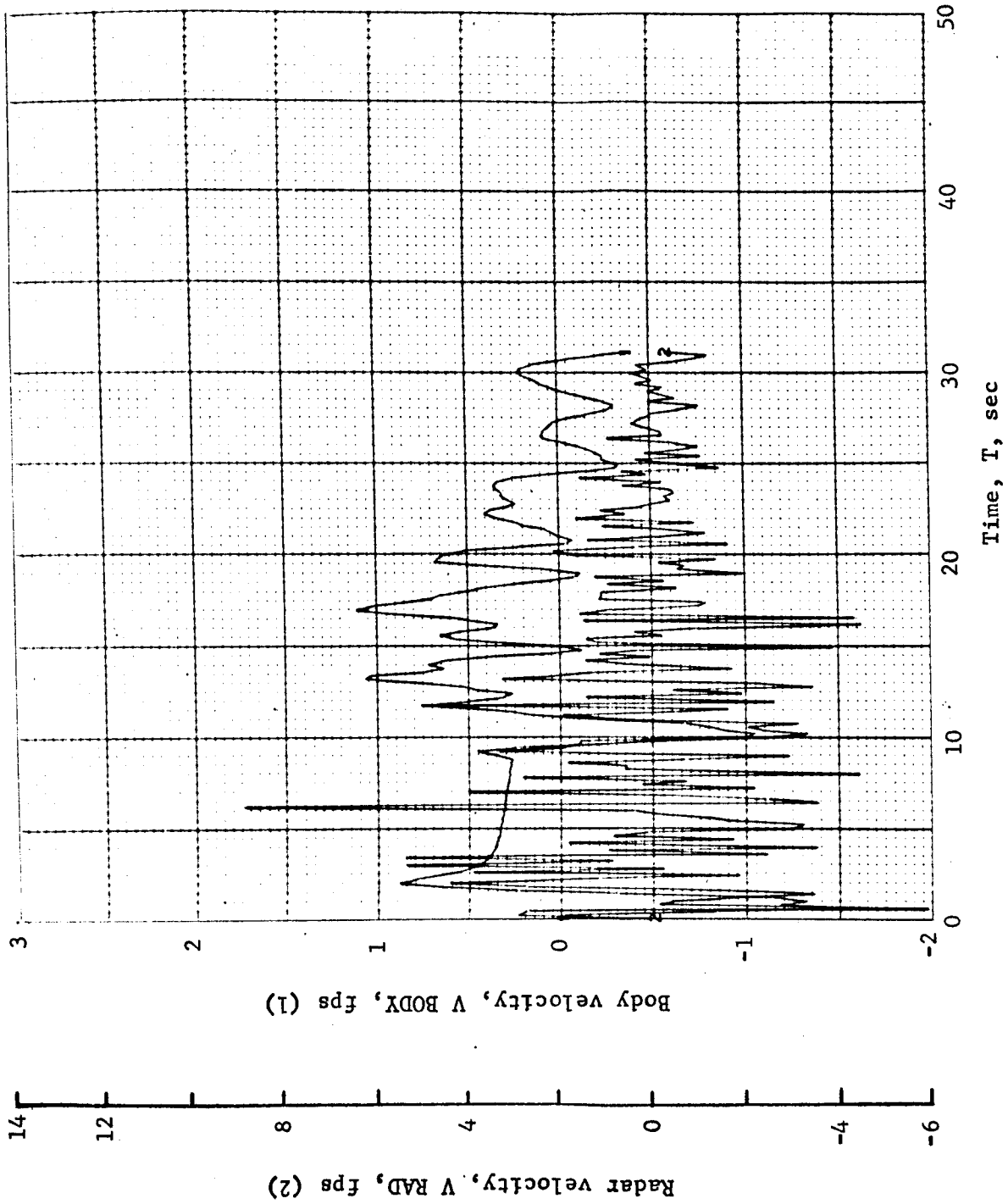


Figure B157.- Configuration 1B, Run 13-3

APPENDIX B

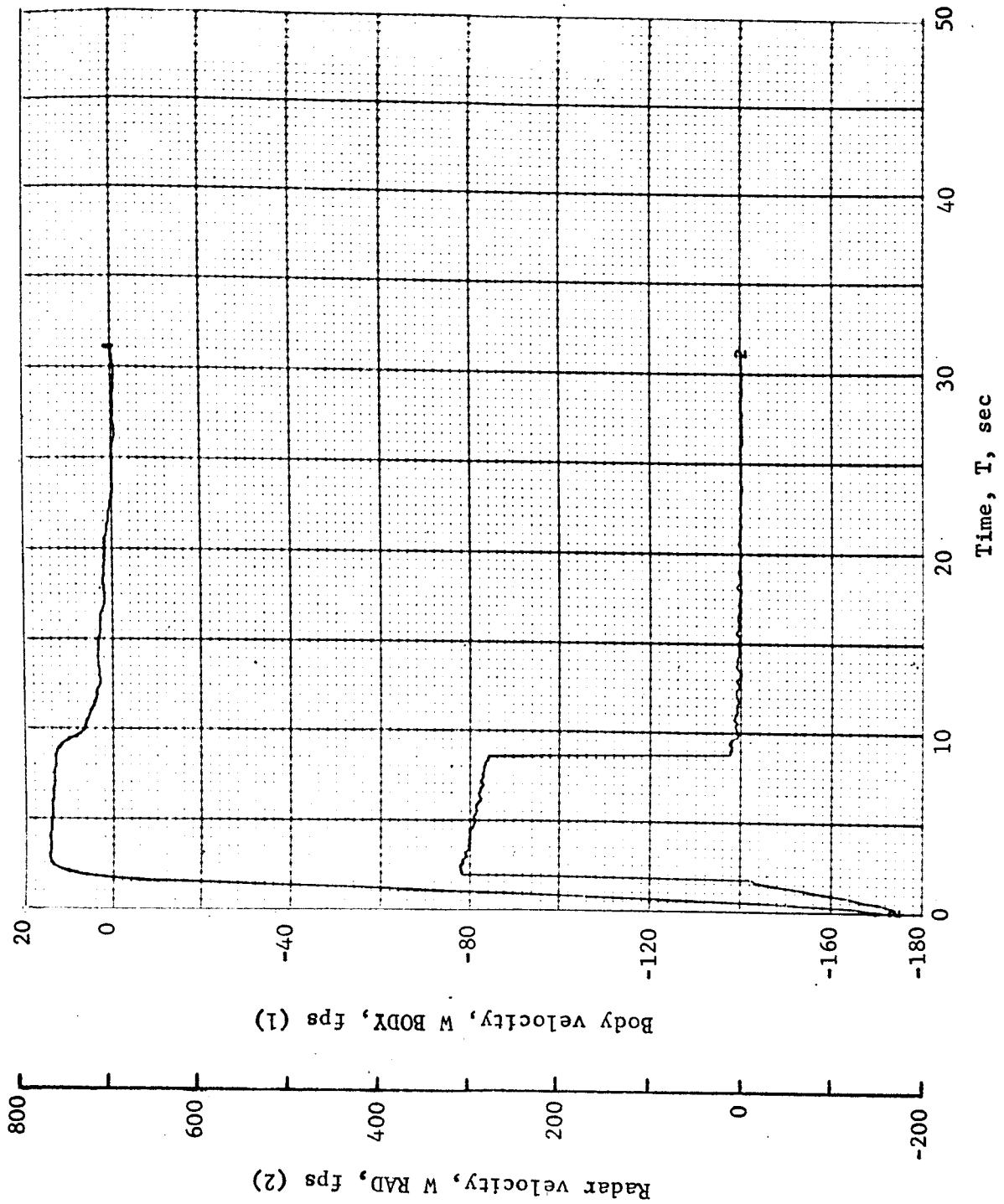


Figure B158.- Configuration 1B, Run 13-4

APPENDIX B

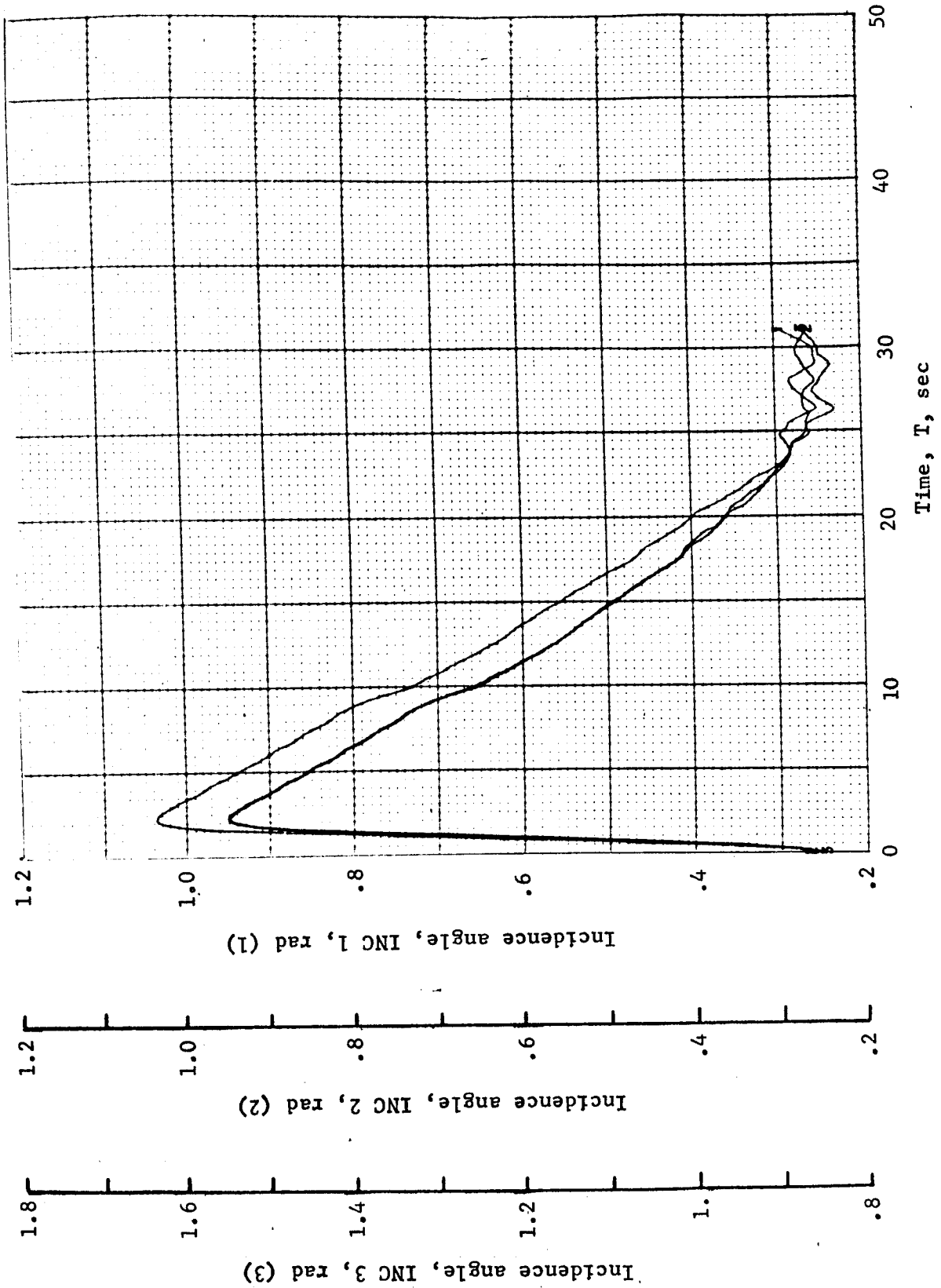


Figure B159.- Configuration 1B, Run 13-5

APPENDIX B

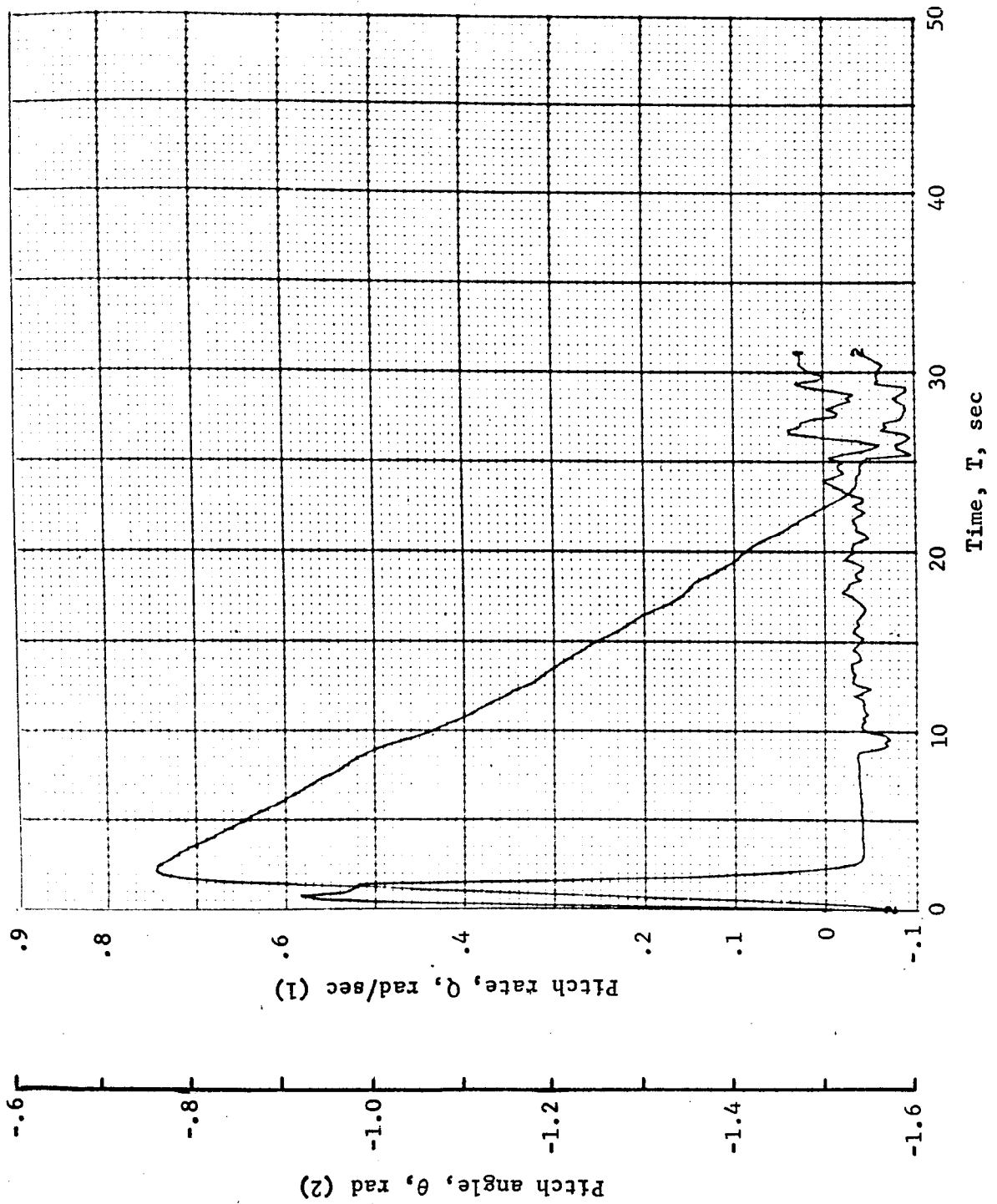


Figure B160.- Configuration 1B, Run 13-6

APPENDIX B

TABLE B14.- RUN 14, CONFIGURATION 1B/MODIFIED LM/RANGE VELOCITY/26.7° DOWNSLOPE

Flight condition	Altitude, ft	Velocity, fps		Pitch angle, deg	Pitch rate, deg/sec	Time, sec	Fuel used, lb	Beams unlocked	Time to reacquire, sec
		Roll axis	Cross axis						
Initial	2300	165	-170	-90	0	0	0	----	----
Mid-pitchup	2224.3	218.5	-81	-64.5	30.6	1	2.7	----	----
Max. pitchup	2127.9	226.4	12.7	-42.9	.34	2.2	5.6	3 at 1.8	----
Thrust aligned	2127.9	226.4	12.7	-42.9	.34	2.2	5.6	3 at 1.9	9.4
Encounter contour	983.1	201.5	7.2	-64	-3.25	12	27	----	----
Constant vel	32.66	12.0	.19	-90.3	-.65	24.2	80.6	----	----
Cutoff eng	8.35	13.	-.22	-91.2	-2.3	26.1	84.3	----	----
Land	.97	18.7	-.68	-92.6	-2.3	26.5	84.3	----	----
Remarks: Last 1B run. Checkout of S1 module used in all lander/support module runs.									

APPENDIX B

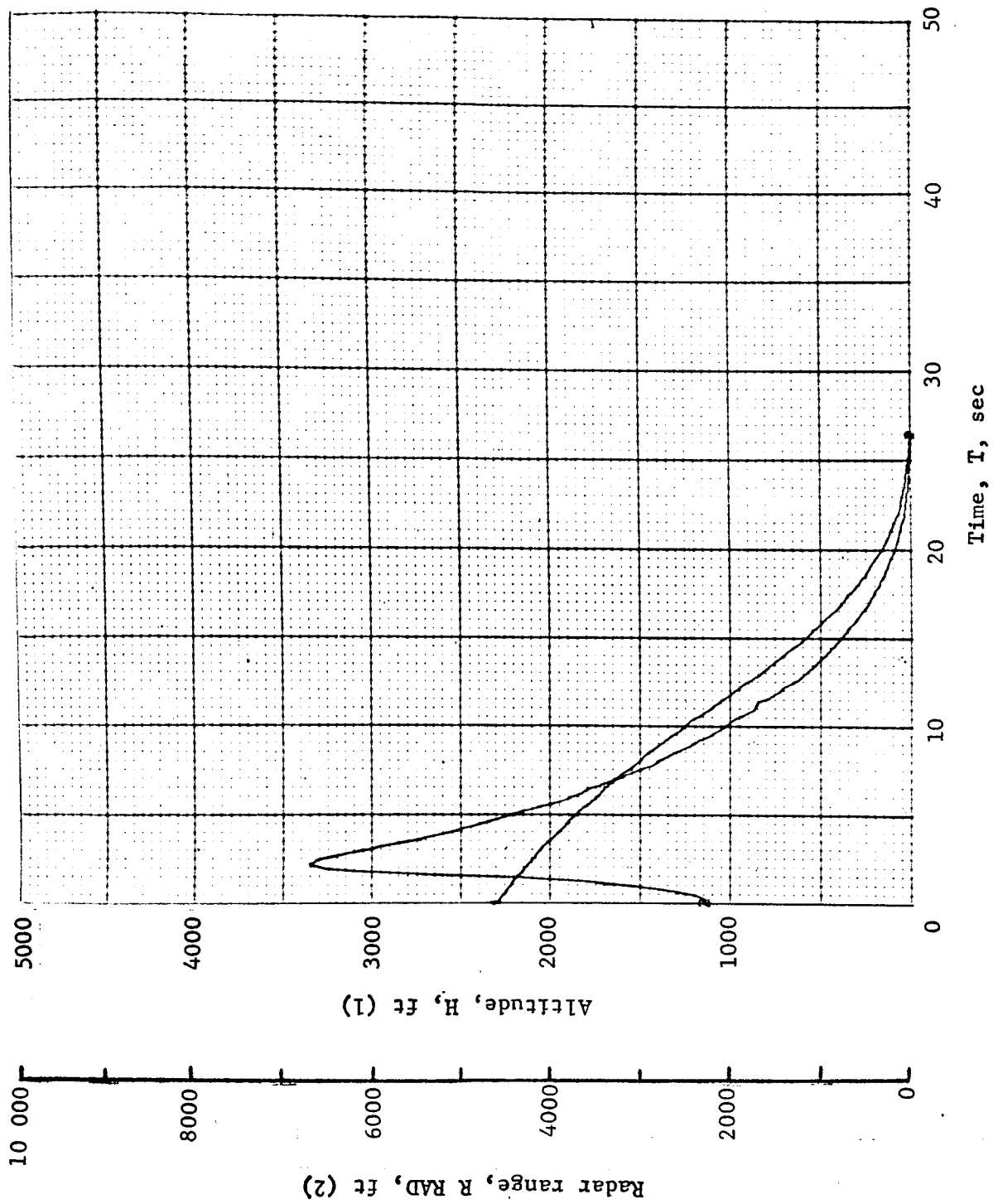


Figure B161.- Configuration 1B, Run 14-1

APPENDIX B

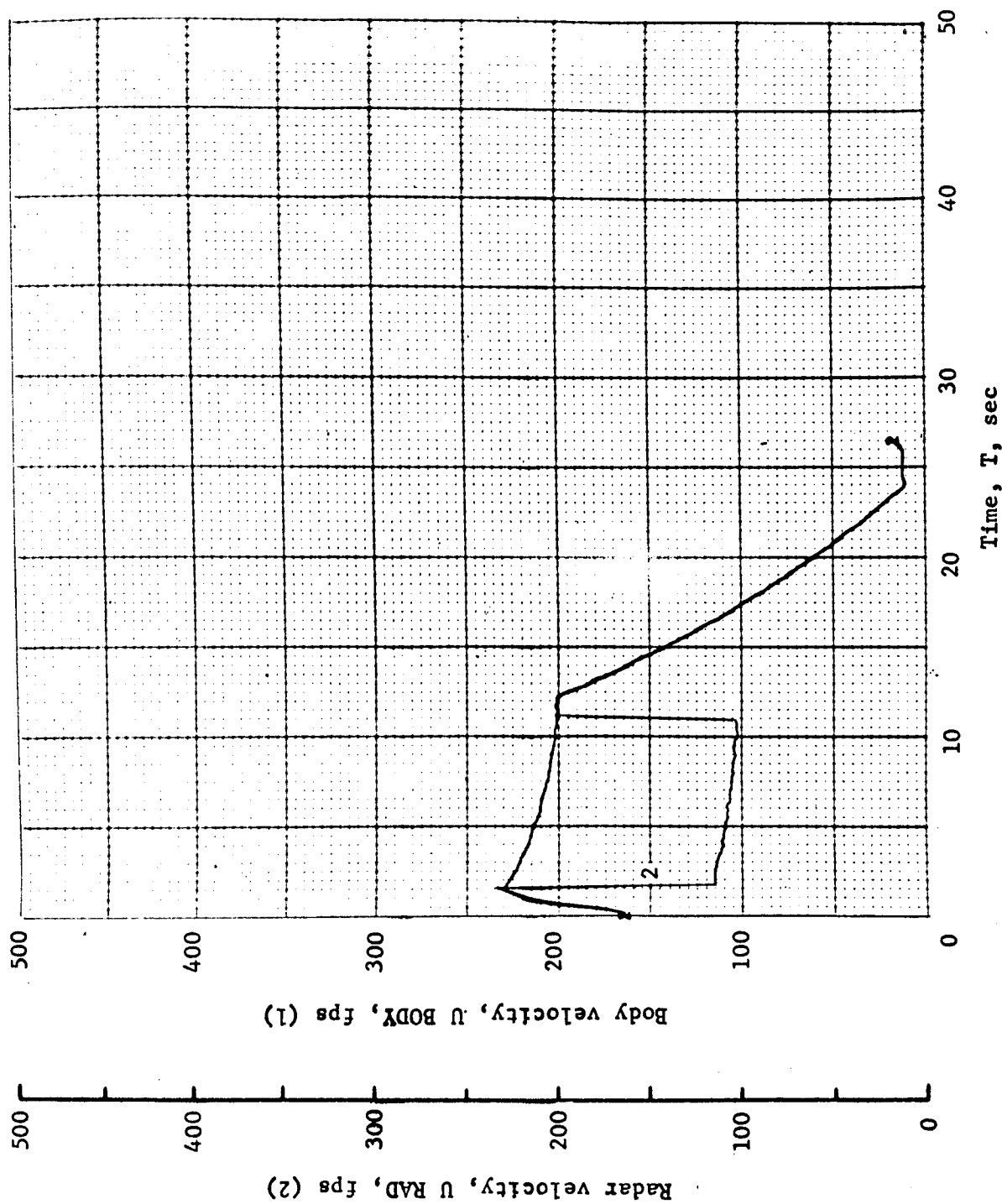


Figure B162.- Configuration 1B, Run 14-2

APPENDIX B

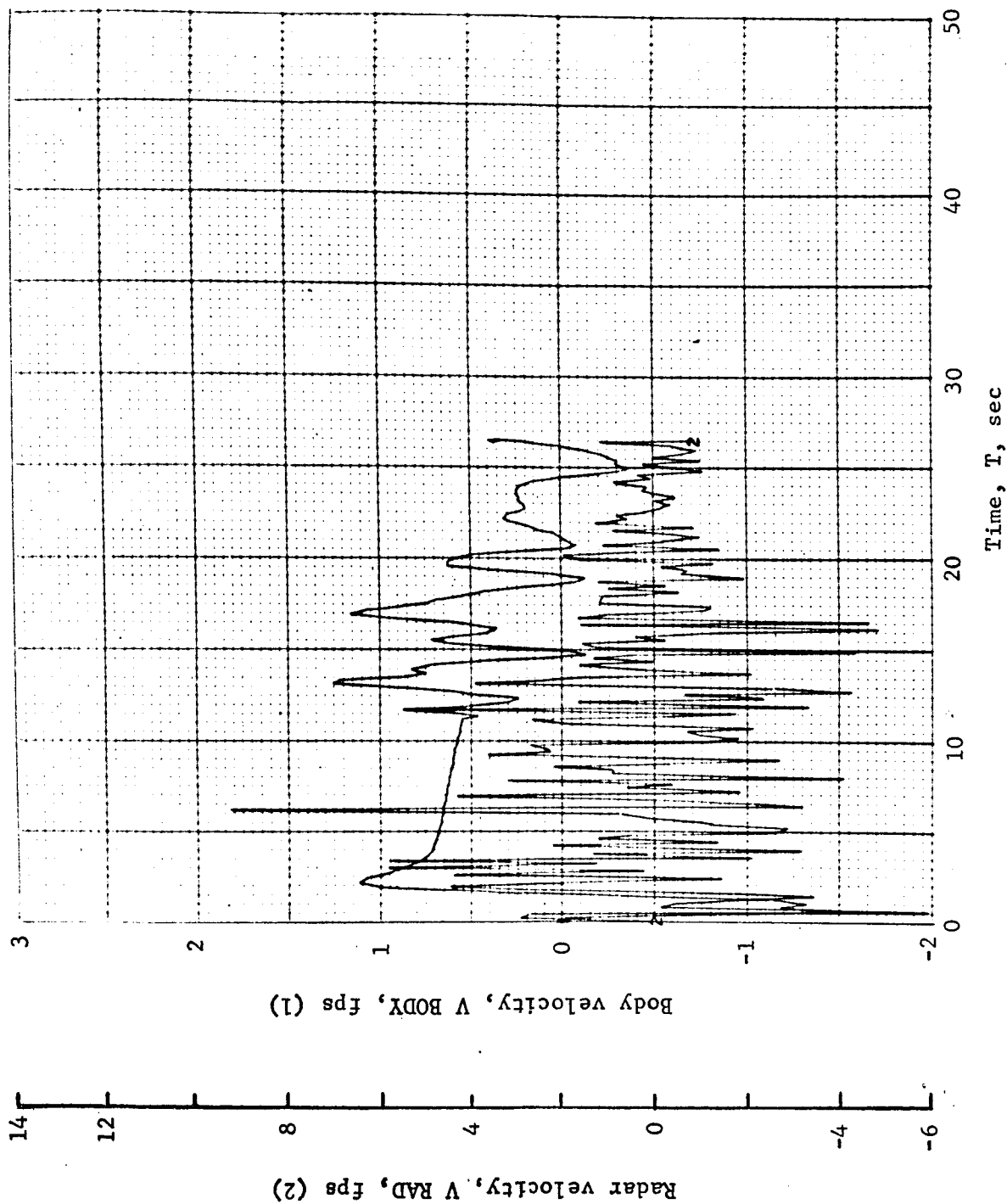


Figure B163.- Configuration 1B, Run 14-3

APPENDIX B

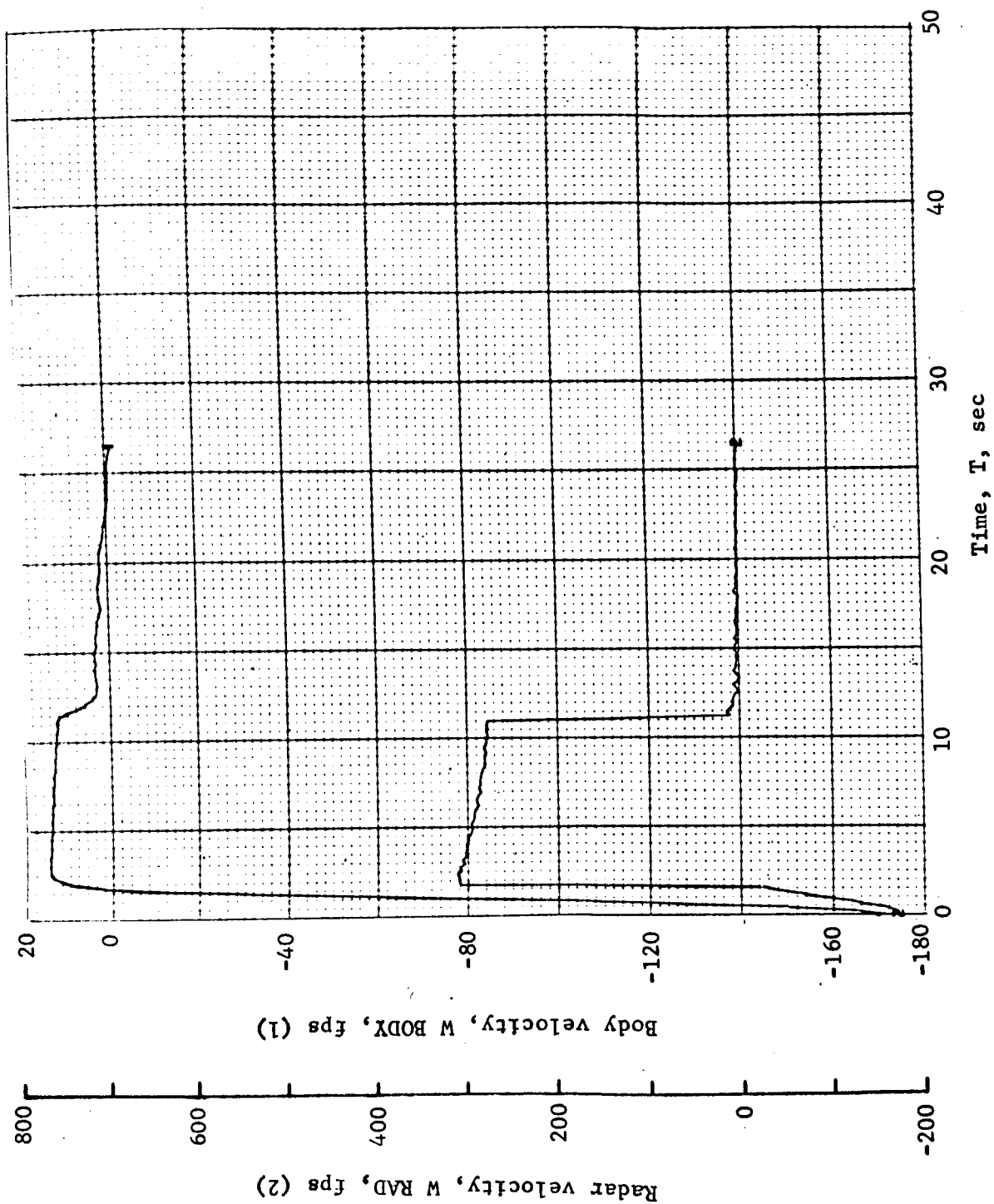


Figure B164.- Configuration 1B, Run 14-4

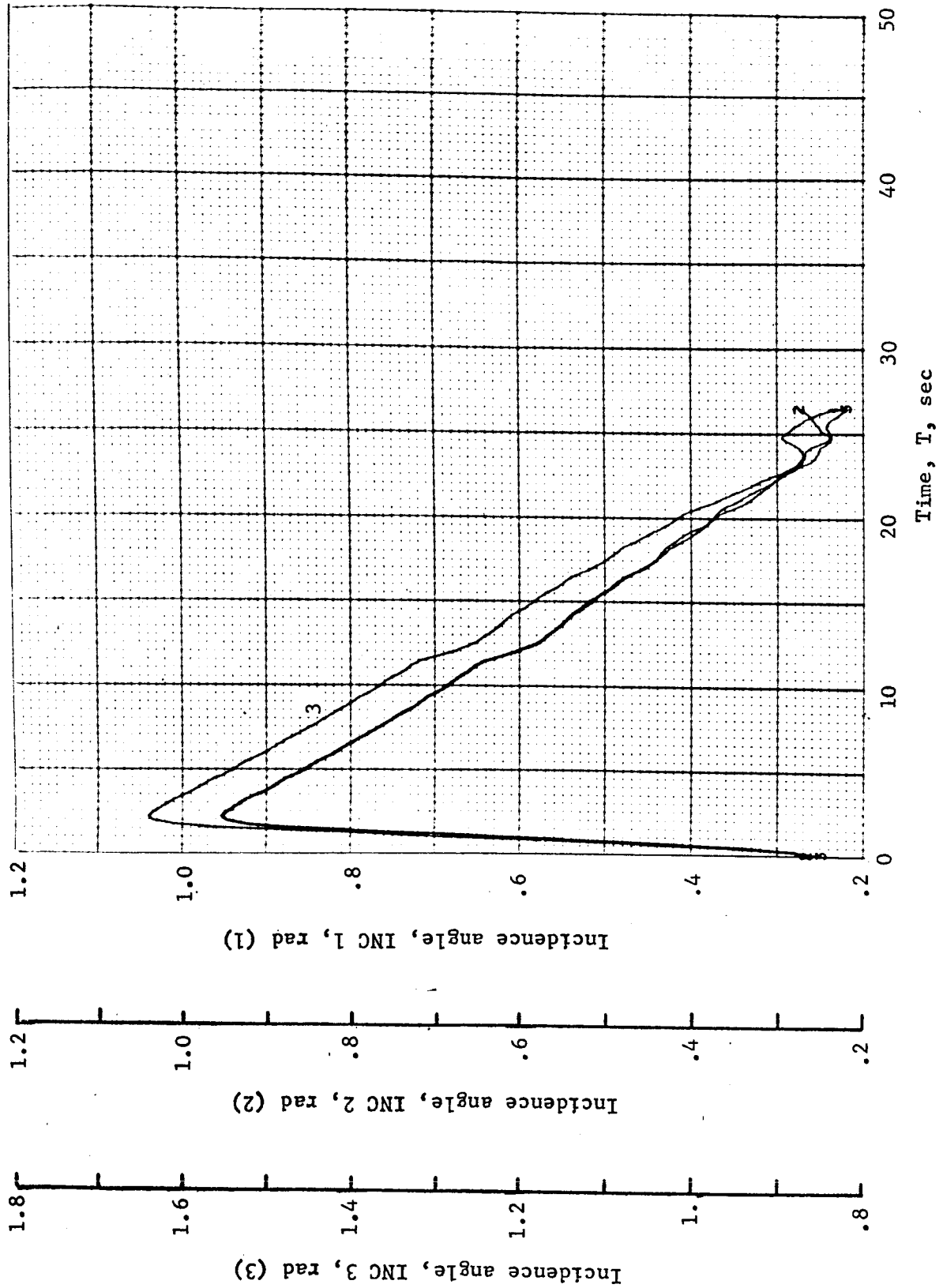


Figure B165.- Configuration 1B, Run 14-5

APPENDIX B

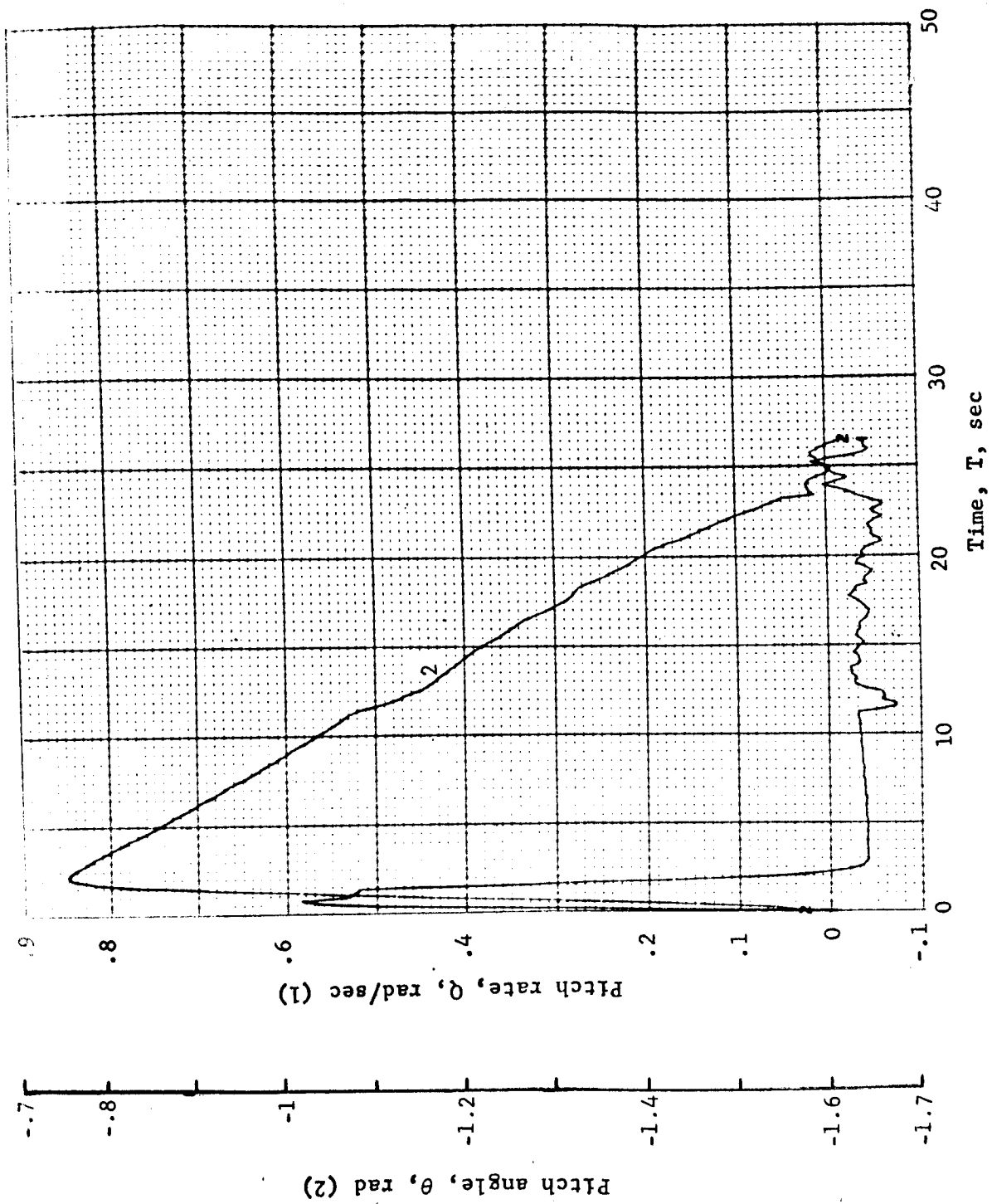


Figure B166.- Configuration 1B, Run 14-6

<p>NASA CR-66728-1, 2 and 3</p> <p>National Aeronautics and Space Administration FINAL SUMMARY REPORT, STUDY OF A SOFT LANDER/ SUPPORT MODULE FOR MARS MISSIONS, Raymond S. Wiltshire, Hugh E. Craig, et al.</p> <p>(NASA CONTRACTOR REPORT NASA CR-66728-1, 2 & 3)</p> <p>This is the final summary report of the work accomplished by Martin Marietta Corporation for the Langley Research Center under Modifica- tion 3 to Contract NAS1-7976, Study of Direct Versus Orbital Entry for Mars Missions. The objective of this study was to determine the conceptual design of an altitude stabilized soft lander capsule and to obtain solutions in the areas of communication, data handling, cost, reliability (in general sense), weight, program implementation of long lead items, and affec- tive use of existing equipment.</p>	<p>I. Wiltshire, Raymond S.; Craig, Hugh E.; et al.</p> <p>II. NASA CR-66728-1, 2 & 3</p> <p>NASA</p>
--	---

<p>NASA CR-66728-1, 2 and 3</p> <p>National Aeronautics and Space Administration FINAL SUMMARY REPORT, STUDY OF A SOFT LANDER/ SUPPORT MODULE FOR MARS MISSIONS, Raymond S. Wiltshire, Hugh E. Craig, et al.</p> <p>(NASA CONTRACTOR REPORT NASA CR-66728-1, 2 & 3)</p> <p>This is the final summary report of the work accomplished by Martin Marietta Corporation for the Langley Research Center under Modifica- tion 3 to Contract NAS1-7976, Study of Direct Versus Orbital Entry for Mars Missions. The objective of this study was to determine the conceptual design of an altitude stabilized soft lander capsule and to obtain solutions in the areas of communication, data handling, cost, reliability (in general sense), weight, program implementation of long lead items, and affec- tive use of existing equipment.</p>	<p>I. Wiltshire, Raymond S.; Craig, Hugh E.; et al.</p> <p>II. NASA CR-66728-1, 2 & 3</p> <p>NASA</p>
--	---

<p>NASA</p>	<p>This report is presented in the following three volumes;</p> <p>NASA CR-66728-1 - Volume I - Summary</p> <p>NASA CR-66728-2 - Volume II - Subsystem Studies</p> <p>NASA CR-66728-3 - Volume III - Appendixes</p>
-------------	---

<p>NASA</p>	<p>This report is presented in the following three volumes;</p> <p>NASA CR-66728-1 - Volume I - Summary</p> <p>NASA CR-66728-2 - Volume II - Subsystem Studies</p> <p>NASA CR-66728-3 - Volume III - Appendixes</p>
-------------	---